

A troubled debut for the world's  
first malaria vaccine p. 1062

Ocean floor observations with  
fiber optics pp. 1076 & 1103

Lactose fuels *Enterococcus* growth  
in GVHD patients pp. 1077 & 1143

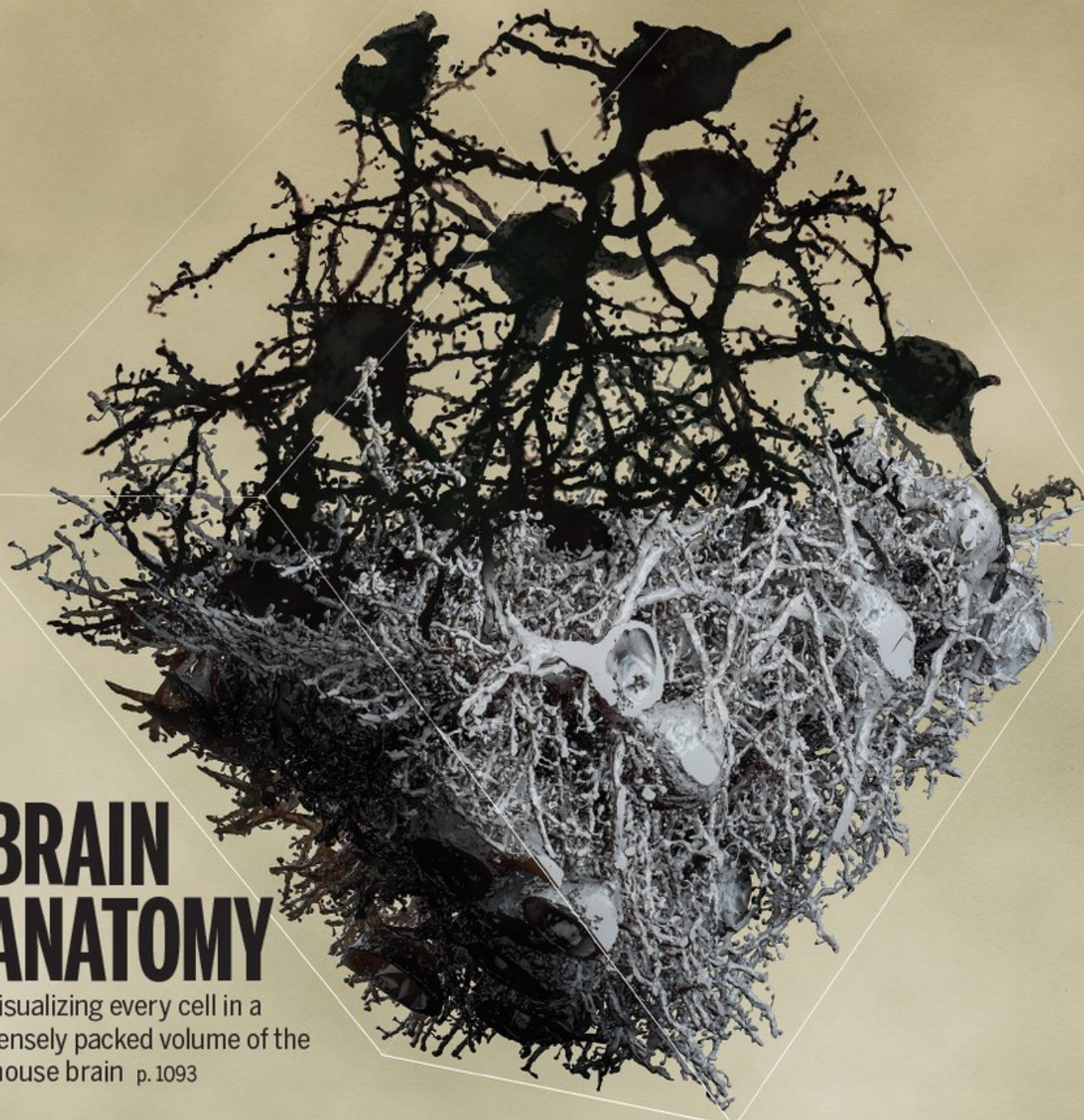
# Science

\$15  
29 NOVEMBER 2019  
[sciencemag.org](http://sciencemag.org)

AAAS

## BRAIN ANATOMY

Visualizing every cell in a  
densely packed volume of the  
mouse brain p. 1093





# CONTENTS

29 NOVEMBER 2019 • VOLUME 366 • ISSUE 6469



1062

In Malawi, a baby has received a new malaria vaccine.

## NEWS

### IN BRIEF

**1054** News at a glance

### IN DEPTH

**1056** **Bacteria-armed mosquitoes make dent in dengue**

Field trials suggest spreading *Wolbachia* could reduce cases of debilitating viruses  
*By K. Servick*

**1057** **Universities move to stop passing the harasser**

Changes in hiring practices ask job candidates to allow employers to disclose findings  
*By J. Mervis*

**1058** **U.K. parties stake out science stances in 'Brexit election'**

Contenders' Brexit policies are starkly different  
*By E. Stokstad*

**1059** **Questions churn about vaping's long-term risks**

Studies in people and animals explore potential chronic harms to the heart and lungs  
*By J. Couzin-Frankel*

**1060** **Top Chinese scientist faces questions about publications**

Case seen as a test of China's efforts to improve research integrity and crack down on scientific misconduct  
*By D. Normile*

**1061** **European Mars rover in a 'race against time' to fix parachutes**

ExoMars team looks to NASA for help after unexplained parachute tears  
*By D. Clery*

### FEATURES

**1062** **A shot of hope**

The first malaria vaccine is finally being rolled out—despite limited efficacy and nagging safety concerns  
*By J. de Vrieze*

## INSIGHTS

### POLICY FORUM

**1066** **Cyber risk research impeded by disciplinary barriers**

Security progress requires cross-disciplinary collaboration  
*By G. Falco et al.*

### PERSPECTIVES

**1070** **A chemical path to quantum information**

Nanoscale graphene can be designed to function as a molecular qubit  
*By S. von Kugelgen and D. E. Freedman*  
REPORT p. 1107

**1071** **Regulation of negative emotional behavior**

A lower-brainstem structure regulates a psychobehavioral state for avoidance behavior  
*By S. Ikemoto*  
RESEARCH ARTICLE p. 1094

**1072** **An unexpected cofactor**

A mystery of bacterial chromosome segregation is explained by a nucleotide cofactor  
*By B. E. Funnell*  
REPORT p. 1129

**1074** **Immunology taught by vaccines**

Systems analysis of vaccine responses reveals the impact of the microbiota on human immunity  
*By B. Pulendran*

**1076** **Illuminating Earth's faults**

Submarine fiber-optic cables drive discovery of fault locations and ocean dynamics  
*By P. Jousset*  
REPORT p. 1103

**1077** **Immunostimulatory gut bacteria**

Some bacterial species stimulate inflammation, autoimmunity, and anticancer immunity  
*By L. Zitvogel and G. Kroemer*  
REPORT p. 1143

**1078** **Surface nanopatterning with polymer brushes**

A variety of surfaces are patterned with precisely defined cylindrical micelles  
*By A. Presa Soto*  
REPORT p. 1095

### BOOKS ET AL.

**1080** **The pursuit of Earth's waters**

A historian shares stories of six scientists who laid foundations for modern climate science  
*By L. Barnett*

**1081** **Arbiters of truth, then and now**

A 40-year-old tome's prescient observations about scientific fact-making resonate today  
*By J. Swift*

### LETTERS

**1082** **Fires scorching Bolivia's Chiquitano forest**

*By A. Romero-Muñoz et al.*



## 1082 Misguided approach to dengue vaccine risk

By A. Wilder-Smith et al.

## 1083 Need for mountain weather stations climbs

By D. S. Hik and S. N. Williamson

## 1083 Technical Comment abstracts

# RESEARCH

### IN BRIEF

**1090** From *Science* and other journals

### RESEARCH ARTICLES

#### 1093 Neuroscience

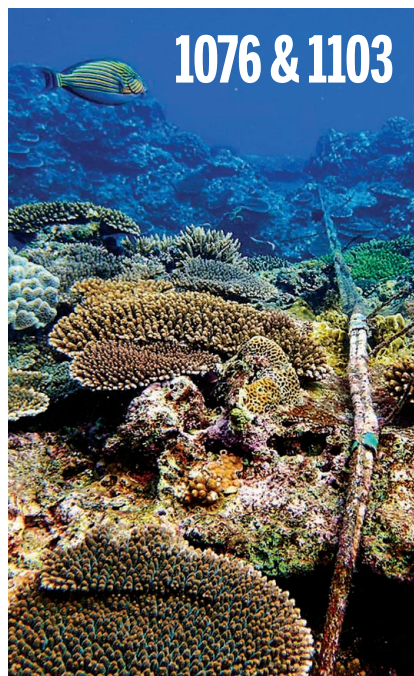
Dense connectomic reconstruction in layer 4 of the somatosensory cortex  
*A. Motta et al.*

RESEARCH ARTICLE SUMMARY; FOR FULL TEXT:  
DX.DOI.ORG/10.1126/SCIENCE.AAY3134

#### 1094 Neuroscience

Median raphe controls acquisition of negative experience in the mouse  
*A. Szőnyi et al.*

RESEARCH ARTICLE SUMMARY; FOR FULL TEXT:  
DX.DOI.ORG/10.1126/SCIENCE.AAY8746  
PERSPECTIVE p. 1071



### REPORTS

#### 1095 Materials science

Tailored multifunctional micellar brushes via crystallization-driven growth from a surface  
*J. Cai et al.*

PERSPECTIVE p. 1078

#### 1099 Superconductivity

Incoherent strange metal sharply bounded by a critical doping in Bi2212  
*S.-D. Chen et al.*

#### 1103 Seismology

Illuminating seafloor faults and ocean dynamics with dark fiber distributed acoustic sensing  
*N. J. Lindsey et al.*

PERSPECTIVE p. 1076; PODCAST

#### 1107 Quantum materials

Quantum units from the topological engineering of molecular grapheneoids  
*F. Lombardi et al.*

PERSPECTIVE p. 1070

#### 1111 Chemical physics

Direct observation of bimolecular reactions of ultracold KRb molecules  
*M.-G. Hu et al.*

#### 1116 Elastocalorics

Fatigue-resistant high-performance elastocaloric materials made by additive manufacturing  
*H. Hou et al.*

#### Magnonics

**1121** Mutual control of coherent spin waves and magnetic domain walls in a magnonic device  
*J. Han et al.*

**1125** Magnetization switching by magnon-mediated spin torque through an antiferromagnetic insulator  
*Y. Wang et al.*

#### 1129 Biochemistry

Self-organization of *parS* centromeres by the ParB CTP hydrolase  
*Y.-M. Soh et al.*

PERSPECTIVE p. 1072

#### 1134 Enhancer genomics

Brain cell type-specific enhancer-promoter interactome maps and disease-risk association  
*A. Nott et al.*

#### 1139 Molecular biology

Comprehensive AAV capsid fitness landscape reveals a viral gene and enables machine-guided design  
*P. J. Ogden et al.*

#### 1143 Microbiome

Lactose drives *Enterococcus* expansion to promote graft-versus-host disease  
*C. K. Stein-Thoeringer et al.*

PERSPECTIVE p. 1077

#### 1150 Protein folding

Watching helical membrane proteins fold reveals a common N-to-C-terminal folding pathway  
*H.-K. Choi et al.*

### DEPARTMENTS

#### 1053 Editorial

An even bigger climate problem  
*By Carolina Schmidt*

#### 1162 Working Life

Giving thanks in China  
*By Barbara Gastel*

### ON THE COVER



Nerve cells from the mouse brain, densely reconstructed in this volume. For a century, neuron reconstruction in the cerebral cortex showed only ~1 in 1000 nerve cells (black); now researchers can use

3D electron microscopy and AI-based image analysis to reconstruct all of them (gray). The connectivity matrix between thousands of axons and dendrites can be measured, yielding insights about the formational patterns of brain circuits and possible imprints of learning in the neuronal network. See page 1093. *Image: V. Altounian/Science; Data: A. Motta et al., Science 366 eaay3134 (2019)*

Science Staff .....	1052
AAAS News & Notes .....	1084
New Products .....	1157
Science Careers .....	1158

SCIENCE (ISSN 0036-8075) is published weekly on Friday, except last week in December, by the American Association for the Advancement of Science, 1200 New York Avenue, NW, Washington, DC 20005. Periodicals mail postage (publication No. 484460) paid at Washington, DC, and additional mailing offices. Copyright © 2019 by the American Association for the Advancement of Science. The title SCIENCE is a registered trademark of the AAAS. Domestic individual membership, including subscription (12 months): \$165 (\$74 allocated to subscription). Domestic institutional subscription (51 issues): \$1971; Foreign postage extra: Mexico, Caribbean (surface mail) \$55; other countries (air assist delivery): \$98. First class, airmail, student, and emeritus rates on request. Canadian rates with GST available upon request. GST #R123074622. Publications Mail Agreement Number 1069624. Printed in the U.S.A. Change of address: Allow 4 weeks, giving old and new addresses and 8-digit account number. Postmaster: Send change of address to AAAS, P.O. Box 96178, Washington, DC 20090-6178. Single-copy sales: \$15 each plus shipping and handling; bulk rate on request. Authorization to reproduce material for internal or personal use under circumstances not falling within the fair use provisions of the Copyright Act can be obtained through the Copyright Clearance Center (CCC), www.copyright.com. The identification code for Science is 0036-8075. Science is indexed in the Reader's Guide to Periodical Literature and in several specialized indexes.



Editor-in-Chief Holden Thorp, hthorp@aaas.org

Executive Editor Monica M. Bradford

Editors, Research Valda Vinson, Jake S. Yeston Editor, Insights Lisa D. Chong

**DEPUTY EDITORS** Julia Fahrenkamp-Uppenbrink (UK), Stella M. Hurlley (UK), Phillip D. Szuromi, Sacha Vignieri **SR. EDITORIAL FELLOW** Andrew M. Sugden (UK) **SR. EDITORS** Gemma Alderton (UK), Caroline Ash (UK), Brent Grocholski, Pamela J. Hines, Paula A. Kiberstis, Marc S. Lavine (Canada), Steve Mao, Ian S. Osborne (UK), Beverly A. Purnell, L. Bryan Ray, H. Jesse Smith, Jelena Stajic, Peter Stern (UK), Valerie B. Thompson, Brad Wible, Laura M. Zahn **ASSOCIATE EDITORS** Michael A. Funk, Priscilla N. Kelly, Tage S. Rai, Seth Thomas Scanlon (UK), Keith T. Smith (UK), Yury V. Suleymanov **LETTERS EDITOR** Jennifer Sills **LEAD CONTENT PRODUCTION EDITORS** Harry Jach, Lauren Kmec **CONTENT PRODUCTION EDITORS** Amelia Beyna, Jeffrey E. Cook, Chris Filatreau, Julia Katris, Nida Masiulis, Suzanne M. White **SR. EDITORIAL COORDINATORS** Carolyn Kyle, Beverly Shields **EDITORIAL COORDINATORS** Aneera Dobbins, Joi S. Granger, Jeffrey Hearn, Lisa Johnson, Maryrose Madrid, Ope Martins, Shannon McMahon, Jerry Richardson, Alana Warnke, Alice Whaley (UK), Anita Wynn **PUBLICATIONS ASSISTANTS** Jeremy Dow, Alexander Kief, Ronnel Navas, Hilary Stewart (UK), Brian White **EXECUTIVE ASSISTANT** Jessica Slater **ASI DIRECTOR, OPERATIONS** Janet Clements (UK) **ASI SR. OFFICE ADMINISTRATOR** Jessica Waldoock (UK)

News Editor Tim Appenzeller

**NEWS MANAGING EDITOR** John Travis **INTERNATIONAL EDITOR** Martin Enserink **DEPUTY NEWS EDITORS** Elizabeth Culotta, Lila Guterman, David Grimm, Eric Hand (Europe), David Malakoff **SR. CORRESPONDENTS** Daniel Clerly (UK), Jon Cohen, Jeffrey Mervis, Elizabeth Pennisi **ASSOCIATE EDITORS** Jeffrey Brinard, Catherine Maticic **NEWS REPORTERS** Adrian Cho, Jennifer Couzin-Frankel, Jocelyn Kaiser, Kelly Servick, Robert F. Service, Erik Stokstad (Cambridge, UK), Paul Voosen, Meredith Wadman **INTERMEDIATE FOX CONTRIBUTING CORRESPONDENTS** Warren Cornwall, Ann Gibbons, Mara Hvistendahl, Sam Kean, Eli Kintisch, Kai Kupferschmidt (Berlin), Andrew Lawler, Mitch Leslie, Eliot Marshall, Virginia Morell, Dennis Normile (Shanghai), Elisabeth Pain (Careers), Charles Piller, Michael Price, Tania Rabesandratana (Barcelona), Emily Underwood, Gretchen Vogel (Berlin), Lizzie Wade (Mexico City) **CAREERS** Donisha Adams, Rachel Bernstein (Editor), Katie Langin **COPY EDITORS** Julia Cole (Senior Copy Editor), Cyra Master (Copy Chief) **ADMINISTRATIVE SUPPORT** Meagan Weiland

Creative Director Beth Rakouskas

**DESIGN MANAGING EDITOR** Marcy Atard **GRAPHICS MANAGING EDITOR** Alberto Cuadra **PHOTOGRAPHY MANAGING EDITOR** William Douthitt **WEB CONTENT STRATEGY MANAGER** Kara Estelle-Powers **SENIOR DESIGNER** Chrystal Smith **DESIGNER** Christina Aycock **GRAPHICS EDITOR** Nirja Desai **INTERACTIVE GRAPHICS EDITOR** Xing Liu **SENIOR SCIENTIFIC ILLUSTRATORS** Valerie Altounian, Chris Bickel **SCIENTIFIC ILLUSTRATOR** Alice Kitterman **SENIOR GRAPHICS SPECIALISTS** Holly Bishop, Nathalie Cary **SENIOR PHOTO EDITOR** Emily Petersen

## Interim Chief Executive Officer and Executive Publisher Alan Leshner

Publisher, Science Family of Journals Bill Moran

**DIRECTOR, BUSINESS SYSTEMS AND FINANCIAL ANALYSIS** Randy Yi **DIRECTOR, BUSINESS OPERATIONS & ANALYSIS** Eric Knott **DIRECTOR OF ANALYTICS** Enrique Gonzales **MANAGER, BUSINESS OPERATIONS** Jessica Tierney **SENIOR BUSINESS ANALYST** Cory Lipman, Meron Kebede **FINANCIAL ANALYST** Alexander Lee **ADVERTISING SYSTEM ADMINISTRATOR** Tina Burks **SENIOR SALES COORDINATOR** Shirley Young **DIGITAL/PRINT STRATEGY MANAGER** Jason Hillman **QUALITY TECHNICAL MANAGER** Marcus Spiegler **ASSISTANT MANAGER DIGITAL/PRINT** Rebecca Doshi **SENIOR CONTENT SPECIALISTS** Steve Forrester, Jacob Hedrick, Antoinette Hodal, Lori Murphy **DIGITAL PRODUCTION MANAGER** Lisa Stanford **CONTENT SPECIALIST** Kimberley Oster **ADVERTISING PRODUCTION OPERATIONS MANAGER** Deborah Tompkins **DESIGNER, CUSTOM PUBLISHING** Jeremy Huntsinger **SR. TRAFFIC ASSOCIATE** Christine Hall **SPECIAL PROJECTS ASSOCIATE** Sarah Dhere **ASSOCIATE DIRECTOR, BUSINESS DEVELOPMENT** Justin Sawyers **GLOBAL MARKETING MANAGER** Allison Pritchard **DIGITAL MARKETING MANAGER** Aimee Aponte **MARKETING MANAGER** Shawana Arnold **MARKETING ASSOCIATES** Tori Velasquez, Mike Romano, Ashley Hylton **DIGITAL MARKETING SPECIALIST** Asleigh Rojanavongse **SENIOR DESIGNER** Kim Huynh **TRADE SHOW AND MEETINGS ASSOCIATE** Andrew Clamp

**DIRECTOR AND SENIOR EDITOR, CUSTOM PUBLISHING** Sean Sanders **ASSISTANT EDITOR, CUSTOM PUBLISHING** Jackie Oberst

**DIRECTOR, PRODUCT & PUBLISHING DEVELOPMENT** Chris Reid **DIRECTOR, BUSINESS STRATEGY AND PORTFOLIO MANAGEMENT** Sarah Whalen **ASSOCIATE DIRECTOR, PRODUCT MANAGEMENT** Kris Bishop **ASSOCIATE DIRECTOR, PRODUCT DEVELOPMENT AND SPJ** Hannah Heckner **SR. PRODUCT ASSOCIATE** Robert Koepke **DIGITAL PRODUCT STRATEGIST** Michael Hardesty **SPJ ASSOCIATE** Samantha Bruno Fuller

**DIRECTOR, INSTITUTIONAL LICENSING** Iquo Edim **ASSOCIATE DIRECTOR, RESEARCH & DEVELOPMENT** Elisabeth Leonard **MARKETING MANAGER** Kess Knight **SENIOR INSTITUTIONAL LICENSING MANAGER** Ryan Rexroth **INSTITUTIONAL LICENSING MANAGER** Marco Castellani **MANAGER, SYSTEMS AND OPERATIONS** Brian Holiahn **MANAGER, AGENT RELATIONS & CUSTOMER SUCCESS** Judy Lillibridge **SENIOR OPERATIONS ANALYST** Lana Guo **FULFILLMENT COORDINATOR** Melody Stringer

**DIRECTOR, GLOBAL SALES** Tracy Holmes **US EAST COAST AND MID WEST SALES** Stephanie O'Connor, Glen Cox **US WEST COAST SALES** Lynne Stickrod **US SALES MANAGER, SCIENCE CAREERS** Claudia Paulsen-Young **US SALES REP, SCIENCE CAREERS** Tracy Anderson **ASSOCIATE DIRECTOR, ROW** Roger Gonçalves **SALES REP, ROW** Sarah Lelarge **SALES ADMIN ASSISTANT, ROW** Bryony Cousins **DIRECTOR OF GLOBAL COLLABORATION AND ACADEMIC PUBLISHING RELATIONS**, ASIA Xiaoying Chu **ASSOCIATE DIRECTOR, INTERNATIONAL COLLABORATION** Grace Yao **SALES MANAGER** Danny Zhao **PROJECT MANAGER** Kilo Lan **ASCA CORPORATION, JAPAN** Kaoru Sasaki (Tokyo), Miyuki Tani (Osaka) **COLLABORATION/CUSTOM PUBLICATIONS/JAPAN** Adarsh Sandhu

**DIRECTOR, COPYRIGHT, LICENSING AND SPECIAL PROJECTS** Emilie David **RIGHTS AND LICENSING COORDINATOR** Jessica Adams **RIGHTS AND PERMISSIONS ASSOCIATE** Elizabeth Sandler **CONTRACTS AND LICENSING ASSOCIATE** Lili Catlett

### MAIN HEADQUARTERS

Science/AAAS  
1200 New York Ave. NW  
Washington, DC 20005

### SCIENCE INTERNATIONAL

Clarendon House  
Clarendon Road  
Cambridge, CB2 8FH, UK

### SCIENCE CHINA

Room 1004, Culture Square  
No. 59 Zhongguancun St.  
Haidian District, Beijing, 100872

### SCIENCE JAPAN

ASCA Corporation  
Sibaura TY Bldg. 4F, 1-14-5  
Shibaura Minato-ku  
Tokyo, 108-0073 Japan

### EDITORIAL

science\_editors@aaas.org

### NEWS

science\_news@aaas.org

### INFORMATION FOR AUTHORS

sciencemag.org/authors/  
science-information-authors

### REPRINTS AND PERMISSIONS

sciencemag.org/help/  
reprints-and-permissions

### MEDIA CONTACTS

scipak@aaas.org

### MULTIMEDIA CONTACTS

SciencePodcast@aaas.org  
ScienceVideo@aaas.org

### INSTITUTIONAL SALES

sciencemag.org/librarian

### PRODUCT ADVERTISING

**& CUSTOM PUBLISHING**  
advertising.sciencemag.org/  
products-services

science\_advertising@aaas.org

### CLASSIFIED ADVERTISING

advertising.sciencemag.org/  
science-careers

### ADVERTISING IN SCIENCE CAREERS

advertise@sciencecareers.org

### JOB POSTING CUSTOMER SERVICE

employers.sciencecareers.org  
support@sciencecareers.org

### MEMBERSHIP AND INDIVIDUAL SUBSCRIPTIONS

sciencemag.org/subscriptions

### MEMBER BENEFITS

aaas.org/membercentral

### AAAS BOARD OF DIRECTORS

**CHAIR** Margaret A. Hamburg  
**PRESIDENT** Steven Chu  
**PRESIDENT-ELECT** Claire M. Fraser  
**TREASURER** Carolyn N. Ainslie  
**INTERIM CHIEF EXECUTIVE OFFICER**  
Alan Leshner  
**BOARD** Cynthia M. Beall  
May R. Berenbaum  
Rosina M. Bierbaum  
Ann Bostrom  
Stephen P.A. Fodor  
S. James Gates, Jr.  
Laura H. Greene  
Kaye Husbands Fealing  
Maria Klawe  
Robert B. Millard  
William D. Provine

### BOARD OF REVIEWING EDITORS (Statistics board members indicated with \$)

Adriano Aguzzi, U. Hospital Zürich  
Takuzo Aida, U. of Tokyo  
Leslie Aiello, Wenner-Gren Foundation  
Judith Allen, U. of Manchester  
Sebastian Amigorena, Institut Curie  
James Analytis, U. of California, Berkeley  
Paola Ariotti, Harvard U.  
Johan Auwerx, EPFL  
David Awschalom, U. of Chicago  
Clare Baker, U. of Cambridge  
Nenad Ban, ETH Zürich  
Franz Bauer, Pontificia Universidad Católica de Chile  
Ray H. Baughman, U. of Texas at Dallas  
Peter Bearman, Columbia U.  
Carlo Beenakker, Leiden U.  
Yasmine Belkaid, NIAID, NIH  
Philip Benfey, Duke U.  
Gabriele Bergers, VIB  
Bradley Bernstein, Mass. General Hospital  
Alessandra Biffi, Harvard Med. School  
Peer Bork, EMBL  
Chris Bowler, Ecole Normale Supérieure  
Ian Boyd, U. of St. Andrews  
Emily Brodsky, U. of California, Santa Cruz  
Ron Brookmeyer, U. of California, Los Angeles (\$) **Christian Büchel, UKE Hamburg**  
Dennis Burton, Scripps Research  
Carter Tribble Butts, U. of California, Irvine  
György Buzsáki, New York U. School of Med.  
Blanche Capel, Duke U.  
Annmarie Carlton, U. of California, Irvine  
Lars-Erik Cederman, ETH Zürich  
Nick Chater, U. of Warwick  
Zhijian Chen, UT Southwestern Med. Ctr.  
Ib Chorkendorff, Denmark TU  
James J. Collins, MIT  
Robert Cook-Deegan, Arizona State U.  
Alan Cowman, Walter & Eliza Hall Inst.  
Carolyn Coyne, U. of Pittsburgh  
Roberta Croce, VU Amsterdam  
Jeff L. Dangel, U. of North Carolina  
Tom Daniel, U. of Washington  
Chiara Darai, Caltech  
Nicolas Dauphas, U. of Chicago  
Frans de Waal, Emory U.  
Claude Desplan, New York U.  
Sandra Diaz, Universidad Nacional de Córdoba  
Hong Ding, Inst. of Physics, CAS  
Jennifer Dionne, Stanford U.  
Dennis Discher, U. of Penn.  
Jennifer A. Doudna, U. of California, Berkeley  
Bruce Dunn, U. of California, Los Angeles  
William Dunphy, Caltech  
Christopher Dye, U. of Oxford  
Todd Ehlers, U. of Tübingen  
Jennifer Elisseeff, Johns Hopkins U.  
Tim Elston, U. of North Carolina  
Andrea Encalada, U. San Francisco de Quito  
Nader Engheta, U. of Penn.  
Karen Ersche, U. of Cambridge  
Barry Everitt, U. of Cambridge  
Vanessa Ezenwa, U. of Georgia  
Michael Feuer, The George Washington U.  
Toren Finkel, U. of Pittsburgh Med. Ctr.  
Gwen Flowers, Simon Fraser U.  
Peter Fratzl, Max Planck Inst. Potsdam  
Elaine Fuchs, Rockefeller U.  
Eileen Furlong, EMBL  
Jay Gallagher, U. of Wisconsin  
Susan Gelman, U. of Michigan  
Daniel Geschwind, U. of California, Los Angeles  
Karl-Heinz Glassmeier, TU Braunschweig  
Ramon Gonzalez, U. of South Florida  
Elizabeth Grove, U. of Chicago  
Nicolas Gruber, ETH Zürich  
Kip Guy, U. of Kentucky College of Pharmacy  
Taekjip Ha, Johns Hopkins U.  
Christian Haass, Ludwig Maximilians U.  
Sharon Hammes-Schiffer, Yale U.  
Wolf-Dietrich Hardt, ETH Zürich  
Louise Harra, U. College London  
Jian He, Clemson U.  
Carl-Philipp Heisenberg, IST Austria  
Ykä Helariutta, U. of Cambridge  
Janet G. Hering, Eawag  
Hans Hilgenkamp, U. of Twente  
Kai-Uwe Hinrichs, U. of Bremen  
David Hodell, U. of Cambridge  
Lora Hooper, UT Southwestern Med. Ctr.  
Fred Hughson, Princeton U.  
Randall Hulet, Rice U.  
Auke Ijspeert, EPFL  
Akiko Iwasaki, Yale U.  
Stephen Jackson, USGS and U. of Arizona  
Kai Johnson, EPFL  
Peter Jonas, IST Austria  
Matt Kaerberlein, U. of Washington  
William Kaelin Jr., Dana-Farber Cancer Inst.  
Daniel Kammen, U. of California, Berkeley  
V. Naray Kim, Seoul Nat. U.  
Robert Kingston, Harvard Med. School  
Nancy Knowlton, Smithsonian Institution  
Etienne Koechlin, Ecole Normale Supérieure  
Alexander Kolodkin, Johns Hopkins U.

Thomas Langer, U. of Cologne  
Mitchell A. Lazar, U. of Penn.  
Ottoline Leyser, U. of Cambridge  
Wendell Lim, U. of California, San Francisco  
Marcia C. Linn, U. of California, Berkeley  
Jianguo Liu, Michigan State U.  
Luis Liz-Marzán, CIC bioMaGUNE  
Jonathan Losos, Washington U. in St. Louis  
Ke Lu, Chinese Acad. of Sciences  
Christian Lüscher, U. of Geneva  
Fabienne Mackay, U. of Melbourne  
Anne Magurran, U. of St. Andrews  
Oscar Marín, King's College London  
Charles Marshall, U. of California, Berkeley  
Christopher Marx, U. of Idaho  
Geraldine Masson, CNRS  
C. Robertson McClung, Dartmouth College  
Rodrigo Medellín, U. of Mexico  
Graham Medley, London School of Hygiene & Tropical Med.  
Jane Memmott, U. of Bristol  
Edward Mielke, U. of Cambridge, Berkeley  
Tom Misteli, NCI, NIH  
Yasushi Miyashita, U. of Tokyo  
Alison Motsinger-Reif, NC State U. (\$) **Daniel Nettle, Newcastle U.**  
Daniel Neumark, U. of California, Berkeley  
Beatriz Noheda, U. of Groningen  
Helga Nowotny, Austrian Council  
Rachel O'Reilly, U. of Warwick  
Harry Orr, U. of Minnesota  
Pilar Ossorio, U. of Wisconsin  
Andrew Oswald, U. of Warwick  
Isabella Pagano, Istituto Nazionale di Astrofisica  
Margaret Palmer, U. of Maryland  
Elizabeth Levy Paluck, Princeton U.  
Jane Parker, Max Planck Inst. Cologne  
Giovanni Parmigiani, Dana-Farber Cancer Inst. (\$) **Samuel Pfaff, Salk Inst. for Biological Studies**  
Julie Pfeiffer, UT Southwestern Med. Ctr.  
Matthieu Piel, Institut Curie  
Kathrin Plath, U. of California, Los Angeles  
Martin Plesner, Ullm U.  
Elvira Poloczanska, Alfred-Wegener-Inst.  
Julia Pongratz, Ludwig Maximilians U.  
Philippe Poulin, CNRS  
Jonathan Pritchard, Stanford U.  
David Randall, Colorado State U.  
Félix A. Rey, Institut Pasteur  
Trevor Robbins, U. of Cambridge  
Amy Rosenzweig, Northwestern U.  
Mike Ryan, U. of Texas at Austin  
Mitunori Saitou, Kyoto U.  
Shimon Sakaguchi, Osaka U.  
Miquel Salmeron, Lawrence Berkeley Nat. Lab  
Nitin Samarth, Penn. State U.  
Jürgen Sandkühn, Med. U. of Vienna  
Alexander Schier, Harvard U.  
Wolfram Schlenker, Columbia U.  
Susannah Scott, U. of California, Santa Barbara  
Rebecca Sear, London School of Hygiene & Tropical Med.  
Vladimir Shaleev, Purdue U.  
Jie Shan, Cornell U.  
Beth Shapiro, U. of California, Santa Cruz  
Jay Shendure, U. of Washington  
Brian Shiochet, U. of California, San Francisco  
Robert Siliciano, Johns Hopkins U. School of Med.  
Lucia Sivilotti, U. College London  
Alison Smith, John Innes Centre  
Richard Smith, U. of North Carolina (\$) **Mark Smyth, QIMR Berghofer**  
Pam Solts, U. of Florida  
John Speakman, U. of Aberdeen  
Tara Spire-Jones, U. of Edinburgh  
Allan C. Spradling, Carnegie Institution for Science  
V. S. Subrahmanian, U. of Maryland  
Ira Tabas, Columbia U.  
Sarah Teichmann, U. of Cambridge  
Rocio Titiunik, Princeton U.  
Shubha Tole, Tata Inst. of Fundamental Research  
Wim van der Putten, Netherlands Inst. of Ecology  
Reinhold Veugelen, KU Leuven  
Bert Vogelstein, Johns Hopkins U.  
Kathleen Vohs, U. of Minnesota  
David Wallach, Weizmann Inst. of Science  
Jane-Ling Wang, U. of California, Davis (\$) **David Waxman, Fudan U.**  
Jonathan Weissman, U. of California, San Francisco  
Chris Winkle, U. of Missouri (\$) **Terrie Williams, U. of California, Santa Cruz**  
Ian A. Wilson, Scripps Research (\$) **Yu Xie, Princeton U.**  
Jan Zaenen, Leiden U.  
Kenneth Zaret, U. of Penn. School of Med.  
Jonathan Zehr, U. of California, Santa Cruz  
Maria Zuber, MIT



# An even bigger climate problem

**H**olding a major international summit on climate change against a backdrop of civil discontent like the kind that has rocked Chile might have given the world the impression that issues like clean energy can be addressed without also confronting problems of social justice. So last month, in the midst of massive protests on cost-of-living burdens and other inequalities, Chile withdrew as the host nation of the United Nations Climate Change Conference (COP25). Instead, COP25 will convene next week in Madrid, Spain. Despite this decision, Chile's commitment to maintain its presidency of COP25 through next year hopefully signals a turning point in climate action—one that further steers Chile and the rest of the global community to recognize connections between social and climate crises, and to support climate policies that do not leave anyone behind.

This year, Chile made bold moves to limit climate change. In September, it launched a broad alliance that encourages nations, regions, cities, businesses, and investors to accelerate measures to reduce greenhouse gas emissions and reduce vulnerability to the effects of climate change. And although Chile contributes a mere 0.25% to global carbon emissions, its proposed nationally determined contribution (NDC)—the reductions in greenhouse gas emissions that are at the heart of the international Paris Agreement to limit global temperature rise—was formulated with Chile's own national agenda of reaching carbon neutrality by 2050.

Achieving a net zero carbon footprint will require one of the fastest coal shutdowns of any country because the fuel accounts for about 40% of Chile's electricity generation. The Mitigation Plan for the Energy Sector is aligned with goals set in Chile's 2050 energy strategy, which has a renewable energy generation target of at least 60% by 2035. Thanks to an Electromobility Strategy, Chile operates the largest electric urban public bus fleet in Latin America, with plans to achieve 100% electric public transport by 2050. These are examples of necessary short-term actions to limit global temperature increase to 1.5°C. In the meantime, a Climate Change Law proposal is under discussion. It is the first Latin American law that formulated a car-

bon neutrality goal in conjunction with the scientific community. It also proposes a Scientific Council and a Civil Society Council to expand input into policies and a Regional Committee on Climate Change to develop local climate action plans.

But dealing with climate change will require not only technical and practical transformations in sectors like energy and transportation, but also social transformations. Climate change amplifies social inequities. Sea level rise, droughts, heat waves, and wildfires, among other hazards, affect food, water, air, land, energy, and other securities. Some groups are affected more than others, depending on where they live and their ability to cope. What is needed are "green transitions" that support people who live in poverty and in indigenous communities with limited resources, as well as those in urban communities struck by higher energy costs and air and water pollution.

How can climate action advance a more sustainable, fairer, and united Chile? Goals, technologies, and policies surrounding climate must be discussed in the context of their impacts across the income distribution. For example, in Chile's updated NDC, a new aggressive goal to reduce up to 30% of carbon emissions by 2030 was created to address the huge pollution problem associated with cities mainly in the south. The complete coal phase-

out program was agreed upon in a roundtable where the government, private sector, local authorities, and civil representatives discussed a transition process that is sensitive to the health and employment of those affected most. And the inclusion of the water security was given priority to address a 10-year drought that has afflicted 70% of the population.

Although the civil protests in Chile contributed to the decision to hold the climate conference elsewhere, the result will hopefully send an important message: Nations cannot address development and prosperity without addressing climate change, and vice versa. Hopefully, the social crisis in Chile will be brought to bear on COP25 in Madrid and the way countries make decisions, including those related to a low-carbon and more resilient economy.

—Carolina Schmidt



**Carolina Schmidt**  
is the Minister  
of Environment of  
Chile, Santiago,  
Chile. [cschmidt@mma.gob.cl](mailto:cschmidt@mma.gob.cl)

**"Nations cannot  
address development  
and prosperity  
without addressing  
climate change,  
and vice versa."**

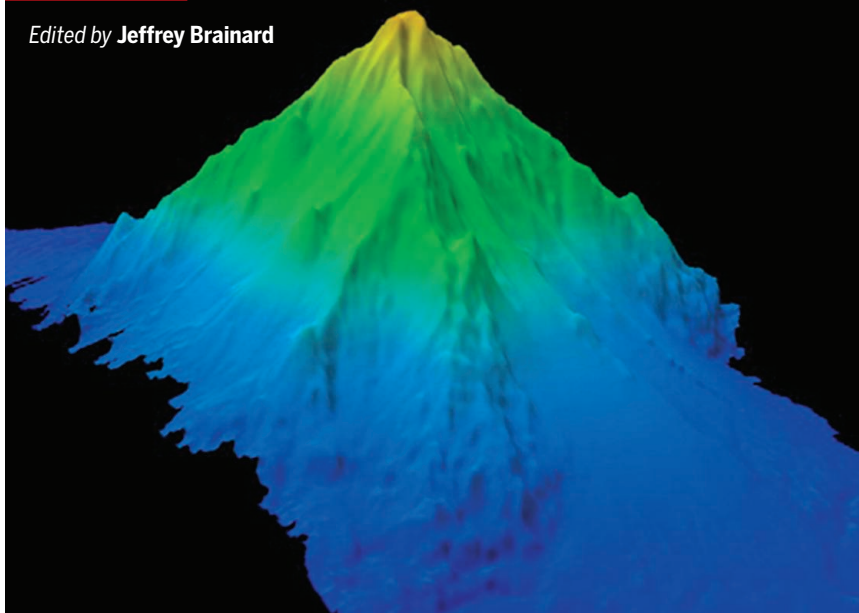


“You’d think we’d be forming ice, but there’s just too much heat left in the ocean.”

Sea ice physicist **Andy Mahoney**, in *Climatewire*, on why November sea ice in the Chukchi Sea north of the Bering Strait is the lowest on record.

## IN BRIEF

Edited by **Jeffrey Brinard**



A map of the sea floor in the Central Pacific Basin includes a 4200-meter-high peak called Kahalewai.

## OCEANOGRAPHY

### United States to survey nearby sea floor

**M**apping of the ocean floor may expand under an order signed by President Donald Trump on 19 November to create a federal plan to explore U.S. coastal waters. The announcement, which does not call for additional funding, comes amid growing international interest in charting the sea floor as unmanned aquatic drones and other new technologies promise to make the work cheaper and faster. The maps, also created by ship-towed sonar arrays, are crucial to understanding basic ocean dynamics, finding biological hot spots, and surveying mineral, oil, and gas deposits. But much of the ocean floor remains unmapped; an international campaign called Seabed 2030 aims to map all of it in detail by 2030. Such maps cover just 40% of the 11.6 million square kilometers in the U.S. exclusive economic zone, which extends 320 kilometers from the coasts of all U.S. states and territories—an area larger than the total U.S. land mass. Today, those maps are a hodgepodge drawn from government, industry, and academic research, says Vicki Ferrini, a marine geophysicist at Columbia University’s Lamont-Doherty Earth Observatory in Palisades, New York. The federal plan, she says, could be a “game changer.”

### Iran sentences conservationists

**STATE SECURITY** | When Iran this summer eased conditions for eight conservationists jailed on espionage charges, allowing more frequent family visits and time outdoors, observers hoped it was a sign of leniency. Those hopes were dashed on 20 November, when six of the detainees were sentenced to 6 to 10 years in prison. (The other two apparently are awaiting sentencing.) Iran’s Islamic Revolutionary Guard Corps had accused the group—all with the Persian Wildlife Heritage Foundation, a nonprofit in Tehran—of using wildlife camera traps to spy on military installations and jailed them in early 2018. The arrests sparked an international outcry. Calling their detainment a “real tragedy,” famed primatologist Jane Goodall last month implored Iran’s leaders to show compassion. Hopes now rest on a long shot: that Iran’s supreme leader, Ayatollah Ali Khamenei, will pardon them.

### Compromise on 5G noise

**METEOROLOGY** | Delegates at an international conference last week approved a standard for electronic noise from a radio band used for 5G, the next generation of wireless communications, that meteorologists say will interfere with weather forecasting. The decision at the United Nations’s World Radiocommunication Conference in Sharm El Sheikh, Egypt, restricts the noise to –33 decibel watts (dBW) outside of the 24-gigahertz communications band. After 8 years, the limit would be tightened to –39 dBW. That’s less stringent than the –55 dBW sought by the World Meteorological Organization to avoid conflicts with the neighboring frequency used by satellites to collect crucial data about humidity. But it’s a tighter limit than the –20 dBW backed by the U.S. Federal Communications Commission, a proposal that triggered months of debate with scientists (*Science*, 9 August, p. 528).

### NOAA nominee withdraws

**LEADERSHIP** | Barry Myers, the controversial nominee to lead the National Oceanic and Atmospheric Administration (NOAA), withdrew from consideration last week,



citing health concerns. Myers, longtime CEO of private weather forecaster AccuWeather, had seen his nomination languish in the Senate for 2 years. Critics faulted his lack of a science background and continued family ties to AccuWeather, founded by his older brother. Before President Donald Trump nominated Myers, the firm had lobbied to restrict forecasts put out by NOAA's National Weather Service that might compete with those from commercial providers. After his nomination, Myers resigned from AccuWeather and divested himself of ownership shares in the company. NOAA's acting head is Neil Jacobs, an atmospheric scientist and its chief of environmental observation and prediction.

## Psychology groups tackle climate

**SCIENTIFIC SOCIETIES** | Psychological associations from more than 40 nations agreed this month to apply their discipline to help advance efforts to combat the effects of climate change. The groups agreed to study effective ways to communicate with the public, policymakers, and other scientists about the problem and promote environmentally friendly behaviors, for example. At the inaugural International Summit on Psychology and Global Health in Lisbon, the groups approved a proclamation supporting the effort and vowed to support a U.N. sustainable development goal of helping countries create climate adaptation strategies and low-carbon development programs.

## A mobile response to disease

**INFECTIOUS DISEASE** | Frustrated by a lack of well-equipped laboratories in developing countries with disease outbreaks, medical researchers have come up with a solution on wheels: a mobile biosafety level 3 lab that can be transported by cargo plane. The need for such a vehicle, showcased last week at the annual meeting of the American Society for Tropical Medicine and Hygiene



A new biosafety lab on wheels could improve research in developing countries on disease outbreaks.



**IN FOCUS** A koi fish hovering over lotus petals won a first prize in the American Society for Microbiology's annual Agar Art Contest. Contestants paint living microbes on agar, a gelatinlike culture medium, under safe conditions. Artist Arwa Hadid colored the petals using *Escherichia coli*, a common gut bacterium, and the water with *Enterococcus faecalis*, which causes urinary tract infections.

near Washington, D.C., became obvious during the West African Ebola epidemic of 2013–16, when diagnosis and research suffered long delays, says Calum Semple, a clinical virologist at the University of Liverpool in the United Kingdom. He and other scientists formed a new company, Integrum Scientific, to build the mobile lab. It boasts a glove box for handling dangerous pathogens, almost 10 meters of lab benches, a  $-80^{\circ}\text{C}$  freezer, and two generators. Semple admits the lab hardly helps developing countries build up their research capacity—a top priority in the global health community—but it will help save lives, he says.

## Prevention studies questioned

**BIOMEDICINE** | Only about one-fourth of prevention research recently funded by the U.S. National Institutes of Health examined the top 10 causes of death in the United States, an analysis by NIH researchers has found. The study, published on 8 November in *JAMA Network Open*, looked at a random sample of more than 11,000 such research projects funded between 2012 and 2017. Only 26% focused on measuring one of the top 10 killers

of Americans—such as heart disease, cancer, or accidents. The authors say “the nation may benefit” from shifting more NIH-funded prevention research toward proposals that study one or more of these causes of death and their risk factors. Prevention research accounted for 23% of NIH's spending on research projects during the study period.

## Shhh! Noise is hard on animals

**ECOLOGY** | Noise pollution from autos, planes, and a variety of human activities is affecting a wide range of animals, suggesting a need for better regulations to protect them, according to research published last week. The findings came from a large meta-analysis of more than 100 studies that measured changes in animal behaviors and hormone levels before and after exposure to noise. Effects varied across species but were not clustered in particular types, the authors wrote in *Biology Letters*. They said noise could harm bats by hampering their echolocation of prey, for example. It could also harm ecosystems by driving away some native species. Other species may benefit, if noise confuses their predators.



A World Mosquito Program staff member releases *Wolbachia* mosquitoes in Brazil.

## INFECTIOUS DISEASES

# Bacteria-armed mosquitoes make dent in dengue

Field trials suggest spreading *Wolbachia* could reduce cases of debilitating viruses

By **Kelly Servick**, in National Harbor, Maryland

In a handful of cities around the world, mosquitoes have been armed with a microscopic weapon against disease. The bacterium *Wolbachia pipientis* blocks the insects' ability to spread fearsome viruses such as dengue, Zika, and chikungunya. Since 2011, researchers have been injecting *Wolbachia* into the eggs of *Aedes aegypti* mosquitoes and releasing the hatched insects, which spread this protection to their offspring. But the field has been waiting for evidence that this approach actually reduces disease in people.

Signs that it does came last week in preliminary results from several trials in tropical areas burdened with mosquito-borne viruses such as dengue. In some release areas, studies conducted by the nonprofit World Mosquito Program (WMP) found as much as a 76% reduction in the rate of dengue, which causes fever and severe joint pain and has no specific treatment.

"The first indications are very promising," says Marcelo Jacobs-Lorena, a geneticist at Johns Hopkins University in Baltimore, Maryland, who wasn't part of the studies.

*Wolbachia* naturally inhabits many insects, though not *A. aegypti*. In mosquito cells, the bacterium can prevent viruses such as dengue from replicating—and thus from spilling into a new host when a mosquito bites. Proponents say the approach could complement traditional methods such as insecticide

sprays, which often fail to control disease. And because the bacterium spreads on its own, it could be more cost effective than population-reducing approaches such as genetic engineering, some of which require ongoing releases.

WMP researchers reported this summer that in more than 4 years after a trial release of infected mosquitoes in Townsville, Australia, only four locally acquired cases of dengue were recorded. No previous period of that length since 2001 had fewer than 69 cases.

But stronger evidence of *Wolbachia's* impact requires comparing rates of disease in release areas with those at untreated sites nearby. At the annual meeting of the American Society of Tropical Medicine and Hygiene here last week, WMP epidemiologist Katie Anders of Monash University in Melbourne, Australia, presented results from such controlled trials on opposite sides of the globe. On the outskirts of Yogyakarta, Indonesia, local health officials documented 76% fewer dengue infections in the 2.5 years after the release of *Wolbachia* mosquitoes than in a nearby control area. And one treated area in Niterói, Brazil, saw 75% fewer chikungunya cases than untreated sites. (A reduction in dengue cases was harder to evaluate because rates were generally low during the trial.)

Those results rely on public health surveillance data, which can include inaccuracies and misdiagnoses, Anders acknowledged. But, "We're still seeing a signal," she said, and seeing it across sites "is giving us confidence."

It isn't always easy to get *Wolbachia* to spread and remain in wild mosquito populations. WMP infectious disease researcher Cameron Simmons, also at Monash University, noted that levels of the bacterium unexpectedly dropped in one study area in Vietnam. Heat may have contributed; lab tests suggest *A. aegypti* larvae that develop in hotter environments harbor less *Wolbachia*.

Another team of researchers is releasing and tracking a different *Wolbachia* strain that may better resist high temperatures. Steven Sinkins, a vector biologist at the University of Glasgow in the United Kingdom, and his collaborators have been releasing infected mosquitoes in and around apartments, houses, and shopping areas in Kuala Lumpur. In a pilot study of six release sites, published last week in *Current Biology*, Sinkins's team reported a 40% reduction in dengue cases compared with similar sites with no releases.

Both teams are now conducting larger trials. In central Yogyakarta, WMP has carved out 24 randomized release and control sites. From local clinics, they will identify patients with dengue and those with other causes of fever, then compare the proportions that live in *Wolbachia*-treated and control areas. That trial is the "gold standard," says Fred Gould, an evolutionary biologist at North Carolina State University in Raleigh. If the results, expected next year, back up the preliminary evidence that *Wolbachia* reduces dengue, he says, the World Health Organization could approve this microbial ally for broader use. ■



## SCIENTIFIC WORKFORCE

# Universities move to stop passing the harasser

Changes in hiring practices ask job candidates to allow employers to disclose findings

By Jeffrey Mervis

**T**he #MeToo movement has shone a spotlight on an ugly tradition in higher education: allowing faculty members found guilty of bullying or sexual harassment to move to a new job without telling their new employer about their past conduct. The practice of “passing the harasser” is abetted by privacy and labor laws that limit how much a prospective employer can be told about a job applicant.

But major research universities are taking steps to penetrate that veil of silence. The Davis and San Diego campuses of the University of California (UC) system are conducting pilot programs that ask certain faculty candidates to waive some privacy protections, and earlier this month, the University of Illinois Board of Trustees adopted the recommendations of a faculty group to conduct a similar pilot.

Even as universities move to tackle the issue, however, a case in which the National Science Foundation (NSF) unwittingly hired an academic shortly before he was suspended for bullying highlights the lack of transparency in hiring practices. NSF didn’t learn about the harasser’s past until he had spent 18 months at the agency because the university ignored an NSF rule requiring immediate notification of any change in employment status. NSF also didn’t take advantage of a new policy at the harasser’s institution that would have given the agency access to its findings.

In July 2018, UC Davis officials started to ask finalists for tenured positions to waive privacy and allow their current employer—and sometimes previous employers—to share any past harassment findings. Such personnel records are typically kept confidential. Any candidate who doesn’t agree to the waiver is considered to have an incomplete application and is excluded from further consideration.

The new policy is having its desired effect, says Philip Kass, UC Davis’s vice provost for academic affairs. Every one of the

21 applicants investigated since the policy was implemented has come up clean, he says. His explanation is that those with a negative finding in their files don’t apply, and he’s not worried that such self-winning will limit the talent pool available to the university. “I’d rather err on the side of excluding someone with a history of harassment rather than allowing someone to sneak through,” Kass says.

Applicants with a harassment finding in their files aren’t automatically rejected, Kass adds, because it’s possible for a faculty member to learn from past mistakes. For similar reasons, he says, UC Davis only seeks records going back 8 to 10 years.

At UC San Diego (UCSD), a “false alarm” involving an allegation of past harassment by a new faculty member prompted it to

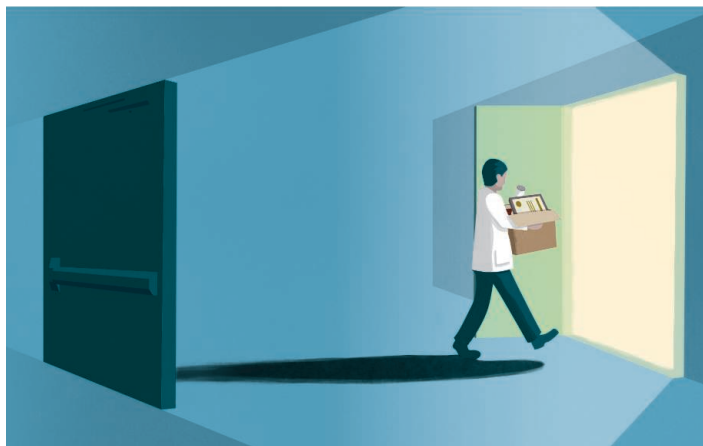
the University of Wisconsin (UW) in Madison concluded in May 2017 that engineering professor Akbar Sayeed had created a toxic environment in his laboratory through a barrage of epithets and intimidation tactics aimed at his students. The investigation was triggered by a query from the family of John Brady, a graduate student in Sayeed’s lab who committed suicide in 2016 after enduring years of such abuse.

In November 2017, UW suspended Sayeed for 2 years without pay. The month before, Sayeed had started to work at NSF’s headquarters in Alexandria, Virginia, as a temporary “rotator” overseeing grants in electrical, communications, and cyber-systems. Despite that suspension, NSF followed its normal practice of reimbursing the university for the rotator’s salary.

Under NSF rules, UW should have immediately informed the agency of Sayeed’s suspension, which would have disqualified him from serving as a rotator. (UW acknowledges it “failed to provide NSF with a timely update of his status.”) Instead, NSF didn’t learn what had happened until April, after the university gave the details to a local newspaper reporter who requested public records on all UW investigations of alleged harassment. NSF promptly terminated Sayeed, and has since reminded universities of the reporting rule.

Jim Brady, John Brady’s father, wonders why Sayeed was allowed to go to NSF. “Obviously, [UW] couldn’t prevent him from finding work during his leave,” says Jim Brady, a Ph.D. chemist who works in industry. But, he says, “The timeline should make anyone queasy. ... Something is awry and needs a bit of attention.”

Ironically, last year the UW system adopted a first-in-the-nation policy requiring all of its institutions to share findings of harassment with any employer that asks. But it doesn’t require the university to be proactive in passing along troubling information. And NSF never asked. Rotators undergo the same criminal background check given to any other federal job applicant, according to NSF, but are not asked about any findings of harassment. ■



launch a similar pilot this summer, says Robert Continetti, UCSD’s senior associate vice chancellor for academic affairs. The policy applies only to tenured positions, Continetti says, because although it is relatively easy to oust an untenured professor found guilty of misdeeds, “it’s a laborious process to remove someone with tenure.”

In Illinois, university trustees this month adopted a faculty report that recommends several steps for combatting sexual misconduct. One would reverse the university’s current policy of not publicly sharing harassment findings, a practice that it says “can lead to poor hiring decisions.” The report also recommends that university officials stop signing nondisclosure agreements related to such incidents.

The NSF episode began after officials at



U.K. Prime Minister Boris Johnson is calling for research funding boosts and a speedy Brexit.

## EUROPE

# U.K. parties stake out science stances in 'Brexit election'

Contenders' Brexit policies are starkly different

By Erik Stokstad

**"G**et Brexit done." "Stop Brexit." "Give people the final say." The campaign slogans of the Conservative, Liberal Democrat, and Labour parties, respectively, betray the biggest issue in a momentous U.K. election on 12 December. When representatives of each party took to a stage last week at the Royal Society in London, they all promised increased funding and easier immigration for scientists. But Brexit loomed over the discussion, says Sarah Main, director of the Campaign for Science and Engineering, an advocacy group in London. "There are huge implications."

For many scientists, the promised benefits would do little to lessen the pain of Brexit. At stake is the roughly £1.5 billion that U.K. researchers win each year from the European Union, more than the U.K. puts into those EU programs. Even now, the mere prospect of Brexit seems to be taking a toll on U.K. research. For example, winners of European fellowships are now less likely to come—and bring their money—to U.K. institutions than they were a few years ago (*Science*, 4 October, p. 24).

Conservative Prime Minister Boris Johnson called for the election to break gridlock over Brexit. The United Kingdom's departure from the European Union, kicked off by a 2016 referendum and now set for 31 January 2020, has been put off twice al-

ready. Johnson has been unable to get Parliament to approve a divorce agreement, and crashing out of the European Union without a deal could cause a recession.

Johnson and the Conservatives want a quick approval for their plan. "I think we need to move on to bigger issues," Stephen Metcalfe, a Conservative member of Parliament (MP) and a member of the House of Commons Science and Technology Committee, said at the Royal Society event. The opposition Labour Party says it will negotiate a better deal with the European Union and then put it to the people in another referendum. The Liberal Democrats, running third in national polls, want to cancel Brexit.

If Brexit happens, the parties all say they would try to reach a science deal with the European Union and pay to participate in its funding programs. They also want to reform immigration for scientists, both to minimize the red tape and fees that EU scientists will face after Brexit and to bring in talent from other parts of the world. Johnson wants to eliminate caps on visas for top researchers and make it easier for universities to sponsor them. At the Royal Society event, Labour and Liberal Democrats said they would make improvements as well. "It's clear the entire system needs reform because it's not working," said Chi Onwurah, a Labour MP and party spokesperson for science and innovation.

Research funding was another point of agreement. The Conservatives started to

boost the budget in 2016, and in 2017 announced a 10-year goal of reaching a national R&D investment of 2.4% of gross domestic product, the average figure among economically developed countries, up from 1.7%. The other parties have pledged to maintain that momentum. "There is a startling degree of consensus across the three main parties," says James Wilsdon, a science policy expert at the University of Sheffield.

A closer look suggests the parties might deploy this money differently. Johnson said last month he wants to create a British Advanced Research Projects Agency, inspired by the U.S. military agency that helped develop the internet, with a total of £800 million over 5 years to work on bold civilian ideas. But Sam Gyimah, a Liberal Democrat MP and a former science minister before he quit the Conservative Party, pointed out that researchers are already adapting to a big new funder, UK Research and Innovation. He warned about the risk of "chopping and changing" the way government distributes research funding.

Labour has a controversial idea of its own, although it didn't get much mention at the Royal Society debate. In September, the party—which favors nationalization of railways, postal service, and utilities—called for a publicly owned drug company to make generic drugs, including versions of drugs still under patent, for the National Health Service. Any profits would support public R&D. In a statement, Richard Torbett of the Association of the British Pharmaceutical Industry in London rejected that idea. "It would send a hugely negative signal to British scientists and would discourage research."

On climate policy, all the parties vow to reduce net carbon emissions to zero and increase renewable energy, but differ on the pace. The Conservatives would aim for zero emissions in 2050, whereas the Liberal Democrats say 2045 is doable. Labour, mindful of supporters who work in oil and gas extraction and energy-intensive industries, recently stepped back from a target of 2030; its platform, released last week, focuses instead on creating jobs in renewable energy.

The election will determine how much of this is practical. Ambitious goals, such as a new funding agency or energy policy, need the approval of what has been a paralyzed Parliament. That inaction might continue if the next ruling party fails to get a significant majority. The parties have so far ruled out forming a coalition government. The end result could be more of the same: an impasse on the issue most important to the country, and to science. ■



## BIOMEDICINE

# Questions churn about vaping's long-term risks

Studies in people and animals explore potential chronic harms to the heart and lungs

By Jennifer Couzin-Frankel

**R**eports of lung injuries from e-cigarettes splash across the news these days, but the nicotine-delivery devices are also spawning a quieter worry: whether users risk long-term health effects that may not manifest for decades. Studies in animals and people are now starting to probe whether e-cigarettes pose chronic risks to the lungs and cardiovascular system and how the chemicals they contain might disrupt healthy biology.

E-cigarettes are battery-powered devices containing nicotine and other substances, such as solvents that dissolve the nicotine and flavorings that enhance their appeal. Heat converts the mix into an aerosol that users inhale. Manufacturers tout e-cigarettes as tools to help smokers quit, although data are mixed. But one thing is clear: Millions of young people who didn't smoke cigarettes have taken up vaping. And given that e-cigarettes vary more than conventional cigarettes in their chemical composition, "We're asking medical science to do a huge, heavy lift" to pinpoint health impacts across people, says James Stein, a preventive cardiologist at the University of Wisconsin in Madison.

He and others believe they have no choice but to try. This month, the National Heart, Lung, and Blood Institute gave a boost to studies of acute and chronic effects when it announced supplemental funds for ongoing

e-cigarette research, on which the institute will spend \$23 million this year.

E-cigarettes have been around in some form for decades but began to soar in popularity about 5 years ago, thanks to thousands of flavoring options and new delivery methods that more closely mimic smoking. Today, about 13 million people in the United States use them, as do millions more worldwide. In March, one hazard emerged when acute lung injuries began to strike; U.S. cases now approach 2300, with 47 deaths. "We were all taken by surprise" by those lung injuries, says Peter Shields, a medical oncologist who specializes in lung cancer at Ohio State University's Comprehensive Cancer Center in Columbus. They look unlike anything seen in cigarette smokers. Health officials now suspect the injuries are linked to a vitamin E oil added to e-cigarettes containing tetrahydrocannabinol, better known as THC.

Animal studies are already yielding clues about longer term effects of e-cigarette use. In September, a paper in *The Journal of Clinical Investigation* described mice exposed to e-cigarettes for 4 months, nearly one-quarter of their life span. Farrah Kheradmand, a pulmonologist at Baylor College of Medicine in Houston, Texas, who led the work, says that, at first, "There was absolutely no emphysema, nothing" in the animals that inhaled aerosol from e-cigarettes. That finding jibes with earlier research showing combustion

products are the cause of airway inflammation in smokers.

Then Kheradmand's graduate student Matthew Madison showed her slides of the animals' lung tissue. She did a double take. Immune cells called macrophages were swollen with fat, an abnormality. Kheradmand guessed at first that the cells had gorged on vegetable glycerin, which is used as a solvent in vaping liquids. But when the scientists cracked open the macrophages, they found they were mistaken. "I couldn't sleep at night," Kheradmand says. "Where is this fat coming from?"

Further experiments revealed a likely explanation. Macrophages protect the body from infections, but they also help recycle lung surfactant, a mix of proteins and lipids that coats the inside of lung air sacs and aids gas exchange. Vegetable glycerin and another solvent in e-cigarettes, propylene glycol, are "capable of not only dissolving nicotine, but dissolving anything that comes their way—including the surfactant," Kheradmand says, and her work suggests the macrophages were filled with the type of fat in surfactant. Affected mice seemed healthy, but when Kheradmand exposed them to a flu virus, those with swollen macrophages died, suggesting their ability to battle infection had weakened.

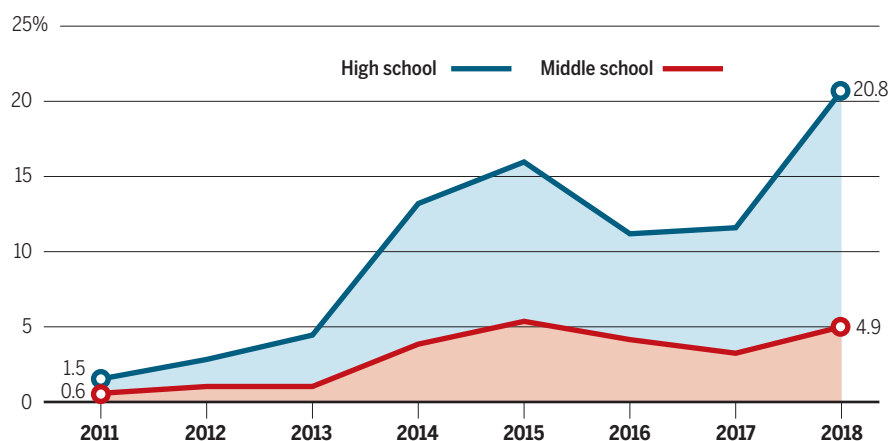
Another vexing concern is whether, like smoking, vaping can lead to cancer. Scientists believe e-cigarettes are likely to be less carcinogenic than tobacco, but last month, a team from New York University School of Medicine in New York City reported in the *Proceedings of the National Academy of Sciences* that mice exposed to e-cigarettes for 54 weeks had an increased risk of lung cancer and showed changes in bladder cells that presage cancer there.

No one knows whether the mouse findings will translate to people. But they reveal "some of the things we should be looking for," says Thomas Eissenberg, a psychologist who co-directs the Center for the Study of Tobacco Products at Virginia Commonwealth University in Richmond and serves as a paid consultant in litigation against the tobacco and e-cigarette industries.

Eissenberg is among those pushing for more human studies. He has applied for funding to work with colleagues who would perform bronchoscopies on healthy e-cigarette users and healthy controls.

## Youth movement

E-cigarettes have soared in popularity among young people in the United States, as shown by data on the percentage who used the products in the past 30 days.



GRAPHIC: CENTERS FOR DISEASE CONTROL AND PREVENTION MORBIDITY AND MORTALITY WEEKLY REPORT, VOL. 67, 12/6, 2015. ADAPTED BY A. CUADRA/SCIENCE

Unlike, say, the skin or the gut, which are adapted to manage outside assaults, “The lungs don’t have a powerful defense mechanism,” he says. “Once things get into the lungs, they can cause a lot of trouble.” Eissenberg wants to look for the lipid-filled macrophages Kheradmand saw in animals. And, he adds, “I’m worried about the throat and the upper airways.” Vegetable glycerin and propylene glycol can dry up tissues, and they’re being inhaled across “membranes that are trying to be kept moist,” Eissenberg says. “I wonder what the long-term effects of that aridity are going to be.”

Shields is one of few researchers who has already probed human lungs for e-cigarettes’ effects. Last month, his group published a paper in *Cancer Prevention Research* that compared 15 healthy volunteers who used e-cigarettes without nicotine for 4 weeks with 15 people who never smoked or vaped. (He did the study before concerns about acute lung injuries surfaced.) Bronchoscopies on the vaping volunteers showed minimal but measurable signs of inflammation in lung tissue and lung fluid. He is now recruiting for a larger trial of 145 people, to include smokers transitioning to e-cigarettes, as well as long-term e-cigarette users. It will look for markers of inflammation; gene expression patterns; the balance of bacteria in the lungs, mouth, and throat; and other signs of lung health and disease. “I have no idea what we’re going to see,” Shields says.

Because cigarette smoking causes cardiovascular disease, researchers wonder whether vaping has similar effects. A study this month in the *Journal of the American College of Cardiology* found some improvements in heart health among 74 smokers who switched to e-cigarettes. But both habits deliver a host of chemicals that are absorbed across the lining of the lungs. And concerns remain about nonsmokers who take up the habit, as well as smokers who try vaping to quit their habit but end up using both forms of nicotine.

Stein is now recruiting 440 volunteers, all of whom either use e-cigarettes exclusively, smoke and use e-cigarettes, or do neither. His team is gathering physiological measurements before and after vaping or smoking, including heart rate, blood pressure, artery thickness and stiffness, and aerobic function while running on a treadmill. The researchers will also collect data on the e-cigarettes themselves, to see whether different products vary in their health effects.

It was decades before science laid bare the long-term risks of cigarettes to human health. Stein and others are hoping that for e-cigarettes, that timeline will be far shorter. Right now, he says, “We have no idea what the harm is.” ■

## RESEARCH INTEGRITY

# Top Chinese scientist faces questions about publications

Case seen as a test of China’s efforts to improve research integrity and crack down on scientific misconduct

By Dennis Normile

One of China’s most prominent scientists is facing a barrage of questions about images in dozens of papers produced by laboratories he leads. The Chinese Academy of Engineering has launched an investigation of the publications, by immunologist Cao Xuetao, president of Nankai University in Tianjin, and the case is getting extensive attention in both traditional and social media.

Cao has defended the scientific validity of the papers, says he is cooperating with the review, and has promised to work with journals to correct any errors. “I most sincerely apologize for any oversight on my part,” he wrote on 17 November on PubPeer, the publications review website where researchers first raised questions about the papers.

The episode highlights long-standing concerns about China’s scientific enterprise, observers say, including whether star scientists can effectively oversee the far-flung research empires they often lead, and whether officials are making progress in stamping out chronic research misconduct.

Cao’s work came under scrutiny after microbiologist Elisabeth Bik, a consultant in San Francisco, California, who searches for doctored images in papers, noted on PubPeer that several images in a 2009 paper in *The Journal of Immunology* “look unexpectedly similar. ... Could the authors please explain what happened here?” she wrote on 14 November. “I am not accusing anyone of misconduct,” Bik subsequently tweeted. The duplications “might just be honest errors.” Other PubPeer contributors soon raised concerns about additional papers.

On 18 November, China’s engineering academy told local media that it would investigate, but provided no details.

The case has renewed discussion in China about the power wielded by elite scientists such as Cao, who simultaneously leads one of the nation’s top universities and directs

three additional laboratories or institutes in different cities. Running Nankai University likely “demands 100% of his efforts,” says Cao Cong, a science policy expert at the University of Nottingham’s campus in Ningbo, China. (He is not related to Cao Xuetao.) That means Cao Xuetao must rely on large teams of graduate students and postdocs to do the actual research, says Huang Futao, a higher education scholar at Hiroshima

University in Japan. But such high-flying scientists often “do not have sufficient time or energy to supervise” those researchers, he notes.

At least one-quarter of the retracted papers recorded by the website Retraction Watch this year were by Chinese authors, says Xiaotian Chen, a library and in-

formation scientist at Bradley University in Peoria, Illinois. The country has launched several initiatives to improve the record, and Cao Xuetao has been involved in such efforts. On 13 November, he gave a speech to some 6000 people in the Great Hall of the People in Beijing that touched on research “integrity, ethics, and morality.” The talk was streamed to universities and 800,000 students watched, according to China’s Xinhua News Agency.

“But it is hard to change the culture,” Chen says. “The cost of research misconduct is either very low or does not exist in China. Academic misconduct in the U.S. and Europe usually leads to resignation or dismissal, but that practice is not very common in China.”

How the authorities handle the Cao Xuetao review will be a test case, says Cao Cong. Over the past 2 years, key government, Communist Party, and scientific bodies have issued guidelines for research integrity and set penalties for misconduct. If Cao Xuetao is found guilty of violating those rules but no action is taken, he says, “it means that various policies to maintain the integrity of scientific research are empty talk.” ■

With reporting by Bian Huihui.





Europe's 35-meter parachute in a 2018 test in Sweden. It will be the largest ever on Mars.

## PLANETARY SCIENCE

# European Mars rover in a 'race against time' to fix parachutes

ExoMars team looks to NASA for help after unexplained parachute tears

By **Daniel Clery**

Getting a probe safely to the surface of Mars is not easy: Numerous landing attempts have ended in a crash. Sufficiently slowing a lander in the thin air requires plenty of sophisticated kit, including designer heat shields, powerful retrorockets, and, sometimes, giant airbags. But the European-Russian ExoMars mission is struggling with a piece of 18th century technology: parachutes.

High-altitude tests earlier this year revealed that ExoMars's chutes were tearing as they were pulled from their bags. The European Space Agency (ESA) has turned to NASA colleagues for help, and this week, a joint team began tests to see whether redesigned bags and chutes now work, and if not, why. It could be their last chance to fix the problem and preserve a launch set for next summer—or face 2 years of delay. "It's a race against time," says David Parker, ESA's director of human and robotic exploration in Noordwijk, the Netherlands.

The ExoMars mission, Europe's largest ever planetary mission and first Mars rover, has been in gestation since 2001. The golf cart-size rover, named after British DNA pioneer Rosalind Franklin, will look for signs of life. It is just one-third of the size of NASA's Mars 2020 rover, which will gather rocks for eventual return to Earth (*Science*, 22 November, p. 932). But uniquely, it has

a drill that can burrow 2 meters below ground to sample material that has been shielded from the harsh radiation that bombards Mars's surface. "It's a hostile place for life, so you have to dig deeper," says Andrew Coates of University College London, principal investigator of the rover's science camera system.

About 10 years ago, ESA teamed up with NASA to transport its rover in a U.S. lander. But in 2012, when the U.S. side pulled out for budgetary reasons, ESA had to find a new landing craft. The agency teamed up with its Russian counterpart, Roscosmos. Russia's landing system does not have retrorockets as powerful as NASA's, so ESA had to devise larger parachutes to slow the craft for landing, says Francois Spoto, ExoMars project manager in Noordwijk.

The parachutes are just one step in a hair-raising descent. But because they unfurl and inflate in unpredictable ways, they are considered risky. When the approaching spacecraft first hits the thin martian atmosphere, drag on its heat shield slows it from 21,000 to 1700 kilometers per hour. Then, a 15-meter-wide parachute, with a large, ring-shaped gap to cope with the supersonic airflow, slows the craft to 400 kilometers per hour. That chute is jettisoned and followed by a 35-meter parachute, the largest ever deployed in a descent to Mars, with multiple ring-shaped slots that create higher drag at low speeds. When that chute has done its

work, it, too, is jettisoned, and at an altitude of 1 kilometer retrorockets take over to lower the 2000-kilogram lander to the surface. "It'll be a real finger-biting time," Coates says.

ESA's 2016 lander, Schiaparelli (*Science*, 28 October 2016, p. 397), tested the 15-meter chute. Although the chute did its job, a software error caused the craft to think it had landed when it was still 4 kilometers high. The parachute was released, thrusters were turned off, and Schiaparelli crashed. "Let's hope this goes better this time," says Francesca Esposito of the Astronomical Observatory of Capodimonte in Naples, Italy, whose instrument DREAMS was destroyed in the crash. Her new instrument on the ExoMars lander, called MicroMED, will study how martian dust forms and how it affects the atmosphere.

In May, engineers tested the two-chute system in Sweden, dropping it from a balloon at an altitude of 30 kilometers, better to mimic the thin air of Mars. Both the 15-meter and 35-meter chutes tore while being pulled from their bags. ESA made adjustments, reinforcing the parachutes and lining the bags with Teflon to make them more slippery. But in an August test, the chutes tore catastrophically.

ESA sought help from NASA's Jet Propulsion Laboratory (JPL) in Pasadena, California, which has designed parachutes for many successful Mars landings. In September, ESA staff traveled to JPL for a 3-day workshop. "It was very open. We received some critical comments on the design," Spoto says. Two JPL engineers traveled to Europe to inspect the damaged chutes and suggested a different lacing system for the bags, which ESA has now adopted.

This week, tests on these new chutes will begin at JPL. The chutes will be hydraulically pulled from the bags in a series of tests, which will gradually ramp up to full extraction speeds of 60 meters per second. If the tests are successful, engineers will perform more high-altitude drop tests in Oregon in February and March 2020. That would leave just enough time for the redesigned chutes to be installed on the spacecraft in Cannes, France, before it is shipped to the Baikonur Cosmodrome in Kazakhstan for its summer launch. "It's very challenging, but it's doable," Parker says.

A final check would come in late April 2020, when the parachute system must pass a qualification review by senior ESA experts. If the parachutes miss that deadline, "it's bye-bye for 2 years," Spoto says—until the next time orbital mechanics bring Mars into line for a suitable launch window. Esposito, who has already seen one of her dreams dashed, would rather be safe than sorry. "I'll be happy to wait," she says. ■



# A SHOT OF HOPE

The first malaria vaccine is finally being rolled out—despite limited efficacy and nagging safety concerns

By **Jop de Vrieze**, in Malawi; Photography by **Thoko Chikondi**

In a small room at the Phalula Health Centre in southern Malawi's Balaka district, two young mothers are sitting on a wooden bench, each with a 5-month-old baby on their lap. Across from them, behind a desk, sits Alfred Kaponya, a community health worker. A colleague is busy preparing a vaccine, tapping the syringe to dislodge bubbles. Kaponya explains the procedure to the women, writes down the vaccines' serial numbers in the children's vaccination booklets, and copies them onto a spreadsheet in his binder.

Then, one of the mothers bares her son's thigh for the shot; he starts to cry, and she strokes his back. The procedure is repeated for the other baby, a girl.

It may sound routine, but it's not. These two children have just received the first malaria vaccine to move beyond the stage of clinical testing—a landmark event in the battle against a disease that each year takes more than 400,000 lives, most of them children in Africa. Thirty years in the making, RTS,S, also known by its brand name, Mosquirix, targets *Plasmodium falciparum*, the most common and most lethal of four ma-

laria parasite species. It is an answer to a dire need. After decades of declining numbers of cases and deaths, the fight against malaria has stalled. Parasites resistant to the most widely used treatment, called artemisinin-based combination therapy, are spreading, while malaria mosquitoes are increasingly resistant to insecticides.

And yet the rollout, here and in two other African countries, isn't quite the breakthrough the field has been waiting for. Mosquirix's efficacy and durability are mediocre: Four doses offer only 30% protection against severe malaria, for no more than 3 years. Some experts question whether that is worth the cost and effort. And it may yet turn out that Mosquirix doesn't even prevent severe malaria, but merely postpones it.

The biggest concerns, however, are about the vaccine's safety. In the largest trial, children who received Mosquirix had a risk of meningitis 10 times higher than those who received a control vaccine. Mosquirix may not have triggered the meningitis cases—there are other possible explanations—but the possible risk worried the global health community so much that, rather than roll-

ing out the vaccine across Africa, the World Health Organization (WHO) in 2015 decided to set up a pilot in Malawi, Ghana, and Kenya in which the vaccine will be given to hundreds of thousands of children.

The pilot is not a clinical trial, but a closely monitored vaccination campaign to collect more data to make sure Mosquirix is safe and effective before wider introduction. "I think the pilot is a scientific and pragmatic way to move forward," says Marcel Tanner, a former director of the Swiss Tropical and Public Health Institute in Basel who has been involved in several clinical studies with the vaccine. "It is a way to monitor all the aspects of the vaccine and watch if something happens."

But monitoring the vaccinated children is a daunting task in a country like Malawi, which lacks digital systems to record health and mortality statistics. "When we decided a pilot was needed, we did not take into account the practical implications," acknowledges epidemiologist Peter Smith of the London School of Hygiene & Tropical Medicine (LSHTM), a scientific adviser to the pilot. And critics are still skeptical the pilot







Emily Phadzula from Bereu, Malawi, holds her daughter Margaret, who has received three doses of Mosquirix, the first malaria vaccine (left).

will deliver a clear verdict about Mosquirix's potential in the real world.

**THE MALARIA PARASITE** is a challenging target for a vaccine. It has a complex life cycle that begins when an infected female mosquito bites a human and spits *Plasmodium* cells called sporozoites into the bloodstream. They multiply in the liver, emerge as another cell type named merozoites, invade red blood cells, and continue to multiply. The blood cells burst, causing fever, headache, chills, muscle aches, and often anemia. (They also flood the blood with gametocytes—the parasite's reproductive cells—ready to be picked up by the next mosquito.) Along the way, the parasite frequently changes its surface proteins. That makes it an elusive target for the immune system, and for a vaccine.

Mosquirix, developed in the 1980s by a team in Belgium at SmithKline-RIT, now part of GlaxoSmithKline (GSK), stimulates an immune response against a protein that occurs only on the sporozoites' surface. To bolster the response, the research team fused the vaccine protein with a hepatitis B surface protein and added an adjuvant. "Many peo-

ple were very skeptical at the time, because there had been so many attempts done and so many failures," says molecular biologist Joe Cohen, who led the effort until he retired from GSK in 2012.

But results of the first large trial, among 2000 children aged 1 to 4 in Mozambique, were promising: Malaria infections during the first 6 months after vaccination were down 58%, Cohen and his colleagues reported in a 2004 paper in *The Lancet*. An even larger trial enrolled 15,000 children in seven African countries between 2009 and 2011 and had mixed results. Among babies, the efficacy was close to zero. That dashed hopes that the vaccine could protect the most vulnerable group and that it could be given together with other routine infant vaccinations, Smith says. But among children between 5 months and 25 months of age, malaria infections overall were down by 40%, and severe infections 30%.

Those are paltry numbers compared with the measles vaccine, which is 97.5% protective. "But nobody really expected to get very high efficacy because malaria is such a complicated disease," Smith says. The trials also

revealed that, even after three shots given 1 month apart, protection drops to near zero in about a year and a half. A booster shot given at that point bolsters the protective effect, but it tapers off again in another 18 months. Still, even a short-lived, partly effective vaccine "could already make a huge difference," Smith says. Cohen notes that it offers some protection during a crucial period: "The real period during which children are at risk of severe disease and death is under 5 years old."

The European Medicines Agency (EMA) agreed. In July 2015, it declared the vaccine was safe and effective enough to be introduced in Africa, under a special procedure designed to help regulatory agencies in developing countries make decisions.

That didn't end the doubts. Some scientists feared the vaccine would be less effective in the real world than in studies, says LSHTM malaria researcher Brian Greenwood, who led the trial, because people might count on the vaccine for protection and become less careful. "What if people no longer went to sleep under their mosquito nets or parents no longer brought their feverish child to a

clinic for a malaria test? That would have to be monitored,” he says. Others worried that the money spent on Mosquirix would come at the expense of other malaria prevention methods. A full series of four shots costs about \$20, versus \$5 for a mosquito net and \$1.50 to give a child malaria drugs prophylactically, during the rainy season. “There are effective measures available that we can use even better,” says Micaela Serafini of Doctors Without Borders in Geneva, Switzerland.

The safety data, meanwhile, were puzzling. About 20 of the 6000 children vaccinated against malaria in the seven-country trial contracted meningitis, compared with one of 3000 children in the control group, who re-

**THE DEBATES ABOUT MOSQUIRIX** came to a head at a meeting at WHO headquarters in Geneva in October 2015. Proponents of rolling out the vaccine, including many African representatives, argued that an imperfect vaccine was better than none. Others, mainly vaccine experts, argued that Mosquirix just wasn’t safe and effective enough for introduction.

A relative outsider at the meeting, Danish anthropologist and vaccine researcher Peter Aaby of the Bandim Health Project in Guinea-Bissau, offered another argument against introduction. After reanalyzing the data from the biggest trial, Aaby discovered that although the vaccinated children had

that contain a living, weakened pathogen—such as the vaccines against measles and tuberculosis—strengthen the immune system generally, Aaby and Stabell Benn say, making recipients better able to fight off other infections. But vaccines that contain a killed pathogen or only bits of it weaken the immune system, their theory goes—especially in girls, because their immune systems seem to respond more strongly to vaccines in general.

Few share Aaby’s concerns about Mosquirix. WHO’s Mary Hamel, who leads the Mosquirix pilot from Geneva, says the trial was not designed to study mortality. Just being enrolled in the trial meant children received better care, and their mortality was 70% lower than among children near the study sites who weren’t enrolled. “So, the difference does not tell us anything about reality,” she says. Tanner says Aaby has “enriched our field” but “has turned a bit into a missionary with regard to the nonspecific immune effects. I am confident that the vaccine will have an overall positive effect on mortality.” Yet Aaby’s presentation at the meeting intensified the doubts. At one point, it appeared the vaccine might be abandoned altogether, Greenwood says.

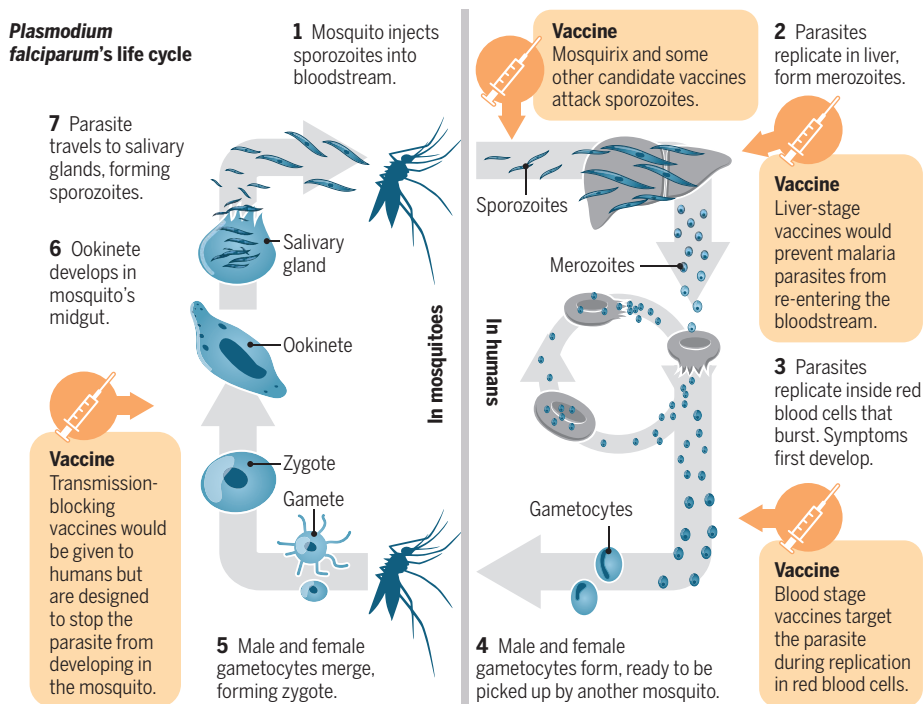
To address the concerns, the attendees agreed to the three-country pilot. In each country, the WHO team and the national government would randomly select areas where about 120,000 children annually would receive the vaccine between 2019 and 2022. Researchers would monitor how well the rollout went and compare rates of malaria, meningitis, and other diseases, as well as mortality, in vaccinated and control areas.

**MALAWI WOULD WELCOME** an effective vaccine. It has seen progress in the fight against malaria—primarily thanks to mosquito nets, rapid diagnostics, and improved access to treatment. Ten years ago, about 60% of children were infected at any given moment, versus 17% today. But Don Mathanga, director of the Malaria Alert Centre at the University of Malawi in Blantyre, says the current infection rate is “not a figure that we are very content with.” The death toll was about 7000 in 2017 and, as in many other countries, the decline has stalled. “So we were very happy to be selected as a pilot country,” Mathanga says.

So are many parents. At the Queen Elizabeth Central Hospital in Blantyre, Jaquiline Masomba, 32, is dabbing the head of her 3-year-old son Edson with a washcloth. He probably contracted malaria from a mosquito that found its way through a hole in her worn-out bed net, she says. “For our living I depend on alcohol distillation,” Masomba says. “And my business has been on hold for 2 weeks” as she cares for Edson. Masomba

## Many ways to thwart a parasite

Malaria vaccines in development interfere with many different parts of the parasite’s complex life cycle. Mosquirix targets so-called sporozoites after they are injected by a mosquito and before they move to the liver.



ceived a rabies vaccine—a 10-fold increase in risk. One-third of the children with meningitis died. The research team and EMA both think this outcome was a fluke. The meningitis episodes occurred at random intervals after vaccination, most of them at two of the seven study sites, and there is no good explanation for why Mosquirix would lead to meningitis, the authors of the *Lancet* paper argue. Other scientists have suggested the difference may be due to the rabies vaccine that control children received. That group had a remarkably low rate of meningitis—suggesting the rabies vaccine may somehow prevent it.

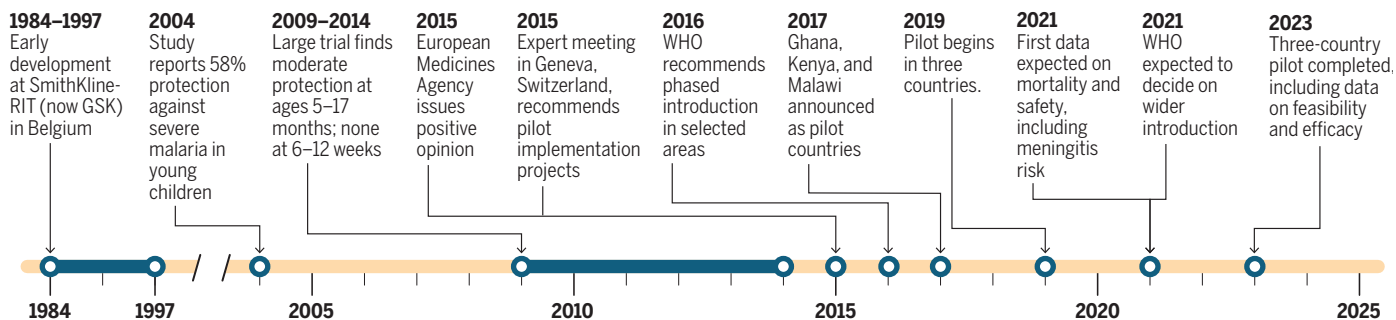
malaria less often, they did not die less often. Among girls, overall mortality was almost doubled, Aaby told his colleagues at the meeting. “This vaccine is killing girls,” he recalls saying. Whereas WHO expects the vaccine to save one life per 200 children vaccinated, Aaby believes one in 200 will die as a result of it; he predicts “a nightmare.”

Aaby and Christine Stabell Benn, a global health professor at the University of Southern Denmark, have an explanation. The married couple has studied routine vaccinations in Africa for decades and believes vaccines can “train” the immune system in ways that don’t affect just the target disease. Vaccines



## The long road to a lackluster vaccine

Development of Mosquirix began in the 1980s. A pilot rollout now underway will help determine whether it should be introduced widely in Africa in the next decade.



had never heard about the vaccine, but now says: “Of course I would like to have it when it becomes available.”

Violet Wilson, 26, in the southern village of Nkwazi, explains that she tries everything to keep her 5-month-old son from becoming infected. Cracks and holes in the walls of her brick house are smeared with loam to keep mosquitoes out. Wilson and her son sleep under a mosquito net every night. If her baby gets a fever, she’ll rush him to a clinic, Wilson says. She was delighted to hear about the arrival of the vaccine, but her son can’t get it because they live in a control area.

Emily Phadzula, 30, from the nearby town of Bereu, was luckier: In late April, her daughter Margaret, then 5 months old, was the first child in her village to be vaccinated. Sitting on the doorstep of her concrete house and tightly holding Margaret, who is wearing a pink sweater, Phadzula explains she heard about the vaccine during a community meeting. “I didn’t have any doubts,” she said. “I was very happy that after having to see my other children suffer so much, finally this child could be better protected.” Margaret has had no side effects except a slight fever—and no malaria. Phadzula says she recommends the shots to other mothers.

By September, almost 35,000 children in Malawi had received at least one shot. Getting the vaccine to these children has been straightforward, but collecting follow-up information is a challenge. “In trials, you have a controlled environment. You know where the participants are, keep track of them, if there is an issue you take care of them,” says Bernhards Ogutu, a pediatrician and malaria researcher at the University of Nairobi who is involved in Kenya’s vaccine pilot program. “But in the pilot, once you’ve given the child the vaccine, they go home.”

As a first step to monitoring them, researchers in Malawi have set up a surveillance system in four “sentinel hospitals” that treat both vaccinated and unvaccinated children. Comparing data about illness and mortality should show the vaccine’s impact, says pediatrician Tisu Mvalo of the University of

North Carolina Project–Malawi in Lilongwe. “We had to train hospital staff to collect these data. We hope that the numbers will be big enough to detect potential differences.”

Keeping track of children who die outside the hospitals is even harder. “Unfortunately, we still have no death registration in this country,” Mathanga says. Instead, the team built a new system based on a cultural practice: In rural Malawi, town chiefs must allocate a place for the dead to be buried. The researchers figured they would know which children have died. Many chiefs are illiterate, however, so they had to be assigned an assistant. Pilot evaluation staff use motorbikes to visit the chiefs regularly and collect the paper files; they also interview relatives of deceased children to identify the most likely cause of death. But these “verbal autopsies” aren’t always correct.

**MEANWHILE**, the pressure to deliver results is rising. In April, WHO’s vaccine advisory committee said it would assess any impact of Mosquirix on meningitis, severe malaria, and mortality—and determine whether the vaccine can be introduced in the rest of Africa—after just 2 years, instead of the

five originally planned. “The evaluation will continue, but we don’t want to keep the rest of Africa waiting any longer,” says David Schellenberg, who left LSHTM in 2016 to join the team at WHO. Another reason to hasten the decision is that GSK needs to know whether it can continue production, Schellenberg says.

Whether the researchers will have enough data to make a decision remains to be seen, however. In Kenya, the pilot was delayed by 4 months, apparently because the government was overwhelmed by the implementation of universal health care. In Ghana, an advocacy group called the Coalition for Ghana’s Independence Now called for a boycott of the vaccine in May, asking for an injury compensation program similar to the one in the United States, to help those who might be harmed by Mosquirix. That, too, might cause delays. What’s more, a declining number of meningitis cases and deaths in the three countries—although good news—may mean researchers need to continue the pilot longer than expected to detect statistically significant differences.

Aaby says showing whether the vaccine increases mortality among girls might also take longer than planned. He worries that even without a clear safety verdict, the global health community will exert enormous pressure to get the vaccine approved around Africa. But the WHO team in Geneva remains confident it will know whether the benefits are worth any risks. “We have a lot of checks on the evaluation. So, this setup should do it,” Hamel says.

Many people in Malawi have no doubts. “The community has welcomed the vaccine,” Kaponya says, after he closes the door behind the two women and their newly vaccinated babies. “The only challenge we are having here, is that people from the non-vaccine areas come and ask for it.” ■

Jop de Vrieze is a science journalist in Amsterdam. With reporting by Saulos Jali in Malawi. This story was supported by the European Journalism Fund.



Health worker Dennis Nkuma opens a vaccine registry book in a health center in southern Malawi.



## POLICY FORUM

### CYBER RISK

# Cyber risk research impeded by disciplinary barriers

Security progress requires cross-disciplinary collaboration

By **Gregory Falco**<sup>1,2,3</sup>, **Martin Eling**<sup>4</sup>, **Danielle Jablanski**<sup>5</sup>, **Matthias Weber**<sup>6,7</sup>, **Virginia Miller**<sup>8</sup>, **Lawrence A. Gordon**<sup>9,10</sup>, **Shaun Shuxun Wang**<sup>11</sup>, **Joan Schmit**<sup>12</sup>, **Russell Thomas**<sup>13,14</sup>, **Mauro Elvedi**<sup>15</sup>, **Thomas Maillart**<sup>16</sup>, **Emy Donovan**<sup>17</sup>, **Simon Dejung**<sup>18</sup>, **Eric Durand**<sup>19</sup>, **Franklin Nutter**<sup>20</sup>, **Uzi Scheffer**<sup>21</sup>, **Gil Arazi**<sup>22</sup>, **Gilbert Ohana**<sup>23</sup>, **Herbert Lin**<sup>24,25,26,27,28,29</sup>

Cyber risk encompasses a broad spectrum of risks to digital systems, such as data breaches or full-fledged cyber attacks on the electric grid. Efforts to systematically advance the science of cyber risk must draw on not only computer science but also fields such as behavioral science, economics, law, management science, and political science. Yet, many scholars believe that they have sufficient

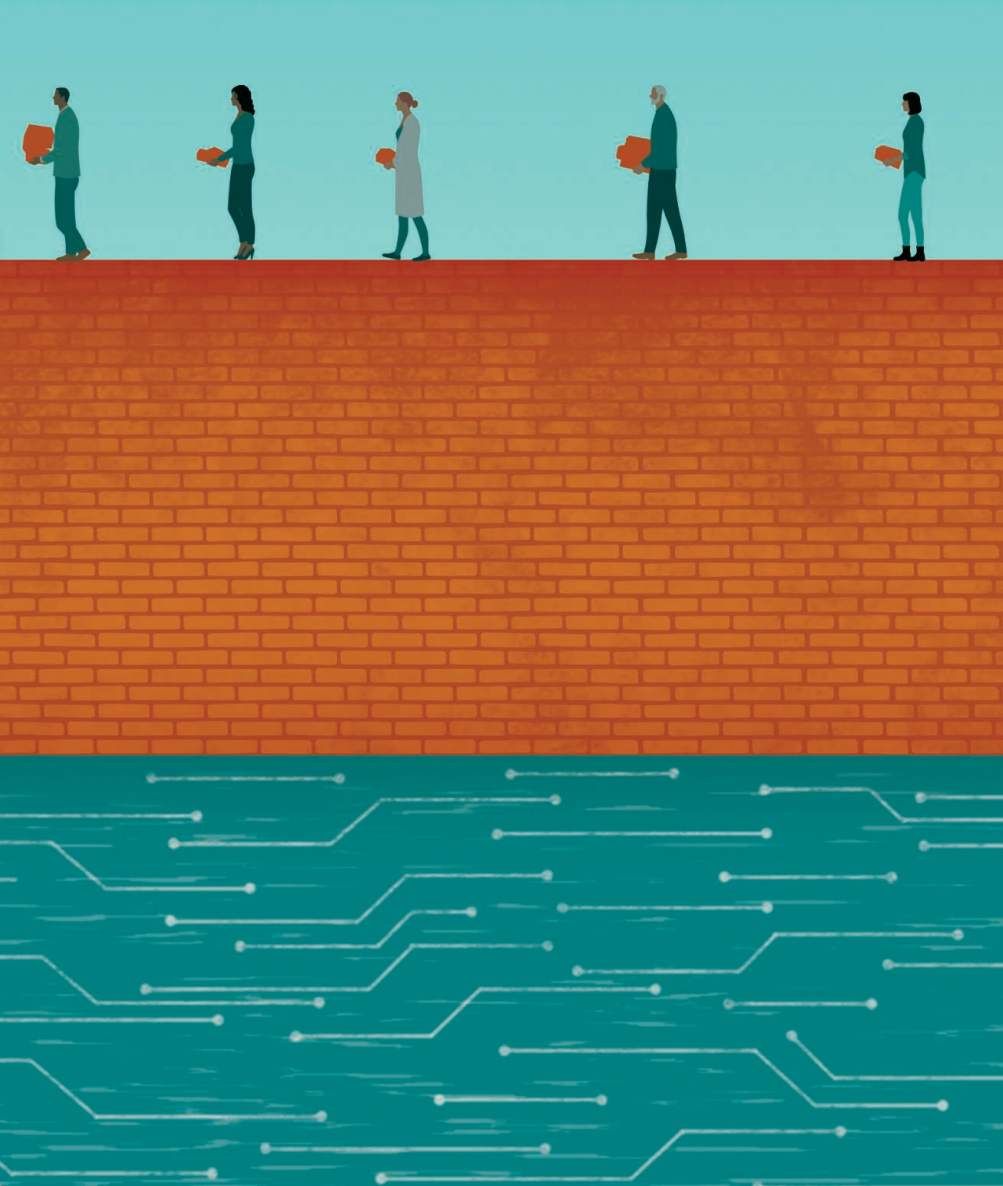
understanding of other fields to comprehensively address the inherently cross-disciplinary nature of cyber risk. For example, a statistician might apply Bayesian modeling to predict future cyber events, even though it is not entirely clear what bearing historical cyber events have on future ones. Computer scientists might write on data protection laws, yet with little knowledge of legal jurisdiction issues. Such questions of disciplinary

ownership, the inability to coordinate across disciplines, and the undefined scope of the problem domain have thus plagued inherently cross-disciplinary cyber risk research. Drawing on global expertise and challenges from industry, academia, nonprofit organizations, and governments, we adapted the classical risk-management process to identify core research questions for cyber risk, gaps in knowledge that need to be addressed for advances in security, and opportunities for cross-disciplinary collaboration for each area. Although we mention specific disciplines reflective of our backgrounds, these are not the only ones that should be conducting cyber risk research.

### CYBER RISK TRADECRAFT

We consider cyber risks to include “operational risks to information and technology assets that have consequences affecting the confidentiality, availability, or integrity of information or information systems” (1). But the scope of cyber risk has nonetheless been difficult to characterize because there





is disagreement about what a cyber event and other pertinent terminology actually entail. Some organizations consider a cyber event to be any unknown connection attempt to their network, but others only consider successful unauthorized access to their network. Still others only consider instances when “loss” is experienced. Such definitional ambiguity is problematic, making it difficult to benchmark security or risk across an industry or even within the same organization. For the purpose of establishing a body of knowledge, clear and consistent terminology is essential (2).

Recently, there has been welcome progress. For example, the International Organization for Standardization established cyber guidance for insurance and machinery. But as seen with the U.S. government’s National Institute of Standards and Technology’s cybersecurity framework, implementation has faltered among those seeking to use the “gold standard” of cyber risk management. One important reason is the high costs associated with appropriate security controls and

the lack of qualified people to implement the standard. In our view, in addition to increased convergence on cyber guidance and standards, there is need for a standard of care that defines how an organization can proceed with enacting a standard. By addressing cyber risk terminology, standards, and implementation principles in a cross-disciplinary fashion, such guidance can be interpretable and usable by a wide variety of companies and nonprofit and governmental organizations that have different agendas. Diversity of thought will likely contribute to richer cyber risk insights.

There is also value to classifying the variety of cyber risks so that they can be addressed appropriately. For example, cyber risks can be classified by motivation (such as financial or reputational), type of attack (such as malware, insider attack, spam, or distributed denial of service), and source (such as terrorists, criminals, or government). Clarification on types of cyber risk can help to develop a common language for the science. Progress has been made by the nonprofit MITRE Corpora-

tion in classifying risk types and establishing terminology. But adaptations of classical risk-management tools such as early detection systems or risk maps are still in their infant stages, also because of measurement and quantification difficulties.

An example of disciplines that could benefit from collaborating on this topic is computer science and law. Increasingly, legislation is being proposed about technical attributes of cyber risk. Computer scientists should contribute to proposed technical regulatory requirements and definitional boundaries. Without collaboration here, legislators will continue to develop reactive measures that run the risk of rapid obsolescence as newer technologies are more widely adopted.

### MEASURING RISK AND ITS COSTS

Consistent metrics for loss frequency and severity that can communicate the extent of cyber risk are important to understanding how well an organization is prepared for cyber risks. Standardized risk management concepts such as “value at risk” may also enable organizations to understand the cost and benefits of investing in cybersecurity.

Security always involves tradeoffs (3). The tradeoff might be convenience, money, or technological progress. These tradeoffs can be abstracted into metrics and ultimately used in models to assess cyber risk costs (4). A science of cyber risk will help to address deficiencies in decision-support models, which are often formulated ad hoc for individual organizations based on point-in-time data and do not adequately capture cyber risk trends that could influence an organization’s risk-management strategy (5). For example, the movement toward cloud providers is a way for organizations to outsource computing security infrastructure. An organization reaps considerable benefits in cost and increased operational efficiency by moving to the cloud. However, if a large number of organizations move to a monoculture of cloud providers, the result could be the exposure of organizations to a new class of systemic risk related to systemic failures across multiple industries. Such risk would not be captured by point-in-time models; instead, analysis requires strategic interorganization decision science that could be enabled with cross-disciplinary research.

Today, calculating indirect costs of cyber risk such as lost revenues or reputational effects is imprecise at best. There are also gaps in measuring how a cyber event in one department affects other departments throughout the organization. Current metrics do not capture bigger economic questions such as measuring risk across organizations. Establishing organizational processes for cyber risk planning and enabling these plans with

measurable success metrics is another problematic aspect of cyber risk that may also help drive organizational accountability. Nonprofit organizations such as the Factor Analysis of Information Risk Institute are working toward developing robust value-at-risk measurements, but more needs to be done as described.

An example of cross-disciplinary collaboration on this topic could be on measuring risk across a portfolio of companies, sectors, or countries. Data scientists could use clustering techniques to determine what other types of catastrophic-loss scenarios are most akin to cyber. Then, economists could develop cyber loss scenarios that are consistent with and comparable with the other types of catastrophic-event loss scenarios.

### CYBER RISK AVOIDANCE

Risk avoidance per se is a largely aspirational goal, given the dependence of modern society on digital technology. It is unrealistic to avoid all cyber risk, although it may be possible in some domains to eliminate certain kinds of cyber risk. One option is to design and use inherently secure systems (6). Most devices, networks, and systems, particularly Internet-of-Things devices, were built without security as a priority. Some new approaches to designing and building software and hardware systems aim to avoid certain security issues entirely. For example, by designing operating systems with built-in limitations on what processes they can run, certain risks are automatically avoided.

Managerial options to avoid cyber risk include minimizing the use of connected computing systems in certain environments. This is not a decision to be taken lightly, considering the benefits that networking affords. However, the thought process behind choosing to unplug is important. Today, society defaults to assuming connectivity is beneficial. Organizations must weigh the tradeoff between convenience and security if they seek to avoid cyber risk.

An example of cross-disciplinary collaboration that would advance understanding

of this topic is between political science and management science. Many political scientists have sought to apply nuclear weapons-deterrence doctrine to cyber, but the parallels are often weak at best. Deterrence scholars could work with management scientists who have studied nontechnical attack and defense dynamics to understand what social dynamics theories may fit with their deterrence conceptualization. Together, they could arrive at alternative mechanisms to avoid risk.

### OPPORTUNITIES TO REDUCE RISK

Many cyber-security researchers use a framework called the Parkerian hexad to evaluate opportunities to reduce risk. It outlines six elements of information security: confidentiality, possession or control, integrity, authenticity, availability, and utility (7). Increasingly, organizations understand that they cannot protect themselves from all risks all the time. They need to prioritize their systems, networks, and data security and evaluate op-

**“Encouraging disciplines to pursue their world view of each question is important, but the disciplines should recognize the limits of their expertise and collaborate...”**

portunities to reduce cyber risk across the hexad (8). The relative importance of each hexad element must be evaluated.

One concrete step toward reducing cyber risk across the hexad is to share threat information; if an organization shares recent attacks with others that may use similar systems, networks, or data, future attacks against others could be prevented (9). Information Sharing Analysis Centers (ISACs) exist across all critical infrastructure sectors in many countries to facilitate information sharing about cyber events, but they have not been equally successful. ISACs are only

as effective as the member organizations' participation. For example, the financial services ISAC is well regarded. One reason for its success is that the banking and financial services regulators in the United States have required participation. Also, U.S. law protects consumers from banking and card services theft, which means that losses from such theft must be absorbed by the industry. This incentivizes companies in financial services to participate. Other ISACs likely will need similar incentives to spur participation. Studying why some sectors engage more effectively with their ISAC, and alternative incentives for participation, may help improve cyber-event prevention in other sectors.

In many ways, cybersecurity can be characterized as a public good. This can lead to underinvestment in reducing cyber risk. From the perspective of an individual organization, it might be optimal to reduce investments in cyber risk reduction. In such cases, public policy might be needed to enforce some minimum standards for cyber risk reduction that apply to all organizations in a given sector (10). In principle, these standards need to be global to be effective, given that cyber risk knows no boundaries. In light of the lack of policy direction in this space, it is important to evaluate market mechanisms, such as cyber insurance (11), that may have cyber risk-reduction effects.

An example of two disciplines that could collaborate here is economists and behavioral scientists. Economists could investigate mechanisms to reduce cyber risk through incentives, which would benefit from working with behavioral scientists, who could provide insight into what drives human interactions and how they engage with technology.

### TRANSFERRING RISK

It is important to consider how organizations can transfer cyber responsibility and risk externally to insurers, capital markets, contracts in indemnity, hold-harmless agreements, or even the government (12). Cyber risk management today mainly focuses on

<sup>1</sup>Freeman Spogli Institute for International Studies, Stanford University, Stanford, CA, USA. <sup>2</sup>Computer Science and Artificial Intelligence Laboratory, Massachusetts Institute of Technology, Cambridge, MA, USA. <sup>3</sup>Belfer Center for Science and International Affairs, Harvard University, Cambridge, MA, USA. <sup>4</sup>Institute of Insurance Economics, University of St. Gallen, St. Gallen, Switzerland. <sup>5</sup>Freeman Spogli Institute for International Studies, Stanford University, Stanford, CA, USA. <sup>6</sup>CyberCube, San Francisco, CA, USA. <sup>7</sup>Next Insurance U.S., Palo Alto, CA, USA. <sup>8</sup>Freeman Spogli Institute for International Studies, Stanford University, Stanford, CA, USA. <sup>9</sup>Robert H. Smith School of Business, University of Maryland, College Park, MD, USA. <sup>10</sup>University of Maryland's Cybersecurity Center, University of Maryland, College Park, MD, USA. <sup>11</sup>Nanyang Business School, Nanyang Technological University, Singapore. <sup>12</sup>Wisconsin School of Business, University of Wisconsin-Madison, Madison, WI, USA. <sup>13</sup>Department of Computational and Data Sciences, George Mason University, Fairfax, VA, USA. <sup>14</sup>Risk Management Solutions, Newark, CA, USA. <sup>15</sup>Institute of Insurance Economics, University of St. Gallen, St. Gallen, Switzerland. <sup>16</sup>Geneva School of Economics and Management, University of Geneva, Geneva, Switzerland. <sup>17</sup>Cyber, Tech & Media Professional Indemnity, Allianz Global Corporate & Specialty, San Francisco, CA, USA. <sup>18</sup>Global Line Engineering, SCOR SE, Paris, France. <sup>19</sup>Cyber Center of Competence, Swiss Re Institute, Zurich, Switzerland. <sup>20</sup>Reinsurance Association of America, Washington, DC, USA. <sup>21</sup>SOSA, Tel-Aviv, Israel. <sup>22</sup>FinTLV Ventures, Tel-Aviv, Israel. <sup>23</sup>FinTLV Ventures, Tel-Aviv, Israel. <sup>24</sup>Freeman Spogli Institute for International Studies, Stanford University, Stanford, CA, USA. <sup>25</sup>The Hoover Institution on War, Revolution, and Peace, Stanford, CA, USA. <sup>26</sup>Computer Science and Telecommunications Board, National Research Council, Washington, DC, USA. <sup>27</sup>Saltzman Institute for War and Peace Studies, Columbia University, New York, NY, USA. <sup>28</sup>Science and Security Board, The Bulletin of Atomic Scientists, Chicago, IL, USA. <sup>29</sup>Center for Long-Term Cyber Security, University of California-Berkeley, Berkeley, CA, USA. Email: falco@stanford.edu



prevention, whereas risk-transfer instruments such as insurance are in their infancy. Insurance coverages are narrow, and pricing is based on heuristic estimations of loss frequency and severity. Such risk transfer must be empirically grounded in science in order to accurately price forward-looking cyber risk. Inaccurate pricing for cyber insurance could result in disproportionate payouts compared with premiums paid. This could be especially damaging if cyber risks accumulate, when an insurer faces the possibility of simultaneous payouts on a large scale because of a single event (for example, an attack on a common technology such as a cloud service provider).

The private sector is unwilling or unable to cover certain cyber events. For example, insurers generally deny coverage for events deemed “cyberwar” because of the potentially large effects of sophisticated nation-state attacks. Scholars need to evaluate government’s role for risk transfer in acts of cyberwar. Different organizations and governments have varying perspectives on what is cyberwar, further complicating risk transfer (13). Pooling of cyber risk as launched in Singapore might be a solution to cover risks on a broader scale, involving the private sector and the government. Standardized insurance conditions as used in Germany also help to reduce uncertainty about coverages and make insurance more broadly available.

An example of potential cross-disciplinary collaboration concerning risk transfer could be between law and management science. Legal scholars could investigate contract mechanisms that would enable risk sharing and transfer—research that would benefit from management scientists, who could provide insight as to how such a contract would affect business operations and a company’s balance sheet.

### MONITOR AND MANAGE RESIDUAL RISK

Regardless of prevention measures taken, there is still some chance that an organization will experience a cyber event. Monitoring such residual cyber risk often falls to the chief information security officer (CISO). However, the actual ownership of cyber risk within an organization is generally unclear—even if the organization has a CISO or chief information officer (CIO) who is supposed to manage information security (14). Because cyber risk is a key part of an organization’s overall business risk, all departments of an organization have a vested interest in how the organization manages residual cyber risk.

Researchers must devise a systematic approach for business units to increase their involvement in cyber decisions rather than these responsibilities being centralized only

in the CISO or CIO role. Business unit operators need better incident response playbooks, including strategies for communicating with internal units, board members, shareholders, government officials, regulatory authorities, and the public (15).

An example of two disciplines that could work together on monitoring and managing residual risk is computer science and political science. Political scientists are actively studying how cyber capabilities contribute to power dynamics across nations. This would benefit from a computer scientist’s ability to actively monitor cyber attacks and capabilities.

### EXPLORING THE MARGINS

To overcome barriers to cross-disciplinary cyber risk research, scholars researching a component of this agenda could develop collaborations and explore questions at the margins of the disciplines. An example of where the authors have done this is in studying extreme cyber-risk scenarios. Initiated by an economist, we set out to establish a consistent approach for modeling extreme cyber-risk scenarios. The team engaged a computer scientist who was able to describe plausible extreme events and the criticality of these events so that the relevant information was analyzed. Neither the economists nor computer scientist had the complete expertise to address the problem.

Another barrier to cross-disciplinary research is the nature of calls for proposals for funding. We cannot assume that cross-disciplinary research projects will all be arrived at organically. Instead, government and private sector research grants for cyber risk must be structured to require collaboration that studies questions on the margins of disciplines. Otherwise, the science of cyber risk will merely borrow from previous studies along disciplinary boundaries—effectively forcing the use of existing methods to imperfectly address cyber issues. For example, a working group at the International Actuarial Association is aiming to develop an economic cyber loss index. To collect incident data, they first need to consult legal scholars to understand what data can be legally collected. Then, computer scientists need to collect data using tools at their disposal. Data scientists need to cleanse this data and prepare it for analysis. Management scientists need to categorize the data’s relevance by sector, and economists ultimately need to model the economic impact. If any single discipline approached this problem alone, there would likely be missteps throughout that could lead to flawed research outcomes.

Industry and government organizations must demonstrate leadership in setting the

direction of cross-disciplinary research. Because digital risk is a daily battle for businesses and public organizations, they must propose and provide data for the most pressing research problems to spur cross-disciplinary-scope projects. One promising concept from the risk-management toolbox that is well established in other contexts (natural catastrophe, terror, and nuclear risks) might be the pooling of risk. However, to implement this, legal, business, and economic preconditions have to be studied. Further discussion on potential standardization and regulation to improve cyber-risk management needs input from various disciplines as well. It is important to understand the economic and political incentives for the proliferation of cyber risk, how society can be trained in dealing with cyber risks, and what legal action can be taken to improve cyber security.

Both the intellectual independence of academia and the experiential knowledge from government and industry are critical for robust, integral research. Integrating practical direction into calls for research proposals that are not catered to a specific discipline can spur cross-disciplinary collaboration—for example, by agencies such as the U.S. Defense Advanced Research Projects Agency. Encouraging disciplines to pursue their world view of each question is important, but the disciplines should recognize the limits of their expertise and collaborate on topics at the margins of disciplines to advance the science of cyber risk. ■

### REFERENCES AND NOTES

1. J. J. Cebula, L. R. Young, “A taxonomy of operational cyber security risks,” Technical note CMU/SEI-2010-TN-028 (Software Engineering Institute, Carnegie Mellon University, 2010).
2. R. Ramirez, N. Choucri, *IEEE Access* **4**, 2216 (2016).
3. G. V. Post, A. Kagan, *Comput. Secur.* **26**, 229 (2007).
4. R. Böhme, S. Laube, M. Riek, *Variance J.* **12**, 161 (2019).
5. L. A. Gordon, M. P. Loeb, *ACM Trans. Inf. Syst. Secur.* **5**, 438 (2002).
6. H. Shrobe, D. L. Shrier, A. Pentland, Eds., *New Solutions for Cybersecurity* (MIT Press, 2018).
7. A. Beauteament, D. J. Pym, paper presented at the Ninth Workshop on the Economics of Information Security, Harvard University, 8 June 2010.
8. G. Falco, C. Caldera, H. Shrobe, *IEEE Internet Things J.* **5**, 4486 (2018).
9. S. Laube, R. Böhme, *ACM Comput. Surv.* **50**, 1 (2017).
10. D. Thaw, *GA. St. UL Rev.* **30**, 287 (2014).
11. M. Eling, W. Schnell, *J. Risk Finance* **17**, 474 (2016).
12. L. Bodin, L. A. Gordon, M. P. Loeb, A. Wang, *J. Account. Public Policy* **37**, 527 (2018).
13. D. Woods, A. Simpson, *J. Cyber Pol.* **2**, 209 (2017).
14. V. Hooper, J. McKissack, *Bus. Horiz.* **59**, 585 (2016).
15. G. Falco, A. Noriega, L. Susskind, *J. Cyber Pol.* **4**, 90 (2019).

### ACKNOWLEDGMENTS

M.W. is a board member and shareholder of CyberCube Analytics. U.S. is a board member and chief executive officer of SOSA. G.F., D.J., V.M., and H.L. thank Swiss Re for research funding.

10.1126/science.aaz4795

## PERSPECTIVES

## QUANTUM MATERIALS

# A chemical path to quantum information

Nanoscale graphene can be designed to function as a molecular qubit

By **Stephen von Kugelen** and  
**Danna E. Freedman**

**T**he second quantum revolution is rapidly transforming fields like structural biology, cryptography, and condensed matter physics. The core quantum unit is the qubit, which has an infinite number of possible configurations through the superposition of its quantum states. This quantum property provides a singular approach for solving problems in computing, sensing, and metrology (1, 2). Creating and manipulating qubits is a grand challenge, leading to a plethora of viable ap-

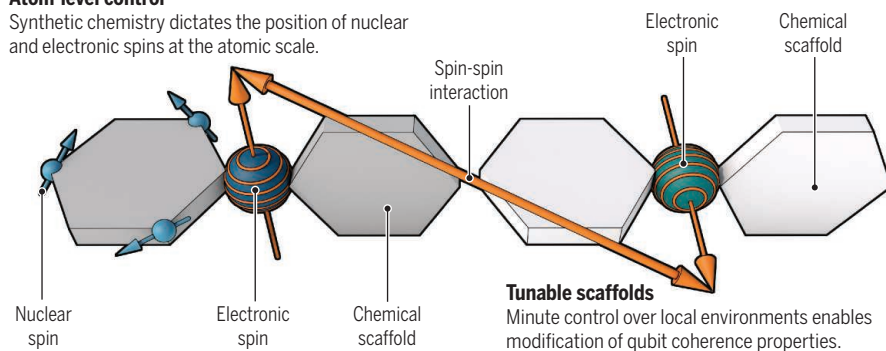
proaches (3). Spin-based molecular qubits are promising because they unify atomic-scale spatial precision with structural customization for systems integration (4). On page 1107 of this issue, Lombardi *et al.* (5) exemplified this approach by constructing an electronic spin-based molecular qubit from a carefully engineered state in nanoscale graphene, providing an elegant example of atomic control over qubit design.

## Quantum information enabled by chemical design

Chemical synthesis of qubits enables a bottom-up approach that controls both local qubit environment and qubit-qubit interactions. The inherent atomistic precision of chemical synthesis supports the creation of designer qubits, each tailored for their intended application.

### Atom-level control

Synthetic chemistry dictates the position of nuclear and electronic spins at the atomic scale.



proaches (3). Spin-based molecular qubits are promising because they unify atomic-scale spatial precision with structural customization for systems integration (4). On page 1107 of this issue, Lombardi *et al.* (5) exemplified this approach by constructing an electronic spin-based molecular qubit from a carefully engineered state in nanoscale graphene, providing an elegant example of atomic control over qubit design.

The bottom-up synthesis of chemical qubits is an emerging field, with comple-

mentary metal-based and organic radical approaches delivering large advances in the past decade (6–8). Chemists can dictate the precise distribution of a qubit's spins through meticulous synthetic control over organic structures or harness ligand fields to finely tune magnetic properties at metal centers (9). An early example of a quantum computation was the implementation of Shor's algorithm using a nuclear spin qubit in a molecule, which highlighted the power of chemical synthesis to enforce the atomically precise relationships that control communication between elements of a quantum system (10). Lombardi *et al.*

showcase a previously untapped strategy in qubit engineering in which their molecular qubit's unpaired spins are created not by an odd number of total electrons but rather by the precise structure of the molecule's bonding (5). They leverage the stability of aromatic  $\pi$  systems to promote an otherwise unfavorable bond configuration that leaves out two unpaired electrons. This enables the rational synthesis of a molecular system that replicates topological defects in graphene in a synthetically tunable platform (see the figure).

Lombardi *et al.* subjected their molecule to a suite of experiments designed to both establish its viability as a qubit and elucidate the mechanisms of the collapse of the superposition state, called decoherence. The molecular system remains in a superposition state, coherence, for times that compare favorably with endohedral fullerene-based systems (6). The 0.33-ms coherence time that the authors observed is similar to the high values achieved with transition metal-based qubits (8). By subjecting the molecule to a series of microwave pulses, the authors demonstrate their control over the qubit by placing it into any arbitrary superposition of states. A benefit of chemically designing qubits is that modulating the local chemical environment can deconvolute processes that lead to the collapse of the superposition state. Lombardi *et al.* demonstrate this with experiments in solids and in solution over a wide range of temperatures, including nuclear decoupling and solvent dependence studies. This rigorous approach should serve as a guide for others vetting new chemical qubits.

A key next step toward quantum sensors is to bring chemical qubits into communication with one another or with other chemical species in a controlled fashion. Constructing multiqubit systems with this level of precision across multiple length scales represents an outstanding challenge in the field. The first step involves progressing from isolated spin-based qubits to understanding two independently controllable, interacting qubits (7). To make this transition, both organic and transition metal-based approaches are promising strategies. Chemical synthesis can expand these quantum systems into many-qubit arrays. The approach from Lombardi *et al.* could be applied to patterned topological defects in other carbon nanomaterials. Alternatively, the bottom-up synthesized qubits could be used to forge molecular qubits into uniformly ordered arrays by bonding them into extended framework materials, which then can be manipulated on the microscale (11). Extending the distances between qubits in these ordered, porous structures would not only control coherence times but also prime them as platforms for quantum sensing of larger chemical species. Ordering qubits could be done in other interesting ways, such as us-

Department of Chemistry, Northwestern University, Evanston, IL 60208-3113, USA.  
Email: danna.freedman@northwestern.edu



ing designer polymer materials like DNA to create tailored soft-matter templates (12).

Defect-based materials such as nitro-gen-vacancy-pair defects in diamond are exceptional candidates for spin-based qubits. An incredible suite of spectroscopies has developed around these defects that exploit their facile optical readout (13). Molecular nanographene-based qubits are one of many ways to create atomically precise analogs of defects that can be read out optically. Lombardi *et al.* show that a bottom-up approach to spin qubits is a promising strategy to expand the usefulness of this spectroscopic infrastructure. Exploiting established spectroscopic approaches by emulating the properties of defect-based systems in these synthetically tunable platforms is an exciting frontier for developing molecular qubits.

The grand challenges of quantum information science present new targets for chemical synthesis. Lombardi *et al.* model a clear path for future chemists to contribute to the advancement of the field. The authors both demonstrate a new strategy

## "This rigorous approach should serve as a guide for others vetting new chemical qubits."

for creating a qubit and expose its intrinsic characteristics through thoughtful application of experimental controls. Through synthetic chemistry, the insights and precision needed for new materials to transform quantum information science are within our reach. ■

### REFERENCES AND NOTES

1. M. A. Nielsen, I. L. Chuang, *Quantum Computation and Quantum Information* (Cambridge Univ. Press, 2010).
2. C. L. Degen, F. Reinhard, P. Cappellaro, *Rev. Mod. Phys.* **89**, 035002 (2017).
3. T. D. Ladd *et al.*, *Nature* **464**, 45 (2010).
4. M. Atzori, R. Sessoli, *J. Am. Chem. Soc.* **141**, 11339 (2019).
5. F. Lombardi *et al.*, *Science* **366**, 1107 (2019).
6. R. M. Brown *et al.*, *Phys. Rev. B* **82**, 033410 (2010).
7. S. Nakazawa *et al.*, *Angew. Chem. Int. Ed.* **51**, 9860 (2012).
8. J. M. Zadrozny, J. Niklas, O. G. Poluektov, D. E. Freedman, *ACS Cent. Sci.* **1**, 488 (2015).
9. J. Ferrando-Soria *et al.*, *Coord. Chem. Rev.* **339**, 17 (2017).
10. L. M. K. Vandersypen *et al.*, *Nature* **414**, 883 (2001).
11. M. J. Graham, J. M. Zadrozny, M. S. Fataftah, D. E. Freedman, *Chem. Mater.* **29**, 1885 (2017).
12. N. C. Seeman, H. F. Sleiman, *Nat. Rev. Mater.* **3**, 17068 (2017).
13. D. D. Awschalom, R. Hanson, J. Wrachtrup, B. B. Zhou, *Nat. Photonics* **12**, 516 (2018).

### ACKNOWLEDGMENTS

D.E.F. and S.v.K. acknowledge support from the U.S. Department of Energy, Office of Science, Basic Energy Sciences under award no. DE-SC0019356.

10.1126/science.aaz4044

## NEUROSCIENCE

# Regulation of negative emotional behavior

## A lower-brainstem structure regulates a psychobehavioral state for avoidance behavior

By Satoshi Ikemoto

Animals and humans must interact with the environment to meet biological needs and avoid dangers. Thus, survival relies on the balance between approach and avoidance behaviors. The median raphe region (MRR), located in the lower brainstem, may play an important role in this balancing process. It is one of two major regions that contain serotonergic neurons that project to the forebrain. The neurotransmitter serotonin is known for the regulation of anxiety and mood. On page 1094 of this issue, Szőnyi *et al.* (1) examined a neglected neuron type—glutamatergic neurons in the MRR that express the vesicular glutamate transporter 2 (vGLUT2)—and show that these MRR-vGLUT2 neurons have a vital role in the regulation of negative emotional states. Their findings have considerable implications for understanding psychiatric illnesses, particularly anxiety and mood disorders.

Accumulating evidence suggests that the MRR suppresses appetitive behaviors. The inhibition of MRR neurons in rodents results in compulsive displays of a variety of behaviors, including feeding, drinking, gnawing, locomotor activity, and reward-seeking behavior (2–4). Moreover, these manipulations induce psychobehavioral states characterized as being anxiolytic and, even, rewarding (5–8). Conversely, the excitation of MRR neurons induces behavioral inhibition and anxiogenic effects (9). Although selective manipulations of MRR serotonergic neurons produce similar, but generally weaker, effects, it has not been investigated how other types of MRR neurons contribute to such behavioral effects. Indeed, until now, no research had been conducted on the functions of MRR-vGLUT2 neurons.

Szőnyi *et al.* found that MRR-vGLUT2 neurons robustly project to three brain regions in mice that have been implicated in the regulation of negative emotional states and memory: the lateral habenula (LHb), the

medial ventral tegmental area (mVTA), and the medial septum and the vertical limbs of the diagonal bands of Broca (MS/VDB) (see the figure). The LHb mediates negative emotion, and its dysregulation has been strongly implicated in major depression (10). Szőnyi *et al.* show that MRR-vGLUT2 neurons establish synapses on LHb-vGLUT2 neurons and confirm that MRR-vGLUT2 neurons release glutamate to provide excitatory inputs to LHb-vGLUT2 neurons. In addition, LHb-vGLUT2 neurons establish excitatory synapses on MRR-vGLUT2 neurons. These results suggest a positive feedback loop between MRR-vGLUT2 neurons and LHb neurons, perhaps for mediating negative emotion-associated functions. Indeed, the presentation of aversive stimuli, which is known to activate LHb neurons, activated MRR-vGLUT2 neurons. In addition, selective stimulation of MRR-vGLUT2 neurons induced negative emotional effects: It increased aggression; when stimulation was paired with the response that delivered food, it diminished the food-seeking responses in hungry mice; and when paired with a place, mice avoided the place. Moreover, repeated stimulation of MRR-vGLUT2 neurons over the course of several weeks resulted in depression-like symptoms in mice.

Threatening environments activate dopamine neurons projecting to various forebrain regions. Particularly, those located in the mVTA and projecting to the medial prefrontal cortex are most sensitive to environmental challenges (11). MRR-vGLUT2 neurons were found to form synapses with such dopamine neurons. These dopamine neurons received inputs from both MRR-vGLUT2 neurons and LHb neurons, suggesting that MRR-vGLUT2 neurons, as well as LHb neurons, regulate the activity of dopamine neurons projecting to the medial prefrontal cortex when animals must cope with environmental challenges.

The hippocampus is critical in memory formation (12) and the MRR plays an important role in hippocampus-dependent memory (13). Szőnyi *et al.* show that MRR-vGLUT2 neurons robustly project to the MS/VDB and establish synapses on MS/VDB neurons that project to the hippocampus.

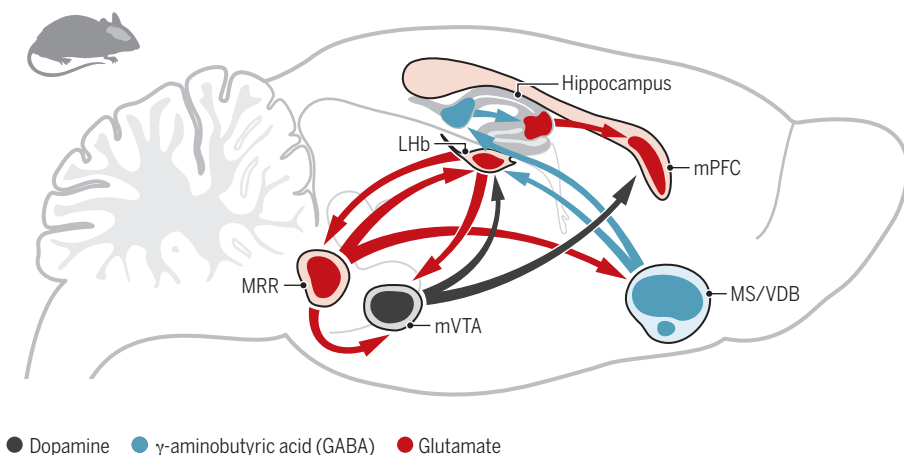
National Institute on Drug Abuse, National Institutes of Health, 251 Bayview Boulevard, Suite 200, Baltimore, MD 21224, USA. Email: satoshi.ikemoto@nih.gov

The MS/VDB plays a critical role in generating hippocampal theta oscillations (HTOs), which are indicative of cognitive processing of environmental information (12). HTOs are coupled with firing activity of LHB neurons (14). Such activity of the two structures may signify a role in the acquisition of emotional memory and may be coordinated by the MS/VDB, which projects to both the hippocampus and LHB (15). Because both MS/VDB and LHB neurons received inputs from the same MRR-vGLUT2 neurons, it is possible that MRR-vGLUT2 neurons contribute to coordinating activities between

sive contexts, MRR-vGLUT2 neurons may be important for active avoidance. LHB-vGLUT2 neurons have synaptic contacts with serotonergic neurons within the MRR, which suggests that LHB-vGLUT2 neurons directly activate serotonergic neurons. Therefore, dysregulation of MRR-vGLUT2 neurons could participate in anxiety and mood disorders by disrupting a positive-feedback interaction with LHB neurons regulating forebrain serotonin, in addition to disrupting the activities of the mVTA and MS/VDB. Such ideas are to be examined by future research. ■

## Neurocircuitry in aversive learning

MRR-vGLUT2 neurons regulate negative emotional behavior in mice through three key structures: LHB-vGLUT2 neurons, mVTA-dopamine neurons, and MS/VDB GABAergic neurons. These structures are linked with the hippocampus and mPFC to regulate higher-order processes, including aversive learning.



LHB, lateral habenula; mPFC, medial prefrontal cortex; MRR, median raphe region; MS/VDB, medial septum and the vertical limbs of the diagonal bands of Broca; mVTA, medial ventral tegmental area; vGLUT2, vesicular glutamate transporter 2.

the hippocampus and the LHB. Therefore, Szőnyi *et al.* hypothesized that MRR-vGLUT2 neurons regulate the acquisition of aversive memory and found that the inhibition of MRR-vGLUT2 neurons during the occurrence of aversive events reduced subsequent avoidance responses triggered by cues that had been previously paired with aversive events. Thus, MRR-vGLUT2 neurons appear to play a role in encoding aversive events for recall.

Unlike the ideas that emerge from non-selective manipulations of neurons, the findings of Szőnyi *et al.* suggest that MRR-vGLUT2 neurons actively regulate negative emotional state. Avoidance behavior can be categorized in two ways—passive avoidance (withdrawal or suppression of ongoing behavior) and active avoidance or active coping behavior—and distinct neural mechanisms are involved between these two behavioral strategies. Because the stimulation of MRR-vGLUT2 neurons increased, instead of decreased, behavioral activity in aver-

## REFERENCES AND NOTES

1. A. Szőnyi *et al.*, *Science* **366**, eaay8746 (2019).
2. M.A. Klitenick, D. Wirtshafter, *Behav. Neural Biol.* **51**, 436 (1989).
3. D. Wirtshafter, T.R. Stratford, M.R. Pitzer, *Behav. Brain Res.* **59**, 83 (1993).
4. A. Lê Dzung *et al.*, *Psychopharmacology (Berl.)* **195**, 605 (2008).
5. P.J. Fletcher, Z.H. Ming, G.A. Higgins, *Psychopharmacology (Berl.)* **113**, 31 (1993).
6. R. Shin, S. Ikemoto, *Psychopharmacology (Berl.)* **208**, 545 (2010).
7. Z.H. Liu, S. Ikemoto, *Eur. J. Neurosci.* **25**, 735 (2007).
8. S.E. File, L.E. Gonzalez, N. Andrews, *J. Neurosci.* **16**, 4810 (1996).
9. L. dos Santos, T.G.C. S. de Andrade, H. Zangrossi Jr., *Psychopharmacology (Berl.)* **179**, 733 (2005).
10. C.D. Proulx, O. Hikosaka, R. Malinow, *Nat. Neurosci.* **17**, 1146 (2014).
11. A.F.T. Arnsten, M.A. Raskind, F.B. Taylor, D.F. Connor, *Neurobiol. Stress* **1**, 89 (2015).
12. G. Buzsáki, E.I. Moser, *Nat. Neurosci.* **16**, 130 (2013).
13. D.V. Wang *et al.*, *Nat. Neurosci.* **18**, 728 (2015).
14. H. Aizawa *et al.*, *J. Neurosci.* **33**, 8909 (2013).
15. G.W. Zhang *et al.*, *Neuron* **99**, 1016 (2018).

## ACKNOWLEDGMENTS

The author is supported by the Intramural Research Program of the National Institute on Drug Abuse.

10.1126/science.aaz8638

## MOLECULAR BIOLOGY

# An unexpected cofactor

A mystery of bacterial chromosome segregation is explained by a nucleotide cofactor

By Barbara E. Funnell

Accurate chromosome segregation is essential for organisms in all kingdoms of life. In bacteria, which do not compartmentalize their chromosomes into nuclei or undergo mitosis, this process is as important as it is in eukaryotes. Bacterial chromosomes typically contain centromere partition sites (*parS*). Centromeres are DNA sites necessary for segregation, which is generally called “partition” in bacteria. The *parS* sites are bound by centromere-binding ParB (partition protein B) proteins. On page 1129 of this issue, Soh *et al.* (1) report the unexpected and remarkable discovery that ParB proteins use cytidine triphosphate (CTP) as a cofactor when they assemble partition complexes, and that ParB is an enzyme capable of CTP hydrolysis in addition to its DNA binding activities. ParB proteins interact with partition adenosine triphosphatases (ATPases) called ParA and, until the study of Soh *et al.*, ATP was believed to be the only nucleotide cofactor required in this type of partition reaction.

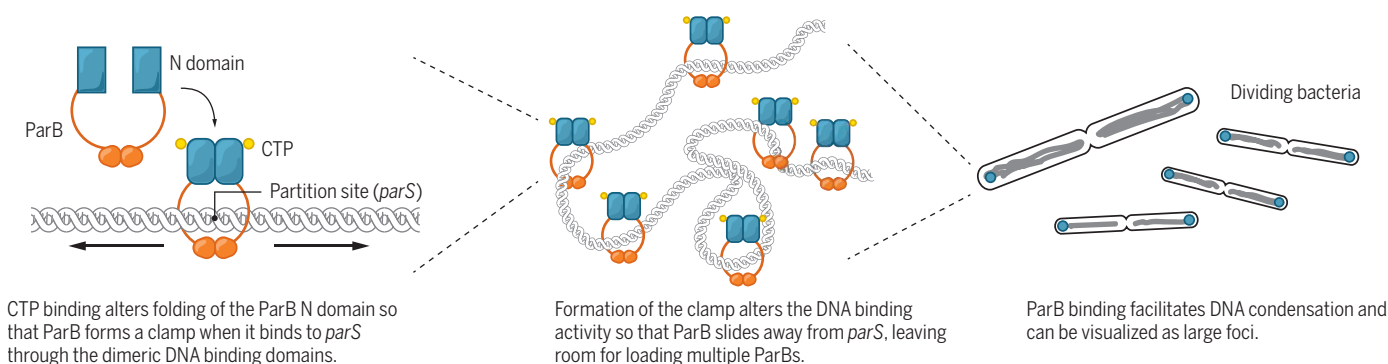
ParABS partition systems facilitate the separation of cellular chromosomes and many plasmids (DNA molecules that replicate independently of the cellular chromosome) (2, 3). ParB proteins were first identified in plasmid partition systems over 35 years ago, and the addition of CTP to the story is an unprecedented and major advance for the field. ParBs share limited sequence conservation among bacterial species and plasmids but possess a common domain arrangement. A central helix-turn-helix DNA binding domain is flanked by a carboxyl-terminal dimer domain (C) and a flexible amino-terminal domain (N) that can interact with itself and with ParA. The region of highest sequence conservation among ParBs is in the N domain and

Department of Molecular Genetics, University of Toronto, Toronto, Ontario M5G 1M1, Canada. Email: b.funnell@utoronto.ca



# The bacterial segrosome

An unusual cofactor, cytidine triphosphate (CTP), is found to promote partition protein B (ParB) binding to DNA for segregation.



resembles an ATP binding motif that occurs in sulfiredoxin (Srx), a eukaryotic protein involved in reduction of the hyperoxidized sulfinic acid form of cysteine (4). This ParB-Srx motif was noted but not originally explored because many experiments showed that the ATPase in ParABS systems was ParA. Soh *et al.* revisited the question over the ParB-Srx motif using ParB from *Bacillus subtilis*, and discovered that it binds CTP and not ATP. Furthermore, they showed that this is a general property because two plasmid ParBs also bound CTP.

ParB proteins exhibit two properties that require the N domain and reflect assembly of multiple molecules of ParB at *parS*. Large foci of ParB are visible in cells when ParB is fluorescently labeled (5), indicating that many hundreds of ParB molecules coalesce near or at *parS*. When measured directly, ParB binding is concentrated at *parS* but also “spreads” to surrounding nonspecific DNA, typically extending many kilobases away from *parS* (6, 7). The ParA ATPase interacts with these large ParB-*parS* partition complexes, and ParA acts as the motor to drive chromosomal movement. However, reconstituting the higher-order ParB complex assembly biochemically has proven challenging, in part because the ParB-ParB interactions between N domains are weak and dynamic (8, 9). The study by Soh *et al.* reveals that the magic ingredient missing in these experiments and in the models of ParB assembly is CTP.

The results lead to a new and intriguing model for how large partition complexes assemble and spread on DNA. Recent models have suggested that ParBs spread by a combination of lateral and bridging interactions across their N domains (8, 9). By contrast, Soh *et al.* propose that CTP binding promotes self-association of the N domain, which closes a “gate” so that ParB encircles DNA after it loads onto *parS* (see the figure).

When the gate closes, ParB is locked onto the DNA but released from *parS* so that it is free to slide; that is, to spread along DNA and form foci. CTP hydrolysis is not necessary at this step, and its role remains to be elucidated. The different spreading models are not mutually exclusive, and further studies are needed to understand the exact architecture involved.

The discovery of CTP as a cofactor opens the door to a wealth of experiments studying ParABS partition. Many different approaches that previously examined ParB proteins will likely be revisited to ask how CTP binding and hydrolysis contribute to ParB action. How does ParB condense *parS*

tates chromosome separation (10), but the mechanistic details of this process are not completely understood and are the focus of much current research. It will be important to understand how the architecture of ParB-CTP-*parS* complexes fits into, and perhaps alters, models of ParA action.

CTP is an unusual nucleotide cofactor in any enzyme outside of those involved in nucleotide metabolism. A recent example is LarC, a bacterial enzyme involved in nickel cofactor synthesis, which requires CTP binding and hydrolysis for activity (11). It seems that prokaryotic ParABS-mediated partition has reserved ATP for ParA and exploited CTP for ParB, implying that the division of nucleotide labor will be important for the regulation of the process. Soh *et al.* suggest that the ParB-Srx CTP binding domain is conserved in diverse proteins. Did CTP binding evolve from the ATP active site of a ParB-Srx motif or vice versa? Moreover, it is important to investigate whether there are other CTP-protein interactions that have been missed simply because no one thought to look for them. ■

“...it is important to investigate whether there are other [cytidine triphosphate]-protein interactions that have been missed...”

sites so that they group together, especially to form the large assemblies visualized as foci inside cells? There are x-ray crystal structures of fragments of ParB, but the full-length protein has proven refractory to crystallization so no complete structure has been solved; will CTP alter protein folding in such a way that makes these approaches feasible? The door is wide open for other biophysical approaches such as cryo-electron microscopy to examine large ParB structures, in the presence of CTP and DNA, to directly visualize the complexes and explore the mechanisms of complex assembly.

Key questions to address are how CTP affects ParB-ParA interactions, and what roles such interactions play in the mechanism of partition. ParA, which binds nonspecifically to the bacterial chromosome in the presence of ATP, forms dynamic gradients of DNA binding in the presence of ParB. The large complexes of ParB at *parS* move along these gradients, which facili-

## REFERENCES AND NOTES

1. Y.-M. Soh *et al.*, *Science* **366**, 1129 (2019).
2. A. Badrinarayanan, T. B. K. Le, M. T. Laub, *Annu. Rev. Cell Dev. Biol.* **31**, 171 (2015).
3. J.-Y. Bouet, B. E. Funnell, *Ecosol Plus* **8**, ESP-0003 (2019).
4. M. K. Basu, E. V. Koonin, *Cell Cycle* **4**, 947 (2005).
5. D. C.-H. Lin, P. A. Levin, A. D. Grossman, *Proc. Natl. Acad. Sci. U.S.A.* **94**, 4721 (1997).
6. O. Rodionov, M. Lobočka, M. Yarmolinsky, *Science* **283**, 546 (1999).
7. A. M. Breier, A. D. Grossman, *Mol. Microbiol.* **64**, 703 (2007).
8. T. G. W. Graham *et al.*, *Genes Dev.* **28**, 1228 (2014).
9. R. E. Debaugny *et al.*, *Mol. Syst. Biol.* **14**, e8516 (2018).
10. A. G. Vecchiarelli, K. C. Neuman, K. Mizuuchi, *Proc. Natl. Acad. Sci. U.S.A.* **111**, 4880 (2014).
11. B. Desguin *et al.*, *J. Biol. Chem.* **293**, 12303 (2018).

## ACKNOWLEDGMENTS

The author is supported by Canadian Institutes of Health Research grant 133613.

10.1126/science.aaz8632

## IMMUNOLOGY

# Immunology taught by vaccines

Systems analysis of vaccine responses reveals the impact of the microbiota on human immunity

By **Bali Pulendran**

**D**espite the success of vaccination in controlling many infectious diseases, there are challenges in designing vaccines against HIV, malaria and tuberculosis, and other pathogens that, in aggregate, afflict billions of people. Vaccine development has been frustrated by a lack of detailed understanding about what types of immune responses are effective at preventing infection, and failure to translate successes in animal models to humans. This problem is compounded by the variability in vaccine efficacy in humans. For example, vaccines against oral pathogens such as *Rotavirus* and *Poliomyelitis* have considerably lower efficacy in children in some low- and middle-income countries (LMICs) compared to those in high-income countries (1). Environmental differences, persistent parasitic infections, malnutrition, and environmental enteropathy may affect immune system function and its ability to respond to vaccination (1, 2). Several studies have also suggested that intestinal microbiota composition plays a role (1, 2).

The microbiota consists of trillions of bacteria in the human gut and in other peripheral tissues such as the skin and lungs, and they outnumber human cells 10-fold (3). Emerging evidence suggests a potent role for this microbial universe in shaping many aspects of physiology, including the immune system, the cardiovascular system, and various aspects of host metabolism (2, 3). Loss of microbial diversity in microbiota (dysbiosis) is strongly associated with many inflammatory diseases, and intestinal dysbiosis is linked to reduced efficacy of various immune interventions, including prevention of HIV infection and immune checkpoint blockade, a form of cancer immunotherapy. However, much of the evidence for this comes from elegant studies in mice administered antibiotics to deplete their microbiota, or in germ-free mice that are devoid of any bacteria from birth. The extent to which these results reflect what happens in humans is uncertain. Many studies have established correlations between particular

species of bacteria and various aspects of human physiology, but there remains little causal evidence.

Immunologists have recently harnessed vaccines as probes to study the human immune system. Systems biological approaches that can measure the expression of genes, proteins, metabolites, and immune cell types have been used to study immune responses to vaccination. The first examples of such studies used the live attenuated yellow fever vaccine (YF-17D) (4, 5), which has been administered to 600 million people worldwide and is one of the most effective vaccines developed. Blood gene expression “signatures” induced within a few days of vaccination with YF-17D correlated with the ensuing CD8<sup>+</sup> T cell and neutralizing antibody response. Machine learning techniques delineated signatures capable of predicting the immunogenicity of the vaccine in individuals (4). Subsequently, systems approaches have been used to identify signatures that predicted the immunogenicity of other vaccines, such as the inactivated seasonal influenza vaccine or malaria vaccine, in diverse populations such as the elderly, infants, and identical twins and in geographically distinct populations (6–8). Such signatures reflect a range of biological processes, such as the early innate immune response and amino acid starvation response, as well as signatures of the antibody-producing cell response (4–8).

Several mechanistic insights have emerged from these studies. One such insight concerns the impact of the microbiota on vaccination in humans. Analysis of blood transcriptional responses induced by vaccination of healthy adults with the inactivated seasonal influenza vaccine revealed a strong correlation between the early expression of the gene encoding Toll-like receptor 5 (*Tlr5*), an innate immune receptor that senses bacterial flagellin, on day 3 after vaccination and the ensuing vaccine-specific antibody titers measured 28 days after vaccination (9). The association between the antibody response to a viral vaccine and the expression of a receptor involved in bacterial sensing was puzzling and suggested a potential link between microbiota and vaccination-induced immunity. Vaccination of mice genetically deficient in *Tlr5* (*Tlr5*<sup>−/−</sup> mice) resulted in impaired antibody responses (9). Antibody responses to influenza vaccination were also impaired

in germ-free mice and mice administered broad-spectrum antibiotics. Moreover, *Tlr5*<sup>−/−</sup> mice and antibiotic-administered mice had impaired antibody responses to the inactivated polio vaccine, which, like the inactivated seasonal influenza vaccine, contains no exogenous adjuvants (or immune-boosting agents). By contrast, *Tlr5*<sup>−/−</sup> mice or antibiotic-administered mice were capable of mounting normal antibody responses to vaccines that contained adjuvants such as the alum-adjuvanted tetanus, diphtheria, and pertussis vaccines (9). This raised the concept that the microbiota could be serving as “endogenous adjuvants” that boost immunity to vaccines lacking adjuvants.

The possibility that the microbiota plays a role in modulating immune responses to vaccination in humans is of particular concern because vaccines are less effective in many regions of LMICs, where widespread and indiscriminate use of antibiotics, particularly in neonates and infants, could cause long-lasting changes in the microbiota (1). However, the effects of the antibiotic azithromycin were examined on the immunogenicity of oral polio vaccine in seronegative infants in India, and the antibody response was unaffected (10). Of note, detailed analysis of immune responses was not performed in this study, so further investigation is warranted.

To comprehensively assess the impact of the microbiota in humans, a clinical trial was performed in which a cocktail of broad-spectrum antibiotics was given to healthy young adults before and after vaccination with the inactivated seasonal influenza vaccine (11). Antibiotics administration resulted in a 10,000-fold reduction in the total quantity of gut bacteria, but this effect was short-lived and normal numbers were regained within a few days. Furthermore, gut bacterial diversity was reduced, and this took longer than 6 months to recover (11). Nonetheless, the antibody responses to vaccination were unaffected. The individuals in this study had high concentrations of influenza-specific antibodies prior to vaccination, indicating recent exposure to the vaccine or influenza virus. Another clinical trial was conducted in which anyone who had either received the influenza vaccine or had been exposed to influenza during the past 3 years was excluded. There was a marked impairment in the immunoglobulin G1 (IgG1) and IgA antibody response specific to the H1N1 strain of influenza, as well as in antibody neutralization to the H1N1 strain (11). In humans, the serum antibody response to vaccination with seasonal influenza vaccine is dominated by the IgG1 subclass (with lower contributions from IgM and IgA antibodies), and IgG1 antibodies can neutralize the virus as well as mediate a range of effector

Institute for Immunity, Transplantation and Infection, School of Medicine, Stanford University, Stanford, CA 94305, USA. Email: bfulend@stanford.edu



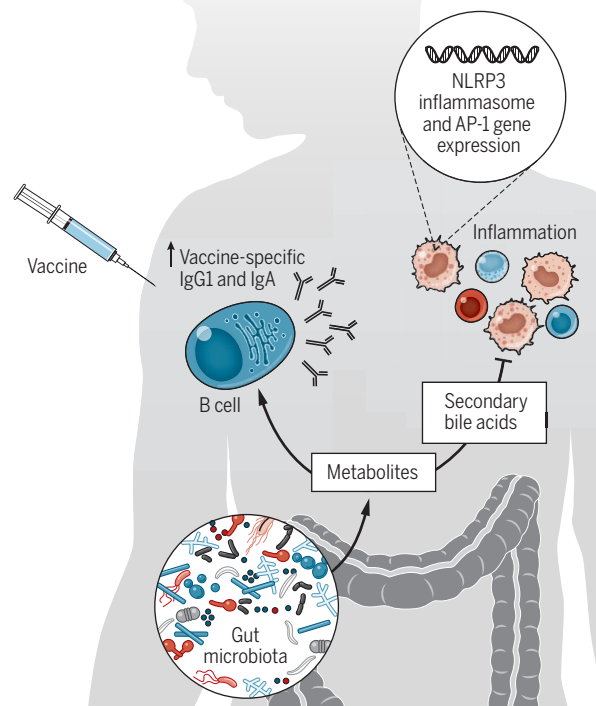
cell functions. Curiously, the impairment in IgG1 and IgA responses was only observed against one of the three influenza strains contained in the vaccine—the H1N1 strain—and not against the H3N2 or B strains. The reason for this is unclear, but it is possible that adults have high H3N2 and B subtype immunological memory due to prior exposure, and thus a higher threshold of memory against these strains could withstand the effects of antibiotics. Thus, the adaptive immune response truly does seem to be adaptive, and resilient to even the most severe perturbations in the microbiota. This resilience of the adaptive immune system is evident in the context of genetic variation. Thus, a previous study has demonstrated that responses to influenza vaccination in identical twins were largely driven by environmental factors such as prior immune exposure and were independent of genetic factors (8).

In addition to these effects on the adaptive immune response, analysis of transcriptional signatures revealed that antibiotics treatment resulted in enhanced innate immune responses, specifically inflammation and in particular several gene expression programs associated with the transcription factors activating protein 1 (AP-1, comprising FOS and JUN) and nuclear receptor 4A1 (NR4A1), which play central roles in mediating inflammatory responses (17) (see the figure). These same transcriptional modules were increased in healthy elderly subjects immunized with the seasonal influenza vaccine (6). These results indicate that antibiotics-driven depletion of the gut microbiota may drive inflammatory responses to vaccines similar to age-associated increases in inflammation and that frequent and long-term usage of antibiotics may accelerate the process called “inflammaging,” a chronic low-grade inflammation that can develop with advanced age and contribute to the pathogenesis of age-associated diseases (12). Future studies should thus explore the potential connection between antibiotics usage, inflammaging, and impaired vaccine immunity in the elderly.

In addition to the effects on the adaptive and innate immune responses, antibiotics administration induced a large perturbation in the blood metabolome of young adults receiving inactivated seasonal influenza vaccine, including changes in bile acids, such as lithocholic acid (LCA). LCA is the most potent agonist of G protein-coupled bile acid receptor 1 (GPBAR1), which inhibits

## The gut microbiota affects vaccination

In healthy humans, the gut microbiota enhances antigen-specific immunoglobulin G1 (IgG1) and IgA antibody responses to vaccination. Secondary bile acids metabolized by gut microbiota suppress excessive inflammation driven by NACHT, LRR, and PYD domains-containing protein 3 (NLRP3) inflammasome and activating protein 1 (AP-1)-associated gene expression.



activation of the NACHT, LRR, and PYD domains-containing protein 3 (NLRP3) inflammasome, a multiprotein complex that detects pathogens and other stress-inducing signals leading to activation of innate immunity, in mice (13). Moreover, antibiotics-driven perturbation of secondary bile acids was associated with increased inflammation, including modules involved in AP-1 signaling and NLRP3 inflammasome activation. These results highlight a potential mechanism by which the microbiota can regulate secondary bile acid production and consequently inflammatory responses in humans, which can also affect vaccine responses. To what extent the dysbiosis-secondary bile acid-inflammation axis contributes to inflammaging in the elderly remains to be determined. It should also be noted that increased gut permeability, which increases with age, could result in systemic exposure to bacterial stimuli such as lipopolysaccharide, flagellin, and other pathogen-associated molecular patterns that could directly trigger up-regulation of the AP-1 and NR4A1 signaling pathways. Further studies in elderly people should thus explore the mechanisms by which gut dysbiosis modulates inflammaging and the age-associated decline in immune function

known as immunosenescence.

These results could have several public health implications. Given that the impact of antibiotics on the antibody response was only evident in subjects with low baseline concentrations of antibody, it could be advantageous to receive the influenza vaccine annually to build up immune memory. A second implication concerns the potential effects of antibiotics on neonates or infants, in which immune imprinting to influenza may be minimal or nonexistent. In infant mice, antibiotics-driven early-life dysbiosis leads to altered vaccine responses (14). A relatively sterile 9-month-old baby in utero experiences a microbial “big bang” during birth, and this microbial universe continues to expand during the first few years of life. The widespread use of antibiotics in neonates and infants raises the possibility that antibiotics-driven gut dysbiosis may exert a considerable toll on vaccination-induced immunity in the very young. Furthermore, antibiotics-driven microbiota disruptions in early life can have long-lasting effects on body weight in adulthood, long after cessation of antibiotics (15). It is therefore possible that antibiotics treatment during childhood could exert long-lasting effects on the immune system, perhaps through epigenetic imprinting. Future studies should thus be aimed at exploring both the short- and long-term effects of antibiotics on vaccine immunity in the very young. In addition, the microbiota-inflammaging axis in aging and its impact on vaccine immunity deserve attention. ■

## REFERENCES AND NOTES

1. I. Praharaj, S. M. John, R. Bandyopadhyay, G. Kang, *Philos. Trans. R. Soc. Lond. B Biol. Sci.* **370**, 20140144 (2015).
2. N. Collins, Y. Belkaid, *Cold Spring Harb. Perspect. Biol.* **10**, a028860 (2018).
3. H. Tilg, N. Zmora, T. E. Adolph, E. Elinav, *Nat. Rev. Immunol.* **10**, 1038/s41577-019-0198-4 (2019).
4. T. D. Querec et al., *Nat. Immunol.* **10**, 116 (2009).
5. D. Gaucher et al., *J. Exp. Med.* **205**, 3119 (2008).
6. H. I. Nakaya et al., *Immunity* **43**, 1186 (2015).
7. J. S. Tsang et al., *Cell* **157**, 499 (2014).
8. P. Brodin et al., *Cell* **160**, 37 (2015).
9. J. Z. Oh et al., *Immunity* **41**, 478 (2014).
10. N. C. Grassly et al., *Lancet Infect. Dis.* **16**, 905 (2016).
11. T. Hagan et al., *Cell* **178**, 1313 (2019).
12. C. Franceschi, P. Garagnani, P. Parini, C. Giuliani, A. Santoro, *Nat. Rev. Endocrinol.* **14**, 576 (2018).
13. C. Guo et al., *Immunity* **45**, 802 (2016).
14. M. A. Lynn et al., *Cell Host Microbe* **23**, 653 (2018).
15. L. M. Cox et al., *Cell* **158**, 705 (2014).

## ACKNOWLEDGMENTS

I am supported by the National Institutes of Health and the Bill and Melinda Gates Foundation for the research performed in my laboratory.

10.1126/science.aau6975

## GEOPHYSICS

# Illuminating Earth's faults

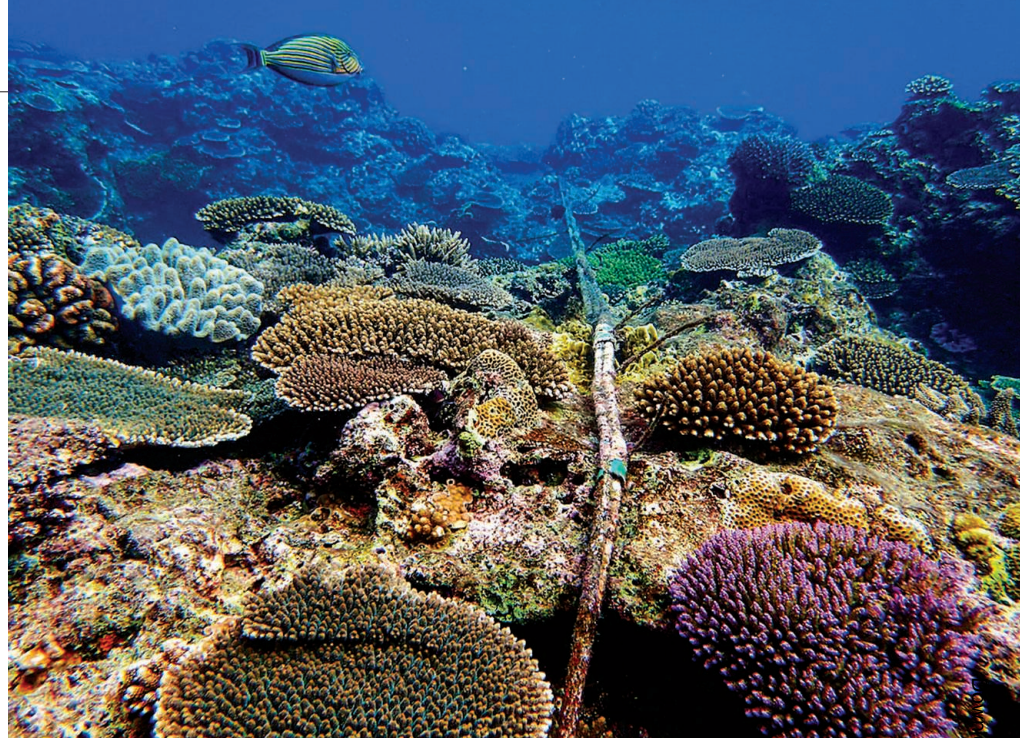
Submarine fiber-optic cables drive discovery of fault locations and ocean dynamics

By Philippe Jousset

Earthquakes are primarily caused by movement of big land masses—tectonic plates—at large physical fractures in Earth's crust (faults). Furthermore, faults sometimes convey mineral-rich fluids, oil, gas, and hot water and thus contribute to our mineral and energy resources. Unfortunately, scientists do not yet know where all of Earth's faults are located, especially when they reside under cities or the seafloor, where their movement can produce large earthquakes and tsunamis. Without a complete map of Earth's faults, economic opportunities may be overlooked and seismic hazards may be underestimated. On page 1103 of this issue, Lindsey *et al.* (1) describe the use of a method—distributed acoustic sensing (DAS)—that makes it possible to discover previously unidentified faults in Monterey Bay, California, the United States.

Various technological developments have allowed scientists to see billions of kilometers, from Earth to space (2), but the underground details of our own planet have remained elusive. Drilling into Earth's crust is an accurate but expensive way to explore what is beneath our feet and also sometimes inflicts environmental damage (3). Fortunately, scientists can probe Earth's interior from its surface with the use of geophysical methods. The main internal structures of our planet were mapped by recording travel times of seismic waves between the source (the fault) and the sensors (seismometers). Furthermore, the imaging of Earth by analyzing seismic ambient noise (microseism) can pinpoint faults (4). This technique requires a large number of well-distributed seismometers, which is not always feasible, especially in underwater locations.

DAS, the relatively new method used by Lindsey *et al.* in Monterey Bay, consists of



DAS technology allows fault mapping and the study of ocean hydrodynamics when used to probe fiber-optic cables on the seafloor that transmit information from submarine observatories (here, Okinawa Institute of Science and Technology Graduate University).

probing a fiber-optic cable with successive coherent laser pulses and using a spectrometer to analyze time of flight and frequency properties of the photons that are reflected back in the direction from which they originated (so-called back-scattered light). This method allows dense, spatially distributed measurement of dynamic strain that results from passing seismic waves along several-kilometers-long fibers. These fiber-optic cables are similar to those typically used for telecommunication and internet transmission. For several years, the oil and gas industry has used DAS with cables deployed in boreholes to image near well-bore areas. In Iceland, DAS was used recently to map land faults at the Earth surface by using telecommunication cables (5). Although DAS is rapidly finding new uses in a variety of disciplines, it is expected to make seminal contributions to geophysical studies as Earth's unknown structural and seismological features can be probed with great accuracy.

One of the most exciting new features of the Lindsey *et al.* study is that the interrogated fiber-optic cable lies underwater. Earthquakes might occur deep in Monterey Bay, where little is known about fault locations. The cable is part of the transmission system for data on underwater activity and aquatic organisms acquired by the Monterey Accelerated Research System (MARS). Most oceanographic instruments that reside on the seafloor have no connection with the land or sea surfaces, so they must run on batteries and store their own data. The MARS cabled observatory removes these restrictions by providing a power supply

for the submarine instruments and transmitting their data to the surface through a fiber-optic cable.

During a 4-day period of cable maintenance, Lindsey *et al.* connected the MARS fiber-optic cables to a DAS interrogator, an instrument that transmits photons in the fiber and analyzes backscattered light. After 4 days of continuous measurement, the authors used the resulting strain data to map previously unknown faults and to hypothesize mechanisms for sources of the microseism.

Another unexpected result from the new study was the ability to record very-long-period strain signals (larger than 10 s), which the authors interpreted as being associated with oceanic hydrodynamics, such as currents modulated by tides. This interpretation remains to be validated in longer studies (more than 4 days) and with other submarine cables.

Other such underwater observatories exist in the world—for example, the European Multidisciplinary Seafloor and Water-column Observatory (EMSO), which has sensors in the Atlantic Ocean and the Mediterranean and Black seas (6). EMSO was designed to gain a better understanding of phenomena occurring in the ocean and below the ocean floor and to decipher the role that these phenomena play in Earth's systems. The ocean floor is a favorable location for detection of seismic events in marine tectonic areas precisely because this area is a critical source of tectonic movement. Through a network of subsea seismometers, the interactions of tectonic plates can

Helmholtz Center Potsdam, GFZ German Research Centre for Geosciences Near-surface Geophysics, Albert Einstein Str. 42-46, 14473 Potsdam, Germany. Email: philippe.jousset@gfz-potsdam.de



be further elucidated. The study of seabed seismic activity can yield a better hazard assessment, thus improving detection, early-warning protocols, emergency response, and disaster preparedness.

As in Monterey Bay, EMSO sea observatories are linked to the shore by optical cables that can be used in concert with DAS and complement the SMART (Science Monitoring And Reliable Telecommunications) cable approach (7). For example, a 41.5-km telecom cable from the EMSO facility in Toulon, France, is being used to measure seafloor strain and ocean–solid Earth interactions from the coast to the abyssal plain (8). Furthermore, two recent studies (9, 10) used EMSO local network service and DAS to explore complex volcanic structures on the seafloor east of Sicily. Eighty percent of volcanic activity occurs in the oceans, and because of inaccessibility, little is known about the characteristics of volcano structures and what they exude.

These studies and that of Lindsey *et al.* demonstrate that DAS is a powerful tool for studying a variety of phenomena on land and under the sea. Data from this diverse research inform scientists on Earth's structure and physical mechanisms that drive mineral deposition, geothermal-fluids migration, and volcanic processes. Fiber-optic networks already laid in cities for telecommunication can be used to assess underground seismic hazards without the need for dense networks of sensors and complement citizen-oriented initiatives such as the Seismic-Catcher network or LastQuake telecom mobile applications (11, 12). Machine learning and automatic classification algorithms are required to process these data in real time and are under development (13). ■

#### REFERENCES AND NOTES

1. N. J. Lindsey, T. C. Dawe, J. B. Ajo-Franklin, *Science* **366**, 1103 (2019).
2. H. Umehata *et al.*, *Science* **366**, 97 (2019).
3. K. M. Keranen, H. M. Savage, G. A. Abers, E. S. Cochran, *Geology* **41**, 699 (2013).
4. N. M. Shapiro, M. Campillo, L. Stehly, M. H. Ritzwoller, *Science* **307**, 1615 (2005).
5. P. Jousset *et al.*, *Nat. Commun.* **9**, 2509 (2018).
6. P. Favali, L. Beranzoli, *Nucl. Instrum. Methods Phys. Res. A* **602**, 21 (2009).
7. B. M. Howe *et al.*, *Front. Mar. Sci.* **6**, 424 (2019).
8. A. Sladen *et al.*, *EarthArXiv* 10.31223/osf.io/ekrfy (2009).
9. M.-A. Gutscher *et al.*, *Photoniques* **3**, 32 (2019).
10. G. Ricobene for the KM3NeT Collaboration, *EPJ Web Conf.* **207**, 09003 (2019).
11. E. S. Cochran, J. F. Lawrence, C. Christensen, R. Jakka, *Seismol. Res. Lett.* **80**, 26 (2009).
12. R. Bossu *et al.*, *Int. J. Disaster Risk Reduct.* **28**, 32 (2018).
13. R. Fielding, L. Davies, *First Break* **37**, 59 (2019).

#### ACKNOWLEDGMENTS

I thank C. Krawczyk, T. Reinsch, and G. Currenti for discussions and comments on the manuscript. This work was supported by the Helmholtz Association.

10.1126/science.aaz7750

#### IMMUNOTHERAPY

# Immunostimulatory gut bacteria

Some bacterial species stimulate inflammation, autoimmunity, and anticancer immunity

By Laurence Zitvogel<sup>1,2,3,4</sup> and Guido Kroemer<sup>4,5,6,7,8</sup>

**S**tudies of the nature of the human-microbial “superorganism” indicate that many diseases are linked to widespread alterations of this hybrid ecosystem. For example, inflammatory disorders and malignancies have been associated with shifts in the composition of the intestinal microbiota, causing a state of dysbiosis that reflects the pathological process and contributes to disease pathogenesis (1, 2). On page 1143 of this issue, Stein-Thoeringer *et al.* (3) find that shifts in several enterococcal bacteria species, in particular an increase in *Enterococcus faecium*, favor severe inflammatory and immune-mediated damage of the intestine in response to allogeneic hematopoietic cell transplantation (allo-HCT), which is used to treat hematological malignancies. This surge in *E. faecium* in the gut correlates with increased graft-versus-host disease (GVHD, in which immune cells from the donor attack the recipient) and reduced survival. These findings suggest that some enterococcal species may have immunostimulatory and pro-inflammatory effects.

Allo-HCT is a severe procedure that requires immunosuppressive preconditioning of patients with high-dose chemotherapy. Following up previous work that suggested that the microbiota modulates the clinical outcome of allo-HCT (4), Stein-Thoeringer *et al.* investigated 1325 adult allo-HCT recipients (organized into two cohorts, a discovery cohort and a multinational validation cohort) and observed a shift in the intestinal microbiota toward domination by enterococci. This shift had no impact on the advancement of the malignant disease, yet coincided with the presence of vancomycin-resistant enterococci (VRE). In several

mouse models of allo-HCT, the authors found a similar domination by enterococci, but also by another species, *E. faecalis*, which translocated beyond the intestinal barrier and into mesenteric lymph nodes. Enterococcal domination was accompanied by a reduction of commensal Clostridia, with the consequent diminution of the anti-inflammatory metabolite butyrate. Among the class of Clostridia, the genus *Blautia*, which produces an antibiotic protein that inhibits VRE (5), was also depleted, suggesting a systemic alteration of the gut microflora.

Analyses of the microbiome (bacterial genomes) from human allo-HCT recipients revealed increased expression of enzymes involved in degradation of the sugars lactose and galactose, which was associated with enterococcal domination. Mice undergoing allo-HCT exhibited a reduced expression of lactase (which degrades lactose) in their duodenum that was mediated by T cell-dependent inflammation, suggesting a state of lactose malabsorption and consequent increase of this disaccharide in the intestinal lumen. Both *E. faecium* and *E. faecalis* require lactose for their growth in vitro (they are lactose auxotrophs). Indeed, feeding mice undergoing allo-HCT with lactose-free chow reduced the *Enterococcus* bloom, mitigated the severity of GVHD, and reduced the signs of T cell activation. These data suggest a causal link between enterococcal domination and GVHD. Notably, Stein-Thoeringer *et al.* found that allo-HCT patients bearing a genetic polymorphism (rs4988235) that reduces lactase expression with attendant lactose malabsorption exhibited prolonged enterococcal domination compared to patients lacking such a polymorphism. These findings suggest that lactose is causally involved in the expansion and maintenance of enterococci in the fecal microbiota of patients. Whether rs4988235 and lactose intake influences the severity of GVHD in patients remains to be determined.

There are other clinical conditions in which enterococci may expand in the gut and contribute to disease pathogenesis. Proton pump inhibitors administered to mice cause the expansion of enterococci, including *E. faecalis* (6). This favors ethanol-induced steatohepatitis (fatty liver disease with inflammation) and involves bacterial translocation into the liver and subsequent inflammation. Patients with gastritis who are treated with

<sup>1</sup>Gustave Roussy Cancer Campus, Villejuif, France. <sup>2</sup>National Institute of Health and Medical Research (INSERM) U1015, Villejuif, France. <sup>3</sup>University Paris XI, Paris Saclay, France. <sup>4</sup>Suzhou Institute for Systems Biology, Chinese Academy of Medical Sciences, Suzhou, China. <sup>5</sup>Equipe labellisée par la Ligue contre le cancer, Université de Paris, Sorbonne Université, INSERM U1138, Centre de Recherche des Cordeliers, Paris, France. <sup>6</sup>Metabolomics and Cell Biology Platforms, Institut Gustave Roussy, Villejuif, France. <sup>7</sup>Pôle de Biologie, Hôpital Européen Georges Pompidou, AP-HP, Paris, France. <sup>8</sup>Karolinska Institute, Department of Women's and Children's Health, Karolinska University Hospital, Stockholm, Sweden. Email: laurence.zitvogel@orange.fr; kroemer@orange.fr

proton pump inhibitors also exhibit fecal expansion of enterococci, and patients with a diagnosis of chronic alcohol abuse have a higher probability of developing alcoholic liver diseases when they use proton pump inhibitors (6). *E. faecalis* expresses a metalloprotease that compromises the intestinal barrier (7). However, in mice, *E. gallinarum*, another *Enterococcus* species that expands with proton pump inhibitors (6) but less so in GVHD (3), compromises ileal barrier function more efficiently than does *E. faecalis*. When present as the dominant bacterial species in the gut, *E. gallinarum* can translocate to the mesenteric lymph node, spleen, and liver, triggering systemic autoimmunity (8).

Another *Enterococcus* species, *E. hirae*, has been found to translocate to the spleen in tumor-bearing mice treated with the chemotherapeutic agent cyclophosphamide. In this context, *E. hirae* improves cyclophosphamide-mediated tumor growth reduction

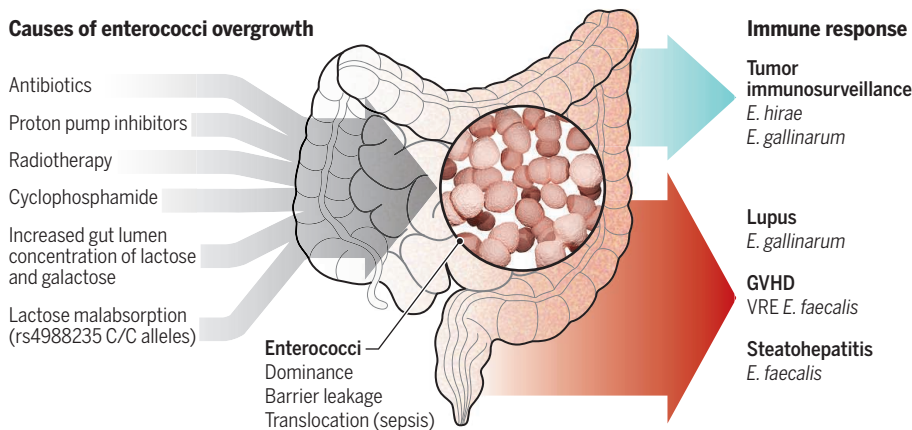
and anticancer immune responses (see the figure). Future research should compare the characteristics of different enterococcal species in a systematic fashion.

It will be important to determine to what extent different *Enterococcus* species and strains are lactose-auxotrophic. Adult lactose intolerance is a prevalent condition, especially among persons of non-European descent, and rs4988235 (lactase persistence) is associated with enhanced milk intake, higher waist circumference, and poor-prognosis cardiometabolic traits (12). Although lactase persistence has no impact on the mortality of the general population (13), it may be advisable to genotype patients at risk of enterococcal infection and to adapt their diet to avoid potentially lethal shifts in their intestinal flora. In addition, it may be useful to treat such patients with specific bacteria that prevent VRE outgrowth, improve intestinal barrier function, and reduce systemic inflammation. ■

## Enterococci in the intestinal ecosystem

Various factors favor the expansion and dominance of enterococci bacteria in the gut, which can lead to translocation to other organs. Dominance of certain *Enterococcus* species can affect inflammation and immunity. For example, vancomycin-resistant enterococci (VRE) can promote graft-versus-host disease (GVHD) in patients receiving allogeneic hematopoietic cell transplantation.

### Causes of enterococci overgrowth



through the stimulation of a T cell-mediated anticancer immune response (9). *E. hirae* also enhanced the efficacy of immune checkpoint blockade in mice with cancer (10). In cancer patients, the fecal abundance of *E. hirae* correlated with the efficacy of immune checkpoint blockade and was associated with improved outcome of chemoimmunotherapy in ovarian and non-small cell lung cancers (9–11).

It appears that a variety of medical treatments (allo-HCT, chemotherapy, immunotherapy, and proton pump inhibitors), as well as lactose intolerance, can favor the expansion of several species of enterococci in the gut, and that several enterococci are facultative pathogens that stimulate pathogenic inflammation of the gut, steatohepatitis, and systemic autoimmunity, yet can also elicit an-

### REFERENCES AND NOTES

1. K. Honda, D. R. Littman, *Nature* **535**, 75 (2016).
2. B. Routy *et al.*, *Nat. Rev. Clin. Oncol.* **15**, 382 (2018).
3. C. K. Stein-Thoeriger *et al.*, *Science* **366**, 1143 (2019).
4. Y. Taur *et al.*, *Blood* **124**, 1174 (2014).
5. S. G. Kim *et al.*, *Nature* **572**, 665 (2019).
6. C. Llorente *et al.*, *Nat. Commun.* **8**, 837 (2017).
7. N. Steck *et al.*, *Gastroenterology* **141**, 959 (2011).
8. S. Manfredo Vieira *et al.*, *Science* **359**, 1156 (2018).
9. R. Daillère *et al.*, *Immunity* **45**, 931 (2016).
10. B. Routy *et al.*, *Science* **359**, 91 (2018).
11. L. Zitvogel *et al.*, *Science* **359**, 1366 (2018).
12. Mendelian Randomization of Dairy Consumption Working Group, *Clin. Chem.* **65**, 751 (2019).
13. H. K. M. Bergholdt *et al.*, *Eur. J. Epidemiol.* **33**, 171 (2018).

### ACKNOWLEDGMENTS

L.Z. and G.K. are co-founders of everImmune, which develops microbes for the treatment of cancer. L.Z. holds patents on enterococcal anticancer probiotics.

10.1126/science.aaz7595

## MATERIALS SCIENCE

# Surface nanopatterning with polymer brushes

A variety of surfaces are patterned with precisely defined cylindrical micelles

By Alejandro Presa Soto

Rational design of patterned surfaces over multiple length scales can be achieved through chemical strategies for fine-tuning the composition and chemical functionality. For example, “grafting-from” methods can tailor the surface properties by using polymer brushes—thin polymer films in which polymer backbones are tethered to a solid interface by one chain end (1). Chemical strategies can pattern surfaces at molecular and macromolecular levels, but precise fabrication of nanopatterned surfaces that bear selected chemical functionalities is still challenging. On page 1095 of this issue, Cai *et al.* (2) present a versatile bottom-up strategy to fabricate well-defined nanostructures with precisely controlled chemical functionalities on a variety of surfaces.

Cylindrical micelles of controlled lengths were grown through living crystallization-driven self-assembly (CDSA) of block copolymers (BCPs) from surface-confined crystallite “micelle seeds.” This strategy was used to control the wettability of surfaces and functionalize them with nanoparticles. This tailoring of surfaces led to demonstrated applications in separation, antibacterial sterilization, and catalysis.

Nature uses nanostructured functional materials to create a variety of surfaces with distinctive characteristics, as in the reduced drag of shark skin or the self-cleaning properties of lotus leaves, and has inspired methods that create artificial mimics of these structures. Self-assembly of BCPs can create a variety of tailored nanostructures with designed and controlled shapes (spheres, cylinders, lamellae,

Department of Organic and Inorganic Chemistry, School of Chemistry, University of Oviedo, 33006 Oviedo, Spain.  
Email: presaalejandro@uniovi.es



gyroids, etc.) and dimensions (3). Moreover, living polymerization techniques, in which chain growth is controlled by the supply of monomers from solution, lead to well-defined blocks that enable exquisite control of BCP assembly pathways. For example, in poly(ferrocenyldimethylsilane) (PFS)-based BCPs, crystallization of the PFS core-forming block directs self-assembly processes, which lead to a variety of nanostructures such as di- and triblock co-micelles (4, 5), complex hierarchical supermicelles (6), or decorated concentric rectangular platelets (7). Recently, the potential of the CDSA approach to grow fibers of PFS-based BCPs on silicon nanoparticles (8) and PFS-coated carbon nanotubes (9) was demonstrated.

Building on previous successes of CDSA processes with PFS-based BCPs, Cai *et al.* report a general method for functionalizing surfaces with cylindrical micelle brushes of controlled length and tailored chemical functionalities (see the figure). Short cylindrical micelle seeds that have PFS crystalline cores and nitrogen-containing poly(2-vinylpyridine) (P2VP) coronas were attached to different substrates. In the case of silicon wafers and graphene oxide (GO) sheets, attachment occurred through hydrogen bonding between pyridine groups of P2VP coronas and hydroxyl groups, and for GO, electrostatic interactions also occurred between pyridine groups and carboxyl groups of GO. The two ends of the surface-attached crystallite seeds have PFS cores that remain active for the addition of PFS-based BCPs ("unimers") from solution.

Further additions of unimers led to cylindrical micelle brushes, and their length could be precisely controlled by the amount of unimers added from solution. This epitaxial growth process is similar to grafting-from approaches but uses longer building blocks (nanometer-sized cylindrical micelles) and has advantages over conventional approaches in terms of uniformity and grafting density. The overall process, which

can be called "micellization-from," allows precise control of the chemical functionalities and properties embodied in the as-modified surfaces through the selection of the coronas of the PFS-based unimers. For example, hydrophobicity of silicon wafers was enhanced by using unimers that had hydrophobic polysiloxane corona-forming blocks.

The outstanding potential and versatility of the micellization-from approach was demonstrated by post-assembly functionalization of P2VP coronas of micelle brushes. Functionalization of silicon wafers with gold nanoparticles created surfaces that could catalyze the reduction of 4-nitrophenol, and surfaces functionalized with silver nanoparticles could resist the growth of Gram-negative *Escherichia coli*. The separation of heptane from a heptane-in-water emulsion was achieved with GO-based membranes coated with micelle brushes that had positively charged P2VP coronas.

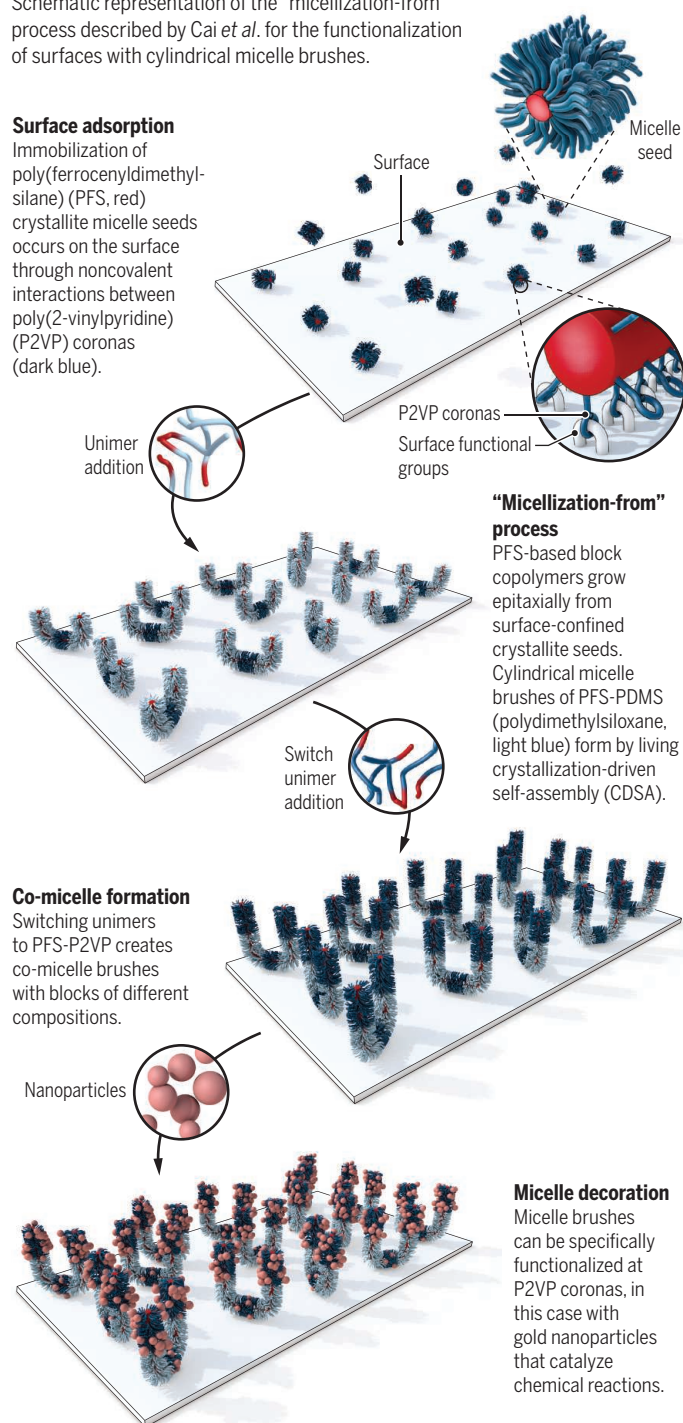
As the demand for advanced functional materials increases, the ability to control the precise functionalization of surfaces represents a major challenge. In this regard, the approach of Cai *et al.* represents a crucial step forward in the search for facile and general methodologies leading to nanopatterned functional surfaces with tailor-made chemical functionalities. The authors take the self-assembly of BCPs, and particularly the CDSA processes, to the next level of complexity by exploiting its advantages to provide reliable and convenient routes to nanofunctionalized surfaces. With this work, they address one of the critical challenges of surface chemistry, the precise functionalization of surfaces, and have created a powerful tool for fabricating advanced functional materials that can open up yet unforeseen applications. ■

## Nanofunctionalization of surfaces

Schematic representation of the "micellization-from" process described by Cai *et al.* for the functionalization of surfaces with cylindrical micelle brushes.

### Surface adsorption

Immobilization of poly(ferrocenyldimethylsilane) (PFS, red) crystallite micelle seeds occurs on the surface through noncovalent interactions between poly(2-vinylpyridine) (P2VP) coronas (dark blue).



### "Micellization-from" process

PFS-based block copolymers grow epitaxially from surface-confined crystallite seeds. Cylindrical micelle brushes of PFS-PDMS (polydimethylsiloxane, light blue) form by living crystallization-driven self-assembly (CDSA).

### Co-micelle formation

Switching unimers to PFS-P2VP creates co-micelle brushes with blocks of different compositions.

### Micelle decoration

Micelle brushes can be specifically functionalized at P2VP coronas, in this case with gold nanoparticles that catalyze chemical reactions.

## REFERENCES AND NOTES

1. C. Feng, X. Huang, *Acc. Chem. Res.* **51**, 2314 (2018).
2. J. Cai *et al.*, *Science* **366**, 1095 (2019).
3. Y. Mai, A. Eisenberg, *Chem. Soc. Rev.* **41**, 5969 (2012).
4. X. Wang *et al.*, *Science* **317**, 644 (2007).
5. P. A. Rupar, L. Chabanne, M. A. Winnik, I. Manners, *Science* **337**, 559 (2012).
6. H. Qiu, Z. M. Hudson, M. A. Winnik, I. Manners, *Science* **347**, 1329 (2015).
7. H. Qiu *et al.*, *Science* **352**, 697 (2016).
8. L. Jia *et al.*, *Nat. Commun.* **5**, 3882 (2014).
9. L. Jia *et al.*, *ACS Nano* **9**, 10673 (2015).

10.1126/science.aay8350



Military meteorologists prepare an instrument that will measure temperature, pressure, and humidity.

BOOKS *et al.*

## ENVIRONMENTAL SCIENCE

# The pursuit of Earth's waters

A historian shares stories of six scientists who laid foundations for modern climate science

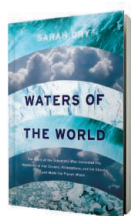
By Lydia Barnett

How did climatology become climate science? More fundamentally, how did the idea of Earth as an interconnected natural system—one of the conceptual foundations of climate science—emerge from a welter of different disciplines? In clear and engaging prose, historian Sarah Dry narrates the life stories of six individuals—from the Victorian British scientist John Tyndall to the late-20th-century Danish glaciologist Willi Dansgaard—whose scientific careers helped lay the foundations for the modern science of climate.

*Waters of the World* takes readers from the lab to the study to the field and back again. In addition to Tyndall and Dansgaard, we meet Charles Piazzi Smyth, a Scottish astronomer who traveled to the Canary Islands in search of the stars and ended up studying the clouds that obscured his view; Gilbert Walker, a meteorologist and mathematician who analyzed weather data for the British Raj; the American meteorologist Joanne Simpson, who developed experi-

mental aircraft to gather data about clouds by flying straight into them; and the American oceanographer Henry Stommel, who once threw a sack of parsnips off the dock of an English lake to puzzle out the fluid dynamics of the world's major ocean currents.

The main thread linking these biographies is, as the book's title suggests, water. Tyndall's studies of glaciers and experiments with water vapor led him to develop the theory of greenhouse gases. Walker's failed attempts to develop a science of monsoon prediction fostered instead a dawning realization that interlocking systems of high and low pressure conspired to produce what he called "world weather." Simpson's lifelong pursuit of tropical clouds and storms generated novel understandings of atmospheric circulation on a



**Waters of the World**  
Sarah Dry  
University of Chicago  
Press, 2019. 338 pp.

global scale, just as her contemporary Stommel's work on the Gulf Stream revealed the interconnectedness of the world's oceans. Dansgaard's fascination with snow and rainwater led him to engineer the method of ice core sampling that proved foundational to the birth of paleoclimatology.

Dry shows how disappointments and dead ends, creative workarounds, and the contingencies of funding, training, family relationships, scholarly networks, health and mental illness, and access to instruments, institu-

tions, and other people's labor all shaped scientific inquiry into the planet's oceans, atmosphere, and ice sheets. As she writes in the book's conclusion, "Global visions are necessarily made up of unglobal things—individuals, places, moments in time."

Although her approach is primarily biographical—each main chapter features one of the six aforementioned scientists—Dry insists that the work of individual scientists cannot be separated from the social and institutional context in which they worked. *Waters of the World* is at its strongest when it situates its protagonists not only in their scientific milieu but also in networks of imperial, military, and technocratic power. The book's middle chapters on Walker and Simpson are especially good in this respect.

Gilbert Walker's ability to collect data for his project on world weather, we learn, depended on the same infrastructure that enabled the British Empire to lay claim to India: telegraphs, railways, the British navy, and imperial networks of correspondence. His orders to find a way to predict monsoons were, above all, a task of imperial governance in the face of repeated, large-scale famines in British India. (It later turned out that the famines were more the product of imperial mismanagement than of natural variability in the monsoon season.)

State interests in predicting and controlling the weather shaped Joanne Simpson's career as well, which unfolded against the backdrop of the Cold War. Dry taps into the rich archive of Simpson's personal papers to reveal her ambivalence about her involvement in Project Stormfury, a weather-modification project sponsored by the U.S. Navy and Department of Commerce. Simpson viewed weather control as a means to fund her real research interests (tropical clouds), although she later expressed regret about her 2-year directorship of the program.

*Waters of the World* is an accessible work of science history that draws on some of the best recent scholarship in the field. As Dry explains in the introduction, she was motivated to write it, in part, to challenge what she sees as "a larger attempt by climate scientists to tell a singular history of a heterogeneous science."

As such, *Waters of the World* is a history that functions as a plea for interdisciplinary work on the problem of climate. The book ends with a call to climate scientists to embrace their interdisciplinary roots and to recognize and celebrate that there are "multiple ways of knowing the planet." ■

The reviewer is at the Department of History, Northwestern University, Evanston, IL 60208, USA. Email: lydia.barnett@northwestern.edu

10.1126/science.aaz2703



## CLASSICS REVISITED

# Arbiters of truth, then and now

A 40-year-old tome's prescient observations about scientific fact-making resonate today

By Joseph Swift

In the 1970s, sociologist Bruno Latour wanted to observe how scientific facts emerged in real time. Preferring not to rely on researchers' own accounts of how discoveries were made, he was keen to witness scientists work in situ. To achieve this, he served for 2 years as a resident anthropologist in Roger Guillemin's laboratory at the Salk Institute for Biological Studies.

The account of his stay, coauthored with Steve Woolgar and published 40 years ago under the title *Laboratory Life: The Social Construction of Scientific Facts*, raised contentious questions about the nature of scientific truths. Challenging the idea that facts are things discovered by scientists that reflect an objective reality, the authors argued that facts are instead tools constructed by scientists themselves. The book's central claim divided scientists, while sociologists hailed it as a watershed moment in the study of science.

Since the 1970s, the public's faith in science as an arbiter of what is and what is not fact has waned. As a seminal work that casts fact-generating as a sort of culture, *Laboratory Life* can help readers make sense of science's ambiguous role in today's society.

Since the Enlightenment, philosophers have debated whether anyone can claim to know anything about reality. Spurred by rapid technological change and the rise of postmodernism, this question experienced a resurgence in the latter part of the 20th century. *Laboratory Life* was part of this revival. Its authors were particularly interested in claims associated with specialized knowledge—the sort of facts that require teams of scientists and sophisticated equipment to reveal.

During his time in Guillemin's lab, Latour noticed the defining role that language played in bringing well-hidden facts to light. He argued that it was not the experiment per se but the scientist's interpretation of an experiment's result that made phenomena real.

When an experiment was conducted for the first time, any discussion about its findings was often hedged with qualifying

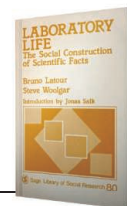
statements (e.g., “it seems like” and “this appears to be”). However, as a finding became more robust—if, for example, it was validated using a different method—the number of possible interpretations scientists drew upon grew smaller. Finally, when a finding became widely reproducible or attained a certain degree of precision, it began to be regarded as having obtained a sort of stability. At this point, the existence of the fact no longer hinged on a scientist's interpretation; it was considered a truth unto itself. But, as Latour and Woolgar noted, the consensus point where an observation was deemed to reach this stability was, by nature, arbitrary.

Sociologists found this troubling. If language is the only way to signal what is a fact and what is not, then one could argue that facts themselves reside in language, not in an external reality. After all, if reality is essentially limitless, then language, which is finite, can never faithfully describe reality. Scientists may dismiss this caveat as academic, but thinking about scientific facts as tools constructed by language helps clarify why current anti-scientific rhetoric is so effective.

Because language allows for a gray area between unsubstantiated claims and concrete facts, the role of the scientific community is to carefully shepherd findings along this continuum. In 1979, when *Laboratory Life* was published, this journey was fairly

## Laboratory Life: The Social Construction of Scientific Facts

Bruno Latour and Steve Woolgar  
Sage Publications, 1979.  
271 pp.

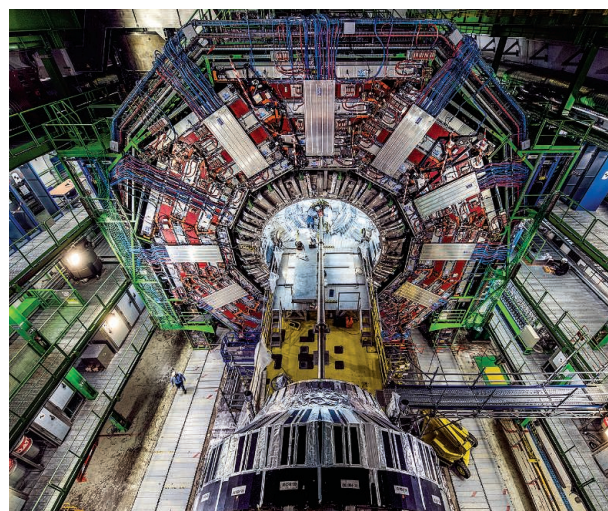


insulated. At that time, discerning between what was fact and what was artifact was left mostly to scientists themselves.

Today, it is a different story. The internet is a wide web of contradiction, where information can move rapidly within social networks. This renders the complicated phenomena that scientists study vulnerable to the turbulence that rhetoric can create. Findings that can upset the status quo—such as the biological mechanisms governing sexual orientation, or the safety of genetically modified food—can be diluted through rhetoric, regardless of whether the findings in question reflect an objective reality. If facts are tools made by language, they can be undone by language too.

Forty years after its publication, *Laboratory Life* remains prescient in its ability to encourage scientists to see that descriptions of reality and reality itself are not the same thing. The gap that separates the two can, however, be made smaller by good science. While we may never touch reality, we can certainly get very close. ■

10.1126/science.aaz3045



The Large Hadron Collider offers insights into the Universe's first moments.

## PODCAST

### At the Edge of Time: Exploring the Mysteries of Our Universe's First Seconds

Dan Hooper  
Princeton University Press,  
2019. 248 pp.

From dark matter to cosmic inflation, the cosmos contains tantalizing hints from the Universe's earliest moments. This week on the *Science* podcast, Dan Hooper unpacks what we know about the first seconds after the Big Bang and reveals how scientists are attempting to test theories about this pivotal period.

10.1126/science.aba0323

The reviewer is at the Salk Institute for Biological Studies, La Jolla, CA 92037, USA. Email: jswift@salk.edu





## LETTERS

Bolivia has lost a substantial portion of its forests to fires.

Edited by Jennifer Sills

## Fires scorching Bolivia's Chiquitano forest

The Chiquitano Dry Forest—endemic to Bolivia, highly biodiverse, and considered the world's best-preserved tropical dry forest (1)—has lost a staggering 1.4 million hectares to fires since July, about 12% of the Chiquitano forest area before the fires (2). As in Amazonia (3), fires in the Chiquitano are a sign of expanding cattle ranching and soybean agriculture: More than 70% of the burned area coincides with the deforestation frontier (4), with widespread evidence of fires being ignited by people (5).

Unfortunately, the Chiquitano also exemplifies wider trends in Bolivia. The country ranks ninth in terms of primary forest globally but is among the five countries with the highest deforestation rates (6). A series of recent legal changes, issued by the Morales administration and aimed at expanding Bolivia's agricultural area from 3 to 13 million hectares by 2025 (7), are worsening these trends. Specifically, Law 741 encourages agricultural expansion; Law 1098 allows biofuel production and associated cropland expansion; and Supreme Decree 3973 legalizes deforestation and controlled burns in lowland forests (8, 9). If current trends continue, Bolivia may lose most of its 50 million hectares of forest by 2050 (10). This jeopardizes sustainable use of forest resources, freshwater provisioning, food security, and the livelihoods of millions of people (8), while fueling climate change to which Bolivia is one of the most vulnerable countries globally (11).

Across Bolivia, fires have already consumed 5.3 million hectares of forests and savannas since July (2). This unprecedented

disaster should trigger a reevaluation of Bolivia's agricultural and economic policies. We urge the new Bolivian government to revise legislation encouraging agricultural expansion, to effectively protect remaining forests and the many ecosystem services they provide, and to encourage evidence-based, sustainable agricultural production in areas already transformed to agriculture.

**Alfredo Romero-Muñoz<sup>1,2\*</sup>, Martin Jansen<sup>3,4</sup>, Angela M. Nuñez<sup>5</sup>, Marisol Toledo<sup>6</sup>, Roberto Vides Almonacid<sup>7</sup>, Tobias Kuemmerle<sup>1,8</sup>**

<sup>1</sup>Geography Department, Humboldt-University Berlin, Berlin, Germany. <sup>2</sup>Fundación Cohabitar, Sucre, Bolivia. <sup>3</sup>Terrestrial Zoology, Senckenberg Research Institute and Nature Museum, Frankfurt, Germany. <sup>4</sup>Centro de Investigaciones Ecológicas Chiquitos, Concepción, Bolivia. <sup>5</sup>Colegio de Biólogos de La Paz, La Paz, Bolivia. <sup>6</sup>Museo de Historia Natural Noel Kempff Mercado, Universidad Autónoma Gabriel René Moreno, Santa Cruz, Bolivia. <sup>7</sup>Fundación para la Conservación del Bosque Seco Chiquitano, Santa Cruz, Bolivia. <sup>8</sup>Integrative Research Institute on Transformations of Human–Environment Systems (IRI THESys), Humboldt-University Berlin, Germany.

\*Corresponding author.  
Email: alfredo.romero@geo.hu-berlin.de

### REFERENCES AND NOTES

1. R. Vides-Almonacid, H. Justiniano, in *Adapting to Change: The State of Conservation of World Heritage Forests in 2011*, M. Patry, R. Horn, S. Haraguchi, Eds. (UNESCO, France, 2011), pp. 91–96.
2. Fundación Amigos de la Naturaleza, "Reporte de incendios forestales en Santa Cruz: 15 de septiembre de 2019" (Fundación Amigos de la Naturaleza, Santa Cruz de la Sierra, Bolivia, 2019) [in Spanish].
3. H. Escobar, *Science* **365**, 853 (2019).
4. J. Hinojosa, "70% del área quemada coincide con avance de frontera agropecuaria," *Los Tiempos* (2019) [in Spanish].
5. "Policía de la Chiquitania encuentra botellas con gasolina y llantas ardiendo en medio del bosque," *ATB Digital* (2019) [in Spanish].
6. D. Morales-Hidalgo, S. N. Oswalt, E. Somanathan, *For. Ecol. Manage.* **352**, 68 (2015).
7. Estado Plurinacional de Bolivia, *Agenda Patriótica 2025* (Ministerio de Autonomías, 2013), vol. 2025.
8. A. Romero-Muñoz et al., *Nat. Ecol. Evol.* **3**, 866 (2019).
9. "En 13 años, Evo aprobó cuatro leyes que afectan a bosques y tierras," *Página Siete* (2019) [in Spanish].
10. G. Tejada et al., *Environ. Res.* **144**, 49 (2016).
11. D. Eckstein, V. Künzel, L. Schäfer, "Global climate risk index 2018," (Germanwatch, Bonn, Germany, 2017).

10.1126/science.aaz7264

## Misguided approach to dengue vaccine risk

In the In Depth News story "Controversy over dengue vaccine risk" (6 September, p. 961), J. Cohen describes the anxiety of parents whose children were vaccinated with Dengvaxia after warnings that the vaccine could lead to severe dengue in rare cases in children who were seronegative (i.e., had never had a prior dengue infection) at the time of first vaccination. Vaccinated children who were seropositive at the time of vaccination experienced substantial protection, whereas children who were seronegative when vaccinated were found to be at higher risk of severe dengue than seronegative unvaccinated children (1). It is natural for parents to fear that their children were seronegative at the time of their vaccination and hence at increased risk, but these fears should not be unnecessarily exacerbated. Cohen quotes Leonila and Antonio Dans, who call for testing of all vaccinated children to retrospectively determine their baseline serostatus before the administration of Dengvaxia. This approach is misplaced.

In a seroprevalence setting in the Philippines estimated to be as high as 85% (2), the vast majority of vaccinated children are seropositive and will benefit from the vaccine. As for many other vaccines, protective efficacy is not complete but reported to be 76% in seropositive vaccinated persons (1). Therefore, one would expect breakthrough disease, including severe dengue, in about 24% of seropositive vaccinated persons as a result of exposure to natural infection given the current dengue outbreak in the country (1). The clinical spectrum of severe dengue in seronegative vaccinated children is the same as



in seropositive vaccinated or seropositive unvaccinated children (1, 4). Thus, clinical management of severe dengue is the same, irrespective of baseline serostatus at the time of administration of Dengvaxia. Testing vaccinated children would not change clinical management.

Moreover, as Cohen points out, commercially available dengue immunoglobulin G enzyme-linked immunosorbent antibody (ELISA) testing will not be able to differentiate the effect of vaccination from the effect of natural dengue infection, and therefore it cannot identify those children who were seronegative at baseline. An elaborate assay such as the novel NS1-based ELISA assay (3) must be used to retrospectively infer baseline serostatus. However, the ability of the NS1 assay to correctly detect “dengue-exposed” individuals as seropositive is estimated to be 95.3%, which means that the false negative rate (seropositive samples misclassified as seronegative) is 4.7%. The ability of the assay to correctly identify dengue unexposed individuals as seronegative is estimated to be 68.6%, which means that the false seropositive rate (seronegative samples misclassified as seropositive by the assay) is 31.4% (4). Therefore, among subjects classified as seropositive by the anti-NS1 assay, a proportion would be actually seronegative and vice versa. This would result in unnecessary anxiety for those tested seronegative although they are actually seropositive and would falsely reassure those tested seropositive who are actually seronegative. Furthermore, given the high annual dengue incidence in the Philippines, many of the originally seronegative children vaccinated in 2016 have meanwhile been exposed to dengue infections and become seropositive. These children would also be misclassified as seropositive.

The costs and logistics of testing about 800,000 children are immense and totally disproportionate to the benefit. The money would be better spent on improving clinical case management and setting up centers of excellence to ensure better health outcomes of dengue patients, regardless of vaccination status.

**Annelies Wilder-Smith<sup>1\*</sup>, Joachim Hombach<sup>2</sup>, Alejandro Cravioto<sup>3</sup>**

<sup>1</sup>Heidelberg Institute of Global Health, University of Heidelberg, Heidelberg, Germany. <sup>2</sup>World Health Organization (WHO) Initiative for Vaccine Research, Geneva, Switzerland. <sup>3</sup>Faculty of Medicine, National Autonomous University of Mexico, Mexico City, Mexico.

\*Corresponding author.

Email: anneliesws@gmail.com

#### REFERENCES AND NOTES

1. S. Sridhar *et al.*, *N. Engl. J. Med.* **379**, 327 (2018).
2. M. LAzou *et al.*, *Trans. R. Soc. Trop. Med. Hyg.* **112**, 158 (2018).
3. E. J. M. Nascimento *et al.*, *J. Virol. Meth.* **257**, 48 (2018).

4. Sage Working Group on Dengue Vaccines, WHO Secretariat, “Background paper on dengue vaccines” (2018); [www.who.int/immunization/sage/meetings/2018/april/2\\_DengueBackgrPaper\\_SAGE\\_Apr2018.pdf](http://www.who.int/immunization/sage/meetings/2018/april/2_DengueBackgrPaper_SAGE_Apr2018.pdf).

#### COMPETING INTERESTS

A.W.-S. is a consultant to WHO. A.C. is the chair of the WHO Strategic Advisory Group of Experts on Immunization. The views expressed here are the authors' alone and do not necessarily represent the decisions or policies of WHO.

10.1126/science.aaz6159

## Need for mountain weather stations climbs

The recent special issue on Mountain Life (13 September, p. 1092) and the Intergovernmental Panel on Climate Change Special Report on the Ocean and Cryosphere in a Changing Climate (1) have highlighted the extent of climate change impacts in mountain environments. Globally, there is also increasing evidence for elevation-dependent warming (EDW), the amplification of warming at higher elevations compared with surrounding lowlands resulting from both local feedback processes and altered patterns of meridional heat transport (2–4). However, our ability to detect EDW remains limited because there are sparse meteorological records from higher elevations in most parts of the world.

The Global Historical Climatology Network Monthly—Version 3 lists only 84 weather stations above 2000 m. They are spread across 20 countries, but 68% of them are located in either the southern Rocky Mountains or greater Tibetan Plateau (5). There are many geographical gaps. For example, the vast mountainous regions of western Canada have few weather stations above the median elevation of glaciers (about 2190 m in southern British Columbia and Alberta) (6). The network lists only one current station in Canada above 1300 m (Banff) (5).

Ground observations are essential for understanding changes occurring at higher elevation. They cannot be replaced entirely by either remote sensing or climate reanalysis data because proxy observations are biased depending on external factors such as the extent of snow cover (7, 8). Informal meteorological stations have been established for a variety of research and avalanche forecasting purposes, but these are insufficient to address the EDW data gap. The World Meteorological Organization Global Cryosphere Watch program (9) has developed standards that should be adopted internationally, and we strongly encourage the establishment of comprehensive and sustained high-elevation meteorological

monitoring networks in order to properly study the influences of climate change on mountain environments.

**David S. Hik<sup>1\*</sup> and Scott N. Williamson<sup>2</sup>**

<sup>1</sup>Department of Biological Sciences, Simon Fraser University, Burnaby, BC, V5A 1S6, Canada. <sup>2</sup>Department of Geography, University of Northern British Columbia, Prince George, BC, V2N 4Z9, Canada.

\*Corresponding author. Email: dhik@sfu.ca

#### REFERENCES AND NOTES

1. H.-O. Pörtner *et al.*, Eds., “Intergovernmental Panel on Climate Change: Summary for Policymakers,” in “IPCC Special Report on the Ocean and Cryosphere in a Changing Climate” (2019).
2. N. Pepin *et al.*, *Nat. Clim. Change* **5**, 424 (2015).
3. N. Pepin, J. Lundquist, *Geophys. Res. Lett.* **35**, L1470 (2008).
4. R. S. Bradley, F. T. Keimig, H. F. Diaz, *Geophys. Res. Lett.* **31**, L16210 (2004).
5. Global Historical Climatology Network Monthly—Version 3 (GHCN-Mv3) ([www.ncdc.noaa.gov/data-access/land-based-station-data/land-based-datasets/global-historical-climatology-network-monthly-version-3](http://www.ncdc.noaa.gov/data-access/land-based-station-data/land-based-datasets/global-historical-climatology-network-monthly-version-3)). The GHCN-Mv3 ftp server provides a list of weather stations ([ftp://ftp.ncdc.noaa.gov/pub/data/ghcn/v3/products/ghcnmv3.first.last](http://ftp.ncdc.noaa.gov/pub/data/ghcn/v3/products/ghcnmv3.first.last)) with associated country codes, station location, elevation, and data duration.
6. A. H. Jarosch *et al.*, *Clim. Dyn.* **38**, 391 (2012).
7. S. N. Williamson *et al.*, *Remote Sens. Environ.* **189**, 14 (2017).
8. L. Lembrechts *et al.*, *Global Ecol. Biogeog.* **28**, 1578 (2019).
9. World Meteorological Organization, Global Cryosphere Watch, Guide to Meteorological Instruments and Methods of Observation (2018); [www.wmo.int/pages/prog/www/IMOP/CIMO-Guide.html](http://www.wmo.int/pages/prog/www/IMOP/CIMO-Guide.html).

10.1126/science.aaz7450

#### TECHNICAL COMMENT ABSTRACTS

##### Comment on “The global tree restoration potential”

**Andrew K. Skidmore, Tiejun Wang, Kees de Bie, Petter Pilesjö**

Bastin *et al.* (Reports, 5 July 2019, p. 76) claim that 205 gigatonnes of carbon can be globally sequestered by restoring 0.9 billion hectares of forest and woodland canopy cover. Reinterpreting the data from Bastin *et al.*, we show that the global land area actually required to sequester human-emitted CO<sub>2</sub> is at least a factor of 3 higher, representing an unrealistically large area.

**Full text:** [dx.doi.org/10.1126/science.aaz0111](https://doi.org/10.1126/science.aaz0111)

##### Response to Comment on “The global tree restoration potential”

**Jean-Francois Bastin, Yelena Finegold, Claude Garcia, Danilo Mollicone, Marcelo Rezende, Devin Routh, Constantin M. Zohner, Thomas W. Crowther**

Our study quantified the global tree restoration potential and its associated carbon storage potential under existing climate conditions. Skidmore *et al.* dispute our findings, using as reference a yearly estimation of carbon storage that could be reached by 2050. We provide a detailed answer highlighting misunderstandings in their interpretation, notably that we did not consider any time limit for the restoration process.

**Full text:** [dx.doi.org/10.1126/science.aaz0493](https://doi.org/10.1126/science.aaz0493)

Cite as: A. K. Skidmore *et al.*, *Science*  
10.1126/science.aaz0111 (2019).

## Comment on “The global tree restoration potential”

Andrew K. Skidmore<sup>1,2\*</sup>, Tiejun Wang<sup>1</sup>, Kees de Bie<sup>1</sup>, Petter Pilesjö<sup>3</sup>

<sup>1</sup>Faculty of Geo-Information Science and Earth Observation (ITC), University of Twente, 7500 AE Enschede, Netherlands. <sup>2</sup>Department of Earth and Environmental Science, Macquarie University, Sydney, Australia. <sup>3</sup>Department of Physical Geography and Ecosystem Science, Lund University, S-223 62 Lund, Sweden.

\*Corresponding author. Email: a.k.skidmore@utwente.nl

Bastin *et al.* (Reports, 5 July 2019, p. 76) claim that 205 gigatonnes of carbon can be globally sequestered by restoring 0.9 billion hectares of forest and woodland canopy cover. Reinterpreting the data from Bastin *et al.*, we show that the global land area actually required to sequester human-emitted CO<sub>2</sub> is at least a factor of 3 higher, representing an unrealistically large area.

Bastin *et al.* (1) modeled the global potential tree coverage and found that there is room for an extra 0.9 billion ha of canopy cover, which could store 205 gigatonnes of carbon (GtC) in areas naturally supporting woodlands and forests. The IPCC modeling of the upper limit from pathways that could limit global warming to 1.5°C by 2050 (2) is 1 billion ha. We note that Bastin *et al.* do not consider forest rotations or biomass accumulation over time. Assuming that the IPCC model represents 30 years of C sequestration after tree restoration, we estimate Bastin *et al.*'s average global forest sequestration rate to be 6.8 GtC year<sup>-1</sup> (= 205 GtC/30 years), or 7.6 tC ha<sup>-1</sup> year<sup>-1</sup> on 0.9 billion ha. Table 1 lists examples of realistic growth rates by biome found in the literature (3–15), with the global average forest sequestration rate being 2.31 tC ha<sup>-1</sup> year<sup>-1</sup>. Thus, the Bastin estimate for sequestration of 7.6 tC ha<sup>-1</sup> year<sup>-1</sup> is greater by approximately a factor of 3.2 (= 7.6/2.31), based on published research from flux towers and forest inventory plots across key global forest biomes (Table 1). In other words, the estimate of 205 GtC by Bastin *et al.* would actually require 2.88 (= 3.2 × 0.9) billion ha, and not 0.9 billion ha, to have an even chance of limiting warming to 1.5°C.

In addition, the Bastin *et al.* estimate can be shown to overestimate the “remaining budget” of 158 GtC calculated by the IPCC. According to the IPCC, 158 GtC forms the threshold to accumulated atmospheric CO<sub>2</sub> for creating an even chance (medium confidence) of limiting global warming to 1.5°C by 2050 on 1 billion ha. The Bastin *et al.* estimate of the “remaining budget” is 205 GtC on 0.9 billion ha, which is 30% higher than the IPCC (= 205/158) target for 1 billion ha. How realistic is restoration on such a scale? An area of 2.88 billion ha is approximately equivalent to the area of Africa, 3 times that of the United States, or 115 times that of the United Kingdom.

The Bastin *et al.* methodology further overestimates global tree restoration potential by assuming that tree cover

in protected areas (PAs) is a proxy for the maximum potential canopy cover for that biome. This premise appears optimistic because of the following issues:

1) The reversibility principle of the IPCC ruled that forests established after 1989 (i.e., <30 years ago) cannot be counted as restored forests; this rule was agreed on to discourage land owners from cutting down trees and then claiming carbon credit payments for the “restoring” forest (16).

2) Herbivores and browsers—including insects—are ecological engineers stopping huge areas of natural grasslands and savannas from converting to forest (17).

3) Disturbance within PAs is not considered; for example, insect attack or wildfire reduces forest biomass accumulation (18).

4) Many biomes are not represented within PAs because of historical land tenure and land use planning decisions.

The claim of Bastin *et al.* that 900 million ha of global forest and woodland could potentially be restored is not supported by our analysis, if we adopt the IPCC modeling of the upper limit from pathways that could limit global warming to 1.5°C by 2050 (2). This is especially the case when we consider that humans have deforested 13 million ha annually for at least the past three decades, and that this deforestation continues despite concerted efforts and substantial financial investment to reduce it.

The seemingly good news in Bastin *et al.* requires an enormous land area. We estimate that the global land area required to sequester human-emitted CO<sub>2</sub> is at least a factor of 3 higher than estimated by Bastin *et al.* As much as we would like to embrace the central conclusion of Bastin *et al.* that ecosystem restoration is “one of the most effective solutions at our disposal to mitigate climate change,” we conclude that the emerging global political myth of massive tree planting and restoration as a panacea for global warming requires an unrealistically large area. Although tree



planting should be welcomed, curbing emissions appears to be the key, albeit politically challenging, action.

## ACKNOWLEDGMENTS

We thank S. Lewis for his review of a draft.

## REFERENCES

1. J.-F. Bastin, Y. Finegold, C. Garcia, D. Mollicone, M. Rezende, D. Routh, C. M. Zohner, T. W. Crowther, The global tree restoration potential. *Science* **365**, 76–79 (2019). [doi:10.1126/science.aax0848](https://doi.org/10.1126/science.aax0848)
2. IPCC, *Global Warming of 1.5°C: An IPCC Special Report on the Impacts of Global Warming of 1.5°C Above Pre-Industrial Levels and Related Global Greenhouse Gas Emission Pathways, in the Context of Strengthening the Global Response to the Threat of Climate Change, Sustainable Development, and Efforts to Eradicate Poverty*, V. Masson-Delmotte et al., Eds. (World Meteorological Organization, Geneva, 2018).
3. A. N. Rencz, A. N. D. Auclair, NPP Boreal Forest: Schefferville, Canada, 1974, R1 (ORNL DAAC, Oak Ridge, TN, 2013). [doi:10.3334/ORNLDAAC/573](https://doi.org/10.3334/ORNLDAAC/573)
4. IPCC National Greenhouse Gas Inventories Programme (IPCC-NGGIP), *Good Practice Guidance for Land Use, Land-Use Change and Forestry*, J. Penman et al., Eds. (Institute for Global Environmental Strategies, Kanagawa, 2003); [www.ipcc.ch/publication/good-practice-guidance-for-land-use-land-use-change-and-forestry/](http://www.ipcc.ch/publication/good-practice-guidance-for-land-use-land-use-change-and-forestry/).
5. A. A. Knorre, A. V. Kiryanov, E. A. Vaganov, Climatically induced interannual variability in aboveground production in forest-tundra and northern taiga of central Siberia. *Oecologia* **147**, 86–95 (2006). [doi:10.1007/s00442-005-0248-4](https://doi.org/10.1007/s00442-005-0248-4)
6. R. T. Busing, NPP Temperate Forest: Great Smoky Mountains, Tennessee, USA, 1968–1992, R1 (ORNL DAAC, Oak Ridge, TN, 2013). [doi:10.3334/ORNLDAAC/804](https://doi.org/10.3334/ORNLDAAC/804)
7. W. L. Webb, W. K. Lauenroth, S. R. Szarek, R. S. Kinerson, Primary production and abiotic controls in forests, grasslands, and desert ecosystems in the United States. *Ecology* **64**, 134–151 (1983). [doi:10.2307/1937336](https://doi.org/10.2307/1937336)
8. J. C. Menaut, J. Cesar, Structure and primary productivity of Lamto savannas, Ivory Coast. *Ecology* **60**, 1197–1210 (1979). [doi:10.2307/1936967](https://doi.org/10.2307/1936967)
9. P. G. Murphy, A. E. Lugo, Ecology of tropical dry forest. *Annu. Rev. Ecol. Syst.* **17**, 67–88 (1986). [doi:10.1146/annurev.es.17.110186.000435](https://doi.org/10.1146/annurev.es.17.110186.000435)
10. M. Maass, A. Martinez-Yrizar, NPP Tropical Forest: Chamela, Mexico, 1982–1995, R1 (ORNL DAAC, Oak Ridge, TN, 2013). [doi:10.3334/ORNLDAAC/578](https://doi.org/10.3334/ORNLDAAC/578)
11. D. A. Clark, NPP Tropical Forest: La Selva, Costa Rica, 1975–1994, R1 (ORNL DAAC, Oak Ridge, TN, 2013). [doi:10.3334/ORNLDAAC/218](https://doi.org/10.3334/ORNLDAAC/218)
12. J. Chave, J. Olivier, F. Bongers, P. Châtelet, P.-M. Forget, P. van der Meer, N. Norden, B. Riéra, P. Charles-Dominique, Above-ground biomass and productivity in a rain forest of eastern South America. *J. Trop. Ecol.* **24**, 355–366 (2008). [doi:10.1017/S0266467408005075](https://doi.org/10.1017/S0266467408005075)
13. Y. Malhi, O. L. Phillips, Tropical forests and global atmospheric change: A synthesis. *Philos. Trans. R. Soc. London Ser. B* **359**, 549–555 (2004). [doi:10.1098/rstb.2003.1449](https://doi.org/10.1098/rstb.2003.1449)
14. M. G. R. Cannell, *World Forest Biomass and Primary Production Data* (Academic Press, 1982).
15. R. A. Sedjo, D. Botkin, Using forest plantations to spare natural forests. *Environment* **39**, 14–30 (1997). [doi:10.1080/00139159709604776](https://doi.org/10.1080/00139159709604776)
16. G. J. Nabuurs et al., in *Climate Change 2007: Mitigation. Contribution of Working Group III to the Fourth Assessment Report of the Intergovernmental Panel on Climate Change*, B. Metz et al., Eds. (Cambridge Univ. Press, 2007).
17. R. M. Pringle, Elephants as agents of habitat creation for small vertebrates at the patch scale. *Ecology* **89**, 26–33 (2008). [doi:10.1890/07-0776.1](https://doi.org/10.1890/07-0776.1)
18. K. Morehouse, T. Johns, J. Kaye, A. Kaye, Carbon and nitrogen cycling immediately following bark beetle outbreaks in southwestern ponderosa pine forests. *For. Ecol. Manage.* **255**, 2698–2708 (2008). [doi:10.1016/j.foreco.2008.01.050](https://doi.org/10.1016/j.foreco.2008.01.050)

6 August 2019; accepted 24 October 2019

Published online 29 November 2019

10.1126/science.aaz0111

**Table 1. Average carbon accumulation for different forest types.** Note that the multiple values and/or ranges given for C production are as stated in the original references.

Type of forest	C production (tonnes ha <sup>-1</sup> year <sup>-1</sup> )	Mean tonnes ha <sup>-1</sup> year <sup>-1</sup>	Reference
Boreal forest	1.0	1.00	(3)
Boreal forest	0.2, 0.4, 0.75	0.45	(4)
Boreal forest	0.025–0.07; 0.025–0.09	0.05	(5)
Temperate forest	1.8–3; 3.6–3.9	3.08	(6)
Temperate forest	2.628	2.63	(7)
Savanna	2.65–5.5; 0.65–1.50	2.58	(4)
Savanna	0.38	0.38	(8)
Tropical dry forest	1.8–3.3	2.55	(9)
Tropical dry forest	3.36–4.05	3.70	(10)
Humid tropical forest	4.2–6.3	5.25	(11)
Humid tropical forest	1.06–1.73	1.40	(12)
Humid tropical forest	0.74–2.75	1.75	(13)
Plantation	2.4–2.6	2.50	(14)
Plantation	5	5.00	(15)
<b>Mean of all forest types</b>		<b>2.31</b>	



Cite as: J.-F. Bastin *et al.*, *Science*  
10.1126/science.aaz0493 (2019).

# Response to Comment on “The global tree restoration potential”

**Jean-Francois Bastin<sup>1\*</sup>, Yelena Finegold<sup>2</sup>, Claude Garcia<sup>3</sup>, Danilo Mollicone<sup>2</sup>, Marcelo Rezende<sup>2</sup>, Devin Routh<sup>1</sup>, Constantin M. Zohner<sup>1</sup>, Thomas W. Crowther<sup>1</sup>**

<sup>1</sup>Crowther Lab, Department of Environmental Systems Science, Institute of Integrative Biology, ETH Zürich, Zürich, Switzerland. <sup>2</sup>Food and Agriculture Organization of the United Nations, Rome, Italy. <sup>3</sup>Department of Environmental Systems Science, Institute of Integrative Biology, ETH Zürich, Zürich, Switzerland.

\*Corresponding author. Email: bastin.jf@gmail.com

**Our study quantified the global tree restoration potential and its associated carbon storage potential under existing climate conditions. Skidmore *et al.* dispute our findings, using as reference a yearly estimation of carbon storage that could be reached by 2050. We provide a detailed answer highlighting misunderstandings in their interpretation, notably that we did not consider any time limit for the restoration process.**

Skidmore *et al.* (1) calculated the yearly carbon storage associated to restoration from numbers provided in the IPCC special report *Global Warming of 1.5°C* (2) and projected them for 30 years. They use this to suggest that our estimates of total potential carbon storage in restoration areas are too high (3). Based on their analysis, they claim that we overestimated the amount of carbon that can be captured in restored trees by a factor of 3. Although we understand their concerns, we highlight several misunderstandings in their interpretation of the analysis that invalidate their comment.

First, in our analysis, we never considered any time limit for the restoration process. Indeed, our study estimates the total carbon stock that can be associated to the optimal state of each ecosystem. As mentioned in the main text of our paper, the accumulation of carbon in forests would take a very long time to reach maximum potential carbon storage—considerably greater than the 30-year analysis (3). Consequently, the comparison proposed by Skidmore *et al.* is not valid.

We stress that our estimations of carbon stock were not calculated from simulated values of yearly accumulation of carbon. Instead, our values correspond to ground-based estimates of the extent of carbon stored in mature forests. Yearly accumulation could eventually be compared to our numbers if the related simulation includes the appropriate nonlinear carbon accumulation and a stationary phase associated to the mature state of the ecosystem. The number of years required to reach this stationary phase should then be calculated for each pixel and then converted in a total increase of carbon stocks. This was not done in the analysis proposed by Skidmore *et al.*

In the second part of the comment by Skidmore *et al.*,

there is a critical misunderstanding. Contrary to what they suggest, our estimation of the 205 gigatonnes of carbon (GtC) that could be captured in restored ecosystems certainly does not reflect the “remaining budget” that we should overcome in order to limit global warming to 1.5°C. Instead, that is the amount of carbon that could potentially be stored in the vegetation and soil of terrestrial ecosystems if forests were restored across all available land. This is a misunderstanding of both our analysis and the IPCC special report (2).

We would like to reexplain the main principles of our analysis. Simply put, we provide a quantitative estimation of the tree cover that could be naturally reached in any place of the world if the human activity were close to null [figure 2A of (3)]. As such, we assessed the natural forest potential of the planet under existing climate conditions. These natural conditions were approximated in building our model only considering protected areas. Here, it is important to note that in contrast to the suggestion of Skidmore *et al.*, the representativeness of each biome in protected areas was very good—a point illustrated by the extremely low level of extrapolation versus interpolation in our methods section [see figure S12 of (3)]. To realistically quantify areas that can potentially be restored, we then removed currently existing forest, urban, and cropland areas from the total forest potential. This gives the “global tree restoration potential” illustrated in figure 2, B and C, of (3). The area of canopy cover (and not forest cover) available for restoration—i.e., 900 million hectares—was then used to estimate the total amount of carbon stored. As previously mentioned, our estimation of 205 GtC does not correspond to the sum of the yearly uptake of carbon in vegetation. It corresponds to the

quantity of carbon associated to the mature state of each ecosystem considered. This calculation was done using numbers published in the literature based on field plot observation in each ecosystem (4, 5). We hope that this explanation helps to clarify our approach.

Finally, our colleagues caution against interpreting these potential restoration estimates as a guide for climate action. Here we must again disagree. Although we would never want to discourage investment in all other climate solutions, we believe that continuing to underappreciate the value of restoration for climate mitigation, as well as for biodiversity and human well-being, is a greater danger. Until now, most of our understanding of restoration potential stemmed from Earth system models with high uncertainties (6) or from “expert opinion” pieces (7) that cannot reflect the full global potential for carbon capture. Quantitative global approaches based on observations, as presented in our study, are needed to understand and promote restoration as one of the most promising solutions at our disposal in the fight against the global threats of climate change and biodiversity loss.

## REFERENCES

1. A. K. Skidmore, T. Wang, K. de Bie, P. Pilesjö, Comment on “The global tree restoration potential”. *Science* **366**, eaaz0111 (2019).
2. IPCC, *Global Warming of 1.5°C: An IPCC Special Report on the Impacts of Global Warming of 1.5°C Above Pre-Industrial Levels and Related Global Greenhouse Gas Emission Pathways, in the Context of Strengthening the Global Response to the Threat of Climate Change, Sustainable Development, and Efforts to Eradicate Poverty*, V. Masson-Delmotte et al., Eds. (World Meteorological Organization, Geneva, 2018).
3. J.-F. Bastin, Y. Finegold, C. Garcia, D. Mollicone, M. Rezende, D. Routh, C. M. Zohner, T. W. Crowther, The global tree restoration potential. *Science* **365**, 76–79 (2019). [doi:10.1126/science.aax0848](https://doi.org/10.1126/science.aax0848) [Medline](#)
4. Y. Pan, R. A. Birdsey, J. Fang, R. Houghton, P. E. Kauppi, W. A. Kurz, O. L. Phillips, A. Shvidenko, S. L. Lewis, J. G. Canadell, P. Ciais, R. B. Jackson, S. W. Pacala, A. D. McGuire, S. Piao, A. Rautiainen, S. Sitch, D. Hayes, A large and persistent carbon sink in the world's forests. *Science* **333**, 988–993 (2011). [doi:10.1126/science.1201609](https://doi.org/10.1126/science.1201609) [Medline](#)
5. J. Grace, J. S. Jose, P. Meir, H. S. Miranda, R. A. Montes, Productivity and carbon fluxes of tropical savannas. *J. Biogeogr.* **33**, 387–400 (2006). [doi:10.1111/j.1365-2699.2005.01448.x](https://doi.org/10.1111/j.1365-2699.2005.01448.x)
6. K. E. O. Todd-Brown, J. T. Randerson, W. M. Post, F. M. Hoffman, C. Tarnocai, E. A. G. Schuur, S. D. Allison, Causes of variation in soil carbon simulations from CMIP5 Earth system models and comparison with observations. *Biogeosciences* **10**, 1717–1736 (2013). [doi:10.5194/bg-10-1717-2013](https://doi.org/10.5194/bg-10-1717-2013)
7. S. L. Lewis, C. E. Wheeler, E. T. A. Mitchard, A. Koch, Restoring natural forests is the best way to remove atmospheric carbon. *Nature* **568**, 25–28 (2019). [doi:10.1038/d41586-019-01026-8](https://doi.org/10.1038/d41586-019-01026-8) [Medline](#)

6 September 2019; accepted 24 October 2019  
Published online 29 November 2019  
[10.1126/science.aaz0493](https://doi.org/10.1126/science.aaz0493)





# Indoor chemical pollution impacts often remain invisible

AAAS Research Competitiveness symposium shows need for transdisciplinary collaboration

By **Becky Ham**

Furniture, flooring, construction materials, and humans and their habits are just some sources of the thousands of particles and gases that surround people living indoors. As scientists collect increasingly sophisticated data on the chemistry of the indoor environment, policy-makers and industry leaders are seeking more information on how to apply these findings to buildings and homes, experts said at an American Association for the Advancement of Science symposium.

The term “environment” has a specific “outdoor” meaning for many policy-makers and the public that has overshadowed the hazards of the indoor environment for pollution and human health, speakers at the event suggested. Such indifference exists even as Americans spend 70 years of an average 79-year life span inside. While the U.S. Environmental Protection Agency is the most prominent regulator of outdoor pollution, research and policy decisions about the indoor environment are spread across several federal agencies.

It may be time for a “national chemistry of the indoor environment initiative, similar to what we have done with the national nanotechnology initiative,” said Vicki Grassian, a professor of physical chemistry at the University of California, San Diego, who moderated the closing session at the 19 September symposium.

“Bridging agencies that have different interests but around the same subject is something that is needed...and would be a very welcome policy change,” to fund multidisciplinary research projects related to the indoor environment, agreed Richard Corsi, dean of the Maseeh College of Engineering and Computer Science at Portland State University in Oregon. Corsi and other symposium participants also spoke at a related Capitol Hill briefing held 18 September for congressional staff members.

The symposium and briefing were organized by AAAS’s Research Competitiveness Program in collaboration with the Alfred P. Sloan Foundation to facilitate “a new vision for what this transdisciplinary field of research has achieved and can achieve,” said Charles Dunlap, the program’s director.

Since 1996, the Research Competitiveness Program has worked to build research capacity in science, technology, engineering, and mathematics by evaluating STEM education programs, helping design and manage peer review competitions, and supporting innovation and entrepreneurship in 130 emerging economies around the world.

As part of the program, “we mobilize experts and bring them together to increase research capacity in a variety of ways,” said Annette Olson, an RCP project director at AAAS who led the organization of the events. “For this symposium, we sought to bring together experts in indoor



Scientist measures indoor volatile organic compounds.

on <http://science.sciencemag.org/> on December 1, 2019

PHOTOS: CALLIE RICHMOND

**Researcher tests emissions after stir fry for study of indoor air.**

chemistry with potential collaborators who could help fund the research moving forward or create new, multidisciplinary research efforts, as well as with agency and industry stakeholders who would be the ones implementing this knowledge directly.

In addition to the speakers and moderators, representatives from 55 organizations were able to attend the symposium."

At the events, experts shared studies that offer a detailed look at the thousands of chemicals and chemical reactions inside buildings, apartments, and homes. Chemical exposure is amplified by the amount of surface area inside buildings, many of the researchers noted.

Surface areas provided by furniture materials such as polyurethane foam, wall paints, and flooring offer complex, dynamic surfaces that both leach and absorb chemicals and provide a place for dynamic chemical reactions. Although exposure to some chemicals, including flame retardants and plasticizers, has been linked to the risk of certain cancers and developmental effects in children, many indoor compounds have not been identified or evaluated for their health impacts, the researchers said.

For instance, there are "about 30,000 different chemicals in indoor dust—and we only know about 280 of them," said Heather Stapleton, an associate professor of exposure science and environmental health at Duke University. "I spend a lot of time and money just trying to figure out what's in consumer products, particularly the flame retardants in polyurethane foam. Yet that information is available within the industry, but unfortunately they're not required to release that information to the public. They're allowed to maintain confidential business information indefinitely."

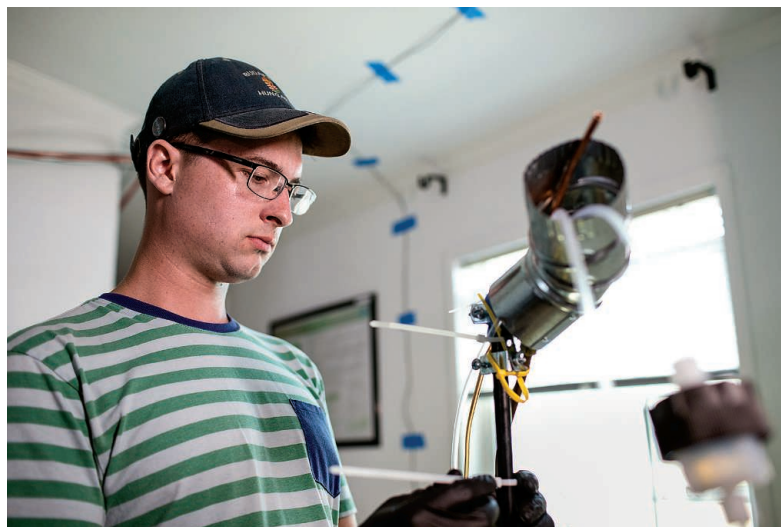
Laura Kolb, EPA's Indoor Environments Division director for scientific analysis, said that more research would better define the risks of indoor chemicals. "I need to know what the implications for public health are, so I can translate it into EPA guidance," she said.

Several symposium participants suggested that the health impacts of chemicals in the indoor environment are still mostly invisible to the public. In his plenary address, Mahesh Ramanujam, president and chief executive officer of the U.S. Green Building Council and Green Business Certification, Inc., cited studies from the Harvard T. H. Chan School of Public Health and others that "found that improved indoor environmental quality can double occupants' cognitive function scores and occupants had increased decision-making performance scores."

Despite this, many people do not know that "green buildings—or buildings at all—can contribute to health and wellness," said Ramanujam.

Health disparities related to the indoor environment are another aspect of the field that deserves more attention, some researchers noted. In one of Stapleton's studies, for instance, children living in public housing with all vinyl flooring had levels of benzyl butyl phthalate plasticizer in their urine that were 15 times higher than children from homes with no vinyl flooring. Lesliam Quirós-Alcalá, an assistant professor of environmental health and engineering at Johns Hopkins Bloomberg School of Public Health, discussed how pest control in low-income housing could lead to increased levels of pesticide exposure for residents.

As scientists study the chemical contents of the indoor environment, their findings also suggest ways to reduce toxic chemical exposures. When Corsi and Glenn Morrison, a professor of environmental sciences and engineering at the University of North Carolina, studied how methamphetamines penetrate wallboard, they found that higher humidity could drive the chemicals off the surface. "If we understood this process a little better," Corsi said, "it might be possible to reduce exposure to indoor pollutants like volatile organic compounds by simultaneously flushing the building while adjusting its temperature and humidity."



Researcher measures organic acids in air for HOMEChem study.

To control indoor pollution, researchers also need to know more about human behavior, Corsi noted. "Trying to understand why some people don't use the exhaust fan on their stove when they cook, or why some people like to burn a lot of incense or why some people like to vacuum 10 times a week as opposed to once a month...all of this affects what people are exposed to indoors."

Connecting research to action is possible and necessary, said Marina Eller Vance, an assistant professor of mechanical engineering from the University of Colorado. Vance shared some of her results from HOMEChem, an ongoing research collaboration that examines the chemistry of the indoor environment in a manufactured "test house" at the University of Texas, Austin.

"Sometimes I feel like I hear that we are powerless to change or to impact people's exposure to indoor pollutants because we can't control what people do within their own homes, but that's not true," she said. "We can educate and interact with industry to make those changes happen upstream in the supply chain."

## AAAS Council reminder

The next meeting of the AAAS Council will take place during the 2020 AAAS Annual Meeting in Seattle, Washington, and will begin at 9:00 a.m. on 16 February 2020, Eliza Anderson (Amphitheater and Foyer).

Individuals or organizations wishing to present proposals or resolutions for possible consideration by the council should submit them in written form to the AAAS Executive Office by 10 January 2020. This will allow time for them to be considered by the Committee on Council Affairs at its winter meeting.

Items should be consistent with AAAS's objectives and be appropriate for consideration by the council. Resolutions should be in the traditional format, beginning with "Whereas" statements and ending with "Therefore be it resolved."

Late proposals or resolutions delivered to the AAAS chief executive officer in advance of the February 2020 open hearing of the Committee on Council Affairs will be considered, provided that they deal with urgent matters and are accompanied by a written explanation of why they were not submitted by the 10 January deadline. The Committee on Council Affairs will hold its open hearing at 2:30 p.m. on 15 February 2020, in the Grand Hyatt Discovery A and B.



## 2019 AAAS Fellows approved by the AAAS Council

In October 2019, the Council of the American Association for the Advancement of Science elected 443 members as Fellows of AAAS. These individuals will be recognized for their contributions to science and technology at the Fellows Forum to be held on 15 February 2020 during the AAAS Annual Meeting in Seattle, Washington. Presented by section affiliation, they are:

### Section on Agriculture, Food, and Renewable Resources

**Lisa Ainsworth**, USDA-ARS/Univ. of Illinois at Urbana-Champaign

**Senthil Asseng**, Univ. of Florida

**Guihua Bai**, U.S. Department of Agriculture-Agricultural Research Service

**Thomas Elmo Clemente**, Univ. of Nebraska-Lincoln

**Karen A. Garrett**, Univ. of Florida

**Jerry D. Glover**, U.S. Agency for International Development

**Niklaus J. Grunwald**, USDA-ARS

**Kater Davis Hake**, Cotton Incorporated

**Dirk Inze**, VIB-UGent Center for Plant Systems Biology/Ghent Univ. (Belgium)

**Isgouhi Kaloshian**, Univ. of California, Riverside

**Susan J. Lamont**, Iowa State Univ.

**Thomas Leustek**, Rutgers, The State Univ. of New Jersey

**Jonathan Lynch**, Pennsylvania State Univ.

**John McKay**, Colorado State Univ.

**Dina A. St. Clair**, Univ. of California, Davis

**Peter Sutovsky**, Univ. of Missouri

**Luther E. Talbert**, Montana State Univ.

**Linda S. Thomashow**, Washington State Univ.

**Leena Tripathi**, International Institute of Tropical Agriculture (ITTA) (Kenya)

### Section on Anthropology

**C. Michael Barton**, Arizona State Univ.

**Rachel Caspari**, Central Michigan Univ.

**Susan Pfeiffer**, Univ. of Toronto (Canada)

**Matt Sponheimer**, Univ. of Colorado Boulder

**Wenda Trevathan**, New Mexico State Univ.

**Sander Ernst van der Leeuw**, Arizona State Univ.

### Section on Astronomy

**William Nielsen Brandt**, Pennsylvania State Univ.

**Kathryn A. Flanagan**, Space Telescope Science Institute

**Vassiliki Vicky Kalogera**, Northwestern Univ.

**Makenzie Lystrup**, Ball Aerospace

**Colin Norman**, Johns Hopkins Univ.

**Sarah T. Stewart**, Univ. of California, Davis

**Farhad Yusef-Zadeh**, Northwestern Univ.

### Section on Atmospheric and Hydrospheric Science

**Waleed Abdalati**, Univ. of Colorado Boulder

**Karl Banse**, Univ. of Washington

**Leo J. Donner**, NOAA Geophysical Fluid Dynamics Laboratory

**John A. Downing**, Univ. of Minnesota

**Jenni L. Evans**, Pennsylvania State Univ.

**Kelly Kenison Falkner**, National Science Foundation

**Lee-Lueng Fu**, Jet Propulsion Laboratory, California Institute of Technology

**Joan Kleypas**, National Center for Atmospheric Research

**Patricia Quinn**, NOAA Pacific Marine Environmental Laboratory

**Eric J. Steig**, Univ. of Washington

**Ping Yang**, Texas A&M Univ.

**Minghua Zhang**, Stony Brook Univ.

### Section on Biological Sciences

**Réka Albert**, Pennsylvania State Univ.

**Zhiqiang An**, The Univ. of Texas Health Science Center

**William D. Beavis**, Iowa State Univ.

**Peter Beerli**, Florida State Univ.

**Andrew Biewener**, Harvard Univ.

**Gail A. Bishop**, Univ. of Iowa

**Ben Bond-Lamberty**, Pacific Northwest National Laboratory

**Lynda Bonewald**, Indiana Univ.

**Jacobus J. (Koos) Boomsma**, Univ. of Copenhagen (Denmark)

**Cheryl Briggs**, Univ. of California, Santa Barbara

**Susan V. Brooks**, Univ. of Michigan

**Robb T. Brumfeld**, Louisiana State Univ.

**Edgar B. Cahoon**, Univ. of Nebraska-Lincoln

**Brian R. Calvi**, Indiana Univ.

**Vernon B. Carruthers**, Univ. of Michigan Medical School

**Bryan Carstens**, The Ohio State Univ.

**Julian Chen**, Arizona State Univ.

**Luis M. Chiappe**, Natural History Museum of Los Angeles County

**James Scott Coleman**, Univ. of Arkansas

**Kathryn L. Cottingham**, Dartmouth College

**Shane Crotty**, La Jolla Institute for Immunology

**William (Bill) S. Currie**, Univ. of Michigan

**Francesco J. DeMayo**, National Institute of Environmental Health Sciences/NIH

**Kanwarpal Singh Dhugga**, International Center for Maize and Wheat Improvement (CIMMYT) (Mexico)

**Enrico Di Cera**, Saint Louis Univ. School of Medicine

**Nikolay Dokholyan**, Pennsylvania State Univ. College of Medicine

**Meghan Duffy**, Univ. of Michigan

**Steven A. Farber**, Carnegie Institution for Science

**Cédric Feschotte**, Cornell Univ.

**Kurt L. Fredrick**, The Ohio State Univ.

**Erica Golemis**, Fox Chase Cancer Center

**Tatyana Golovkina**, Univ. of Chicago

**Christina M. Grozinger**, Pennsylvania State Univ.

**John S. Gunn**, Nationwide Children's Hospital/The Ohio State Univ.

**Melina Elisabeth Hale**, Univ. of Chicago

**John Hammond**, USDA-ARS

**Nissim Hay**, Univ. of Illinois at Chicago

**Simon Iain Hay**, Univ. of Washington

**Eileen Anne Hebets**, Univ. of Nebraska-Lincoln

**Eric Linke Hegg**, Michigan State Univ.

**Oleh Hornykiewicz**, Medical Univ. of Vienna (Austria)

**Zhiqiang Hu**, Univ. of Missouri

**Henriette Jager**, Oak Ridge National Laboratory

**Jean X. Jiang**, The Univ. of Texas Health Science Center

**Igor Jouline**, The Ohio State Univ.

**Cheryl A. Kerfeld**, Michigan State Univ./Lawrence Berkeley National Laboratory

**Laura S. Kubatko**, The Ohio State Univ.

**Justin P. Kumar**, Indiana Univ.

**Michael Lagunoff**, Univ. of Washington

**Olivier Lichtarge**, Baylor College of Medicine

**Eric R. Mackow**, Stony Brook Univ.

**Michael T. Madigan**, Southern Illinois Univ.

**Louis James Maher III**, Mayo Clinic College of Medicine and Science

**Harmit Singh Malik**, Fred Hutchinson Cancer Research Center

**Chuanbin Mao**, Univ. of Oklahoma

**Emília P. Martins**, Arizona State Univ.

**Robert T. Mason**, Oregon State Univ.

**Maureen C. McCann**, Purdue Univ.

**Victoria Meller**, *Wayne State Univ.*

**Pamela L. Mellon**, *Univ. of California, San Diego*

**Raymond J. Monnat Jr.**, *Univ. of Washington*

**Kirankumar S. Mysore**, *Noble Research Institute, LLC.*

**Knute Nadelhoffer**, *Univ. of Michigan*

**Wayne L. Nicholson**, *Univ. of Florida*

**Thomas W. Okita**, *Washington State Univ.*

**David M. Ornitz**, *Washington Univ. School of Medicine in St. Louis*

**Caryn Elizabeth Outten**, *Univ. of South Carolina*

**Craig Packer**, *Univ. of Minnesota*

**Lawrence Page**, *Florida Museum of Natural History*

**John (Sandy) S. Parkinson**, *Univ. of Utah*

**Julia K. Parrish**, *Univ. of Washington*

**Nicola Partridge**, *New York Univ.*

**Charles Perrings**, *Arizona State Univ.*

**Karin Pfennig**, *Univ. of North Carolina at Chapel Hill*

**Elizabeth A. Platz**, *Johns Hopkins School of Medicine*

**Kenneth D. Poss**, *Duke Univ. Medical Center*

**David M. Post**, *Yale Univ.*

**Ellen Puré**, *Univ. of Pennsylvania*

**Jeffrey C. Rathmell**, *Vanderbilt Univ. Medical Center*

**John P. Reganold**, *Washington State Univ.*

**Howard Riessen**, *SUNY-Buffalo State College*

**Wilson K. Rumbeiha**, *Iowa State Univ.*

**David V. Schaffer**, *Univ. of California, Berkeley*

**Emily E. Scott**, *Univ. of Michigan*

**Alessandro Sette**, *La Jolla Institute for Immunology*

**Lindsey N. (Les) Shaw**, *Univ. of South Florida*

**Aleem Siddiqui**, *Univ. of California, San Diego*

**Stephen T. Smale**, *David Geffen School of Medicine at Univ. of California, Los Angeles*

**Douglas Soltis**, *Univ. of Florida*

**Andrew V. Suarez**, *Univ. of Illinois at Urbana-Champaign*

**Michele S. Swanson**, *Univ. of Michigan Medical School*

**David G. Thanassi**, *Stony Brook Univ.*

**Shirley M. Tilghman**, *Princeton Univ.*

**David M. Tobin**, *Duke Univ.*

**David S. Ucker**, *Univ. of Illinois College of Medicine*

**Meng C. Wang**, *Baylor College of Medicine*

**Henry Neal Williams**, *Florida A&M Univ.*

## Section on Chemistry

**Rebecca Abergel**, *Univ. of California, Berkeley/Lawrence Berkeley National Laboratory*

**Mark A. Beno**, *Argonne National Laboratory*

**Stephen Bradforth**, *Univ. of Southern California*

**Amanda C. Bryant-Friedrich**, *The Univ. of Toledo*

**Julia Chan**, *The Univ. of Texas at Dallas*

**Aurora Evelyn Clark**, *Washington State Univ.*

**Paula Diaconescu**, *Univ. of California, Los Angeles*

**Andrey V. Dobrynin**, *The Univ. of Akron*

**Arlene A. Garrison**, *Oak Ridge Associated Universities*

**Steven McGrath Graham**, *St. John's Univ.*

**R. Kiplin Guy**, *Univ. of Kentucky*

**Adam L. Hamilton**, *Southwest Research Institute*

**Paul J. Hergenrother**, *Univ. of Illinois at Urbana-Champaign*

**Andrew C. Hillier**, *Iowa State Univ.*

**Jennifer A. Hollingsworth**, *Los Alamos National Laboratory*

**Xuefei Huang**, *Michigan State Univ.*

**Nicholas V. Hud**, *Georgia Institute of Technology*

**Bart Kahr**, *New York Univ.*

**Todd D. Krauss**, *Univ. of Rochester*

**Carsten Krebs**, *Pennsylvania State Univ.*

**George I. Makhatadze**, *Rensselaer Polytechnic Institute*

**Thomas Graves Mason**, *Univ. of California, Los Angeles*

**Michael G. Matturro**, *ExxonMobil Research and Engineering*

**Gagik G. Melikyan**, *California State Univ., Northridge*

**Benjamin L. Miller**, *Univ. of Rochester*

**Tina M. Nenoff**, *Sandia National Laboratories*

**Thuc-Quyen Nguyen**, *Univ. of California, Santa Barbara*

**Peter Nickias**, *Dow Chemical Company*

**Marc D. Porter**, *Univ. of Utah*

**Carol Beth Post**, *Purdue Univ.*

**Krishnan Raghavachari**, *Indiana Univ.*

**Susan Richardson**, *Univ. of South Carolina*

**Kenneth Ruud**, *Univ. of Tromsø – The Arctic Univ. of Norway (Norway)*

**Zachary Schultz**, *The Ohio State Univ.*

**George C. Shields**, *Furman Univ.*

**Zuzanna Siwy**, *Univ. of California, Irvine*

**Peter J. Tonge**, *Stony Brook Univ.*

**Marek Urban**, *Clemson Univ.*

**David Van Vranken**, *Univ. of California, Irvine*

**Michael VanNieuwenhze**, *Indiana Univ.*

**Helma Wennemers**, *ETH Zurich (Switzerland)*

**Hao Yan**, *Arizona State Univ.*

## Section on Dentistry and Oral Health Sciences

**Carolyn W. Gibson**, *Penn Dental Medicine*

**Janet Moradian-Oldak**, *Univ. of Southern California*

**Lynne A. Opperman**, *Texas A&M Univ. College of Dentistry*

**Michael W. Russell**, *Univ. at Buffalo, The State Univ. of New York*

**Kelly G. Ten Hagen**, *National Institute of Dental and Craniofacial Research/NIH*

## Section on Education

**Carol A. Brewer**, *Univ. of Montana*

**Anthony Carpi**, *John Jay College of Criminal Justice, CUNY*

**Jennifer Lynn Cutaro**, *Science Storytellers*

**Zoubeida R. Dagher**, *Univ. of Delaware*

**Susan Elrod**, *Indiana Univ. South Bend*

**Barbara L. Gonzalez**, *California State Univ., Fullerton*

**Robert Hilborn**, *American Association of Physics Teachers*

**Toby Horn**, *Retired*

**Kenneth L. Huff**, *Mill Middle School*

**Elizabeth F. Karplus**, *Mills College*

**Eric Klopfer**, *Massachusetts Institute of Technology*

**Michael C. Lach**, *Township High School District 113*

**Joseph S. Levine**, *Freelance author and editor*

**Michael Mayhew**, *Science Education Solutions*

**Marisa L. Pedulla**, *Montana Technological Univ.*

**Maria Varelas**, *Univ. of Illinois at Chicago*

## Section on Engineering

**Douglas E. Adams**, *Vanderbilt Univ.*

**Avinash Kumar Agarwal**, *Indian Institute of Technology Kanpur (India)*

**Andrew G. Alleyne**, *Univ. of Illinois at Urbana-Champaign*

**Andrea Alù**, *CUNY Advanced Science Research Center*

**Rajeevan Amirtharajah**, *Univ. of California, Davis*

**Arthur B. Baggeroer**, *Massachusetts Institute of Technology*

**John Ballato**, *Clemson Univ.*

**Ravi Bellamkonda**, *Duke Univ.*

**Robert H. Bishop**, *Univ. of South Florida*

**David Cahill**, *Univ. of Illinois at Urbana-Champaign*

**Ashutosh Chilkoti**, *Duke Univ.*

**George Chrisikos**, *NA*

**Cristina Davis**, *Univ. of California, Davis*

**Matthew Delisa**, *Cornell Univ.*

**Dan Fleetwood**, *Vanderbilt Univ.*

**David H. Gracias**, *Johns Hopkins Univ.*

**Piotr Grodzinski**, *National Cancer Institute/NIH*

**Carol Klein Hall**, *North Carolina State Univ.*

**Wesley L. Harris**, *Massachusetts Institute of Technology*



**Tony Jun Huang**, *Duke Univ.*

**Sheldon H. Jacobson**, *Univ. of Illinois at Urbana-Champaign*

**David C. Jiles**, *Iowa State Univ.*

**Alexander H. King**, *Iowa State Univ.*

**Thomas C. M. Lee**, *Univ. of California, Davis*

**Y. A. Liu**, *Virginia Tech*

**Guru Madhavan**, *National Academy of Sciences, Engineering, and Medicine*

**Vinothan N. Manoharan**, *Harvard Univ.*

**Radenka Maric**, *Univ. of Connecticut/UConn Health*

**Eyad Masad**, *Texas A&M Univ./Texas A&M Univ. at Qatar (Qatar)*

**Clare McCabe**, *Vanderbilt Univ.*

**Achille Messac**, *Howard Univ.*

**Randolph L. (Randy) Moses**, *The Ohio State Univ.*

**G.R. Odette**, *Univ. of California, Santa Barbara*

**Gopal R. Rao**, *Materials Research Society (MRS)*

**Asok Ray**, *Pennsylvania State Univ.*

**Sharon L. Walker**, *Drexel Univ.*

**Lihong Wang**, *California Institute of Technology*

**Rosemarie D. Wesson**, *The City College of New York*

**Yang Yang**, *Univ. of California, Los Angeles/Westlake Univ. (China)*

## Section on General Interest in Science and Engineering

**Monica M. Bradford**, *AAAS /Science*

**Lee Ann Brogie**, *American Junior Academy of Science*

**Ronnie Coffman**, *Cornell Univ.*

**Rebecca Finlay**, *CIFAR - Canadian Institute for Advanced Research (Canada)*

**Julia M. Gelfand**, *Univ. of California, Irvine*

**John Charles Nemeth**, *Education and Research Consulting*

**Clayton E. Teague**, *National Institute of Standards and Technology*

## Section on Geology and Geography

**Roland Bürgmann**, *Univ. of California, Berkeley*

**Renee M. Clary**, *Mississippi State Univ.*

**Laura Crossey**, *Univ. of New Mexico*

**Annette Summers Engel**, *Univ. of Tennessee, Knoxville*

**Christopher M. Fedo**, *Univ. of Tennessee, Knoxville*

**Andrew T. Fisher**, *Univ. of California, Santa Cruz*

**Jeff T. Freymueller**, *Michigan State Univ.*

**Richard Gordon**, *Rice Univ.*

**Chansheng He**, *Western Michigan Univ.*

**Hugo A. Loaiciga**, *Univ. of California, Santa Barbara*

**Michael Manga**, *Univ. of California, Berkeley*

**Petra Mudie**, *Natural Resources Canada (Canada)*

**Alan T. Murray**, *Univ. of California, Santa Barbara*

**Nathan A. Niemi**, *Univ. of Michigan*

**Eric Rignot**, *Univ. of California, Irvine*

**Patricia Soranno**, *Michigan State Univ.*

**John R. G. Townshend**, *Univ. of Maryland*

**David Valentine**, *Univ. of California, Santa Barbara*

**Christa von Hillebrandt-Andrade**, *National Weather Service*

**Qihao Weng**, *Indiana State Univ.*

**Shuhai Xiao**, *Virginia Tech*

## Section on History and Philosophy of Science

**Don Ihde**, *Stony Brook Univ.*

**Margaret Jacob**, *Univ. of California, Los Angeles*

**Nicolas Rasmussen**, *Univ. of New South Wales (Australia)*

**Zuoyue Wang**, *California State Polytechnic Univ., Pomona*

## Section on Industrial Science and Technology

**Ray H. Baughman**, *The Univ. of Texas at Dallas*

**Elizabeth R. Cantwell**, *Univ. of Arizona*

**Sara Kenkare-Mitra**, *Genentech*

**Willie E. May**, *Morgan State Univ.*

**Janice G. Pero**, *NA (most recently OmniGene Bioproducts Inc.)*

**William D. Provine**, *Delaware Innovation Space/DuPont*

**Ellen D. Williams**, *Univ. of Maryland*

## Section on Information, Computing, and Communications

**Daniel Atkins**, *Univ. of Michigan*

**Elizabeth M. Belding**, *Univ. of California, Santa Barbara*

**Kevin W. Bowyer**, *Univ. of Notre Dame*

**Guohong Cao**, *Pennsylvania State Univ.*

**William J. Clancey**, *Florida Institute for Human and Machine Cognition*

**Noshir S. Contractor**, *Northwestern Univ.*

**Isabel F. Cruz**, *Univ. of Illinois at Chicago*

**Ewa Deelman**, *Univ. of Southern California*

**Michael Franz**, *Univ. of California, Irvine*

**Roscoe C. Giles**, *Boston Univ.*

**Zhu Han**, *Univ. of Houston*

**Abdelsalam Sumi Helal**, *Univ. of Florida/Lancaster Univ. (UK)*

**Odest Chadwicke Jenkins**, *Univ. of Michigan*

**Norman P. Jouppi**, *Google, Inc.*

**Sampath Kannan**, *Univ. of Pennsylvania*

**John J. Leonard**, *Massachusetts Institute of Technology*

**Herbert S. Lin**, *Stanford Univ.*

**Donald W. Loveland**, *Duke Univ.*

**Michael A. McRobbie**, *Indiana Univ.*

**Klara Nahrstedt**, *Univ. of Illinois at Urbana-Champaign*

**Rob Rutenbar**, *Univ. of Pittsburgh*

**Reid G. Smith**, *i2k Connect*

**Tao Xie**, *Peking Univ. (China)*

**Yuan Xie**, *Univ. of California, Santa Barbara*

## Section on Linguistics and Language Sciences

**Jennifer Cole**, *Northwestern Univ.*

**Suzanne Flynn**, *Massachusetts Institute of Technology*

**Allard Jongman**, *Univ. of Kansas*

**Dan Jurafsky**, *Stanford Univ.*

## Section on Mathematics

**David M. Bressoud**, *Macalester College*

**Lisa J. Fauci**, *Tulane Univ.*

**John S. Lowengrub**, *Univ. of California, Irvine*

**Michael J. Miksis**, *Northwestern Univ.*

**Kavita Ramanan**, *Brown Univ.*

**Jinchao Xu**, *Pennsylvania State Univ.*

**Kevin Zumbrun**, *Indiana Univ.*

## Section on Medical Sciences

**Mary Aramian**, *Johns Hopkins School of Medicine*

**Brian D. Athey**, *Univ. of Michigan Medical School*

**Nicole Baumgarth**, *Univ. of California, Davis*

**David A. Bloom**, *Univ. of Michigan*

**Subbarao Bondada**, *Univ. of Kentucky*

**Gary A. Churchill**, *The Jackson Laboratory*

**Samuel M. Cohen**, *Univ. of Nebraska Medical Center*

**Nicholas Davidson**, *Washington Univ. School of Medicine in St. Louis*

**Channing Der**, *Univ. of North Carolina at Chapel Hill*

**Donna L. Farber**, *Columbia Univ. Irving Medical Center*

**Robert D. Frisina**, *Univ. of South Florida*

**Mary J. C. Hendrix**, *Shepherd Univ.*

**Darren E. Higgins**, *Harvard Medical School*

**James E. Klaunig**, *Indiana Univ.*

**Kenneth M. Langa**, *Univ. of Michigan*

**Jun Li**, *Univ. of Michigan*

**Marsha A. Moses**, *Harvard Medical School/ Boston Children's Hospital*

**Kevin G. Osteen**, *Vanderbilt Univ. School of Medicine*

**Kornelia Polyak**, *Dana-Farber Cancer Institute*

**Claire Pomeroy**, *Albert and Mary Lasker Foundation*

**Joan Y. Reede**, *Harvard Medical School*

**José Rafael Romero**, *Univ. of Arkansas for Medical Sciences*

**Linda C. Samuelson**, *Univ. of Michigan*

**Julianne M. Serovich**, *Univ. of South Florida*

**Dale Richman (Rick) Sumner Jr.**, *Rush Univ. Medical Center*

**Dan Theodorescu**, *Cedars-Sinai Medical Center*

**Samuel O. Thier**, *Harvard Medical School/ Massachusetts General Hospital*

**Jack R. Wands**, *The Liver Research Center, Rhode Island Hospital and Brown Univ.*

**Dyann F. Wirth**, *Harvard T. H. Chan School of Public Health*

**Joseph C. Wu**, *Stanford Univ. School of Medicine*

**Sarah Y. Yuan**, *Univ. of South Florida*

**Mone Zaidi**, *Ichann School of Medicine at Mount Sinai*

**David L. Zeale**, *Vanderbilt Univ. Medical Center*

**Yuan Zhu**, *Children's National Research Institute of Children's National Hospital*

**Weiping Zou**, *Univ. of Michigan*

## Section on Neuroscience

**Kathryn Albers**, *Univ. of Pittsburgh*

**Tallie Z. Baram**, *Univ. of California, Irvine*

**Robert F. Berman**, *Univ. of California, Davis*

**Maria G. Castro**, *Univ. of Michigan Medical School*

**Peter Dayan**, *Max Planck Institute for Biological Cybernetics (Germany)*

**R. Douglas Fields**, *National Institute of Child Health and Human Development/NIH*

**Michael J. Friedlander**, *Virginia Tech*

**David L. Glanzman**, *Univ. of California, Los Angeles*

**John Francis Greden**, *Univ. of Michigan*

**Suzanne M. Moenter**, *Univ. of Michigan*

**Thomas J. Park**, *Univ. of Illinois at Chicago*

**Vijayalakshmi Ravindranath**, *Centre for Brain Research, Indian Institute of Science (India)*

**David J. Schulz**, *Univ. of Missouri*

**Robert Schwarcz**, *Univ. of Maryland School of Medicine*

**Piali Sengupta**, *Brandeis Univ.*

**Michael Shipley**, *Univ. of Maryland School of Medicine*

**Styliani-Anna (Stella) E. Tsirka**, *Stony Brook Univ.*

**Marcelo A. Wood**, *Univ. of California, Irvine*

**Teresa Wood**, *New Jersey Medical School, Rutgers Univ.*

## Section on Pharmaceutical Sciences

**John A. Beutler**, *National Cancer Institute at Frederick/NIH*

**Robert Clarke**, *Georgetown Univ.*

**Sara A. Courtneidge**, *Oregon Health & Science Univ.*

**Jay Irwin Goodman**, *Michigan State Univ.*

**Douglas A. Lauffenburger**, *Massachusetts Institute of Technology*

**Leonard Schleifer**, *Regeneron*

**Neil Stahl**, *Regeneron*

**Nicholas K. Tonks**, *Cold Spring Harbor Laboratory*

**Shaomeng Wang**, *Univ. of Michigan*

## Section on Physics

**Beverly K. Berger**, *National Science Foundation (retired)*

**Robert Caldwell**, *Dartmouth College*

**Vincent H. Crespi**, *Pennsylvania State Univ.*

**Dale E. Gary**, *New Jersey Institute of Technology*

**Kurt Gibble**, *Pennsylvania State Univ.*

**Frederick J. Gilman**, *Carnegie Mellon Univ.*

**Tao Han**, *Univ. of Pittsburgh*

**Barbara A. Jones**, *IBM Research - Almaden*

**Jacqueline Krim**, *North Carolina State Univ.*

**Reiner Kruecken**, *TRIUMF/Univ. of British Columbia (Canada)*

**Albert J. Libchaber**, *The Rockefeller Univ.*

**Kai Liu**, *Georgetown Univ./Univ. of California, Davis*

**Arthur B. McDonald**, *Queen's Univ. (Canada)*

**Noureddine Melikechi**, *Univ. of Massachusetts, Lowell*

**Vincent Meunier**, *Rensselaer Polytechnic Institute*

**Ivan I. Oleynik**, *Univ. of South Florida*

**J. Ritchie Patterson**, *Cornell Univ.*

**Mark George Raizen**, *The Univ. of Texas at Austin*

**Marcos Rigol**, *Pennsylvania State Univ.*

**Natalie A. Roe**, *Lawrence Berkeley National Laboratory*

**Vladimir Shiltsev**, *Fermi National Accelerator Laboratory*

**James Siegrist**, *U.S. Department of Energy*

**Leonid A. Turkevich**, *The National Institute for Occupational Safety and Health/CDC*

**David S. Weiss**, *Pennsylvania State Univ. College of Medicine*

**James Wells**, *Univ. of Michigan*

**Edward Witten**, *Institute for Advanced Study*

**Lilia M. Woods**, *Univ. of South Florida*

## Section on Psychology

**Michelle Suzanne Bourgeois**, *Univ. of South Florida*

**Richard Gerrig**, *Stony Brook Univ.*

**Richard Ivry**, *Univ. of California, Berkeley*

**Kevin LaBar**, *Duke Univ.*

**Gordon D. Logan**, *Vanderbilt Univ.*

**Sharon Landesman Ramey**, *Virginia Tech*

**Paul Elliott Spector**, *Univ. of South Florida*

**Margaret Beale Spencer**, *Univ. of Chicago*

**Bethany Ann Teachman**, *Univ. of Virginia*

**David H. Zald**, *Vanderbilt Univ.*

## Section on Social, Economic, and Political Sciences

**Maria Charles**, *Univ. of California, Santa Barbara*

**Claudio Cioffi-Revilla**, *George Mason Univ.*

**Dalton Conley**, *Princeton Univ.*

**Kathleen Mullan Harris**, *Univ. of North Carolina at Chapel Hill*

**Catherine L. Kling**, *Cornell Univ.*

**Stephen Marks**, *Harvard T. H. Chan School of Public Health*

**David Neumark**, *Univ. of California, Irvine*

**William Alex Pridemore**, *Univ. at Albany, The State Univ. of New York*

**Thomas P. Tomich**, *Univ. of California, Davis/ UC Division of Agriculture and Natural Resources*

## Section on Societal Impacts of Science and Engineering

**Margaret M. Betchart**, *Betchart Expeditions, Inc.*

**William S. Kisaalita**, *Univ. of Georgia*

**Gary Marchant**, *Arizona State Univ.*

**Marie Lynn Miranda**, *Rice Univ.*

**William R. Moomaw**, *Tufts Univ.*

**Margaret Race**, *SETI Institute*

**Melanie Roberts**, *Pacific Northwest National Laboratory*

**Dahlia Sokolov**, *United States House of Representatives*

## Section on Statistics

**F. DuBois Bowman**, *Univ. of Michigan*

**Ronald D. Fricker Jr.**, *Virginia Tech*

**Jiming Jiang**, *Univ. of California, Davis*

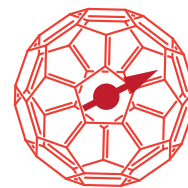
**Nandini Kannan**, *Indo-U.S. Science and Technology Forum (IUSSTF)*

**J. Jack Lee**, *Univ. of Texas MD Anderson Cancer Center*

**Kathryn Roeder**, *Carnegie Mellon Univ.*

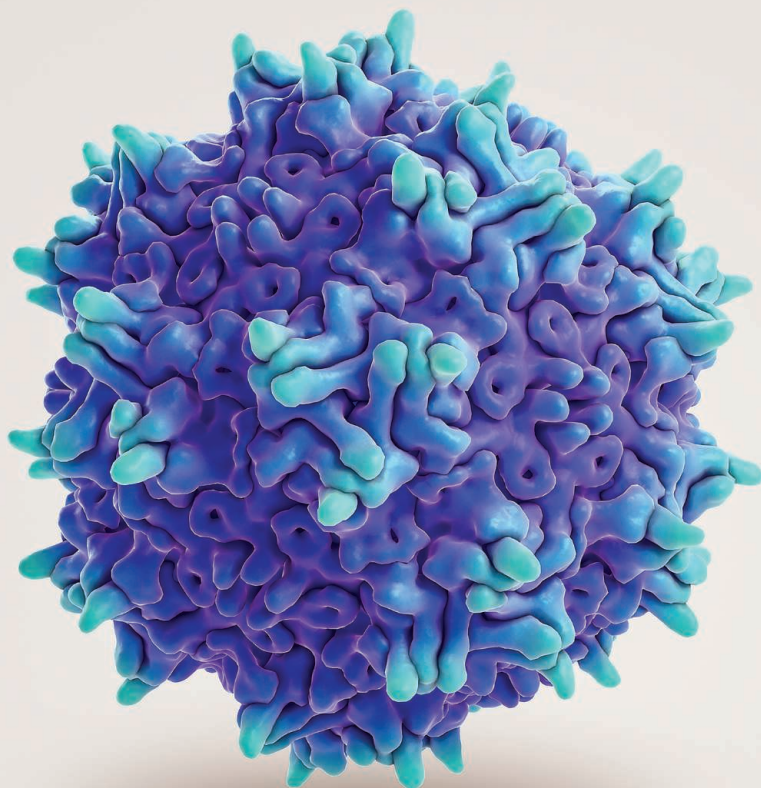
**Susan M. Shortreed**, *Kaiser Permanente Washington Health Research Institute*





## IN SCIENCE JOURNALS

Edited by **Stella Hurtley**



### MOLECULAR BIOLOGY

## The fitness landscape of AAV

**A**deno-associated virus (AAV) is an important gene therapy vector. Using tools from synthetic biology, Ogden *et al.* provide a comprehensive view of how sequence changes in capsid proteins affect AAV properties. After saturation mutagenesis of the AAV2 capsid gene, the resulting library was subjected to multiplexed phenotypic analyses, including virus production, immunity, thermostability, and biodistribution. The mutant distribution to major organs in mice revealed dominant trends affecting *in vivo* delivery. Moreover, the findings uncovered a viral accessory protein with a role in viral production. Finally, a model built from the capsid fitness landscape enabled machine-guided design of useful variants with much higher efficiency than random mutagenesis. —SYM

*Science*, this issue p. 1139

Computer-generated image of the atomic structure of adeno-associated virus

### SUPERCONDUCTIVITY

## A sharp boundary in the cuprates

Many physicists working on cuprate superconductors believe that the so-called strange metal phase in the cuprate phase diagram is associated with a quantum critical point. Within this picture, the quantum critical point gives rise to a V-shaped region in the doping-temperature phase diagram of the cuprates: the strange metal phase. Chen *et al.* used angle-resolved photoemission spectroscopy in the cuprate family Bi2212 to challenge this

view. By taking comprehensive measurements as a function of doping and temperature—and making sure that the signal was not affected by environmental conditions—they found an incoherent strange metal phase that was sharply separated from a conventional phase by a temperature-independent vertical line in the phase diagram. —JS

*Science*, this issue p. 1099

### ELASTOCALORICS

## A million times cooler

Elastocaloric materials can be used for solid-state cooling applications because they can

pump heat out of a system using a reversible phase transformation. However, many such materials fail after a small number of cycles. Hou *et al.* found that laser melting of elastocaloric metals can create fatigue-resistant microstructures. A nickel-titanium-based alloy could be cycled a million times and still produce a cooling of about 4 kelvin. This processing method could improve elastocaloric performance and move us closer to using these materials more widely for solid-state cooling applications. —BG

*Science*, this issue p. 1116

### MATERIALS SCIENCE

## Growing polymer brushes from surfaces

Surface functionalization is important in a broad range of fields. One approach involves polymer brushes, where polymer chains are grafted onto a surface. Cai *et al.* describe the nanoscale functionalization of surfaces by exploiting the living crystallization-driven self-assembly of polyferrocenyl-based block copolymers (see the Perspective by Presa Soto). Small crystalline cylindrical micelle seeds were attached using noncovalent bonds to

a variety of surfaces, including silicon wafers, graphene oxide nanosheets, and gold. Addition of dissolved unimers over the seed-coated surfaces allowed micellar brushes to grow. Protonation and post-decoration with gold and silver nanoparticles demonstrated the applicability of such modified surfaces in catalysis, as antibacterial agents, and in separation processes. —MSL

*Science*, this issue p. 1095;  
see also p. 1078

## ENHANCER GENOMICS

### Linking enhancers to disease

Enhancers are genomic regions that regulate gene expression, sometimes in a cell-dependent manner. However, most of our knowledge of human brain cell-type enhancers derives from studies of bulk human brain tissue. Nott *et al.* examined chromatin and promoter activity in cell nuclei isolated from human brains. Genetic variants associated with brain traits and disease showed cell-specific patterns of enhancer enrichment. These data indicate that Alzheimer's disease is regulated by genetic variants within microglial cells, whereas psychiatric diseases tend to affect neurons. —LMZ

*Science*, this issue p. 1134

## MICROBIOME

### Lactose can fuel GVHD

Allogeneic hematopoietic cell transplantation (allo-HCT) is used to treat certain hematopoietic malignancies, but patients have a risk of developing graft-versus-host disease (GVHD). Stein-Thoeriger *et al.* performed a large-scale analysis of more than 1300 patients treated with allo-HCT across four clinical centers (see the Perspective by Zitvogel and Kroemer). High levels of bacteria from the *Enterococcus* genus were associated with greater incidence of GVHD and mortality. Lactose appears to provide a substrate for *Enterococcus*

growth, and patients with a lactose-malabsorption genotype had a greater abundance of *Enterococcus*. A lactose-free diet limited *Enterococcus* growth, reduced the severity of GVHD, and improved survival in gnotobiotic mouse models. —PNK

*Science*, this issue p. 1143;  
see also p. 1077

## HIV

### Early to treat, early to thrive

Timing of antiretroviral therapy (ART) initiation for HIV can influence viral-reservoir seeding and also the immune response. However, this has not been well characterized in neonatal HIV infection. To discern how ART affects neonates, Garcia-Broncano *et al.* studied infants from Botswana who were placed on ART hours or months after birth. Early initiation of therapy reduced seeding of the viral reservoir and also modulated natural killer cell and T cell responses to HIV. Thus, immediate ART initiation—earlier than the current guidelines of a few weeks—could provide real benefit to infants with HIV. —LP

*Sci. Transl. Med.* **11**, eaax7350 (2019).

## TUMOR IMMUNOTHERAPY

### New cell therapy fights brain tumors

An adoptive cellular therapy that expands clonal T cells could help fight deadly heterogeneous brain tumors, medulloblastoma, and glioblastoma. Working in mice, Flores *et al.* used dendritic cells expressing tumor RNA to expand polyclonal T cells that quickly react against a variety of different antigens within different brain tumors. Promising results were also obtained in a patient with recurrent medulloblastoma. Although previous adoptive T cell therapies have proven effective against several advanced cancers, the current method could provide patients with effective T cell therapy for brain tumors. —SMF

*Sci. Adv.* 10.1126/sciadv.aav9879 (2019).

## IN OTHER JOURNALS

Edited by **Caroline Ash**  
and **Jesse Smith**



## DRUG SOLVATION

### A spoonful of sugar for your coffee

**A**lthough we brew coffee and tea in water, the psychoactive drug we crave, caffeine, is moderately hydrophobic and becomes more so as the temperature of a beverage decreases. Stacked aggregates of caffeine molecules, which may have different properties, can form at saturation. Shumilin *et al.* investigated the distribution of caffeine aggregates and monomers in response to increasing concentration of a common excipient: sugar. Although various sugars decreased overall caffeine solubility, they had a preferential effect on oligomers and resulted in a higher relative proportion of caffeine in the monomer form. —MAF

*J. Am. Chem. Soc.* **141**, 18056 (2019).

**Adding sugar to coffee can change the solubility and aggregation behavior of caffeine molecules.**

## HEART DISEASE

### Exercise finds its niche

Regular physical activity is associated with a lower rate of death from heart disease, but the underlying mechanisms are not fully understood. Frodermann *et al.* examined the effect of exercise on cardiovascular inflammation, a known risk factor for atherosclerosis,

by studying mice that voluntarily ran for long distances on exercise wheels. They found that these physically active mice had fewer inflammatory cells (leukocytes) than sedentary mice, an effect they traced to diminished activity of hematopoietic stem and progenitor cells (HSPCs). The lower activity of HSPCs was due at least in part to exercise-induced reduction in the levels



Honey bee,  
*Apis mellifera*,  
feeding on  
a strawberry  
flower



## MUTUALISM

### Root to shoot protection

**N**oble rot caused by the gray mold *Botrytis cinerea* is essential to producing the world's finest wines, but under different conditions, this mold devastates soft fruit crops. Kim *et al.* investigated how plants and their microbial partners defend against this ubiquitous greenhouse pathogen. They identified a filamentous *Streptomyces* sp. bacterium, a genus renowned for synthesizing antibiotic-like molecules, associated with strawberry plants. *Streptomyces globisporus* SP6C4 was found in all vascular tissues of the plants, even in the pollen. The occurrence of SP6C4 associated with low levels of mold disease. In greenhouse experiments, honey bees ingested the SP6C4-laden strawberry pollen and not only benefited from a reduction in potential insect pathogens but also acted as vectors of the protective SP6C4 to mold-susceptible greenhouse plants. The natural products produced by SP6C4 have not yet been characterized. —CA

*Nat. Commun.* **10**, 4802 (2019).

of leptin, a hormone produced by fat tissue that regulates cells within the hematopoietic bone marrow niche. —PAK

*Nat. Med.* **25**, 1761 (2019).

## CELL BIOLOGY

### Prising open the human brain

Meningococcus (*Neisseria meningitidis*) causes meningitis and rapidly progressing fatal shock, but only in humans. To invade the brain, meningococcus uses its filamentous pili to hijack the  $\beta_2$ -adrenergic receptor ( $\beta_2$ AR), inducing an allosteric  $\beta$ -arrestin-biased signaling cascade in endothelial cells lining the capillaries of the brain. This cascade allows bacterial colonies to tether to endothelial cells, despite the shear stress of blood flow, and also promotes opening of endothelial junctions, which allows bacteria to penetrate the brain. Virion *et al.* sought to understand how a G protein-coupled receptor is activated by bacterial type IV pili proteins to

transduce a signaling cascade that normally needs a cognate ligand. They found that  $\beta_2$ AR activation requires two asparagine-branched glycan chains with terminally exposed sialic acid residues. Meningococcus triggers receptor signaling by exerting mechanical forces on  $\beta_2$ AR glycans with its retractable pili. Because human glycans are unusual in exposing sialic acid residues on their glycans, this mechanism may help explain the specificity of meningococcus to its human host. —SMH

*Nat. Commun.* **10**, 4752 (2019).

## NEUROSCIENCE

### How to assemble a glutamate receptor

The biogenesis of the AMPA glutamate receptor, which mediates fast synaptic transmission in the central nervous system, is not understood. Using a variety of high-resolution techniques, as well as behavioral studies, Schwenk *et al.* identified the protein constituents of the

production line in the endoplasmic reticulum that assembles functional AMPA receptors in the mammalian brain. These protein constituents help to generate tetrameric assemblies from monomers of pore-forming receptor subunits. Genetic deletion of the oligomerizing proteins profoundly altered AMPA receptor-mediated neurotransmission and synaptogenesis, abolished activity-driven plasticity, and severely impaired learning in mice. —PRS

*Neuron* **10.1016/j.neuron.2019.08.033** (2019).

## ARCTIC WARMING

### Snow job

What is the cause of the observed reduction of surface albedo in the Arctic since the early 1980s? This surface albedo reduction is thought to be a major reason that the Arctic has warmed at a rate two to three times greater than the global average. Zhang *et al.* show that reductions of terrestrial snow cover, snow cover fraction over sea ice, and sea ice

extent are coequally responsible for the albedo decline and that the decrease in snow cover is primarily due to rising surface air temperatures. Soot deposition has not been an important factor in the albedo change. —HJS

*Proc. Natl. Acad. Sci. U.S.A.* **10.1073/pnas.1915258116** (2019).

## INORGANIC CHEMISTRY

### Aluminum squared

Three-coordinate aluminum compounds are potent Lewis acids: They readily attract electron donors, binding them to form a saturated tetrahedral product. Ebner *et al.* now report that four-coordinate aluminum can act as a Lewis acid, too, so long as it's forced ahead of time into a square planar geometry. To attain this unusual bonding motif, they embedded an aluminum(III) ion within a macrocycle of four negatively charged pyrrole donors. In addition to binding tetrahydrofuran, this aluminum center accepted hydride and fluoride ligands. —JSY

*J. Am. Chem. Soc.* **141**, 18009 (2019).

ALSO IN *SCIENCE* JOURNALS

Edited by Stella Hurlley

## NEUROSCIENCE

**Brain anatomy revealed in startling detail**

The mammalian cerebral cortex is an enormously complex network of neuronal processes that are long and thin, branching, and extremely densely packed. This high packing density has made the reconstruction of cortical neuronal networks challenging. Motta *et al.* used advanced automated imaging and analysis tools to reconstruct with high spatial resolution the morphological features of 89 neurons and their connections in the mouse barrel cortex. The reconstruction covered an area more than two orders of magnitude larger than earlier neuroanatomical mapping attempts. This approach revealed information about the connectivity of inhibitory and excitatory synapses of corticocortical as well as excitatory thalamocortical connections. —PRS

*Science*, this issue p. 1093

## SEISMOLOGY

**Marine observations with optics**

Placing sensors on the seafloor is difficult, but a sensor network has huge potential for observing processes occurring both below and above the seafloor. Lindsey *et al.* measured acoustic vibrations collected by attaching a laser to the Monterey Accelerated Research System's subsea optical fiber during a maintenance period (see the Perspective by Jousset). Acoustic waves were monitored by changes in laser light along the cable. The observations from just a few days allowed mapping of an unknown fault system and detection of several dynamic processes in the water column above. —BG

*Science*, this issue p. 1103;  
see also p. 1076

## QUANTUM MATERIALS

**Controlling quantum defects in graphene**

The development of quantum technologies relies on the ability to fabricate and engineer materials with robust quantum properties. The controlled introduction of defects in semiconductors is one of the most promising platforms under development. With the capability to precisely position point defects (five-membered rings) in the graphene honeycomb lattice, Lombardi *et al.* explored recent theoretical work suggesting that such defects should display enhanced quantum properties (see the Perspective by von Kugelgen and Freedman). The spin-bearing properties of the defects and the engineered control of their interactions open up exciting possibilities for graphene-based spintronics and quantum electronics. —ISO

*Science*, this issue p. 1107;  
see also p. 1070

## CHEMICAL PHYSICS

**Glimpsing an exchange of partners**

When two diatomic molecules collide, they can sometimes swap partners. For instance, two potassium-rubidium (KRb) molecules can produce  $K_2$  and  $Rb_2$ . The four-atom intermediate formed upon collision is typically too scarce and short-lived to spot, even using ultrafast techniques. Hu *et al.* circumvented this problem by studying the reaction at temperatures approaching 0 kelvin. Using a combination of mass spectrometry and velocity-map imaging, the authors directly characterized the ionized  $K_2Rb_2$  complex as well as the reactant and product populations. —JSY

*Science*, this issue p. 1111

## NEUROSCIENCE

**Keeping tabs on bad experiences**

Identifying the neural basis underlying how we acquire, process, and store negative experiences could help the search for effective treatments for mood disorders. Szőnyi *et al.* used a range of neuroscientific tools to elucidate the role of a specific neural circuit that originates in the median raphe region of the murine brainstem (see the Perspective by Ikemoto). A subpopulation of excitatory neurons projected to aversive brain areas and received recurrent feedback from the lateral habenula and convergent feedback from a range of fear-related circuitry. These neurons were activated by aversive stimuli, and artificial stimulation promoted aversion or anxiety-related behavior. This group of cells thus plays a pivotal role in a network that helps to mediate aversive motivation. —PRS

*Science*, this issue p. 1094;  
see also p. 1071

## MAGNONICS

**Toward magnonic devices**

The field of magnonics aims to use spin waves (SWs) and their associated quasiparticles—magnons—as carriers of information. Compared with the movement of charge in conventional electronics, a major advantage of SWs is reduced Joule heating. However, SWs are trickier to direct and control. Two groups now go a step further toward magnon-based devices. Han *et al.* show that in multilayer films, domain walls can be used to change the phase and magnitude of a spin wave. Wang *et al.* demonstrate how magnon currents can be used to switch the magnetization of an adjacent layer. —JS

*Science*, this issue p. 1121, p. 1125

## BIOCHEMISTRY

**CTP hydrolysis organizes chromosomes**

The bacterial DNA *parS* centromere recruits the ParB protein to the bacterial chromosome. Soh *et al.* found that the widespread family of ParB proteins not only bind DNA but also bind and hydrolyze cytidine triphosphate (CTP) (see the Perspective by Funnell). ParB CTP hydrolysis is stimulated by *parS* and regulates the spreading of ParB protein to the *parS* flanking regions, which is crucial for organizing the bacterial chromosome. The cytidine triphosphatase domain is conserved in a large variety of protein sequences, suggesting its potential roles in other cellular processes. —SYM

*Science*, this issue p. 1129;  
see also p. 1072

## PROTEIN FOLDING

**A pathway for helical membrane proteins**

Membrane proteins are inserted into cell membranes while they are being translated and may fold concurrently into their secondary and tertiary structures. Choi *et al.* describe a single-molecule force microscopy technique that allowed them to monitor folding of helical membrane proteins in vesicles and bicelles. Two helical membrane proteins, the *Escherichia coli* rhomboid protease GlpG and the human  $\beta_2$ -adrenergic receptor, both folded from the N to the C terminus, with structures forming in units of helical hairpins. In the cell, this would allow these proteins to begin folding while being translated. —VV

*Science*, this issue p. 1150



## IMMUNOLOGY

**Microbiota influence vaccine responses**

Responses to vaccines can be variable, and recent findings suggest a potential explanation may lie in the influence of gut microbiota. In a Perspective, Pulendran discusses how systematic analyses of vaccination responses—for example, to the influenza vaccine—are revealing insights into vaccine responses and the importance of the gut microbiota in forming immunogenicity to infectious disease. This has implications for vaccine design and for stratifying individuals according to likely vaccine response. —GKA

*Science*, this issue p. 1074

## T CELLS

**Charting MAIT cell development**

Mucosal-associated invariant T (MAIT) cells are a distinct subset of T cells that recognize vitamin B metabolites presented by major histocompatibility complex class I–related protein (MR1). Koay *et al.* used bulk and single-cell RNA sequencing and flow cytometric analysis to characterize the development of murine and human MAIT cells. In addition to providing a clearer picture of MAIT cell development in the thymus, the studies uncovered several molecules that play key roles in regulating this process. Genetic inactivation experiments in mice confirmed the functions some of these molecules—including SAP, SATB1, CXCR6, and CCR7—in regulating MAIT cell development. —IW

*Sci. Immunol.* **4**, eaay6039 (2019).

stress-granule formation. After DNA stimulation of human cells, cGAS associated in an RNA-dependent manner with G3BP1 and was found in cytoplasmic foci that also contained messenger RNA and the RNA-dependent kinase PKR. Formation of cytoplasmic cGAS condensates necessary for DNA-stimulated type I interferon production required G3BP1 and PKR activity. —ERW

*Sci. Signal.* **12**, eaav7934 (2019).

## INNATE IMMUNITY

**A convergence for RNA and DNA sensing**

In response to cytosolic DNA, cyclic GMP-AMP synthase (cGAS) initiates a type I interferon response. Hu *et al.* found that endogenous cGAS bound to the nucleotide helicase G3BP1, which is involved in

## RESEARCH ARTICLE SUMMARY

## NEUROSCIENCE

## Dense connectomic reconstruction in layer 4 of the somatosensory cortex

Alessandro Motta\*, Manuel Berning\*, Kevin M. Boergens\*, Benedikt Staffler\*, Marcel Beining, Sahil Loomba, Philipp Hennig, Heiko Wissler, Moritz Helmstaedter†

**INTRODUCTION:** The brain of mammals consists of an enormously dense network of neuronal wires: the axons and dendrites of nerve cells. Their packing density is so high that light-based imaging methods have so far only been able to resolve a very small fraction of nerve cells and their interaction sites, the synapses, in mammalian cortex. Recent advances in three-dimensional (3D) electron microscopy allow researchers to image every nerve cell and all chemical synapses in a given piece of brain tissue, opening up the possibility of mapping neuronal networks densely, not just sparsely. Although there have been substantial advances in imaging speed, the analysis of such 3D image data is still the limiting step. Therefore, dense reconstructions

of cortical tissue have thus far been limited to femtoliter-scale volumes, keeping the systematic analysis of axons, neuronal cell bodies and their dendrites of different types, and the dense connectome between them out of reach.

**RATIONALE:** Image analysis has made decisive progress using artificial intelligence-based methods, but the resulting reconstructions of dense nerve tissue are still too error-prone to be scientifically meaningful as is. To address this, human data analysis has been integrated into the generation of connectomes and it is the efficiency of this human-machine data analysis that now determines progress in connectomics. We therefore focused on efficiency gains by: (i)

improving the automated segmentation quality, (ii) analyzing the automated segmentation for locations of likely errors and directing the human work to these locations only, and (iii) optimizing human data interaction by helping annotators to immediately understand

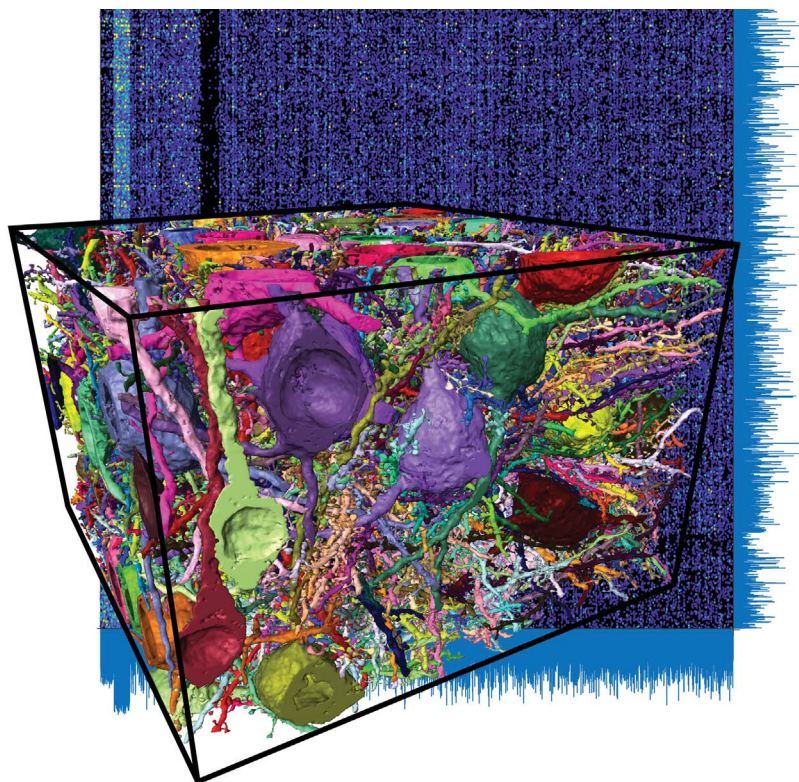
## ON OUR WEBSITE

Read the full article at <http://dx.doi.org/10.1126/science.aay3134>

With this, close to 100 student annotators solved hundreds of thousands of reconstruction problems within just 29 s each, including all preparation and transition time.

**RESULTS:** We reconstructed 2.7 m of neuronal wires densely in layer 4 of mouse somatosensory cortex within only ~4000 invested human work hours, yielding a reconstruction ~300 times larger than previous dense cortical reconstructions at ~20-fold increased efficiency, a leap for the dense reconstruction of connectomes. The resulting connectome between 6979 presynaptic and 3719 postsynaptic neurites with at least 10 synapses each, comprising 153,171 synapses total, was then analyzed for the dense circuit structure in the cerebral cortex. We found that connectomic data alone allowed the definition of inhibitory axon types that showed established principles of synaptic specificity for subcellular postsynaptic compartments, but that at scales beyond ~5  $\mu\text{m}$ , geometric predictability of the circuit structure was low and coarser models of random wiring needed to be rejected for dense cortical neuropil. A gradient of thalamocortical synapse density along the cortical axis yielded an enhanced variability of synaptic input composition at the level of single L4 cell dendrites. Finally, we quantified connectomic imprints consistent with Hebbian synaptic weight adaptation, obtaining upper bounds for the fraction of the circuit that could have undergone long-term potentiation.

**CONCLUSION:** By leveraging human-machine interaction for connectomic analysis of neuronal tissue, we acquired the largest connectome from the cerebral cortex to date. Using these data for connectomic cell-type definition and the mapping of upper bounds for the learned circuit fraction, we establish an approach for connectomic phenotyping of local dense neuronal circuitry in the mammalian cortex, opening the possibility for the connectomic screening of nervous tissue from various cortices, layers, species, developmental stages, sensory experience, and disease conditions. ■



Dense reconstruction of ~500,000 cubic micrometers of cortical tissue yielding 2.7 m of neuronal cables (~3% shown, front) implementing a connectome of ~400,000 synapses between 34,221 axons and 11,400 postsynaptic processes (fraction shown, back). These data were used for connectomic cell-type definition, geometrical circuit analysis, and measurement of the possible plastic fraction (the "learnedness") of the circuit.

The list of author affiliations is available in the full article online.

\*These authors contributed equally to this work.

†Corresponding author. Email: [mh@brain.mpg.de](mailto:mh@brain.mpg.de)

Cite this article as A. Motta et al., *Science* 366, eaay3134 (2019); DOI: 10.1126/science.aay3134



## RESEARCH ARTICLE

## NEUROSCIENCE

## Dense connectomic reconstruction in layer 4 of the somatosensory cortex

Alessandro Motta<sup>1\*</sup>, Manuel Berning<sup>1\*</sup>, Kevin M. Boergens<sup>1\*</sup>, Benedikt Staffler<sup>1\*</sup>, Marcel Beining<sup>1</sup>, Sahil Loomba<sup>1</sup>, Philipp Hennig<sup>2</sup>, Heiko Wissler<sup>1</sup>, Moritz Helmstaedter<sup>1†</sup>

The dense circuit structure of mammalian cerebral cortex is still unknown. With developments in three-dimensional electron microscopy, the imaging of sizable volumes of neuropil has become possible, but dense reconstruction of connectomes is the limiting step. We reconstructed a volume of ~500,000 cubic micrometers from layer 4 of mouse barrel cortex, ~300 times larger than previous dense reconstructions from the mammalian cerebral cortex. The connectomic data allowed the extraction of inhibitory and excitatory neuron subtypes that were not predictable from geometric information. We quantified connectomic imprints consistent with Hebbian synaptic weight adaptation, which yielded upper bounds for the fraction of the circuit consistent with saturated long-term potentiation. These data establish an approach for the locally dense connectomic phenotyping of neuronal circuitry in the mammalian cortex.

**T**he cerebral cortex of mammals houses an enormously complex intercellular interaction network implemented with neuronal processes that are long and thin, branching, and extremely densely packed. Early estimates indicated that 4 km of axons and 400 m of dendrites are compressed into a cubic millimeter of cortical tissue (1). This high packing density of cellular processes has made the locally dense mapping of neuronal networks in the cerebral cortex challenging.

So far, reconstructions of cortical tissue have been either sparse (2–7) or restricted to small volumes of up to 1500  $\mu\text{m}^3$  (8–10). Consequently, the detailed network architecture of the cerebral cortex is unknown. Particular open questions are to what degree local neuronal circuits are explainable by geometric rules alone (1, 2, 11–13) and on which spatial scales cortical connectivity is only explainable by innervation preferences beyond such geometric models (5, 8, 9, 14, 15). Similarly, although numerous cortical neuronal cell types have been described based on protein expression, morphology, and electrophysiological characteristics (16), and these have been shown to have particular synaptic target patterns (17), the inverse question—whether, at the level of the dense cortical circuit, axons represent a continuum of synaptic preference or a set of distinct innervation paradigms that would allow for a purely connectomic cell type definition [as has been successful in the retina

(18, 19)]—is still open. Next, at the level of synaptic input to the primary dendrites of cortical excitatory cells, it is not known whether the typically three to 10 primary dendrites of a cortical neuron that leave the cell body homogeneously sample the available excitatory and inhibitory synaptic inputs or if there is an enhanced heterogeneity of synaptic input composition, making it possible to exploit the numerous mechanisms that have been discussed for the nonlinear integration of local synaptic inputs (20–23). Finally, whereas the change of synaptic weights in response to electrical and sensory stimulation has been widely studied (24–28) and connectomic data consistent with LTP have been described (29, 30), the fraction of a given cortical circuit that is plausibly shaped by processes related to Hebbian learning under undisturbed conditions is still unknown.

We used dense connectomic reconstruction to quantitatively address these questions about the formational principles of a dense cortical circuit.

## Results

We acquired a three-dimensional (3D) EM dataset from upper layer 4 of primary somatosensory cortex of a 28-day-old mouse (Fig. 1, A to D, likely located within a barrel, see supplementary materials) using serial block-face electron microscopy [SBEM (31); dataset size:  $61.8 \times 94.8 \times 92.6 \mu\text{m}^3$ ; voxel size:  $11.24 \times 11.24 \times 28 \text{ nm}^3$ ]. For dense reconstruction (Fig. 1, E to H), we 3D aligned the images and applied a sequence of automated analyses [SegEM (32), SynEM (33), ConnectEM, and TypeEM; Fig. 2, supplementary materials and methods, and table S2], followed by focused manual annotation (FocusEM). We reconstructed 89 neurons that had their cell body in the dataset

(Fig. 1, E and F). These neurons constituted only 2.6% of the total path length (69 mm; Fig. 1G). To reconstruct axons, which constitute most of the wiring in the dense circuit (1.79 m, 66.6%, Fig. 1H), we applied a scalable distributed annotation strategy that identified locations of uncertainty in the automated reconstruction, which were then resolved by targeted manual annotation. To reduce the required manual annotation time, it was critical to obtain an automated reconstruction with low error rates, to use efficient algorithms for identifying locations for focused manual inspection (queries), and to minimize the time spent per user query. For this (Fig. 2A), we developed artificial intelligence–based algorithms that evaluated the EM image data and convolutional neural network (CNN)–filtered versions of the image data in the surrounding of interjunctions between segmented pieces of neurites (Fig. 2B). Together with classifiers that computed the probability of volume segments belonging to an axon, a dendrite, a spine head, or a glial process (using, among others, shape features; Fig. 2C), this allowed us to automatically connect parts of dendrites, attach spine heads to dendritic shafts (by a greedy stepwise agglomeration initiated at the spine head, Fig. 2D; 58.9% of spine heads unaffected by the dataset boundary were automatically attached), and reconstruct parts of axons. Similarly, synapses were automatically detected by evaluating pre- and postsynaptic volumes at neurite interfaces [Fig. 2E and figs. S2 to S5 (33); for shaft synapses, additional CNN-based classifiers for vesicle clouds and mitochondria were used]. To manually correct remaining errors in axons (Fig. 2, F to H), we detected ending locations of automatically reconstructed axon pieces (Fig. 2F) and directed user queries to these locations. For this, we used an egocentric 3D image display mode [“flight mode,” Fig. 2G (34)] and oriented the user annotation along the axis of the neurite for which a local annotation (“query”) was requested (movie S2). Together with data preloading, this yielded a low-latency, targeted neurite annotation in which individual user queries took 29.4 s to resolve (traveled path length per query:  $5.49 \mu\text{m}$ ). These queries could be easily distributed among 87 annotators. Similarly, we detected locations of likely mergers between axons (Fig. 2H, “chiasmata”) and directed user queries to reconnect the chiasma exits along actual axons. Using this scalable annotation architecture, we obtained a dense reconstruction of 2.69 m of neuronal processes (Fig. 1, G and H) with a total investment of 3981 human work hours, ~10 times faster than a recent dense reconstruction in the fly larval brain (35) (Fig. 2, I and J), ~20 times faster than the previous dense reconstruction in the mammalian retina (18), and ~25 times faster than the

<sup>1</sup>Department of Connectomics, Max Planck Institute for Brain Research, D-60438 Frankfurt, Germany. <sup>2</sup>Probabilistic Numerics Group, Max Planck Institute for Intelligent Systems, D-72076 Tübingen, Germany.

\*These authors contributed equally to this work.

†Corresponding author. Email: mh@brain.mpg.de

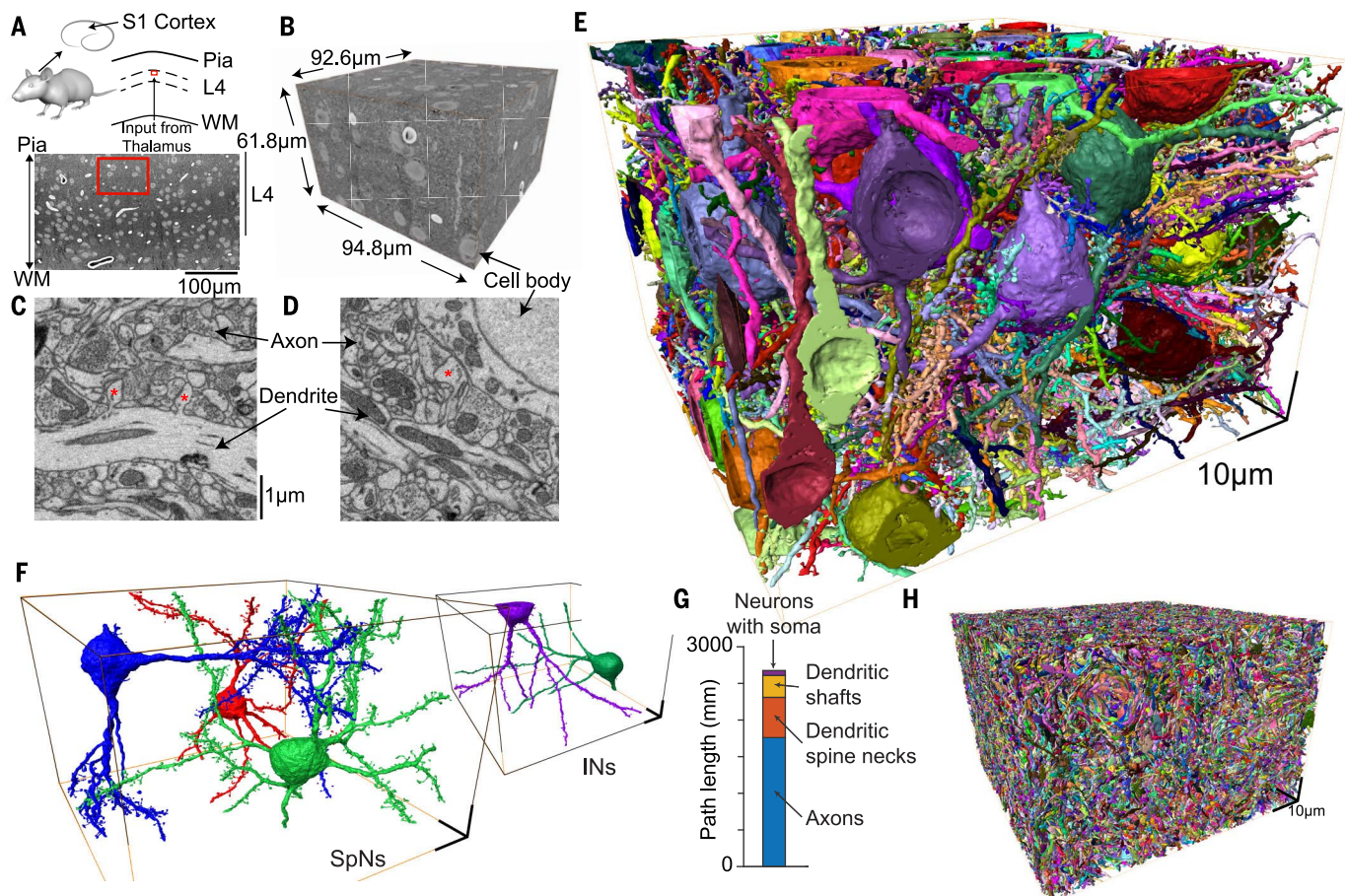


**Fig. 1. Dense connectomic reconstruction of cortical neuropil from layer 4 of mouse primary somatosensory cortex.** (A to D) Location [(A), red] of the 3D EM dataset (B). WM, white matter. High-resolution example images are shown in (C) and (D). Asterisks indicate examples of dendritic spines. Direct links to data browser webKnossos are as follows: <https://wklmk.org/9276> (B), <https://wklmk.org/7101> (C), and <https://wklmk.org/8906> (D). (E) Reconstruction of  $n = 89$  neurons with a cell body and dendrites in the dataset. (F) Three spiny neurons (SpNs) and two INs (see movie S1). (G) Quantification of circuit components in the dense reconstruction. Most of the circuit path length (total: 2.69 m) is contributed by nonproximal axons (1.79 m, 66.6%), spine necks (0.55 m, 20.5%), and dendritic shafts (0.28 m, 10.3%) not connected to any cell body in the volume. (H) Display of all 34,221 reconstructed axons contained in the dataset. Scale bars in (D) are as in (C); scale bar in (F) is 10  $\mu\text{m}$ .

previous dense reconstruction in mammalian cortex (9) (Fig. 2, I and J). To quantify remaining reconstruction error rates in this dense neuropil reconstruction, we measured the remaining errors in a set of 10 randomly chosen axons and found 12.8 errors per millimeter of path length (of these, there were 8.7 continuity errors per millimeter; see materials and methods). This is indistinguishable from the error rates previously found in fast human annotations (18, 34, 36).

We obtained a connectome (Fig. 3) between 34,221 presynaptic axonal processes and 11,400 postsynaptic processes [6979  $\times$  3719 connectivity matrix (Fig. 3E) when restricted to those pre- and postsynaptic neurites that established at least 10 synapses]. Among the postsynaptic processes, we classified  $n = 169$  apical dendrites (ADs) that traversed the dataset along the cortical axis without connection to one of the neuronal cell bodies in the dataset (Fig. 2A), 246 smooth dendrites (SDs, Fig. 2B),

80 somata, 116 axon initial segments (AISs; Fig. 2C), and 89 proximal dendrite (PD) trees connected to a soma in the dataset (movie S1; note that some of these neurons also had ADs that were classified as PDs and not included in the AD definition above; see materials and methods and tables S1 and S2).

#### Connectomic definition of axon types

We investigated whether, based solely on connectomic information (Fig. 3), we could extract the rules of subcellular innervation preference described for inhibitory axons in the mammalian cortex (17) and if such synaptic target preference could also be found for excitatory axons. We first measured the preference of each axon for innervating dendritic spine heads versus dendritic shafts and other targets (Fig. 4, A and B) because, in the mammalian cortex, most axons of inhibitory interneurons (INs) preferentially innervate the dendrites' shafts or neuronal somata (17)

and most excitatory glutamatergic axons preferentially innervate the spine heads of dendrites (1). The fraction of primary spine synapses per axon (out of all synapses of that axon) accordingly allowed the identification of spine-preferring, likely excitatory axons with at least 50% primary spine innervations ( $n = 5894$  axons) and shaft-preferring, likely inhibitory axons with <20% primary spine innervations ( $n = 893$  axons, or 13.2% of all axons; for exceptions to this rule and control measurements, see the supplementary materials and tables S1 and S2).

We then determined for each of the subcellular synaptic target classes defined above (Figs. 3 and 4C) the per-synapse innervation probability that would best explain whether an inhibitory axon establishes at least one synapse onto each of these targets. These inhibitory "single-hit" binomial innervation probabilities were 4.2% (somata), 17.8% (PD), 4.9% (SD), 3.3% (AD), and 0.5% (AIS) (Fig. 4D). We



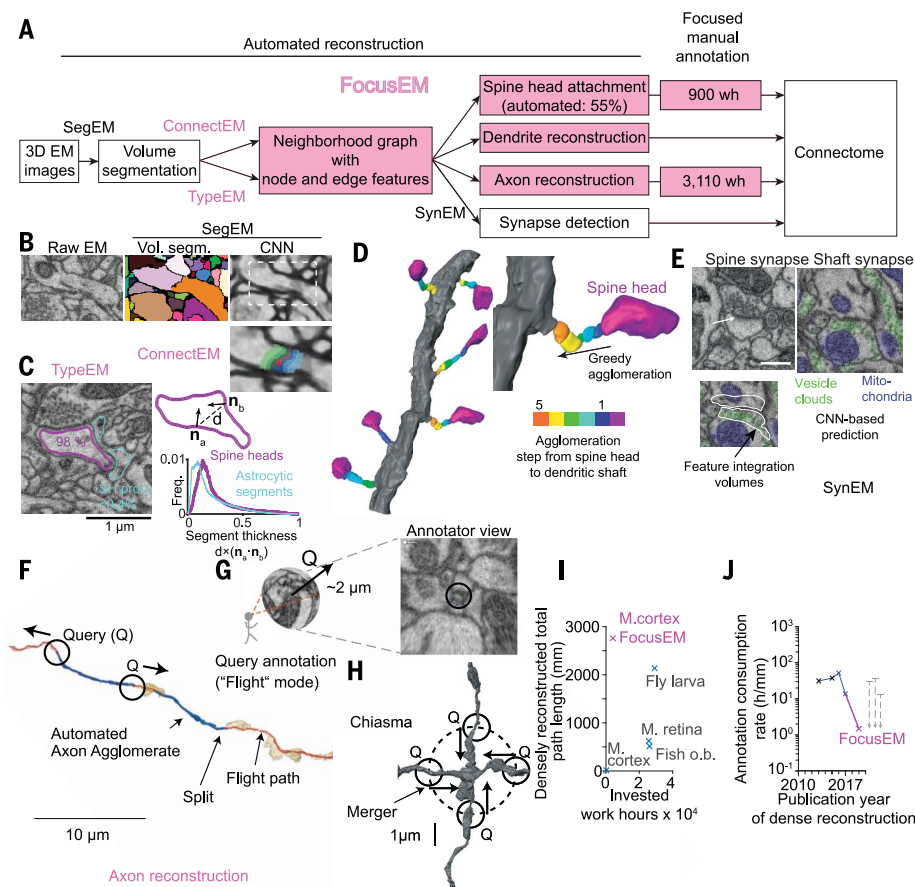


**Fig. 2. Methods for the efficient dense connectomic reconstruction.** (A) Simplified diagram of reconstruction steps [fig. S1, detailed in (B) to (H)]. wh, annotation work hours. (B) ConnectEM classifier for combining neurite pieces from the CNN-based volume segmentation (32): at junctions of volume segments (bottom right), raw data, CNN, and shape features were evaluated. (C) TypeEM classifier for assigning cellular identity to volume segments: the probability of axons, dendrites, spine heads, and glial processes was evaluated. Shown is an illustration of spine head (purple) and astrocyte (cyan) classification; one of the 985 features is illustrated (segment thickness). Numbers indicate the probability of the segment being a spine head. Precision and recall of spine head detection were 92.6 and 94.4%, respectively. (D) Process for automatically attaching spine heads to the dendritic shaft by stepwise agglomeration of volume segments along the highest-probability transition between neighboring segments [according to the ConnectEM score (B)]. An example of six neighboring spine heads that were all automatically attached is shown. In total, 58.9% of spine heads were automatically attached (A). (E) Automated detection of spine and shaft synapses [here, vesicle clouds (green) and mitochondria (blue) were detected and used as additional features for the SynEM (33) classifier]. (F to H) Focused annotation strategy for directing human annotation queries (Q) to ending locations of the automatically reconstructed axon pieces [(F), blue], oriented along the axon's main axis [traced in webKnossos using flight mode (G {34}), yielding flight paths of  $5.5 \pm 8.8 \mu\text{m}$  length ( $21.3 \pm 36.1 \text{ s}$  per ending annotation,  $n = 242,271$ , movie S2)]. Neurite mergers (H) were detected as "chiasmatic" configurations, and queries (Q) directed from the exits of the chiasma toward its center were used to determine correct neurite continuities (fig. S1). (I and J) Quantification of circuit size and invested work hours for dense circuit reconstructions in connectomics and resulting order-of-magnitude improvement provided by FocusEM compared with previous dense reconstructions (m). Fish o.b., zebrafish olfactory bulb (59); M. retina, mouse retina IPL (18); Fly larva, mushroom body in larval stage of *D. melanogaster* (35); M. cortex, mouse somatosensory cortex [(9) and this study (magenta)]. Only completed dense reconstructions were included in the comparison.

then computed the expected distribution of synapses per axon made onto each target class assuming the double-hit, triple-hit, etc., innervation probabilities are the same as the probability to establish at least one synapse onto that target. When comparing these target dis-

tributions with the measured distributions of synapses per axon onto each target class (Fig. 4E), we found that inhibitory axons established enhanced preference for somata ( $p = 2.4 \times 10^{-34}$ ,  $n = 893$ , one-sided Kolmogorov-Smirnov test), PDs ( $p = 6.0 \times 10^{-77}$ ), ADs ( $p =$

$2.5 \times 10^{-4}$ ), and to a lesser degree for SDs ( $p = 1.7 \times 10^{-3}$ , table S1), but no enhanced preference for AISs in L4 ( $p = 0.648$ ). AISs were synaptically innervated by 0.172 input synapses per micrometer of AIS length, but these innervations were not made by axons with an enhanced preference for AISs, unlike in supragranular and infragranular layers (37).

When performing the same analysis for excitatory axons (Fig. 4F), we found clear target preference for ADs ( $p = 2.5 \times 10^{-34}$ , Fig. 4F), SDs ( $p = 7.6 \times 10^{-25}$ ), and PDs ( $p = 1.3 \times 10^{-169}$ ). By contrast, thalamocortical (TC) axons [detected using the criteria reported in (38); see fig. S6 and materials and methods] indicated a target preference for PDs ( $p = 2.5 \times 10^{-31}$ ), but not for ADs ( $p = 0.019$ ) or SDs ( $p = 0.723$ ). To determine the fraction of inhibitory and excitatory axons that had an unexpectedly high synaptic preference for one (or multiple) of the subcellular target classes, we applied the false detection rate criterion used for the determination of significantly expressed genes [ $q$  value (39); see materials and methods] and obtained lower bounds on the fractions of axons in the tissue that preferentially innervate the various subcellular target classes (Fig. 4G; at least 58.0% of inhibitory and 24.4% of excitatory axons). Inhibitory axons (Fig. 4H), but not excitatory axons (Fig. 4I), showed higher-order innervation preferences, indicating that at the level of the dense cortical circuit, synaptic target preferences established by axons were not a continuum but allowed cell-type classification without the need for measurements of neuronal morphology, electrical activity, protein expression, or transcription levels.

### Geometric sources of synaptic innervations

Could these local connectivity rules have been derived solely from the geometry of axons and dendrites? We first quantified the overall relation between the spatial distribution of axons and dendrites and the establishment of synapses between them (Fig. 5). One paradigm, originally proposed by Peters (17), states that TC axons entering a certain cortical tissue volume would sample the available cortical dendrites for synaptic innervation according to their relative prevalence in the tissue (1). This model (Fig. 5A) predicted the TC innervation of most cortical dendrites rather well, with the exception of smooth dendrites [an exception reported by White et al. (14)] and the enhanced TC innervation of PDs of layer 4 cells (27). When applied to corticocortical excitatory and inhibitory axons (Fig. 5A), we found that this model predicted excitatory innervation of most spiny dendrites rather well, but again failed to predict innervation of SDs and the proximal bias of inhibitory synapses. Because this model [which has been most widely used for circuit inference



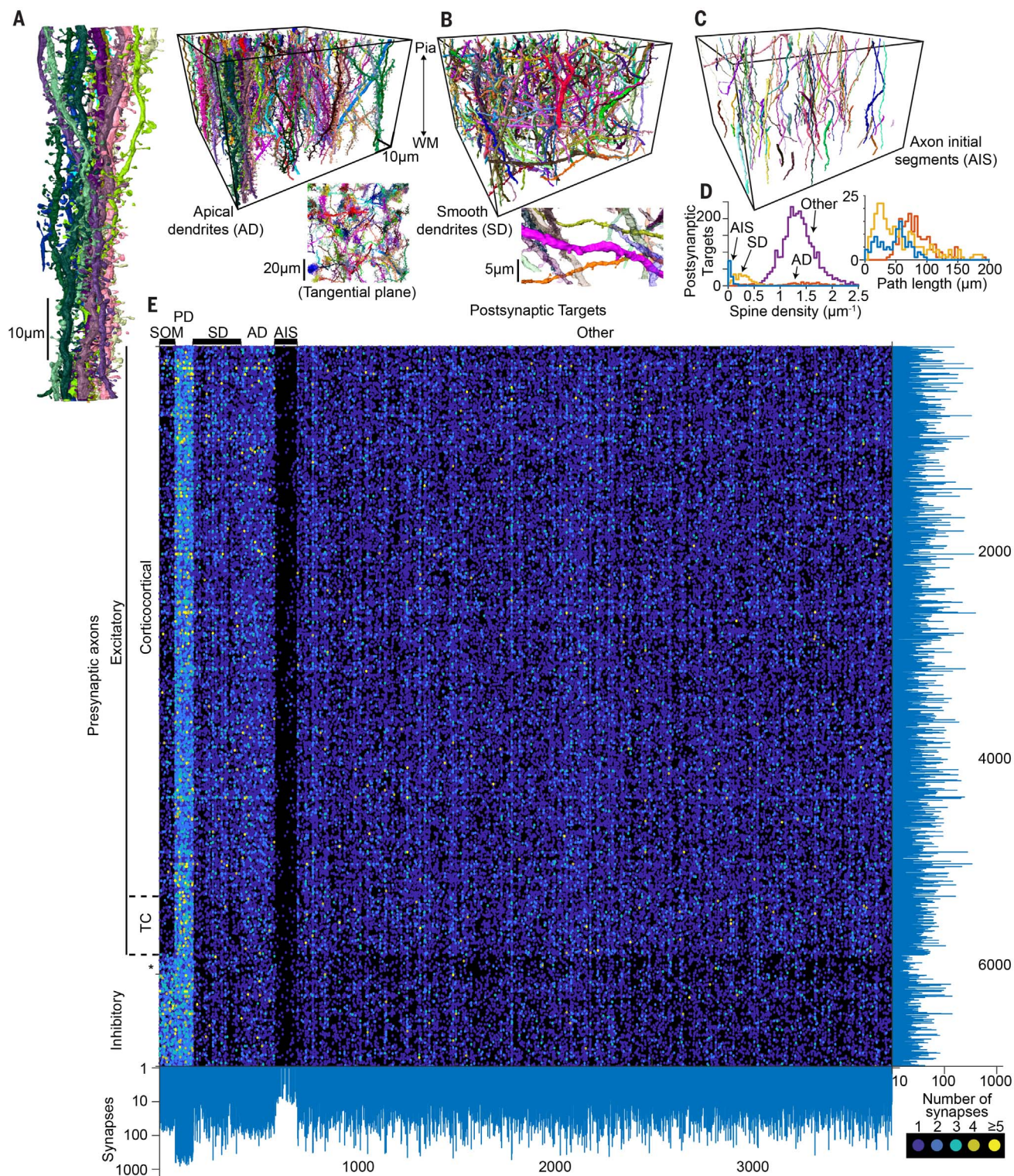


**Fig. 3. Postsynaptic target classes and dense cortical connectome.** (A to D) Display of all ADs [(A), magnified one-AD bundle (left) and top view in tangential plane illustrating AD bundles], SDs [(B), magnification inset illustrating low rate of spines], AISs (C), and their respective path length and spine density distributions (D). Note that spine density is underestimated by ~20% (table S1). (E) Display of connectome between all axons ( $n = 6979$ ) and postsynaptic targets ( $n = 3719$ ) in the volume with at

least 10 synapses each, establishing a total of 153,171 synapses (of 388,554 synapses detected in the volume). For the definition of postsynaptic target classes, see (A) to (D); for the definition of presynaptic axon classes, see Fig. 4 and fig. S6. AISs with fewer than 10 input synapses are also shown. SOM, neuronal somata; Note that some of these PD dendrites are L4 ADs not included in the AD definition above. Asterisks indicate remaining unassigned axons.



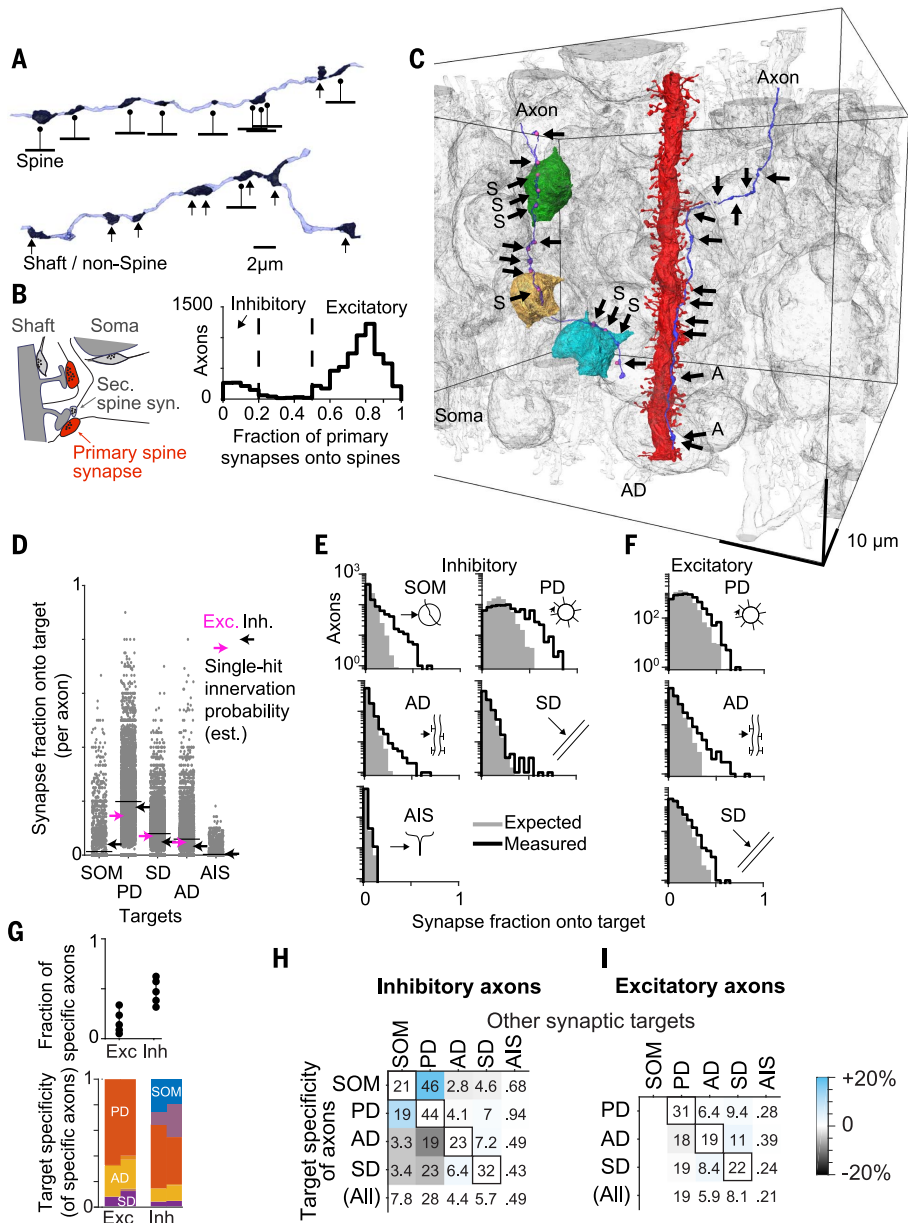


**Fig. 4. Connectomic definition of axon classes.** (A) Example axons with high (top) and low (bottom) fraction of output synapses made onto dendritic spines. (B) Distribution of spine-targeting fraction over all  $n = 6979$  axons; dashed lines indicate thresholds applied to distinguish non-spine-preferring, likely inhibitory axons (<20% spine innervation,  $n = 893$ , 12.8% of all axons) from spine-preferring, mostly excitatory axons (>50% spine innervation,  $n = 5,894$ , 84.5%). Diagram shows the definition of primary spine innervations. (C to I) Connectomic definition of axon classes by preferential synaptic innervation of subcellular targets. (C) Two example axons innervating three somata [left,  $n = 6$  synapses onto somata (S) of 14 total, arrows] and an AD (right,  $n = 2$  synapses onto AD of 13 total), respectively. All other cell bodies and ADs are shown in gray. (D) Fraction of synapses onto somata, PDs, ADs, SDs, and AISs for all axons. Binomial probabilities are shown over axons to establish at least one synapse onto the respective target (arrows: magenta, excitatory; black, inhibitory). Black lines indicate the average over axons. (E) Comparison of predicted synapse fraction onto target classes per inhibitory axon on the basis of the binomial probability to innervate the target at least once [gray shading; see arrows in (D)] and measured distribution of synapse fractions onto targets (black lines). (F) Same as (E) but for excitatory axons. (G) Fraction of target-preferring excitatory (Exc.) and inhibitory (Inh.) axons identified using the false detection rate criterion [ $q = 5$  to 30% (39)]. Colored bars indicate the distribution for  $q = 5\%$  (left) and  $q = 30\%$  (right). Mixed colors indicate axons specific for both somata and PDs. [(H) and (I)] Second-order innervation preference by target-specific axons; numbers indicate fractional innervation by remaining synapses per axon; colors indicate underfrequent (black) or overfrequent (blue) innervation. Diagonal entries are the fraction of synapses onto the same target (black boxes).

(2, 12)] implicitly accounts for the density of synapses along the presynaptic axons, it was capable of capturing the increased synapse density of TC axons (Fig. 5A). A simpler variant of the Peters model (1, 15) (Fig. 5B), which uses the density of pre- and postsynaptic path length as basis for the synaptic innervation prediction, failed at predicting the TC innervation but captured the corticocortical innervation of spiny dendrites (Fig. 5B). We then analyzed whether a Peters model normalized for postsynaptic synapse density (Fig. 5C) would better capture synaptic innervation and found that, in fact, the dendritic model was a far better predictor of synaptic innervation (compare Fig. 5, C and B). This indicated that SDs and ADs sampled synaptic input according to the relative path length of the presynaptic axons (Fig. 5C). We then investigated whether a Peters model accounting for pre- and postsynaptic synapse densities would improve the innervation prediction (Fig. 5D). In this model, both the output and the input of cortical excitatory neurites were properly predicted, but the suppressed innervation of SDs and ADs by TC axons and the proximal bias of inhibitory axons was not. Notably, none of the Peters models could account for this proximal bias of inhibitory synapses [Fig. 5D; for other failures of Peters predictions, see, e.g., (3, 6, 8, 9)].

More recently, the Peters model has been investigated for the close proximity between axons and dendrites on the scale of few micrometers (8, 9) and concluded poor (8) or absent (9) geometric predictability of synaptic innervation. We used our larger dense reconstruction to investigate the geometric prediction over a substantially broader spatial scale from 1 to ~30  $\mu$ m and accounted for inhibitory axons, excitatory axons, and postsynaptic target types (Fig. 5, E to H). We measured whether the postsynaptic membrane surface available within a certain radius  $r_{\text{pred}}$  around a given axon (Fig. 5E) would be a predictor of synaptic innervation for that given axon. We measured the available membrane surface belonging to the five subcellular target classes around all 6979 axons (Fig. 5F) and used a linear multinomial regression model to predict synaptic innervation from these data (Fig. 5G). Then, we computed the coefficient of determination ( $R^2$ ) reporting the fraction of axonal synaptic innervation variance that could be explained purely based on the geometrical information (Fig. 5H; for details, see the materials and methods). In fact, for small spatial scales of 1 to 5  $\mu$ m, the membrane surface available around an axon was a rather good predictor of synaptic innervation from excitatory axons (range, 16 to 90%, Fig. 5H; less so for inhibitory axons: range, 23 to 79%).

Would this imply that axonal and dendritic proximity at the single-axon level can be used

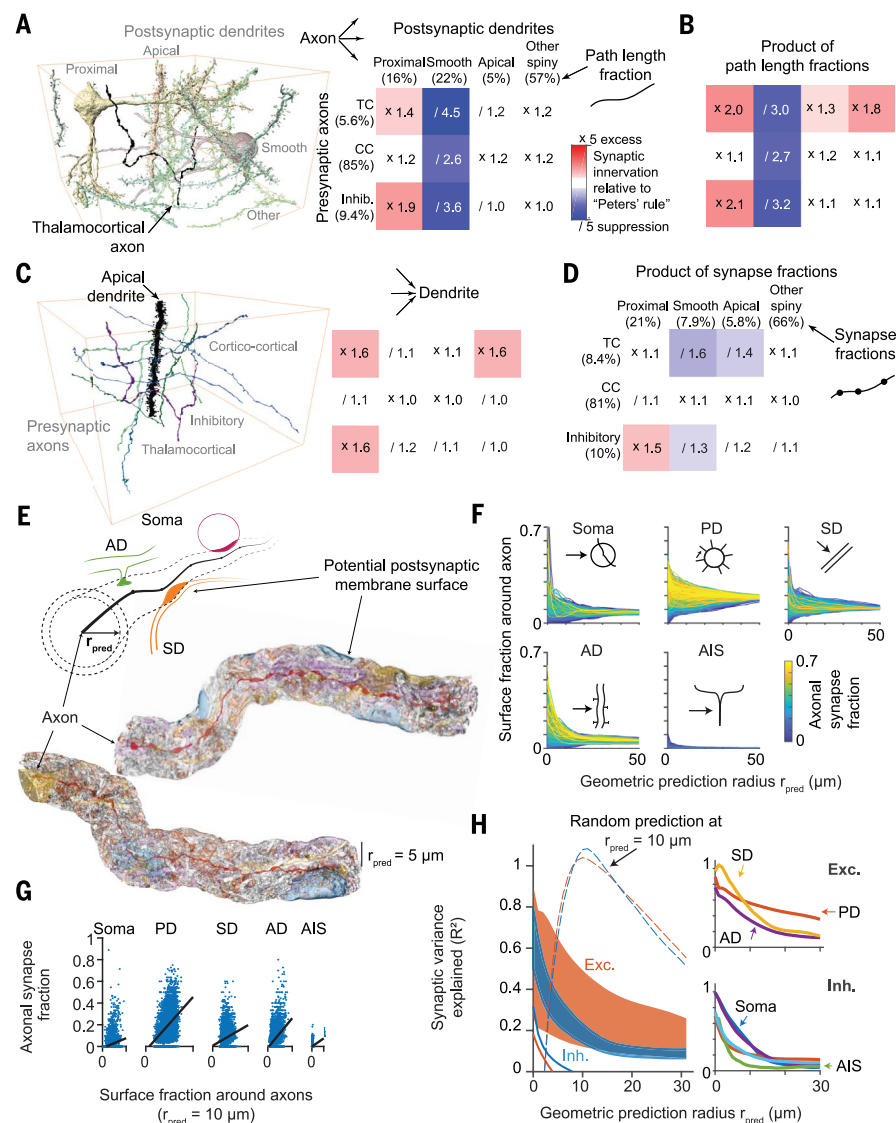


**Fig. 5. Contribution of neurite geometry and membrane availability to cortical wiring.** (A to D) Quantitative test of various formulations of Peters' rule: comparison of actual synaptic innervation to the prediction of synaptic innervation on the basis of the availability of postsynaptic path length in the dataset (A), the product of pre- and postsynaptic path length (B), the sampling of presynaptic partners by their relative prevalence (C), and the product of pre- and postsynaptic synapse density (D). Log likelihood ratios were as follows:  $-1.1 \times 10^3$  (A),  $-11 \times 10^3$  (C), and  $-12 \times 10^3$  (D), all compared with the simple model in (B);  $p < 10^{-14}$  (corrected for degrees of freedom). (E to H) Prediction of single-axon synaptic target preference by distance-dependent postsynaptic surface sampling. (E) Diagram of the surface area of the various subcellular postsynaptic target classes (colors) within a distance  $r_{pred}$  from a given axon (black) and example surfaces around two axons within a prediction radius  $r_{pred} = 5 \mu m$ . (F) Surface fraction of target classes around all  $n = 6979$  axons in dependence of  $r_{pred}$  around axons. Colors indicate the fraction of synapses of a given axon actually innervating the respective target. (G) Relationship between the surface fraction around all axons and synaptic innervation by these axons for each target ( $r_{pred} = 10 \mu m$ ). Black lines indicate linear regression for geometrical innervation prediction. (H)  $R^2$  reporting the fraction of synaptic innervation variance [over all axons; see (G)] explained by a multivariate linear innervation model using the available postsynaptic surface area around axons [shaded areas: red, excitatory axons (Exc.); blue, inhibitory axons (Inh.)]; lower end of shades indicates prediction; upper ends indicate correction by the variance contributed by the multinomial sampling of targets along axons; solid lines represent direct prediction of innervation from surface fraction. Dashed lines indicate modeled prediction for a purely geometric forward model at  $r_{pred} = 10 \mu m$ . Insets (right) show sampling-corrected predictive power of excitatory (top) and inhibitory (bottom) axons for the innervation of target classes.

to infer synaptic connectivity in the cortex (13)? We found that for the spatial alignment scales that can be achieved in light-microscopy-based neuron reconstructions from multiple animals (10 to 20  $\mu m$ ), predictability dropped substantially (Fig. 5H), making circuit inference by an emulation of growth processes based on light-microscopically aligned data (13, 40) implausible.

### Subcellular synapse placement

We used our dense reconstruction to study the spatial distribution of synapses along somata and dendrites in the cortical neuropil. The density of TC synapses had a substantial dependence on cortex depth (Fig. 6, A to D): the absolute density of TC synapses in the volume increased by  $\sim 93\%$  over 50  $\mu m$  cortex depth (Fig. 6, A and B); the TC excitatory synapse fraction  $TC/(TC+CC)$  (where CC is cortico-cortical) increased by 82.6%, corresponding to an absolute increase in the TC synapse fraction of 5.8% per 50  $\mu m$  cortex depth (Fig. 6D). This gradient was consistent with light-microscopic analyses of TC synapses indicating a decrease of TC synapse density from lower to upper L4 (41). Neither the inhibitory nor the corticocortical excitatory synapse densities showed a comparable spatial profile (Fig. 6C).

How is the synaptic TC gradient mapped onto the dendrites of L4 neurons along the cortex axis (Fig. 6, E to G)? One possibility is that the TC synapse gradient is used to enhance the variability of synaptic input composition between different primary dendrites of the L4 neurons such that a neuron's dendrites pointing upward toward the pia would sample relatively less TC input than dendrites pointing toward the white matter. Alternatively, mechanisms to establish synaptic target preference (such as those reported in Fig. 4) could be used to counterbalance this synaptic gradient and equilibrate the synaptic input fractions on the differently oriented dendrites. Our analysis showed that, in fact, even at the level of single primary dendrites, TC input fractions were 1.28-fold higher for dendrites pointing upward toward the cortical surface versus downward toward the white matter (Fig. 6, F and G; TC input fractions of each dendrite were corrected for the entire neuron's TC input fraction; for this analysis, see the materials and methods). We then investigated whether this differential composition of the inhibitory input is accompanied by different compositions of the inhibitory input synapses (Fig. 6, H to L). We found that the fraction of TC input to a neuron's dendrites was anticorrelated to the fraction of inhibitory synapses that originated from AD-preferring inhibitory axons (Figs. 6I and 4), both at the level of the input to L4 neurons and at the level of single primary dendrites of L4 neurons



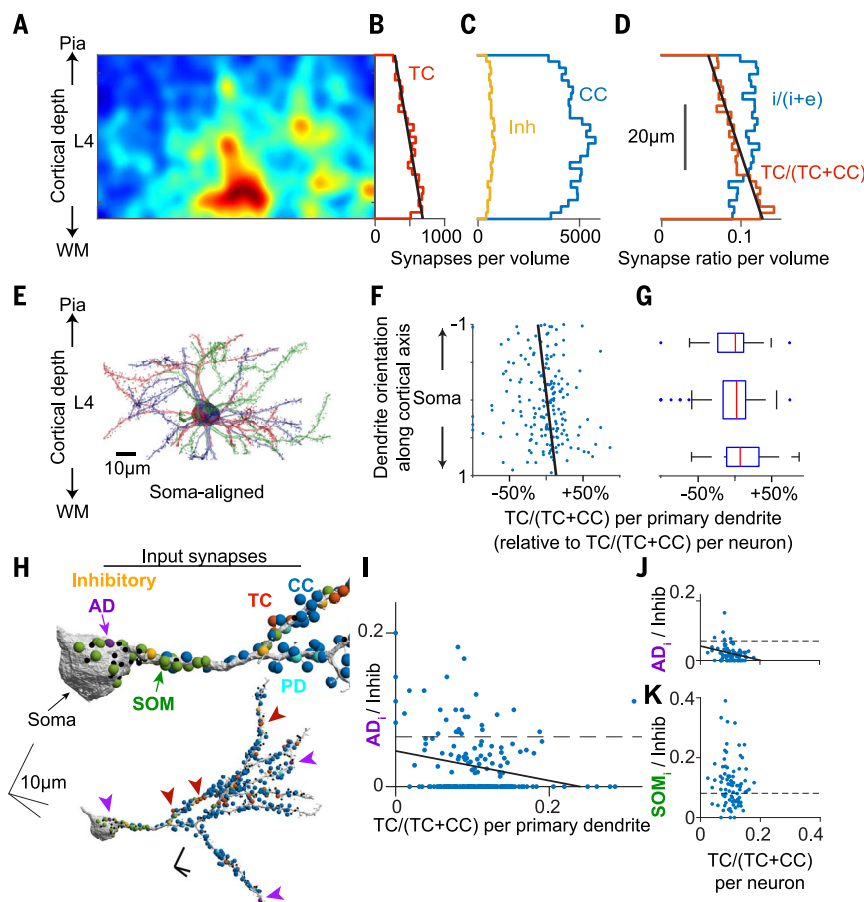


**Fig. 6. Gradient of TC synapse density in L4 and ensuing variability of synaptic input composition in L4 neurons.** (A to D) Distribution of TC synapses within the L4 dataset (A): gradient along the cortical axis (B), which is absent for inhibitory (yellow) or CC (blue) synapses (C). (D) Resulting gradient in TC synapse fraction [increase by 83% from 7.0 to 12.8% (+5.8%) within 50  $\mu\text{m}$  along the cortical axis; line fit,  $p < 1.1 \times 10^{-12}$ ,  $n = 134,537$  synapses]. (E to G) Analysis of the variability of TC input onto the primary dendrites of neurons possibly resulting from the TC synapse gradient (D): example reconstructions (E) aligned to the somata; (F) fraction of excitatory input synapses originating from TC axons evaluated for each primary dendrite, plotted according to the direction of the dendrite relative to cortical axis (–1, aligned toward pia; +1, aligned toward WM). TC input fraction [TC/(TC+CC)] of each dendrite compared with the TC input fraction of its entire parent neuron (ratios shown). (G) Summary analysis of relation between dendrite direction and relative TC input fraction showing that the TC input fraction is determined by the dendrites' orientation relative to the cortex axis (1.28-fold higher relative TC fraction for downward- than upward-pointing dendrites,  $n = 183$ ,  $p = 0.026$ , two-sided  $t$  test for dendrites with a normalized absolute projection  $>0.5$ ; bars correspond to ranges –1 to –0.5; –0.5 to 0.5; and 0.5 to 1). (H to K) Enhanced TC synaptic input (red spheres) is correlated to reduced inhibitory input from AD-preferring inhibitory axons (purple spheres and arrows in H) at the level of single dendrites ( $r = -0.24$ ,  $p = 0.0095$ ,  $n = 183$ , Pearson's correlation after Bonferroni's correction) and for neurons [(J),  $r = -0.27$ ,  $p = 0.01$ ,  $n = 84$ ], but not soma-preferring inhibitory axons [green in (H) and (K),  $r = 0.08$ ,  $p = 0.49$ ,  $n = 84$ ].

(Fig. 6, I and J). The effect was absent for all other synapse classes, most notably the soma-preferring inhibitory axons (Fig. 6K; see discussion).

#### Connectomic mapping of the plasticity-consistent circuit fraction

The concept of Hebbian plasticity, thought to be at the core of experience-dependent changes of synaptic weights in the brain, makes predictions about the temporal evolution of syn-

aptic weights in multiple synaptic contacts between the same pre- and postsynaptic neurons (AADD joint synapses; Fig. 7, A and B): Because Hebbian synaptic plasticity is dependent on the electrical activity of the pre- and postsynaptic neurons, which in a first approximation can be assumed to be similar at joint synapses, long-term potentiation (LTP) predicts joint synapses to become stronger and relatively more similar in weight (especially if synaptic weight saturates) and long-term depression

(LTD) predicts joint synapses to become weaker and relatively more dissimilar in weight (but more similar if synaptic weights saturate; Fig. 7A). Models of LTP and LTD thus make particular predictions about the temporal evolution of joint synaptic weights, and the mapping of synaptic weights and synaptic weight similarity in the connectome allows the quantification of upper bounds on the fraction of the circuit that can have undergone such particular patterns of weight change before the connectomic experiment (we denote those synapse pairs for which such patterns of weight change occurred to a sufficient degree as “having undergone LTP/LTD”; see discussion).

We set out to leverage our large connectomic dataset ( $n = 5290$  excitatory joint synaptic pairs onto spines; Fig. 7C) to map the relation between synaptic size and synaptic size similarity in joint synapse pairs [Fig. 7E; for visualization, the figure reports relative synaptic size dissimilarity on the x-axis; for the utilization of the axon–spine interface area (Fig. 7D) as an indicator of synaptic weight (42, 43)]. These data would allow us to determine upper bounds on the plasticity-consistent fraction of the circuit beyond the previous finding that in joint synapse pairs, synaptic size is more similar than for randomly shuffled synapse pairs (9, 29, 30, 44).

Synaptic size similarity in joint synapse pairs showed a broad distribution (Fig. 7E). When comparing this distribution with the synaptic size and synaptic size similarity distribution obtained from a random assignment of the same synapses into “random pairs” (Fig. 7F and fig. S7, C and D), we observed that the population of oversimilar synapse pairs (Fig. 7F) was split into a region of oversimilar and large synapses (mean synaptic size 0.23 to 1.19  $\mu\text{m}^2$ ; 16 to 20% of all joint synapse pairs are found in this region; the above-random synapse pairs constitute 3.6 to 3.9% of all joint synapse pairs; see fig. S7, C and D, and the materials and methods for details of the region definition and statistics), and oversimilar and small synapses (mean synaptic size 0.06 to 0.2  $\mu\text{m}^2$ ; 15 to 19% of all joint synapse pairs were found in this region; 3.0 to 3.4% of all joint synapse pairs were above random in this region). With this information, we obtained upper bounds on the fraction of the circuit that can have undergone LTP and LTD with weight saturation (compare Fig. 7, F and A).

To what degree was the observed synaptic weight similarity a result of subtypes of neurons establishing differently sized synapses? Although the quantification of the upper bounds of the plasticity-consistent circuit fraction would remain unaffected, we could use this more detailed analysis to understand whether the plasticity-consistent

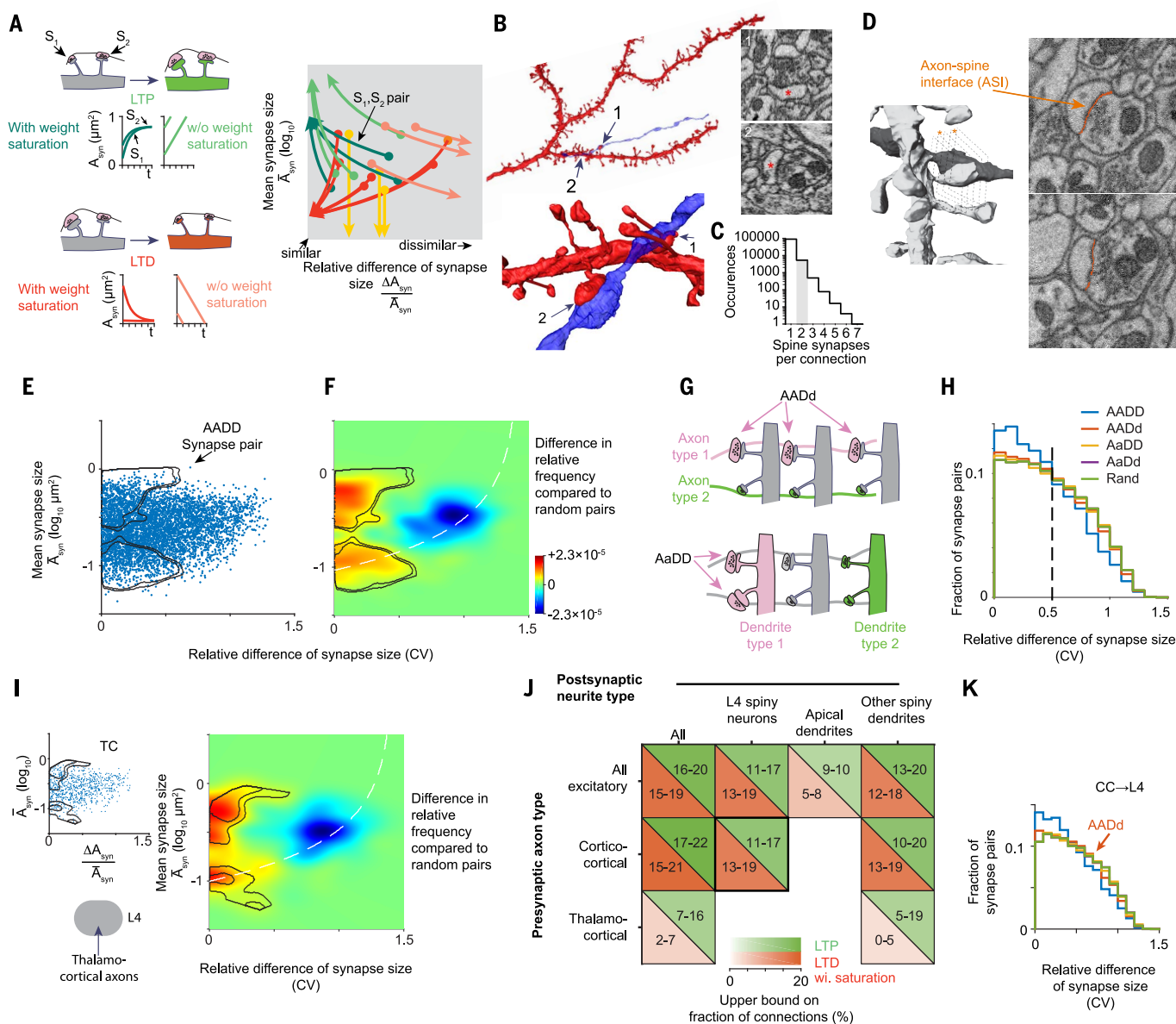


**Fig. 7. Connectomic mapping of the plasticity-consistent circuit fraction.**

(A) Hebbian LTP makes predictions about the temporal evolution of synaptic size and size similarity in AADD synapse pairs (green; insets show example model trajectories of synapse pairs exposed to LTP with and without weight saturation), yielding a region in the size-similarity plane (right) where synaptic pairs that have undergone LTP are predicted to be found (colors in right panel as in temporal plots on the left). For Hebbian LTD, pairs of synapses behave accordingly only if synaptic size saturates at low values (red). Arrows indicate trajectories of synapse pairs with randomly drawn initial size that undergo LTP with (dark green) or without (light green) weight saturation; LTD with (red) and without (pink and yellow indicate linear and exponential decay, respectively) weight saturation. (B) Example AADD synapse pair (arrows) onto dendritic spines between the same axon (blue) and same dendrite (red). Direct links to datasets are as follows: <https://wklinc.org/3356> (synapse 1) and <https://wklinc.org/6145> (synapse 2). (C) Frequency of joint synapse pairs in the dataset ( $n = 5290$  spine-synapse pairs, shaded, analyzed here). (D) ASI as a representative measure of synapse weight (42, 43), dataset link <https://wklinc.org/5780> (E) Distribution of mean synaptic size and synaptic size

similarity for all pairs of AADD synapses from excitatory axons; each dot corresponds to one synapse pair. Isolines indicate statistical regions defined in (F). (F) Map of the relation between synaptic size and synaptic size similarity in AADD pairs, reported as the difference of (E) to random synapse pairs (fig. S7, C and D). Isolines indicate significance levels ( $p = 0.05$  and  $0.005$  for outer and inner isolines, respectively) outlining overfrequency of synapse pairs that are similar in size and large (upper area) and similar in size and small (lower area). (G and H) Analysis of AADD and AaDD synapse pairs that would indicate a contribution of cell-type-dependent connection size differences. No oversimilarity can be found in these cases (H). (I) Analysis as in (E) and (F) but for TC connections. Note upper bound of 16% of connections consistent with stabilized LTP. (J) Summary of fraction of synapse pairs that resided in the regions identified in (F) and (I) as upper bounds (for the interaction between the two upper bounds, see the supplementary materials). Numbers indicate the ranges for different significance thresholds [see (F) and (I) and fig. S7, C and D]. (K) Analysis as in (G) and (H) but for CC-to-L4 neuron connections only, refuting subtypes of CC connections as the source of the observed oversimilarity (see fig. S7, A and B). Image width is 2 μm in (B) and (D).



circuit fractions were specific to types of neuronal connections.

First, we considered the possibility that certain presynaptic cell types made consistently larger or consistently smaller synapses (Fig. 7G). In this case, the distribution of synaptic weight similarity for same-axon different-dendrite (AADD) synapse pairs would also show a bias toward more similarly sized synapses. However, we found no such evidence (Fig. 7H), excluding cell-type-specific synapse size of either presynaptic (axonal) or postsynaptic (dendritic) origin as the cause of the observed oversimilar synapse pairs.

Next, we separated those connections established by TC axons from those made by the remaining excitatory (i.e., CC) axons (Fig. 7I and fig. S7, A and B). We found an excess of oversimilar synapse pairs in the TC connections as well, with 7 to 16% of pairs found in a region of overly similar and large synapses (i.e., an upper bound of 16% on LTP). The region of overly similar and small synapse pairs, however, only comprised 2 to 7% of joint synapse pairs. This remaining number of overly similar small synapse pairs could in fact be induced by the overly similar large synapse pairs (see the supplementary materials). At 28 days of age, ~3 weeks after the proposed critical period during which LTP can be induced in TC connections (45, 46), a fraction of up to 16% of joint synapse pairs was still consistent with previous episodes of LTP that led to stabilized potentiated synapse pairs at dendritic spines (47, 48), but 84% were not.

Repeating these analyses for other combinations of pre- and postsynaptic neurite types (Fig. 7J), we found upper bounds for LTP and LTD of ~10 to 20%. For each of these subtype-specific connections, we could then again analyze whether any purely presynaptic or purely postsynaptic subtype within the already type-selected connections (corresponding to squares in the table of Fig. 7J) could be the cause of the observed synapse similarity. For example, the connections from corticocortical axons onto spiny L4 neurons (49) showed no evidence for presynaptic axonal subtypes yielding oversimilar synapses (Fig. 7K; for additional controls of these findings, see the supplementary materials; fig. S7, A and B; and table S1).

Together, these results provided a first quantitative upper bound on the fraction of the circuit consistent with previous episodes of saturated Hebbian synaptic plasticity leading to strengthening or weakening of synapses (a “connectomic fingerprint” of the maximum possible plasticity fraction of the circuit) and excluded obvious cell-type-based connection strength differences as the origin of these observations. Because these results were obtained from brains of untrained animals and were not the result of electrical or other stimulation (“plasticity induction”), these data may

represent an unbiased screening of upper bounds of plasticity traces in local cortical circuits, for which the dense connectomic mapping was essential.

## Discussion

Using FocusEM, we obtained the first dense circuit reconstruction from the mammalian cerebral cortex at a scale that allowed the analysis of axonal patterns of subcellular innervation, ~300 times larger than previous dense reconstructions from cortex (9). Inhibitory axon types preferentially innervating certain postsynaptic subcellular compartments could be defined solely on the basis of connectomic information (Figs. 3 and 4). In addition to inhibitory axons, a fraction of excitatory axons also exhibited such subcellular innervation preferences (Fig. 4). The geometrical arrangement of axons and dendrites explained only a moderate fraction of synaptic innervation, revoking coarse random models of cortical wiring (Fig. 5). A substantial TC synapse gradient in L4 gave rise to an enhanced heterogeneity of synaptic input composition at the level of single cortical dendrites (Fig. 6), which was accompanied by a reduced innervation from AD-preferring inhibitory inputs. The consistency of synapse size between pairs of axons and dendrites signified fractions of the circuit consistent with saturated synaptic plasticity, placing an upper bound on the “learned” fraction of the circuit (Fig. 7). FocusEM allowed the dense mapping of circuits in the cerebral cortex at a throughput that enables connectomic screening.

### Synaptic input composition along L4 dendrites

Our finding of a covariation of enhanced TC inputs to L4 excitatory cells with reduced direct inhibitory input from AD-preferring INs (Fig. 6, H to K) could be interpreted in the context of a disinhibitory circuit described previously (50, 51). Taking into account the preferential targeting of ADs and of soma-preferring parvalbumin (PV)-positive INs by somatostatin (SST)-positive INs, this could imply that SST-IN-based disinhibition can enhance TC input by silencing perisomatic PV inputs recruited by feedforward inhibition (52) and concomitantly reducing the direct inhibitory component from SST INs. In any case, this finding of per-dendrite input variation points to a circuit configuration in which TC input variability is enhanced between neurons of the same excitatory type in cortical layer 4, and furthermore provides evidence for a per-dendrite synaptic input composition of enhanced heterogeneity.

### Connectomic traces of plasticity

We interpreted the joint synapse data (Fig. 7) in terms of upper bounds of synapse pairs that could have undergone certain models of plas-

ticity. Although this analysis detects those synapse pairs that were exposed to saturating plasticity (i.e., the possible plasticity event led to a final weight state of both synapses), an alternative interpretation is a dynamic circuit in which at any given point in time, only a fraction of synapses has expressed saturated plasticity, whereas other (or all) synapses are in the process of undergoing plastic changes. We expect that more elaborate plasticity models of entire circuits will also make testable predictions that are accessible by connectomic snapshot experiments as shown here.

## Outlook

The presented methods and results open the path to the connectomic screening of nervous tissue from various cortices, layers, species, developmental stages, sensory experiences, and disease conditions. The fact that even a small piece of mammalian cortical neuropil contains a high density of relevant information so rich as to allow the extraction of possible connectomic signatures of the “learnedness” of the circuit makes this approach a promising endeavor for the study of the structural setup of mammalian nervous systems.

## Materials and Methods

### Animal experiments

A wild-type (C57BL/6) male mouse was transcardially perfused at postnatal day 28 under isoflurane anesthesia using a solution of 2.5% paraformaldehyde and 1.25% glutaraldehyde (pH 7.4) following the protocol in (53). All procedures followed the animal experiment regulations of the Max Planck Society and were approved by the local animal welfare authorities (Regierungspräsidien Oberbayern and Darmstadt).

### Tissue sampling and staining

The brain was removed from the skull after 48 hours of fixation and sliced coronally using a vibratome. Two samples were extracted using a 1-mm biopsy punch (Integra Miltex, Plainsboro, NJ) from a 1-mm-thick slice 5 mm from the front of the brain targeted to layer 4 in the somatosensory cortex of the right hemisphere. The corresponding tissue from the left hemisphere was further sliced into 70- $\mu$ m-thick slices followed by cytochrome oxidase staining, indicating the location of the coronal slice to be in barrel cortex.

Next, the extracted tissue was stained as described previously (53). Briefly, the tissue was immersed in a reduced osmium tetroxide solution (2% OsO<sub>4</sub>, 0.15 M CB, 2.5 M KFeCN), followed by a 1% thiocarbonylhydrazide step and a 2% OsO<sub>4</sub> step for amplification. After an overnight wash, the sample was further incubated with 1.5% uranyl acetate solution and a 0.02 M lead(II) nitrate solution. The sample was dehydrated with propylene oxide and

EtOH, embedded in Epon Hard (Serva Electrophoresis GmbH, Germany), and hardened for 48 hours at 60°C.

### 3D electron microscopy experiment

The embedded sample was placed on an aluminum stub and trimmed such that the tissue was directly exposed on all four sides of the sample. The sides of the sample were covered with gold in a sputter coater (Leica Microsystems, Wetzlar, Germany). Then, the sample was placed into an SBEM setup [(37), Magellan scanning electron microscope, FEI Company, Hillsboro, OR, equipped with a custom-built microtome courtesy of W. Denk]. The sample was oriented so that the radial cortex axis was in the cutting plane. The transition between L4 and L5A was identified in overview electron microscopy (EM) images by the sudden drop in soma density between the two layers (Fig. 1C). A region of size  $96 \times 64 \mu\text{m}^2$  within L4 was selected for imaging using a  $3 \times 3$  image mosaic, a pixel size of  $11.24 \times 11.24 \text{ nm}^2$ , an image acquisition rate of 10 MHz, a nominal beam current of 3.2 nA (thus a nominal electron dose of  $15.8 \text{ e}^-/\text{nm}^2$ ), an acceleration voltage of 2.5 kV, and a nominal cutting thickness of 28 nm. The effective data rate, including overhead time spent during motor movements for cutting and tiling, was 0.9 MB/s. A total of 3420 image planes were acquired, yielding 194 GB of data.

### Image alignment

After 3D EM dataset acquisition, all images were inspected manually and marked for imaging artifacts caused by debris present on the sample surface during imaging. Images with debris artifacts were replaced by the images at the same mosaic position from the previous or subsequent plane. First, rigid translation-only alignment was performed based on the procedures in (53). The following modifications were applied. When shift vectors were obtained that yielded offsets of  $>100$  pixels, these errors were iteratively corrected by manually reducing the weight of the corresponding entry in the least-squares relaxation by a factor of 1000 until the highest remaining residual error was  $<10$  pixels. Shift calculation of subsequent images in cutting direction was found to be the most reliable measurement and was therefore weighted 3-fold in the weighted least-squares relaxation. The resulting shift vectors were applied (shift by integer voxel numbers) and the 3D image data were written in KNOSSOS format (34, 36). For further improvement, subimage alignment was applied (see the supplementary materials and methods).

### Methods description for software code

All routines described in the following are available as software at <https://gitlab.mpgdf.mpg.de/connectomics/L4dense>, which is the

relevant reference for the exact sequence of processing steps applied. The following descriptions and the more detailed ones in the supplementary materials and methods are aimed at pointing to the key algorithmic steps rather than enumerating all detailed computations.

### Workflow for dense circuit reconstruction

The workflow for volume reconstruction of the acquired 3D EM volume (Fig. 2 and fig. S1) was as follows. We first detected blood vessels and cell bodies using automated heuristics, and then processed the remaining image volume using machine-learning-based image segmentation [CNN and watershed as described in SegEM (32)]. The result of this processing was 15 million volume segments corresponding to pieces of axons, dendrites, and somata (volume:  $0.0295 \pm 0.3846 \mu\text{m}^3$ , mean  $\pm$  SD). We then constructed the neighborhood graph between all these volume segments and computed the properties of interfaces between directly adjacent volume segments. On the basis of these features, we trained a connectivity classifier (ConnectEM; Fig. 2, A and B) to determine whether two segments should be connected (along an axon or a dendrite or a glial cell) or if they should be disconnected. Using the SynEM classifier (33), we determined whether an interface between two disconnected processes corresponded to a chemical synapse and, if so, which was the presynaptic and which was the postsynaptic neurite segment (see below for more details). We further trained a set of classifiers (TypeEM; Fig. 2C) to compute for each volume segment the probability of being part of an axon, a dendrite, a spine head, or a glia cell (precision and recall were 91.8 and 92.9% for axons, 95.3 and 90.7% for dendrites, 97.2 and 85.9% for astrocytes, and 92.6 and 94.4% for spine heads, respectively; see table S2).

### Cell body–based neuron reconstruction

We next reconstructed those neurons that had their cell bodies in the tissue volume (Fig. 1, E and F, cell gallery in movie S1;  $n = 125$  cell bodies; of these, 97 were neuronal and of these 97, 89 were reconstructed with dendrites in the dataset). For this, we used a set of simple growth rules for automatically connecting neurite pieces on the basis of the segment-to-segment neighborhood graph and the connectivity and neurite type classifiers (fig. S1, “automated agglomeration”; see the supplementary materials and methods). As a result, we obtained fully automated reconstructions of the neuron’s soma and dendritic processes. With a minimal additional manual correction investment of 9.7 hours for 89 cells (54.5 mm dendritic and 2.1 mm axonal path length), the dendritic shafts of these neurons could be reconstructed without merge errors, but there were 37 remaining split errors, at 87.3% den-

dritic length recall (table S2). This reconstruction efficiency compares favorably to recent reports of automated segmentation of neurons in 3D EM data from the bird brain obtained at  $\sim 2$ -fold higher imaging resolution (54), which reports soma-based neuron reconstruction at an error rate of beyond 100 errors per 66 mm dendritic shafts at lower (68%) dendritic length recall with a similar resource investment (see the supplementary materials and methods).

In addition to the dendritic shafts, the dendritic spines constitute a major fraction of the dendritic path length in cortical neuropil (Fig. 1G). Using our spine head classifier (part of the TypeEM classifiers; Fig. 2C), we found 415,797 spine heads in the tissue volume, which is a density of 0.784 per  $\mu\text{m}^3$  (0.98 per  $\mu\text{m}^3$  of neuropil, when excluding somata and blood vessels). To connect these to the corresponding dendritic shafts, we trained a spine neck continuity algorithm that was able to automatically attach 58.9% of these spines (evaluated in the center of the dataset at least  $10 \mu\text{m}$  from the dataset border), yielding a dendritic spine density of 0.672 per  $\mu\text{m}$  dendritic shaft length [comparable to spine densities in the bird brain (55)]. However, in mammalian cerebral cortex, the density of spines along dendrites is even higher (at least 1 per  $\mu\text{m}$  dendritic shaft length). The remaining spine heads were then attached to their dendritic shafts by seeding manual reconstructions at the spine heads and asking annotators to continue along the spine necks to the dendritic shafts. This annotation was performed in the “orthogonal mode” configuration of webKnossos (34), in which the annotator viewed three orthogonal image planes to decide where to continue the respective spine neck [as in KNOSSOS (36)]. The annotation of all remaining spine necks consumed an additional 900 hours of human work for the attachment of 98,221 spines, resulting in a final overall spine density of 0.959 per  $\mu\text{m}$  dendritic shaft length.

### Dense tissue reconstruction

The reconstruction of neurons starting from their cell bodies, however, was not the main challenge. Rather, the remaining processes, axons and dendrites not connected to a cell body within the dataset and densely packed in the tissue constitute  $\sim 97\%$  of the total neuronal path length in this volume of cortex (Fig. 1G). To reconstruct this vast majority of neurites (Fig. 1H), we first used our connectivity and neurite type classifiers (ConnectEM and TypeEM, respectively; Fig. 2) to combine neurite pieces into larger dendritic and axonal agglomerates (“automated agglomeration,” fig. S1 and supplementary materials and methods). Then, we took those agglomerates that had a length of at least  $5 \mu\text{m}$  ( $n = 74,074$  axon agglomerates), detected their endings that were



not at the dataset border, and directed focused human annotation to these endings (“queries,” Fig. 2, F and G).

For human annotation, we used an egocentric directed 3D image data view (“flight mode” in webKnossos), which we had previously found to provide maximized human reconstruction speed along axons and dendrites in cortex (34). Here, however, instead of asking human annotators to reconstruct entire dendrites or axons, we only queried their judgment at the endings of automatically reconstructed neurite parts. To make these queries efficient, we made three additions to webKnossos: (i) we oriented the user along the estimated direction of the neurite at its ending, reducing the time the user needs to orient within the 3D brain tissue; (ii) we dynamically stopped the user’s flight along the axon or dendrite whenever another of the already reconstructed neurite agglomerates had been reached; and (iii) we preloaded the next query while the user was annotating (Fig. 2, F and G). Movie S2 illustrates this annotation process for cases of splits and mergers, respectively. Note that the user was able to switch quickly to the next query and, based on its 3D orientation, spent little time orienting in the tissue at the new location. With this, the average user interaction time was  $21.3 \pm 36.1$  s per query, corresponding to an average of  $5.5 \pm 8.8$   $\mu$ m traveled per query. In total, 242,271 axon-ending queries consumed 1978 paid-out work hours (i.e., including all overheads, 29.4 s per query).

However, we had to account for a second kind of reconstruction error, so-called mergers, which can originate from the original segmentation, the agglomeration procedure, or erroneous flight paths from human queries (Fig. 2H). To detect such mergers, we started with the notion that most of these merger locations will yield a peculiar geometrical arrangement of a 4-fold neurite intersection once all neurite breaks have been corrected (Fig. 2H, “chiasma”). Because such chiasmatic configurations occur rarely in branching neurites, we directed human focused annotation to these locations. First, we automatically detected these chiasmatic locations using a simple heuristic to detect locations at which axon-centered spheres intersected more than three times with the axon [Fig. 2H,  $n = 55,161$  chiasmata; for approaches to detect such locations by machine learning, see (56, 57)]. Then, we positioned the user queries at a certain distance from the chiasma location pointing inward (Fig. 2H) and used a set of case distinctions to query a given chiasma until its configuration had been resolved (see the supplementary materials and methods for details). Chiasma annotation consumed an additional 1132 work hours [note that the detection of endings and chiasmata was iterated eight times for axons (see the supplementary materials and methods) and

that, in a final step, we also detected and queried 3-fold neurite configurations to remove remaining mergers].

### Synapse detection, types of postsynaptic targets, and connectome reconstruction

Given the reconstructed pre- and postsynaptic neurites in the tissue volume, we then went on to extract their connectome. For this, we used SynEM (33) to detect synapses between the axonal presynaptic processes and the postsynaptic neurites (Fig. 2E).

We trained a dedicated interface classifier for nonspine synapses using training data containing only shaft and soma synapses (Figs. S2 to S5; see the supplementary material and methods). This classifier also used four additional texture filters compared with SynEM in (33), which originated from the voxelwise predictions of a multiclass CNN trained on synaptic junctions, vesicle clouds, mitochondria, and a background class (Fig. 2E).

Because we were interested in analyzing the subcellular specificity of neuronal innervation, we had to also classify which of the postsynaptic membranes belonged to cell bodies; to classify spiny dendrites as belonging to excitatory cells and smooth dendrites as belonging to INs; and to detect AISs and those dendrites that were likely ADs of neurons located in deeper cortical layers. We developed semiautomated heuristics to detect these subcellular compartments (Fig. 3, A to D; see the supplementary materials and methods for details).

### Definition of excitatory and inhibitory axons

We used the fraction of primary spine synapses per axon (out of all synapses of that axon, only axons with at least 5  $\mu$ m path length and at least 10 synapses were analyzed), which had a peak at ~80% (Fig. 4, A and B), to identify spine-preferring, likely excitatory axons with at least 50% primary spine innervations. Similarly, we identified shaft-preferring, likely inhibitory axons with <20% primary spine innervations. Together, this yielded 6449 axons with clear shaft or spine preferences. For the remaining  $n = 528$  axons with primary spine innervations >20% and <50%, we first wanted to exclude remaining mergers between excitatory and inhibitory axons (that would yield intermediate spine innervation rates) and split these axons at possible merger locations (at least 3-fold intersections). Of these, 338 now had at least 10 synapses and spine innervation rates <20% or >50%. The remaining  $n = 192$  axons (2.75% of all axons with at least 10 synapses) were not included in the following analyses. This together yielded  $n = 5894$  excitatory and  $n = 893$  inhibitory axons in our data. For additional controls, see the supplementary materials.

TC axons were defined following parameters described previously (38) (see the supplementary materials and methods).

### Analysis of subcellular synaptic target preference

First, we assumed that all synapses of a given axon class have the same probability to innervate a particular postsynaptic target class (as above). We then inferred this single-hit innervation rate for all combinations of presynaptic axon classes and postsynaptic target classes by determining the probability that best explains whether an axon innervated the target class under a binomial model. The optimized binomial model was then used together with the measured number of synapses of each axon to calculate the expected distribution of target innervation rates. A one-sided Kolmogorov–Smirnov test was used to search for the existence of a subpopulation with an increased target innervation rate. To identify those axons that innervated a given target class beyond chance (Fig. 4G), we computed the probability  $p^{(t)}_{\text{meas},i,k}$  of finding at least the measured fraction of synapses onto target  $t$  for each axon  $i$  from axon class  $k$ . The  $p$  values were also calculated for the expected distribution of target innervation rates and combined with  $p^{(t)}_{\text{meas},i,k}$  to estimate the  $p$ -value threshold  $\hat{p}^{(t)}_k$  at which the false discovery rate  $q$  (39) crosses 20%. Eighty percent of the axons with  $p^{(t)}_{\text{meas},i,k} < \hat{p}^{(t)}_k$  innervate target  $t$  with a rate above the single-hit innervation probability and are thus considered to be  $t$  preferring.

For the analysis of second-order innervation preference (Fig. 4, H and I), we reported the fraction of synapses onto target  $\tau$  by  $t$ -preferring axons of class  $k$  after removal of synapses onto  $t$ . This innervation rate was compared against the fraction of synapses onto target  $\tau$  by all axons of class  $k$ .

### Geometrical predictability analysis

Peters’ rule (1) stipulates that synapses between classes of axons and dendrites are established in proportion to the prevalence of these classes. One variant of Peters’ rule considered (Fig. 5B) makes the prediction that the fraction of synapses from axon class A onto target class T is the product of  $p_A$  and  $q_T$ , where  $p_A$  is the proportion of axonal path length made up by class A, and  $q_T$  is the proportion of dendritic path length (excluding spines) made up by class T. The measured synapse fractions were compared against the predictions by calculating the ratio of observed to predicted synapse fractions.

Other formulations evaluate these predictions independently for each axon class (Fig. 5A) or each dendrite class (Fig. 5C).

Finally, to assess the effect of incorporating explicit knowledge about the synapse densities of different axon and dendrite classes,

a fourth variant of Peters' rule (Fig. 5D) was considered in which the predicted synapse fraction from axon class A onto target class T is the product of  $p'_A$  and  $q'_T$ , the overall fractions of synapses originating from A and innervating T, respectively.

How much additional information about the neuropil composition around an axon helps to predict its postsynaptic targets was assessed as follows. For each axon, we determined the total surface area of the target classes that were contained within the cylinder of radius  $r_{\text{pred}}$  around the axon (Fig. 5E) and compared it with the actually innervated target fraction of each axon (Fig. 5, E and F). We then analyzed the correlation between the availability of the target surfaces and the established synapses on these target classes (Fig. 5G).

We then computed  $R^2$  using the following model. For all axons of a given type, we used the fraction of target innervations and fractional surface availabilities in a surround of radius  $r_{\text{pred}}$  to find the optimal multivariate linear regression parameters. To estimate best-case geometric predictability, we then calculated  $R^2$  as 1 minus the ratio between the squared residuals of the regression and the synaptic variance on the same axons used for parameter optimization. Here, we corrected for the variance introduced by the finite number of synapses per axon: we used the axons' fractional surface availabilities within  $r_{\text{pred}}$  and absolute synapse numbers to calculate the expected binomial variance and subtracted it from the squared residuals.

This analysis made several assumptions that were in favor of a geometrical explanation of synaptic innervation [therefore, the conclusions about a minimal predictability (Fig. 5H) are still upper-bound estimates]. It was assumed that the number of synapses for a given axon was already known; in most settings, only average synapse rates are known for a given circuit. It also assumed that a precise knowledge of the axonal trajectory and the surrounding target surface fractions were available; again, this is usually only available as an average on the scale of  $r_{\text{pred}}$  of several tens of micrometers.

To relax the assumption of complete knowledge about target availabilities, we repeated the above  $R^2$  analysis for a model in which the predicted fractional innervation of a target is the fractional surface availability of that target.

The computational routine used can be found at [https://gitlab.mpcdf.mpg.de/connectomics/L4dense\\_in\\_connectEM/Connectome/plotGeometricPredictability.m](https://gitlab.mpcdf.mpg.de/connectomics/L4dense_in_connectEM/Connectome/plotGeometricPredictability.m).

### Synapse-size consistency analysis

To determine the consistency of primary spine synapses between a given axon–dendrite pair,

we calculated the axon–spine interface area (ASI) (42, 43) of a synapse as the total contact area between the corresponding axon and spine head agglomerates. For axon–dendrite pairs connected by exactly two primary spine synapses, we then calculated the coefficient of variation (CV) of the ASI areas by  $CV = 2^{1/2}(ASI_1 - ASI_2)/(ASI_1 + ASI_2)$ , where  $ASI_1$  and  $ASI_2$  are the larger and smaller of the two ASI areas, respectively. To avoid false same-axon, same-dendrite (AADD) pairs caused by remaining merge errors in the axon reconstruction, this analysis was performed only after splitting axons at their branch points. The measured distribution of CV values was compared against the CV values obtained by randomly drawing pairs from all AADD synapses and against the CV values of observed AADD synapse pairs and pairs from different axons onto the same dendrite (AaDD) and from different axons onto different dendrites (AaDd; Fig. 7H). To test whether AADD primary spine synapse pairs are more similar in size than pairs in the control conditions, a one-sided Kolmogorov–Smirnov test was used. We calculated the decimal logarithm of the average ASI area (in square micrometers) and the CV of the ASI areas of each synapse pair to map the size-similarity plane (Fig. 7, F and I). The kernel density estimate of the observed distribution was compared against the distribution expected from random pairs (5000 Monte Carlo samples; fig. S7C) to identify statistically significantly overrepresented regions. Contour lines show the intersection of the significance regions for  $p$ -value thresholds of 0.5% and 5% (Fig. 7, E, F, I, and fig. S7, C and D), with the convex hull around the set of all data points. The fraction of data points contained within a contour was used as the upper bound on the fraction of connections consistent with saturated Hebbian plasticity (Fig. 7J).

### Statistical methods

The following statistical tests were performed (in order of presentation in the figures):

The existence of axon subpopulation with unexpectedly high synapse rate onto a given target class was tested using the one-sided Kolmogorov–Smirnov test (Fig. 4, E and F). Axons belonging to a given target-preference class were identified on the basis of the false detection rate criterion [ $q = 20\%$  (39)] (Fig. 4G).

The degree to which synaptic variance is explainable by geometry-based models was evaluated using  $R^2$  (Fig. 5H). Binomial variance was corrected for by subtracting the surface fraction-based expected binomial variance from the squared residuals.

$F$  tests were used to evaluate synaptic gradients as function of cortical depth (Fig. 6, B and D) or dendritic orientation (Fig. 6, F and G). For correlation of the TC input fraction with other synaptic input fractions along den-

drites, the inhibitory input fraction and seven target-preferential inhibitory and excitatory synapse types were tested. AD-preferring inhibitory synapses were the only ones with significant and substantial correlation (Pearson's correlation after Bonferroni's correction for  $n = 8$  multiple tests). The correlation was also significant at the soma level (Pearson's correlation). Both correlations were also significant using Spearman's rank correlation.

The four variants of Peters' rule (Fig. 5, A to D) were compared using a likelihood-ratio test based on the following multinomial model. It was assumed that the pre- and postsynaptic classes of each synapse in the connectome were sampled either after the path-length fractions of these classes ( $p_A$  and  $q_T$ ) or after the product of the path length and a class-specific likelihood-maximizing relative synapse density. Wilks' theorem was used to compute the corresponding  $p$  values.

To test whether the axon–spine interface areas of a given spine–synapse pair configuration were more similar than randomly sampled pairs, a one-sided Kolmogorov–Smirnov test was used (Fig. 7, H and K).

### REFERENCES AND NOTES

1. V. Braitenberg, A. Schüz, *Cortex: Statistics and Geometry of Neuronal Connectivity*. (Springer, 1998).
2. J. Lübke, A. Roth, D. Feldmeyer, B. Sakmann, Morphometric analysis of the columnar innervation domain of neurons connecting layer 4 and layer 2/3 of juvenile rat barrel cortex. *Cereb. Cortex* **13**, 1051–1063 (2003). doi: [10.1093/cercor/13.10.1051](https://doi.org/10.1093/cercor/13.10.1051); pmid: [12967922](https://pubmed.ncbi.nlm.nih.gov/12967922/)
3. N. M. da Costa, K. A. Martin, Selective targeting of the dendrites of corticothalamic cells by thalamic afferents in area 17 of the cat. *J. Neurosci.* **29**, 13919–13928 (2009). doi: [10.1523/JNEUROSCI.2785-09.2009](https://doi.org/10.1523/JNEUROSCI.2785-09.2009); pmid: [19890002](https://pubmed.ncbi.nlm.nih.gov/19890002/)
4. D. D. Bock et al., Network anatomy and in vivo physiology of visual cortical neurons. *Nature* **471**, 177–182 (2011). doi: [10.1038/nature09802](https://doi.org/10.1038/nature09802); pmid: [21390124](https://pubmed.ncbi.nlm.nih.gov/21390124/)
5. W. C. Lee et al., Anatomy and function of an excitatory network in the visual cortex. *Nature* **532**, 370–374 (2016). doi: [10.1038/nature17192](https://doi.org/10.1038/nature17192); pmid: [27018655](https://pubmed.ncbi.nlm.nih.gov/27018655/)
6. H. Schmidt et al., Axonal synapse sorting in medial entorhinal cortex. *Nature* **549**, 469–475 (2017). doi: [10.1038/nature24005](https://doi.org/10.1038/nature24005); pmid: [28959971](https://pubmed.ncbi.nlm.nih.gov/28959971/)
7. Y. Han et al., The logic of single-cell projections from visual cortex. *Nature* **556**, 51–56 (2018). doi: [10.1038/nature26159](https://doi.org/10.1038/nature26159); pmid: [29590093](https://pubmed.ncbi.nlm.nih.gov/29590093/)
8. Y. Mishchenko et al., Ultrastructural analysis of hippocampal neuropil from the connectomics perspective. *Neuron* **67**, 1009–1020 (2010). doi: [10.1016/j.neuron.2010.08.014](https://doi.org/10.1016/j.neuron.2010.08.014); pmid: [20869597](https://pubmed.ncbi.nlm.nih.gov/20869597/)
9. N. Kasthuri et al., Saturated reconstruction of a volume of neocortex. *Cell* **162**, 648–661 (2015). doi: [10.1016/j.cell.2015.06.054](https://doi.org/10.1016/j.cell.2015.06.054); pmid: [26232230](https://pubmed.ncbi.nlm.nih.gov/26232230/)
10. C. Cali et al., The effects of aging on neuropil structure in mouse somatosensory cortex-A 3D electron microscopy analysis of layer 1. *PLOS ONE* **13**, e0198131 (2018). doi: [10.1371/journal.pone.0198131](https://doi.org/10.1371/journal.pone.0198131); pmid: [29966021](https://pubmed.ncbi.nlm.nih.gov/29966021/)
11. A. Peters, Thalamic input to the cerebral cortex. *Trends Neurosci.* **2**, 183–185 (1979). doi: [10.1016/0166-2236\(79\)90074-2](https://doi.org/10.1016/0166-2236(79)90074-2)
12. T. Binzegger, R. J. Douglas, K. A. Martin, A quantitative map of the circuit of cat primary visual cortex. *J. Neurosci.* **24**, 8441–8453 (2004). doi: [10.1523/JNEUROSCI.1400-04.2004](https://doi.org/10.1523/JNEUROSCI.1400-04.2004); pmid: [15456817](https://pubmed.ncbi.nlm.nih.gov/15456817/)
13. H. Markram et al., Reconstruction and simulation of neocortical microcircuitry. *Cell* **163**, 456–492 (2015). doi: [10.1016/j.cell.2015.09.029](https://doi.org/10.1016/j.cell.2015.09.029); pmid: [26451489](https://pubmed.ncbi.nlm.nih.gov/26451489/)
14. E. L. White, G. Benshalom, S. M. Hersch, Thalamic cortical and other synapses involving nonspiny multipolar cells of mouse Sml cortex. *J. Comp. Neurol.* **229**, 311–320 (1984). doi: [10.1002/cne.902290303](https://doi.org/10.1002/cne.902290303); pmid: [6501606](https://pubmed.ncbi.nlm.nih.gov/6501606/)



15. G. M. Shepherd, A. Stepanyants, I. Bureau, D. Chklovskii, K. Svoboda, Geometric and functional organization of cortical circuits. *Nat. Neurosci.* **8**, 782–790 (2005). doi: [10.1038/nrn1447](https://doi.org/10.1038/nrn1447); pmid: [1588011](https://pubmed.ncbi.nlm.nih.gov/1588011/)
16. G. A. Ascoli et al., Petilla terminology: Nomenclature of features of GABAergic interneurons of the cerebral cortex. *Nat. Rev. Neurosci.* **9**, 557–568 (2008). doi: [10.1038/nrn2402](https://doi.org/10.1038/nrn2402); pmid: [18568015](https://pubmed.ncbi.nlm.nih.gov/18568015/)
17. Y. Majota, F. Karube, M. Nomura, Y. Kawaguchi, The diversity of cortical inhibitory synapses. *Front. Neural Circuits* **10**, 27 (2016). doi: [10.3389/fncir.2016.00027](https://doi.org/10.3389/fncir.2016.00027); pmid: [27199670](https://pubmed.ncbi.nlm.nih.gov/27199670/)
18. M. Helmstaedter et al., Connectomic reconstruction of the inner plexiform layer in the mouse retina. *Nature* **500**, 168–174 (2013). doi: [10.1038/nature12346](https://doi.org/10.1038/nature12346); pmid: [23925239](https://pubmed.ncbi.nlm.nih.gov/23925239/)
19. J. S. Kim et al., Space-time wiring specificity supports direction selectivity in the retina. *Nature* **509**, 331–336 (2014). doi: [10.1038/nature13240](https://doi.org/10.1038/nature13240); pmid: [24805243](https://pubmed.ncbi.nlm.nih.gov/24805243/)
20. G. Major, M. E. Larkum, J. Schiller, Active properties of neocortical pyramidal neuron dendrites. *Annu. Rev. Neurosci.* **36**, 1–24 (2013). doi: [10.1146/annurev-neuro-062111-150343](https://doi.org/10.1146/annurev-neuro-062111-150343); pmid: [23841837](https://pubmed.ncbi.nlm.nih.gov/23841837/)
21. H. Jia, Z. Varga, B. Sakmann, A. Konnerth, Linear integration of spine Ca<sup>2+</sup> signals in layer 4 cortical neurons in vivo. *Proc. Natl. Acad. Sci. U.S.A.* **111**, 9277–9282 (2014). doi: [10.1073/pnas.1408525111](https://doi.org/10.1073/pnas.1408525111); pmid: [24927564](https://pubmed.ncbi.nlm.nih.gov/24927564/)
22. M. Lavzin, S. Rapoport, A. Polsky, L. Garion, J. Schiller, Nonlinear dendritic processing determines angular tuning of barrel cortex neurons in vivo. *Nature* **490**, 397–401 (2012). doi: [10.1038/nature11451](https://doi.org/10.1038/nature11451); pmid: [22940864](https://pubmed.ncbi.nlm.nih.gov/22940864/)
23. T. Branco, B. A. Clark, M. Häusser, Dendritic discrimination of temporal input sequences in cortical neurons. *Science* **329**, 1671–1675 (2010). doi: [10.1126/science.1189664](https://doi.org/10.1126/science.1189664); pmid: [20705816](https://pubmed.ncbi.nlm.nih.gov/20705816/)
24. E. Fíková, A. Van Harreveld, Long-lasting morphological changes in dendritic spines of dentate granular cells following stimulation of the entorhinal area. *J. Neurocytol.* **6**, 211–230 (1977). doi: [10.1007/BF01261506](https://doi.org/10.1007/BF01261506); pmid: [856951](https://pubmed.ncbi.nlm.nih.gov/856951/)
25. H. Markram, J. Lübke, M. Frotscher, B. Sakmann, Regulation of synaptic efficacy by coincidence of postsynaptic APs and EPSPs. *Science* **275**, 213–215 (1997). doi: [10.1126/science.275.5297.213](https://doi.org/10.1126/science.275.5297.213); pmid: [8985014](https://pubmed.ncbi.nlm.nih.gov/8985014/)
26. V. Egger, D. Feldmeyer, B. Sakmann, Coincidence detection and changes of synaptic efficacy in spiny stellate neurons in rat barrel cortex. *Nat. Neurosci.* **2**, 1098–1105 (1999). doi: [10.1038/16026](https://doi.org/10.1038/16026); pmid: [10570487](https://pubmed.ncbi.nlm.nih.gov/10570487/)
27. M. Matsuzaki, N. Honkura, G. C. Ellis-Davies, H. Kasai, Structural basis of long-term potentiation in single dendritic spines. *Nature* **429**, 761–766 (2004). doi: [10.1038/nature02617](https://doi.org/10.1038/nature02617); pmid: [15190253](https://pubmed.ncbi.nlm.nih.gov/15190253/)
28. I. Sáez, M. J. Friedlander, Plasticity between neuronal pairs in layer 4 of visual cortex varies with synapse state. *J. Neurosci.* **29**, 15286–15298 (2009). doi: [10.1523/JNEUROSCI.2980-09.2009](https://doi.org/10.1523/JNEUROSCI.2980-09.2009); pmid: [19955381](https://pubmed.ncbi.nlm.nih.gov/19955381/)
29. T. M. Bartol Jr et al., Nanoconnectomic upper bound on the variability of synaptic plasticity. *eLife* **4**, e10778 (2015). doi: [10.7554/eLife.10778](https://doi.org/10.7554/eLife.10778); pmid: [26618907](https://pubmed.ncbi.nlm.nih.gov/26618907/)
30. K. E. Sorra, K. M. Harris, Occurrence and three-dimensional structure of multiple synapses between individual radiatum axons and their target pyramidal cells in hippocampal area CA1. *J. Neurosci.* **13**, 3736–3748 (1993). doi: [10.1523/JNEUROSCI.13-09-03736.1993](https://doi.org/10.1523/JNEUROSCI.13-09-03736.1993); pmid: [8366344](https://pubmed.ncbi.nlm.nih.gov/8366344/)
31. W. Denk, H. Horstmann, Serial block-face scanning electron microscopy to reconstruct three-dimensional tissue nanostructure. *PLOS Biol.* **2**, e329 (2004). doi: [10.1371/journal.pbio.0020329](https://doi.org/10.1371/journal.pbio.0020329); pmid: [15514700](https://pubmed.ncbi.nlm.nih.gov/15514700/)
32. M. Berning, K. M. Boergens, M. Helmstaedter, SegEM: Efficient Image Analysis for High-Resolution Connectomics. *Neuron* **87**, 1193–1206 (2015). doi: [10.1016/j.neuron.2015.09.003](https://doi.org/10.1016/j.neuron.2015.09.003); pmid: [26402603](https://pubmed.ncbi.nlm.nih.gov/26402603/)
33. B. Staffler et al., SynEM, automated synapse detection for connectomics. *eLife* **6**, e26414 (2017). doi: [10.7554/eLife.26414](https://doi.org/10.7554/eLife.26414); pmid: [28708060](https://pubmed.ncbi.nlm.nih.gov/28708060/)
34. K. M. Boergens et al., webKnossos: Efficient online 3D data annotation for connectomics. *Nat. Methods* **14**, 691–694 (2017). doi: [10.1038/nmeth.4331](https://doi.org/10.1038/nmeth.4331); pmid: [28604722](https://pubmed.ncbi.nlm.nih.gov/28604722/)
35. K. Eichler et al., The complete connectome of a learning and memory centre in an insect brain. *Nature* **548**, 175–182 (2017). doi: [10.1038/nature23455](https://doi.org/10.1038/nature23455); pmid: [28796202](https://pubmed.ncbi.nlm.nih.gov/28796202/)
36. M. Helmstaedter, K. L. Briggman, W. Denk, High-accuracy neurite reconstruction for high-throughput neuroanatomy. *Nat. Neurosci.* **14**, 1081–1088 (2011). doi: [10.1038/nn.2868](https://doi.org/10.1038/nn.2868); pmid: [21743472](https://pubmed.ncbi.nlm.nih.gov/21743472/)
37. H. Taniguchi, J. Lu, Z. J. Huang, The spatial and temporal origin of chandelier cells in mouse neocortex. *Science* **339**, 70–74 (2013). doi: [10.1126/science.1227622](https://doi.org/10.1126/science.1227622); pmid: [23180771](https://pubmed.ncbi.nlm.nih.gov/23180771/)
38. R. Bopp, S. Holler-Rickauer, K. A. Martin, G. F. Shuhknecht, An ultrastructural study of the thalamic input to layer 4 of primary motor and primary somatosensory cortex in the mouse. *J. Neurosci.* **37**, 2435–2448 (2017). doi: [10.1523/JNEUROSCI.2557-16.2017](https://doi.org/10.1523/JNEUROSCI.2557-16.2017); pmid: [28137974](https://pubmed.ncbi.nlm.nih.gov/28137974/)
39. J. D. Storey, R. Tibshirani, Statistical significance for genomewide studies. *Proc. Natl. Acad. Sci. U.S.A.* **100**, 9440–9445 (2003). doi: [10.1073/pnas.1530509100](https://doi.org/10.1073/pnas.1530509100); pmid: [12883005](https://pubmed.ncbi.nlm.nih.gov/12883005/)
40. M. W. Reimann, J. G. King, E. B. Muller, S. Ramaswamy, H. Markram, An algorithm to predict the connectome of neural microcircuits. *Front. Comput. Neurosci.* **9**, 120 (2015). doi: [10.3389/fncom.2015.00120](https://doi.org/10.3389/fncom.2015.00120); pmid: [26500529](https://pubmed.ncbi.nlm.nih.gov/26500529/)
41. M. Oberlaender, A. Ramirez, R. M. Bruno, Sensory experience restructures thalamocortical axons during adulthood. *Neuron* **74**, 648–655 (2012). doi: [10.1016/j.neuron.2012.03.022](https://doi.org/10.1016/j.neuron.2012.03.022); pmid: [22632723](https://pubmed.ncbi.nlm.nih.gov/22632723/)
42. C. E. Cheetham, S. J. Barnes, G. Albiéri, G. W. Knott, G. T. Finnerty, Pansynaptic enlargement at adult cortical connections strengthened by experience. *Cereb. Cortex* **24**, 521–531 (2014). doi: [10.1093/cercor/bhs334](https://doi.org/10.1093/cercor/bhs334); pmid: [23118196](https://pubmed.ncbi.nlm.nih.gov/23118196/)
43. L. de Vivo et al., Ultrastructural evidence for synaptic scaling across the wake/sleep cycle. *Science* **355**, 507–510 (2017). doi: [10.1126/science.aah5982](https://doi.org/10.1126/science.aah5982); pmid: [28154076](https://pubmed.ncbi.nlm.nih.gov/28154076/)
44. E. B. Bloss et al., Single excitatory axons form clustered synapses onto CA1 pyramidal cell dendrites. *Nat. Neurosci.* **21**, 353–363 (2018). doi: [10.1038/s41593-018-0084-6](https://doi.org/10.1038/s41593-018-0084-6); pmid: [29459763](https://pubmed.ncbi.nlm.nih.gov/29459763/)
45. M. C. Crair, R. C. Malenka, A critical period for long-term potentiation at thalamocortical synapses. *Nature* **375**, 325–328 (1995). doi: [10.1038/375325a0](https://doi.org/10.1038/375325a0); pmid: [7753197](https://pubmed.ncbi.nlm.nih.gov/7753197/)
46. H. Li et al., Laminar and columnar development of barrel cortex relies on thalamocortical neurotransmission. *Neuron* **79**, 970–986 (2013). doi: [10.1016/j.neuron.2013.06.043](https://doi.org/10.1016/j.neuron.2013.06.043); pmid: [24012009](https://pubmed.ncbi.nlm.nih.gov/24012009/)
47. J. Grutzendler, N. Kasthuri, W. B. Gan, Long-term dendritic spine stability in the adult cortex. *Nature* **420**, 812–816 (2002). doi: [10.1038/nature01276](https://doi.org/10.1038/nature01276); pmid: [12490949](https://pubmed.ncbi.nlm.nih.gov/12490949/)
48. J. T. Trachtenberg et al., Long-term in vivo imaging of experience-dependent synaptic plasticity in adult cortex. *Nature* **420**, 788–794 (2002). doi: [10.1038/nature01273](https://doi.org/10.1038/nature01273); pmid: [12490942](https://pubmed.ncbi.nlm.nih.gov/12490942/)
49. D. Feldmeyer, V. Egger, J. Lübke, B. Sakmann, Reliable synaptic connections between pairs of excitatory layer 4 neurones within a single 'barrel' of developing rat somatosensory cortex. *J. Physiol.* **521**, 169–190 (1999). doi: [10.1111/j.1469-7793.1999.00169.x](https://doi.org/10.1111/j.1469-7793.1999.00169.x); pmid: [10562343](https://pubmed.ncbi.nlm.nih.gov/10562343/)
50. C. K. Pfeffer, M. Xue, M. He, Z. J. Huang, M. Scanziani, Inhibition of inhibition in visual cortex: The logic of connections between molecularly distinct interneurons. *Nat. Neurosci.* **16**, 1068–1076 (2013). doi: [10.1038/nn.3446](https://doi.org/10.1038/nn.3446); pmid: [23817549](https://pubmed.ncbi.nlm.nih.gov/23817549/)
51. J. Yu, H. Hu, A. Agmon, K. Svoboda, Recruitment of GABAergic interneurons in the barrel cortex during active tactile behavior. *Neuron* **104**, 412–427.e4 (2019). doi: [10.1016/j.neuron.2019.07.027](https://doi.org/10.1016/j.neuron.2019.07.027); pmid: [31466734](https://pubmed.ncbi.nlm.nih.gov/31466734/)
52. J. T. Porter, C. K. Johnson, A. Agmon, Diverse types of interneurons generate thalamus-evoked feedforward inhibition in the mouse barrel cortex. *J. Neurosci.* **21**, 2699–2710 (2001). doi: [10.1523/JNEUROSCI.21-08-02699.2001](https://doi.org/10.1523/JNEUROSCI.21-08-02699.2001); pmid: [11306623](https://pubmed.ncbi.nlm.nih.gov/11306623/)
53. K. L. Briggman, M. Helmstaedter, W. Denk, Wiring specificity in the direction-selectivity circuit of the retina. *Nature* **471**, 183–188 (2011). doi: [10.1038/nature09818](https://doi.org/10.1038/nature09818); pmid: [21390125](https://pubmed.ncbi.nlm.nih.gov/21390125/)
54. M. Januszewski et al., High-precision automated reconstruction of neurons with flood-filling networks. *Nat. Methods* **15**, 605–610 (2018). doi: [10.1038/s41592-018-0049-4](https://doi.org/10.1038/s41592-018-0049-4); pmid: [30013046](https://pubmed.ncbi.nlm.nih.gov/30013046/)
55. J. Kornfeld et al., EM connectomics reveals axonal target variation in a sequence-generating network. *eLife* **6**, e24364 (2017). doi: [10.7554/eLife.24364](https://doi.org/10.7554/eLife.24364); pmid: [28346140](https://pubmed.ncbi.nlm.nih.gov/28346140/)
56. D. Rolnick, N. Shavit, Morphological error detection in 3D segmentations. [arXiv:1705.10882](https://arxiv.org/abs/1705.10882) [cs.CV] (30 May 2017).
57. J. Zung, I. Tartavull, K. Lee, H. S. Seung, An error detection and correction framework for connectomics. [arXiv:1708.02599](https://arxiv.org/abs/1708.02599) [cs.CV] (8 August 2017).
58. Y. Hua, P. Laserstein, M. Helmstaedter, Large-volume en-bloc staining for electron microscopy-based connectomics. *Nat. Commun.* **6**, 7923 (2015). doi: [10.1038/ncomms8923](https://doi.org/10.1038/ncomms8923); pmid: [26235643](https://pubmed.ncbi.nlm.nih.gov/26235643/)
59. A. A. Wanner, C. Genoud, R. W. Friedrich, 3-dimensional electron microscopic imaging of the zebrafish olfactory bulb and dense reconstruction of neurons. *Sci. Data* **3**, 160100 (2016). doi: [10.1038/sdata.2016.100](https://doi.org/10.1038/sdata.2016.100); pmid: [27824337](https://pubmed.ncbi.nlm.nih.gov/27824337/)

## ACKNOWLEDGMENTS

We thank Y. Hua and K. M. Harris for discussions; A. Gour, Y. Hua, P. Laserstein, and H. Schmidt for discussing unpublished observations; B. Cowgill for experimental contributions; E. Eulig, R. Hesse, C. Schramm, and M. Zecevic for code contributions; C. Guggenberger for compute infrastructure; Scalable Minds for implementation of the fast-swapping user queries in webKnossos; and annotators (see the supplementary materials) for reconstruction work. **Funding:** Funding was provided by the Max Planck Society. **Author contributions:** M.H. conceived, initiated, and supervised the project; K.M.B. performed experiments; P.H. provided analysis methods; A.M., M.B., K.M.B., and B.S. developed and performed analyses with contributions by all authors; and A.M. and M.H. wrote the manuscript with contributions by all authors. **Competing interests:** The authors declare no competing financial interests. **Data and materials availability:** The raw EM data are available for browsing at <https://wklink.org/9276> (see data links in the figure legends). All data and code are publicly available at <https://L4dense2019.brain.mpg.de> and in updated form at <https://gitlab.mpcdf.mpg.de/connectomics/L4dense>. Less than 2% of the 3D EM image dataset using the initial image alignment was previously published (32–34, 58).

## SUPPLEMENTARY MATERIALS

[science.sciencemag.org/content/366/6469/eaay3134/suppl/DC1](https://science.sciencemag.org/content/366/6469/eaay3134/suppl/DC1)  
Materials and Methods  
Supplementary Text  
Figs. S1 to S7  
Tables S1 and S2  
Captions for Movies S1 and S2  
References (60–72)

[View/request a protocol for this paper from Bio-protocol.](#)

7 June 2019; accepted 11 October 2019  
Published online 24 October 2019  
[10.1126/science.aay3134](https://doi.org/10.1126/science.aay3134)

## RESEARCH ARTICLE SUMMARY

## NEUROSCIENCE

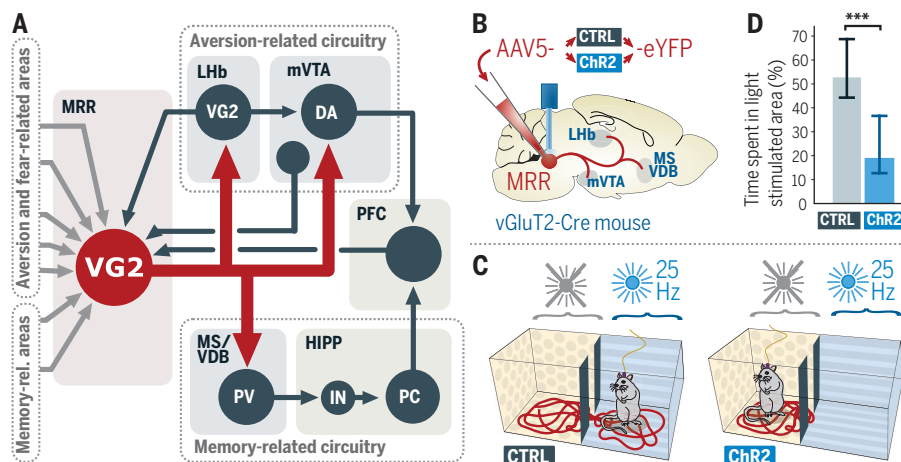
## Median raphe controls acquisition of negative experience in the mouse

András Szőnyi\*, Krisztián Zichó\*, Albert M. Barth, Roland T. Gönczi, Dániel Schlingloff, Bibiána Török, Eszter Sipos, Abel Major, Zsuzsanna Bardóczy, Katalin E. Sos, Attila I. Gulyás, Viktor Varga, Dóra Zelena, Tamás F. Freund, Gábor Nyiri†

**INTRODUCTION:** Coping with negative experience is essential for survival. Animals must quickly recognize a harmful situation, produce an adequate response, and learn its context, so that they can predict the reoccurrences of similar experiences. This process requires the lateral habenula (LHb) and the medial ventral tegmental area (mVTA) for evaluating and predicting aversive stimuli. LHb neurons promote encoding of aversive behavior; learn to respond to cues that predict aversive stimuli, and activate negative experience-processing mVTA dopaminergic (DA) neurons. Overexcitation of LHb neurons leads to depression-like symptoms, whereas their inactivation has an antidepressant effect. Coping with negative experience also requires the septohippocampal system to record and recall contextual memories of events. This process necessitates increased firing of pace-maker parvalbumin (PV)-positive neurons in the medial septum and the vertical limbs of the diagonal bands of Broca (MS/VDB) and subsequent theta oscillations in the hip-

pocampus. However, how all these brain centers coordinate their activity during adverse events is poorly understood.

**RATIONALE:** Because the LHb does not project directly to the septohippocampal system, the brainstem median raphe region (MRR) has been proposed to coordinate their activity. Although MRR plays an important role in regulating mood, fear, and anxiety, and neuronal projections from it have been extensively studied for decades, it is still unclear how MRR neurons process these negative experiences. Using cell type-specific neuronal tract tracing, monosynaptic rabies tracing, block-face scanning immunoelectron microscopy, and in vivo and in vitro electrophysiological methods, we investigated the neurons of mouse MRR that are responsible for these functions. We used in vivo optogenetics combined with behavioral experiments or electrophysiological recordings to explore the role of MRR neurons responsible for the acquisition of negative experience.



**MRR vGluT2 neurons serve as a key hub for aversive behavior.** (A) MRR vGluT2 (VG2) neurons process aversive events by activating LHb and mVTA neurons and hippocampus (HIPP)–projecting memory acquisition–promoting PV-positive cells in MS/VDB. PFC, prefrontal cortex; IN, interneuron; PC, pyramidal cell. After viruses made MRR vGluT2 neurons light-sensitive (B), mice were light-stimulated in a specific area (C), which caused significant avoidance of that area compared with response in control mice (D). Medians and interquartile ranges; \*\*\* $P = 0.00034$ ; Mann-Whitney  $U$  test. AAV5, adeno-associated virus serotype 5; CTRL, control; ChR2, channelrhodopsin 2; eYFP, enhanced yellow fluorescent protein.

**RESULTS:** We discovered that the MRR harbors a vesicular glutamate transporter 2 (vGluT2)–positive cell population that gives rise to the largest ascending output of the MRR. These neurons received extensive inputs from negative sensory experience-related brain centers, whereas their excitatory fibers projected to the LHb, mVTA, and MS/VDB (see figure). MRR vGluT2 neurons mainly innervated MRR- or mVTA-projecting cells in the medial (limbic) LHb, creating a direct feedback in the MRR-LHb-mVTA axis. MRR vGluT2 neurons were selectively activated by aversive but not rewarding stimuli in vivo. Stimulation of MRR vGluT2 neurons induced strong aversion (see figure), agitation, and aggression and suppressed reward-seeking behavior; whereas their chronic activation induced depression-related anhedonia. The latter can at least partly be explained by our three-dimensional electron microscopy data showing highly effective synaptic targeting of LHb neurons and by our in vitro data showing that MRR vGluT2 terminals can trigger depressive behavior-related bursting activity of LHb neurons.

## ON OUR WEBSITE

Read the full article at <http://dx.doi.org/10.1126/science.aay8746>

MRR vGluT2 neurons seem to be involved in active responses to negative experience, therefore inducing aggression or avoidance, classical fight-or-flight responses. Suppression of MRR vGluT2 neurons precisely at the moment of the aversive stimulus presentation strongly disrupted the expression of both contextual and cued fear memories and prevented fear generalization. MRR vGluT2 neurons could facilitate the learning of negative experience, because their LHb-projecting axons bifurcated and selectively innervated pace-maker MS/VDB PV-positive neurons that projected to the hippocampus. Consequently, in vivo stimulation of MRR vGluT2 neurons instantly evoked memory acquisition–promoting hippocampal theta oscillations in mice.

**CONCLUSION:** Our results revealed that the MRR harbors a previously unrecognized brainstem center that serves as a key hub for the acquisition of negative experience. MRR vGluT2 neurons could activate the aversion- and negative prediction-related LHb-mVTA axis and could swiftly transform the state of the septohippocampal system for immediate acquisition of episodic memories of the negative experience. Maladaptations in processing negative experience form the basis of several types of mood disorders, which have a huge social and economic impact on individuals and society. Selective targeting of this neural hub may form the basis of new therapies. ■

The list of author affiliations is available in the full article online.

\*These authors contributed equally to this work.

†Corresponding author. Email: [nyiri.gabor@koki.mta.hu](mailto:nyiri.gabor@koki.mta.hu)

Cite this article as A. Szőnyi et al., *Science* 366, eaay8746 (2019). DOI: 10.1126/science.aay8746



## RESEARCH ARTICLE

## NEUROSCIENCE

## Median raphe controls acquisition of negative experience in the mouse

András Szőnyi<sup>1\*†‡</sup>, Krisztián Zichó<sup>1\*</sup>, Albert M. Barth<sup>1</sup>, Roland T. Gönczi<sup>1</sup>, Dániel Schlingloff<sup>1,2</sup>, Bibiána Török<sup>2,3</sup>, Eszter Sipos<sup>3</sup>, Abel Major<sup>1</sup>, Zsuzsanna Bardóczi<sup>1</sup>, Katalin E. Sos<sup>1,2</sup>, Attila I. Gulyás<sup>1</sup>, Viktor Varga<sup>1</sup>, Dóra Zelena<sup>3</sup>, Tamás F. Freund<sup>1</sup>, Gábor Nyiri<sup>1§</sup>

Adverse events need to be quickly evaluated and memorized, yet how these processes are coordinated is poorly understood. We discovered a large population of excitatory neurons in mouse median raphe region (MRR) expressing vesicular glutamate transporter 2 (vGluT2) that received inputs from several negative experience-related brain centers, projected to the main aversion centers, and activated the septohippocampal system pivotal for learning of adverse events. These neurons were selectively activated by aversive but not rewarding stimuli. Their stimulation induced place aversion, aggression, depression-related anhedonia, and suppression of reward-seeking behavior and memory acquisition-promoting hippocampal theta oscillations. By contrast, their suppression impaired both contextual and cued fear memory formation. These results suggest that MRR vGluT2 neurons are crucial for the acquisition of negative experiences and may play a central role in depression-related mood disorders.

To survive, animals must quickly recognize a harmful situation, produce an adequate response, and learn its context to help predict the occurrence of similar negative experiences in the future (1–6). This process requires the lateral habenula (LHb) and medial ventral tegmental area (mVTA) for evaluating and predicting aversive stimuli and also requires the septohippocampal system to record and recall memories of these adverse events. Yet how these brain centers coordinate their activity during adverse events is poorly understood. Because the LHb does not project directly to the septohippocampal system, the brainstem median raphe region (MRR) has been proposed to coordinate their activity (7–14). Although the MRR plays an important role in regulating mood, fear, and anxiety, its role in processing negative experience remains elusive (13, 15, 16). It contains projection neurons expressing serotonin [5-hydroxytryptamine (5-HT)] and/or type 3 vesicular glutamate transporter (vGluT3), yet after decades of studies, it is still unclear how MRR neurons can support these functions (17–19). Although projections from the MRR to the LHb, mVTA,

and medial septum and the vertical limbs of the diagonal bands of Broca (MS/VDB) must be crucial to understanding negative experience-related behavior, the identity of key MRR neurons responsible for these connections remains unknown (20, 21).

#### Most MRR projection neurons are vGluT2-positive

In mice, the transmitter phenotypes and targets of almost 25% of MRR neurons are unknown (22). In this study, injections of the Cre-dependent tracer virus AAV5-eYFP (AAV5, adeno-associated virus serotype 5; eYFP, enhanced yellow fluorescent protein) into the MRR of vGluT2-Cre mice, together with complete stereological measurements, revealed that at least 20% of the MRR neurons are vGluT2-positive (Fig. 1, A to C; table S5; and supplementary materials). MRR vGluT2-positive neurons were evenly distributed both in the median and the paramedian part of the MRR. Fluorescent immunohistochemistry demonstrated that this group of cells was distinct from 5-HT- and/or vGluT3-positive neurons in the MRR (Fig. 1B). Terminals of eYFP-expressing MRR neurons of vGluT2-Cre mice were positive for vGluT2 (fig. S1, A and B), but they do not express the plasma membrane serotonin transporter, vesicular GABA transporter (vGAT), or vGluT3 (fig. S1C).

#### MRR vGluT2 neurons are linked to negative experience-related brain regions

Viral labeling of vGluT2 neurons with Cre-dependent AAV5-eYFP in vGluT2-Cre mice revealed that they strongly innervate the LHb and the mVTA (Fig. 1, E and F), as well as other neurons locally (fig. S1D). We did not observe similar innervation patterns after

injecting surrounding brain areas in vGluT2-Cre mice, nor after injecting AAV5-eYFP into the MRR of tryptophan hydroxylase (TpH)-Cre, vGluT3-Cre, or vGAT-Cre mice [labeling serotonergic, vGluT3-positive, and  $\gamma$ -aminobutyric acid-releasing (GABAergic) MRR neurons, respectively] (fig. S3, A to I).

Injections of Cre-dependent AAV5-eYFP into the MRR of vGluT2-Cre mice showed that MRR vGluT2 neuronal projections avoided positive reinforcement-related lateral VTA dopaminergic (DA) cells (Fig. 1G). Instead, they innervated mVTA DA neurons (Fig. 1, G and H). Glutamatergic LHb neurons also innervate mVTA DA cells to regulate negative reward predictions and aversive behavior (1–3, 23). Indeed, when we simultaneously injected AAV5-mCherry into the LHb and AAV5-eYFP into the MRR of the same vGluT2-Cre mice, we detected that both LHb and MRR vGluT2 neurons targeted the mVTA specifically (Fig. 1, G and H).

Aversion-related mVTA DA cells target the medial prefrontal cortex (mPFC) (23, 24). We injected the retrograde tracer cholera toxin B subunit (CTB) into the mPFC and Cre-dependent AAV5-eYFP into the MRR of vGluT2-Cre mice (fig. S1E). vGluT2-positive MRR terminals established synaptic contacts with those mVTA DA neurons that project to the mPFC (fig. S1, F and G), showing that vGluT2-positive MRR neurons target DA cells related to negative reward predictions.

Glutamatergic LHb neurons (primarily in the medial part of the LHb) also innervate the MRR (25), but the identity of their target cells is unknown. We injected Cre-dependent AAV5-eYFP into the MRR and AAV5-mCherry into the LHb of vGluT2-Cre mice and found that MRR vGluT2 neurons primarily targeted the medial part of the LHb (Fig. 1E), whereas at least 39% of LHb terminals innervated vGluT2-positive neurons in the MRR (Fig. 1, I to L). Serotonergic and vGluT3-positive MRR neurons were also targeted by LHb vGluT2 neurons (for the exact ratios, see fig. S2, F and G). Using combined anterograde and retrograde tracing, we also found that there is a direct reciprocal connection between the LHb-projecting vGluT2-positive MRR neurons and the MRR-projecting vGluT2-positive LHb neurons (Fig. 1I) (for measured ratios, see figs. S1, H to J, and S2, A to E, and supplementary materials). vGluT2-positive MRR neurons also innervate LHb neurons that project to the mVTA (fig. S1, H to J). These results indicate an excitatory positive-feedback loop between the vGluT2 neurons of the MRR and LHb. Both of these neuronal populations project to the aversion-encoding mVTA as well.

To identify upstream brain areas that synaptically target the MRR vGluT2-positive neurons, we used mono-transsynaptic rabies tracing (26). We used a Cre-dependent helper

<sup>1</sup>Laboratory of Cerebral Cortex Research, Department of Cellular and Network Neurobiology, Institute of Experimental Medicine, Hungarian Academy of Sciences, Budapest, Hungary.

<sup>2</sup>János Szentágothai Doctoral School of Neurosciences, Semmelweis University, Budapest, Hungary. <sup>3</sup>Laboratory of Behavioral and Stress Studies, Department of Behavioral Neurobiology, Institute of Experimental Medicine, Hungarian Academy of Sciences, Budapest, Hungary.

\*These authors contributed equally to this work.

†Present address: Laboratory for Cellular Mechanisms of Learning and Memory, Friedrich Miescher Institute for Biomedical Research, Basel, Switzerland.

‡Present address: Laboratory of Cellular Neurophysiology, Department of Cellular and Network Neurobiology, Institute of Experimental Medicine, Hungarian Academy of Sciences, Budapest, Hungary.

§Corresponding author. Email: nyiri.gabor@koki.mta.hu

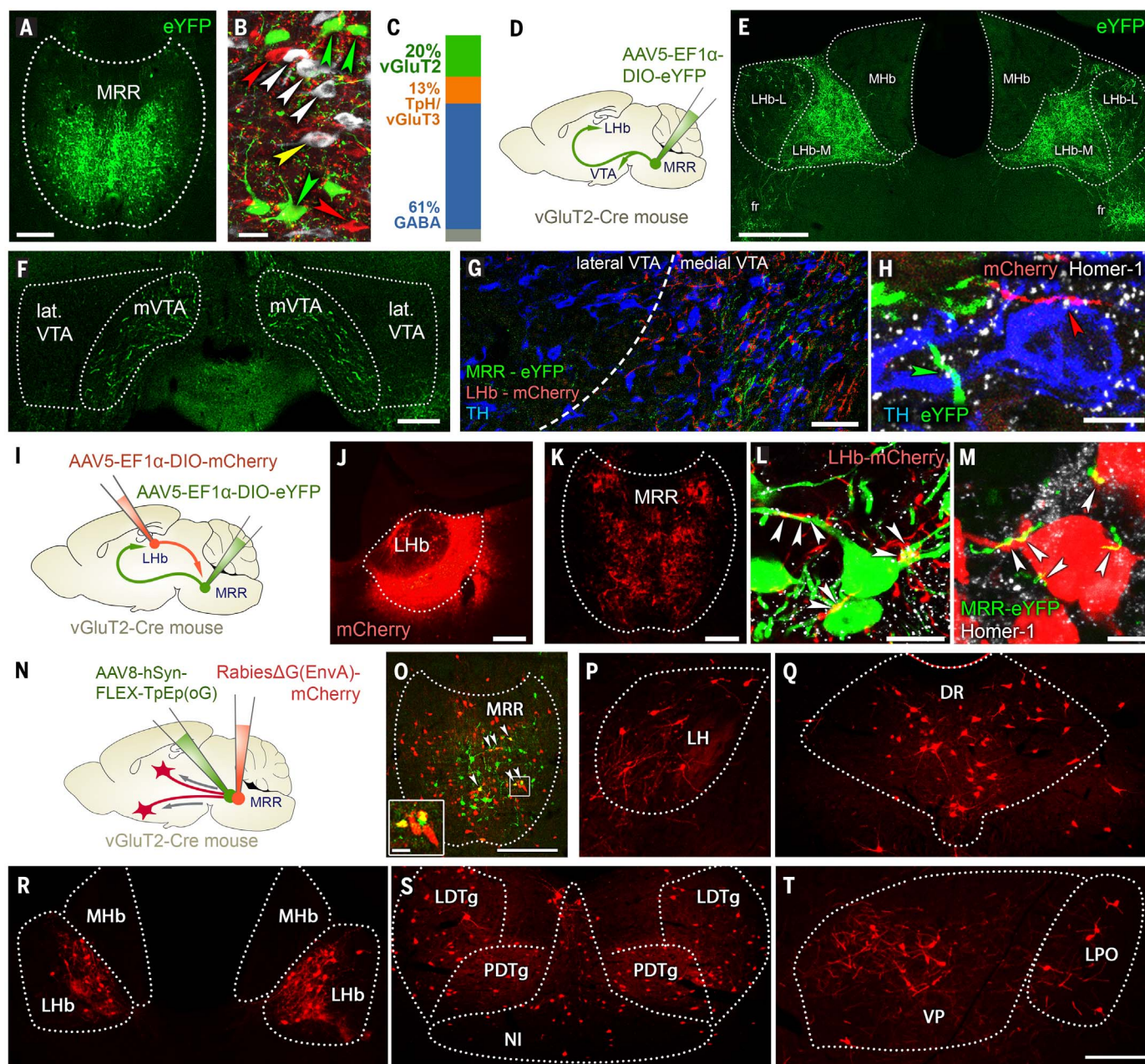


**Fig. 1. vGluT2 neurons are the largest population of projection cells in the MRR.** (A) AAV5-eYFP labeling in the MRR in vGluT2-Cre mice. Scale bar: 200  $\mu$ m. (B) eYFP-labeled vGluT2-positive (green arrows), immunolabeled Tph-positive (white arrows), vGluT3-positive (red arrows), and Tph/vGluT3 double positive (yellow arrow) cells in MRR. Scale bar: 20  $\mu$ m. (C) At least 20% of the MRR neurons are vGluT2-positive. (For stereological statistical details, see table S5). (D) AAV2/5-EF1 $\alpha$ -DIO-eYFP was injected into the MRR of vGluT2-Cre mice ( $n = 3$ ). (E and F) Virally labeled vGluT2-positive MRR fibers innervate the Lhb (primarily the medial part) and mVTA. fr, fasciculus retroflexus; Lhb-L, lateral habenula, lateral division; Lhb-M, lateral habenula, medial division; MHb, medial habenula; VTA, ventral tegmental area. Scale bars: 200  $\mu$ m. (G) vGluT2-positive fibers from MRR (green) and Lhb (red) innervate the same medial VTA but not the lateral VTA. DA cells were labeled with anti-tyrosine hydroxylase (TH, blue). Scale bar: 50  $\mu$ m. Statistical details for all figures are provided in the supplementary text section of the supplementary materials. (H) vGluT2-positive MRR axon terminal (green) and an Lhb terminal (red) establish Homer-1 (white) positive synaptic contacts with the same dopaminergic

cell (TH, blue) in mVTA. Scale bar: 5  $\mu$ m. (I) AAV2/5-EF1 $\alpha$ -DIO-eYFP was injected into the MRR and AAV2/5-EF1 $\alpha$ -DIO-mCherry was injected into the Lhb of vGluT2-Cre mice bilaterally ( $n = 2$ ). (J and K) Injection site in the Lhb (J) and its vGluT2-positive fibers in the MRR (K). Scale bar: 200  $\mu$ m. (L) vGluT2-positive Lhb fibers (red) establish Homer-1 (white) positive synaptic contacts (white arrowheads) with vGluT2-positive MRR neurons (green). Scale bar: 10  $\mu$ m. (M) vGluT2-positive MRR fibers (green) establish Homer-1 (white) positive synaptic contacts (white arrowheads) with vGluT2-positive Lhb neurons (red). Scale bar: 5  $\mu$ m. (N) A helper AAV2/8-hSyn-FLEX-TpEp(oG) was injected into the MRR of vGluT2-Cre mice, followed by an injection of Rabies( $\Delta$ G)-EnvA-mCherry 2 weeks later ( $n = 3$  mice). (O) Injection site of helper (green) and rabies (red) viruses into the MRR of vGluT2-Cre mice. Inset shows some starter neurons expressing both viruses. Scale bar: 100  $\mu$ m (main image), 10  $\mu$ m (inset). (P to T) Rabies-labeled neurons in different brain areas establish synapses on vGluT2-positive MRR neurons. Scale bar: 100  $\mu$ m. LDTg, laterodorsal tegmental nucleus; LPO, lateral preoptic area; PDTg, posterodorsal tegmental nucleus; VP, ventral pallidum. For detailed analysis, see table S6.



virus encoding both an avian tumor virus receptor A (TVA) and an optimized rabies glycoprotein, and we used a TVA-receptor-dependent and glycoprotein-deleted rabies virus in vGluT2-Cre mice (supplementary materials and Fig. 1, N and O)—the specificity of this virus combination was validated in our previous study (27). Brain areas that play an essential role in negative experience-related behavior, including the dorsal raphe (DR), lateral hypothalamus (LH), periaqueductal gray, and zona incerta, showed a strong convergence onto vGluT2-positive MRR cells (Fig. 1, P to T; for details, see table S6). The LHb accounts for most of the monosynaptically labeled input cells (Fig. 1R). Areas related to the encoding of aversive memories [such as the mammillary areas, the pontine reticular nucleus, or the nucleus incertus (NI)] also sent

strong projections onto vGluT2-positive MRR neurons (table S6).

### MRR vGluT2 neurons establish multiple burst-promoting synapses on LHb neurons

Negative experience-related behavior and subsequent depression-like symptoms are strongly promoted by the excitatory inputs of LHb neurons (28–30). Using block-face scanning electron microscopy, we revealed that MRR vGluT2 neurons provide an extensive synaptic coverage on LHb neurons (Fig. 2, A, B, E, and F), and most of the axon terminals of MRR vGluT2 neurons established more than one synapse on the same or different target cells (Fig. 2D). *N*-methyl-D-aspartate (NMDA) receptor-dependent burst-firing in LHb neurons play a key role in the development of depression (28, 30). We found that MRR

vGluT2 neurons established NMDA receptor-containing excitatory glutamatergic synapses on LHb neurons (Fig. 2C). In the LHb, astroglia cooperate with excitation to regulate neuronal bursting and depression-like symptoms (28). These glial processes enwrapped most synapses of MRR vGluT2 terminals in the LHb (Fig. 2, B, E, and F).

To test the physiological effect of MRR vGluT2 neurons on the activity of the LHb neurons, we selectively activated MRR vGluT2 fibers in the LHb in vitro using channelrhodopsin 2 (ChR2)-containing Cre-dependent AAV5-ChR2-eYFP in optogenetic experiments (Fig. 3A). Light stimulation of ChR2-containing MRR vGluT2-positive fibers reliably evoked glutamatergic excitatory postsynaptic currents (EPSCs) in voltage-clamped neurons of the LHb (Fig. 3B and fig. S4, A and B), which

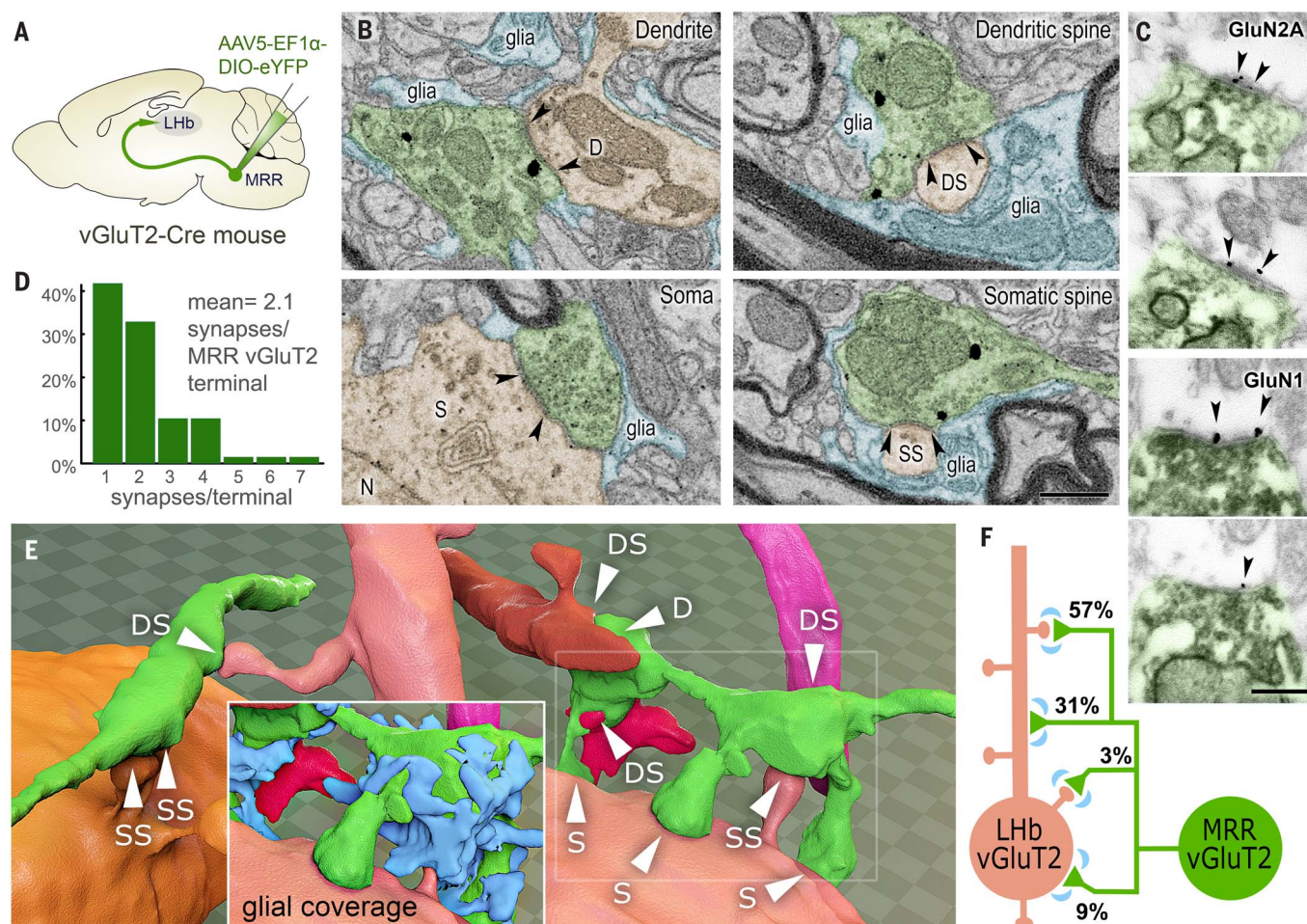


**Fig. 2. MRR vGluT2 neurons establish glia-enwrapped glutamatergic synapses on LHb neurons.** (A) AAV5/5-EF1 $\alpha$ -DIO-eYFP was injected into the MRR of vGluT2-Cre mice. (B) Scanning electron micrographs represent different types of synaptic contacts established by eYFP-positive MRR terminals (immunogold labeling, black spheres) on different subcellular compartments of LHb neurons. Arrows indicate synaptic edges. D, dendrite; DS, dendritic spine; N, nucleus; S, soma; SS, somatic spine. Scale bar: 500 nm. (C) AAV-eYFP positive terminals [serial sections of immunoperoxidase labeling, dark 3,3' diaminobenzidine (DAB) precipi-

tate] establish synapses on LHb neurons that contain the GluN2A (top two images) or GluN1 (bottom two images) NMDA-receptor subunits (immunogold particles indicated with arrowheads). Scale bar: 300 nm. (D) MRR vGluT2 terminals establish more than one synapse on LHb neurons (from two mice). (E) 3D reconstruction of MRR vGluT2 fibers (green) shows their synapses with different membrane domains of LHb neurons. Inset shows the abundant glial coverage around MRR vGluT2 terminals (blue). (F) Schematic illustration of the proportion of MRR vGluT2 synapses on different membrane domains of LHb neurons (from two mice).

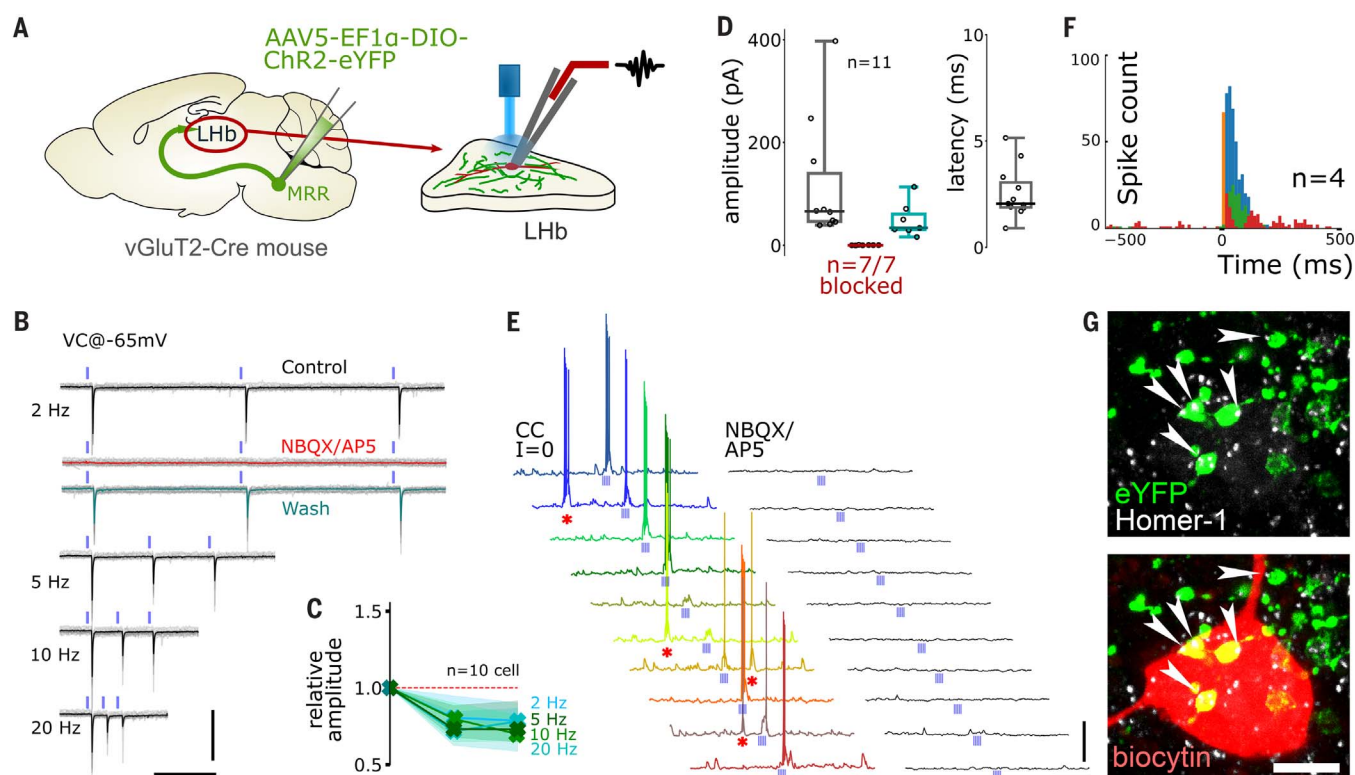


**Fig. 3. Fibers of MRR vGluT2 neurons evoke burst firing in Lhb neurons.**

(A) AAV2/5-EF1 $\alpha$ -DIO-ChR2-eYFP was injected into the MRR of vGluT2-Cre mice ( $n = 3$ ). Six weeks later, 300- $\mu$ m-thick horizontal in vitro slices were prepared from the Lhb. Neurons in the Lhb were whole-cell patch clamped in voltage-clamp mode (see supplementary methods). (B) Light stimulations of MRR vGluT2 fibers evoked EPSCs in Lhb neurons. The average responses to 2-ms light pulses are shown above individual gray traces. Responses are strong in control conditions (black); they were completely abolished (red trace) by 20- $\mu$ M NBQX (AMPA/kainite receptor antagonists) and 50- $\mu$ M AP5 (NMDA antagonist) and partially recovered after washout (teal). Scale bars: 200 ms, 200 pA. (C) Cells displayed short-term depression of EPSC amplitudes at all stimulation frequencies (averages from 10 cells). (D) EPSC amplitude

and latency distributions from all 11 recorded neurons (in gray). Excitatory postsynaptic potentials were sensitive to glutamatergic antagonists in 7 out of 7 tested cells (red) and partially recovered after washout (teal). (E) Traces show representative current-clamped ( $I = 0$ ) Lhb neurons displaying spontaneous (asterisks) and light-evoked (pale blue lines, 5 pulses at 20 Hz) bursts. Ten consecutive stimulations are shown. Both spontaneous and light-evoked bursts were abolished by application of NBQX and AP5 (traces on the right). Scale bars: 1 s, 20 mV. (F) Peristimulus time histogram shows action potential distributions upon light stimuli ( $n = 4$  cells). (G) A representative, recorded Lhb cell (biocytin labeling, red) receives Homer-1-positive (white) synaptic contacts (white arrowheads) from eYFP-positive MRR fibers (green). Scale bar: 5  $\mu$ m.

received MRR vGluT2 terminals (Fig. 3G). These EPSCs showed strong short-term depression and were abolished by the simultaneous blockade of  $\alpha$ -amino-3-hydroxy-5-methyl-4-isoxazolepropionic acid (AMPA)- and NMDA-type glutamate receptors (Fig. 3, B to D). After activating ChR2-expressing vGluT2-positive MRR terminals in the Lhb, we frequently observed the induction of burst-firing in Lhb neurons (Fig. 3, E and F), whereas some spontaneous burst-firing was also present in these neurons. Bursting disappeared after the combined blockade of AMPA- and NMDA-type glutamate receptors (Fig. 3E).

#### MRR vGluT2 neurons are selectively activated by aversive stimuli in vivo

We explored the in vivo response of identified MRR vGluT2 neurons to aversive and rewarding stimuli. We used a combination of multi-channel recording and optogenetic tagging in

the MRR of Cre-dependent, AAV-ChR2-eYFP-injected vGluT2-Cre mice. Awake mice were head-fixed on top of an air-supported spherical treadmill, while multiple single units were simultaneously recorded from the MRR using a multichannel silicone probe. Light pulses that were used to tag vGluT2 neurons were delivered through an optic fiber positioned above the MRR (Fig. 4, A and B). Tagged neurons reliably responded to brief blue laser light pulses with short latency and small jitter (Fig. 4C). A large set of optogenetically identified vGluT2-positive MRR neurons were robustly activated by strongly aversive air puffs (Fig. 4, D to F). By contrast, MRR vGluT2 neurons were practically never affected by rewarding stimuli (water drops) (Fig. 4, D to F). Mildly aversive light-emitting diode (LED) flashes triggered a slight, transient elevation of activity in a small subgroup of vGluT2-positive MRR neurons, partially overlapping with the air-puff

activated group (fig. S4, G and H), but this effect was significantly lower than that of air-puff stimulation (Fig. 4, D to F).

#### Optogenetic activation of MRR vGluT2 neurons causes strongly aversive behavior

The rapid, adverse experience-specific in vivo activity of MRR vGluT2 neurons suggests that they specifically process negative experience. To light-activate MRR vGluT2 neurons selectively in vivo, we injected ChR2-containing Cre-dependent AAV5-ChR2-eYFP into the MRR of vGluT2-Cre mice ("ChR2 mice"). Control mice were injected with a control virus that expressed no ChR2 ("CTRL mice"). Then, we implanted an optic fiber over the MRR (supplementary materials, Fig. 5A, and fig. S5). After handling, mice were placed in a chamber containing two different areas with different visual cues (Fig. 5A). In the habituation session, mice did not show a preference for one



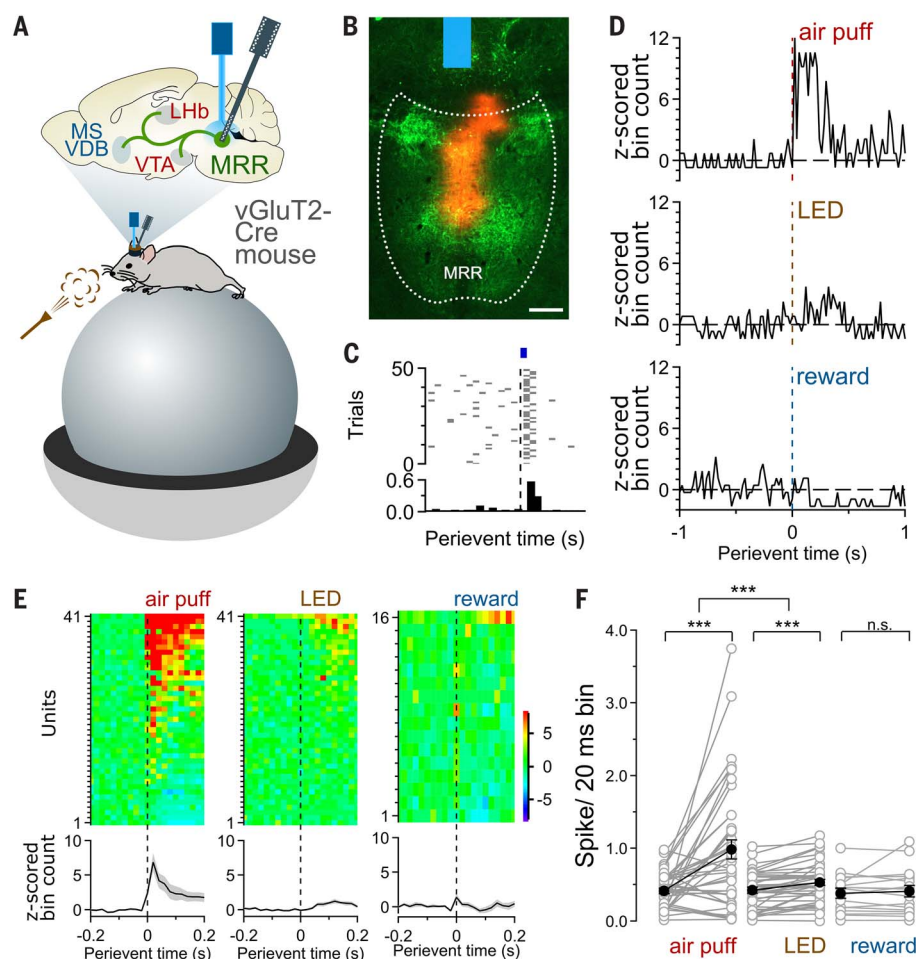


**Fig. 4. In vivo, MRR vGluT2 neurons selectively respond to aversive stimuli.** (A) AAV2/5-EF1 $\alpha$ -DIO-ChR2-eYFP was injected into the MRR of vGluT2-Cre mice. A silicone probe was inserted into and an optical fiber was placed above the MRR. Mice were head-fixed on top of an air-supported spherical treadmill, and strongly aversive (air puff), mildly aversive (LED flash), and rewarding (water drops) stimuli were randomly presented to the awake animals (eight mice). (B) A representative image of virus expression (green) and the position of the implanted optic fiber (blue) and silicone probe (red Dil labeling) in the MRR of a vGluT2-Cre mouse. Scale bar: 200  $\mu$ m. (C) A raster plot and a peristimulus time histogram, corresponding to an optogenetically tagged vGluT2 neuron in the MRR, shows short latency, high success rate, and low jitter of the responses. The blue square indicates the light pulse. (D) A representative MRR vGluT2 neuron was robustly activated by an aversive air puff, was only weakly activated by a slightly aversive LED stimulus, and showed no response to water reward. (E) Top matrices show the reaction of individual MRR vGluT2 neurons to different stimuli (each row is one neuron's z-scored peristimulus time histogram), sorted by descending response magnitudes. Bottom plots show average response across all tagged units (from eight animals, mean  $\pm$  SEM). (F) Paired plots of cells [same as those displayed in (E)] show the baseline versus stimulus-evoked firing activity of MRR vGluT2 neurons (gray, individual tagged neurons; black, mean  $\pm$  SEM). Air puffs evoked significantly larger responses than did LED flashes. Reward induced no significant population response.

area over the other (fig. S6, A and B). Twenty-four hours later, mice were returned to the same chamber and received optogenetic stimulation (25 Hz) only in one area of the chamber (area selection was systematically random). ChR2 mice, but not CTRL mice, showed a powerful and immediate real-time place aversion to the stimulation-linked area (Fig. 5, A and B, and fig. S6, A and B). The following day, previously stimulated ChR2 mice, but

not CTRL mice, showed a strong conditioned aversion to the area that was previously linked to stimulation (Fig. 5, A and B, and fig. S6, A and B).

We investigated whether the activity of MRR vGluT2 neurons is powerful enough to counteract the strongly positive expectation of a motivated, food-seeking animal. The above-mentioned ChR2 and CTRL mice were food-restricted and trained for 10 days in an

operant conditioning task to nose-poke for food rewards (Fig. 5C and supplementary materials). On the last day of their training, both groups of mice reached a plateau in the total number of nose-pokes during the 30-min-long operant conditioning session (Fig. 5C). Twenty-four hours later, mice received blue laser stimulation that started after each rewarded nose-poke during the entire 30-min-long session. ChR2 mice, but not CTRL mice, poked significantly less for reward pellets during the day of the stimulation experiment compared with the frequency of poking on the last day of their training (Fig. 5, D and E).

We also tested whether the activation of these cells can induce passive coping. We performed an optogenetic contextual fear conditioning experiment with the same cohort of mice that participated in the operant conditioning task (fig. S6C). Mice were allowed 3 days to rest and regain their original weight, and on the 25th day they were placed in a novel environment, where they received 15-s-long laser stimulation 10 times. Twenty-four hours later, mice were tested in the same environment. Neither ChR2 mice nor CTRL mice showed any sign of freezing behavior during light stimulation or 24 hours later in the same environment (fig. S6C).

#### Activation of MRR vGluT2 neurons induces aggression and depressive symptoms

Neuronal activity in the LHb is related to aggressive behavior (31). Therefore, we investigated whether activation of MRR vGluT2 neurons induces the prediction of negative experience in a social context and whether it promotes an aggressive behavior in mice during these social interactions. We used a DREADD (designer receptors exclusively activated by designer drugs)-containing AAV-based chemogenetic tool that expresses mutant receptors that activates cells upon binding to clozapine-N-oxide (CNO). We injected either Cre-dependent excitatory DREADD virus AAV8-h3MDq-mCherry ("hM3Dq mice") or Cre-dependent AAV8-mCherry virus ("CTRL mice") into the MRR of vGluT2-Cre mice. Then, both hM3Dq and CTRL mice received intraperitoneal injections of CNO (Fig. 6A and supplementary materials) and performed two behavioral tests. In the social interaction test, mice were placed in a novel environment 30 min after CNO injections, together with an unfamiliar mouse. CTRL mice showed mostly prosocial behavior toward the conspecific (Fig. 6B). In contrast, hM3Dq mice became highly aggressive (Fig. 6B and fig. S4, C to F). Five days later, we carried out a resident-intruder test. Thirty minutes after CNO injections, a subordinate intruder mouse was placed into the home cage of the CTRL or hM3Dq mice. Again, hM3Dq mice became highly aggressive

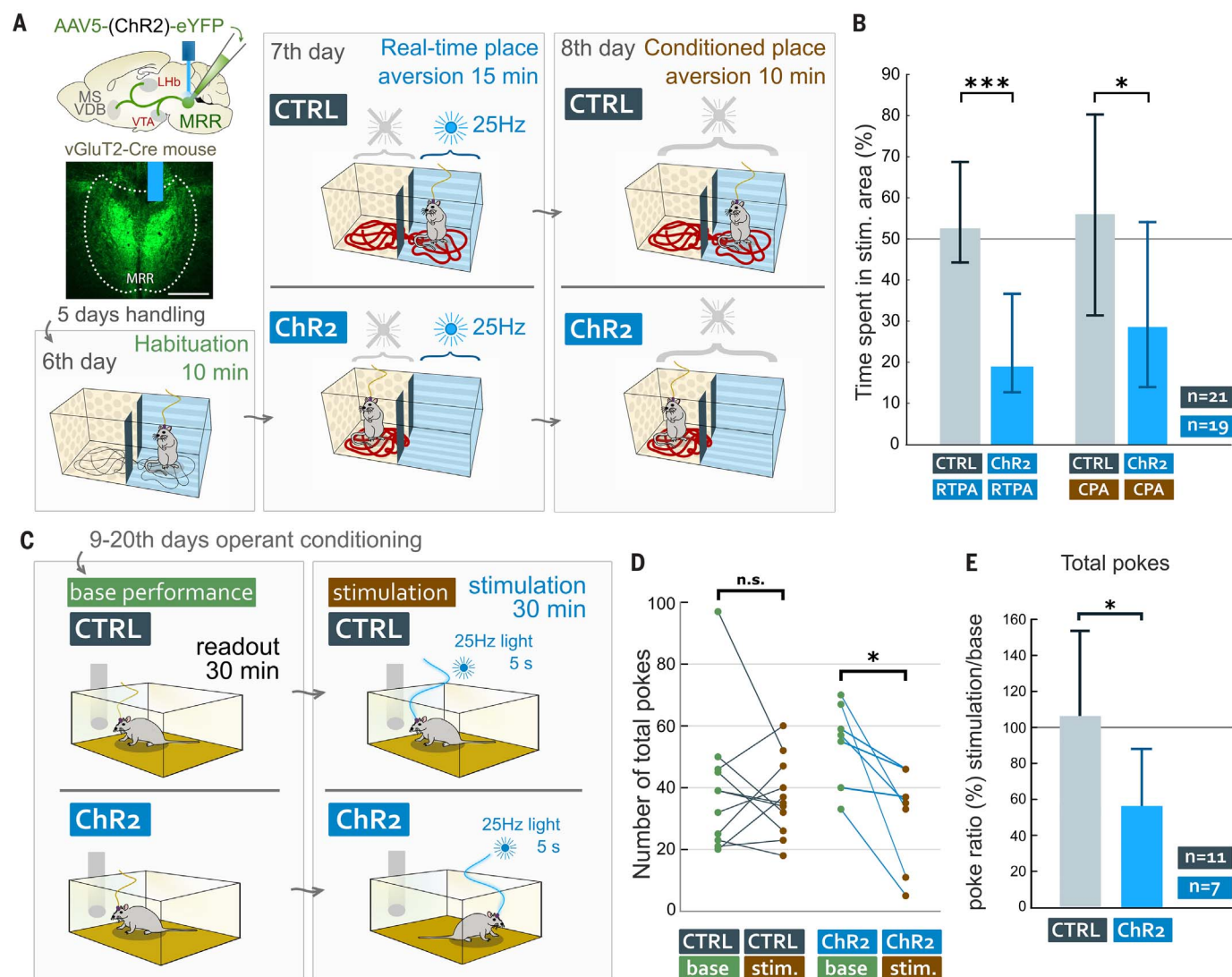


**Fig. 5. MRR vGluT2 neurons induce active avoidance of negative experience.** (A) After injecting ChR2-containing AAV2/5-EF1 $\alpha$ -DIO-ChR2-eYFP (“ChR2 mice”) or control (only eYFP-containing) Cre-dependent AAV5 (“CTRL mice”) into the MRR of vGluT2-Cre mice, we implanted an optic fiber over the MRR. Image represents an injection site in MRR and the position of the optic fiber (blue). Scale bar: 500  $\mu$ m. Four weeks later, mice were habituated to a chamber with two areas. On day 7, mice received 25-Hz light illumination in one of the areas of the chamber. ChR2 mice showed immediate, significant real-time place aversion (RTPA) of the stimulated area. On day 8, no light was presented, but ChR2 mice displayed a significant conditioned place aversion (CPA), suggesting

that the activity of MRR vGluT2 neurons can directly induce real-time and learned active contextual avoidance (see also fig. S6A). (B) RTPA and CPA tests show significant effects (medians and interquartile ranges). (C) Between days 9 and 21, mice were food-restricted and learned to nose-poke for reward pellets. On day 22, mice received 5-s 25-Hz light stimulation on nose-pokes. Compared with base performance (on day 21), ChR2 mice performed significantly fewer nose-pokes when nose-pokes were paired with laser stimulation (on day 22). (D) The total number of nose-pokes for rewards during the base and stimulation performance in the operant conditioning task. (E) Nose-poke ratios of stimulation/base performance in the operant conditioning task (mean and SD).

toward the intruder (Fig. 6C and fig. S4, C to F). In a separate experiment, chemogenetic activation of AAV8-h3MDq-expressing MRR vGluT2 neurons by CNO injections also induced significantly higher motor activities in a Y-maze compared with CTRL mice (fig. S4I).

Aggressive behavior frequently accompanies the depressive state (32–34), which is also promoted by chronic overactivation and burst-firing of LHB neurons (28–31, 35). Using the above-mentioned types of CTRL and hM3Dq

mice, we tested whether chronic activation of MRR vGluT2 neurons promoted depression-like symptoms. Mice received intraperitoneal injections of the DREADD-agonist CNO three times a week for 3 weeks (Fig. 6A and supplementary materials). On day 19, mice were tested in a sucrose preference test, which can detect anhedonia, a classic symptom of depression (36). CTRL mice preferred the 1% sucrose solution over water significantly more than hM3Dq mice did (Fig. 6D). The postmortem weight of

the adrenal glands of hM3Dq mice was significantly higher than that of CTRL mice (fig. S4J).

#### MRR vGluT2 neurons activate memory acquisition—promoting MS/VDB neurons

Fast and effective processing of negative experience requires the immediate induction of memory acquisition, which necessitates a rapid change in the state of the MS/VDB-hippocampal system (37). After AAV5-eYFP labeling of MRR vGluT2 neurons, we observed



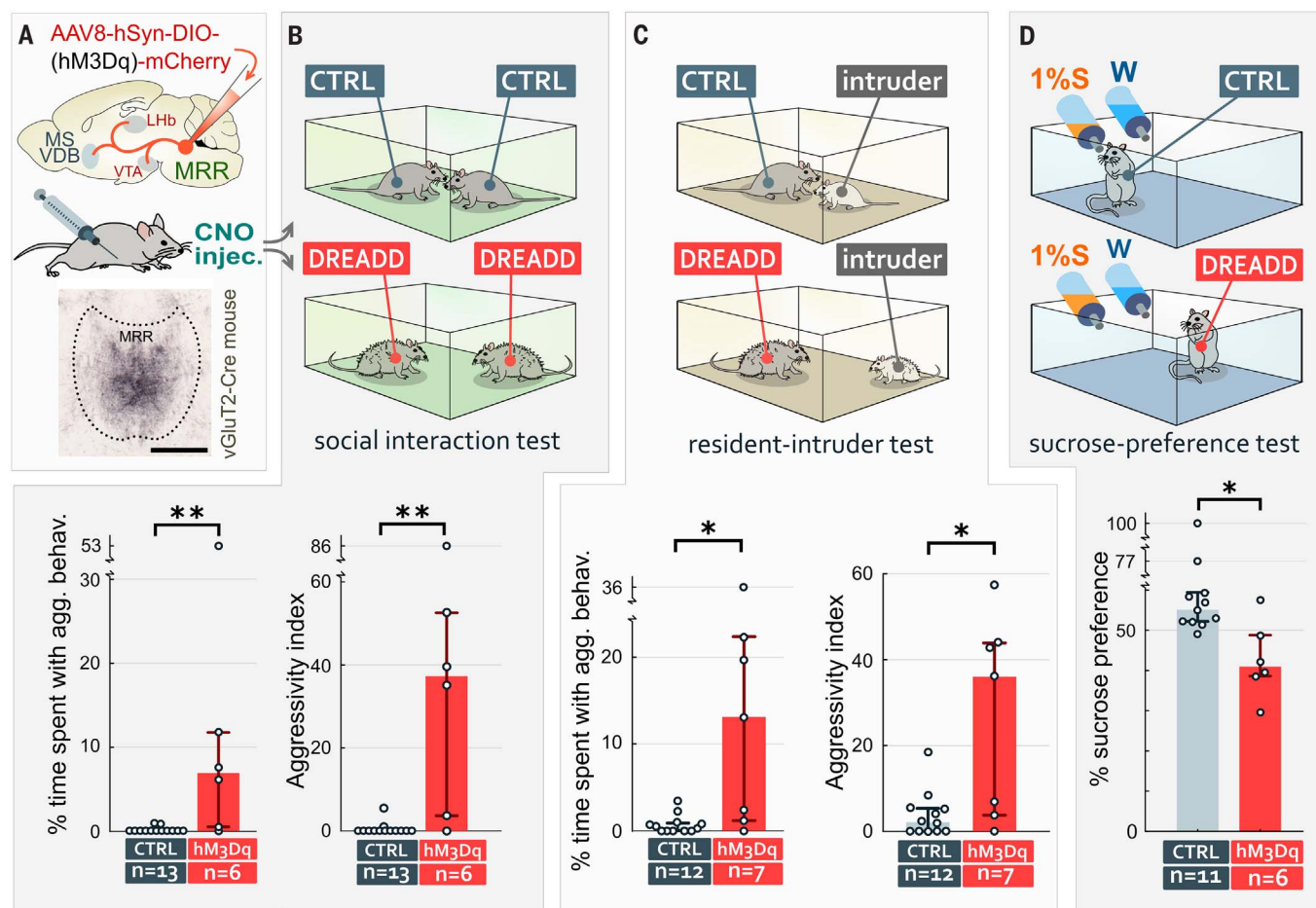


**Fig. 6. Chronic overactivation of MRR vGluT2 neurons induces aggression and anhedonia.** (A) AAV2/8-hSyn-DIO-hM3D(Gq)-mCherry or control AAV2/8-hSyn-DIO-mCherry was injected into the MRR of vGluT2-Cre mice (14 CTRL mice and 8 hM3Dq mice). All mice received hM3Dq-agonist clozapine-*N*-oxide (CNO, 1 mg 10 ml<sup>-1</sup> kg<sup>-1</sup> intraperitoneally, 30 min before testing). Image represents a DAB-labeled injection site in the MRR. Scale bar: 500  $\mu$ m. (B and C) Social interaction (B) and resident-intruder (C) tests. Percentage of time spent with aggressive

interactions and aggressivity index are shown at the bottom. Chemogenetic stimulation of MRR vGluT2 neurons led to highly aggressive behavior, suggesting the induction of active coping with a perceived strongly negative experience. (D) Testing anhedonia in a sucrose preference test (see supplementary methods for details). Chronic stimulation of MRR vGluT2 neurons in hM3Dq mice led to a significant difference in sucrose preference compared to CTRL mice, suggesting the induction of depression-related anhedonia. Graphs show medians and 25%–75% quartiles.

an abundant axonal labeling in the MS/VDB (Fig. 7, A and B). MRR vGluT2 neurons established NMDA receptor-containing excitatory synapses selectively with parvalbumin (PV)-positive GABAergic cells in the MS/VDB (Fig. 7, A to E; fig. S1K; and supplementary text). Using hippocampal injections of the retrograde tracer FluoroGold, in combination with AAV5-mCherry, into the MRR of vGluT2-Cre mice, we found that MRR vGluT2 neurons directly innervate hippocampus-projecting PV neurons in MS/VDB (Fig. 7, F to H). These PV neurons are the pacemakers of memory acquisition—promoting hippocampal theta rhythm (38, 39).

The theta-rhythmic activity of LHB neurons and the hippocampal network are phase-locked, and their concerted activity is necessary for proper memory formation (8, 14). Therefore, we investigated whether individual axons of

MRR vGluT2 neurons bifurcate and target both areas. We performed double retrograde tracing by injecting CTB into the LHB and FluoroGold into the MS/VDB of vGluT2-Cre mice, and we labeled vGluT2-positive MRR cells with AAV5-mCherry (Fig. 7, I and J). At least 61% of MRR vGluT2 neurons retrogradely labeled from the MS/VDB were retrogradely labeled from the LHB as well (Fig. 7K).

We also investigated the effect of activation of MRR vGluT2 neurons on hippocampal network activity in vivo. Using AAV5-ChR2-eYFP, we expressed ChR2 in MRR vGluT2 neurons and implanted an optic fiber over the MRR and a Buzsaki probe into the dorsal CA1 (Fig. 8A). Ten-second-long stimulation of MRR vGluT2 neurons by a 25-Hz light train triggered some movement (possibly related to the above-mentioned active avoidance of the stimuli)

and it triggered hippocampal theta oscillations (Fig. 8, B to D) known to facilitate the formation of memories.

#### MRR vGluT2 neurons are necessary for fear memory acquisition

MRR vGluT2 neurons are specifically excited by negative experience, which they relay to aversion centers and to the septohippocampal system, likely promoting memory encoding. We injected Cre-dependent Archaelrhodopsin T-3 (ArchT 3.0)-containing AAV5-ArchT-GFP (ArchT mice) or control Cre-dependent AAV5-eYFP (CTRL mice) into the MRR of vGluT2-Cre mice and implanted an optic fiber over the MRR (Fig. 8E and fig. S5). After handling, mice were tested in a delay cued fear conditioning paradigm. First, we placed mice into a novel environment “A,” where they received three

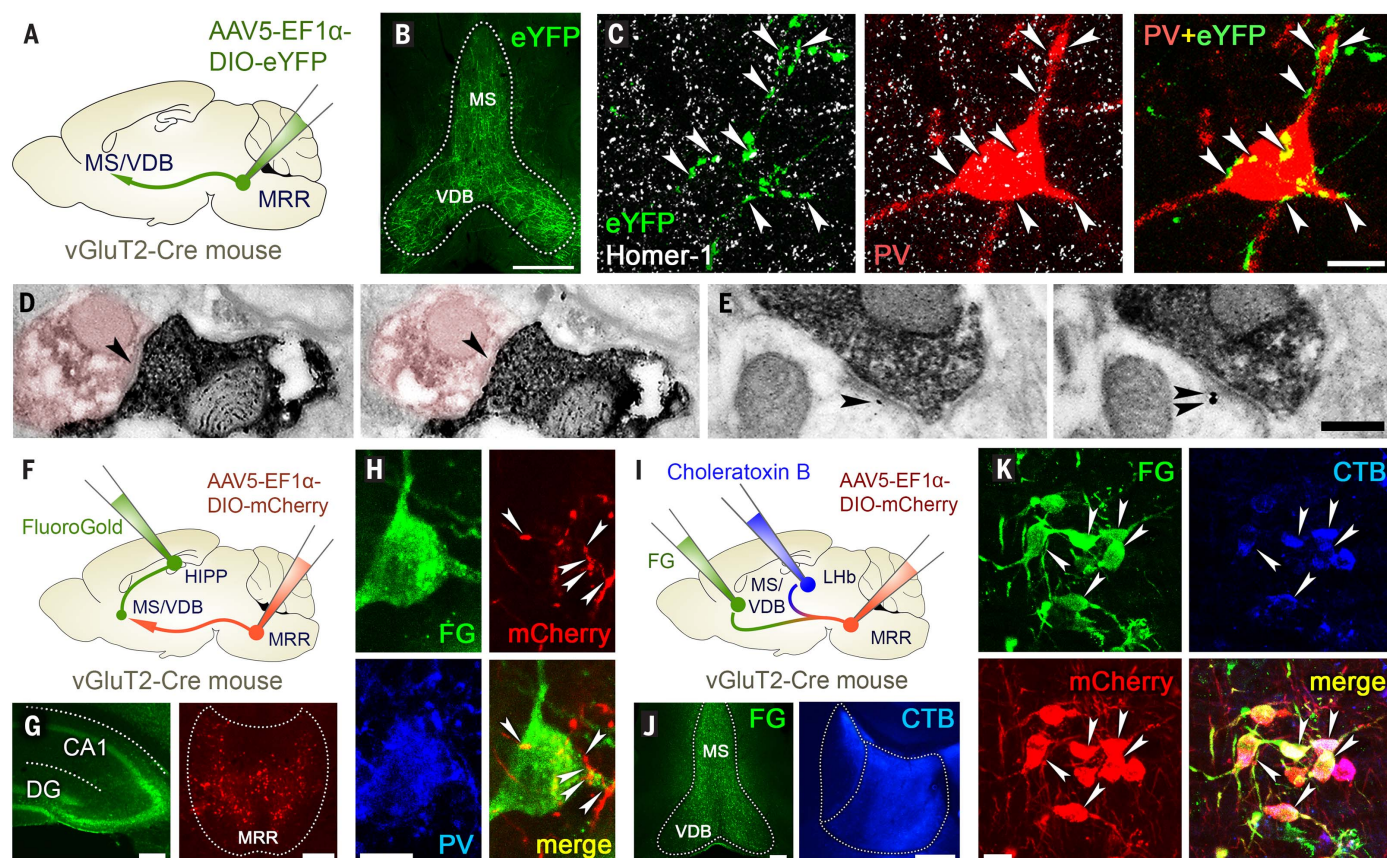


**Fig. 7. MRR vGluT2 neurons selectively innervate PV-positive MS/VDB neurons.** (A) AAV2/5-EF1 $\alpha$ -DIO-eYFP was injected into the MRR of vGluT2-Cre mice ( $n = 3$ ). (B) MRR vGluT2 neuronal fibers innervate the MS/VDB. Scale bar: 200  $\mu$ m. (C) A representative MS/VDB PV-positive neuron (red) is innervated by basket-like multiple synapses of vGluT2-positive MRR fibers (green), establishing Homer-1-positive (white) synaptic contacts (white arrowheads). Scale bar: 10  $\mu$ m. (D and E) Electron microscopic images show serial sections of synapses of vGluT2-positive MRR terminals (dark SI-DAB). (D) PV-positive dendrite (false red colored, DAB-Ni precipitate) in the VDB received synaptic contacts (at least 12 synapses were reconstructed; black arrowheads). (E) Synapses contained GluN2A subunit of the NMDA receptors (immunogold labeling, black arrowheads) postsynaptically. Scale bar: 300 nm. (F) AAV2/5-EF1 $\alpha$ -DIO-mCherry was injected into the MRR and FluoroGold into the bilateral

hippocampus of vGluT2-Cre mice ( $n = 2$ ). (G) Representative injection sites in the hippocampus [green FluoroGold (FG) labeling] and MRR (red AAV-mCherry). Scale bars: 200  $\mu$ m. (H) AAV-mCherry containing vGluT2-positive MRR terminals (red) establish several putative contacts (white arrowheads) with a FG-positive (green) septohippocampal PV-positive (blue) neuron. Scale bar: 10  $\mu$ m. (I) Double retrograde tracing was performed by injecting FG into the MS/VDB and CTB into the Lhb, bilaterally, and AAV2/5-EF1 $\alpha$ -DIO-mCherry was injected into the MRR to virally label vGluT2-positive neurons in vGluT2-Cre mice ( $n = 2$ ). (J) Representative injection sites in the MS/VDB (FG labeling) and in the Lhb (CTB labeling). Scale bars: 200  $\mu$ m. (K) MRR vGluT2 neurons (red) contain both FG (green) and CTB retrograde labeling (blue), which shows that bifurcating axons of these neurons simultaneously target both the MS/VDB and Lhb. Scale bar: 20  $\mu$ m.

auditory tones, at the end of which they received foot shocks and light illuminations. Light delivery was precisely aligned to foot shocks (Fig. 8E). All mice displayed equally strong immediate reactions to foot shocks. In the tests that followed, mice received no light illumination. Twenty-four hours later, mice were placed into the same environment “A” to test their contextual memories. CTRL mice expressed strong contextual freezing behavior, whereas ArchT mice showed almost no freezing behavior (Fig. 8E). The next day, we placed mice into a different, neutral environment (environment “B”), where ArchT mice showed significantly lower generalized fear compared with CTRL mice (Fig. 8E). Then, in the same neutral environment,

we presented mice with an auditory cue. CTRL mice showed very high levels of freezing. In contrast, light-inhibited ArchT mice showed significantly diminished freezing, indicating impaired fear memory formation (Fig. 8E). Even after cue presentation was completed, the difference between the fear levels of ArchT and CTRL mice remained significant (fig. S6D).

#### MRR vGluT2 neurons serve as a key hub for the acquisition of negative experience

Animals must recognize adverse events quickly and decide whether to fight or flee, while at the same time efficiently learning the context of that event so that they can predict it in the future. The Lhb and mVTA are activated during the acquisition of negative experience

(7, 23, 24, 40), which initiates the encoding of “negative reward prediction errors” and aversion in these nuclei (5, 41). Activation of mVTA DA neurons is also aversive (23, 42), whereas the activity of lateral VTA neurons plays a role in positive reinforcement. The Lhb contains nearly exclusively glutamatergic neurons, which encode aversive behavior and activate DA neurons of the mVTA (23–25, 43). Lhb activity also indirectly inhibits encoding of positive reinforcement in the lateral VTA (23, 44). These processes fine-tune future strategies in similar situations (5, 41, 45–48). The Lhb and mVTA convey information related to negative predictions and learn to respond to cues that predict aversive stimuli (3, 42, 49–53).



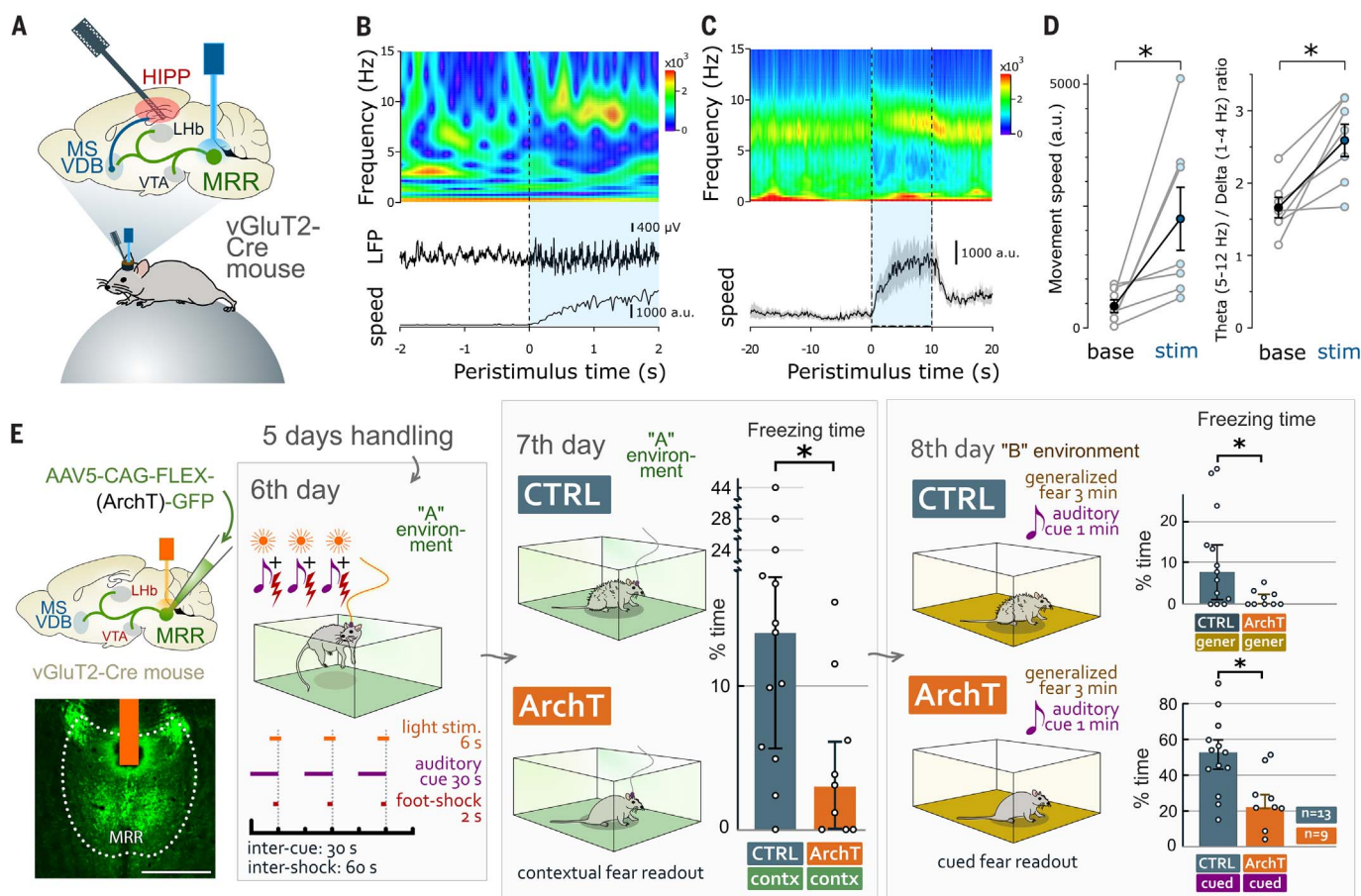


**Fig. 8. MRR vGluT2 neurons promote hippocampal theta rhythm and are necessary for fear memory formation.** (A) AAV2/5-EF1 $\alpha$ -DIO-ChR2-eYFP was injected into the MRR of vGluT2-Cre mice. An optical fiber was inserted into the MRR and a silicone probe was implanted into the hippocampal CA1 region to measure concurrent hippocampal network activity ( $n = 7$  mice). Mice were head-fixed on top of an air-supported spherical treadmill and their behavior was monitored. (B) Running speed (bottom), local field potential (LFP) recordings from the pyramidal layer of the dorsal hippocampal CA1 region (middle), and corresponding wavelet spectrogram (top). Vertical dashed line indicates the onset of laser stimulation, which rapidly induced a switch to theta oscillation. (C) Average running speed (mean  $\pm$  SEM) (bottom) and corresponding averaged wavelet spectrogram (seven mice) (top). Vertical dashed lines highlight the MRR laser illumination period. (D) Paired plots indicating movement speed (left) and

theta/delta ratios (right) during baseline (10-s window before laser onset) versus stimulation (10-s window after laser onset) periods (gray, individual animals; black, mean  $\pm$  SEM). (E) Design of cued fear conditioning experiments with optogenetic inhibition of MRR vGluT2 neurons. Fluorescent image represents one of the injection sites to label MRR vGluT2 neurons, and the orange area represents the position of the optic fiber. Scale bar: 500  $\mu$ m. After handling, light illumination of MRR was switched on precisely during foot shocks that mice received at the end of the auditory cue presentation on day 6. On days 7 and 8, mice received no more light. On day 7, contextual freezing behavior in ArchT mice in the same environment was almost completely diminished (below the 5% threshold) compared with CTRL mice, which received virus without ArchT. On day 8, ArchT mice showed significantly less generalized fear and cued fear in a novel environment compared with CTRL mice. Medians and interquartile ranges are shown on the graphs.

Meanwhile, the MS/VDB-hippocampal system must also be switched into the state optimal for memory acquisition to record the context of such events (8, 14). These processes are also necessary for the prediction and prevention of negative experience in the future. Yet it was not clear which neuronal pathway orchestrates the coordinated activation of these networks. Although the MRR was known to play a central role in processing negative experience (13, 15), its known cell types did not project to the LHB, and the transmitter phenotypes and targets of almost 25% of the MRR neurons were not even known (22).

We discovered that these previously unrecognized vGluT2-positive MRR neurons project heavily into the LHB, mVTA, and MS/VDB (fig. S7). They are the largest population of projection neurons from the MRR, are glutamatergic, and do not express 5-HT, vGluT3, or vGAT. We detected an extensive convergence of monosynaptic inputs to MRR vGluT2 neurons from several environmental experience-related brain centers (fig. S7) (7, 40, 54). MRR vGluT2 neurons predominantly innervate the medial (limbic) division of the LHB that projects to the MRR and mVTA, but they mostly avoid lateral (pallidal) division of the LHB that receives a different set of inputs

(25, 51, 55, 56). MRR vGluT2 neurons directly innervate MRR- or mVTA-projecting LHB cells, creating a direct feedback in the MRR-LHB-mVTA axis.

Our *in vivo* physiological measurements confirmed the central and specific role of MRR vGluT2 neurons in the formation of negative experience. MRR vGluT2 neurons were strongly and specifically activated by strong aversive stimuli, mildly activated by weak aversive stimuli, and unaffected by rewarding stimuli. This suggests that these neurons are primarily responsible and necessary for relaying negative experience in the brainstem. Indeed, specific optogenetic inhibition

of these neurons precisely during the presentation of adverse stimuli eliminated or significantly decreased hippocampus-dependent contextual or hippocampus-independent cued fear memories, respectively. These data showed that this neural hub is essential for processing negative experience.

The elevation of excitatory transmission in the LHB and the stimulation of the mVTA have similar effects (23, 46, 57, 58). MRR vGluT2 neurons heavily project to the LHB and also selectively innervate mVTA DA neurons (but do not innervate neurons in lateral VTA that are mostly reward-related), suggesting that they can effectively activate negative prediction centers. Indeed, their optogenetic activation triggered immediate behavioral changes by inducing acute place aversion. The adverse event was effectively memorized because it induced conditioned place aversion. Furthermore, the selective activation of MRR vGluT2 neurons could negate an otherwise strongly rewarding behavior in an operant conditioning task. The activation of MRR vGluT2 neurons did not induce passive freezing behavior directly; instead, MRR vGluT2 neurons seem to be involved in active responses to negative experience, and therefore they induce avoidance or flight-or-fight behavior.

Depression is thought to be a result of a learning mechanism based on chronically sustained negative experiences (59, 60). Glutamatergic synapses on LHB neurons show long-term plasticity mechanisms, and LHB neurons can learn to respond to cues preceding aversive events (28, 29, 50, 67). The chronic elevation of glutamatergic transmission in the LHB causes depressive disorder through the promotion of burst-firing of LHB neurons, which is also regulated by adjacent glial cell coverage (28–30, 50, 62, 63). MRR vGluT2 neurons massively innervate LHB neurons with different types of NMDA receptor-containing excitatory contacts that are mostly covered by glial processes on LHB neurons. They can also evoke burst-firing of LHB neurons. We revealed an abundant reciprocal excitatory connection between vGluT2-positive glutamatergic neurons of the LHB and MRR that may result in a reverberation and may support pathological learning and excessive activation of LHB neurons if the loop is not controlled effectively. To mimic a chronically maladapted circuitry, we chemogenetically induced chronic overactivation of vGluT2-positive MRR neurons and it caused anhedonia in the sucrose-preference test, which is a typical sign of depressive disorder in mice.

Aggression is another well-known symptom of depression in mice and humans (32–34), and both the LHB and MS/VDB play a role in the emotional processing of aggressive behavior (31). The activation of MRR vGluT2

neurons also promoted aggressive behavior. Aggression is commonly associated with agitation, the most distinguishing features of which include restlessness, pacing, and motor activities. We observed elevated locomotor activity and exploration in chemogenetically stimulated mice, which together suggest that activation of vGluT2-positive MRR neurons promotes agitation and active aversive behaviors (flight-or-fight responses) in neutral or social situations.

MRR has a complex effect on MS/VDB-hippocampal activity and the formation of contextual fear memories, although its mechanism is not well understood (9, 11). In vivo optogenetic activation of MRR promoted memory acquisition-related theta rhythm through a mechanism conveyed by a non-serotonergic and non-GABAergic MRR cell population (13). Activation of pacemaker PV-positive MS/VDB neurons is essential for the generation of hippocampal theta rhythm and proper episodic memory formation (38, 39, 64). PV-positive MS/VDB neurons are innervated by glutamatergic cells of the MRR (18, 65, 66), but the identity of those neurons was unknown. We discovered that MRR vGluT2 neurons not only project to the LHB-mVTA aversion axis, but the axons of most of these MRR vGluT2-positive excitatory neurons bifurcate and simultaneously innervate PV-positive neurons in the MS/VDB and can instantly and reliably promote hippocampal theta rhythm generation necessary for memory acquisition. MRR vGluT2 neurons increased theta rhythm-related exploratory behavior, while animals exhibited conditioned place aversion on the day after stimulation, suggesting the facilitation of strong memory formation. MRR vGluT2 neurons may also facilitate the phase-locking of theta rhythm in the LHB and the hippocampus.

Our data revealed that the MRR vGluT2-positive neuronal population is a previously unrecognized neural hub of the brain that is both necessary and sufficient for the acquisition of negative experience, but which is not activated by positive rewarding experience. MRR vGluT2 neurons receive extensive convergence of inputs from sensory experience-related brain areas, their inhibition disrupts aversive memory formation, and their activation promotes agitated and aversive behavior and flight, which quickly negates motivated behavior. If flight is not an option during social interaction, MRR vGluT2 neurons provoke fight and aggression. MRR vGluT2 neurons also facilitate long-term memory formation related to negative experience, and their chronic activation produces a depression-like phenotype, likely through inducing long-term bursting activity in LHB neurons (28, 30), which we showed in our *in vitro* experiments. Therefore, vGluT2-positive

MRR neurons control the acquisition of negative experience by simultaneously triggering the activity of brain aversion centers and hippocampal episodic memory encoding. Maladaptations in processing negative experience are the basis of several types of mood disorders, which have a huge social and economic impact on individuals and society. Selective targeting of this neural hub may form the basis of new therapies.

## Materials and methods summary

### *Ethical considerations and mouse strains*

All experiments were performed in accordance with regulations. For details, see the supplementary methods section of the supplementary materials. We used male and female vGluT2-iRES-Cre, vGAT-iRES-Cre, BAC-vGluT3/iCre, and TpH2/iCre-ERT2 mice and males C57Bl/6 wild-type mice. We used adult (at least 6-week-old) mice.

### *Viral gene transfer, retrograde and mono-transsynaptic rabies tracing, and optic fiber implantations*

Mice were anesthetized and mounted in an animal stereotaxic frame. A microinjector pump was used for injections. For anterograde tracing, optogenetic and chemogenetic experiments, we injected different amounts of viruses into the target brain areas. For retrograde tracing experiments, we injected FluoroGold or cholera toxin B subunit into the target areas. For behavioral experiments, 4 to 6 weeks after virus injections, optic fibers were implanted over the MRR. Positions of the optic fibers are illustrated in fig. S5. See (26) for a detailed description of the monosynaptic rabies tracing technique used.

### *Perfusions*

Mice were anesthetized and were perfused transcardially with different solutions, depending on the experiments. After perfusions, brains were cut into 30- $\mu$ m-thick sections using a sliding microtome or into 50-, 60-, or 100- $\mu$ m-thick sections using a vibratome.

### *Immunohistochemistry and antibodies*

Generally, perfusion-fixed sections were cryoprotected, and after antigen retrieval they were incubated in a blocking medium, and sections were incubated in a mixture of primary antibodies. This was followed by extensive washes and incubation in the mixture of appropriate secondary antibodies. Then, sections were placed on slides and covered with mounting medium. Fluorescent immunohistochemistry for laser-scanning confocal microscopy, immunoperoxidase labeling for localization of virus injections, immunogold-immunoperoxidase double labeling for electron microscopy, silver-gold intensified and nickel-intensified immunoperoxidase double



labeling, and sample preparation for 3D block-face scanning electron microscopy required different procedures, which are described in detail in the supplementary methods.

The list and specifications of the primary and secondary antibodies used can be found in tables S1 and S2. Combinations of the used primary and secondary antibodies in the different experiments are listed in tables S3 and S4.

#### Block-face scanning electron microscopy and image analysis

We used an FEI Apreo VolumeScope. Images in the z-stacks measured 16,384 pixels  $\times$  16,383 pixels with 70 nm thickness, and the final z-stacks contained 300 slices. Voxel size was 4 nm  $\times$  4 nm  $\times$  70 nm. All image post-processing was done in FIJI ImageJ. Segmentation was performed manually. Data were analyzed using Tibco Statistica 13.4. After segmentation, the models were exported in .obj format and imported into Blender (Blender Foundation, Amsterdam, the Netherlands) for further investigation and visualization.

#### Stereology measurements

Unbiased design-based stereological measurements were carried out using the optical fractionator method. Cell counting was carried out in Stereo Investigator 10.0 stereology software, while cells were identified parallel using NIS Elements AR 4.3 software.

#### In vitro electrophysiological experiments

In all slice experiments, mice were decapitated under deep isoflurane anesthesia. The brain was removed, and coronal slices of 300  $\mu$ m thickness were cut using a vibratome. Slices were placed into an interface-type holding chamber, and cells were recorded. Drugs were administered from stock solutions via pipettes into the ACSF-containing superfusion system. All data were processed and analyzed off-line using standard built-in functions of Python 2.7.0. Latency was defined as a time between light stimulus onset and time of reaching 10% of maximal EPSC amplitude. Throughout this article, for in vitro electrophysiology data, we used median, first, and third quartiles for the description of data groups because they did not show Gaussian distribution.

#### In vivo electrophysiological recordings in head-fixed mice

Animals were anesthetized and mounted in a stereotaxic frame. After surgery, mice were continuously monitored. After a recovery period of 3 to 7 days, mice were water-restricted and habituated for 10 to 14 days to the spherical treadmill setup with their head fixed. Ani-

mal weight was monitored, and when a mouse reached 85% of the initially measured baseline weight, the daily volume of water supplement was individually adjusted in order to maintain this 85% target weight. Habituation is described in the supplementary methods. On the day of the experiment, the animal was head-fixed above the air-supported spherical treadmill. Hippocampal and median raphe silicone probes were lowered through the cranial window. Ground electrode was placed above the cerebellum. Electrophysiological recordings were performed by a signal multiplexing head-stage. At the end of each recording session, brief laser pulses were applied for offline identification of responsive units. Units (i.e., neurons) were categorized as “tagged” if their firing followed the laser pulse with short latency (within 4 ms) and >50% success rate.

The mean baseline firing rate values and standard deviations were calculated from a 4-s time window preceding stimulus onset. A change in firing rate was declared significant if it deviated more than 2 standard deviations from the mean baseline value ( $z$ -score larger than 2 or smaller than  $-2$ ) in a 200-ms time window after stimulus onset. Both responsive neurons (which increased their firing frequency) and nonresponsive neurons distributed across animals. All statistical analyses were performed with standard Igor Pro 8 functions.

#### Optogenetic behavioral experiments

After optic fiber implantations, mice were transferred to the animal room of the behavioral unit of the institute to rest and then received 5 days of handling. We carried out real-time place-aversion tests (RTPA), conditioned place-aversion tests (CPA), operant conditioning tests, optogenetic contextual fear conditioning tests (Opto-CFC), and delayed cued-fear conditioning tests (CuedFC). The experimenters evaluating behavioral experiments were blind to the conditions and treatment of the mice. Experimental data were collected and analyzed using the Noldus EthoVision 13.0 and Tibco Statistica 13.4 software.

#### Behavioral test battery for chemogenetic experiments

We carried out a series of behavioral tests with mice that were injected either with the hM3Dq-containing virus [that expressed a clozapine-*N*-oxide (CNO)-sensitive, excitatory G protein-coupled receptor plus a fluorescent protein] or with a control virus (that expressed only a fluorescent protein). Mice were allowed 48 to 72 hours of rest between tests. To activate the hM3Dq virus, CNO (1 mg/kg in 10 ml saline, Tocris) was injected intraperitoneally 30 min before each behavioral test. Tests were video recorded and analyzed later by an observer blind to the treatment protocols. After this battery of behavioral tests, mice were

sacrificed, and their adrenal glands were removed and weighed.

#### REFERENCES AND NOTES

1. E. S. Bromberg-Martin, M. Matsumoto, H. Nakahara, O. Hikosaka, Multiple timescales of memory in lateral habenula and dopamine neurons. *Neuron* **67**, 499–510 (2010). doi: [10.1016/j.neuron.2010.06.031](https://doi.org/10.1016/j.neuron.2010.06.031); pmid: [20696385](https://pubmed.ncbi.nlm.nih.gov/20696385/)
2. E. S. Bromberg-Martin, O. Hikosaka, Lateral habenula neurons signal errors in the prediction of reward information. *Nat. Neurosci.* **14**, 1209–1216 (2011). doi: [10.1038/nn.2902](https://doi.org/10.1038/nn.2902); pmid: [21857659](https://pubmed.ncbi.nlm.nih.gov/21857659/)
3. E. S. Bromberg-Martin, M. Matsumoto, O. Hikosaka, Distinct tonic and phasic anticipatory activity in lateral habenula and dopamine neurons. *Neuron* **67**, 144–155 (2010). doi: [10.1016/j.neuron.2010.06.016](https://doi.org/10.1016/j.neuron.2010.06.016); pmid: [20624598](https://pubmed.ncbi.nlm.nih.gov/20624598/)
4. C. A. Orsini, D. E. Moorman, J. W. Young, B. Setlow, S. B. Floresco, Neural mechanisms regulating different forms of risk-related decision-making: Insights from animal models. *Neurosci. Biobehav. Rev.* **58**, 147–167 (2015). doi: [10.1016/j.neubiorev.2015.04.009](https://doi.org/10.1016/j.neubiorev.2015.04.009); pmid: [26072028](https://pubmed.ncbi.nlm.nih.gov/26072028/)
5. C. M. Stopper, S. B. Floresco, What's better for me? Fundamental role for lateral habenula in promoting subjective decision biases. *Nat. Neurosci.* **17**, 33–35 (2014). doi: [10.1038/nn.3587](https://doi.org/10.1038/nn.3587); pmid: [24270185](https://pubmed.ncbi.nlm.nih.gov/24270185/)
6. C. M. Stopper, M. T. L. Tse, D. R. Montes, C. R. Wiedman, S. B. Floresco, Overriding phasic dopamine signals redirects action selection during risk/reward decision making. *Neuron* **84**, 177–189 (2014). doi: [10.1016/j.neuron.2014.08.033](https://doi.org/10.1016/j.neuron.2014.08.033); pmid: [25220811](https://pubmed.ncbi.nlm.nih.gov/25220811/)
7. P. M. Baker, S. E. Oh, K. S. Kidder, S. J. Y. Mizumori, Ongoing behavioral state information signaled in the lateral habenula guides choice flexibility in freely moving rats. *Front. Behav. Neurosci.* **9**, 295 (2015). doi: [10.3389/fnbeh.2015.00295](https://doi.org/10.3389/fnbeh.2015.00295); pmid: [26582981](https://pubmed.ncbi.nlm.nih.gov/26582981/)
8. R. Goutagny *et al.*, Interactions between the lateral habenula and the hippocampus: Implication for spatial memory processes. *Neuropsychopharmacology* **38**, 2418–2426 (2013). doi: [10.1038/npp.2013.142](https://doi.org/10.1038/npp.2013.142); pmid: [23736315](https://pubmed.ncbi.nlm.nih.gov/23736315/)
9. R. Crooks, J. Jackson, B. H. Bland, Dissociable pathways facilitate theta and non-theta states in the median raphe–Septohippocampal circuit. *Hippocampus* **22**, 1567–1576 (2012). doi: [10.1002/hipo.20999](https://doi.org/10.1002/hipo.20999); pmid: [22180148](https://pubmed.ncbi.nlm.nih.gov/22180148/)
10. A. Domonkos *et al.*, Divergent in vivo activity of non-serotonergic and serotonergic VGLUT3-neurons in the median raphe region. *J. Physiol.* **594**, 3775–3790 (2016). doi: [10.1113/JP272036](https://doi.org/10.1113/JP272036); pmid: [27028801](https://pubmed.ncbi.nlm.nih.gov/27028801/)
11. J. Jackson, C. T. Dickson, B. H. Bland, Median raphe stimulation disrupts hippocampal theta via rapid inhibition and state-dependent phase reset of theta-related neural circuitry. *J. Neurophysiol.* **99**, 3009–3026 (2008). doi: [10.1152/jn.00065.2008](https://doi.org/10.1152/jn.00065.2008); pmid: [18436639](https://pubmed.ncbi.nlm.nih.gov/18436639/)
12. G. Viana Di Prisco, Z. Albo, R. P. Vertes, B. Kocsis, Discharge properties of neurons of the median raphe nucleus during hippocampal theta rhythm in the rat. *Exp. Brain Res.* **145**, 383–394 (2002). doi: [10.1007/s00221-002-1123-8](https://doi.org/10.1007/s00221-002-1123-8); pmid: [12136388](https://pubmed.ncbi.nlm.nih.gov/12136388/)
13. D. V. Wang *et al.*, Mesopontine median raphe regulates hippocampal ripple oscillation and memory consolidation. *Nat. Neurosci.* **18**, 728–735 (2015). doi: [10.1038/nn.3998](https://doi.org/10.1038/nn.3998); pmid: [25867120](https://pubmed.ncbi.nlm.nih.gov/25867120/)
14. H. Aizawa *et al.*, The synchronous activity of lateral habenula neurons is essential for regulating hippocampal theta oscillation. *J. Neurosci.* **33**, 8909–8921 (2013). doi: [10.1523/JNEUROSCI.4369-12.2013](https://doi.org/10.1523/JNEUROSCI.4369-12.2013); pmid: [23678132](https://pubmed.ncbi.nlm.nih.gov/23678132/)
15. T. G. C. S. Andrade, H. Zangrossi Jr., F. G. Graeff, The median raphe nucleus in anxiety revisited. *J. Psychopharmacol.* **27**, 1107–1115 (2013). doi: [10.1177/0269881113499208](https://doi.org/10.1177/0269881113499208); pmid: [23999409](https://pubmed.ncbi.nlm.nih.gov/23999409/)
16. D. G. Balázsfi *et al.*, Median raphe region stimulation alone generates remote, but not recent fear memory traces. *PLOS ONE* **12**, e0181264 (2017). doi: [10.1371/journal.pone.0181264](https://doi.org/10.1371/journal.pone.0181264); pmid: [28708877](https://pubmed.ncbi.nlm.nih.gov/28708877/)
17. T. F. Freund, A. I. Gulyás, L. Acsády, T. Görös, K. Tóth, Serotonergic control of the hippocampus via local inhibitory interneurons. *Proc. Natl. Acad. Sci. U.S.A.* **87**, 8501–8505 (1990). doi: [10.1073/pnas.87.21.8501](https://doi.org/10.1073/pnas.87.21.8501); pmid: [1700433](https://pubmed.ncbi.nlm.nih.gov/1700433/)
18. J. Jackson, B. H. Bland, M. C. Antle, Nonserotonergic projection neurons in the midbrain raphe nuclei contain the vesicular glutamate transporter VGLUT3. *Synapse* **63**, 31–41 (2009). doi: [10.1002/syn.20581](https://doi.org/10.1002/syn.20581); pmid: [18925658](https://pubmed.ncbi.nlm.nih.gov/18925658/)

19. V. Varga *et al.*, Fast synaptic subcortical control of hippocampal circuits. *Science* **326**, 449–453 (2009). doi: [10.1126/science.1178307](https://doi.org/10.1126/science.1178307); pmid: [19833972](https://pubmed.ncbi.nlm.nih.gov/19833972/)
20. S. J. Bang, P. Jensen, S. M. Dymecki, K. G. Commons, Projections and interconnections of genetically defined serotonin neurons in mice. *Eur. J. Neurosci.* **35**, 85–96 (2012). doi: [10.1111/j.1460-9568.2011.07936.x](https://doi.org/10.1111/j.1460-9568.2011.07936.x); pmid: [22151329](https://pubmed.ncbi.nlm.nih.gov/22151329/)
21. C. Leranthe, R. P. Vertes, Median raphe serotonin innervation of medial septum/diagonal band of broca (MSDB) parvalbumin-containing neurons: Possible involvement of the MSDB in the desynchronization of the hippocampal EEG. *J. Comp. Neurol.* **410**, 586–598 (1999). doi: [10.1002/\(SICI\)1096-9861\(19990809\)410:4<586::AID-CNE6>3.0.CO;2-H](https://doi.org/10.1002/(SICI)1096-9861(19990809)410:4<586::AID-CNE6>3.0.CO;2-H); pmid: [10398050](https://pubmed.ncbi.nlm.nih.gov/10398050/)
22. K. E. Sos *et al.*, Cellular architecture and transmitter phenotypes of neurons of the mouse median raphe region. *Brain Struct. Funct.* **222**, 287–299 (2017). doi: [10.1007/s00429-016-1217-x](https://doi.org/10.1007/s00429-016-1217-x); pmid: [27044051](https://pubmed.ncbi.nlm.nih.gov/27044051/)
23. S. Lammel *et al.*, Input-specific control of reward and aversion in the ventral tegmental area. *Nature* **491**, 212–217 (2012). doi: [10.1038/nature11527](https://doi.org/10.1038/nature11527); pmid: [23064228](https://pubmed.ncbi.nlm.nih.gov/23064228/)
24. S. Lammel, B. K. Lim, R. C. Malenka, Reward and aversion in a heterogeneous midbrain dopamine system. *Neuropharmacology* **76**, 351–359 (2014). doi: [10.1016/j.neuropharm.2013.03.019](https://doi.org/10.1016/j.neuropharm.2013.03.019); pmid: [23578393](https://pubmed.ncbi.nlm.nih.gov/23578393/)
25. L. A. Quina *et al.*, Efferent pathways of the mouse lateral habenula. *J. Comp. Neurol.* **523**, 32–60 (2015). doi: [10.1002/cne.23662](https://doi.org/10.1002/cne.23662); pmid: [25099741](https://pubmed.ncbi.nlm.nih.gov/25099741/)
26. I. R. Wickersham *et al.*, Monosynaptic restriction of transsynaptic tracing from single, genetically targeted neurons. *Neuron* **53**, 639–647 (2007). doi: [10.1016/j.neuron.2007.01.033](https://doi.org/10.1016/j.neuron.2007.01.033); pmid: [17329205](https://pubmed.ncbi.nlm.nih.gov/17329205/)
27. A. Szőnyi *et al.*, Brainstem nucleus incertus controls contextual memory formation. *Science* **364**, eaaw0445 (2019). doi: [10.1126/science.aaw0445](https://doi.org/10.1126/science.aaw0445); pmid: [31123108](https://pubmed.ncbi.nlm.nih.gov/31123108/)
28. Y. Cui *et al.*, Astroglial Kir4.1 in the lateral habenula drives neuronal bursts in depression. *Nature* **554**, 323–327 (2018). doi: [10.1038/nature25752](https://doi.org/10.1038/nature25752); pmid: [29446379](https://pubmed.ncbi.nlm.nih.gov/29446379/)
29. K. Li *et al.*,  $\beta$ CaMKII in lateral habenula mediates core symptoms of depression. *Science* **341**, 1016–1020 (2013). doi: [10.1126/science.1240729](https://doi.org/10.1126/science.1240729); pmid: [23990563](https://pubmed.ncbi.nlm.nih.gov/23990563/)
30. Y. Yang *et al.*, Ketamine blocks bursting in the lateral habenula to rapidly relieve depression. *Nature* **554**, 317–322 (2018). doi: [10.1038/nature25509](https://doi.org/10.1038/nature25509); pmid: [29446381](https://pubmed.ncbi.nlm.nih.gov/29446381/)
31. S. A. Golden *et al.*, Basal forebrain projections to the lateral habenula modulate aggression reward. *Nature* **534**, 688–692 (2016). doi: [10.1038/nature18601](https://doi.org/10.1038/nature18601); pmid: [27357796](https://pubmed.ncbi.nlm.nih.gov/27357796/)
32. L. A. Martin, H. W. Neighbors, D. M. Griffith, The experience of symptoms of depression in men vs women: Analysis of the National Comorbidity Survey Replication. *JAMA Psychiatry* **70**, 1100–1106 (2013). doi: [10.1001/jamapsychiatry.2013.1985](https://doi.org/10.1001/jamapsychiatry.2013.1985); pmid: [23986338](https://pubmed.ncbi.nlm.nih.gov/23986338/)
33. N. Verdolini *et al.*, Aggressiveness in depression: A neglected symptom possibly associated with bipolarity and mixed features. *Acta Psychiatr. Scand.* **136**, 362–372 (2017). doi: [10.1111/acps.12777](https://doi.org/10.1111/acps.12777); pmid: [28741646](https://pubmed.ncbi.nlm.nih.gov/28741646/)
34. C. R. Yang *et al.*, Enhanced aggressive behaviour in a mouse model of depression. *Neurotox. Res.* **27**, 129–142 (2015). doi: [10.1007/s12640-014-9498-4](https://doi.org/10.1007/s12640-014-9498-4); pmid: [25376807](https://pubmed.ncbi.nlm.nih.gov/25376807/)
35. B. Li *et al.*, Synaptic potentiation onto habenula neurons in the learned helplessness model of depression. *Nature* **470**, 535–539 (2011). doi: [10.1038/nature09742](https://doi.org/10.1038/nature09742); pmid: [21350486](https://pubmed.ncbi.nlm.nih.gov/21350486/)
36. S. J. Russo, E. J. Nestler, The brain reward circuitry in mood disorders. *Nat. Rev. Neurosci.* **14**, 609–625 (2013). doi: [10.1038/nrn3381](https://doi.org/10.1038/nrn3381); pmid: [23942470](https://pubmed.ncbi.nlm.nih.gov/23942470/)
37. G. Buzsáki, E. I. Moser, Memory, navigation and theta rhythm in the hippocampal-entorhinal system. *Nat. Neurosci.* **16**, 130–138 (2013). doi: [10.1038/nrn3304](https://doi.org/10.1038/nrn3304); pmid: [23354386](https://pubmed.ncbi.nlm.nih.gov/23354386/)
38. B. Hangya, Z. Borhegyi, N. Szilágyi, T. F. Freund, V. Varga, GABAergic neurons of the medial septum lead the hippocampal network during theta activity. *J. Neurosci.* **29**, 8094–8102 (2009). doi: [10.1523/JNEUROSCI.5665-08.2009](https://doi.org/10.1523/JNEUROSCI.5665-08.2009); pmid: [19553449](https://pubmed.ncbi.nlm.nih.gov/19553449/)
39. Z. Borhegyi, V. Varga, N. Szilágyi, D. Fábó, T. F. Freund, Phase segregation of medial septal GABAergic neurons during hippocampal theta activity. *J. Neurosci.* **24**, 8470–8479 (2004). doi: [10.1523/JNEUROSCI.1413-04.2004](https://doi.org/10.1523/JNEUROSCI.1413-04.2004); pmid: [15456820](https://pubmed.ncbi.nlm.nih.gov/15456820/)
40. D. J. Barker *et al.*, Lateral preoptic control of the lateral habenula through convergent glutamate and GABA transmission. *Cell Rep.* **21**, 1757–1769 (2017). doi: [10.1016/j.celrep.2017.10.066](https://doi.org/10.1016/j.celrep.2017.10.066); pmid: [29141211](https://pubmed.ncbi.nlm.nih.gov/29141211/)
41. M. Stephenson-Jones *et al.*, A basal ganglia circuit for evaluating action outcomes. *Nature* **539**, 289–293 (2016). doi: [10.1038/nature19845](https://doi.org/10.1038/nature19845); pmid: [27652894](https://pubmed.ncbi.nlm.nih.gov/27652894/)
42. J. W. de Jong *et al.*, A neural circuit mechanism for encoding aversive stimuli in the mesolimbic dopamine system. *Neuron* **101**, 133–151.e7 (2019). doi: [10.1016/j.neuron.2018.11.005](https://doi.org/10.1016/j.neuron.2018.11.005); pmid: [30503173](https://pubmed.ncbi.nlm.nih.gov/30503173/)
43. K. Brinschwitz *et al.*, Glutamatergic axons from the lateral habenula mainly terminate on GABAergic neurons of the ventral midbrain. *Neuroscience* **168**, 463–476 (2010). doi: [10.1016/j.neuroscience.2010.03.050](https://doi.org/10.1016/j.neuroscience.2010.03.050); pmid: [20353812](https://pubmed.ncbi.nlm.nih.gov/20353812/)
44. T. C. Zhou, S. Geisler, M. Marinelli, B. A. Degarmo, D. S. Zahm, The mesopontine rostromedial tegmental nucleus: A structure targeted by the lateral habenula that projects to the ventral tegmental area of Tsai and substantia nigra compacta. *J. Comp. Neurol.* **513**, 566–596 (2009). doi: [10.1002/cne.21891](https://doi.org/10.1002/cne.21891); pmid: [19235216](https://pubmed.ncbi.nlm.nih.gov/19235216/)
45. S. Hong, T. C. Zhou, M. Smith, K. S. Saleem, O. Hikosaka, Negative reward signals from the lateral habenula to dopamine neurons are mediated by rostromedial tegmental nucleus in primates. *J. Neurosci.* **31**, 11457–11471 (2011). doi: [10.1523/JNEUROSCI.1384-11.2011](https://doi.org/10.1523/JNEUROSCI.1384-11.2011); pmid: [21832176](https://pubmed.ncbi.nlm.nih.gov/21832176/)
46. A. M. Stamatakis, G. D. Stuber, Activation of lateral habenula inputs to the ventral midbrain promotes behavioral avoidance. *Nat. Neurosci.* **15**, 1105–1107 (2012). doi: [10.1038/nn.3145](https://doi.org/10.1038/nn.3145); pmid: [22729176](https://pubmed.ncbi.nlm.nih.gov/22729176/)
47. J. Tian, N. Uchida, Habenula lesions reveal that multiple mechanisms underlie dopamine prediction errors. *Neuron* **87**, 1304–1316 (2015). doi: [10.1016/j.neuron.2015.08.028](https://doi.org/10.1016/j.neuron.2015.08.028); pmid: [26365765](https://pubmed.ncbi.nlm.nih.gov/26365765/)
48. M. Matsumoto, O. Hikosaka, Lateral habenula as a source of negative reward signals in dopamine neurons. *Nature* **447**, 1111–1115 (2007). doi: [10.1038/nature05860](https://doi.org/10.1038/nature05860); pmid: [17522629](https://pubmed.ncbi.nlm.nih.gov/17522629/)
49. H. Li, D. Pullmann, T. C. Zhou, Valence-encoding in the lateral habenula arises from the entopeduncular region. *eLife* **8**, e41223 (2019). doi: [10.7554/eLife.41223](https://doi.org/10.7554/eLife.41223); pmid: [30855228](https://pubmed.ncbi.nlm.nih.gov/30855228/)
50. F. J. Meye *et al.*, Cocaine-evoked negative symptoms require AMPA receptor trafficking in the lateral habenula. *Nat. Neurosci.* **18**, 376–378 (2015). doi: [10.1038/nn.3923](https://doi.org/10.1038/nn.3923); pmid: [25643299](https://pubmed.ncbi.nlm.nih.gov/25643299/)
51. C. D. Proulx, O. Hikosaka, R. Malinow, Reward processing by the lateral habenula in normal and depressive behaviors. *Nat. Neurosci.* **17**, 1146–1152 (2014). doi: [10.1038/nn.3779](https://doi.org/10.1038/nn.3779); pmid: [25157511](https://pubmed.ncbi.nlm.nih.gov/25157511/)
52. M. Trusel *et al.*, Punishment-predictive cues guide avoidance through potentiation of hypothalamus-to-habenula synapses. *Neuron* **102**, 120–127.e4 (2019). doi: [10.1016/j.neuron.2019.01.025](https://doi.org/10.1016/j.neuron.2019.01.025); pmid: [30765165](https://pubmed.ncbi.nlm.nih.gov/30765165/)
53. D. Wang *et al.*, Learning shapes the aversion and reward responses of lateral habenula neurons. *eLife* **6**, e23045 (2017). doi: [10.7554/eLife.23045](https://doi.org/10.7554/eLife.23045); pmid: [28561735](https://pubmed.ncbi.nlm.nih.gov/28561735/)
54. D. H. Root, C. A. Mejias-Aponte, J. Qi, M. Morales, Role of glutamatergic projections from ventral tegmental area to lateral habenula in aversive conditioning. *J. Neurosci.* **34**, 13906–13910 (2014). doi: [10.1523/JNEUROSCI.2029-14.2014](https://doi.org/10.1523/JNEUROSCI.2029-14.2014); pmid: [25319687](https://pubmed.ncbi.nlm.nih.gov/25319687/)
55. D. S. Zahm, D. H. Root, Review of the cytology and connections of the lateral habenula, an avatar of adaptive behaving. *Pharmacol. Biochem. Behav.* **162**, 3–21 (2017). doi: [10.1016/j.pbb.2016.06.004](https://doi.org/10.1016/j.pbb.2016.06.004); pmid: [28647565](https://pubmed.ncbi.nlm.nih.gov/28647565/)
56. U. Kim, Topographic commissural and descending projections of the habenula in the rat. *J. Comp. Neurol.* **513**, 173–187 (2009). doi: [10.1002/cne.21951](https://doi.org/10.1002/cne.21951); pmid: [19123238](https://pubmed.ncbi.nlm.nih.gov/19123238/)
57. J. Tooley *et al.*, Glutamatergic ventral pallidum neurons modulate activity of the habenula-ventral tegmental circuitry and constrain reward seeking. *Biol. Psychiatry* **83**, 1012–1023 (2018). doi: [10.1016/j.biopsych.2018.01.003](https://doi.org/10.1016/j.biopsych.2018.01.003); pmid: [29452828](https://pubmed.ncbi.nlm.nih.gov/29452828/)
58. A. M. Stamatakis *et al.*, Lateral hypothalamic area glutamatergic neurons and their projections to the lateral habenula regulate feeding and reward. *J. Neurosci.* **36**, 302–311 (2016). doi: [10.1523/JNEUROSCI.1202-15.2016](https://doi.org/10.1523/JNEUROSCI.1202-15.2016); pmid: [26758824](https://pubmed.ncbi.nlm.nih.gov/26758824/)
59. J. Kauffling, Alterations and adaptation of ventral tegmental area dopaminergic neurons in animal models of depression. *Cell Tissue Res.* **377**, 59–71 (2019). doi: [10.1007/s00441-019-03007-9](https://doi.org/10.1007/s00441-019-03007-9); pmid: [30848354](https://pubmed.ncbi.nlm.nih.gov/30848354/)
60. S. F. Maier, M. E. P. Seligman, Learned helplessness at fifty: Insights from neuroscience. *Psychol. Rev.* **123**, 349–367 (2016). doi: [10.1037/rev0000033](https://doi.org/10.1037/rev0000033); pmid: [27337390](https://pubmed.ncbi.nlm.nih.gov/27337390/)
61. I. Lazaridis *et al.*, A hypothalamus-habenula circuit controls aversion. *Mol. Psychiatry* **24**, 1351–1368 (2019). doi: [10.1038/s41380-019-0369-5](https://doi.org/10.1038/s41380-019-0369-5); pmid: [30755721](https://pubmed.ncbi.nlm.nih.gov/30755721/)
62. D. Knowland *et al.*, Distinct ventral pallidal neural populations mediate separate symptoms of depression. *Cell* **170**, 284–297.e18 (2017). doi: [10.1016/j.cell.2017.06.015](https://doi.org/10.1016/j.cell.2017.06.015); pmid: [28689640](https://pubmed.ncbi.nlm.nih.gov/28689640/)
63. A. Friedman *et al.*, Electrical stimulation of the lateral habenula produces an inhibitory effect on sucrose self-administration. *Neuropharmacology* **60**, 381–387 (2011). doi: [10.1016/j.neuropharm.2010.10.006](https://doi.org/10.1016/j.neuropharm.2010.10.006); pmid: [20955718](https://pubmed.ncbi.nlm.nih.gov/20955718/)
64. G. Gangadharan *et al.*, Medial septal GABAergic projection neurons promote object exploration behavior and type 2 theta rhythm. *Proc. Natl. Acad. Sci. U.S.A.* **113**, 6550–6555 (2016). doi: [10.1073/pnas.1605019113](https://doi.org/10.1073/pnas.1605019113); pmid: [27208094](https://pubmed.ncbi.nlm.nih.gov/27208094/)
65. S. Aznar, Z. X. Qian, G. M. Knudsen, Non-serotonergic dorsal and median raphe projection onto parvalbumin- and calbindin-containing neurons in hippocampus and septum. *Neuroscience* **124**, 573–581 (2004). doi: [10.1016/j.neuroscience.2003.12.020](https://doi.org/10.1016/j.neuroscience.2003.12.020); pmid: [14980728](https://pubmed.ncbi.nlm.nih.gov/14980728/)
66. A. Szőnyi *et al.*, The ascending median raphe projections are mainly glutamatergic in the mouse forebrain. *Brain Struct. Funct.* **221**, 735–751 (2016). doi: [10.1007/s00429-014-0935-1](https://doi.org/10.1007/s00429-014-0935-1); pmid: [25381463](https://pubmed.ncbi.nlm.nih.gov/25381463/)
67. A. M. Barth, LFP\_analysis, software, Figshare (2019); <https://doi.org/10.6084/m9.figshare.8924771.v1>

## ACKNOWLEDGMENTS

We thank S. Arthaud (INSERM, Lyon, France) for help with vGlut2-Cre mice. We thank L. Barna, the Nikon Microscopy Center at IEM, Nikon Austria GmbH, and Auro-Science Consulting Ltd. for fluorescent imaging technical support. We thank K. Demeter, C. Fazekas, D. Várkonyi, and the Behavior Studies Unit of IEM-HAS for behavioral experiment support. We thank É. Mikics, M. Aliczki, and Z. Balogh for help in planning and evaluating the operant conditioning experiments. We thank Z. Erdélyi, F. Erdélyi, and the staff of the Animal Facility and the Medical Gene Technology Unit of IEM-HAS for expert technical help with the breeding and genotyping of the mouse strains used in this study. We thank Z. Hajós, E. Szépné Simon, M. Mayer, and N. Kriczky for help with experiments and A. Kriczky, K. Iványi, and G. Goda for other assistance. We thank J. Budd and L. Acady for comments on an earlier version of this manuscript.

**Funding:** This work was supported by the European Research Council (ERC-2011-ADG-294313, SERRACO); the National Research, Development and Innovation Office, Hungary (OTKA K119521, OTKA K115441, OTKA K109790, OTKA KH124345, OTKA NN125643, FK129019, PD121248, EFOP-3.6.3-VEKOP-16-2017-00009, NKFIH K120311, and VKSZ\_14-1-2015-0155); the U.S. National Institutes of Health (NS030549); the Human Brain Project of the EU (EU H2020 720270); and the Hungarian Brain Research Program (2017-1.2.1-NKP-2017-00002). The New National Excellence Program of the Ministry of Human Capacities, Hungary, supported D.S. (UNKP-16-3-IV), A.S. (UNKP-17-3-III-SE-9), A.M. (UNKP-18-02-I-SE-20), A.M.B. (UNKP-18-4-SE-126), and K.Z. (UNKP-18-2-I-SE-22). A.M.B. was supported by the Bolayai János Research Fellowship of the Hungarian Academy of Sciences. **Author contributions:** Conceptualization, A.S., K.Z., and G.N.; Investigation: A.S., K.Z., R.T.G., Z.B., and K.E.S. performed and analyzed fluorescent and transmission electron microscopy experiments, supervised by G.N.; A.M. and Z.B. performed and analyzed the scanning electron microscopy experiments, supervised by G.N.; A.S., K.Z., and R.T.G. performed and analyzed the optogenetic behavioral experiments, supervised by G.N.; A.M.B. performed and analyzed the in vivo optogenetic tagging in head-fixed EEG recording experiments, supervised by V.V.; D.S. planned the in vitro experiments and recorded and analyzed the data, supervised by A.I.G.; B.T., E.S., and D.Z. performed and analyzed the chemogenetic behavioral experiments, supervised by D.Z.; Writing – Original Draft, A.S., K.Z., T.F.F., and G.N.; Writing – Review & Editing, all authors; Funding Acquisition, A.M.B., A.I.G., V.V., D.Z., G.N., and T.F.F.

**Competing interests:** The authors have no competing interests. **Data and materials availability:** Viruses used in this study were obtained under material transfer agreements, as follows: AAV2/5-EF1α-DIO-eYFP, AAV2/5-EF1α-DIO-mCherry, and AAV2/5-CAG-FLEX-ArchT-GFP from the UNC Vector Core; AAV2/5-EF1α-DIO-hChR2 (H134R)-eYFP from the Penn Vector Core; AAV2/8-hSyn-DIO-mCherry and AAV2/8-hSyn-DIO-hm3D(Gq)-mCherry from Addgene; and AAV2/8-hSyn-FLEX-TVA-p2A-eGFP-p2A-oG and Rabies(ΔG)-EnvA-mCherry from the Salk GT3 Vector Core. Data generated and analyzed during this study are presented in the manuscript or in the supplementary materials, and additional custom written codes for in vivo electrophysiological recordings are available online (67).

## SUPPLEMENTARY MATERIALS

[science.sciencemag.org/content/366/6469/eaay8746/suppl/DC1](https://science.sciencemag.org/content/366/6469/eaay8746/suppl/DC1)  
Supplementary Methods  
Supplementary Text  
Figs. S1 to S7  
Tables S1 to S6  
References (68–79)

[View/request a protocol for this paper from Bio-protocol.](#)

25 July 2019; accepted 8 October 2019  
10.1126/science.aay8746



## REPORT

## MATERIALS SCIENCE

## Tailored multifunctional micellar brushes via crystallization-driven growth from a surface

Jiandong Cai<sup>1,2,3,4</sup>, Chen Li<sup>2</sup>, Na Kong<sup>1</sup>, Yi Lu<sup>1</sup>, Geyu Lin<sup>2</sup>, Xinyan Wang<sup>1</sup>, Yuan Yao<sup>1</sup>, Ian Manners<sup>2,5,6\*</sup>, Huibin Qiu<sup>1,2\*</sup>

The creation of nanostructures with precise chemistries on material surfaces is of importance in a wide variety of areas such as lithography, superhydrophobicity, and cell adhesion. We describe a platform for surface functionalization that involves the fabrication of cylindrical micellar brushes on a silicon wafer through seeded growth of crystallizable block copolymers at the termini of immobilized, surface-confined crystallite seeds. The density, length, and coronal chemistry of the micellar brushes can be precisely tuned, and post-growth decoration with nanoparticles enables applications in catalysis and antibacterial surface modification. The micellar brushes can also be grown on ultrathin two-dimensional materials such as graphene oxide nanosheets and further assembled into a membrane for the separation of oil-in-water emulsions and gold nanoparticles.

A variety of conventional methods, including physical techniques [e.g., spray-based methods (1) and spin-coating (2)] and chemical routes [e.g., electrochemical deposition (3) and heat treatment (4)], have been developed to endow material surfaces with a wide range of targeted properties. Surface-initiated polymer brushes (5–8), where one of the polymer chain ends is covalently attached to a solid substrate, have emerged as a powerful and versatile approach to surface functionalization. The living characteristic of the covalent polymerizations used to create polymer brushes allows for tailoring

of the surface chemistry at the molecular level. However, the precise fabrication of patterned surfaces using building blocks on longer length scales represents a key challenge.

Block copolymers (BCPs) with a short, crystallizable poly(ferrocenyldimethylsilane) (PFS) core-forming block tend to form cylindrical (or fiber-like) micelles with a crystalline PFS core in selective solvents for the complementary segment (9). The cylindrical micelle termini remain active to the addition of further added PFS BCP in the dissolved (unimer) state through an epitaxial growth process termed living crystallization-driven self-assembly (CDSA)

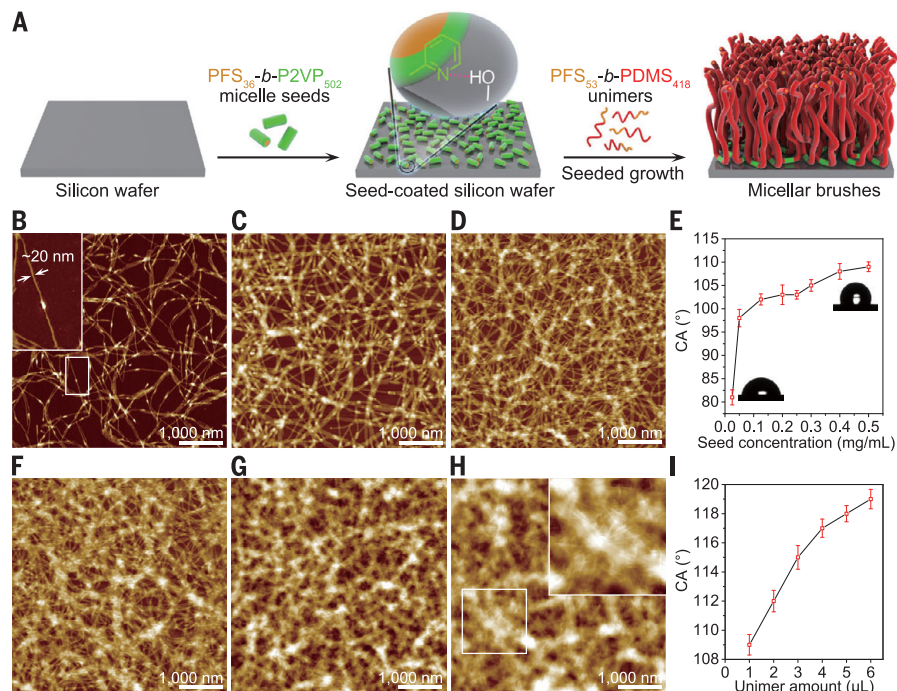
(10–14). Sonication of longer cylindrical micelles with a crystalline PFS core yields small seed micelles that function as initiators for living CDSA. Colloidally dispersed seeds have been used to prepare a variety of nanostructures, including amphiphilic triblock co-micelles (10), concentric platelet micelles (15), and hierarchical assemblies on longer length scales (16). In addition, hybrid assemblies have been fabricated by preceding the living CDSA step by surface confinement of the seeds. This approach has allowed the growth of fibers on seed-covered silica nanoparticles (17) and homopolymer crystal-coated carbon nanotubes (18). We extend this technique to the functionalization of surfaces through the immobilization of short cylindrical micelle seeds of PFS BCPs on silicon wafers and other substrates, and the subsequent growth of cylindrical micellar brushes via *in situ* living CDSA.

A silicon wafer was selected as a model material on which to immobilize the small seeds of PFS-*b*-P2VP [P2VP, poly(2-vinylpyridine)] on the basis of the high density of surface silanol groups, which should allow tenacious

<sup>1</sup>School of Physical Science and Technology, ShanghaiTech University, Shanghai 201210, China. <sup>2</sup>School of Chemistry and Chemical Engineering, Frontiers Science Center for Transformative Molecules, State Key Laboratory of Metal Matrix Composites, Shanghai Jiao Tong University, Shanghai 200240, China. <sup>3</sup>Shanghai Institute of Organic Chemistry, Chinese Academy of Sciences, Shanghai 200032, China. <sup>4</sup>University of Chinese Academy of Sciences, Beijing 100049, China. <sup>5</sup>School of Chemistry, University of Bristol, Bristol BS8 1TS, UK. <sup>6</sup>Department of Chemistry, University of Victoria, Victoria, BC V8P 5C2, Canada. \*Corresponding author. Email: hbqiu@sjtu.edu.cn (H.Q.); imanners@uvic.ca (I.M.)

**Fig. 1. Seeded growth of hydrophobic PFS<sub>53</sub>-*b*-PDMS<sub>418</sub> micellar brushes on a silicon wafer.**

(A) Schematic illustration of the process, which involves the immobilization of PFS<sub>53</sub>-*b*-P2VP<sub>502</sub> seeds ( $L_n = 139$  nm,  $L_w/L_n = 1.04$ ) on a silicon wafer via H-bonding (and probably also assisted by electrostatic interactions) followed by crystallization-driven epitaxial growth of PFS<sub>53</sub>-*b*-PDMS<sub>418</sub> micellar brushes. (B to D) AFM height images of PFS<sub>53</sub>-*b*-PDMS<sub>418</sub> micellar brushes of different densities formed under a constant unimer-to-seed mass ratio (1:1 in the feed) but different seed concentrations: (B) 0.125 mg/ml, (C) 0.25 mg/ml, (D) 0.5 mg/ml. (E) Plot of the dependence of contact angle (CA) value on seed concentration. Insets are photographs of the water droplets on the micellar brush-coated silicon wafers prepared with seed concentrations of 0.025 mg/ml (left) and 0.5 mg/ml (right). (F to H) AFM height images of PFS<sub>53</sub>-*b*-PDMS<sub>418</sub> micellar brushes formed at a constant seed concentration (0.5 mg/ml) but different amounts of unimers: (F) 2  $\mu$ l, (G) 4  $\mu$ l, (H) 6  $\mu$ l. Insets in (B) and (H) are enlargements of the boxed areas. (I) Plot of the dependence of CA value on unimer amount. Error bars in (E) and (I) denote SD of the measured CA values ( $\geq 5$  locations for each sample).



attachment through hydrogen bonding (H-bonding) with the P2VP corona. Low-dispersity PFS<sub>36</sub>-*b*-P2VP<sub>502</sub> (where the subscripts refer to the number-average degree of polymerization of each block) micelle seeds with  $L_n = 139$  nm [ $L_w/L_n = 1.04$ , where  $L_n$  and  $L_w$  are the number- and weight-average lengths, respectively, determined by atomic force microscopy (AFM)] prepared from the sonication of preformed long polydisperse cylinders (10) (fig. S1) were anchored to the silicon wafer via H-bonding (Fig. 1A). An AFM height image (fig. S1D) showed that the PFS<sub>36</sub>-*b*-P2VP<sub>502</sub> crystallite seeds were relatively evenly distributed on the silicon surface. The seed-coated silicon wafer was then immersed in a mixture of isopropanol and hexane (1:1, v/v), and molecularly dissolved PFS<sub>53</sub>-*b*-PDMS<sub>418</sub> (PDMS, polydimethylsiloxane) in the unimer state was added as a solution in tetrahydrofuran (THF). Unimers grew at the termini of the immobilized seeds and eventually formed a layer of nanoscopic brushes on the surface, as revealed by AFM (Fig. 1, B to D and F to H, and fig. S2). AFM analysis indicated that the micellar brushes were ~20 nm in diameter (Fig. 1B, inset) and had an extended fiber-like morphology with lengths of ~1 μm. This indicated that the crystalline seeds immobilized on the silicon wafer remained active and enabled the living growth. Control experiments demonstrated that the micellar brushes were almost entirely formed by seeded growth that initiated on the surface (figs. S2 and S3). The density of the micellar brushes could be varied by the feed concentration of seeds (Fig. 1, B to D, and fig. S1, D and E). As a result of the presence of a PDMS corona, the formation of a series of surfaces with tunable hydrophobicity was revealed by contact angle (CA) values ranging from 81° to 109° (Fig. 1E). Furthermore, on the basis of the characteristics of living CDSA processes performed in homogeneous solution, the length of these brushes should be adjustable through the addition of further unimer (Fig. 1, F to H). With an increase in the amount of unimeric PFS<sub>53</sub>-*b*-PDMS<sub>418</sub>, the CA increased steadily from 109° to 119° (Fig. 1I); this can be attributed to the elongation of the hydrophobic fibers forming a brush layer.

Further utility of the PFS-*b*-PDMS micellar brushes was restricted by their collapse after drying (fig. S4), probably as a consequence of the thin, high-aspect ratio cylindrical structures, as well as the very soft, low- $T_g$  (glass transition temperature, ~-123°C) PDMS corona, and also by the lack of facile coronal functionalization chemistries. We therefore used PFS-*b*-P2VP BCPs for the seeded growth, taking advantage of the higher  $T_g$  (~104°C, which may provide additional rigidity after drying in addition to that provided by the crystalline PFS core) (19) and the more readily functionalized corona-forming P2VP block. In

addition, substantially shorter PFS<sub>36</sub>-*b*-P2VP<sub>502</sub> seeds ( $L_n = 58$  nm,  $L_w/L_n = 1.03$ ) at the same concentration (0.5 mg/ml) were immobilized on the silicon wafer (Fig. 2C) to favor the growth of denser micellar brush arrays. Upon addition of the PFS<sub>20</sub>-*b*-P2VP<sub>140</sub> unimers (Fig. 2A), micellar brushes with increased diameter of ~25 nm grew from the seeds on the substrate and formed coral-like nanoassemblies comprising pillars (revealed by the AFM height images both in the solution and dry state) (Fig. 2B and fig. S5). As a result of the hydrophilic nature of the P2VP coronas, the hydrophilicity was increased as the CA decreased to 67°. Such coral-like nanoassem-

blies could be fabricated on a large scale covering a 1 cm × 1 cm piece of silicon wafer with relatively few defects (undergrown or overgrown sites) (fig. S6). The micellar brushes remained standing as the length further increased by the addition of unimer, but they eventually collapsed beyond average heights of ~40 nm (Fig. 2D and fig. S7).

Previous studies have established that PFS BCPs with a longer PFS core-forming block tend to form cylindrical micelles with a larger core diameter (20). Hence, the use of PFS<sub>30</sub>-*b*-P2VP<sub>226</sub> with a longer PFS core-forming block and relatively larger block ratio ( $R_{P2VP/PFS} = 7.5$  versus 7.0 for PFS<sub>20</sub>-*b*-P2VP<sub>140</sub>, where  $R$  is

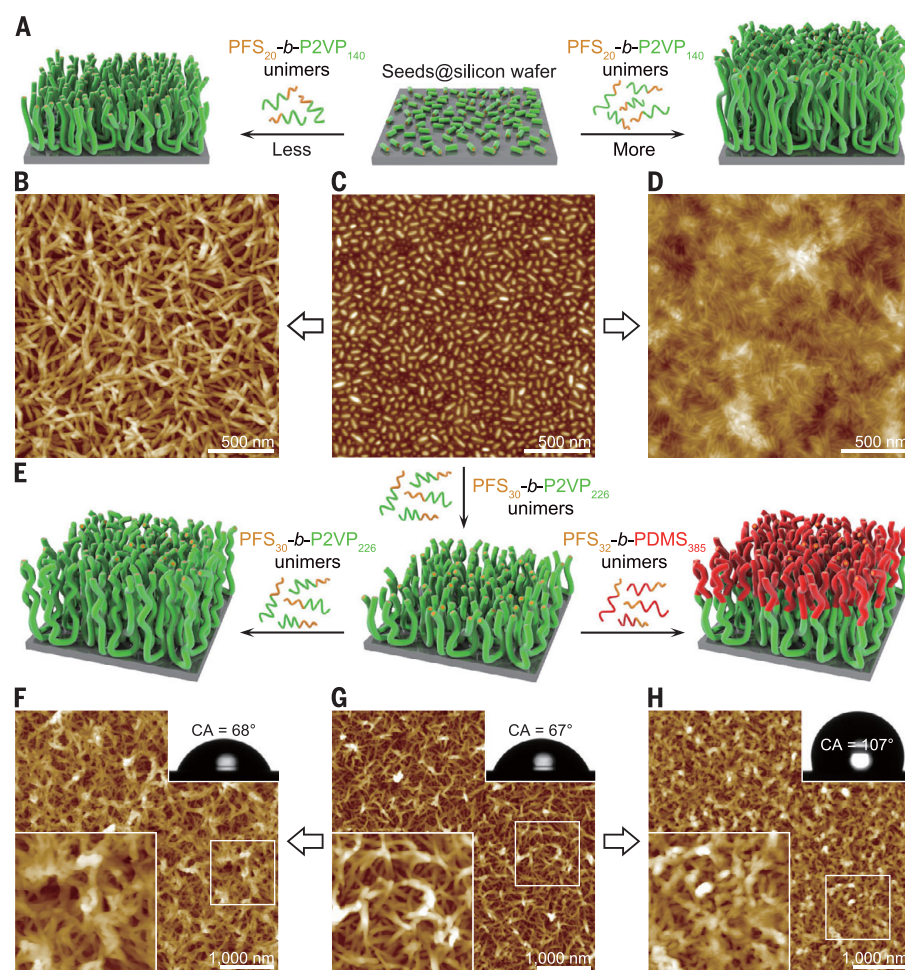


**Fig. 2. Seeded growth of hydrophilic PFS-*b*-P2VP and segmented micellar brushes on a silicon wafer.** (A) Schematic illustration of the growth process for PFS<sub>20</sub>-*b*-P2VP<sub>140</sub> micellar brushes. (B to D) AFM height images of (C) PFS<sub>36</sub>-*b*-P2VP<sub>502</sub> seed-coated silicon wafer (for seeds,  $L_n = 58$  nm,  $L_w/L_n = 1.03$ , concentration = 0.5 mg/ml in isopropanol) and PFS<sub>20</sub>-*b*-P2VP<sub>140</sub> micellar brushes formed by the addition of (B) 4 μl and (D) 10 μl of solution of PFS<sub>20</sub>-*b*-P2VP<sub>140</sub> unimers, respectively. (E) Schematic illustration of the growth process for PFS<sub>30</sub>-*b*-P2VP<sub>226</sub> micellar brushes and segmented micellar brushes. (F to H) AFM height images of (G) short PFS<sub>30</sub>-*b*-P2VP<sub>226</sub> micellar brushes formed by the addition of 3 μl of PFS<sub>30</sub>-*b*-P2VP<sub>226</sub> unimer solution, (F) elongated micellar brushes formed by further addition of 3 μl of PFS<sub>30</sub>-*b*-P2VP<sub>226</sub> unimer solution to the short micellar brushes shown in (G), and (H) segmented micellar brushes formed by further addition of 3 μl of PFS<sub>32</sub>-*b*-PDMS<sub>385</sub> unimer solution to the short micellar brushes shown in (G). Insets at lower left are enlargements of the respective boxed areas; insets at upper right are photographs of water droplets on the surfaces, showing the corresponding CA results.



the block ratio) favored the formation of thicker and presumably more rigid micellar brushes (cylinder diameter of  $\sim 35$  nm and average brush height of  $\sim 125$  nm by AFM; Fig. 2G and fig. S8). The coral-like nanoassemblies thus can be further elongated by subsequent addition of PFS<sub>30</sub>-*b*-P2VP<sub>226</sub> unimers (Fig. 2, E and F, and fig. S8). Moreover, segmented micellar brushes can be generated by sequential addition of PFS<sub>30</sub>-*b*-P2VP<sub>226</sub> and PFS<sub>32</sub>-*b*-PDMS<sub>385</sub> unimers (Fig. 2H and fig. S9), as evidenced by the transformation of

wettability (CA of  $67^\circ$  for the PFS<sub>30</sub>-*b*-P2VP<sub>226</sub> micellar brushes compared to a value of  $107^\circ$  for the segmented brushes).

We attempted post-assembly functionalization of the PFS-*b*-P2VP micellar brushes based on the functional P2VP corona and the redox-active PFS core (Fig. 3A). First, protonation of the P2VP corona was conducted by immersing the micellar brushes in a solution of CF<sub>3</sub>COOH (Fig. 3A, i) (21). This led to the yield of positively charged micellar brushes with structurally retained integrity and a highly hydrophilic

surface (CA =  $26^\circ$  versus  $67^\circ$  for the neutral micellar brush precursor) (Fig. 3B, inset). The P2VP corona was also manipulated to provide a viable platform for functionalization with inorganic nanoparticles (Fig. 3A, ii) (15, 22). For example, the brushes were selectively decorated by gold nanoparticles (AuNPs; diameter  $\sim 15$  nm) via coordination interactions (Fig. 3C), allowing the fabrication of a functional hybrid surface. This was confirmed by scanning electron microscopy (SEM) and selected-area energy-dispersive x-ray (EDX) spectroscopy mapping (fig. S10A). The AuNP-decorated micellar brushes were found to possess useful catalytic activity toward the borohydride-mediated reduction of 4-nitrophenol (Nip) to 4-aminophenol (Amp) (23) (Fig. 3E); they also appeared to be durable and recyclable, as the catalytic performance was retained with similar activity over 15 cycles (Fig. 3, E to G). Furthermore, the redox-active PFS core provides another route to generate nanoparticle arrays (Fig. 3A, iii) (9, 24). In situ reduction of AgNO<sub>3</sub> by the Fe(II) sites in the core gave rise to a highly dense array of silver nanoparticles (AgNPs; diameter  $\sim 35$  nm) (Fig. 3D and fig. S10B). We found that the antibactericidal activity of AgNPs (25) readily renders the silicon wafer resistant to the growth of Gram-negative *Escherichia coli* (fig. S11).

To expand our approach to other material surfaces, we also explored the formation of micellar brushes on graphene oxide (GO) sheets (26) [Fig. 4A; additional anchoring techniques and substrates were also explored, such as coordination interactions for metallic substrates and covalent immobilization for hydroxylated surfaces (figs. S20 and S21)]. Seed-coated GO sheets were prepared by addition of the PFS<sub>30</sub>-*b*-P2VP<sub>226</sub> seeds ( $L_n = 46$  nm,  $L_w/L_n = 1.04$ ) to a suspension of GO in isopropanol, followed by a sedimentation/redispersal process (fig. S12, A to C). Transmission electron microscopy (TEM) and AFM height images (Fig. 4, B and C) showed that the PFS<sub>30</sub>-*b*-P2VP<sub>226</sub> seeds were densely immobilized on the GO sheets, presumably as a result of the H-bonding and electrostatic interactions between the pyridyl groups in the P2VP corona and the carboxyl and hydroxyl groups of GO. The sheets retained the unilaminar structure and no obvious aggregation was observed. Upon addition of the PFS<sub>30</sub>-*b*-P2VP<sub>226</sub> unimers, fiber-like micelles grew from the GO surface and eventually formed a compact hairy brush layer (Fig. 4, D and E, and figs. S12D and S13). These hairy GO sheets were found to be colloidal stable over several months, probably as a result of the solubility arising from the voluminous micellar brushes. In a similar manner to the silicon wafer system, elongated or segmented micellar brushes could be constructed by subsequent addition of PFS<sub>30</sub>-*b*-P2VP<sub>226</sub> or

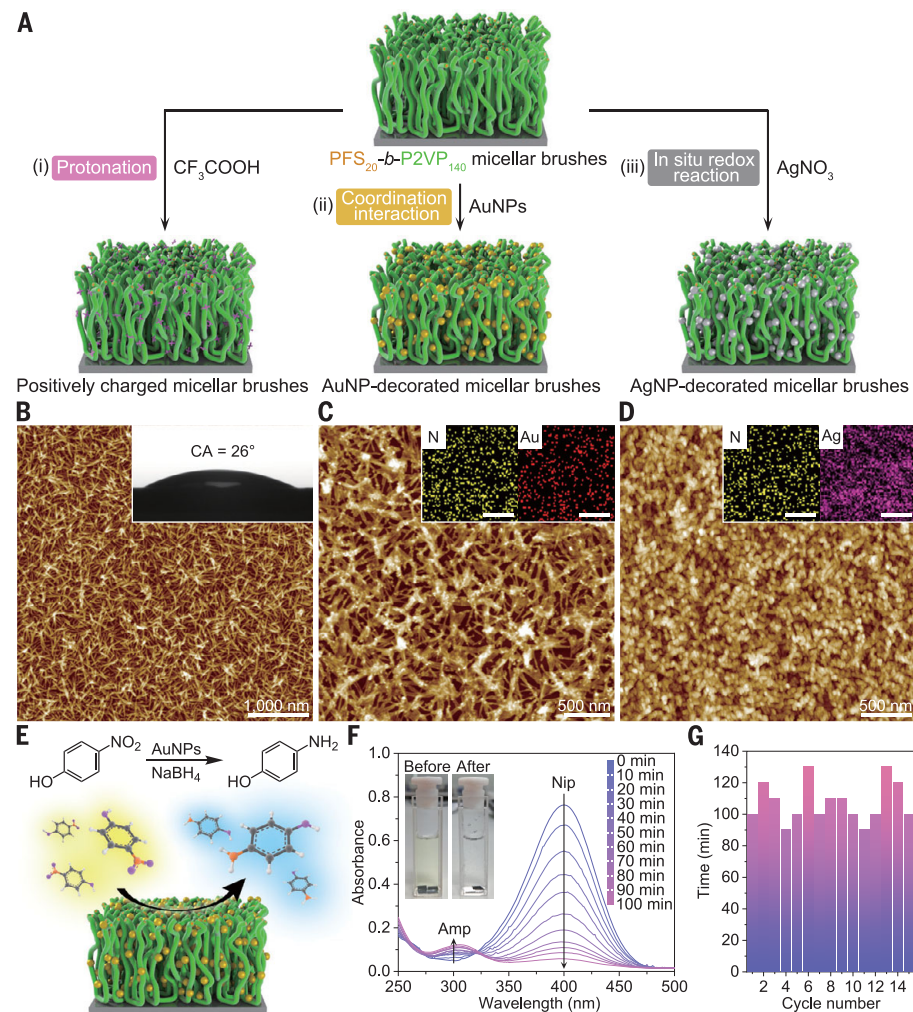


**Fig. 3. Functionalization and application of PFS-*b*-P2VP micellar brushes.** (A) Schematic illustration of the pathways for the functionalization of PFS<sub>20</sub>-*b*-P2VP<sub>140</sub> micellar brushes: (i) protonation, (ii) coordination interaction, and (iii) in situ redox chemistry. (B to D) AFM height images of micellar brushes bearing (B) positive charges (the inset photograph shows a water droplet on the surface), (C) AuNPs, and (D) AgNPs. Insets in (C) and (D) are SEM-assisted EDX mapping images, where the yellow features represent N existing in the P2VP coronas of the micellar brushes, the red features identify Au, and the pink features identify Ag. Scale bars, 200 nm [inset in (C)], 2  $\mu$ m [inset in (D)]. (E) Schematic illustration of the borohydride-mediated reduction of 4-nitrophenol (Nip) to 4-aminophenol (Amp) catalyzed by AuNP-decorated micellar brushes in aqueous solution at room temperature. (F) Ultraviolet-visible (UV-vis) spectrum monitoring the reduction process of Nip in aqueous solution with an interval of 10 min. The reduction was accomplished in  $\sim 100$  min; the solution color changed from yellow to colorless (inset photographs). (G) Recyclability test for AuNP-decorated micellar brushes for the reduction of Nip. The data variability over the 15 cycles is attributed to the absence of stirring, as the reaction was run in a cuvette within a UV-vis spectrophotometer.

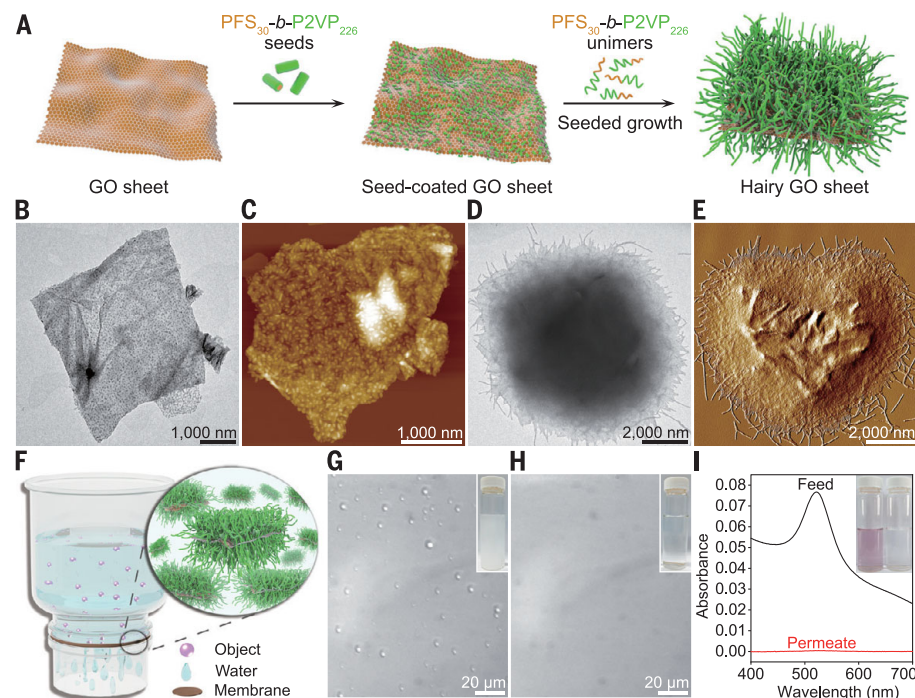


**Fig. 4. Seeded growth of PFS-*b*-P2VP micellar brushes on GO sheets.** (A) Schematic illustration of the process, which involves the immobilization of PFS<sub>30</sub>-*b*-P2VP<sub>226</sub> seeds on GO via H-bonding and electrostatic interactions followed by living growth of PFS<sub>30</sub>-*b*-P2VP<sub>226</sub> micellar brushes. (B and C) TEM (B) and AFM (C) height images of PFS<sub>30</sub>-*b*-P2VP<sub>226</sub> seed-coated GO sheets ( $L_n = 46$  nm,  $L_w/L_n = 1.04$ ) after removal of the excess seeds. (D and E) TEM (D) and AFM [(E); derived from the peak force error channel] images of hairy GO sheets formed by the addition of 10  $\mu$ l of PFS<sub>30</sub>-*b*-P2VP<sub>226</sub> unimer solution (10 mg/ml in THF) to 1 ml of solution of PFS<sub>30</sub>-*b*-P2VP<sub>226</sub> seed-coated GO (GO of 0.02 mg/ml in isopropanol). (F) Schematic illustration describing the vacuum filtration process, which rejects specific objects by means of a laminated membrane assembled from the hairy GO sheets. (G and H) Optical microscopy images and photographs (insets) of a heptane-in-water emulsion before (G) and after (H) filtration by the membrane. The absence of heptane droplets in (H) compared with the feed emulsion shown in (G) indicates that heptane was rejected by the membrane, presumably as a result of the hydrophilic corona of the micellar brush layer. (I) UV-vis spectra and photographs of a AuNP solution before and after filtration by the membrane. The AuNPs were removed, as evidenced by the absence of the peak at 523 nm and the transparent filtrate compared with the original purple solution.

PFS<sub>32</sub>-*b*-PDMS<sub>385</sub> unimers (fig. S14). Analogous to the “grafting-from” method applied in the synthesis of polymer brushes (8), this seeded growth approach provided a facile bottom-up approach to fabricate GO-based hybrid assemblies with controllable brush layer functionalization. The method also has advantages over conventional approaches involving direct anchoring of long fibers on GO sheets (fig. S15) in terms of uniformity and grafting density (27).

The hairy GO sheets can be functionalized using various post-assembly chemistries. For example, fluorescent dyes can be covalently anchored onto the P2VP corona via quaternization, making them observable in solution through stimulated emission depletion (STED) microscopy (fig. S12, E to G). In addition, facile decoration by nanoparticles is possible using noncovalent interactions, such as coordination (e.g., for AuNPs; fig. S16) and H-bonding (e.g., for silica nanoparticles; fig. S17). For demon-

stration of potential utility, a thin laminated membrane (thickness of  $\sim 60$  nm) was further assembled from the hairy GO sheets (fig. S18). This membrane exhibited higher water permeance upon subsequent protonation with trifluoroacetic acid, with substantially higher flux ( $4520$  liters hour<sup>-1</sup> m<sup>-2</sup> bar<sup>-1</sup>) compared to the original membrane ( $226$  liters hour<sup>-1</sup> m<sup>-2</sup> bar<sup>-1</sup>) (see supplementary materials for details) and similar to the fluxes of recently reported GO-based membranes (27, 28). Because of the nanoporosity and hydrophilicity of the protonated P2VP corona of the constitutive micellar brushes, the membrane efficiently separated heptane from a heptane-in-water emulsion (Fig. 4, F to H, and fig. S19) and filtered AuNPs (diameter  $\sim 15$  nm) from an aqueous solution (Fig. 4I and fig. S19).

We have demonstrated a versatile bottom-up strategy that represents a platform for the controlled functionalization of surfaces, using the crystallization-driven growth of BCP micellar brushes with precisely controlled chem-

istry. In principle, this approach should be suitable for any arbitrary material surface given the existence of an effective anchoring technique for the micelle seeds, thereby enabling a range of applications.

## REFERENCES AND NOTES

1. I. S. Yang *et al.*, *Nano Energy* **32**, 414–421 (2017).
2. J. H. Heo, D. H. Song, S. H. Im, *Adv. Mater.* **26**, 8179–8183 (2014).
3. T. Ozel *et al.*, *Nano Lett.* **17**, 4502–4507 (2017).
4. C. Yan *et al.*, *Nat. Energy* **3**, 764–772 (2018).
5. J. O. Zoppe *et al.*, *Chem. Rev.* **117**, 1105–1318 (2017).
6. J. M. Giussi, M. L. Cortez, W. A. Marmisollé, O. Azzaroni, *Chem. Soc. Rev.* **48**, 814–849 (2019).
7. G. Sun *et al.*, *J. Am. Chem. Soc.* **135**, 4203–4206 (2013).
8. W. Zong *et al.*, *Angew. Chem. Int. Ed.* **55**, 3690–3693 (2016).
9. R. L. N. Hailes, A. M. Oliver, J. Gwyther, G. R. Whittell, I. Manners, *Chem. Soc. Rev.* **45**, 5358–5407 (2016).
10. X. Wang *et al.*, *Science* **317**, 644–647 (2007).
11. J. Schmelz, A. E. Schedl, C. Steinlein, I. Manners, H. Schmalz, *J. Am. Chem. Soc.* **134**, 14217–14225 (2012).
12. D. Tao *et al.*, *J. Am. Chem. Soc.* **139**, 7136–7139 (2017).
13. M. C. Arno *et al.*, *J. Am. Chem. Soc.* **139**, 16980–16985 (2017).
14. S. Shin *et al.*, *J. Am. Chem. Soc.* **140**, 6088–6094 (2018).
15. H. Qiu *et al.*, *Science* **352**, 697–701 (2016).
16. H. Qiu, Z. M. Hudson, M. A. Winnik, I. Manners, *Science* **347**, 1329–1332 (2015).
17. L. Jia *et al.*, *Nat. Commun.* **5**, 3882 (2014).
18. L. Jia *et al.*, *ACS Nano* **9**, 10673–10685 (2015).
19. M.-S. Hsiao, S. F. M. Yusoff, M. A. Winnik, I. Manners, *Macromolecules* **47**, 2361–2372 (2014).
20. H. Qiu *et al.*, *J. Am. Chem. Soc.* **137**, 2375–2385 (2015).
21. J. G. Kennemur, *Macromolecules* **52**, 1354–1370 (2019).
22. S. Mei, H. Qi, T. Zhou, C. Y. Li, *Angew. Chem. Int. Ed.* **56**, 13645–13649 (2017).
23. B. Baruah, G. J. Gabriel, M. J. Akbashev, M. E. Boohar, *Langmuir* **29**, 4225–4234 (2013).
24. H. Wang, X. Wang, M. A. Winnik, I. Manners, *J. Am. Chem. Soc.* **130**, 12921–12930 (2008).
25. M. L. W. Knecht, L. H. Koole, *Polymers* **3**, 340–366 (2011).
26. V. Georgakilas *et al.*, *Chem. Rev.* **116**, 5464–5519 (2016).
27. R. Xiong *et al.*, *Angew. Chem. Int. Ed.* **57**, 8508–8513 (2018).
28. H. Huang *et al.*, *Chem. Commun.* **4**, 2979 (2013).

## ACKNOWLEDGMENTS

We thank P. Choi, V. A. Du, and Y. Gao (University of Bristol) for providing some of the block copolymer samples; the Analytical Instrumentation Center and Center for High-Resolution Electron Microscopy (School of Physical Science and Technology, ShanghaiTech University) for AFM and TEM; and the Instrumental Analysis Center (Shanghai Jiao Tong University) for SEM, confocal laser scanning microscopy (CLSM), and STED. **Funding:** H.Q. thanks the National Natural Science Foundation of China (21674062, U1632117), the Science and Technology Commission of Shanghai Municipality (16ZR1422600, 17JC1400700, 18JC1415500), and the Shanghai Education Development Foundation and the Shanghai Municipal Education Commission (16SG54) for financial support. I.M. thanks the University of Bristol, the Canadian Government for a Canada 150 Research Chair, and the Chinese Government for a Thousand Talents Distinguished Visiting Professor position at Shanghai Jiao Tong University.

**Author contributions:** J.C. and H.Q. conceived the project; polymer samples were prepared in I.M.’s group; J.C. performed the experiments with assistance from C.L. and N.K.; J.C. and C.L. prepared the hairy GO sheets and performed the filtration experiments; J.C., N.K., Y.L., and Y.Y. conducted the antibacterial experiments; J.C., C.L., and G.L. performed the EDX imaging; J.C. and X.W. performed the fluid AFM analysis; and J.C., I.M., and H.Q. analyzed the data and prepared the manuscript with input from all the other authors. The project was supervised by I.M. and H.Q. **Competing interests:** A relevant patent application has been submitted to the State Intellectual Property Office of China.

**Data and materials availability:** All data are available in the manuscript or the supplementary materials.

## SUPPLEMENTARY MATERIALS

science.sciencemag.org/content/366/6469/1095/suppl/DC1  
Materials and Methods  
Figs. S1 to S21  
References (29–35)

3 May 2019; accepted 17 October 2019  
10.1126/science.aax9075



## SUPERCONDUCTIVITY

## Incoherent strange metal sharply bounded by a critical doping in Bi2212

Su-Di Chen<sup>1,2\*</sup>, Makoto Hashimoto<sup>3\*</sup>, Yu He<sup>1,2,†</sup>, Dongjoon Song<sup>4,‡</sup>, Ke-Jun Xu<sup>1</sup>, Jun-Feng He<sup>1,2,§</sup>, Thomas P. Devereaux<sup>2,5</sup>, Hiroshi Eisaki<sup>4</sup>, Dong-Hui Lu<sup>3</sup>, Jan Zaanen<sup>1,6</sup>, Zhi-Xun Shen<sup>1,2,‡#</sup>

In normal metals, macroscopic properties are understood using the concept of quasiparticles. In the cuprate high-temperature superconductors, the metallic state above the highest transition temperature is anomalous and is known as the “strange metal.” We studied this state using angle-resolved photoemission spectroscopy. With increasing doping across a temperature-independent critical value  $p_c \sim 0.19$ , we observed that near the Brillouin zone boundary, the strange metal, characterized by an incoherent spectral function, abruptly reconstructs into a more conventional metal with quasiparticles. Above the temperature of superconducting fluctuations, we found that the pseudogap also discontinuously collapses at the very same value of  $p_c$ . These observations suggest that the incoherent strange metal is a distinct state and a prerequisite for the pseudogap; such findings are incompatible with existing pseudogap quantum critical point scenarios.

Landau’s theory of Fermi liquids successfully explains the behavior of interacting electrons in normal metals. In a Fermi liquid, electronic states evolve adiabatically with increasing electron-electron interactions. Therefore, they remain in a one-to-one correspondence with the states in a Fermi gas and can be described in the language of quasiparticles. Soon after the discovery of cuprate high-transition temperature (high- $T_c$ ) superconductors, it was realized that the cuprates fall into a different regime (1). The starting point is a Mott insulator with one hole per Cu site. The holes are localized thanks to strong on-site Coulomb repulsion and become mobile with increasing doping. At the optimal doping where  $T_c$  is maximized, the metallic state above  $T_c$  breaks the Fermi liquid rules (1–3). With sufficient overdoping, a key aspect of Fermi liquid behavior is eventually recovered: Quasiparticles have been directly observed by angle-resolved photoemission spectroscopy (ARPES), spanning up a genuine Fermi

surface (4–6). Here, we report the surprising way in which these quasiparticles spring into existence in  $(\text{Bi,Pb})_2\text{Sr}_2\text{CaCu}_2\text{O}_{8+\delta}$  (Bi2212), one of the most studied high- $T_c$  superconductors.

We performed ARPES measurements over a wide temperature range on Bi2212 single crystals in fine doping steps. Such measurements are challenging because the increased outgassing from the sample environment at high temperature can easily contaminate the sample surface and alter the signal, given the small probe depth of ultraviolet photoemission. To overcome this problem, we controlled the sample temperature using a local heater and preserved the sample environment as a cold trap for contaminants throughout the measurements (7, 8). The spectra showed good consistency before and after thermal cycles between cryogenic and room temperatures (fig. S1), which has rarely been demonstrated in prior work.

In Fig. 1, A to F, we show the doping evolution of the ARPES spectra collected at 250 K along the Brillouin zone (BZ) boundary. On the heavily overdoped side, the spectra feature two parabolic-like dispersions known as the antibonding band (AB) and bonding band (BB) (3), consistent with band structure predictions for  $\text{CuO}_2$  bilayers. However, once the doping level drops below  $p_c \sim 0.19$ , the spectra markedly broaden and dispersions are no longer identifiable. In Fig. 1, G and H, we also present the nodal spectra immediately below and above  $p_c$ , respectively. These two spectra show similar dispersions with almost identical sharpness, indicating that the change across  $p_c$  is intrinsic to the antinode and highly anisotropic.

We now try to understand this change in quasiparticle terms. In Fermi liquid-like sys-

tems, quasiparticles appear as poles in the spectral function,

$$A(k, \omega) = \frac{1}{\pi} \text{Im} \left[ \frac{1}{\varepsilon_k - \omega + \Sigma(k, \omega)} \right] \quad (1)$$

where  $\omega$  is the energy,  $k$  is the momentum,  $\varepsilon_k$  is the bare band dispersion, and  $\Sigma(k, \omega)$  is the perturbative self energy that captures interaction effects. For Bi2212, it has been reported that the normal-state self energy takes the marginal Fermi liquid form (9, 10):

$$\Sigma(k, \omega) = \lambda \left[ \omega \ln \left( \frac{x}{\omega_c} \right) - i \left( \frac{\pi}{2} \right) x \right] - i\Gamma_0 \quad (2)$$

with

$$x = \sqrt{\omega^2 + \pi^2 k_B^2 T^2} \quad (3)$$

where  $\lambda$  is a coupling constant,  $\omega_c$  is a cutoff energy,  $\Gamma_0$  is an energy-independent scattering rate,  $k_B$  is the Boltzmann constant, and  $T$  is the absolute temperature. Immediately above  $p_c$ , we indeed find that the energy distribution curve (EDC) at  $(-\pi, 0)/a_0$  (antinode;  $a_0$  is the unit cell dimension) can be well fitted using this self energy (Fig. 1I) (8). Furthermore, the same set of parameters also reasonably describes the momentum distribution curve (MDC) (Fig. 1J) (8). In contrast, below  $p_c$ , the fitting becomes unstable as the antinodal EDC abruptly broadens and the quasiparticle peaks are replaced by an incoherent continuum (Fig. 1I). Intriguingly, no substantial change is observed in the MDC linewidth across  $p_c$  (Fig. 1J and fig. S2). This indicates that the disappearance of quasiparticle peaks is not a consequence of trivial elastic impurity scattering.

To further reveal the distinct spectral properties below and above  $p_c$ , we show the temperature dependence of spectra in Fig. 2 (see fig. S3 for the complete dataset). Upon cooling, the antinodal EDC below  $p_c$  gains two important features with well-separated temperature scales (Fig. 2A). The first is the pseudogap (2, 3), a low-energy spectral intensity depletion that gradually develops from far above  $T_c$  (red arrow; see also Fig. 3A). The second is the Bogoliubov quasiparticle (BQP) peak, which emerges as an intensity shoulder around 130 K and rapidly grows into a sharp peak with further decreasing temperature (blue stripe). These two features are further accentuated by the temperature difference spectra, where the pseudogap manifests as a spectral weight transfer from near the chemical potential to a wide energy window (Fig. 2B), and the BQP arises as a rather flat dispersion in a temperature range moderately above  $T_c$  (Fig. 2C).

In contrast to the two-temperature-scale behavior below  $p_c$ , we find a more conventional

<sup>1</sup>Departments of Applied Physics and Physics, Stanford University, Stanford, CA 94305, USA. <sup>2</sup>Stanford Institute for Materials and Energy Sciences, SLAC National Accelerator Laboratory and Stanford University, Menlo Park, CA 94025, USA. <sup>3</sup>Stanford Synchrotron Radiation Lightsource, SLAC National Accelerator Laboratory, Menlo Park, CA 94025, USA. <sup>4</sup>National Institute of Advanced Industrial Science and Technology, Tsukuba, Ibaraki 305-8568, Japan. <sup>5</sup>Department of Materials Science and Engineering, Stanford University, Stanford, CA 94305, USA. <sup>6</sup>Institute Lorentz for Theoretical Physics, Leiden University, 2300 RA Leiden, Netherlands.

\*These authors contributed equally to this work. †Present address: Department of Physics, University of California, Berkeley, CA 94709, USA. ‡Present address: Center for Correlated Electron Systems, Institute for Basic Science, Seoul 08826, Republic of Korea. §Present address: Department of Physics, University of Science and Technology of China, Hefei 230026, China.

#Corresponding author. Email: zxshen@stanford.edu

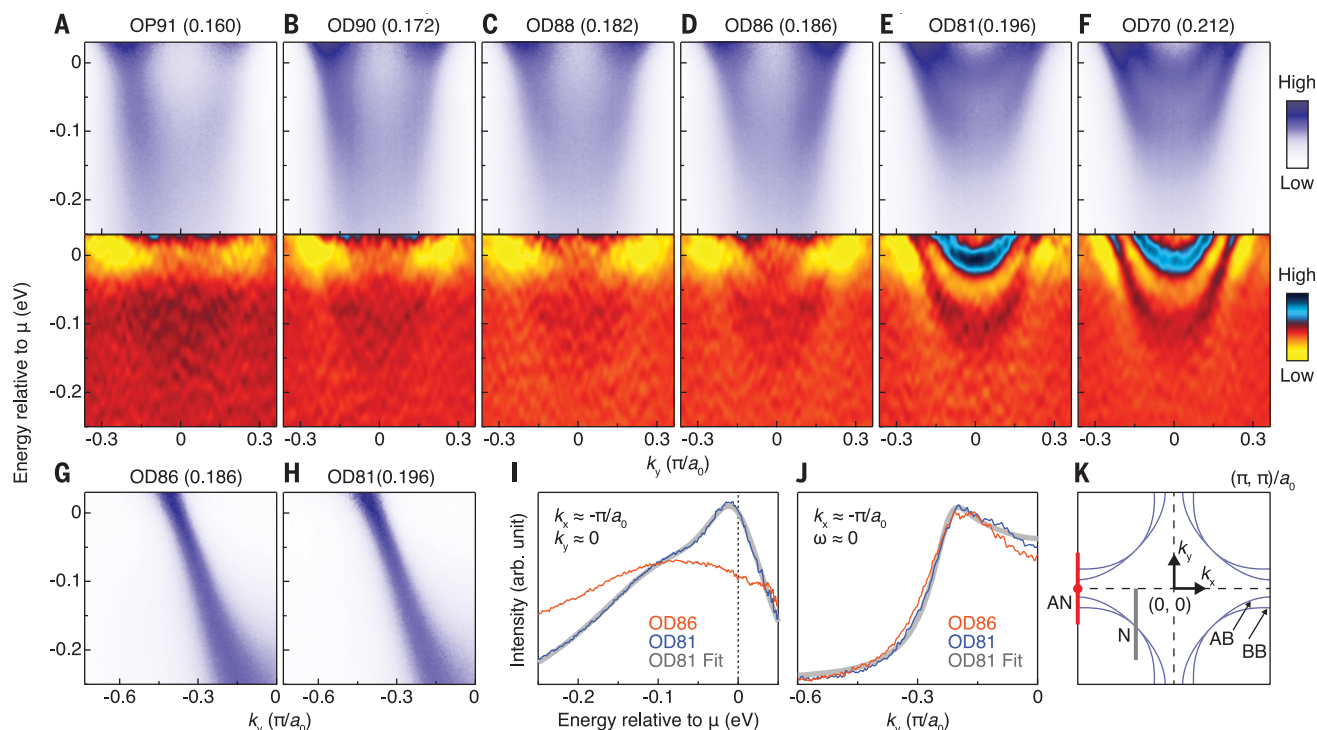


**Fig. 1. Doping dependence of the electronic structure at 250 K in Bi2212.** (A to F) ARPES spectra (top) and their second energy derivatives (bottom) at six doping levels, taken along the Brillouin zone (BZ) boundary as indicated by the red line in (K);  $a_0$  is the unit cell dimension. The corresponding sample (doping  $p$ ) is marked at the top of each panel. Samples are named by their transition temperatures ( $T_c$ , in kelvin) rounded to the nearest integer with the prefix OD for overdoped and OP for optimally doped. The critical doping  $p_c$  is between OD86 and OD81. All data are divided by the resolution-convolved Fermi function. (G and H) ARPES spectra near the node (N) along

the gray line in (K) from OD86 and OD81, respectively. (I and J) Energy distribution curves (EDCs) at the antinode [AN, red dot in (K)], and momentum distribution curves (MDCs) along the BZ boundary at the chemical potential  $\mu$ , respectively. A momentum-independent background is subtracted (8). Curves are normalized by the area under them in the plotted horizontal axis range for better comparison. Data from OD81 are fitted to a marginal Fermi liquid model (8–10), and the results are plotted in gray. (K) Schematics of the Fermi surfaces formed by the antibonding band (AB) and bonding band (BB) in the first BZ.

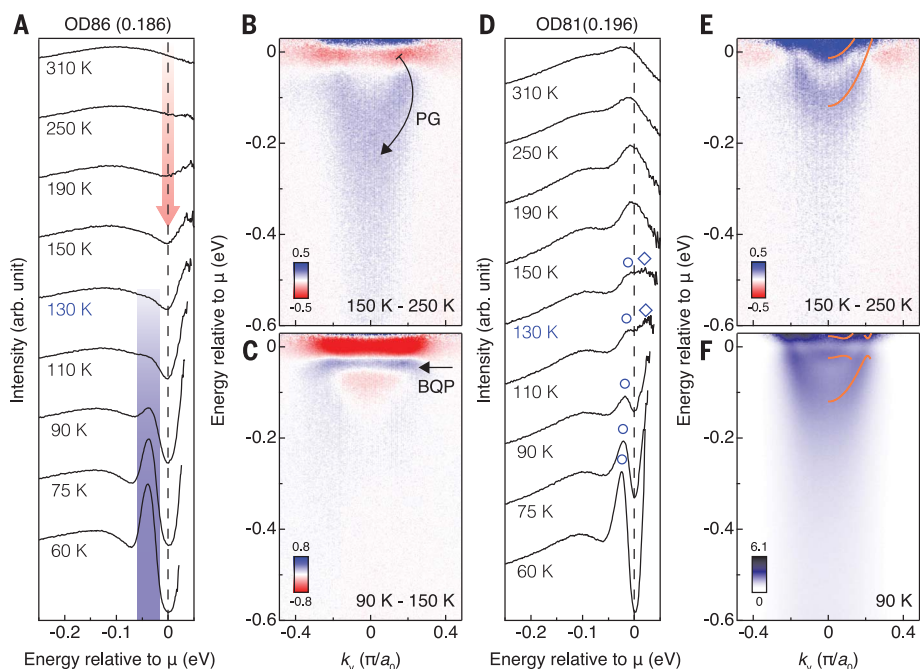


**Fig. 2. Temperature dependence of the electronic structure immediately below and above  $p_c$ .** (A) Temperature evolution of antinodal EDCs in OD86 ( $p \sim 0.186$ ). The curves are offset for clarity. The red arrow indicates the development of the pseudogap (PG). The blue stripe highlights the intensity shoulder and its evolution into the sharp Bogoliubov quasiparticle (BQP) peak. All data are divided by the Fermi function. (B) Difference between the ARPES spectra taken at 150 K and 250 K along the BZ boundary in OD86. The original spectra at each temperature are normalized such that the average intensity between  $-0.6$  and  $-0.5$  eV equals 1. The black arrow indicates the spectral weight transfer due to the PG. (C) Same as (B) but between spectra taken at 90 K and 150 K. The black arrow highlights the emergence of the BQP. (D and E) Same as (A) and (B) but taken for OD81 ( $p \sim 0.196$ ). The open diamonds and circles in (D) are guides to the eye and denote the BQP peaks above and below the chemical potential, respectively. (F) ARPES spectra taken at 90 K along the BZ boundary in OD81. The orange curves in (E) and (F) are guides to the eye and highlight the normal quasiparticle and BQP dispersions, respectively.



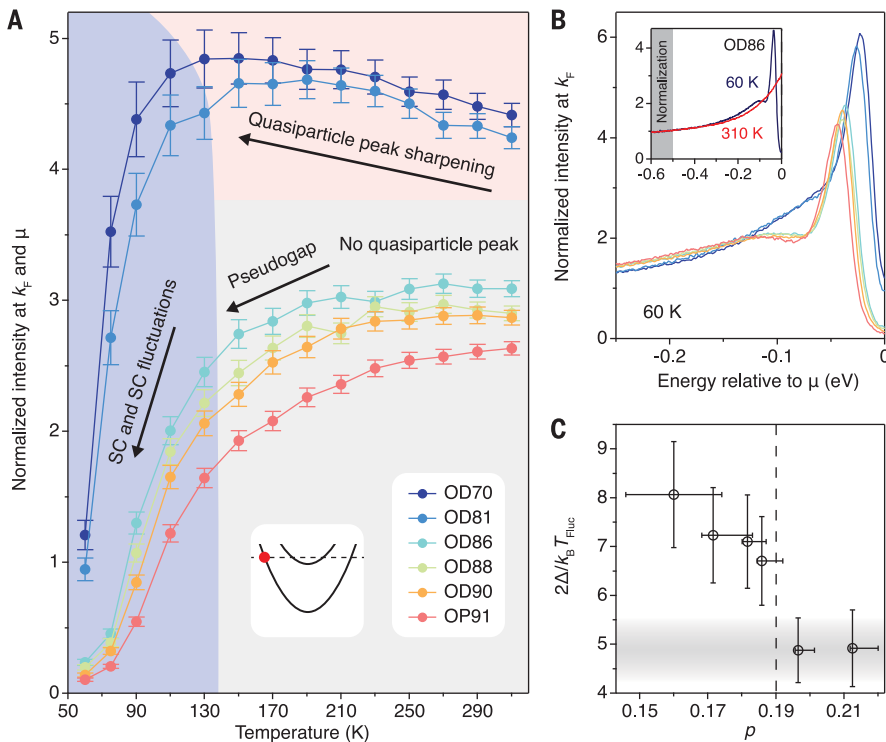


**Fig. 3. Marked changes of spectral properties across  $p_c$ .** (A) Temperature dependence of spectral intensity at the BZ-boundary BB Fermi momentum ( $k_F$ ) and  $\mu$  (red dot in inset). The error bars reflect the noise level in the ARPES data and uncertainties in determining  $k_F$  and  $\mu$ . (B) Doping evolution of EDCs at the BZ-boundary BB  $k_F$  and 60 K. All data in (A) and (B) are background-subtracted (8), divided by the Fermi function, and normalized such that the average EDC intensity between  $-0.6$  and  $-0.5$  eV equals 1. The inset shows examples of intensity normalization using OD86 data. (C) Doping dependence of  $2\Delta/k_B T_{Fluc}$ , where  $\Delta$  is the antinodal superconducting gap size,  $k_B$  is the Boltzmann constant, and  $T_{Fluc}$  is the temperature scale of superconducting fluctuations. The horizontal error bars are caused by uncertainties in  $T_c$  measurements; the vertical error bars reflect uncertainties in determining  $\Delta$  and  $T_{Fluc}$ .

**Fig. 4. Phase diagram of Bi2212.** (A) The color plot (outlined in white) shows the spectral intensity at the BZ-boundary BB  $k_F$  and  $\mu$  (same data as in Fig. 3A) plotted as a function of both temperature and doping.

For  $p < p_c$ , this intensity reduces with decreasing temperature and doping, reflecting the development of the pseudogap. Also plotted are the transition temperatures of various broken symmetries in Bi2212 and  $YBa_2Cu_3O_{6+\delta}$  (YBCO): magnetic order ( $T_{Mag}$ ) (24–26), charge order ( $T_{CDW}$ ) (27–29), nematicity ( $T_{Nem}$ ) (30), time-reversal symmetry breaking ( $T_{TR}$ ) (31), and inversion-symmetry breaking ( $T_{Inv}$ ) (32). The black curve marks  $T_c$ ; the vertical dashed line marks  $p_c$ .

(B)  $T_{Fluc}$  in Bi2212 observed by various probes: ARPES in the antinodal (AN) region (this work), laser ARPES in the near-nodal (NN) region (7), torque magnetometry (11), Nernst effect (11), specific heat (12), and high-frequency conductivity (13). Error bars indicate uncertainties in estimating these temperatures. Gray, pink, and blue background shadings are guides to the eye and indicate the existence of the pseudogap, normal quasiparticles, and BQPs, respectively. Insets are schematics of the antinodal ARPES spectra; the horizontal dashed lines mark the chemical potential, the hatched area indicates incoherent spectra, and the black and blue curves indicate the normal quasiparticle and BQP dispersions, respectively.

temperature evolution above  $p_c$ . With decreasing temperature, the quasiparticle peaks first sharpen with no sign of the pseudogap (Fig. 2, D and E, and Fig. 3A). Then at around 130 K, a gap opens with the rise of one additional peak.

The peak can be attributed to the back-bending AB above the chemical potential (Fig. 2, D and F), consistent with the formation of BQP dispersions when a superconducting gap opens. With further decreasing temperature, the gap

and low-energy peaks become more prominent. Yet as superconductivity develops, no other major changes are observed in the electronic structure. These observations imply that both the gaps above and below  $T_c$  here

are associated with superconductivity. The absence of additional gap-like features also indicates that the pseudogap suddenly collapses at  $p_c$  with overdoping. Furthermore, by following the BQP shoulder for doping  $p < p_c$  and the gap above  $T_c$  for  $p > p_c$  (figs. S3 and S4), we establish a temperature scale for superconducting fluctuations,  $T_{\text{Fluc}}$ , that smoothly follows the  $T_c$  dome. This is consistent with results from other studies (7, 11–13), as summarized in Fig. 4B.

We further compare the spectra across  $p_c$  in the superconducting state. In Fig. 3B we show the doping dependence of EDCs at 60 K, a temperature where the growth of the superconducting gap is almost complete (14). These EDCs are taken from the BB Fermi momentum to minimize bilayer effects. Below  $p_c$ , the EDCs exhibit the anomalous peak-dip-hump line shape, and the gap-to- $T_{\text{Fluc}}$  ratio gradually decreases with increasing doping (Fig. 3C). Once above  $p_c$ , we find that the dip rapidly weakens and the gap-to- $T_{\text{Fluc}}$  ratio saturates. These changes reflect the impact of the normal state on the superconducting phase, echoing previous observations of low-temperature anomalies across the very same  $p_c$  (14–20).

We now discuss the implications of our results. Previously, the low-temperature anomalies at  $p_c$  were sometimes viewed as evidence of a conventional order undergoing a continuous quantum phase transition. In this picture, the order parameter would couple to the electrons and cause the pseudogap, and its quantum critical fluctuations would give rise to the strange metal within a V-shaped region in the temperature-doping phase diagram (1). However, this scenario is hard to reconcile with several studies in the normal state, where the experimental observations are indicative of a change of quasiparticle coherence across  $p_c$  at elevated temperatures (15, 21–23). Consistent with these studies, our data provide direct microscopic evidence that  $p_c$  is not associated with a V-shaped quantum critical region, but instead represents a temperature-independent boundary between the incoherent strange metal and the overdoped quasiparticle metal. Furthermore, we find that upon cooling, the pseudogap develops only inside the incoherent strange metal and in turn serves as a parent state for various broken symmetries that occur at even lower temperatures (Fig. 4A) (24–32). These observations suggest that the pseudogap is a subordinate phenomenon to the incoherent strange metal and does not form a quantum critical point.

A remaining puzzle is the incoherent antinodal line shape. It has been suggested that incoherence may arise from strong coupling between electrons and bosonic modes such as spin excitations (4) and phonons

(33, 34). However, this alone cannot produce the discontinuous change of spectral function at  $p_c$ . In fact, as the impact of this change persists to high energy and temperature, conventionally it would be associated with a first-order phase transition. One possibility is the involvement of a structural transition. For example, an abrupt change of  $\text{CuO}_2$  plane dimpling has been reported in  $\text{YBa}_2\text{Cu}_3\text{O}_{6+\delta}$  near optimal doping (35). Yet it remains to be seen whether a similar structural transition happens at  $p_c$  in  $\text{Bi2212}$  and strongly affects the bare band dispersions and mode coupling properties. Moreover, certain short-range orders, such as the short-range charge density wave (14) and nematic glass (36), may also contribute to the broadening of antinodal spectra. Considering these factors, it seems possible that our data can be explained by a conventional theory. However, such explanations become debatable when results from other probes are considered. A first-order phase transition must be accompanied by jump discontinuities in the macroscopic electronic properties. Nonetheless, to our knowledge, such discontinuities have not been observed at high temperature. Although future experiments with continuous and in situ doping tuning capability may bring important insights, the nature of this hidden “first-order transition” remains to be resolved.

Perhaps these observations signal that the incoherent strange metal is a form of matter governed by unknown emergence principles. A potential culprit is dense many-body entanglement (37). Because the Hilbert space of a quantum many-body system grows exponentially with the system size, to compute the properties of densely entangled states in such systems is beyond the capacity of classical computers. However, because these states are delocalized in the vast Hilbert space, their excitations are generically not organized around single-particle quantum numbers and can manifest a broad spectral function (37). This encapsulates a possible explanation for the incoherent ARPES spectra. Meanwhile, it offers a loophole for the hidden “first-order transition,” as rules for transitions between densely entangled and Fermi liquid-like states are not known. Could it be that this would explain the experimental observations? We present our study as a challenge to the theory community and a potential benchmark test for quantum computing efforts.

## REFERENCES AND NOTES

- B. Keimer, S. A. Kivelson, M. R. Norman, S. Uchida, J. Zaanen, *Nature* **518**, 179–186 (2015).
- T. Timusk, B. Statt, *Rep. Prog. Phys.* **62**, 61–122 (1999).
- A. Damascelli, Z. Hussain, Z. X. Shen, *Rev. Mod. Phys.* **75**, 473–541 (2003).
- Z. X. Shen, J. R. Schrieffer, *Phys. Rev. Lett.* **78**, 1771–1774 (1997).

- Z. M. Yusuf et al., *Phys. Rev. Lett.* **88**, 167006 (2002).
- A. Kaminski et al., *Phys. Rev. Lett.* **90**, 207003 (2003).
- T. Kondo et al., *Nat. Commun.* **6**, 7699 (2015).
- See supplementary materials.
- E. Abrahams, C. M. Varma, *Proc. Natl. Acad. Sci. U.S.A.* **97**, 5714–5716 (2000).
- A. Kaminski et al., *Phys. Rev. B* **71**, 014517 (2005).
- Y. Wang et al., *Phys. Rev. Lett.* **95**, 247002 (2005).
- J. L. Tallon, J. G. Storey, J. W. Loram, *Phys. Rev. B* **83**, 092502 (2011).
- J. Corson, R. Mallozzi, J. Orenstein, J. N. Eckstein, I. Bozovic, *Nature* **398**, 221–223 (1999).
- M. Hashimoto et al., *Nat. Mater.* **14**, 37–42 (2015).
- J. L. Tallon, J. W. Loram, *Physica C* **349**, 53–68 (2001).
- J. L. Tallon, J. W. Loram, J. R. Cooper, C. Panagopoulos, C. Bernhard, *Phys. Rev. B* **68**, 180501 (2003).
- I. M. Vishik et al., *Proc. Natl. Acad. Sci. U.S.A.* **109**, 18332–18337 (2012).
- K. Fujita et al., *Science* **344**, 612–616 (2014).
- S. Badoux et al., *Nature* **531**, 210–214 (2016).
- Y. He et al., *Science* **362**, 62–65 (2018).
- F. Venturini et al., *Phys. Rev. Lett.* **89**, 107003 (2002).
- J. L. Tallon, J. W. Loram, C. Panagopoulos, *J. Low Temp. Phys.* **131**, 387–394 (2003).
- R. A. Cooper et al., *Science* **323**, 603–607 (2009).
- B. Fauqué et al., *Phys. Rev. Lett.* **96**, 197001 (2006).
- S. De Almeida-Didry et al., *Phys. Rev. B* **86**, 020504 (2012).
- L. Mangin-Thro, Y. Sidis, A. Wildes, P. Bourges, *Nat. Commun.* **6**, 7705 (2015).
- E. H. da Silva Neto et al., *Science* **343**, 393–396 (2014).
- S. Blanco-Canosa et al., *Phys. Rev. B* **90**, 054513 (2014).
- M. Hückler, N. B. et al., *Phys. Rev. B* **90**, 054514 (2014).
- Y. Sato et al., *Nat. Phys.* **13**, 1074–1078 (2017).
- J. Xia et al., *Phys. Rev. Lett.* **100**, 127002 (2008).
- L. Zhao et al., *Nat. Phys.* **13**, 250–254 (2017).
- K. M. Shen et al., *Phys. Rev. Lett.* **93**, 267002 (2004).
- T. Cuk et al., *Phys. Rev. Lett.* **93**, 117003 (2004).
- E. Kaldis et al., *Phys. Rev. Lett.* **79**, 4894–4897 (1997).
- K. Lee, S. A. Kivelson, E. A. Kim, *Phys. Rev. B* **94**, 014204 (2016).
- J. Zaanen, *SciPost Phys.* **6**, 061 (2019).
- S.-D. Chen et al., Replication data for “Incoherent strange metal sharply bounded by a critical doping in  $\text{Bi2212}$ ”. Harvard Dataverse, Version 1 (2019). <https://doi.org/10.7910/DVN/VPANTG>

## ACKNOWLEDGMENTS

We thank D.-H. Lee, J. L. Tallon, S. A. Kivelson, C. M. Varma, R. Hackl, W. S. Lee, S.-L. Yang, E. W. Huang, B. Moritz, and T. Jia for discussions. ARPES experiments were performed at Beamline 5-4, Stanford Synchrotron Radiation Lightsource, SLAC National Accelerator Laboratory. **Funding:** Supported by the U.S. Department of Energy, Office of Science, Office of Basic Energy Sciences, Division of Materials Sciences and Engineering, under contract DE-AC02-76SF00515. **Author contributions:** S.-D.C., M.H., Y.H., and J.-F.H. performed the ARPES experiment. D.S., H.E., S.-D.C., and K.-J.X. prepared the samples. M.H. and D.-H.L. developed the ARPES setup. S.-D.C. analyzed the data. S.-D.C., M.H., Y.H., T.P.D., J.Z., and Z.-X.S. interpreted the data and wrote the manuscript with input from all authors. Z.-X.S. supervised the project. **Competing interests:** The authors declare no competing interests. **Data and materials availability:** All data presented in this work are available online at Harvard Dataverse (38).

## SUPPLEMENTARY MATERIALS

science.sciencemag.org/content/366/6469/1099/suppl/DC1  
Materials and Methods  
Supplementary Text  
Figs. S1 to S7  
Table S1  
References (39–45)

4 February 2019; accepted 1 November 2019  
10.1126/science.aaw8850



## SEISMOLOGY

# Illuminating seafloor faults and ocean dynamics with dark fiber distributed acoustic sensing

Nathaniel J. Lindsey<sup>1,2\*</sup>, T. Craig Dawe<sup>3</sup>, Jonathan B. Ajo-Franklin<sup>2,4</sup>

Distributed fiber-optic sensing technology coupled to existing subsea cables (dark fiber) allows observation of ocean and solid earth phenomena. We used an optical fiber from the cable supporting the Monterey Accelerated Research System during a 4-day maintenance period with a distributed acoustic sensing (DAS) instrument operating onshore, creating a ~10,000-component, 20-kilometer-long seismic array. Recordings of a minor earthquake wavefield identified multiple submarine fault zones. Ambient noise was dominated by shoaling ocean surface waves but also contained observations of in situ secondary microseism generation, post–low-tide bores, storm-induced sediment transport, infragravity waves, and breaking internal waves. DAS amplitudes in the microseism band tracked sea-state dynamics during a storm cycle in the northern Pacific. These observations highlight this method's potential for marine geophysics.

**T**he underwater environment that covers 70% of Earth's surface poses major logistical challenges to seafloor studies. Marine geophysical research is conducted with large research vessels, temporary ocean-bottom seismometers (1), and a limited number of permanent tethered observatories (2, 3). Emerging float networks, seafloor global navigation satellite system, and high-frequency remote sensing are beginning to infill major data gaps with promising near-real-time cov-

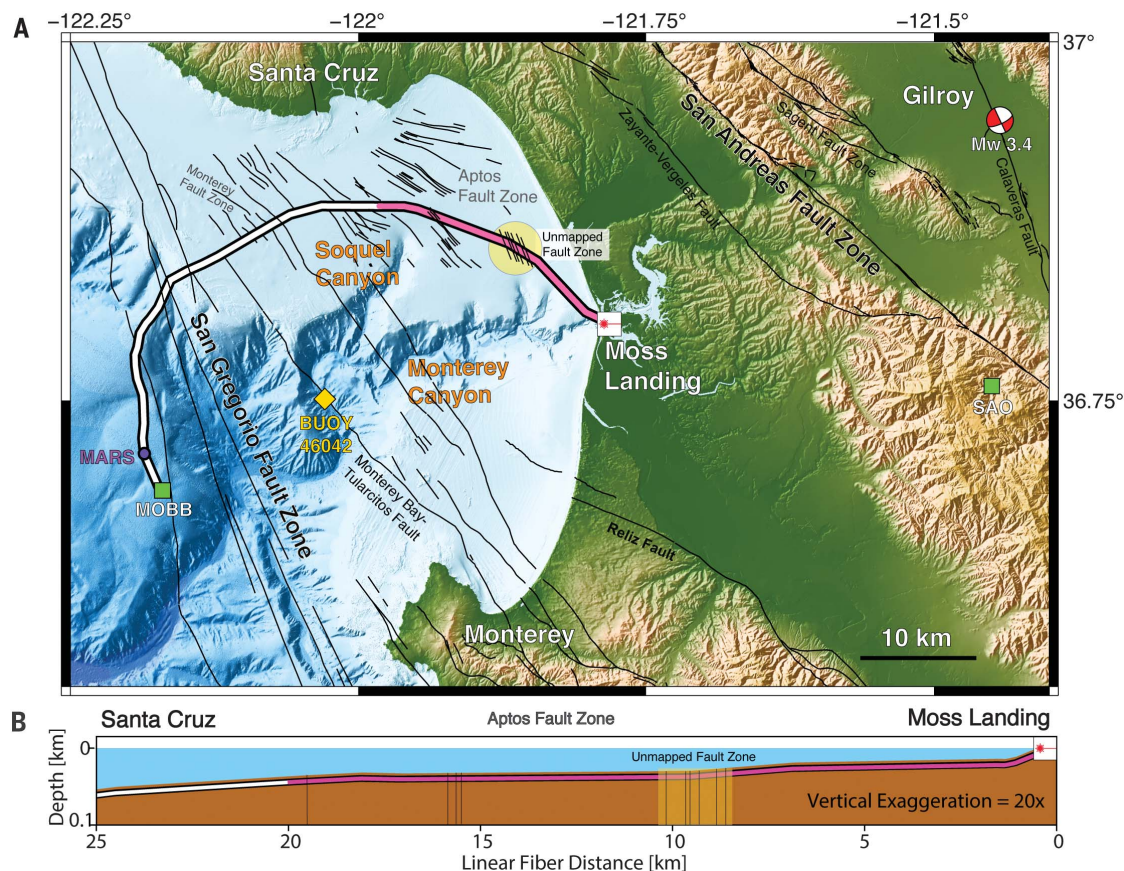
erage. The impact has included quantification of offshore seismic hazards (4, 5), submarine volcanism (6), marine ecology, and ocean transport (7), yet many oceanographic and solid-earth processes remain spatially aliased.

Fiber-optic sensing is an emerging means of recording dense geophysical information onshore (8, 9) and should be equally useful offshore, using existing dark fiber seafloor optical fibers. Marra *et al.* (10) proposed using transmission time-of-flight of ultrastable laser

pulses inside transoceanic subsea fibers to record cable-averaged seafloor strain. To examine seafloor strain with higher spatial resolution, we used backscattered laser pulses with phase-based coherent optical time-domain reflectometry ( $\phi$ -OTDR), otherwise known as distributed acoustic sensing (DAS), inside the Monterey Accelerated Research System (MARS) science cable that spans the continental shelf offshore of California (Fig. 1) (11). In contrast to the approach of Marra *et al.*, DAS multiplexes the optical analysis and thus resolves the seafloor strain field every 10 m, which in our case produced an array dataset totaling 3.2 TB collected over 4 days.

We recorded the 11 March 2018 strike-slip earthquake near Gilroy, CA, using the MARS cable. Figure 2 shows this earthquake wavefield DAS record after minimal data processing (11). P, pP, PP, S, and SS phase arrivals matched predicted arrival times for the U.S. Geological Survey-cataloged event solution and

**Fig. 1. MARS DAS experiment.** (A) Map of Monterey Bay, CA, shows MARS cable (DAS, pink portion), mapped faults, Gilroy earthquake (red-and-white beach ball), seismometers BK.SAO and BK.MOBB (green squares), NOAA buoy 46042 (yellow diamond), and major bathymetric features. (B) Cross-section illustration of MARS cable used for DAS.





cable geometry. The P-wave was barely visible over cable segments, potentially owing to the suboptimal orientation of particle motion relative to the fiber axis ( $\theta > 71^\circ$ ). Converted pP and PP phases with greater horizontal components were more robustly observed. Time-domain beamforming of the record found that energy arrived with equal components from the epicentral backazimuth of  $81^\circ\text{N}$  and a direction around  $45^\circ\text{N}$  (Fig. 2E), interpreted as seismic multipathing through the complex three-dimensional North American-Pacific plate boundary (12). A second source of scattering was found to originate from local structure immediately below the seafloor cable.

After each seismic phase, we observed strong coherent seismic energy propagating outward with apparent velocity of 200 to 600 m/s from discrete points between 15.1 and 16.3 km on the MARS cable and also between 8.4 and 10.3 km (Fig. 2, B to D). We interpreted this as body

wave conversion into Scholte waves at subvertical seafloor faults, which act as point scatterers. Scholte waves have Rayleigh-type wave motion and propagate at the ocean-solid earth interface. Wavefront tracking of the main SS phase showed slowdown between 14.5 and 16.5 km, coincident with observed scattering (Fig. 2D). Assuming wave propagation in the cable axis plane, velocity decreased from 2.1 km/s to 1.2 km/s over  $<1$  km. We interpreted this as a waveguide effect where seismic energy interacts with highly fractured, low-velocity fault zone gouge layers (13). Similar observations were made for the subsequent magnitude 2.7 aftershock.

Recent high-resolution seismic reflection imaging from this section of the continental shelf near Monterey and Soquel canyons identified extensive paleocanyon deposits and the NW-SE striking Aptos Fault Zone, a major step-over relay between the San Andreas Fault

Zone onshore and the San Gregorio Fault Zone offshore (14, 15). Four subvertical Aptos faults mapped in (14) transect the MARS cable around 15 to 17 km and near 19 km at an oblique angle (Fig. 1). These fault locations correlate with observed secondary scattering locations from the Gilroy event. We identified a number of unmapped faults (Fig. 1 for locations; strike based on regional information) in a segment extending the Aptos Fault Zone 15 to 20 km SSE parallel to shore, potentially connecting to the Monterey Canyon.

Ocean-solid earth interactions generate Rayleigh waves between 0.05 and 0.5 Hz, which are globally recorded as primary and secondary microseisms (16–19). In principle, horizontal seafloor fibers have zero strain sensitivity to primary microseism (PM) hydrostatic load changes. To test this hypothesis, we fit a PM model based on buoy wave height records to DAS strain data at 0.05 to 0.15 Hz (11). We

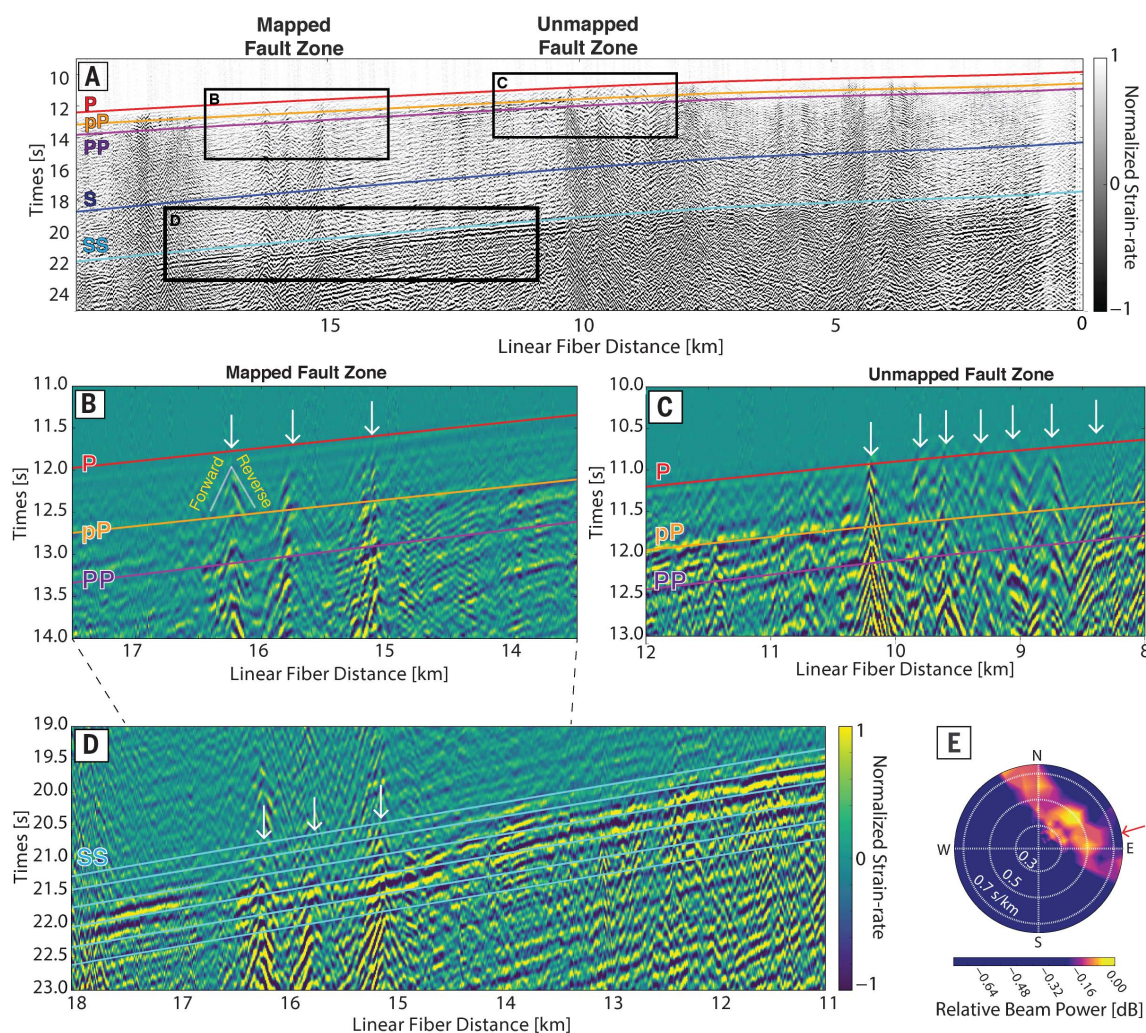


**Fig. 2. Magnitude 3.4 11 March 2018 Gilroy earthquake wavefield.** (A) Full array observation (0 indicates the shore) with predicted seismic phase arrivals (colored lines). (B) Inset shows scattering with recently mapped submarine fault locations (white arrows). (C) Same as (B), for an unmapped fault zone.

(D) Observed 0.25-s wavefront delay in mapped fault zone from (B). Lines show predicted constant phase arrivals immediately after the first SS wavefront. (E) Time-domain beamforming solution shows energy arriving from ENE azimuths, while red arrow shows predicted backazimuth.



found that these DAS records can be explained as PM (fig. S1), likely because the fiber package experiences a Poissonian strain response (20) or an unquantified transverse seafloor current motion in the shallow waters of Monterey Bay.

Tracking microseism energy over 4 days (Fig. 3), we observed a consistent response between buoy wave motion, seafloor DAS strain,

and seismometer noise onshore (11). All three instruments record high amplitudes during the initial period of high storm activity on 10 March 2018. Recorded amplitudes decrease as the first storm loses energy and then increase as the second storm builds. Small absolute frequency shifts and amplitude discrepancies between the three records could

be the result of a number of variables, including complicated energy partitioning, that is, the quality and character of microseism energy conversion at the ocean-continent interface; fiber and seismometer coupling; lateral separation and water-depth differences between the buoy and fiber (18); and poorly constrained ocean site effects (21).

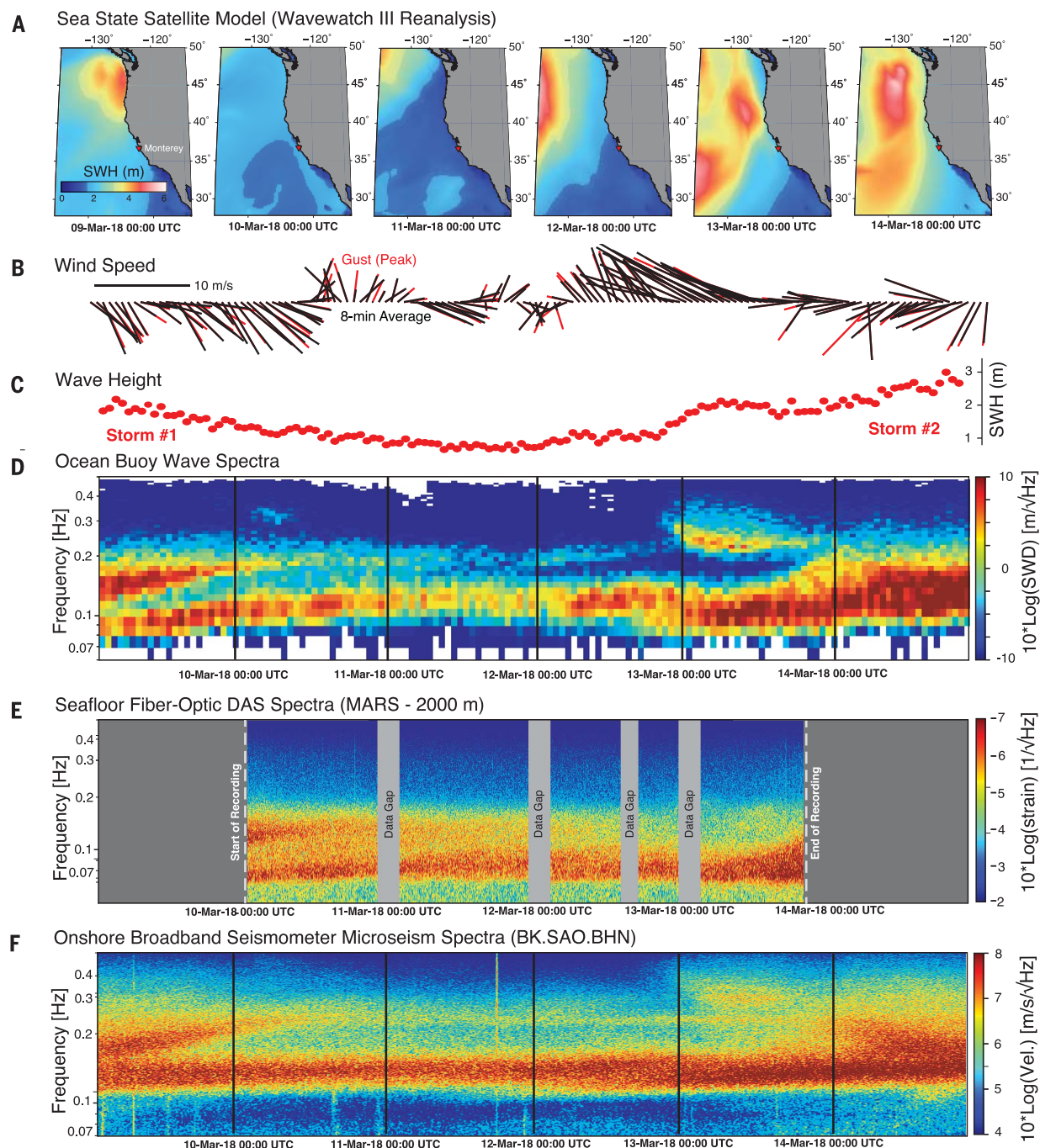


**Fig. 3. Multi-instrument analysis of sea-state evolution.** (A) Wavewatch III reanalysis of satellite remote-sensing data shows ocean wave height outside Monterey Bay (red triangle). (B to D) NOAA buoy 46042 8-min average measurements of wave speed and direction (black) and peak gust (red), and 10-min average wave height and spectral wave density (SWD) measurements.

(E) Seafloor DAS strain from cable location 2 km averaged over a 15-min sliding window. (F) North component of ground velocity from onshore broadband inertial seismometer BK.SAO averaged over a 15-min sliding window. Buoy, DAS, and seismometer measurements show time-lapse interactions of primary and secondary ocean microseism between two Pacific storm cycles.

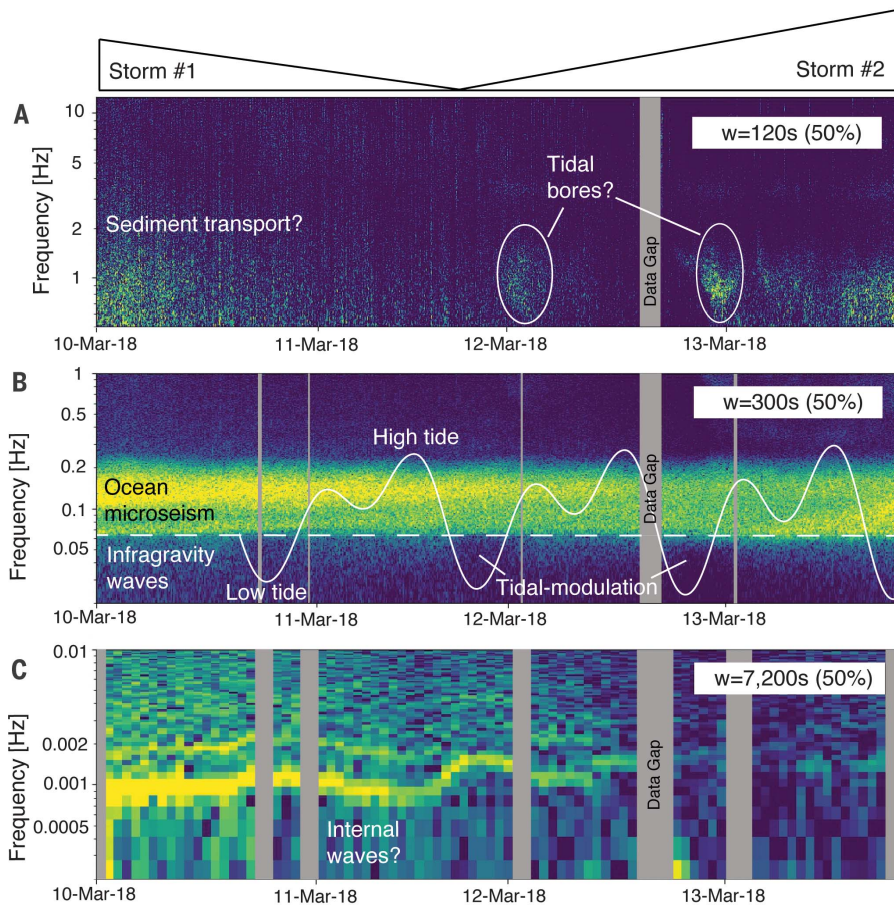


**Fig. 4. Broadband hydrodynamic signals.** DAS data for cable location 5.5 km analyzed with a sliding window ( $w$ ) of 120-, 300-, or 7200-s duration, 50% overlap. **(A)** 0.5 to 11 Hz: high-frequency noise consistent with timing of expected storm-induced sediment transport (see Fig. 3A for storm activity) and tidal bore activity. **(B)** 0.02 to 1 Hz: primary and secondary microseism observations changing energy with storm activity, with tidally modulated infragravity noise below 0.05 Hz; NOAA tide gauge 9413745 from Santa Cruz, CA, plotted for reference (mean lower low water level minimum =  $-0.03$  m, maximum =  $1.42$  m). **(C)** 0.0002 to 0.01 Hz: tidally modulated harmonic noise, potentially caused by bay seiche or breaking internal waves at the continental shelf. Data gaps change with window duration.

To assess energy partitioning, we decomposed the wavefield in the frequency-wavenumber domain. Shoaling wave loads in shallow water produce PMs (18, 22) that obey the dispersion equation

$$\omega^2 = g k \tanh(kH)$$

where  $\omega$  is angular frequency,  $g$  is gravitational acceleration,  $k$  is wavenumber, and  $H$  is water depth. DAS PM recordings were found to be strongly dispersive (fig. S2). Because PMs are caused by local wave height, outgoing components are the result of coast reflection. We thus computed that the reflected PM energy is  $\sim 1\%$  of the incoming energy.

The leading hypothesis for secondary microseism (SM) generation is that opposing wind-wave trains mix nonlinearly and produce Scholte waves at near-acoustic speeds (23, 24).

Testing this hypothesis requires observation of both opposing ocean waves and the resulting Scholte wave generation, which has only been documented in one deep-ocean environment (25). In Monterey Bay, we observed weak energy at 0.25 to 1.5 Hz and very low wavenumber ( $0.003 \text{ m}^{-1}$ ) with symmetric amplitude components traveling at 400 to 1000 m/s, faster than observed wind-wave speeds. We interpreted this as in situ SM generation ultimately produced by the nonlinear interaction of the aforementioned incoming and outgoing wind-waves (fig. S2C). This suggests that SMs are generated even when one wind-wave component is vanishingly small. SM amplitudes were 1.5 to 2 dB below PM, likely owing to the shallow water environment.

We detected a number of nonmicroseism hydrodynamic signals (Fig. 4). At 0.5 to 5 Hz, we observed decreasing amplitude as the first

storm lost energy, consistent with seafloor current-driven sediment transport similar to noise profiles of bedload transport observed onshore near rivers (26, 27). At 1 to 2 Hz, we observed transients coincident with rising tide, interpreted as thermal strain related to semi-diurnal internal tidal bores (28–31). At 0.005 to 0.05 Hz, we observed tidally modulated infragravity waves previously observed using the Monterey Bay seismometer supported by MARS (32). At  $\sim 0.001$  Hz, we also observed a strong gliding signal with harmonics declining in energy from 10 March 2018. Signal gliding correlated with high and low tide. The signal may be related to the higher harmonics of the Monterey Bay seiche (33), but water level monitoring documented stable seiche amplitudes (34). An alternative hypothesis is that this is a solid-earth tilt response to slow-moving internal gravity waves, vertical oscillations of the ocean stratification interface, which break near steep bathymetric features such as the Monterey Canyon (28, 35–37). Internal waves enhance cross-shelf transport of fluid and biology and are therefore foundational in models of thermohaline ocean circulation and marine ecology (38). Independent of the source mechanism, this low-frequency DAS signal highlights the potential utility of the method for studying quasi-geodetic strain phenomena.

#### REFERENCES AND NOTES

1. C. Deplus *et al.*, *Geology* **26**, 131 (1998).
2. B. Romanowicz, P. McGill, D. Neuhauser, D. Dolenc, *Seismol. Res. Lett.* **80**, 197–202 (2009).
3. J. Trowbridge *et al.*, *Front. Mar. Sci.* **6**, 74 (2019).
4. E. Gràcia, J. Dañoebitia, J. Vergés, P. A. R. S. I. F. A. L. Team, *Geology* **31**, 83 (2003).
5. S. Ruiz, R. Madariaga, *Tectonophysics* **733**, 37–56 (2018).
6. T. Mittal, B. Delbridge, *Earth Planet. Sci. Lett.* **511**, 105–116 (2019).
7. L. A. Levin *et al.*, *Front. Mar. Sci.* **6**, 241 (2019).
8. P. Jousset *et al.*, *Nat. Commun.* **9**, 2509 (2018).
9. J. B. Ajo-Franklin *et al.*, *Sci. Rep.* **9**, 1328 (2019).
10. G. Marra *et al.*, *Science* **361**, 486–490 (2018).
11. Materials and methods are available as supplementary materials.
12. A. J. Rodgers, A. Pitarka, N. A. Petersson, B. Sjögren, D. B. McCallen, *Geophys. Res. Lett.* **45**, 739–747 (2018).
13. Y.-G. Li, P. Leary, K. Aki, P. Malin, *Science* **249**, 763–766 (1990).
14. S. Y. Johnson *et al.*, *Ocean Coast. Manage.* **140**, 88–104 (2017).
15. K. L. Maier, S. Y. Johnson, P. Hart, *Mar. Geol.* **404**, 24–40 (2018).
16. R. A. Haubrich, K. McCamy, *Rev. Geophys.* **7**, 539 (1969).
17. T. Herbers, R. Guza, *J. Phys. Oceanogr.* **21**, 1740–1761 (1991).
18. P. D. Bromirski, F. K. Duennebie, *J. Geophys. Res. Solid Earth* **107**, 2166 (2002).
19. J. Zhang, P. Gerstoft, P. D. Bromirski, *Geophys. Res. Lett.* **37**, L15301 (2010).
20. M. Becker, C. Ciervo, M. Cole, T. Coleman, M. Mondanos, *Geophys. Res. Lett.* **44**, 7295–7302 (2017).
21. L. Gualtieri *et al.*, *Geophys. J. Int.* **197**, 1096–1106 (2014).
22. S. C. Webb, *Rev. Geophys.* **36**, 105–142 (1998).
23. M. S. Longuet-Higgins, *Philos. Trans. R. Soc. London Ser. A* **243**, 1–35 (1950).
24. K. Hasselmann, *Rev. Geophys.* **1**, 177 (1963).
25. E. Muzert, *Geophysics* **72**, U21–U26 (2007).
26. L. Hsu, N. J. Finnegan, E. E. Brodsky, *Geophys. Res. Lett.* **38**, L13407 (2011).



27. B. Schmandt *et al.*, *Geology* **45**, 299–302 (2017).
28. G. S. Carter, M. C. Gregg, R.-C. Lien, *Cont. Shelf Res.* **25**, 1499–1520 (2005).
29. R. K. Walter, C. B. Woodson, R. S. Arthur, O. B. Fringer, S. G. Monismith, *J. Geophys. Res. Oceans* **117**, C07017 (2012).
30. F. Cazenave, Y. Zhang, E. McPhee-Shaw, J. G. Bellingham, T. P. Stanton, *Limnol. Oceanogr. Methods* **9**, 571–581 (2011).
31. J. A. Colosi, N. Kumar, S. H. Suanda, T. M. Freismuth, J. H. MacMahān, *J. Phys. Oceanogr.* **48**, 123–143 (2018).
32. D. Dolenc, B. Romanowicz, D. Stakes, P. McGill, D. Neuhauser, *Geochem. Geophys. Geosyst.* **6**, Q09002 (2005).
33. L. C. Breaker, Y. Tseng, X. Wang, *Prog. Oceanogr.* **86**, 380–395 (2010).
34. J. Park, W. Sweet, R. Heitsenrether, *Ocean Sci.* **11**, 439–453 (2015).
35. C. Garrett, W. Munk, *Annu. Rev. Fluid Mech.* **11**, 339–369 (1979).
36. W. S. Holbrook, I. Fer, *Geophys. Res. Lett.* **32**, L15604 (2005).
37. E. Kunze, L. K. Rosenfeld, G. S. Carter, M. C. Gregg, *J. Phys. Oceanogr.* **32**, 1890–1913 (2002).
38. M. H. Alford *et al.*, *Nature* **521**, 65–69 (2015).
39. N. J. Lindsey, njlindsey/Photonic-seismology-in-Monterey-Bay-Dark-fiber1DAS-illuminates-offshore-faults-and-coastal-ocean: doi generation, Version 1, Zenodo (2019); doi.org/10.5281/zenodo.3475631.

#### ACKNOWLEDGMENTS

We thank D. Dreger, B. Romanowicz, S. Holbrook, L. Retailleau, L. Gualtieri, T. Mittal, S. Maurya, D. Neuhauser, C. Paull, three anonymous reviewers, and the editor for their insight. We thank Silixa for long-term support of our DAS acquisitions. **Funding:** N.J.L. was supported by NSF GRFP (DGE 1106400). J.B.A.-F. was supported by LBNL Laboratory Directed Research and Development Program (USDOE DE-AC02-05CH11231), which also supported the experiment. Analysis was supported in part by the GoMCarb Project (USDOE DE-AC02-05CH11231). MARS is funded under NSF Award 1514756 with additional support from the David and Lucille Packard Foundation/MBARI.

**Author contributions:** N.J.L. conceived of and designed the experiment, recorded and analyzed data, and wrote the manuscript. T.C.D. enabled MARS cable access and assisted in field operations. J.B.A.-F. supported the project, contributed to the manuscript, and supervised the project and analysis.

**Competing interests:** The authors have no competing interests.

**Data and materials availability:** Data used to generate the figures and support the findings of this manuscript are available at <https://github.com/njlindsey/Photonic-seismology-in-Monterey-Bay-Dark-fiber1DAS-illuminates-offshore-faults-and-coastal-ocean> and in (39).

#### SUPPLEMENTARY MATERIALS

[science.sciencemag.org/content/366/6469/1103/suppl/DC1](https://science.sciencemag.org/content/366/6469/1103/suppl/DC1)

Materials and Methods

Figs. S1 and S2

References (40–51)

1 July 2019; accepted 8 October 2019

10.1126/science.aay5881

## QUANTUM MATERIALS

## Quantum units from the topological engineering of molecular graphenoids

Federico Lombardi<sup>1</sup>, Alessandro Lodi<sup>1</sup>, Ji Ma<sup>2</sup>, Junzhi Liu<sup>2\*</sup>, Michael Slota<sup>1</sup>, Akimitsu Narita<sup>3†</sup>, William K. Myers<sup>4</sup>, Klaus Müllen<sup>3‡</sup>, Xinliang Feng<sup>2</sup>, Lapo Bogani<sup>1§</sup>

Robustly coherent spin centers that can be integrated into devices are a key ingredient of quantum technologies. Vacancies in semiconductors are excellent candidates, and theory predicts that defects in conjugated carbon materials should also display long coherence times. However, the quantum performance of carbon nanostructures has remained stunted by an inability to alter the sp<sup>2</sup>-carbon lattice with atomic precision. Here, we demonstrate that topological tailoring leads to superior quantum performance in molecular graphene nanostructures. We unravel the decoherence mechanisms, quantify nuclear and environmental effects, and observe spin-coherence times that outclass most nanomaterials. These results validate long-standing assumptions on the coherent behavior of topological defects in graphene and open up the possibility of introducing controlled quantum-coherent centers in the upcoming generation of carbon-based optoelectronic, electronic, and bioactive systems.

Current hopes of developing radically new technologies (1, 2) in computation, communications, security, and sensing rely on the quantum manipulation of charges (3), spins (4), or photons (5). One of the main approaches is defect engineering (1, 2), which has produced robust quantum systems in diamond and silicon carbide. Conjugated sp<sup>2</sup>-carbon nanomaterials would, in principle, be extremely appealing for quantum applications because they can be integrated into engineered devices (6) and possess intriguing mechanical (7) and transport properties (8). Methods to add spins to carbon nanomaterials include encaging heteroatoms inside fullerenes (9), confining electrons into carbon nanotubes (10), and functionalizing graphene nanoribbons (Fig. 1) (11). The manipulation of the honeycomb lattice (12, 13) using topological defects (14) is the approach that has seen most theoretical attention and could provide robustness against decoherence (15), single-photon optical control (16), and spintronic manipulation (17). On the other hand, the difficulty of reliably engineering point defects leaves it largely unexplored.

The desired level of control of the graphene lattice has become possible only recently, with the synthesis of molecules containing many fused rings in an sp<sup>2</sup>-carbon framework (18), where pentagonal rings can be introduced reliably at precise positions (19). It is useful to relate these structures, obtained with bottom-up synthesis, to their equivalents on a graphene lattice (Fig. 1). After two (1,0) dislocations form (Stone-Wales defect), the heptagon-pentagon pairs can migrate. The lattice can then be trimmed down along the graphene stripe containing the dislocations to the desired geometry. Chemical stabilization by reso-

nance will still occur, but the resonance structure with the most disjoint benzene-like moieties is the most relevant (Clar's  $\pi$ -sextet rule) (16). The resulting extended open-shell molecule, with singlet and triplet states separated (20) by an energy gap  $2J$ , is, in essence, one small graphene quantum dot with topology and defect positions shaped with atomic precision. Although the associated chemistry is seeing a veritable explosion for optoelectronic, biological, and energy applications (21), the potential of these molecules for quantum devices remains unexplored and untapped.

Our molecule of choice is a saddle-shaped diindeno-fused bischrysene (**1**) with highly stable open-shell biradical feature (22) (Fig. 2A). It contains a conjugated aromatic backbone and two pentagonal rings; as compared with the perfect heptagon-pentagon pairs, the difference is an unformed bond in each heptagonal ring. It is synthesized from the 11,11'-dibromo-5,5'-bischrysene (**S1**) in five steps (Fig. 2A and supplementary materials). The synthesis of such radicaloids has one often-overlooked feature: Incomplete dehydrogenation in the final step can lead to open-shell monoradical species (**1b**) at impurity concentrations, which are hard to identify by structural characterization methods. For instance, because **1b** differs by one single hydrogen, it cannot be completely removed from **1** and is undetectable by mass spectrometry. For our purposes, **1b** is useful because it allows for determining the behavior of single pentagonal

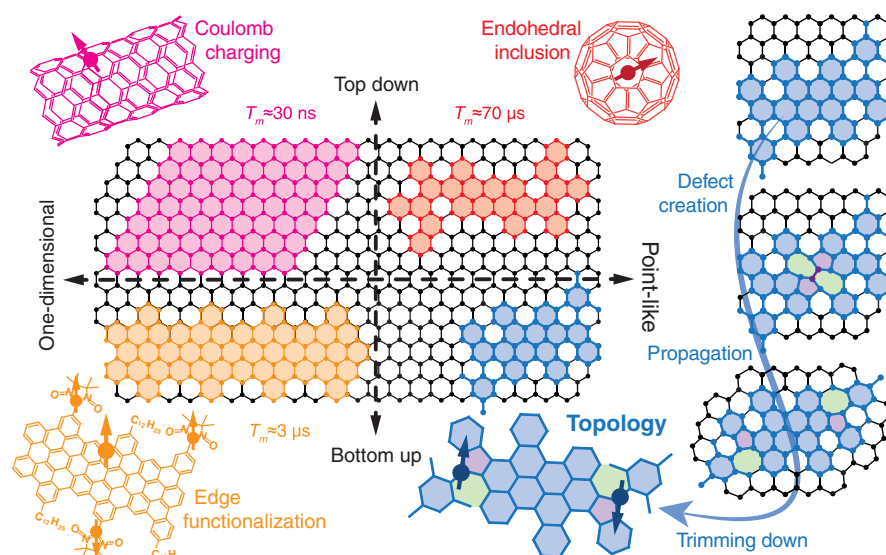


**Fig. 1. Strategies toward obtaining aromatic quantum units.** Quantum spin properties are introduced by heteroatom inclusion for endohedral fullerenes (red), Coulomb charging for carbon nanotubes (magenta), and side-functionalization in graphene nanoribbons (orange). Coherence times refer to room temperature, except for carbon nanotubes (mK). Topological stabilization of magnetic centers is obtained by rational synthetic tailoring of the lattice with atomic precision at preconceived sites (blue). The result is akin to a sequence (right) of introducing a Stone-Wales defect (purple and green), followed by propagation and trimming down.

<sup>1</sup>Department of Materials, University of Oxford, 16 Parks Road, OX1 3PH Oxford, UK. <sup>2</sup>Center for Advancing Electronics Dresden (cfaed), Faculty of Chemistry and Food Chemistry, Technische Universität Dresden, Mommsenstraße 4, 01069 Dresden, Germany. <sup>3</sup>Max Planck Institut für Polymerforschung, Ackermannweg 10, 55128 Mainz, Germany. <sup>4</sup>Inorganic Chemistry, University of Oxford, South Parks Road, OX1 3QR Oxford, UK.

\*Present address: Department of Chemistry and State Key Laboratory of Synthetic Chemistry, The University of Hong Kong, Pokfulam Road, Hong Kong, China. †Present address: Organic and Carbon Nanomaterials Unit, Okinawa Institute of Science and Technology Graduate University, 1919-1 Tancha, Onna-son, Kunigami, Okinawa 904-0495, Japan. ‡Present address: Institute of Physical Chemistry, Johannes Gutenberg-University Mainz, Duesbergweg 10-14, D-55128 Mainz, Germany.

§Corresponding author. Email: lapo.bogani@materials.ox.ac.uk



elements in the honeycomb lattice—that is, a positive disclination—which is particularly relevant at graphene edges (23). Although the signal from **1b** is overshadowed by **1** at room temperature, it is selectively addressable at low temperature,  $T$ , where **1** is completely in the singlet state.

The room-temperature electron paramagnetic resonance (EPR) spectrum shows a single peak of width 0.8 mT in a magnetic field and electron Landé factor  $g = 2.0027 \pm 0.0002$  (Fig. 2B). This matches the expected signal for completely delocalized unpaired electrons in graphene, where dipolar and hyperfine couplings are weak (24). The linewidth (<1 mT) is incompatible with metal ions and analogous to the signals reported for radicaloids (20–22). Simulation with a spin  $S = 1$  in the high-

exchange limit provides excellent agreement. Interestingly, no half-field signal is observed, nor any fine structure, possibly indicating a curvature-induced spin-orbit coupling higher than our accessible energy scale (25), as is the case for the curvature displayed by **1**. The integrated EPR signal decreases rapidly on lowering  $T$  and levels off at  $\sim 90$  K, below which temperature **1b** is selectively addressable (Fig. 2C). Fitting with the Bleaney-Bowers equation (11) plus a paramagnetic species indicates that  $\sim 2\%$  of the molecules are **1b** and that **1** has an antiferromagnetic  $2J = 50 \pm 2$  meV.

The quantum evolution of a spin is often visualized as a movement over the Bloch sphere: Zenith positions indicate pure  $|1/2\rangle$  and  $|-1/2\rangle$  states, and any possible quantum state  $|\sigma\rangle = \cos(\frac{\vartheta}{2})|1/2\rangle + e^{i\varphi}\sin(\frac{\vartheta}{2})|-1/2\rangle$  is represented by a

point on the spherical surface. The spin-flip time,  $T_1$ , represents vertical displacement (variations of  $\vartheta$ ), whereas the evolution of the quantum phase  $\varphi$  is described by the azimuthal movement and the associated time  $T_2$ . We measure  $T_1$  with inversion recovery (26) and a lower bound of  $T_2$  that also contains spin- and spectral-diffusion effects that are absent in single-molecule measurements, called  $T_m$ , by the Hahn-echo sequence (Fig. 3A). The coherence times of the two species, when discernible, are hereby labeled  $T_{m1}$  and  $T_{m1b}$ . We fit the spin recovery via a biexponential function (Fig. 3B and supplementary materials) and the Hahn-echo decay with the function  $Y(\tau) = Y_0 \left[ \xi_1 e^{-\left(\frac{2\tau}{T_{m1}}\right)^x} + \xi_{1b} e^{-\left(\frac{2\tau}{T_{m1b}}\right)^x} \right] \Xi$ , where  $Y(\tau)$  is the echo signal,  $Y_0 = Y(\tau = 0)$ , and

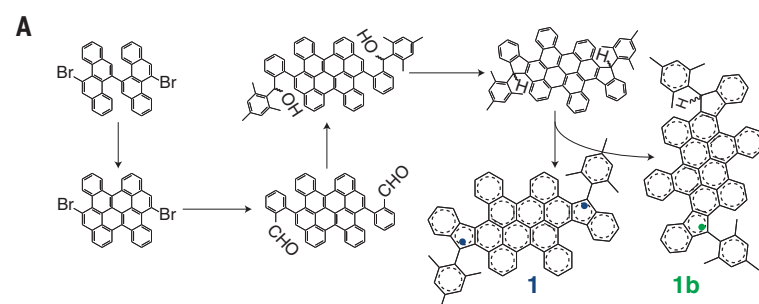


**Fig. 2. Polycyclic aromatic radicaloids.** (A) Synthesis of **1**, including the monoradical **1b**, produced by incomplete dehydrogenation in the final step. (B) EPR spectrum of **1** (blue) and simulation (black).  $B$ , static magnetic field. (C) Temperature dependence of the integrated EPR intensity (circles), fitted to a Bleaney-Bowers equation (black line). The bottom panel displays the signal fraction  $\xi$  produced, at every temperature, by **1** (blue) and by **1b** (green). The error bars arise from uncertainties in the quality factor of the resonator.

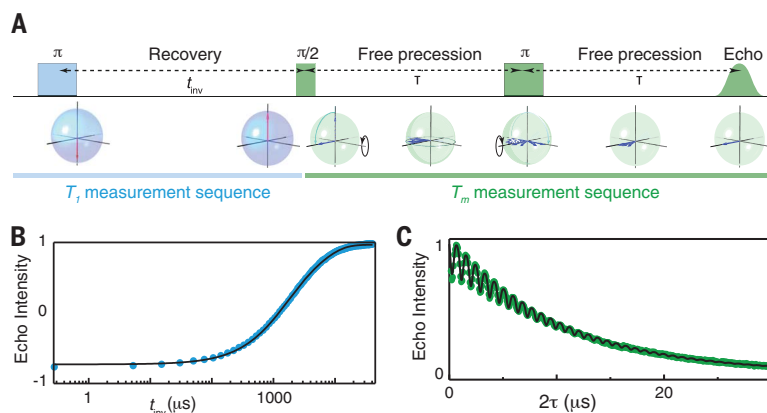
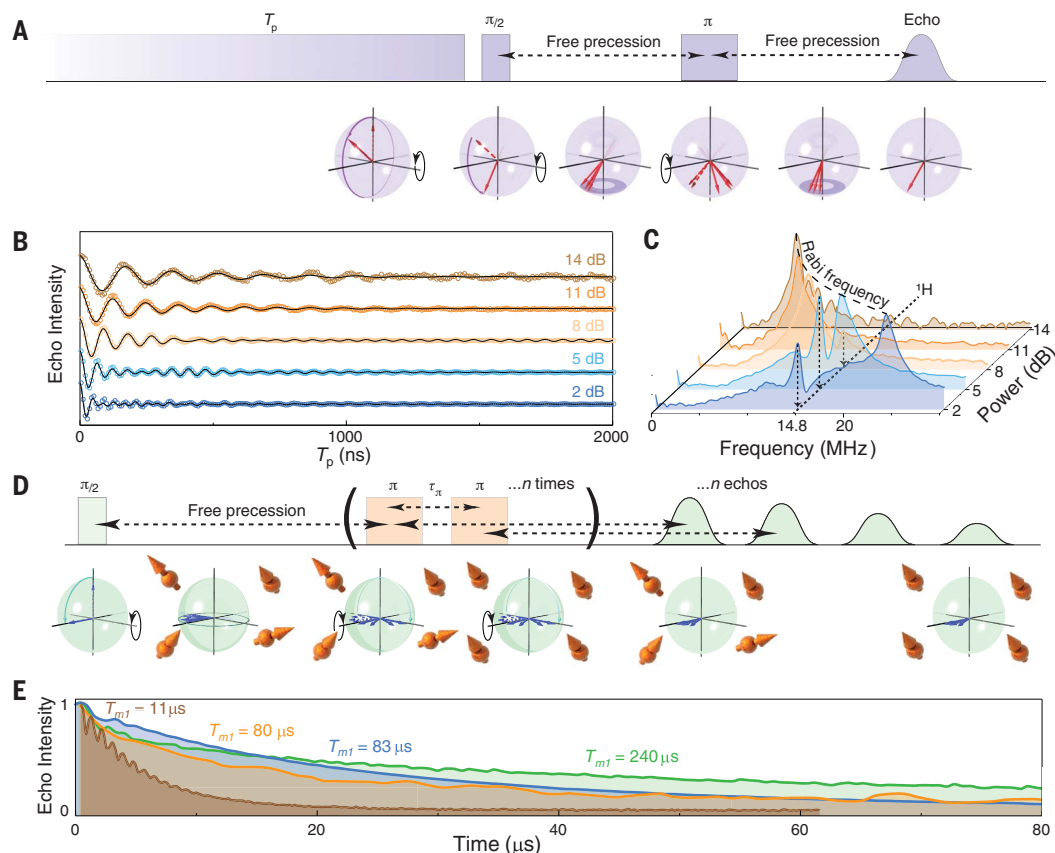


**Fig. 3. Spin-lattice and coherence times.** (A) Pulse sequence used for the detection of the spin-lattice (azure) and coherence (green) times, together with a Bloch sphere representation.  $t_{inv}$ , recovery time. (B) Example of signal recovery, from which  $T_1$  is extracted ( $T = 100$  K; line is fit to the data, see text). (C) Hahn-echo intensity versus delay time, from which  $T_m$  is extracted ( $T = 100$  K; line is fit to the data, see text). (D) Temperature dependence of the inverse spin-lattice relaxation time (top) and of the spin coherence time

(bottom) in powders (blue full circles), toluene (green half-filled circles), *d*-toluene (blue open symbols), and  $CS_2$  (green open symbols). Circles represent **1**, and pentagons represent **1b**. Arrows and full hexagons represent values with nuclear decoupling (Fig. 4). Errors are smaller than the symbols. Lines for  $T_1$  are fits to the data (see text), with the different dynamic regimes shaded. Lines for  $T_m$  are guides to the eye. Vertical dashed lines indicate the freezing temperatures of toluene and  $CS_2$ .

**Fig. 4. Rabi oscillations and nuclear demodulation.** (A) Pulse sequence for the measurement of Rabi oscillations. The nutation pulse length  $T_p$  is tuned so as to vary the azimuthal position on the Bloch sphere, followed by detection. (B) Echo intensity versus  $T_p$ , at different pulse powers ( $T = 80$  K). Black lines are fits to the data. (C) Spectral composition of the time-domain data showing the quadratic dependence of the Rabi frequency on the microwave power (dashed) and the power-independent  $^1\text{H}$  frequency. (D) Pulse sequence used to progressively cancel the dephasing effect of all nuclei (orange) with Larmor precession time  $\tau_\pi$ , leading to multiple echoes. (E) Echo signal decays at  $T = 120$  K without (brown represents *d*-toluene, and orange represents  $\text{CS}_2$ ) and with nuclear decoupling, with interpulse spacing  $\tau_\pi = 840$  ns for *d*-toluene (blue) and  $\tau_\pi = 680$  ns for  $\text{CS}_2$  (green). The corresponding coherence times are reported beside the curves.



$\xi_1$  and  $\xi_{1b} = 1 - \xi_1$  are the weights of **1** and **1b**, from Fig. 2C.  $\Xi = [1 + k_1 \sin(2\omega\tau + \varphi_1) + k_2 \sin(4\omega\tau + \varphi_2)]$  does not affect the extracted decoherence, describing the modulation at a nucleus-specific frequency  $\omega/2\pi = 14.8$  MHz for  $^1\text{H}$  and 2.4 MHz for  $^2\text{H}$ , with amplitudes  $k_1$  and  $k_2$  and phases  $\varphi_1$  and  $\varphi_2$  for first- and second-order effects (Fig. 3C). Good agreement is always found with stretching parameter  $0.9 < x < 1$  (27).

The spin environment strongly affects both  $T_1$  and  $T_2$ . For example, the coherence time of anionic nitrogen-vacancy-pair defects is severely suppressed when in close proximity to the diamond surface (28). Hereafter, we thus assess the behavior of **1** and **1b** in crystalline powders and toluene, deuterated-toluene, and carbon disulfide ( $\text{CS}_2$ ) solutions (Fig. 3D).

For powders,  $T_1$  increases from 1  $\mu\text{s}$  at room temperature to 100  $\mu\text{s}$  at 5 K, in overall agreement with semiconductors (29, 30). Both spectral diffusion and intermolecular electronic effects, such as  $\pi$ -stacking interactions, likely limit  $T_1$  in such a closely packed arrangement in the solid state, and dissolution into solvents produces a 1000-fold increase in  $T_1$ , up to 1 s at 5 K. In solutions,  $T_1$  is limited by molecular tumbling and increases only slightly on lowering  $T$ . At lower temperatures (170 K for toluene and 160 K for  $\text{CS}_2$ ), the solvents turn into a glassy matrix and a two-phonon Raman pro-

cess becomes dominant down to 15 K, below which direct processes dominate the spin-flip mechanism. Good agreement (Fig. 3D) is obtained with the expression  $T_1^{-1} = A_{\text{dir}} T + A_{\text{Ram}} \left(\frac{T}{\vartheta_D}\right)^9 \int_0^{\vartheta_D/T} x^8 e^x / (e^x - 1)^2 dx$ , where  $A_i$  are weights for the two processes and  $\vartheta_D$  is the Debye temperature (11). In the solid state,  $\Xi = 1$  and  $Y(\tau)$  is monoexponential, yielding  $T_m \approx 300$  ns in the whole  $T$  range. Dipolar and hyperfine interactions cannot be solely responsible for the decoherence mechanism; were this true,  $T_m$  would increase and approach the  $\text{CS}_2$  solution value below 80 K, where only **1b** contributes, and a modulation of the echo decay would be observed (e.g., as in Fig. 3C). Decoherence is likely driven by electron-electron scattering along the  $\pi$ -stacks, which are broken up by solvation. In this sense, these molecular systems behave differently from very-large-bandgap semiconductors—for example, diamond—and rational chemical design eliminating the  $\pi$ -stacking interactions could improve the solid-state coherence.

The suppression of stacking by solvation increases  $T_m$  more than 30-fold, and reduction of the solvent nuclear bath by deuteration and by  $\text{CS}_2$  produces a further increase. Several  $T_m$ -limiting mechanisms can be identified. Above the solvent freezing point,  $\Xi = 1$  and  $Y(\tau)$  is monoexponential, because molecular tumbling

limits both  $T_m$  and  $T_1$ . Upon freezing,  $\Xi$  reveals hyperfine modulation by  $^1\text{H}$  and  $^2\text{H}$  and no modulation for  $\text{CS}_2$ , showing dominant solvent hyperfine coupling. In toluene,  $Y(\tau)$  is always monoexponential, whereas in *d*-toluene and  $\text{CS}_2$ , the suppression of solvent  $^1\text{H}$ -hyperfine interactions allows for resolving both  $T_{m1}$  and  $T_{m1b}$ , and  $Y(\tau)$  is biexponential wherever **1** and **1b** coexist.  $T_{m1b}$  displays a maximum, with the low- $T$  behavior dominated by decoherence via intramolecular hyperfine coupling and modulated by the progressive blocking of the methyl rotational motion (31). In *d*-toluene,  $T_{m1}$  is found to rise steadily up to 28  $\mu\text{s}$  at 80 K, and in  $\text{CS}_2$ , the same trend is found but with much improved times, with  $T_{m1}$  reaching 0.1 ms at  $T = 90$  K.

To verify that the spins can be initialized into an arbitrary superposition of states, we performed nutation experiments (Fig. 4A), detecting Rabi oscillation decays (Fig. 4B) (32). Fourier analysis confirms the quantum behavior, with the Rabi frequency proportional to the square root of the applied power (Fig. 4C). Because  $2J \sim 10$  THz is much higher than the 10- to 100-MHz driving, which is in turn much higher than the axial spin anisotropy, no unusual evolution of the Rabi is expected (33), as is indeed observed. This analysis also indicates how to improve coherence: The power-independent peak at 14.8 MHz



corresponds to the  $^1\text{H}$  Larmor frequency, meaning that microwave initialization pulses can also drive and decouple the nuclei—for example, by a train of  $\pi$ -pulses, with interpulse intervals  $\tau_\pi$  that are multiples of the inverse of the nuclear Larmor frequency,  $1/\nu_L$  (Fig. 4D) (34). In *d*-toluene, decoupling from the solvent nuclei yields a fivefold improvement, producing times comparable to those in  $\text{CS}_2$  (e.g.,  $T_{\text{mib}} = 38\ \mu\text{s}$  and  $T_{\text{m1}} = 260\ \mu\text{s}$  at 80 K). The role of the intramolecular hyperfine interactions is revealed by decoupling from the molecular hydrogens in  $\text{CS}_2$ : We observe a threefold increase of the coherence, up to  $T_{\text{m1}} = 290\ \mu\text{s}$  at 80 K. At room temperature, the decoupling allows for reaching  $T_{\text{m}} = 2\ \mu\text{s}$ , close to the maximum attainable limit  $2T_1 = 4.5\ \mu\text{s}$ .

These observations confirm experimentally the possibility of superior quantum performance in carbon-based nanostructures. The coherence times, although still below those of defects implanted deep into bulk semiconductors (1, 2, 35) and semiconducting quantum dots at millikelvin temperatures (36), outshine the latter at high temperatures and show overall agreement with predictions for graphene quantum dots with  $>10$  nuclear spins (37). Although the quantum performance already beats the quantum behavior of diamondoids and shallowly implanted defects (25), there is ample room for optimization: The measured room-temperature values are limited by tumbling in the solvent, and very basic optimization—for example, by immobilization in an oriented diamagnetic matrix or on surfaces—is likely to produce large improvements. These results can now be used to reconsider the quantum magnetic states of graphene devices, where spins are introduced by similar defects (38). Chemical inclusion into conducting nanostructures, such as nanoribbons and graphene sheets, or fusing several molecules into double and multiple quantum dots, opens the path to using quantum effects in the next generation of optoelectronic, electric, and bioactive systems. When considering the body of work already dedicated

to the integration of similar molecules into electronic devices and biologically relevant environments (18), these outcomes appear well within grasp. Optical detection and manipulation are particularly appealing—for example, via the observed single-photon emission (16)—and we may anticipate that these systems will evolve soon into synthetic analogs to optically active quantum centers in semiconductors. In this sense, it is crucial that these observations offer a rational synthetic pathway to add any desired functionality to a graphene quantum unit, opening up an unprecedented multitude of options for the optics and magnetism of quantum nanomaterials.

## REFERENCES AND NOTES

1. M. Atătute, D. Englund, N. Vamivakas, S.-Y. Lee, J. Wrachtrup, *Nat. Rev. Mater.* **3**, 38–51 (2018).
2. D. D. Awschalom, L. C. Bassett, A. S. Dzurak, E. L. Hu, J. R. Petta, *Science* **339**, 1174–1179 (2013).
3. L. M. K. Vandersypen et al., *npj Quantum Inf.* **3**, 34 (2017).
4. A. Gaita-Ariño, F. Luis, S. Hill, E. Coronado, *Nat. Chem.* **11**, 301–309 (2019).
5. D. D. Awschalom, R. Hanson, J. Wrachtrup, B. B. Zhou, *Nat. Photonics* **12**, 516–527 (2018).
6. M. M. Shulaker et al., *Nature* **501**, 526–530 (2013).
7. B. Lassagne, Y. Tarakanov, J. Kinaret, D. Garcia-Sanchez, A. Bachtold, *Science* **325**, 1107–1110 (2009).
8. E. A. Laird et al., *Rev. Mod. Phys.* **87**, 703–764 (2015).
9. M. Mehring, W. Scherer, A. Weidinger, *Phys. Rev. Lett.* **93**, 206603 (2004).
10. T. Cubaynes et al., *npj Quantum Inf.* **5**, 47 (2019).
11. M. Slota et al., *Nature* **557**, 691–695 (2018).
12. P. Recher, B. Trauzettel, *Nanotechnology* **21**, 302001 (2010).
13. O. V. Yazyev, S. G. Louie, *Phys. Rev. B Condens. Matter Mater. Phys.* **81**, 195420 (2010).
14. J. C. Meyer et al., *Nano Lett.* **8**, 3582–3586 (2008).
15. B. Trauzettel, D. V. Bulaev, D. Loss, G. Burkard, *Nat. Phys.* **3**, 192–196 (2007).
16. S. Zhao et al., *Nat. Commun.* **9**, 3470 (2018).
17. W. Han, R. K. Kawakami, M. Gmitra, J. Fabian, *Nat. Nanotechnol.* **9**, 794–807 (2014).
18. A. Narita, X. Y. Wang, X. Feng, K. Müllen, *Chem. Soc. Rev.* **44**, 6616–6643 (2015).
19. N. Martín, L. T. Scott, *Chem. Soc. Rev.* **44**, 6397–6400 (2015).
20. Z. Zeng et al., *Chem. Soc. Rev.* **44**, 6578–6596 (2015).
21. T. Y. Gopalakrishna, W. Zeng, X. Lu, J. Wu, *Chem. Commun.* **54**, 2186–2199 (2018).
22. J. Ma et al., *Angew. Chem. Int. Ed.* **56**, 3280–3284 (2017).
23. J. Li et al., *Sci. Adv.* **4**, eaq0582 (2018).
24. S. Perumal, B. Minaev, H. Ågren, *J. Chem. Phys.* **136**, 104702 (2012).
25. D. Huertas-Hernando, F. Guinea, A. Brataas, *Phys. Rev. B Condens. Matter Mater. Phys.* **74**, 155426 (2006).
26. G. R. Eaton, S. S. Eaton, *Multifrequency Electron Paramagnetic Resonance: Theory and Applications* (Wiley, 2011).
27. J. R. Klauder, P. W. Anderson, *Phys. Rev.* **125**, 912–932 (1962).
28. B. A. Myers, A. Ariyaratne, A. C. B. Jayich, *Phys. Rev. Lett.* **118**, 197201 (2017).
29. V. A. Dediu, L. E. Hueso, I. Bergenti, C. Taliani, *Nat. Mater.* **8**, 707–716 (2009).
30. C. Volk et al., *Nat. Commun.* **4**, 1753 (2013).
31. A. Lund, S. Masaru, Eds., *EPR of Free Radicals in Solids I: Trends in Methods and Applications* (Progress in Theoretical Chemistry and Physics Series Book 24, Springer, 2012).
32. G. D. Fuchs et al., *Nat. Phys.* **6**, 668–672 (2010).
33. R. Glenn, M. E. Limes, B. Saam, C. Boehme, M. E. Raikh, *Phys. Rev. B Condens. Matter Mater. Phys.* **87**, 165205 (2013).
34. P. C. Maurer et al., *Science* **336**, 1283–1286 (2012).
35. G. Balasubramanian et al., *Nat. Mater.* **8**, 383–387 (2009).
36. M. Veldhorst et al., *Nat. Nanotechnol.* **9**, 981–985 (2014).
37. J. Fischer, B. Trauzettel, D. Loss, *Phys. Rev. B Condens. Matter Mater. Phys.* **80**, 155401 (2009).
38. R. R. Nair et al., *Nat. Commun.* **4**, 2010 (2013).
39. F. Lombardi, L. Bogani, Dataset: Quantum units from the topological engineering of molecular graphenoids. Oxford University Research Archive (2019); doi: 10.5287/oxdilean:j1EEx741w.

## ACKNOWLEDGMENTS

We thank A. Ardavan for useful discussions. **Funding:** This work was funded by the European Union (ERC-StG-338258-OptoQMol, ERC-CoG-773048-MMGNr, ERC-CoG-819698-T2DCP, Graphene Flagship-Core2-696656, and European Social Fund); the Royal Society (University Research Fellow and URF grant); UK-EPSC EP/L011972/1; German DFG (Excellence Cluster CFAED and EnhanceNano-391979941); and the Max Planck Gesellschaft and Saxony ESF-Project-GRAPHD. **Author contributions:** F.L. and A.L. performed the EPR measurements, and M.S. and W.K.M. assisted them. J.M. synthesized the compounds and performed the chemical characterization, for which J.L. and X.F. provided supervision. F.L. and L.B. performed the data analysis. L.B. coordinated the experiments and wrote the paper. **Competing interests:** The authors declare no competing interests. **Data and materials availability:** All data are available in the main text or the supplementary materials. All raw data and scripts are stored in the computer center of the University of Oxford. All datasets are freely available at the Oxford University Research Archive at <https://ora.ox.ac.uk/objects/uuid:99b46501-e3c5-4410-91ac-0e643939a4a6> (39).

## SUPPLEMENTARY MATERIALS

[science.sciencemag.org/content/366/6469/1107/suppl/DC1](https://science.sciencemag.org/content/366/6469/1107/suppl/DC1)  
Materials and Methods  
Supplementary Text  
Figs. S1 to S10  
References (40–43)

12 July 2019; accepted 30 October 2019  
10.1126/science.aay7203

## CHEMICAL PHYSICS

## Direct observation of bimolecular reactions of ultracold KRb molecules

M.-G. Hu<sup>1,2,3\*</sup>, Y. Liu<sup>2,1,3\*</sup>, D. D. Grimes<sup>1,2,3</sup>, Y.-W. Lin<sup>1,2,3</sup>, A. H. Gheorghe<sup>2</sup>, R. Vexiau<sup>4</sup>, N. Bouloufa-Maafa<sup>4</sup>, O. Dulieu<sup>4</sup>, T. Rosenband<sup>2</sup>, K.-K. Ni<sup>1,2,3,†</sup>

Femtochemistry techniques have been instrumental in accessing the short time scales necessary to probe transient intermediates in chemical reactions. In this study, we took the contrasting approach of prolonging the lifetime of an intermediate by preparing reactant molecules in their lowest rovibronic quantum state at ultralow temperatures, thereby markedly reducing the number of exit channels accessible upon their mutual collision. Using ionization spectroscopy and velocity-map imaging of a trapped gas of potassium-rubidium (KRb) molecules at a temperature of 500 nanokelvin, we directly observed reactants, intermediates, and products of the reaction  $^{40}\text{K}^{87}\text{Rb} + ^{40}\text{K}^{87}\text{Rb} \rightarrow \text{K}_2\text{Rb}_2^* \rightarrow \text{K}_2 + \text{Rb}_2$ . Beyond observation of a long-lived, energy-rich intermediate complex, this technique opens the door to further studies of quantum-state-resolved reaction dynamics in the ultracold regime.

The creation of ensembles of molecules at ultralow temperatures enables a variety of high-resolution spectroscopic studies, allows broader exploration of reaction phase space, and promises quantum-state control over the outcome of chemical reactions. Already, investigations of single partial-wave collisions have provided detailed benchmarks of short-range molecular potentials (1, 2), exotic conditions at low temperatures have facilitated the synthesis of new chemical species (3), and highly sensitive and precise methods of detection have traced state-to-state reactions between atoms and weakly bound Feshbach molecules (4). Further, chemical reaction rates for barrierless reactions can be altered (5, 6), in some case by orders of magnitude, merely by changing the nuclear spins of the reactants and entering quantum degeneracy (7). These studies all rely on the substantial control attainable over the quantum states of the ultracold molecules.

Despite recent advances in ultracold molecule studies, a key capability has been missing: namely, characterization of transient reaction intermediates and final products. Previous experiments have shown evidence of ultracold reactions between alkali molecules through the quantum-state-specific detection of loss of reactants (5), similar to that shown in the inset to Fig. 1, providing insights into how long-range forces determine the kinetic collision rates of the reactants. These reactions have been observed to occur with a high probability after just a single collision, approaching unity in certain cases (5, 8, 9). Despite four-de-force

levels of control over the precise rovibrational quantum state of the reactants to open up additional energetically allowed reaction chan-

nels, no substantial differences based on the reactant species or initial quantum state have yet been observed (8, 9), and the nature of the molecular loss is still a matter of debate (10).

When two molecules approach one another, they initially form an energy-rich intermediate collision complex, the dynamics of which could hold the key for understanding the details of the ensuing ultracold, barrierless, bimolecular reactions. In higher-temperature reactions, this transient complex persists for only one or two vibrational periods and, at most, on the order of a rotational period (~1 ps) (11, 12). Studying the dynamics or kinetics of such complexes in the gas phase has typically required ultrafast (13–17) or stabilizing collisional (18–20) techniques. Structural investigations of these complexes have been previously obtained by photodetachment (21, 22), photoabsorption (23), or photodissociation (24). On the basis of the Rice-Ramsperger-Kassel-Marcus (RRKM) theory, the lifetime of an intermediate complex is given by  $\tau_c = 2\pi\rho_c/N_o$ ,

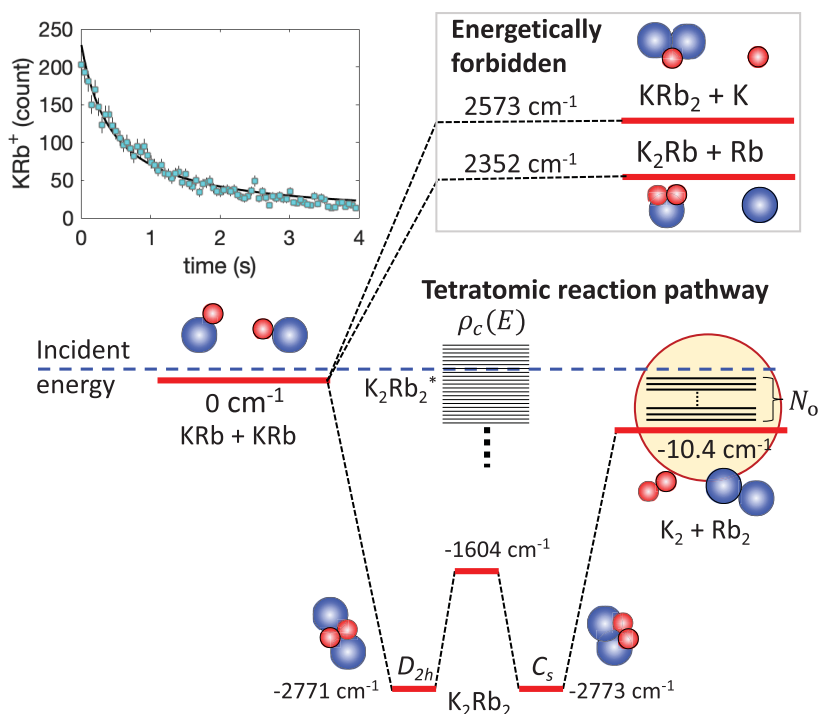


**Fig. 1. Energetics of the bimolecular reactions of ultracold KRb molecules.** The ground-state energies are obtained from spectroscopic data for KRb (28), K<sub>2</sub> (38), and Rb<sub>2</sub> (39) and from calculation for KRB<sub>2</sub>, K<sub>2</sub>Rb, and K<sub>2</sub>Rb<sub>2</sub> at the equilibrium configuration (40). Here, we define the incident energy of two free KRb molecules as zero energy. Because the energies of the triatomic reaction channels are much higher than those of the reactants, these channels are energetically forbidden. In comparison, the tetratomic reaction channel KRb + KRb → K<sub>2</sub>Rb<sub>2</sub>\* → K<sub>2</sub> + Rb<sub>2</sub> is exothermic and therefore energetically allowed. K<sub>2</sub>Rb<sub>2</sub>\* denotes the transient intermediate complex.  $\rho_c(E)$  is the density of states of K<sub>2</sub>Rb<sub>2</sub>\* near the incident energy  $E$ . Two isomers of K<sub>2</sub>Rb<sub>2</sub> with D<sub>2h</sub> and C<sub>s</sub> symmetries connect to the KRb + KRb and K<sub>2</sub> + Rb<sub>2</sub> dissociation limits, respectively.  $N_o$  is the number of exit channels that consist of all combinations of quantum states of K<sub>2</sub> and Rb<sub>2</sub> that have a total energy below  $E$ . The inset (at top left) shows the number decay of KRb molecules measured by ionization detection. Each data point is accumulated over 300 experimental cycles. The error bars denote shot noise. The black curve is a weighted fit to the two-body decay model used in (5), with a root mean square error (RMSE) of 1.37.

<sup>1</sup>Department of Chemistry and Chemical Biology, Harvard University, Cambridge, MA 02138, USA. <sup>2</sup>Department of Physics, Harvard University, Cambridge, MA 02138, USA. <sup>3</sup>Harvard-MIT Center for Ultracold Atoms, Cambridge, MA 02138, USA. <sup>4</sup>Laboratoire Aimé Cotton, CNRS, Université Paris-Saclay, ENS Paris-Saclay, Université Paris-Saclay, 91405 Orsay cedex, France.

\*These authors contributed equally to this work.

†Corresponding author. Email: ni@chemistry.harvard.edu



where  $\rho_c(E)$  denotes the density of states of the intermediate complex near the incident energy  $E$ , and  $N_o$  is the number of energetically allowed exit channels (Fig. 1). Preparing reactant KRb molecules in the pure rovibronic ground state in the ultralow-temperature regime tightly constrains the number of energetically allowed exit channels, greatly extending the lifetime of the intermediate complex. For reactions between bialkali molecules, depending on the species,  $\tau_c$  has been estimated to be on the order of hundreds of nanoseconds to microseconds (25, 26), which makes direct observation of the complex a possible goal. However, no such observations have been made because all previous work has been based on the observation of loss of reactants. Direct multispecies detection methods are necessary to fully describe the details of these ultracold reactions (27).

Here, we report the direct detection of a predicted intermediate as well as products in the ultracold chemical metathesis reaction  $^{40}\text{K}^{87}\text{Rb} + ^{40}\text{K}^{87}\text{Rb} \rightarrow \text{K}_2\text{Rb}_2^* \rightarrow \text{K}_2 + \text{Rb}_2$  (Fig. 1) (25, 26). In our study, we combined precise quantum-state preparation of the ultracold reactants with an ionization-based detection method that allows for direct and simultaneous detection of reactants (KRb), intermediates ( $\text{K}_2\text{Rb}_2^*$ ), and final products ( $\text{K}_2$  and  $\text{Rb}_2$ ).

We began by implementing an established protocol (28) to create an optically trapped gas of  $v = 0$ ,  $N = 0$ ,  $X^1\Sigma^+$  ground-state KRb molecules. Here,  $v$  and  $N$  are the vibrational and rotational quantum number of the molecules, respectively. In brief, ultracold K and Rb atoms are first converted to weakly bound molecules with 20% efficiency by a magnetic field sweep (1.4 ms) through a Feshbach resonance at 546.62 G (29). Then a pair of Raman beams is applied in a stimulated Raman adiabatic passage (STIRAP) (30) pulse sequence (4  $\mu\text{s}$ ) to coherently transfer the weakly bound molecules into a single hyperfine state of the rovibronic ground state with 85% efficiency. Residual Rb and K atoms are removed 8  $\mu\text{s}$  after the STIRAP pulse sequence. The atom-to-molecule transfer is mostly coherent and, therefore, can be reversed with high efficiency. To detect the ground-state KRb molecules, a reversed STIRAP sequence is applied, followed by absorption imaging on an atomic transition (Fig. 2A). Typically,  $5 \times 10^3$  KRb molecules are created at 500 nK, with a peak density of  $10^{12} \text{ cm}^{-3}$ , and trapped by a crossed optical dipole trap (ODT) at a laser wavelength of 1064 nm.

Because the absorption imaging detection is tied directly to the quantum-state-specific STIRAP transfer, it is sensitive to only the KRb molecules in the STIRAP populated quantum state. To probe chemical reaction products and the intermediate complex, we chose a

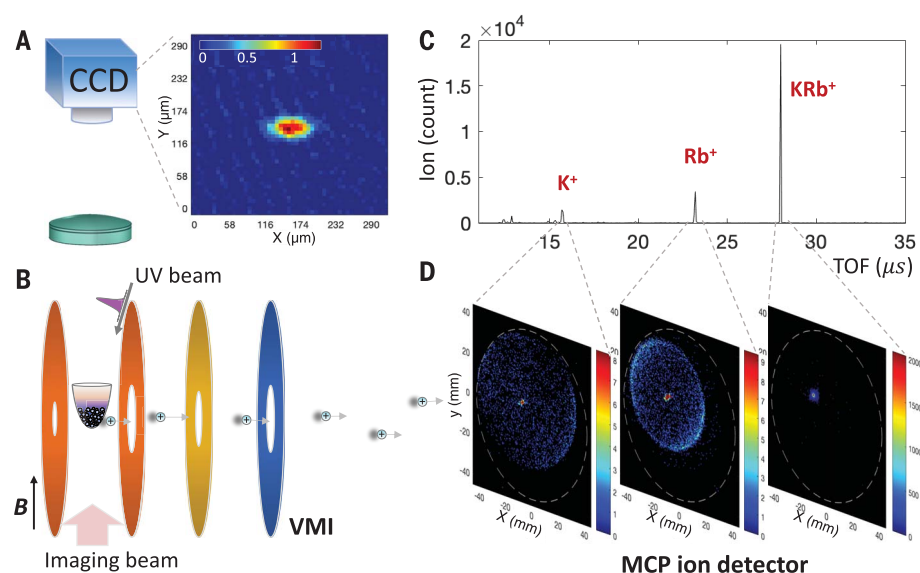


**Fig. 2. Schematic of our ultracold chemistry apparatus.** Ground-state KRb molecules at 500 nK are trapped by a crossed optical dipole trap. (A) Absorption image of KRb molecules. The colorbar indicates the optical depth of the KRb cloud. CCD, charge-coupled device. (B) The trapped molecules are surrounded by VMI ion optics (31), which consist of a series of disk-shaped electrodes. We use a pulsed UV laser to photoionize the molecules.  $B$ , magnetic field. (C) Example TOF spectrum, which can be converted to a mass spectrum using the following relation:  $\text{mass} = 0.16248(\text{u}/\mu\text{s}^2) \times \text{TOF}^2$  (where  $u$  is the unified atomic mass unit). (D) For each species identified in the mass spectrum, we also obtain a VM image from which the momentum distribution can be inferred.

more general detection method that entailed photoionization of neutral reaction species into bound molecular ions, acceleration of the ions in an electric field, and measurement of their arrival time and position on a multichannel plate (MCP) (Fig. 2C). By combining mass spectrometry and velocity-map imaging (VMI) (31) in our ultracold molecule apparatus, we could thereby identify reacting species and study reaction dynamics.

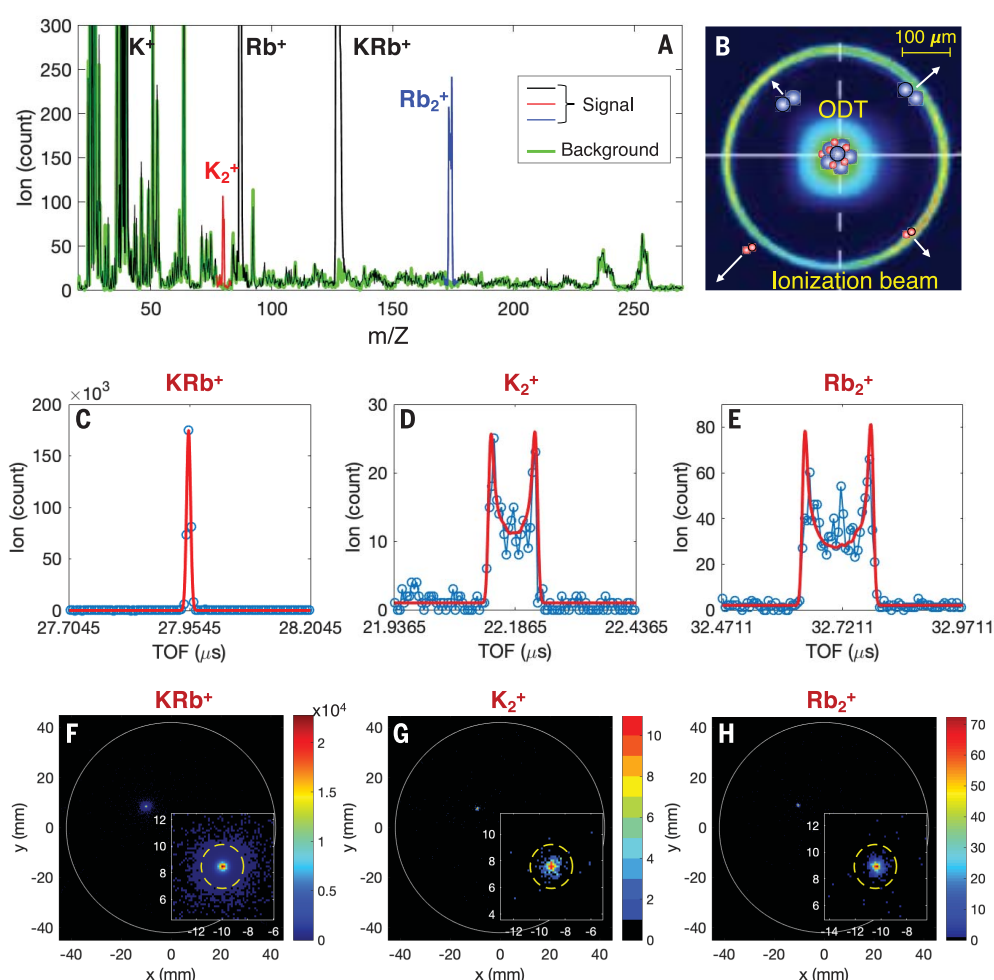
We performed three separate experiments to probe the reactants, intermediate complex, and products of the ultracold reaction. The detection procedure worked as follows: After KRb creation but before the ionization pulse, we ramped the magnetic field down to 30 G within 15 ms to reduce subsequent Lorentz forces that might deflect ions away from the detector, housed 1 m downstream. We then applied an ultraviolet (UV) ionization pulse while simultaneously triggering the MCP to record ion signals. For the detection of reactants and products, we chose a photoionization wavelength of 285 nm, which is above the ionization threshold of KRb, K, Rb, and any species composed of combinations of multiple K and Rb atoms (table S1). For the detection of the intermediate complex, the wavelength was varied over a range of 285 to 356 nm. To avoid space-charge effects, the laser power was kept low enough to ensure that, at most, one ion was generated per UV pulse. The ODT was switched off for a variable

time period during and before the ionization pulse to preclude its influence on the chemical reaction, the lifetime of the intermediate collisional complex, and the photoionization process. We repeated this detection procedure at 1 kHz for the reactant and product detection (see timing diagram in fig. S1) and at 7 kHz for the intermediate complex detection. The mass, and thereby elemental composition, of each detected ion could be inferred from its time of flight (TOF), whereas the momentum of the ion was mapped through its location on the VM image (32).

To demonstrate the ionization detection capability in our ultracold molecular apparatus and to gain information beyond absorption imaging, we first probed the trapped KRb molecules in the ODT (Fig. 2, C and D). As expected, the dominant signal results from  $\text{KRb}^+$ . The VM image for the  $\text{KRb}^+$  signal has a width limited by the detector resolution, consistent with the negligible translational energy in the ultracold regime. Measurable amounts of  $\text{Rb}^+$  and  $\text{K}^+$  were also detected. The VM images for  $\text{K}^+$  and  $\text{Rb}^+$  both show two distinct components: an isotropic central peak and an anisotropic ring. The ions forming the central peak originate from residual ultracold atoms from the molecule-creation process after the cleanup pulses. On the basis of the known ionization cross sections and estimated ion detection efficiencies (table S1), we put an upper bound of 250 atoms of each

**Fig. 3. Identification of the reaction products.**

**(A)** Mass spectrum of the reaction products ionized by 285-nm UV laser pulses. Color-coded ion signals correspond to species associated with the reaction of two KRB molecules compared with the ionization background (the green trace). Noise ions that show up in both the signal and the background spectra have no appreciable effect on the ion signals of interest (section S6).  $m/z$ , mass/charge ratio. **(B)** Geometries of the relevant beams with schematic representations of the reactants and products superimposed. The Gaussian beam spot in the center is the ODT and the ring surrounding it is the ionization beam. **(C to E)** TOF data for the  $\text{KRb}^+$ ,  $\text{K}_2^+$ , and  $\text{Rb}_2^+$  ions, respectively. The red curve in (C) is a time resolution-limited Gaussian to describe TOF line shape for the ions generated in the center, whereas the curves in (D) and (E) are simulated TOF line shapes for the ions generated in the ring. For the simulation, we use physical parameters of our system such as the diameter of the hollow-bottle beams (0.45 mm), the intersection angle of the two hollow beams ( $40^\circ$ ), and the VMI electric field (section S3). The only fitting parameter in this model is the overall amplitude of the signal. **(F to H)** Momentum distributions of the  $\text{KRb}^+$ ,  $\text{K}_2^+$ , and  $\text{Rb}_2^+$  ions, respectively. White solid circles represent the active area of the detector; yellow dashed circles represent the momenta corresponding to  $10.4 \text{ cm}^{-1}$  of translational energy.



species in the trap. These populations are small compared with the  $\text{KRb}$  population, ensuring that the dominant reaction in the subsequent study is the desired bimolecular reaction. The sensitivity of ionization detection allowed us to quantify the small number of residual atoms in the ODT, which are not detected through absorption imaging. To analyze the  $\text{Rb}^+$  ions that form the ring pattern, we extracted the translational energy release (TER) from the diameter of the ring to obtain a TER of  $8.3 \times 10^3 \text{ cm}^{-1}$ . By comparing this TER to the calculated molecular potentials of  $\text{KRb}$  and  $\text{KRb}^+$  (33), we identified a two-photon dissociative ionization pathway that contributes to this atomic ion signal. The same analysis also applies to the ring pattern of the  $\text{K}^+$  ions (fig. S3).

After  $\text{KRb}$  molecules are created, the bimolecular reaction occurs continuously with a measured decay rate coefficient of  $7.6(3) \times 10^{-12} \text{ cm}^3/\text{s}$  until the reactants are depleted (Fig. 1, inset), consistent with previous studies (5). To probe the products of the bimolecular reaction while reducing the perturbation to the

reactants during ionization, we shaped our ionization beam into a “hollow bottle” (Fig. 3B) with the laser intensity concentrated in a ring outside of the ODT to keep the reactants in the dark; the measured intensity contrast between the peak and center of the beam was 500 (32). To further reduce the hollow volume for higher-efficiency ionization, we crossed two hollow-bottle beams at a  $40^\circ$  angle centered on the ODT (32). To observe the bimolecular reaction without the possible influence of the ODT light, we shut off the ODT for 170  $\mu\text{s}$  before each ionization pulse, thereby precluding any role of the ODT in the formation of all but those products with translational energy  $< 0.0127 \text{ cm}^{-1}$  (34).

The dominant peaks in the mass spectrum (Fig. 3A) are again  $\text{K}^+$ ,  $\text{Rb}^+$ , and  $\text{KRb}^+$ , primarily from photoionization of trapped  $\text{KRb}$  molecules by the residual intensity at the centers of the hollow-bottle beams. Aside from these dominant peaks, we can clearly identify ions corresponding to the masses of  $\text{K}_2^+$  and  $\text{Rb}_2^+$ . All peaks aside from these five species appear with comparable intensities in a back-

ground spectrum (green trace) taken in the absence of ultracold atoms and molecules.

We postulate that  $\text{K}_2^+$  and  $\text{Rb}_2^+$  come from direct ionization of the reaction products  $\text{K}_2$  and  $\text{Rb}_2$  (Fig. 1). To support such an assignment, we draw evidence from the TOF line shapes and the VM images. The TOF line shapes characterize the spatial origin of the ions in the ionization beam. The  $\text{KRb}^+$  line shape (Fig. 3C) is sharp and described well by the time resolution-limited Gaussian for ions that originate from the central part of the hollow ionization beams, which coincides with the position of the ODT.  $\text{K}_2^+$  and  $\text{Rb}_2^+$  share similar TOF line shapes, as shown in Fig. 3, D and E, which are much wider than that of  $\text{KRb}^+$ . The simulated line shape (with only total amplitude as a free parameter; see section S3 in the supplementary materials) based on the beam geometry for particles ionized by the ring portion of the hollow ionization beams matches well to the data, which supports the assignment that these signals are from reaction products escaping the central  $\text{KRb}$  cloud. The presence of a center peak in Fig. 3E that



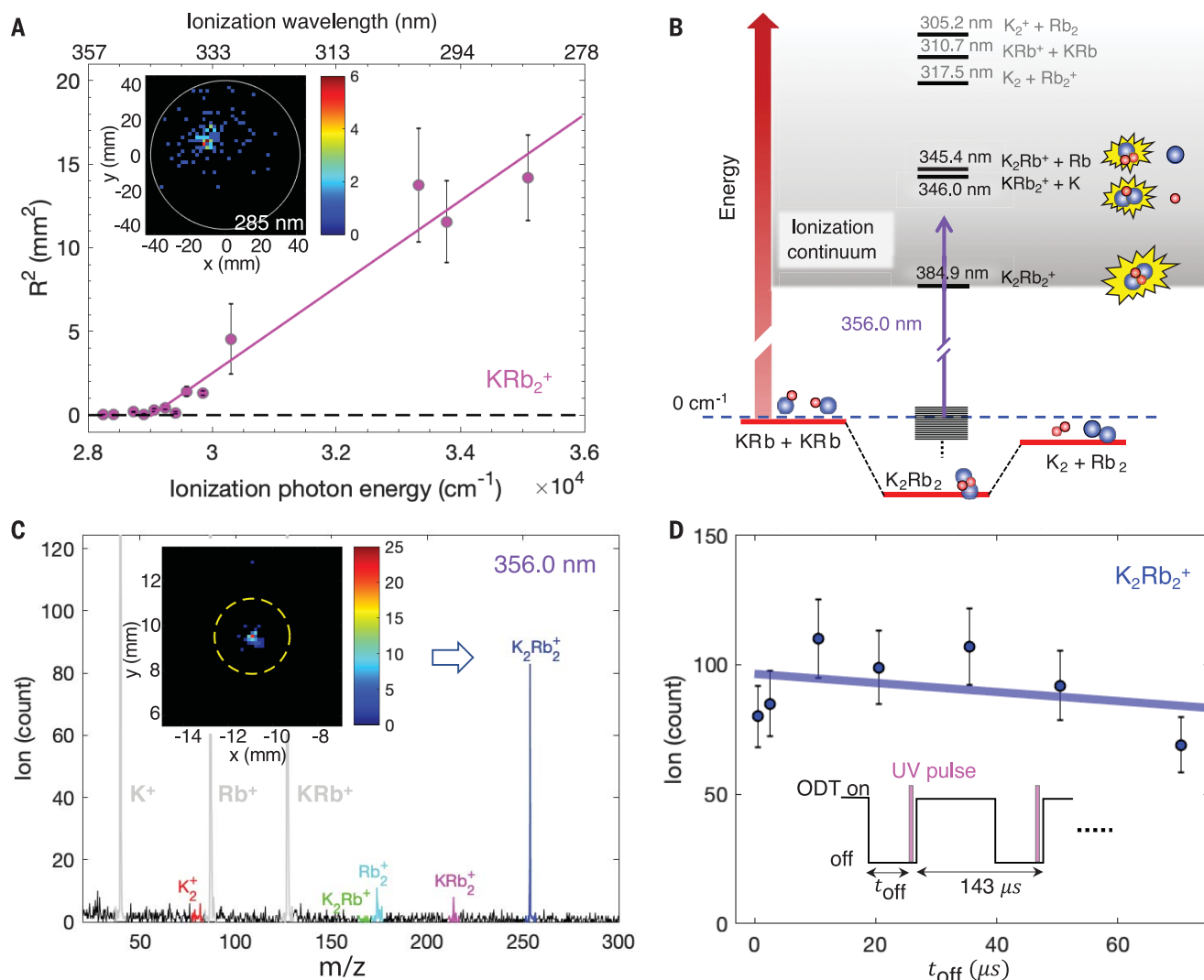


**Fig. 4. Direct detection of the intermediate complex  $K_2Rb_2^+$ .** (A) (Inset) VM image of detected  $K_2Rb_2^+$  ions (using an ionization laser wavelength of 285 nm). For each wavelength,  $R^2$  is extracted from such an image, where  $R$  is the Gaussian width of the ion spatial distribution and  $R^2$  is proportional to the TER. The measured TER of the  $K_2Rb_2^+$  ions is plotted versus the ionization photon energy. Error bars denote the standard deviation of the mean (standard error). Fits are described in section S5. The solid line is an unweighted linear fit to the data above  $2.9 \times 10^4$  cm<sup>-1</sup>, with a RMSE of 1.44, from which an experimental dissociative ionization threshold wavelength of  $345 \pm 4$  nm is determined. (B) Calculated threshold wavelengths of the direct photoionization and dissociative ionization of the intermediate

complex. The energies for the dissociative ionization thresholds are those corresponding to the equilibrium geometry of the ionic complex (table S1) and are therefore lower bounds on the ionization energy. (C) TOF mass spectrum produced using an ionization laser wavelength of 356 nm. (Inset) Corresponding VM image of the detected  $K_2Rb_2^+$  ions. The yellow dashed circle corresponds to  $10.4$  cm<sup>-1</sup>. We do not observe any species larger than  $K_2Rb_2$ , up to  $m/z = 1500$ . (D)  $K_2Rb_2^+$  counts are plotted against  $t_{off}$ , where  $t_{off}$  denotes the length of ODT off-time before UV photoionization. Error bars include shot noise and 10% molecule number fluctuations. A weighted linear fit (blue line) with a RMSE of 1.17 determines a slope of  $-0.2 \pm 0.2$ , consistent with a zero value.

is not captured by the simulated curve is likely due to the product ionization at the center of the hollow beams, where the beams are not perfectly dark. We also rule out the role of ion-neutral reactions, owing to their negligible estimated rates (section S4).

In addition to the mass spectrometry of the  $K_2^+$  and  $Rb_2^+$  ions, we simultaneously recorded the momentum distribution of the  $K_2^+$  and  $Rb_2^+$  ions with VMI (Fig. 3, G and H). To characterize the radius of the distribution, we performed Bayesian fits (section S5) to the images, assuming a circular Gaussian density on

a flat background with uninformative priors. The radius of  $K_2^+$  (or  $Rb_2^+$ ) corresponds to a translational energy of  $0.59$  cm<sup>-1</sup> ( $0.29$  cm<sup>-1</sup>), well above the MCP resolution of  $0.02$  cm<sup>-1</sup>. The ionization process of  $K_2$  ( $Rb_2$ ) would impart to the resulting ion a photon recoil energy of  $0.0159$  cm<sup>-1</sup> ( $0.0112$  cm<sup>-1</sup>), too small to substantially affect the momentum distribution of the ions. Therefore, the measured  $K_2^+$  and  $Rb_2^+$  translational energies closely resemble those of their parent neutrals. The sum of measured translational energies is smaller than the exothermicity,  $10.4$  cm<sup>-1</sup>, of the bimolecular KRB

reaction (Fig. 1). Further, their translational energy ratio,  $0.49 \pm 0.06$ , is consistent with the expected ratio, 0.46, originating from two different mass products flying apart with zero center-of-mass momentum. This finding provides further evidence to support the identification of  $K_2^+$  and  $Rb_2^+$  ions as arising from ionization of the products of the  $KRb + KRb$  chemical reaction.

Next, we focused on the transient intermediate collision complex,  $K_2Rb_2^+$ . To observe the complexes that by conservation of momentum should exist only in the vicinity of the

reactants, we shaped the UV ionization beam into a Gaussian beam profile. After data accumulation, we observed signals consistent with the masses of  $\text{K}_2\text{Rb}^+$  and  $\text{KRb}_2^+$  (fig. S2). On the basis of their VM images, which show large translational energies (Fig. 4A, inset), we hypothesize that these ions are from dissociative ionization of  $\text{K}_2\text{Rb}_2^*$ . To substantiate this idea, we varied the wavelength of the ionization beam to determine the relationship between the translational energy of the triatomic ions and the energy of the photon. We found that the characteristic translational energy associated with the  $\text{KRb}_2^+$  ion decreases as the ionization energy decreases. The ionization energy where the translational energy becomes zero (at  $345 \pm 4$  nm) agrees with our theoretical predictions ( $346 \pm 2$  nm) of the dissociative ionization threshold for the transient intermediate,  $\text{K}_2\text{Rb}_2^* + h\nu \rightarrow \text{KRb}_2^+ + \text{K} (4s) + e^-$  ( $h$ , Planck's constant;  $\nu$ , photon frequency;  $e^-$ , electron).

These theoretical calculations of ionization threshold energies of diatomic, triatomic, and tetratomic K- and Rb-containing molecules (Fig. 4B) are based on the same methodology used in (35) and references therein. Briefly, each alkali-metal atom was modeled as a one-electron system in the field of an ionic core ( $\text{K}^+$  or  $\text{Rb}^+$ ). We used a semiempirical effective core potential plus a core polarization potential to represent the correlation between the valence electron and the core electrons (32). The  $\text{K}_2\text{Rb}^+$  and  $\text{KRb}_2^+$  triatomic ions were modeled as two-valence electron systems and the  $\text{K}_2\text{Rb}_2^+$  ion as a three-valence electron molecule. In the framework of such a simplification, the ground-state potential energy surface can be obtained with good accuracy via the diagonalization of the full electronic Hamiltonian (i.e., full configuration interaction) expressed on a large Gaussian basis set. For all molecular and atomic species, the energies were computed with respect to the same origin—namely, the energy of the four cores ( $\text{K}^+ + \text{K}^+ + \text{Rb}^+ + \text{Rb}^+$ ). This allowed for the determination of transition energies between different species.

To directly observe the transient intermediate complex  $\text{K}_2\text{Rb}_2^*$ , we tuned the wavelength of our ionization laser to 356 nm, with energy well below the lowest dissociative ionization channel. Figure 4C displays a mass spectrum obtained with ionization at 356 nm, and a strong signal of  $\text{K}_2\text{Rb}_2^+$  is evident. Notably, the ionization process transforms the transient intermediate into a bound molecular ion that has no energetically allowed dissociation channel (Fig. 4B) and can therefore survive its flight to the MCP. Although we have not yet directly measured the lifetime of the complex, owing to the technical challenges of precisely establishing a zero of time, the signal strength of our direct observation enables an estimated life-

time of 350 ns (or 3  $\mu\text{s}$ ), assuming the ionization cross section of the  $\text{K}_2\text{Rb}_2$  intermediate complex is 10 Mb (or 1 Mb). This cross section has not been reported in the literature.

The origin of the observed intermediate complex has been the subject of previous debate (10, 25). The long-lived transient complex could potentially collide with another  $\text{KRb}$ , causing the prior's decay into a deeply bound  $\text{K}_2\text{Rb}_2$  molecule and leading to the conversion of its internal energy into a large, observable TER (25, 26). In contrast, we observe a detector resolution-limited small momentum distribution of the  $\text{K}_2\text{Rb}_2^+$  ions (Fig. 4C, inset), consistent with the zero-momentum transient intermediate.

Moreover, because the reactants are trapped in the ODT, a light-assisted process could be a competing, confounding factor, as suggested by Christiansen *et al.* (10). To examine the role of the ODT on the detected intermediate complex, we varied the time that the ODT was switched off before ionization from 1 to 70  $\mu\text{s}$  (see inset of Fig. 4D). If the ODT contributed to the formation of deeply bound  $\text{K}_2\text{Rb}_2$  molecules, which have no radiative decay pathway and only potentially leave the probed volume on a millisecond time scale if untrapped,  $\text{K}_2\text{Rb}_2$  would steadily build up in concentration in the presence of the ODT. As a result, the concentration of  $\text{K}_2\text{Rb}_2$  should decrease monotonically as the ODT off-duration increases. Instead, we find that the yield of  $\text{K}_2\text{Rb}_2^+$  ions has no monotonic trend with the ODT off-duration (Fig. 4D). This result is evidence that the intermediates we observe are formed upon collision of two  $\text{KRb}$  molecules, with no notable effect from the ODT.

The direct observation of  $2\text{KRb} \rightarrow \text{K}_2\text{Rb}_2^* \rightarrow \text{K}_2 + \text{Rb}_2$  opens numerous possibilities of exploring the detailed role of quantum mechanics in ultracold chemical reaction dynamics by measuring the lifetime of the intermediate complex (25, 26), testing the transition from quantum to semiclassical reactions (36), and resolving the quantum states of the reaction products (37) and the intermediate.

## REFERENCES AND NOTES

- A. B. Henson, S. Gersten, Y. Shagam, J. Narevicius, E. Narevicius, *Science* **338**, 234–238 (2012).
- H. Yang *et al.*, *Science* **363**, 261–264 (2019).
- P. Puri *et al.*, *Science* **357**, 1370–1375 (2017).
- D. K. Hoffmann, T. Paintner, W. Limmer, D. S. Petrov, J. H. Denschlag, *Nat. Commun.* **9**, 5244 (2018).
- S. Ospelkaus *et al.*, *Science* **327**, 853–857 (2010).
- A. Kilaj *et al.*, *Nat. Commun.* **9**, 2096 (2018).
- L. De Marco *et al.*, *Science* **363**, 853–856 (2019).
- X. Ye, M. Guo, M. L. González-Martínez, G. Quémener, D. Wang, *Sci. Adv.* **4**, eaq0083 (2018).
- P. D. Gregory *et al.*, *Nat. Commun.* **10**, 3104 (2019).
- A. Christiansen, M. W. Zwiernik, G. C. Groenenboom, T. Karman, *Phys. Rev. Lett.* **123**, 123402 (2019).
- S. Bauer, *Annu. Rev. Phys. Chem.* **30**, 271–310 (1979).
- W. Miller, S. Safran, D. Herschbach, *J. Chem. Phys.* **56**, 3581–3592 (1972).
- P. R. Brooks, *Chem. Rev.* **88**, 407–428 (1988).
- A. H. Zewail, *J. Phys. Chem. A* **104**, 5660–5694 (2000).
- M. Gruebele, I. Sims, E. Potter, A. Zewail, *J. Chem. Phys.* **95**, 7763–7766 (1991).
- I. Sims, M. Gruebele, E. Potter, A. Zewail, *J. Chem. Phys.* **97**, 4127–4148 (1992).
- J. C. Polanyi, A. H. Zewail, *Acc. Chem. Res.* **28**, 119–132 (1995).
- C. C. Womack, M.-A. Martin-Drumel, G. G. Brown, R. W. Field, M. C. McCarthy, *Sci. Adv.* **1**, e1400105 (2015).
- B. J. Bjork *et al.*, *Science* **354**, 444–448 (2016).
- T. Q. Bui *et al.*, *Sci. Adv.* **4**, eaao4777 (2018).
- E. Garand, J. Zhou, D. E. Manolopoulos, M. H. Alexander, D. M. Neumark, *Science* **319**, 72–75 (2008).
- R. E. Continetti, H. Guo, *Chem. Soc. Rev.* **46**, 7650–7667 (2017).
- Y.-T. Su, Y.-H. Huang, H. A. Witek, Y.-P. Lee, *Science* **340**, 174–176 (2013).
- H. Sato, *Chem. Rev.* **101**, 2687–2726 (2001).
- M. Mayle, G. Quémener, B. P. Ruzic, J. L. Bohn, *Phys. Rev. A* **87**, 012709 (2013).
- A. Christiansen, T. Karman, G. C. Groenenboom, *Phys. Rev. A* **100**, 032708 (2019).
- D. J. Nesbitt, *Chem. Rev.* **112**, 5062–5072 (2012).
- K.-K. Ni *et al.*, *Science* **322**, 231–235 (2008).
- T. D. Cumby, R. A. Shewmon, M.-G. Hu, J. D. Perreault, D. S. Jin, *Phys. Rev. A* **87**, 012703 (2013).
- N. Vitanov, M. Fleischhauer, B. Shore, K. Bergmann, *Adv. At. Mol. Opt. Phys.* **46**, 55–190 (2001).
- A. T. Eppink, D. H. Parker, *Rev. Sci. Instrum.* **68**, 3477–3484 (1997).
- See details in the supplementary materials.
- M. Korek, G. Younes, A. Allouche, *Int. J. Quantum Chem.* **92**, 376–380 (2003).
- It would take 170  $\mu\text{s}$  for a  $\text{Rb}_2$  molecule with translational energy of  $0.0127 \text{ cm}^{-1}$  to travel from the center of the  $\text{KRb}$  cloud to the ionization ring with a diameter of 0.45 mm.
- R. Vexiau *et al.*, *Int. Rev. Phys. Chem.* **36**, 709–750 (2017).
- B. Gao, *Phys. Rev. Lett.* **105**, 263203 (2010).
- J. F. E. Croft *et al.*, *Nat. Commun.* **8**, 15897 (2017).
- S. Falke, I. Sherstov, E. Tiemann, Ch. Lisdat, *J. Chem. Phys.* **125**, 224303 (2006).
- C. Amiot, *J. Chem. Phys.* **93**, 8591–8604 (1990).
- J. N. Byrd, J. A. Montgomery Jr., R. Côté, *Phys. Rev. A* **82**, 010502 (2010).
- M.-G. Hu *et al.*, Replication Data for Direct observation of bimolecular reactions of ultracold  $\text{KRb}$  molecules, Version V1, Harvard Dataverse (2019); <https://doi.org/10.7910/DVN/MDFLOZ>.

## ACKNOWLEDGMENTS

We thank D. Herschbach, L. Zhu, T. Karman, and J. Ye for discussion; K. Liu for introducing us to the VMI techniques; T. Pfau, E. Narevicius, and M. Greiner for discussions on apparatus design; J. Doyle for loaning laser equipment; and W. Stwalley, P. Gould, and the late E. Eyer for sharing  $\text{KRb}$  spectroscopy literature. The  $^{40}\text{K}$  isotope used in this research was supplied by the U.S. Department of Energy (DOE), Office of Science, by the Isotope Program in the Office of Nuclear Physics. **Funding:** This work is supported by the DOE Young Investigator Program, the David and Lucile Packard Foundation, and the NSF through the Harvard-MIT CUA. **Author contributions:** The experimental work and data analysis were carried out by M.-G.H., Y.L., D.D.G., Y.-W.L., A.H.G., T.R., and K.-K.N. Theoretical calculations were done by R.V., N.B.-M., and O.D. All authors contributed to interpreting the results and writing the manuscript. **Competing interests:** The authors declare no competing interests. **Data and materials availability:** Data from the main text and supplementary materials are available through the Harvard Dataverse (41).

## SUPPLEMENTARY MATERIALS

[science.sciencemag.org/content/366/6469/1111/suppl/DC1](https://science.sciencemag.org/content/366/6469/1111/suppl/DC1)  
Supplementary Text  
Figs. S1 to S4  
Tables S1 to S2  
References (42–52)

31 July 2019; accepted 4 November 2019  
10.1126/science.aay9531



## ELASTOCALORICS

# Fatigue-resistant high-performance elastocaloric materials made by additive manufacturing

Huilong Hou<sup>1\*</sup>, Emrah Simsek<sup>2</sup>, Tao Ma<sup>2</sup>, Nathan S. Johnson<sup>3</sup>, Suxin Qian<sup>4</sup>, Cheikh Cissé<sup>3</sup>, Drew Stasak<sup>1</sup>, Naila Al Hasan<sup>1</sup>, Lin Zhou<sup>2</sup>, Yunho Hwang<sup>5</sup>, Reinhard Radermacher<sup>5</sup>, Valery I. Levitas<sup>2,6,7</sup>, Matthew J. Kramer<sup>2,8</sup>, Mohsen Asle Zaeem<sup>3</sup>, Aaron P. Stebner<sup>3</sup>, Ryan T. Ott<sup>2</sup>, Jun Cui<sup>2,8</sup>, Ichiro Takeuchi<sup>1,9†</sup>

Elastocaloric cooling, a solid-state cooling technology, exploits the latent heat released and absorbed by stress-induced phase transformations. Hysteresis associated with transformation, however, is detrimental to efficient energy conversion and functional durability. We have created thermodynamically efficient, low-hysteresis elastocaloric cooling materials by means of additive manufacturing of nickel-titanium. The use of a localized molten environment and near-eutectic mixing of elemental powders has led to the formation of nanocomposite microstructures composed of a nickel-rich intermetallic compound interspersed among a binary alloy matrix. The microstructure allowed extremely small hysteresis in quasi-linear stress-strain behaviors—enhancing the materials efficiency by a factor of four to seven—and repeatable elastocaloric performance over 1 million cycles. Implementing additive manufacturing to elastocaloric cooling materials enables distinct microstructure control of high-performance metallic refrigerants with long fatigue life.

Space cooling and refrigeration consume about one-fifth of the entire electricity demand worldwide (1). Vapor compression is a mature technology that dominates the market, but its efficiency has plateaued, and the high global-warming potential of the refrigerants remains a major concern. Solid-state cooling technologies, including thermoelectric (2) and passive radiative cooling (3), represent attractive green alternatives to vapor compression. Particularly promising are caloric (magnetocaloric, mechanocaloric, and electrocaloric) cooling techniques (4–7), which have the potential to surpass the efficiency of vapor compression. Because caloric materials enlist active heat-pumping through manipulation of their functional properties (magnetization, stress-state, and electric polarization) (7), they can be exploited for giant cooling effects. However, hysteresis in the properties is caloric materials' Achilles heel because hysteresis represents work lost in every heat-pumping cycle as dissipated heat.

Hysteresis also ultimately leads to material fatigue and failure. Although the long-term fatigue properties are critical for developing applications for caloric materials, evaluating these properties over a large number of cycles is not common.

The martensitic phase transformation of shape memory alloys (SMAs) may manifest in dramatic temperature-triggered shape change, enabling solid-state actuation technologies (8). The martensitic transformation can also be triggered by stress, resulting in superelasticity (9). During superelastic cycles, latent heat is released or absorbed upon loading or unloading, respectively, because of the exothermic-endothermic nature of the phase transformation. This stress-induced heat-pumping of SMAs is elastocaloric cooling (10, 11), one type of mechanocaloric cooling. Adiabatic temperature change ( $\Delta T_{ad}$ ) of elastocaloric materials can be as large as 31.5 K (12), and the largest reported isothermal entropy change ( $\Delta S$ ) of an SMA is 70.7 J kg<sup>−1</sup> K<sup>−1</sup> (13). Such unparalleled cooling potential has made elastocaloric cooling a front runner among the crowded field of alternative cooling technologies (14). Functioning elastocaloric cooling prototypes with capacity over 100 W have been developed (15), and elastocaloric regenerative heat pumps with  $\Delta T_{ad}$  as large as 19 K have been demonstrated by using commercially available nickel-titanium (Ni–Ti) materials (16, 17). However, thermomechanical hysteresis of elastocaloric SMAs can limit the efficiency of cooling devices, and its impact on long-term performance has not been addressed.

We synthesized elastocaloric materials consisting of alloy matrix and intermetallic phases arranged in nanocomposite microstructures using the powder-feed laser-directed-energy

deposition (L-DED) technique. This method results in a local melting of metal powders followed by rapid solidification (18, 19). When a Ni-rich blend of elemental Ni and Ti powders are mixed during this process, nanocomposite microstructures—composed of transforming, elastocaloric binary NiTi alloy matrix and a nontransforming Ni<sub>3</sub>Ti intermetallic phase—form in a two-phase mixture of comparable volume fractions, with intricate dendritic structures. This configuration enlists the non-transforming intermetallic phase for biasing the phase transformation, leading to considerable improvement in elastocaloric efficiency and transformation reversibility through work hysteresis minimization.

The L-DED-produced Ni–Ti nanocomposite exhibits substantially reduced hysteresis with a quasi-linear stress-strain behavior, resulting in a multifold increase in the materials efficiency, which is defined as the ratio of materials coefficient of performance ( $COP_{materials}$ ) to Carnot  $COP$ . We show that the elastocaloric thermodynamic cycle of these materials is stable over more than a million cycles. In contrast to rate-dependent hysteresis commonly observed in traditionally processed SMAs (20, 21), the hysteresis of the L-DED Ni–Ti nanocomposite is nearly rate-independent (from 0.0002 to 0.2 s<sup>−1</sup>), facilitating high-frequency elastocaloric operations. We used a constitutive model and in situ synchrotron x-ray diffraction experiments to confirm that their properties originate from kinematics of load transfer between transforming and nontransforming phases.

The key features of the L-DED process (Fig. 1A) are a millimeter-scale molten pool of mixed powders and a rapid cooling rate of greater than 10<sup>3</sup> K s<sup>−1</sup> (22). Metal nanocomposites made by, for example, melt-casting (23) can display a stress-transfer mechanism responsible for high strength, a desirable attribute of functional alloys. Because eutectic solidification can naturally lead to the formation of composites, we used the eutectic point in the Ni-rich composition range (Fig. 1B) of binary Ni–Ti to obtain elastocaloric nanocomposite using L-DED (24). Optimization of processing parameters (such as layer thickness and hatching space) was guided by use of a normalized processing map (25) for high denseness ( $\approx 99\%$ ) and mechanical integrity, and the molten pool temperature in operation was maintained to be 1973 to 2173 K, as measured in situ with a ThermoViz pyrometer. We adjusted the ratio of the flow rate of elemental Ni and Ti powders to print different compositions of Ni–Ti materials in a range of geometries (Fig. 1, C to H).

Rapid cooling of the molten pool during L-DED enables precipitation from off-eutectic compositions in a volume fraction comparable with that of eutectic structures, as predicted

<sup>1</sup>Department of Materials Science and Engineering, University of Maryland, College Park, MD 20742, USA. <sup>2</sup>Division of Materials Science and Engineering, Ames Laboratory, Ames, IA 50011, USA. <sup>3</sup>Department of Mechanical Engineering, Colorado School of Mines, Golden, CO 80401, USA.

<sup>4</sup>Department of Refrigeration and Cryogenic Engineering, Xi'an Jiaotong University, Xi'an, Shaanxi 710049, People's Republic of China. <sup>5</sup>Center for Environmental Energy Engineering, Department of Mechanical Engineering, University of Maryland, College Park, MD 20742, USA.

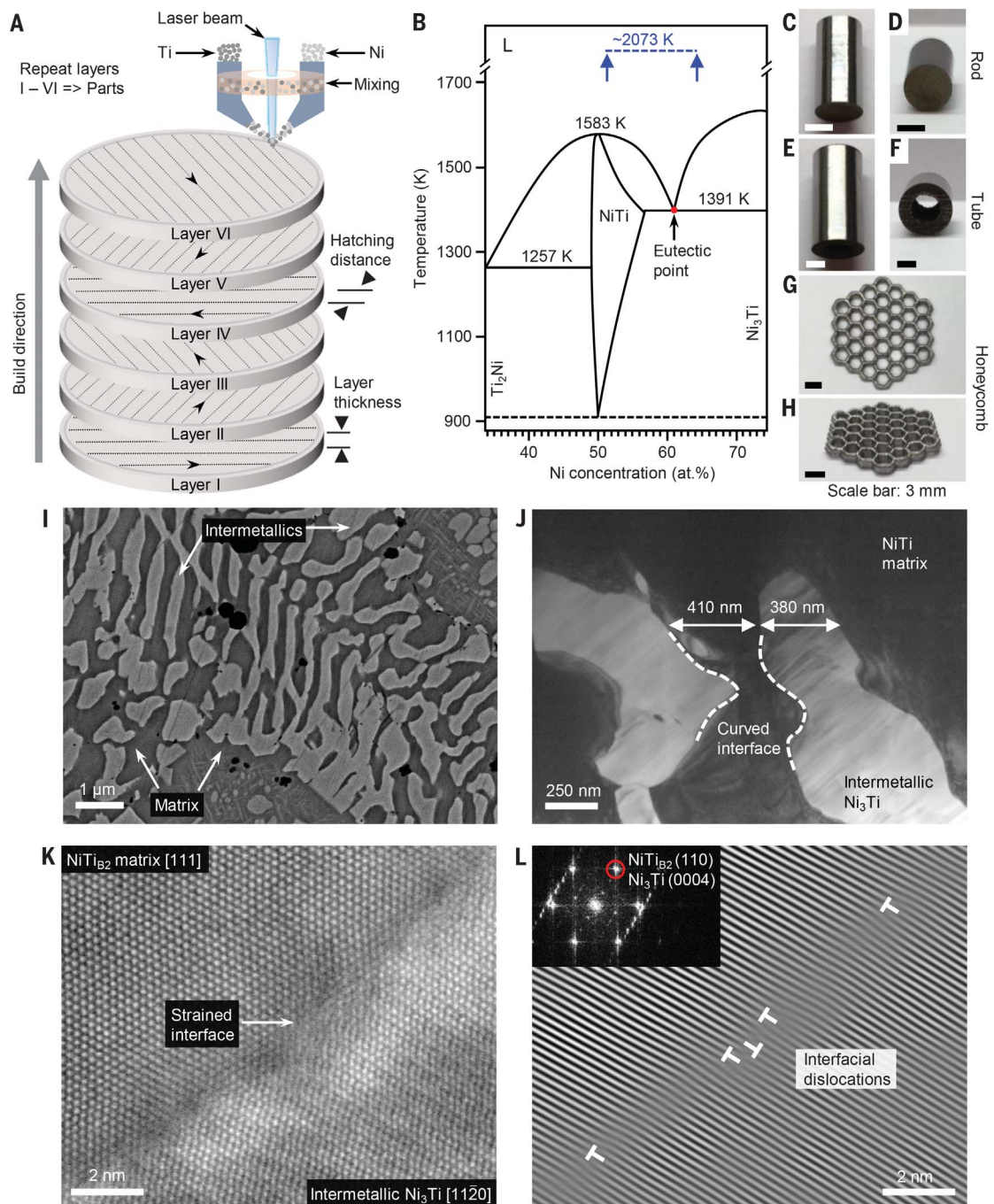
<sup>6</sup>Department of Aerospace Engineering, Iowa State University, Ames, IA 50011, USA. <sup>7</sup>Department of Mechanical Engineering, Iowa State University, Ames, IA 50011, USA.

<sup>8</sup>Department of Materials Science and Engineering, Iowa State University, Ames, IA 50011, USA. <sup>9</sup>Maryland Quantum Materials Center, University of Maryland, College Park, MD 20742, USA.

†Corresponding author. Email: takeuchi@umd.edu

\*Present address: School of Aeronautic Science and Engineering, Beihang University, Beijing 100191, People's Republic of China.

**Fig. 1. Design of elastocaloric Ni–Ti nanocomposite by directed energy deposition.** (A) Schematic representation of an L-DED process. Flows of Ni and Ti powders are individually controlled. The Ni and Ti powders are mixed and then fed to the laser beam. An induced molten pool moves to build materials layer by layer (fig. S1). (B) Phase diagram of Ni–Ti [adapted with permission from (53)] highlighting in blue the Ni-rich composition near a eutectic point and the molten pool temperature used in this work. (C to H) Photographs of L-DED-produced Ni–Ti nanocomposite rods, tubes, and honeycombs in [(C), (E), and (G)] top and [(D), (F), and (H)] front views, respectively. (I to K) Scanning electron microscopy (SEM) image (I), bright-field transmission electron microscopy (TEM) image (J), and high-resolution high-angle annular dark-field scanning TEM (HAADF-STEM) image (K) of as-built  $\text{Ni}_{51.5}\text{Ti}_{48.5}/\text{Ni}_3\text{Ti}$  nanocomposite. In (I), the regions with different contrasts are crystallographically identified to be NiTi and  $\text{Ni}_3\text{Ti}$  phases (figs. S2 and S3). In (J), typical curved interfaces are delineated. In (K) (a zoomed-in view of a curved interface), NiTi and  $\text{Ni}_3\text{Ti}$  phases have an orientation relationship of  $\text{NiTi}_{[111]}||\text{Ni}_3\text{Ti}_{[1120]}$ , although each is slightly off the zone axis because of lattice strains within the interface (fig. S4). (L) Inverse fast Fourier transform (IFFT) image from the circled spot in the FFT image [inset; generated from (K)]. Interfacial dislocations are identified and marked with “T” symbols.



by the Scheil model (22, 26). We observed a substantial fraction of precipitates (up to  $\approx 50\%$ ) in a wide compositional range of the Ni–Ti produced with L-DED (Fig. 1B). Curved microstructures can nucleate and grow because the temperature gradient (highest at the center and lowest at the periphery) of the molten pool leads to circulation of mass and heat within the pool driven by Marangoni shear stress (27), creating local perturbations

of solute concentration and equilibrium temperature (28) on solid–liquid interfaces and breaking up the plane front in growth of steady-state eutectics. As a result of non-equilibrium conditions, a typical microstructure of the L-DED-produced Ni–Ti nanocomposite consists of transforming NiTi and nontransforming  $\text{Ni}_3\text{Ti}$  phases with large aspect ratios, curved interfaces, and comparable volume fractions (Fig. 1I). The size

scale of the microstructure is inversely proportional to the cooling rate (26), which is at least two orders of magnitude higher in L-DED than that of casting ( $\approx 0.1 \text{ K s}^{-1}$ ), leading to a mixture of two phases at a submicrometer scale (Fig. 1J).

Large interfacial curvatures between the cubic B2-ordered NiTi phase and the hexagonal  $\text{D}_{024}$ -ordered  $\text{Ni}_3\text{Ti}$  phase (Fig. 1J) can be naturally accommodated with small lattice



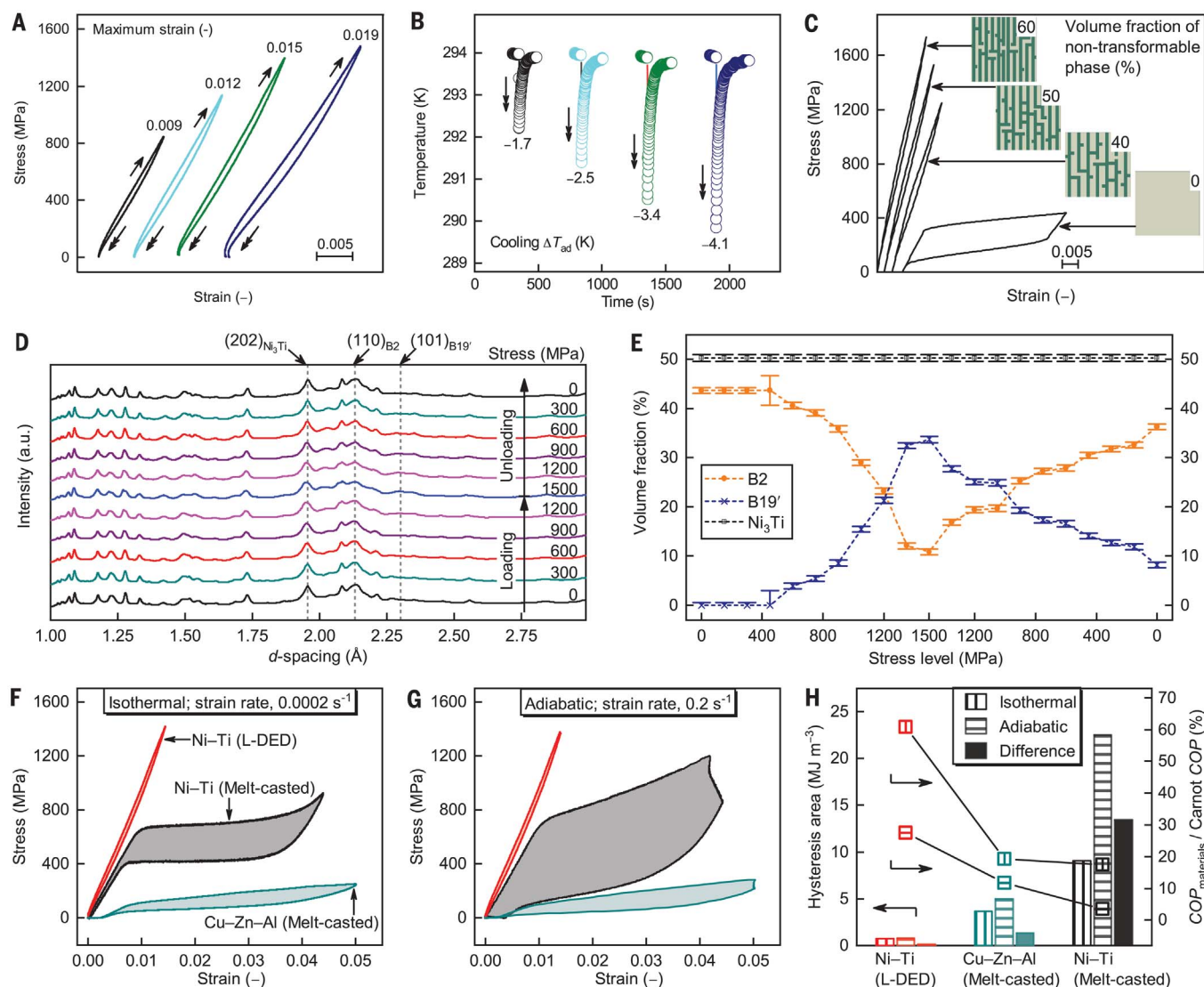


**Fig. 2. Recoverable behaviors and elastocaloric properties of Ni-Ti nanocomposite.** (A and B) The stress-strain curves (A) and corresponding elastocaloric cooling at room temperature (B) of L-DED-produced  $\text{Ni}_{51.5}\text{Ti}_{48.5}/\text{Ni}_3\text{Ti}$  nanocomposite aged at 923 K for 3 hours. The single arrows in (A) denote loading, and the double arrows in (A) and (B) correspond to unloading. (C) Simulated stress-strain curves from a micromechanics model that accounts for the volume fraction of nontransforming phase (insets). (D and E) Synchrotron x-ray diffraction patterns (D) during in situ loading and unloading and the (E) determined volume fraction of primary phases at different stress levels during the cycle. (F and

G) Comparison of stress-strain curves for L-DED-produced  $\text{Ni}_{51.5}\text{Ti}_{48.5}/\text{Ni}_3\text{Ti}$  nanocomposite and melt-casted  $\text{Ni}_{50.8}\text{Ti}_{49.2}$  and  $\text{Cu}_{68}\text{Zn}_{16}\text{Al}_{16}$  alloys at the strain rate of (F)  $0.0002 \text{ s}^{-1}$  for isothermal loading and unloading and (G)  $0.2 \text{ s}^{-1}$  for adiabatic loading and unloading. In (F) and (G), the area enclosed by the loading and unloading curves represents total dissipation energy per unit volume associated with hysteresis. (H) Comparison of hysteresis area under isothermal and adiabatic loading and unloading as well as the ratio of  $\text{COP}_{\text{materials}}$  to Carnot COP for L-DED nanocomposite and melt-casted alloys at maximum transformations. The color code for each material is common for (F) to (H).

mismatches to make their interfaces semi-coherent. An atomic-scale view of the adjacent regions displays strained boundaries (Fig. 1K) where interfacial dislocations are located (Fig. 1L). Preexisting sites of high nucleation potency such as dislocations have been reported to trigger atomic shearing for nucleation of martensite (29), in which a nucleation energy barrier is lowered [or completely suppressed in the case of spontaneous growth (30)]. These interfacial dislocations inherent to the curvatures and additional dislocations

induced through mechanical pretreatment (fig. S5) therefore serve as preexisting nucleation sites to reduce energy barriers for martensite during the forward transformation and for austenite during the reverse transformation. In addition, these same nucleation sites can act as “micropockets” to accommodate remnant austenite and martensite after forward and reverse transformations, respectively, eliminating the necessity of a barrier-overcoming stage for nucleation during cyclic loading. After proper self-organization, pre-

straining, and prestressing (fig. S5, shake-down state), the intricate nanoscale network of connected microstructure suppresses the dislocation motion (31) and limits transformation dissipation, resulting in enhanced cyclic stability.

The L-DED-produced Ni-Ti nanocomposite exhibits quasi-linear behaviors and substantially reduced hysteresis (Fig. 2A). The full strain recovery upon unloading is accompanied by a cooling  $\Delta T_{\text{ad}}$  (Fig. 2B), a signature of martensitic transformation, which reaches

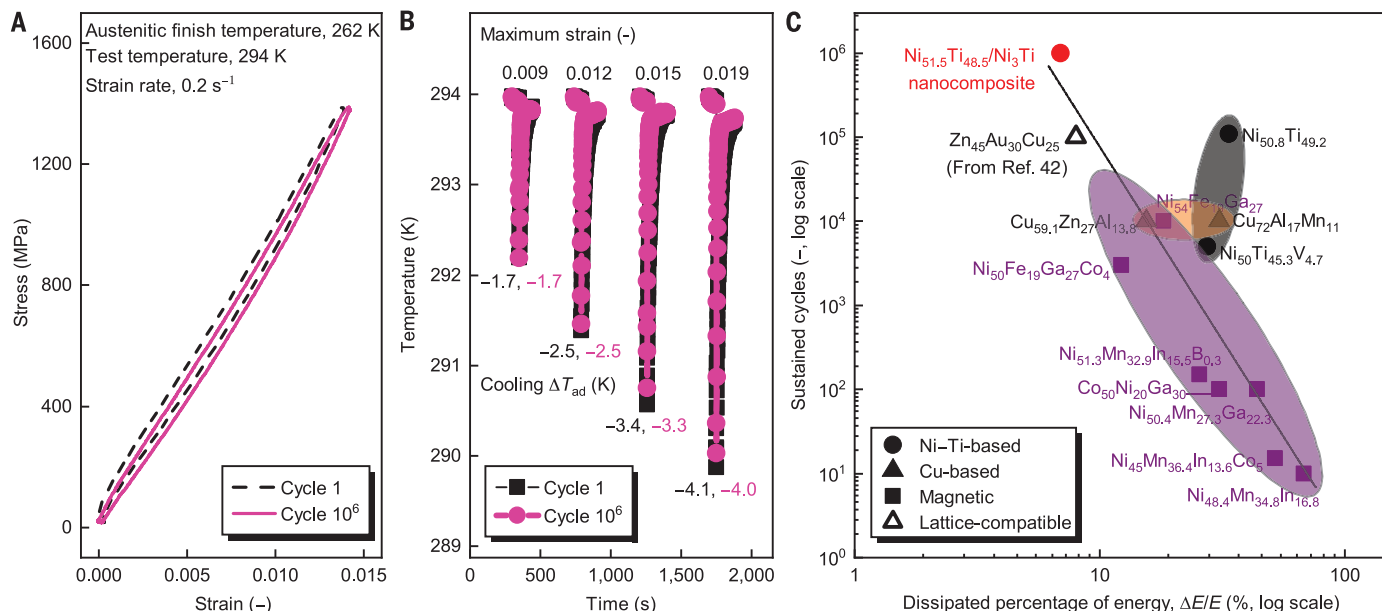


**Fig. 3. Stability of Ni-Ti nanocomposite over 1 million compression cycles and comparison with other reported bulk elastocaloric materials.**

(A and B) Compressive stress-strain curves (A) and elastocaloric cooling (B) of L-DED-produced  $Ni_{51.5}Ti_{48.5}/Ni_3Ti$  nanocomposite aged at 923 K for 3 hours before and after 1 million cycles. (C) Log-log plot of the dissipated fraction of input energy,  $\Delta E/E$ , versus sustained compressive cycles for bulk elastocaloric materials in this work as well as those reported in the literature.

A dissipated fraction of energy is the ratio of hysteresis area  $\Delta E$  in a transformation cycle to the input energy  $E$ . "Lattice-compatible" refers to the alloy in which the lattice parameters of transformed and untransformed phases exhibit exceptional lattice compatibility (42). The straight line is a linear fit. The data from both polycrystalline and single-crystal materials are included. The numerical values used in this plot, as well as strain amplitude and references, are listed in table S1.

4.1 K. In a caloric cooling system,  $\Delta T_{ad}$  of caloric materials can be boosted into a large temperature span across a device by use of active regeneration schemes (16, 32, 33). The quasi-linear recovery behavior arises from the load transfer between the nontransforming intermetallic phase and the transforming non-load-bearing phase and has previously been also observed in melt-casted alloys after aging and/or cold-working (23, 34, 35). The effective modulus of the L-DED-produced Ni-Ti nanocomposite (~80–90 GPa) is higher than the typical austenite (~50 to 60 GPa), which indicates the effect of the nontransforming intermetallic  $Ni_3Ti$  phase in the nanocomposite. As a result, as the austenite transforms to martensite, the intermetallic phase continues to carry the load elastically, and the resulting overall behavior is quasi-linear. To confirm this mechanism, we simulated the crossover from a regular superelastic to quasi-linear behavior by varying the volume fraction of nontransforming intermetallic phase and observed the appearance of quasi-linear behavior at a level of 40, 50, and 60% (Fig. 2C).

The small hysteresis we observed is due to the topology- and defect-controlled kinematics of numerous nucleation events and coalescence, in which spatially dispersed preexisting nucleation sites (Fig. 1L) favor continual, heterogeneous nucleation of a new martensite followed by the sites' coalescence. The resulting volumetric densities of obstacles that austenite-

martensite transformation fronts meet in the course of transformation are reduced and require a decreased amount of frictional work to overcome, as observed in Cu-Zn-Al alloys (36). Additionally, the intermetallic phase has a large volume fraction (~50%) and effectively guides the transformation process through elastic interaction with the transforming phase. This process in turn tempers multiple instabilities that occur during traditional nucleation and fast growth and reduces energy dissipation and effective interfacial friction. We captured the progression in in situ synchrotron x-ray diffraction measurements (Fig. 2, D and E).

We attributed the commonly observed rate-dependent hysteresis (for example, the difference in hysteresis curves between Fig. 2, F and G) to transformation-related heat in SMAs in which surface convection dominates heat transfer. From an explicit integral equation of the specific dissipated energy  $\Delta E$  (which is equal to the generated heat) (37), we can approximate  $\Delta E$  as

$$\Delta E \cong E_{fr} + \Delta T_{ad} \cdot \Delta s$$

where  $E_{fr}$  is the irreversible specific energy that is the generated heat through interface friction and  $\Delta s$  is the specific entropy change associated with the phase transformation. The  $\Delta E$  during a stress-strain cycle manifests itself as the hysteresis area (divided by density) and increases with enlarged hysteresis. This relation

can also explain the nearly rate-independent hysteresis we observed in the Ni-Ti nanocomposite (Fig. 2H) in which thermal conduction (thermal conductivity  $\approx 18 \text{ W m}^{-1} \text{ K}^{-1}$ ) through a large-volume fraction of nontransforming phase and surface convection (with convective heat transfer coefficient  $\approx 4 \text{ W m}^{-2} \text{ K}^{-1}$ ) collectively facilitate effective heat transfer and rejection in a transformation cycle. In this example, the second term on the right of Eq. 1 becomes small owing to the rate of heat dissipation approaching the rate of heat generation.

Decreasing  $E_{fr}$  contributes to additional reduction in  $\Delta E$ .  $E_{fr}$  consists of two components:  $E_{fr} = E_f + E_p$  (38), where  $E_f$  is the heat dissipated from frictional work in a transformation cycle, and  $E_p$  is the heat dissipated by plastic work within austenite-martensite interfaces because of their coherency loss. Although friction is ubiquitous in the propagation of austenite-martensite interfaces (39), reducing extended interfacial motions by having uniformly distributed sites for nucleation and coalescence can substantially curtail frictions, leading to reduced  $E_f$ . The resultant minimization of  $E_f$  accounts for the substantial reduction in  $E_{fr}$  (Fig. 2H). In other alloy systems, relaxing local strain energy associated with phase transformation through improving lattice compatibility was found to lead to considerable reduction in  $E_p$  (40–42).  $E_{fr}$  remains constant at different rates and plays a role in



the rate independence of hysteresis in the Ni-Ti nanocomposite.

Thermodynamics of cooling devices dictates that small hysteresis during isothermal loading and unloading in Stirling-like cycles leads to high efficiencies (15, 43). However, under the same heat-exchange conditions as that of the Brayton-like cycle, Stirling-like operation cycles require much longer time per cycle (leading to reduced output wattage) and additional system components for effective heat transfer (43). In comparison, adiabatic loading and unloading in Brayton-like cycles (44) can operate much faster with relatively simple heat-exchange systems, albeit suffering from lower intrinsic efficiency because of the larger hysteresis (Fig. 2G).  $COP_{\text{materials}}$  in Brayton-like cycles are governed by the directly measured  $\Delta T_{\text{ad}}$  with the adiabatic hysteresis, and  $COP_{\text{materials}}$  in Stirling-like cycles are regulated by the latent heat with the isothermal hysteresis, on the basis of thermodynamically derived equations with full work recovery (24). The hysteresis of the L-DED-produced Ni-Ti nanocomposite is extremely small in both cycles and has a negligible difference (indicating rate independence). With a Carnot  $COP = 37.5$  for hot heat-exchanger temperature ( $T_h$ ) = 308 K and cold heat-exchanger temperature ( $T_c$ ) = 300 K, the ratio of  $COP_{\text{materials}}$  to Carnot  $COP$  of the L-DED-produced Ni-Ti nanocomposite is  $\approx 7$  times that of melt-casted Ni-Ti for adiabatic Brayton-like cycles (and  $\approx 4$  times that for isothermal Stirling-like cycles) at maximum transformations (Fig. 2H).

We studied the long-term stability of the L-DED-produced Ni-Ti nanocomposite. We found that the Ni-Ti nanocomposite is stable in its mechanical behavior and elastocaloric response for more than 1 million cycles (Fig. 3, A and B), indicating its potential for use in regular commercial products with a typical 10-year life [operating at  $<1$  Hz (15)]. This performance is in contrast to other cycled 3D-printed Ni-Ti materials (45, 46). Here, small hysteresis enabled by the nanostructured  $\text{Ni}_3\text{Ti}$  reinforcements is one important factor responsible for long-term stability. We previously showed that by tuning the lattice compatibility using stoichiometry in ternary alloys, we could minimize hysteresis of martensitic transformation and improve its reversibility to extended numbers of cycles (40, 47). However, a comparison of different SMA materials revealed that the absolute value of hysteresis is not the only determining factor. Magnetic SMAs such as polycrystalline Ni-Mn-In and Ni-Fe-Ga (table S1) seem to deteriorate quickly after a small number of cycles ( $\sim 100$ ), even with a hysteresis area as small as  $1.2 \text{ MJ m}^{-3}$ . For stress-induced fatigue, the endurance limit (that is, the stress amplitude able to attain a prescribed number of cycles, usually  $10^7$ , at zero mean

stress) is proportional to the ultimate strength of materials by a factor of  $\approx 0.33$  (48). Across a spectrum of elastocaloric materials, it is the ratio of hysteresis area,  $\Delta E$ , to the input work,  $E$ , that ultimately determines the number of cycles over which the materials can sustain their performance (Fig. 3C).

To understand this trend, we considered an analogy to the well-known  $S$ - $N$  concept conceived by Wöhler in 1858 (49) that connects the stress amplitude ( $S$ ) to the cycles to failure ( $N$ ) in the structural fatigue of materials and obtained a correlation of  $\Delta E/E$  (hysteresis as a fraction of input energy) to the cycles to “functional failure,”  $N$ , (which we define as the number of cycles at the onset of loss of their functionality) (Fig. 3C). In an ideal case of  $\Delta E/E = 0$  (transformation with no hysteresis), the number of cycles to functional failure would asymptotically approach infinity (or extremely large numbers). SMAs typically exhibit hysteresis in superelastic cycles; the best  $\Delta E/E$  hitherto reported for cycling are from  $\text{Zn}_{45}\text{Au}_{30}\text{Cu}_{25}$  alloys optimized through tuning the lattice parameters (42) and a  $\text{Ni}_{51.5}\text{Ti}_{48.5}/\text{Ni}_3\text{Ti}$  nanocomposite with friction-limited kinematics in this work, both of which possess a  $\Delta E/E$  less than 10%. Because of similarity in the hysteresis behavior associated with input work among different materials, the energy-based  $(\Delta E/E)$ - $N$  correlation observed here for elastocaloric materials could in principle apply to other caloric materials (magnetocaloric and electrocaloric materials). Even though the data on fatigue behavior of other caloric materials are somewhat limited (table S1), our preliminary analysis indicates that the same correlation holds for them as well. Caloric materials based on first-order transitions with reported low cyclability (such as  $<10,000$  cycles) can potentially have their functional fatigue lives extended if their  $\Delta E/E$  can be decreased through, for example, materials processing.

The conventional wisdom in the SMA community is that presence of nonequiatom phases such as  $\text{Ni}_3\text{Ti}$  in the NiTi matrix is detrimental to materials integrity because the presence of brittle phases precipitated along grain boundaries can lead to fracture from local stress concentration (50) and mismatch stress generated from transformation-induced shape distortions in neighboring grains (51). The nonequiatom phases have also plagued the self-propagating high-temperature synthesis used for porous Ni-Ti materials for decades because they occur inevitably and produce chemical inhomogeneity in porous implants (52). We created a Ni-Ti-based elastocaloric material whose exceptional stability and unusual operational efficiency are derived from their distinct and intricate nanocomposite structures made by means of additive manufacturing. This demonstration shows the po-

tential for using additive manufacturing to optimize caloric cooling by providing a highly desirable topology flexibility into materials components that serve as both refrigerants and heat exchangers.

## REFERENCES AND NOTES

- D. Coulomb, J.-L. Dupont, A. Pichard, *The Role of Refrigeration in the Global Economy* (International Institute of Refrigeration, 2015).
- J. He, T. M. Tritt, *Science* **357**, eaak9997 (2017).
- Y. Zhai et al., *Science* **355**, 1062–1066 (2017).
- X. Moya, S. Kar-Narayan, N. D. Mathur, *Nat. Mater.* **13**, 439–450 (2014).
- S. Fährler et al., *Adv. Eng. Mater.* **14**, 10–19 (2012).
- L. Mañosa, A. Planes, M. Acet, *J. Mater. Chem. A Mater. Energy Sustain.* **1**, 4925–4936 (2013).
- I. Takeuchi, K. Sandeman, *Phys. Today* **68**, 48–54 (2015).
- D. C. Lagoudas, *Shape Memory Alloys: Modeling and Engineering Applications* (Springer, 2008).
- K. Otsuka, X. Ren, *Prog. Mater. Sci.* **50**, 511–678 (2005).
- E. Bonnot, R. Romero, L. Mañosa, E. Vives, A. Planes, *Phys. Rev. Lett.* **100**, 125901 (2008).
- J. Cui et al., *Appl. Phys. Lett.* **101**, 073904 (2012).
- D. Cong et al., *Phys. Rev. Lett.* **122**, 255703 (2019).
- G. J. Pataky, E. Ertekin, H. Sehitoglu, *Acta Mater.* **96**, 420–427 (2015).
- W. Goetzler, R. Zogg, J. Young, C. Johnson, “Energy savings potential and RD&D opportunities for non-vapor-compression HVAC technologies” (Navigant Consulting, prepared for the U.S. Department of Energy, 2014).
- S. Qian et al., *Int. J. Refrig.* **64**, 1–19 (2016).
- J. Tušek et al., *Nat. Energy* **1**, 16134 (2016).
- K. Engelbrecht et al., *J. Phys. D Appl. Phys.* **50**, 424006 (2017).
- M. Elahinia et al., *Prog. Mater. Sci.* **83**, 630–663 (2016).
- S. Dadbakhsh, M. Speirs, J. Van Humbeeck, J.-P. Kruth, *MRS Bull.* **41**, 765–774 (2016).
- O. A. Shaw, *Int. J. Plast.* **16**, 541–562 (2000).
- O. P. Bruno, P. H. Leo, F. Reith, *Phys. Rev. Lett.* **74**, 746–749 (1995).
- T. DebRoy et al., *Prog. Mater. Sci.* **92**, 112–224 (2018).
- S. Hao et al., *Science* **339**, 1191–1194 (2013).
- Materials and methods are available as supplementary materials.
- M. Thomas, G. J. Baxter, I. Todd, *Acta Mater.* **108**, 26–35 (2016).
- S. Kou, *Welding Metallurgy* (Wiley, 2003).
- T. DebRoy, S. A. David, *Rev. Mod. Phys.* **67**, 85–112 (1995).
- J. H. Martin et al., *Nature* **549**, 365–369 (2017).
- A. Ibarra, D. Caillard, J. San Juan, M. L. No, *Appl. Phys. Lett.* **90**, 101907 (2007).
- I. W. Chen, Y. H. Chiao, *Acta Metall.* **33**, 1827–1845 (1985).
- M. J. Buehler, A. Misra, *MRS Bull.* **44**, 19–24 (2019).
- W. Steyert, *J. Appl. Phys.* **49**, 1216–1226 (1978).
- J. Liu, T. Gottschall, K. P. Skokov, J. D. Moore, O. Gutfleisch, *Nat. Mater.* **11**, 620–626 (2012).
- L. Casalena et al., *Adv. Eng. Mater.* **20**, 1800046 (2018).
- A. Ahadi, Q. P. Sun, *Appl. Phys. Lett.* **103**, 021902 (2013).
- S. M. Ueland, C. A. Schuh, *Acta Mater.* **61**, 5618–5625 (2013).
- Y. Chen, C. A. Schuh, *Acta Mater.* **59**, 537–553 (2011).
- R. F. Hamilton, H. Sehitoglu, Y. Chumlyakov, H. J. Maier, *Acta Mater.* **52**, 3383–3402 (2004).
- P. Sedmák et al., *Science* **353**, 559–562 (2016).
- J. Cui et al., *Nat. Mater.* **5**, 286–290 (2006).
- C. Chluba et al., *Science* **348**, 1004–1007 (2015).
- Y. Song, X. Chen, V. Dabade, T. W. Shield, R. D. James, *Nature* **502**, 85–88 (2013).
- A. Kitanovski, J. Tušek, U. Tomc, U. Plaznik, M. Ožbolt, A. Poredoš, *Magnetocaloric Energy Conversion* (Springer, 2015).
- J. Tušek et al., *Adv. Energy Mater.* **5**, 1500361 (2015).
- S. Bernard, V. Krishna Balla, S. Bose, A. Bandyopadhyay, *J. Mech. Behav. Biomed. Mater.* **13**, 62–68 (2012).
- A. Bagheri, M. J. Mahtabi, N. Shamsaei, *J. Mater. Process. Technol.* **252**, 440–453 (2018).
- R. Zarnetta et al., *Adv. Funct. Mater.* **20**, 1917–1923 (2010).
- M. Ashby, H. Shercliff, D. Cebon, *Materials: Engineering, Science, Processing and Design* (Butterworth-Heinemann, 2007).
- G. Eggeler, E. Hornbogen, A. Yawny, A. Heckmann, M. Wagner, *Mater. Sci. Eng. A* **378**, 24–33 (2004).
- Y. Tanaka et al., *Science* **327**, 1488–1490 (2010).

51. A. Lai, Z. Du, C. L. Gan, C. A. Schuh, . *Science* **341**, 1505–1508 (2013).
52. A. Bansiddhi, T. D. Sargeant, S. I. Stupp, D. C. Dunand, *Acta Biomater.* **4**, 773–782 (2008).
53. T. B. Massalski, H. Okamoto, P. R. Subramanian, L. Kacprzak, *Binary Alloy Phase Diagrams* (ASM International, ed. 2, 1990).

#### ACKNOWLEDGMENTS

We thank N. M. Wereley and T. Pillsbury of the University of Maryland for assistance in cyclic experiments and J.-S. Park of the Argonne National Laboratory for support in configuring and aligning the x-ray diffraction experiments. **Funding:** Advanced Research Projects Agency-Energy (ARPA-E) of the U.S. Department of Energy (DOE) supported the original characterization of shape memory alloys at the University of Maryland under grant ARPA-E DEAR0000131. The use of the laser-engineered net shaping (LENS) equipment was supported by the Critical Materials Institute, an Energy Innovation Hub funded by the Advanced Manufacturing Office of the Office of Energy Efficiency and Renewable Energy of the DOE. The work at Ames Laboratory was also supported by the Division of Materials Science and Engineering of the Basic Energy Sciences Programs of the Office

of Science of the DOE under contract DE-AC02-07CH11358 with Iowa State University. A.P.S. and C.C. acknowledge the funding from the National Science Foundation (Career Award CMMI-1454668), and N.S.J. acknowledges a Los Alamos National Laboratory Additive Manufacturing Graduate Fellowship given to the Alliance for the Development of Additive Processing Technologies (ADAPT). V.I.L. acknowledges the funding from the National Science Foundation (MMN-1904830) and Army Research Office (W911NF-17-1-0225). The in situ x-ray diffraction experiments were performed at the 1-ID-E beamline of the Advanced Photon Source, a DOE Office of Science User Facility operated for the DOE Office of Science by Argonne National Laboratory under contract DE-AC02-06CH11357. **Author contributions:** I.T. initiated and supervised the research. H.H., J.C., and I.T. planned the experiments and designed the samples. E.S. and R.T.O. prepared the materials using the LENS. D.S. and N.A.H. characterized the composition of materials. H.H. carried out the experiments—including heat treatment, DSC measurement, superelastic tests, elastocaloric cooling measurements, and long-cycle tests—and analyzed the data. T.M., L.Z., and M.J.K. conducted SEM and TEM analysis. N.S.J., C.C., and A.P.S. performed and analyzed the in situ x-ray diffraction experiments,

and C.C., M.A.Z., and A.P.S. performed the finite element modeling. S.Q., Y.H., and R.R. discussed the thermodynamic cycles. V.I.L. discussed the mechanism involving interfacial dislocations and shakedown. H.H., A.P.S., J.C., and I.T. wrote the paper with substantial input from other authors. All authors contributed to the discussion of the results. **Competing interests:** I.T. is a founder of Maryland Energy & Sensor Technologies, a company that works on elastocaloric technologies. **Data and materials availability:** All data are available in the manuscript or the supplementary materials.

#### SUPPLEMENTARY MATERIALS

science.sciencemag.org/content/366/6469/1116/suppl/DC1  
Materials and Methods  
Supplementary Text  
Figs. S1 to S8  
Table S1  
References (54–85)

12 August 2019; accepted 1 November 2019  
10.1126/science.aax7616



## MAGNONICS

# Mutual control of coherent spin waves and magnetic domain walls in a magnonic device

Jiahao Han, Pengxiang Zhang, Justin T. Hou, Saima A. Siddiqui, Luqiao Liu\*

The successful implementation of spin-wave devices requires efficient modulation of spin-wave propagation. Using cobalt/nickel multilayer films, we experimentally demonstrate that nanometer-wide magnetic domain walls can be applied to manipulate the phase and magnitude of coherent spin waves in a nonvolatile manner. We further show that a spin wave can, in turn, be used to change the position of magnetic domain walls by means of the spin-transfer torque effect generated from magnon spin current. This mutual interaction between spin waves and magnetic domain walls opens up the possibility of realizing all-magnon spintronic devices, in which one spin-wave signal can be used to control others by reconfiguring magnetic domain structures.

As propagating oscillations of magnetic moments, spin waves (SWs) can transmit spin information over macroscopic distances in the absence of Joule heating (1–6). To manipulate the propagation of SWs, various methods such as lithographically defined synthetic crystals (7, 8), static magnetic fields (9, 10), and electrical currents (11–14) have been used. The large size (above the micrometer scale) of control terminals and high power consumption in these devices pose obstacles for practical applications. Magnetic textures such as magnetic domain walls (DWs) have been suggested as an alternative. It has been predicted that DWs can cause substantial changes in the phase and magnitude of SWs within the length scale of nanometers (15–19). This prediction, in combination with reconfigurability (20, 21) and nonvolatility (22) of DWs, makes DWs promising candidates for modulating SWs. However, little experimental progress has been reported in this direction (23). A major challenge for experimentally studying the SW transmission in the presence of DWs is that resonant excitation and coherent propagation of SWs require well-defined quantization axes for spins. In existing studies, this condition is usually realized through the application of a large external magnetic field (8–10, 12–14), which prevents the formation of more than one magnetic domain. To achieve the coexistence of DWs and zero-field ferromagnetic resonance (FMR), thin films with strong magnetic anisotropy and low damping are highly desirable. In addition to DW-modulated SW transmission, the mutual interactions between SWs and DWs can enable the inverse effect: the SW-induced DW movement. As shown in Fig. 1A, SWs carry magnon spin currents along their propagation direction. On the two sides of a DW, the magnons have opposite spin angular momen-

tum and flow in the same direction, leading to a net spin injection into the DW. This provides the possibility of manipulating the orientation of magnetic domains through magnon-induced spin-transfer torque (24).

In this study, we employed magnetic films with perpendicular magnetic anisotropy (PMA) to achieve the mutual control of SWs and DWs. The magnetic films used in our experiments consist of substrate/Ti(8)/Pt(7)/[Co(0.4)/Ni(0.35–0.4)]<sub>9</sub>/Ru(3) (numbers indicate width in nanometers). The Co/Ni multilayer films were chosen for their high PMA, large magnetic volume, and low magnetic damping. Different from other films with interfacial PMA such as Ta/CoFeB/MgO or Pt/Co/AlO<sub>x</sub>, in which only one thin layer of magnetic material can be used to carry SWs, our perpendicularly magnetized Co/Ni multilayers (25) have a much larger total magnetic thickness, carrying larger amounts of power through SWs. In addition, Co/Ni films exhibit moderate magnetic damping (26) compared with other bulk PMA films, enabling propagation of SWs over detectable distances. FMR spectra (Fig. 1B) were obtained on an unpatterned film by sweeping the field with fixed microwave frequency, and a moderate Gilbert damping factor of 0.024 was determined (Fig. 1C) (25). Moreover, a zero-field FMR was reached at 7.5 GHz (Fig. 1B), which made it possible to excite coherent SWs while maintaining the DW structure.

To study the SW propagation, we patterned films into strips with width between 3 and 6  $\mu\text{m}$  and then deposited SiO<sub>2</sub> mesas (50 nm thick) for electrical isolation. A pair of microwave antennae was further deposited for SW excitation and detection (27, 28). Following the design in (28), we fabricated the antennae as ground-signal-ground coplanar waveguides with three meanders to obtain a well-defined wavelength (3.2  $\mu\text{m}$ ) corresponding to a wave number of  $k = 1.96 \mu\text{m}^{-1}$  (Fig. 2, A and B). This design ensures the resonant generation of highly coherent SWs with more uniform wavelength, in contrast to other approaches that

use thermal gradient (29), spin injection (6, 30), or broadband microstrip (9, 10, 12) to excite SWs. The excitation and transmission of SWs were monitored with a 20-GHz vector network analyzer through the *S*-parameter measurement. The spectra of microwave reflection coefficient  $S_{11}$  and transmission coefficient  $S_{21}$  of a uniformly magnetized channel at zero dc field are shown in Fig. 2C and the upper trace of Fig. 2D, respectively; both exhibit resonant features at 7.8 GHz. To verify the magnetic origin of the observed resonant signal, we measured  $S_{21}$  spectra under different applied external fields  $H_{\text{ext}}$  with the resonant frequency  $f$  versus  $H_{\text{ext}}$  relationship summarized in the inset of Fig. 2D. A typical spectrum at  $H_{\text{ext}} = 200 \text{ Oe}$  is shown as the bottom trace in Fig. 2D. The oscillating real and imaginary parts with a 90° phase difference are typical characteristics of propagating SWs. In a control sample with a 2.6- $\mu\text{m}$ -wide gap in the magnetic strip between two antennae (inset of Fig. 2E), no transmission signal was detected within the resolution of our setup (Fig. 2E). Moreover,  $S_{21}$  spectra with different propagation lengths were measured, for which the SW decay length (31) of  $\sim 3 \mu\text{m}$  was extracted and the propagating SW picture was further confirmed (fig. S3).

We then studied the transmission of SWs through a DW by using microwave circuits integrated with a magneto-optic Kerr effect (MOKE) microscope (Fig. 3A). Figure 3, B and C, shows typical MOKE images, with bright and dark colors representing oppositely oriented domains. By applying millisecond magnetic field pulses, we toggled the magnetic strip between a uniformly magnetized state (Fig. 3B) and a DW state (Fig. 3C). The DW width is estimated to be  $\sim 20 \text{ nm}$  (25). During the measurement, the edge of the SiO<sub>2</sub> mesa assists the pinning of the DW, allowing for repeatable formation of DWs at the same location. By comparing the  $S_{21}$  spectra that correspond to the two different magnetic states in Fig. 3, B and C (Fig. 3, D and E, respectively), we found that when SWs pass through a DW, they keep the same resonance frequency as the uniform state but experience a magnitude attenuation by a factor of 4.3 (or, equivalently, a power reduction by a factor of 18). This observed reduction in the transmitted SW magnitude is consistent with the previous experiment on more complicated Landau domain structures (23), which can be explained by the reflection of SWs at the DW edge caused by the quasi-rigid boundary condition for magnetic moments. Aside from the attenuation in magnitude, a 175° phase shift appears for the SWs propagating through the DW (see the real and imaginary parts of  $S_{21}$  in Fig. 3, D and E). This nearly 180° phase shift is robust across our fabricated devices and immune to specific DW configuration (i.e., up-down or down-up). Five devices with the same design

Department of Electrical Engineering and Computer Science, Massachusetts Institute of Technology, Cambridge, MA 02139, USA.

\*Corresponding author. Email: luqiao@mit.edu

have been checked and similar results have been obtained, with variance of the magnitude attenuation and the phase shift being within 10% (figs. S5 and S6). Control of wave phases lies at the heart of physical implementation of wave-based computing and signal processing. Various magnonic logic devices (4, 15, 19, 32), which rely on the interference between SWs with different phases, have been previously proposed. The experimental discovery of the phase-shifting effect can therefore be useful for realizing those devices.

To better understand the DW-induced SW modulation, we carried out micromagnetic simulations (33) by using material parameters consistent with our real samples. Figure 3F presents the top view of a magnetic channel with propagating SWs, described by the  $x$  component of magnetization ( $m_x$ ). We chose to monitor  $m_x$  in the simulations because of its direct correlation with the experimental observable in our sample geometry (25). A radio frequency magnetic field was locally applied near one end of the channel to excite SWs. Considering the magnetostatic nature of our SW, we set the aspect ratio between the channel width and the SW wavelength to be the same as that of the real device. By comparing the top and bottom panels of Fig. 3F, it is evident that when the SWs encounter a DW, the oscillating  $m_x$  experiences an attenuation in magnitude and a shift of  $\sim 180^\circ$  in phase, consistent with our experimental results. The phase shift in the narrow DW limit can also be possibly explained by considering the magnetic field boundary conditions at the opposite ends of the DW (25).

Similar to spin-valve structures, in which magnetic orientation may result in resistance change (giant or tunneling magnetoresistance) and current may induce magnetic switching (spin-transfer torque), the device structure studied in our experiments can also exhibit this pair of inverse effects. In the structure shown in Fig. 1A, the SWs carry magnon spin current  $J_s$  with spin angular momentum antiparallel to the local equilibrium direction. Across the DW, the spins carried by  $J_s$  reverse sign, resulting in net spin current divergence, which can further cause spin-transfer torque-induced magnetic switching. To observe this effect experimentally, we applied large-magnitude SWs by increasing the driving microwave power. Moreover, we adopted a simple antenna design with one meander (Fig. 4A), whose reduced resistance optimizes the impedance matching with the microwave circuit. In addition, a single antenna, rather than antenna pairs, was employed for clearer observation of the DW movement at longer length scales. In this measurement, an up-down DW was nucleated close to the antenna with external magnetic field pulses, as shown by the boundary between the bright and dark regions

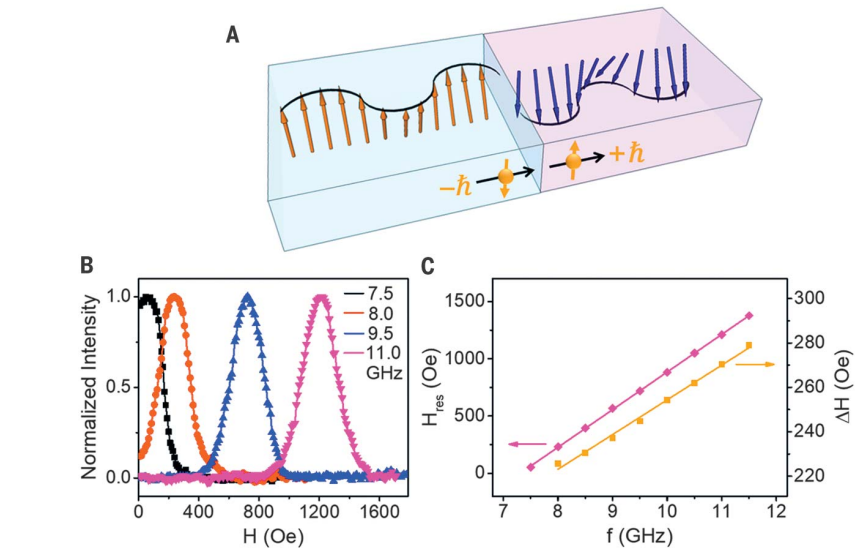


**Fig. 1. Illustration of the basic concept and FMR measurements of thin-film samples.** (A) Schematic of SWs passing through a DW. The magnons at different sides of the DW carry opposite spins, which leads to a spin angular momentum transfer to the DW.  $\pm\hbar$  represents the angular momentum of each magnon. (B) FMR spectra of unpatterned Co/Ni films at different microwave frequencies. The field is applied out of plane. (C) FMR resonant field ( $H_{res}$ ) and linewidth ( $\Delta H$ ) as a function of microwave frequency.

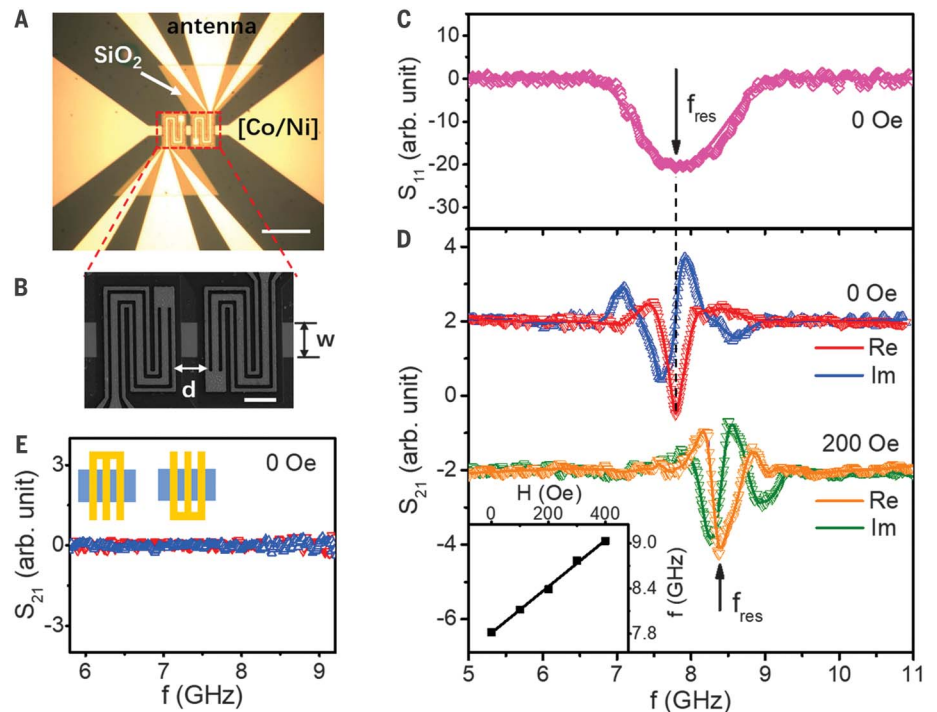


**Fig. 2. SW transmission in uniformly magnetized devices.** (A) Optical image of the device. Scale bar, 30  $\mu\text{m}$ . (B) Scanning electron microscopy (SEM) image of the center of the device. The width of the magnetic channel is  $w = 6 \mu\text{m}$  and the distance between the antennae is  $d = 6.4 \mu\text{m}$ . Scale bar, 6  $\mu\text{m}$ . (C) Reflection spectrum  $S_{11}$  at zero field. (D) Transmission spectrum  $S_{21}$  with external fields of 0 (top) and 200 Oe (bottom). The (arbitrary) unit is the same for  $S_{11}$  and  $S_{21}$ , enabling a comparison of their values. Re, real; Im, imaginary. (Inset) Resonant frequency as a function of external field measured from  $S_{21}$ . (E) Transmission spectrum of a control sample, where the magnetic strip is discontinuous with a 2.6- $\mu\text{m}$ -wide gap between the antennae. A microwave power of 4  $\mu\text{W}$  was used for all measurements depicted in this figure.



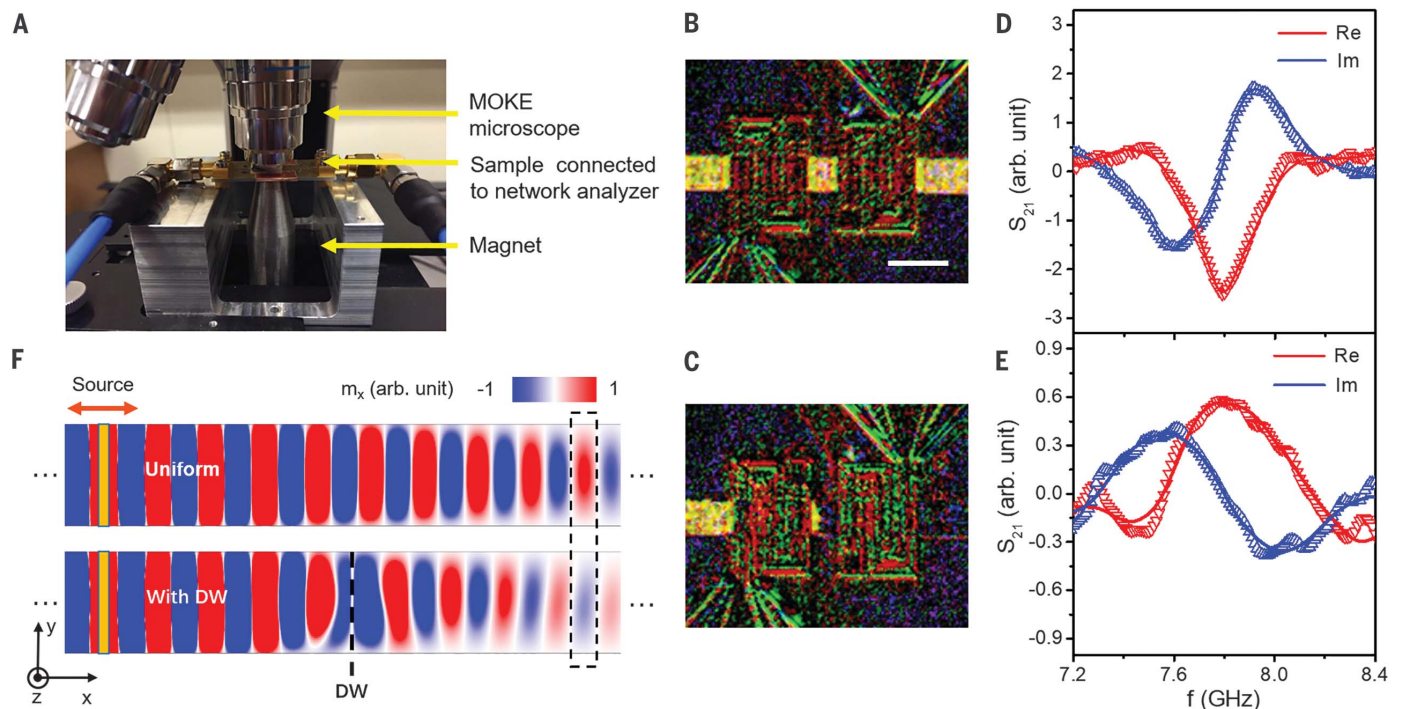


**Fig. 3. SW propagation across a DW.** (A) Photo of the experimental setup. (B and C) MOKE images of the device in a uniformly magnetized state and a DW state, respectively. The bright and dark regions in the magnetic channel represent domains with up and down magnetization. In the DW state, the wall is located between the two antennae. Scale bar, 10  $\mu\text{m}$ . (D and E)  $S_{21}$  spectra for (B) and (C). A microwave power of 4  $\mu\text{W}$  was used for the measurement. (F) Simulated SW propagation in a 600-nm-wide magnetic channel without (top) and with (bottom) a DW. The SW wavelength is 320 nm.  $m_x$  represents the  $x$  component of the magnetization. The dashed rectangle indicates a typical region for comparing the magnitude and phase of the transmitted SWs in the uniform channel and the channel with a DW.

in the top panel of Fig. 4B. With the application of the SW, the DW moves toward the SW source in the absence of any dc magnetic field and stops underneath the antenna (bottom panel of Fig. 4B). A similar effect was observed for the down-up DW (see the movement of the boundary between dark and bright regions in Fig. 4C). When the device was driven with off-resonance microwave signals at the same power, no DW motion was detected. In our experiment, DWs always move against the SW-flowing direction, consistent with the magnonic spin-transfer torque mechanism (24, 34) and in contrast to the linear momentum transfer picture (35). This observed DW movement direction differs from the recently observed field-induced DW movement under the assistance of transient SWs (36), where SWs help DWs move along the wave-flowing direction. Using the microwave power in our DW motion experiment, we can estimate the spin current density carried by the SW to be on the order of  $10^7 (\hbar/2e)\text{A}/\text{cm}^2$  ( $\hbar$ , Planck's constant divided by  $2\pi$ ;  $e$ , elementary charge) (25), similar to the typical threshold spin current density needed for current-induced DW motion (22). Under this magnon spin current density, the DW velocity is expected to be  $\sim 10$  m/s (24, 25), comparable to the velocities obtained in the spin-transfer torque configuration (22).

To further verify the spin-transfer torque origin of the observed DW motion, we experimentally determined the switching phase diagram of the DW under applied SW and external fields. The depinning field ( $H_{\text{depin}}$ ) was measured by simultaneously applying external magnetic field pulses and continuous microwave power at the resonant frequency. Using the magnetometry mode of MOKE microscope, we determined the switching curves of magnetic domains (Fig. 4D). Under the application of SWs,  $H_{\text{depin}}$  exhibits an overall shift, indicating that the SWs assist the DW to move toward the antenna and hamper the motion in the opposite direction.  $H_{\text{depin}}$  as a function of the driving microwave power is summarized in Fig. 4E under both on-resonance frequency (8.8 GHz) and off-resonance frequency (7 GHz). For the off-resonance case, a simple reduction of  $H_{\text{depin}}$  in both directions was observed, which can be explained by a trivial thermal effect that suppresses the switching energy barrier. By comparing the slopes of the two groups of curves, we found that, whereas the thermal effects are similar, only the on-resonance data show asymmetries in  $H_{\text{depin}}$  of the two different switching directions, indicating that coherent magnons other than thermally induced spin flow (29) play a major role in the observed DW motion. To exclude the contribution from the extra heating effect

caused by FMR, we used the anomalous Hall effect to quantitatively characterize the magnetization change in the two experimental situations, as well as to compare them with the change caused by dc current-induced Joule heating. We found that the heating-induced reduction in magnetization cannot account for the observed effect (25). Finally,  $H_{\text{depin}}$  under different driving frequencies is summarized in Fig. 4G, consistent with the SW absorption spectrum (Fig. 4F).

The transfer of spin current with magnon flow represents an energy-efficient process. To transfer one unit of spin angular momentum ( $\hbar$ ), the energy of a magnon ( $\hbar\omega$ ) must be consumed, corresponding to tens of micro-electron volts for gigahertz SWs. This amount is smaller than the energy consumption in other spin current-generation methods such as tunnel junctions or spin valves, for which the corresponding value is in the range of milli-electron volts to sub-electron volts. Substantial differences still exist between the power carried by the SW in the device and that generated at our microwave source, which mainly comes from the low efficiency associated with the inductive generation of SWs using the antenna, degrading the overall power performance of the studied device. This can be improved by using energy-efficient SW generation mechanisms (37, 38). In the meantime, the energy

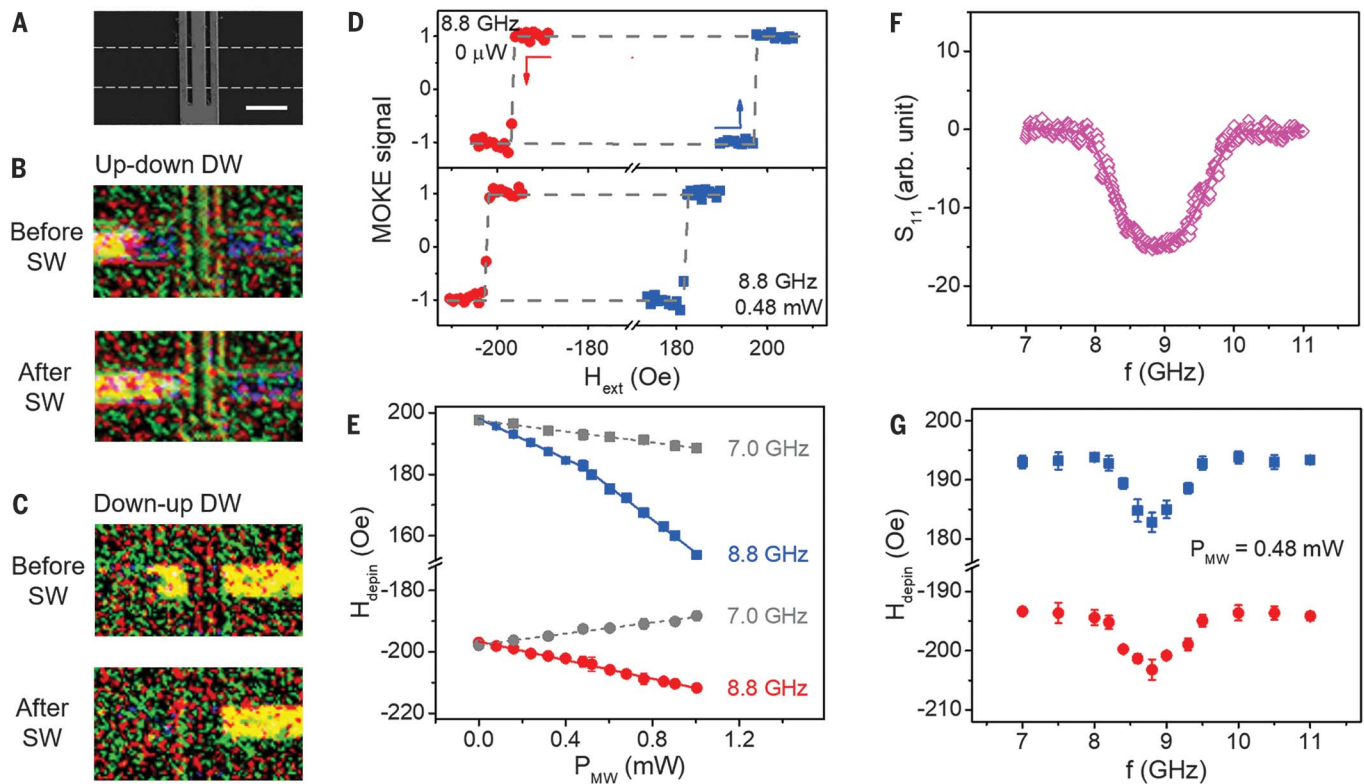


**Fig. 4. Magnetic domain switching induced by SWs.** (A) SEM image of the device. The magnetic strip under  $\text{SiO}_2$  is marked by the dashed lines. Scale bar, 4  $\mu\text{m}$ . (B and C) MOKE images showing the movement of the up-down and down-up DWs under zero dc magnetic field. The bright and dark regions in the magnetic channel represent domains with up and down magnetization. The microwave power applied onto the antenna is  $P_{\text{MW}} = 2.2$  mW at resonant frequency (8.8 GHz for this sample, slightly higher than the previous value, owing to the stronger anisotropy

field). See (25) for the power calibration methods. (D) Magnetic switching around the DW location measured from a MOKE magnetometer, under microwave power of  $P_{\text{MW}} = 0.48$  mW at 8.8 GHz. (E)  $H_{\text{depin}}$  as a function of microwave power. (F) SW reflection spectrum at zero dc field. (G)  $H_{\text{depin}}$  as a function of microwave frequency. The microwave power is fixed at  $P_{\text{MW}} = 0.48$  mW. The applied field in this measurement is small compared with the linewidth of this sample, so the SWs still propagate across the DW with slightly reduced power.

efficiency of magnonic devices can be enhanced by keeping signals in the SW domain and avoiding frequent interconversions between electrical and SW signals. Our experimental results of the mutual control between SWs and DWs thus facilitate the possibility of using one SW to modulate the transmission of others by reconfiguring the magnetic domain structures.

#### REFERENCES AND NOTES

- V. V. Kruglyak, S. O. Demokritov, D. Grundler, *J. Phys. D* **43**, 264001 (2010).
- A. Khitun, M. Bao, K. L. Wang, *J. Phys. D* **43**, 264005 (2010).
- B. Lenk, H. Ulrichs, F. Garbs, M. Münzenberg, *Phys. Rep.* **507**, 107–136 (2011).
- A. V. Chumak, V. I. Vasyuchka, A. A. Serga, B. Hillebrands, *Nat. Phys.* **11**, 453–461 (2015).
- G. Csaba, Á. Papp, W. Porod, *Phys. Lett. A* **381**, 1471–1476 (2017).
- Y. Kajiwara et al., *Nature* **464**, 262–266 (2010).
- Z. K. Wang et al., *Appl. Phys. Lett.* **94**, 083112 (2009).
- H. Yu et al., *Nat. Commun.* **7**, 11255 (2016).
- T. Schneider et al., *Appl. Phys. Lett.* **92**, 022505 (2008).
- S. O. Demokritov et al., *Phys. Rev. Lett.* **93**, 047201 (2004).
- S.-M. Seo, K.-J. Lee, H. Yang, T. Ono, *Phys. Rev. Lett.* **102**, 147202 (2009).
- Z. Wang, Y. Sun, M. Wu, V. Tiberkevich, A. Slavin, *Phys. Rev. Lett.* **107**, 146602 (2011).
- A. Hamadeh et al., *Phys. Rev. Lett.* **113**, 197203 (2014).
- V. V. Vlasov, M. Bailleul, *Science* **322**, 410–413 (2008).
- R. Hertel, W. Wulfhekel, J. Kirschner, *Phys. Rev. Lett.* **93**, 257202 (2004).
- C. Bayer, H. Schultheiss, B. Hillebrands, R. L. Stamps, *IEEE Trans. Magn.* **41**, 3094–3096 (2005).
- S. Macke, D. Goll, *J. Phys. Conf. Ser.* **200**, 042015 (2010).
- J. S. Kim et al., *Phys. Rev. B* **85**, 174428 (2012).
- F. J. Buijsters, Y. Ferreiros, A. Fasolino, M. I. Katsnelson, *Phys. Rev. Lett.* **116**, 147204 (2016).
- E. Albisetti et al., *Nat. Nanotechnol.* **11**, 545–551 (2016).
- K. Wagner et al., *Nat. Nanotechnol.* **11**, 432–436 (2016).
- S. S. P. Parkin, M. Hayashi, L. Thomas, *Science* **320**, 190–194 (2008).
- P. Pirro et al., *Appl. Phys. Lett.* **106**, 232405 (2015).
- P. Yan, X. S. Wang, X. R. Wang, *Phys. Rev. Lett.* **107**, 177207 (2011).
- Detailed discussions are available in the supplementary materials.
- J.-M. Beaupour, D. Ravelosona, I. Tudosa, E. E. Fullerton, A. D. Kent, *Phys. Rev. B* **80**, 180415(R) (2009).
- M. Bailleul, D. Olligs, C. Fermon, S. O. Demokritov, *Europhys. Lett.* **56**, 741–747 (2001).
- V. Vlasov, M. Bailleul, *Phys. Rev. B* **81**, 014425 (2010).
- W. Jiang et al., *Phys. Rev. Lett.* **110**, 177202 (2013).
- L. J. Cornelissen, J. Liu, R. A. Duine, J. Ben Youssef, B. J. van Wees, *Nat. Phys.* **11**, 1022–1026 (2015).
- N. Loayza, M. B. Jungfleisch, A. Hoffmann, M. Bailleul, V. Vlasov, *Phys. Rev. B* **98**, 144430 (2018).
- K.-S. Lee, S.-K. Kim, *J. Appl. Phys.* **104**, 053909 (2008).
- M. J. Donahue, D. G. Porter, “OOMMF User’s Guide, version 1.0” (National Institute of Standards and Technology, 1999).
- Y. Cheng, K. Chen, S. Zhang, *Appl. Phys. Lett.* **112**, 052405 (2018).
- X. Wang, G. Guo, Y. Nie, G. Zhang, Z. Li, *Phys. Rev. B* **86**, 054445 (2012).
- S. Woo, T. Delaney, G. S. D. Beach, *Nat. Phys.* **13**, 448–454 (2017).
- V. E. Demidov et al., *Nat. Mater.* **11**, 1028–1031 (2012).
- Z. Duan et al., *Nat. Commun.* **5**, 5616 (2014).
- J. Han, P. Zhang, J. T. Hou, S. A. Siddiqui, L. Liu, Data from: Mutual control of coherent spin waves and magnetic domain walls in a magnonic device. Version 1, Zenodo (2019); <https://doi.org/10.5281/zenodo.3483803>.

#### ACKNOWLEDGMENTS

The simulations were performed on the Engaging Cluster at the Massachusetts Green High Performance Computing Center (MGHPCC). J.H. acknowledges J. Han and H. Wang for help with device fabrication and SEM imaging. **Funding:** This work was supported by AFOSR under award FA9550-19-1-0048 and the National Science Foundation under award ECCS-1653553. **Author contributions:** L.L. proposed and directed the study. J.H. prepared the samples and carried out the measurements, with help from S.A.S. P.Z. conducted micromagnetic simulations. J.T.H. helped with the measurement setup. J.H., P.Z., and L.L. analyzed the data and wrote the manuscript. All authors commented on the manuscript. **Competing interests:** The authors declare no competing interests. **Data and materials availability:** All data shown in the main text and the supplementary materials are deposited in the Zenodo public repository (39). The micromagnetic simulations are performed by using the open-source code OOMMF (Object Oriented Micromagnetic Framework) (33).

#### SUPPLEMENTARY MATERIALS

[science.sciencemag.org/content/366/6469/1121/suppl/DC1](https://science.sciencemag.org/content/366/6469/1121/suppl/DC1)  
Materials and Methods  
Supplementary Text  
Figs. S1 to S13  
References (40–71)

24 May 2018; resubmitted 21 November 2018  
Accepted 4 November 2019  
10.1126/science.aau2610



## MAGNONICS

# Magnetization switching by magnon-mediated spin torque through an antiferromagnetic insulator

Yi Wang<sup>1,2\*</sup>, Dapeng Zhu<sup>1\*</sup>, Yumeng Yang<sup>1</sup>, Kyusup Lee<sup>1</sup>, Rahul Mishra<sup>1</sup>, Gyungchoon Go<sup>3</sup>, Se-Hyeok Oh<sup>4</sup>, Dong-Hyun Kim<sup>5</sup>, Kaiming Cai<sup>1</sup>, Enlong Liu<sup>1</sup>, Shawn D. Pollard<sup>1</sup>, Shuyuan Shi<sup>1</sup>, Jongmin Lee<sup>1</sup>, Kie Leong Teo<sup>1</sup>, Yihong Wu<sup>1</sup>, Kyung-Jin Lee<sup>3,4,5,6</sup>, Hyunsoo Yang<sup>1†</sup>

Widespread applications of magnetic devices require an efficient means to manipulate the local magnetization. One mechanism is the electrical spin-transfer torque associated with electron-mediated spin currents; however, this suffers from substantial energy dissipation caused by Joule heating. We experimentally demonstrated an alternative approach based on magnon currents and achieved magnon-torque-induced magnetization switching in Bi<sub>2</sub>Se<sub>3</sub>/antiferromagnetic insulator NiO/ferromagnet devices at room temperature. The magnon currents carry spin angular momentum efficiently without involving moving electrons through a 25-nanometer-thick NiO layer. The magnon torque is sufficient to control the magnetization, which is comparable with previously observed electrical spin torque ratios. This research, which is relevant to the energy-efficient control of spintronic devices, will invigorate magnon-based memory and logic devices.

Spin current, a flow of spin angular momentum, is the essential ingredient for spin-transfer torque. One class of spin currents is the electrical spin current  $J_S$ , which is associated with electron spins (1–3). When  $J_S$  is absorbed by a magnet, the magnetization experiences an electrical spin torque, and its direction is reoriented (Fig. 1A). The electrical spin torque has opened the era for electrically controlled magnetic device applications—for example, magnetic random access memories (3). However,  $J_S$  is commonly associated with charge flow so that Joule heat and corresponding power dissipation are unavoidable. Moreover, the spin propagation length (diffusion length) of  $J_S$  is relatively short, typically on the order of nanometers (4), which prevents the delivery of spin information over long distances.

These limitations could be overcome by another class of spin currents, the magnon current  $J_M$ , for which the spin angular momentum is carried by precessing spin moments rather than moving electrons (5). The magnon torque associated with  $J_M$  shows several advantages in comparison with the electrical spin torque. There is no electron movement in  $J_M$ ; therefore, much less Joule heat dissipation is expected. Moreover,  $J_M$  can flow even in in-

sulators for distances up to several micrometers (6–9), and thus, material systems for the magnon torque are not limited to electrical conductors. As  $J_M$  approaches a magnet, it interacts with the magnetization through the exchange coupling, and consequently, the magnetization can be reoriented by the magnon torque (Fig. 1B). However, most studies on magnon currents have focused on long-distance transport (6–9), whereas experimental works on magnon-mediated spin torques (10–13) have been limited to magnetic excitations or thermally driven domain wall motion (14–16), and the magnetization switching has been realized only by the electrical spin torque. In this work, we observed a giant magnon torque with a ratio for the  $J_M$  generation of ~0.3, which is comparable with the electrical spin torque ratio of topological insulators (17–19), and we experimentally demonstrated that the magnetization can be efficiently switched by the magnon torque without any external magnetic field at room temperature.

We fabricated Bi<sub>2</sub>Se<sub>3</sub> (8 nm)/NiO ( $t_{\text{NiO}}$  = 0 to 100 nm)/NiFe (Py, 6 nm) structures, where  $t_{\text{NiO}}$  is the thickness of NiO, with the Bi<sub>2</sub>Se<sub>3</sub> (fig. S1 and materials and methods) (20) acting as a highly efficient spin current source (17–19). In-plane current injection to the Bi<sub>2</sub>Se<sub>3</sub> produces electrical spin currents at the Bi<sub>2</sub>Se<sub>3</sub>/NiO interface and excites  $J_M$  in the NiO layer. We chose NiO, an antiferromagnetic insulator, as a magnon-current medium because magnons are the sole spin angular momentum carriers (6–9, 21–24) in the NiO layer.

Because antiferromagnetic ordering has a crucial role in magnon transport through antiferromagnets (25), we first characterized the thickness dependence of the antiferromagnetic ordering in the NiO layer by measuring hysteresis loops. The antiferromagnetic ordering can be estimated by the exchange

bias field or coercivity; both increase as the antiferromagnetic ordering improves (26). The temperature-dependent exchange bias field  $H_{\text{ex}}$  of Bi<sub>2</sub>Se<sub>3</sub>/NiO/Py is shown in Fig. 2A for various  $t_{\text{NiO}}$ .  $H_{\text{ex}}$  increases with the NiO thickness at  $t_{\text{NiO}} \leq 25$  nm at 2 K. The blocking temperature  $T_b$ , at which the  $H_{\text{ex}}$  becomes zero, increases as  $t_{\text{NiO}}$  increases (Fig. 2B). A similar trend is observed for the coercivity  $H_c$  at room temperature (Fig. 2C);  $H_c$  increases with  $t_{\text{NiO}}$  for  $t_{\text{NiO}} \leq 30$  nm.  $H_c$  then slightly decreases with increasing  $t_{\text{NiO}}$ , which is a typical behavior of antiferromagnetic films. The results suggest that the antiferromagnetic ordering in the NiO layer gradually improves as  $t_{\text{NiO}}$  increases. The smaller  $T_b$  than that in NiO bulk (Fig. 2B) is related to the polycrystalline structure of NiO grown on Bi<sub>2</sub>Se<sub>3</sub> (Fig. 2D). When the NiO layer is directly deposited on the c-plane sapphire substrate, it shows a good crystallinity with the dominant (111) plane. However, when the NiO layer is deposited on Bi<sub>2</sub>Se<sub>3</sub>, it is polycrystalline, possibly because of the lattice mismatch between the NiO and Bi<sub>2</sub>Se<sub>3</sub> layers.

We next characterized the magnon torque using the spin torque ferromagnetic resonance (ST-FMR) measurement (Fig. 3A) (17, 20, 27, 28). A radio frequency current ( $I_{\text{RF}}$ ; current density  $J_C$  in the Bi<sub>2</sub>Se<sub>3</sub> layer) was applied to the device and generated electrical spin currents with a spin polarization denoted in Fig. 3A with a red arrow at the Bi<sub>2</sub>Se<sub>3</sub>/NiO interface.  $J_M$  is then induced in the NiO layer through the exchange interaction between the spins and nearby NiO moments (29). Passing through the NiO layer,  $J_M$  exerts a magnon torque on the Py layer. Consequently, the Py magnetization is excited into the precession mode, generating a ST-FMR signal  $V_{\text{mix}}$  (Fig. 3B, open symbols) from a representative device with  $t_{\text{NiO}} = 25$  nm is fitted by  $V_{\text{mix}} = V_S F_S + V_A F_A$ , where  $V_S F_S$  and  $V_A F_A$  are the symmetric and antisymmetric components, respectively. By adopting an established analysis method (17, 20, 27), we evaluated the spin torque ratio ( $\theta_i = J_i/J_C$ ) for the symmetric component, which is analogous to the spin Hall angle in the electrical spin-orbit torque scheme (17, 27).  $\theta_i$  is caused either by the electrical spin torque (stemming from  $J_S$ ,  $i = S$ ) or by the magnon torque (stemming from  $J_M$ ,  $i = M$ ), depending on the NiO thickness, which is discussed later.

Shown in Fig. 3C is  $\theta_i$  versus  $t_{\text{NiO}}$  at room temperature, at which the NiO/Py interface contribution is subtracted [fig. S2 and (20), section 2]. For the device without the NiO layer—the Bi<sub>2</sub>Se<sub>3</sub>/Py bilayer— $\theta_i$  is 0.67, which is consistent with a previous report for Bi<sub>2</sub>Se<sub>3</sub> (18). We observed that  $\theta_i$  abruptly decreases from 0.67 to ~0 by inserting only a 2-nm NiO layer between the Bi<sub>2</sub>Se<sub>3</sub> and Py layers. In this NiO-thickness range, no noticeable exchange

<sup>1</sup>Department of Electrical and Computer Engineering, National University of Singapore, 117576, Singapore. <sup>2</sup>Key Laboratory of Materials Modification by Laser, Ion and Electron Beams (Ministry of Education), Dalian University of Technology, Dalian 116024, China. <sup>3</sup>Department of Materials Science and Engineering, Korea University, Seoul 02841, Korea. <sup>4</sup>Department of Nano-Semiconductor and Engineering, Korea University, Seoul 02841, Korea. <sup>5</sup>Department of Semiconductor Systems Engineering, Korea University, Seoul 02841, Korea. <sup>6</sup>KU-KIST Graduate School of Converging Science and Technology, Korea University, Seoul 02841, Korea.

\*These authors contributed equally to this work.

†Corresponding author. Email: eleyang@nus.edu.sg

bias nor enhanced coercivity was observed, even at low temperature (Fig. 2). It indicates that the antiferromagnetic ordering is weak, and corresponding magnon torque has a negligible role in this thickness range. Therefore, the small  $\theta_i$  would be of purely electrical origin—electron spin tunneling through a normal insulator such as MgO or SiO<sub>2</sub> (21, 22).

The presence of magnon torque is evident for larger values of NiO thickness in which magnons are the only spin-angular-momentum carriers. We found that  $\theta_i$  starts to increase as  $t_{\text{NiO}}$  increases above 10 nm (Fig. 3C).  $\theta_i$  shows a peak value of  $\sim 0.3$  at  $t_{\text{NiO}} = 25$  nm and then gradually decreases with further increasing  $t_{\text{NiO}}$  up to 100 nm. The peak  $\theta_i$  value is of similar magnitude to the electrical spin Hall angle of topological insulators (17–19) and is higher than that of heavy metals Pt and Ta (30).

We used independent terahertz emission measurements to double check the NiO thickness-dependent behavior [fig. S3 and (20), section 3]. The terahertz emission amplitude characterizes the spin-to-charge conversion, which is the reciprocal process of the ST-FMR measurements (charge-to-spin) (31, 32). A similar trend in Fig. 3C by using both ST-FMR and terahertz techniques validates our observations of NiO thickness-dependent magnon torques. As a control experiment, we inserted a 6-nm MgO layer between Bi<sub>2</sub>Se<sub>3</sub> and NiO layers to block the spins through the NiO layer (33), and the obtained  $\theta_i$  is negligible (Fig. 3C, star symbol). This rules out the possibility that observed torque is generated at the NiO/Py interface [table S1 and (20), section 4]. The temperature dependence of  $\theta_i$  measured for Bi<sub>2</sub>Se<sub>3</sub>/NiO ( $t_{\text{NiO}} = 2, 5$  and 25 nm)/NiFe devices is shown in Fig. 3D. The  $\theta_i$  shows a peak at a certain temperature close to the antiferromagnetic transition in the NiO layer for each device, at which the enhanced spin fluctuations and magnons facilitate the spin transport, which is in line with the previous reports (23, 24, 34, 35). These results confirm the magnon-originated nature of the spin torque.

To gain insight into the thickness dependence of  $\theta_i$ , we estimated a transverse magnon current at the NiO/Py interface using a simple drift-diffusion model. Because the NiO layer is polycrystalline (Fig. 2D), we assumed that magnon propagation in the NiO layer is diffusive (25, 36). In this model, the resultant transverse magnon current  $J_m^\perp$  at the NiO/Py interface is

$$J_m^\perp = \theta_i J_C$$

$$= \eta \theta_i J_C \frac{2G_{\text{A/F}}^\perp l_m \kappa}{G_{\text{A/F}}^\perp l_m (1 + \kappa^2) + 2\pi \sigma_m (1 - \kappa^2)} \quad (1)$$

where  $\theta$  is the spin Hall angle of Bi<sub>2</sub>Se<sub>3</sub> layer;  $\eta$  is the angular momentum loss at the

Bi<sub>2</sub>Se<sub>3</sub>/NiO interface;  $G_{\text{A/F}}^\perp$  is the interfacial magnon conductance for the transverse component between NiO and Py (36), which is analogous to the mixing conductance of the spin transport theory (37);  $\kappa = \exp(-t_{\text{NiO}}/l_m)$ ; and  $l_m$  and  $\sigma_m$  are the magnon diffusion length and magnon conductivity of the NiO layer, respectively [(20), section 5]. The red curve in Fig. 3C is the fit of experimental data to Eq. 1. For the fitting, we assumed that  $l_m$  increases with  $t_{\text{NiO}}$  and saturates at  $\sim 30$  nm (Fig. 3C, inset); the value of 30 nm was estimated from the exponential decrease of  $\theta_i$  for

$t_{\text{NiO}} \geq 25$  nm in Fig. 3C; the saturation  $l_m$  of  $\sim 30$  nm is consistent with that recently reported in polycrystalline NiO (38). This assumption is motivated by the experimental results shown in Fig. 2; the behaviors of  $H_{\text{ex}}$  (or  $T_b$ ) and  $H_c$  with  $t_{\text{NiO}}$  suggest an improvement of antiferromagnetic ordering with  $t_{\text{NiO}}$ . To support this assumption, we performed atomistic lattice spin model calculations for the relation between the antiferromagnetic ordering and  $l_m$  and found that they are correlated (fig. S5). The reasonable fit shown in Fig. 3C implies that the  $t_{\text{NiO}}$ -dependent change

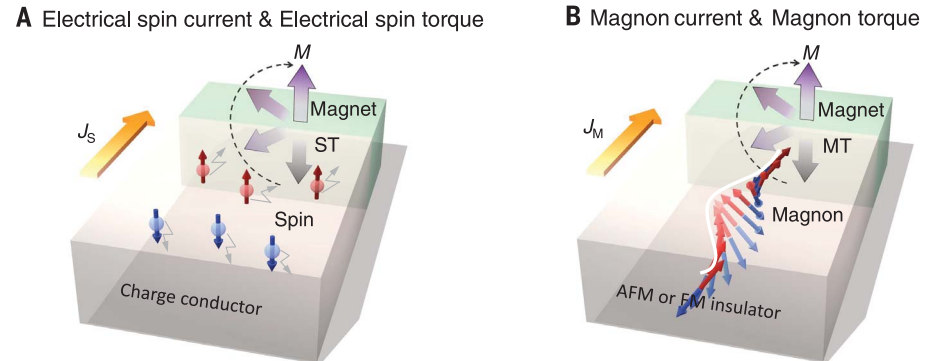


**Fig. 1. Two types of spin-angular-momentum-transfer torque.** (A) Illustration of the magnetization ( $M$ ) reorientation driven by the electrical spin torque (ST) by means of the electrical spin current  $J_s$ . (B) Illustration of the magnetization ( $M$ ) reorientation driven by the magnon torque (MT) by means of the magnon current  $J_m$ . AFM, antiferromagnet; FM, ferromagnet.

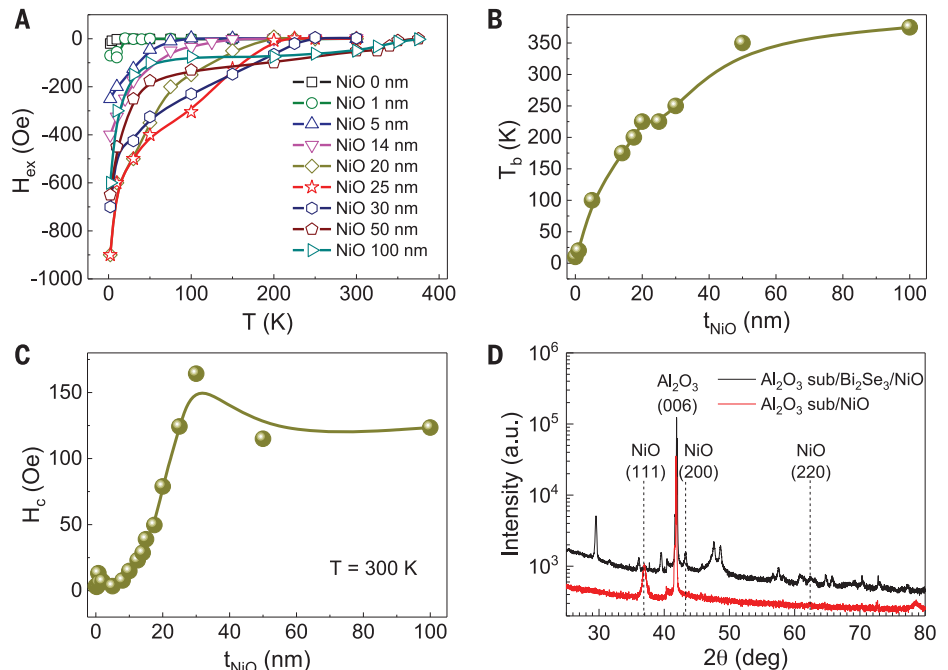


**Fig. 2. Characterization of Bi<sub>2</sub>Se<sub>3</sub>/NiO/Py structures.** (A) The exchange bias as a function of temperature for various NiO thicknesses ( $t_{\text{NiO}}$ ). (B) The blocking temperature deduced from (A). (C) The coercivity as a function of  $t_{\text{NiO}}$  at room temperature. (D) X-ray diffraction patterns of sapphire substrate/Bi<sub>2</sub>Se<sub>3</sub> (8 nm)/NiO (100 nm) and sapphire substrate/NiO (100 nm).



of  $L_m$  is a possible explanation for the experimental observation, even though a more detailed study is required for a quantitative understanding.

Last, we demonstrated magnetization switching induced by the magnon torque in the  $\text{Bi}_2\text{Se}_3/\text{NiO}/\text{Py}$  heterostructure at room temperature (Fig. 4). In switching devices, the Py layer was patterned into a rectangular shaped island to prohibit current shunting through the Py layer (Fig. 4, A and B) (20). The switching results for  $t_{\text{NiO}} = 25$  nm are shown in Fig. 4,

C to F, measured with a magneto-optic Kerr effect (MOKE) microscope by injecting a pulsed current  $I$ . We first saturated the magnetization in the Py island (Fig. 4C, yellow box) along the  $+y$  axis with an in-plane magnetic field. Then, we removed the field and applied  $I$  ( $J_C \sim 1.27 \times 10^7 \text{ A cm}^{-2}$ ) along the  $+x$  axis. We found that the Py magnetization was switched to the  $-y$  axis, indicated by the contrast change from dark to light in the yellow box (Fig. 4D). We then initialized the Py magnetization along the  $-y$  axis (Fig. 4E) and applied  $I$  ( $J_C \sim -1.27 \times$

$10^7 \text{ A cm}^{-2}$ ) along the  $-x$  axis. The Py magnetization was switched to the  $+y$  axis (Fig. 4F). This bidirectional switching depending on the current polarity excludes the possibility that the switching is governed by Joule heating-induced effects. This magnon torque-driven magnetization switching is reproducible in other devices (fig. S6). We also demonstrated magnetization switching induced by magnon torques in  $\text{Bi}_2\text{Se}_3/\text{NiO}$  (25 nm)/ $\text{Co}_{40}\text{Fe}_{40}\text{B}_{20}$  (CoFeB) trilayers at room temperature (fig. S7).

**Fig. 3. ST-FMR measurement of magnon torque.**

(A) A diagram of the ST-FMR measurements, illustrating the magnetization precession driven by the spin torque, including the damping-like torque  $\tau_{\text{DL}}$  and/or field-like torque  $\tau_{\text{FL}}$ . The black arrow denotes the direction of  $I_{\text{RF}}$  with a current density  $J_C$ . The red and blue arrows indicate spin polarizations and magnon current  $J_M$ , respectively. (B) A typical ST-FMR signal (open symbols) from a  $\text{Bi}_2\text{Se}_3/\text{NiO}$  (25 nm)/Py (6 nm) device at 10 GHz and 300 K with fits (solid lines), where the blue and green lines indicate the symmetric ( $V_{\text{SFS}}$ ) and antisymmetric Lorentzian ( $V_{\text{AFA}}$ ) component, respectively. (C) The spin torque ratio  $\theta_i$  deduced from the ST-FMR data (solid circles) and the terahertz emission amplitude (open circles) as a function of  $t_{\text{NiO}}$  at 300 K. The red curve is a fit using Eq. 1. For the fitting, we used  $\eta\theta = 0.8$  and  $G_{\text{A/F}}^{\perp}/\sigma_m = 3 \times 10^8 \text{ m}^{-1}$ . (Inset) The assumed magnon diffusion length ( $l_m$ ) as a function of  $t_{\text{NiO}}$ . The star symbol corresponds to  $\theta_i$  obtained from the ST-FMR measurement of the control device with 6-nm MgO insertion between  $\text{Bi}_2\text{Se}_3$  and NiO layers. (D) Temperature dependence of  $\theta_i$  for  $\text{Bi}_2\text{Se}_3/\text{NiO}$  ( $t_{\text{NiO}} = 2, 5$ , and 25 nm)/Py (6 nm) devices.

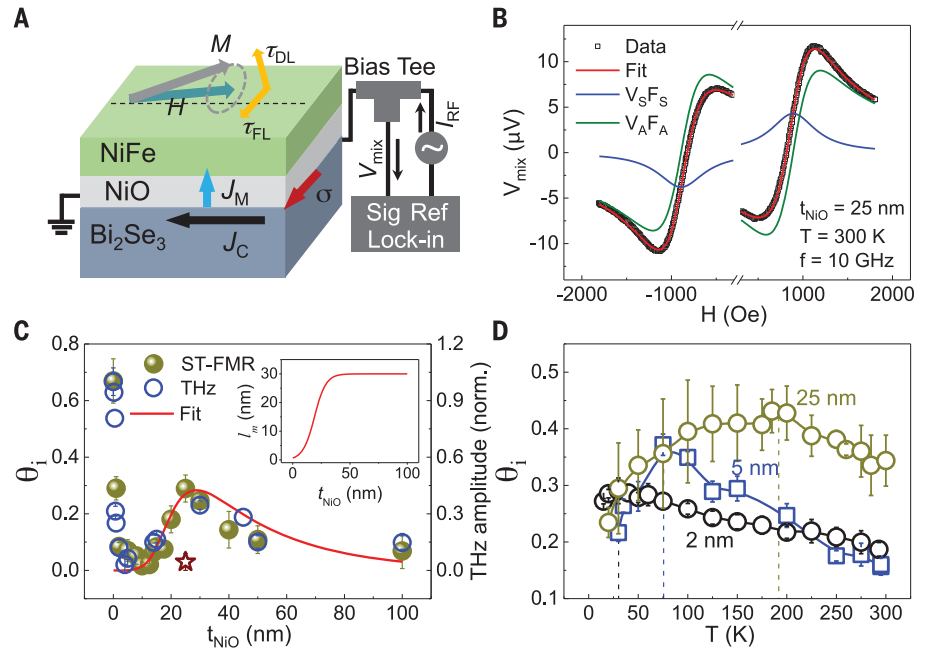
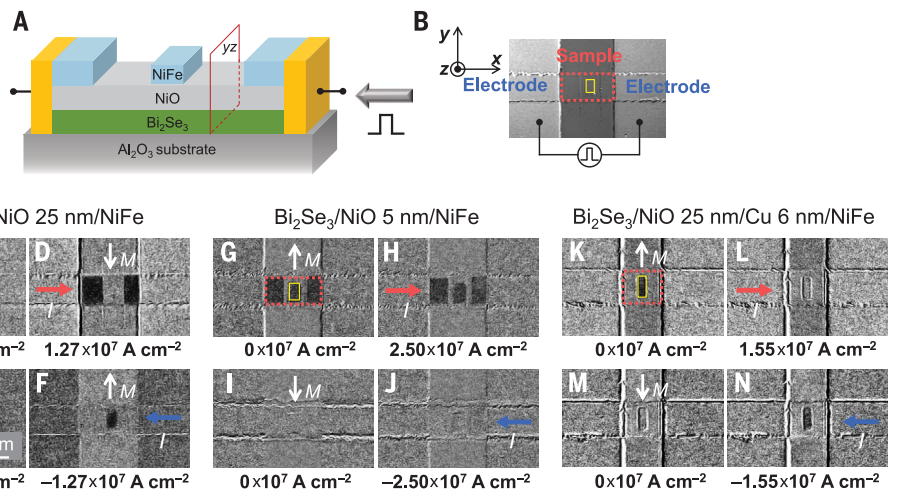


**Fig. 4. Magnetization switching induced by magnon torque in the  $\text{Bi}_2\text{Se}_3/\text{NiO}/\text{Py}$  devices at room temperature.**

(A) Illustration of the structure of the magnon torque switching device with an isolated Py rectangle defined on top of the NiO layer. (B) Optical microscope image of a device with electrodes, where the sample functional region is indicated with a red dotted box and an isolated Py rectangle is denoted with a yellow box. (C to F) MOKE images for magnon-torque-driven magnetization switching in the  $\text{Bi}_2\text{Se}_3/\text{NiO}$  (25 nm)/Py device by injecting a pulsed current  $I$  along the [(C) and (D)]  $+x$  axis or [(E) and (F)]  $-x$  axis at room temperature. (G to J) MOKE images for a  $\text{Bi}_2\text{Se}_3/\text{NiO}$  (5 nm)/Py device by injecting  $I$  along the [(G) and (H)]  $+x$  axis or [(I) and (J)]  $-x$  axis at room temperature. (K to N) MOKE images for the  $\text{Bi}_2\text{Se}_3/\text{NiO}$  (25 nm)/Cu (6 nm)/Py device by injecting  $I$  along the [(K) and (L)]  $+x$  axis or [(M) and (N)]  $-x$  axis at room temperature. In (C) to (N), the dark contrast represents the magnetization along the  $+y$  axis, and the light contrast represents the magnetization along the  $-y$  axis. The direction of magnetization is indicated with white arrows. The current density  $J_C$  in the  $\text{Bi}_2\text{Se}_3$  layer is denoted underneath each image.



The switching experiments on another device of  $\text{Bi}_2\text{Se}_3/\text{NiO}$  (5 nm)/Py are shown in Fig. 4, G to J, in which  $\theta_i$  estimated from ST-FMR is negligible (Fig. 3C). Following the same measurement procedures as in Fig. 4, C to F, we could not observe the magnetization switching, even with a larger  $J_C$ . This behavior was reproducible in other devices with  $t_{\text{NiO}} = 5$  nm. It excludes a possibility that the current-induced Oersted field, which is also present in the devices with  $t_{\text{NiO}} = 5$  nm, is the origin of the magnetization switching observed in the devices with  $t_{\text{NiO}} = 25$  nm. We also performed switching experiments on other devices with isolated Py islands at various  $t_{\text{NiO}}$  and found that the switching efficiency is qualitatively consistent with  $\theta_i$  estimated from ST-FMR (fig. S9). Therefore, our results provide unambiguous evidence that the switching is governed by the magnon torque.

From the above experiments, one question is whether direct exchange coupling between NiO and Py magnetic moments is essential for large magnon torques or not. To answer this, we performed switching experiments in  $\text{Bi}_2\text{Se}_3/\text{NiO}$  (25 nm)/Cu (6 nm)/Py devices, in which the Cu layer breaks direct exchange coupling but allows spin transmission through the transfer of spin angular momentum from magnons to electrons (Fig. 4, K to N). Both the Py and Cu insertion layer were patterned into a rectangular shaped island to eliminate current shunting through the Cu/Py bilayer. Following the same measurement procedures as in Fig. 4, C to F, we observed robust magnetization switching with  $J_C \sim 1.55 \times 10^7$  A  $\text{cm}^{-2}$ , which was reproducible in other devices with a Cu insertion (fig. S8). The observations confirm that direct exchange coupling between the NiO and Py magnetic moments is not essential for the magnon torque-induced magnetization switching.

Our demonstration reveals the ability of magnon torque to switch magnetization, a process that is as energy efficient as electrical

spin torques. This research will broaden the scope of not only magnon-related studies that are mainly focused on magnon transport (6–9, 21–24, 39) but also spintronics studies, in which advances have relied largely on the electrical spin torque. In this study, we induced the magnon torque in an antiferromagnetic insulator by injecting the electric current to a  $\text{Bi}_2\text{Se}_3$  layer as a proof of principle. However, our work is just a starting point to explore the magnon torque-driven magnetization switching. We expect that all-magnon-driven magnetization switching, without involving electrical parts, could be achieved in the near future.

## REFERENCES AND NOTES

- J. C. Slonczewski, *J. Magn. Magn. Mater.* **159**, L1–L7 (1996).
- L. Berger, *Phys. Rev. B* **54**, 9353–9358 (1996).
- A. Brataas, A. D. Kent, H. Ohno, *Nat. Mater.* **11**, 372–381 (2012).
- J. Bass, W. P. Pratt Jr., *J. Phys. Condens. Matter* **19**, 183201 (2007).
- A. Chumak, V. Vasyuchka, A. Serga, B. Hillebrands, *Nat. Phys.* **11**, 453–461 (2015).
- Y. Kajiwara *et al.*, *Nature* **464**, 262–266 (2010).
- L. Cornelissen, J. Liu, R. Duine, J. B. Youssef, B. Van Wees, *Nat. Phys.* **11**, 1022–1026 (2015).
- W. Yuan *et al.*, *Sci. Adv.* **4**, eaat1098 (2018).
- R. Lebrun *et al.*, *Nature* **561**, 222–225 (2018).
- J. C. Slonczewski, *Phys. Rev. B* **82**, 054403 (2010).
- P. Yan, X. S. Wang, X. R. Wang, *Phys. Rev. Lett.* **107**, 177207 (2011).
- D. Hinzke, U. Nowak, *Phys. Rev. Lett.* **107**, 027205 (2011).
- A. A. Kovalev, Y. Tserkovnyak, *EPL* **97**, 67002 (2012) (Europhysics Letters).
- W. Jiang *et al.*, *Phys. Rev. Lett.* **110**, 177202 (2013).
- T. Moriyama *et al.*, *Appl. Phys. Lett.* **106**, 162406 (2015).
- S. Woo, T. Delaney, G. S. Beach, *Nat. Phys.* **13**, 448–454 (2017).
- A. R. Mellnik *et al.*, *Nature* **511**, 449–451 (2014).
- Y. Wang *et al.*, *Nat. Commun.* **8**, 1364 (2017).
- J. Han *et al.*, *Phys. Rev. Lett.* **119**, 077702 (2017).
- Materials and methods are available as supplementary materials.
- C. Hahn *et al.*, *EPL* **108**, 57005 (2014) (Europhysics Letters).
- H. Wang, C. Du, P. C. Hammel, F. Yang, *Phys. Rev. Lett.* **113**, 097202 (2014).
- W. Lin, K. Chen, S. Zhang, C. L. Chien, *Phys. Rev. Lett.* **116**, 186601 (2016).
- D. Hou *et al.*, *Phys. Rev. Lett.* **118**, 147202 (2017).
- S. Rezende, R. Rodríguez-Suárez, A. Azevedo, *Phys. Rev. B* **93**, 054412 (2016).
- J. Nogués, I. K. Schuller, *J. Magn. Magn. Mater.* **192**, 203–232 (1999).
- Y. Wang *et al.*, *Phys. Rev. Lett.* **114**, 257202 (2015).
- Y. Wang, R. Ramaswamy, H. Yang, *J. Phys. D Appl. Phys.* **51**, 273002 (2018).
- S. S.-L. Zhang, S. Zhang, *Phys. Rev. B* **86**, 214424 (2012).
- A. Hoffmann, *IEEE Trans. Magn.* **49**, 5172–5193 (2013).
- Y. Wu *et al.*, *Adv. Mater.* **29**, 1603031 (2017).
- L. Cheng *et al.*, *Nat. Phys.* **15**, 347–351 (2019).
- O. Mosendz, J. Pearson, F. Fradin, S. Bader, A. Hoffmann, *Appl. Phys. Lett.* **96**, 022502 (2010).
- Z. Qiu *et al.*, *Nat. Commun.* **7**, 12670 (2016).
- A. Prakash, J. Brangham, F. Yang, J. P. Heremans, *Phys. Rev. B* **94**, 014427 (2016).
- Y. Cheng, K. Chen, S. Zhang, *Appl. Phys. Lett.* **112**, 052405 (2018).
- A. Brataas, Y. V. Nazarov, G. E. Bauer, *Phys. Rev. Lett.* **84**, 2481–2484 (2000).
- T. Ikebuchi, T. Moriyama, H. Mizuno, K. Oda, T. Ono, *Appl. Phys. Express* **11**, 073003 (2018).
- C. Y. Guo *et al.*, *Phys. Rev. B* **98**, 134426 (2018).
- Y. Wang *et al.*, Replication Data and Code for: Magnetization switching by magnon-mediated spin torque through an antiferromagnetic insulator, Harvard Dataverse (2019); doi:10.7910/DVN/OCWIDN.

## ACKNOWLEDGMENTS

We thank J. W. Yu for illustration-making assistance. **Funding:** This work was supported by SpOT-LITE program (A\*STAR grant, A18A6b00057) through RIE2020 funds and the National Research Foundation (NRF), Prime Minister's Office, Singapore, under its Competitive Research Programme (CRP award NRFCRP12-2013-01). K.-J.L. was supported by the National Research Foundation of Korea (NRF-015M3D1A1070465 and 2017R1A2B2006119) and the KIST Institutional Program (project 2V05750). Y.W. was supported by the Fundamental Research Funds for the Central Universities (project 82232016). **Author contributions:** Y.Wa. and H.Y. conceived of the research; Y.Wa., Y.Y., R.M., and K.C. fabricated the devices; D.Z., Y.Wa., and E.L. grew films; Y.Wa., S.D.P., J.L., K.L., and S.S. performed measurements; G.G. and K.-J.L. contributed to the theoretical model; S.-H.O., D.-H.K., and K.-J.L. performed the atomistic model calculation; Y.Wa., K.-J.L. and H.Y. wrote the manuscript; all authors commented the manuscript; and H.Y. led the project. **Competing interests:** The authors declare no competing interests. **Data and materials availability:** Data reported in this paper are archived online at Harvard Dataverse (40).

## SUPPLEMENTARY MATERIALS

science.sciencemag.org/content/366/6469/1125/suppl/DC1  
Materials and Methods  
Supplementary Text  
Figs. S1 to S9  
Table S1  
References (41–53)

22 October 2018; resubmitted 21 August 2019

Accepted 4 November 2019

10.1126/science.aav8076



## BIOCHEMISTRY

Self-organization of *parS* centromeres by the ParB CTP hydrolaseYoung-Min Soh<sup>1</sup>, Iain Finley Davidson<sup>2</sup>, Stefano Zamuner<sup>3</sup>, Jérôme Basquin<sup>4</sup>, Florian Patrick Bock<sup>1</sup>, Michael Taschner<sup>1</sup>, Jan-Willem Veening<sup>1</sup>, Paolo De Los Rios<sup>3</sup>, Jan-Michael Peters<sup>2</sup>, Stephan Gruber<sup>1\*</sup>

ParABS systems facilitate chromosome segregation and plasmid partitioning in bacteria and archaea. ParB protein binds centromeric *parS* DNA sequences and spreads to flanking DNA. We show that ParB is an enzyme that hydrolyzes cytidine triphosphate (CTP) to cytidine diphosphate (CDP). *parS* DNA stimulates cooperative CTP binding by ParB and CTP hydrolysis. A nucleotide cocrystal structure elucidates the catalytic center of the dimerization-dependent ParB CTPase. Single-molecule imaging and biochemical assays recapitulate features of ParB spreading from *parS* in the presence but not absence of CTP. These findings suggest that centromeres assemble by self-loading of ParB DNA sliding clamps at *parS*. ParB CTPase is not related to known nucleotide hydrolases and might be a promising target for developing new classes of antibiotics.

Sister chromosomes separate from one another and distribute within bacterial cells by means of the ParABS system and the SMC complex. Bacterial centromeres— assembled from ParB proteins and 16–base pair (bp) palindromic *parS* sites—initiate chromosome segregation soon after replication initiation by recruiting SMC condensin and by moving along ParA adenosine triphosphatase (ATPase) gradients (1–5). Multiple ParB proteins localize to a given *parS* site, thereby forming distinctive clusters in the cell (6, 7). ParB recognizes *parS* and enriches in ~15-kb-wide DNA regions flanking *parS* (6, 8–10). ParB spreading is hindered by DNA binding protein “roadblocks” engineered next to *parS* (10–12). Several models for ParB spreading have been proposed (6, 13). However, despite being critical for chromosome segregation, spreading has not yet been faithfully recon-

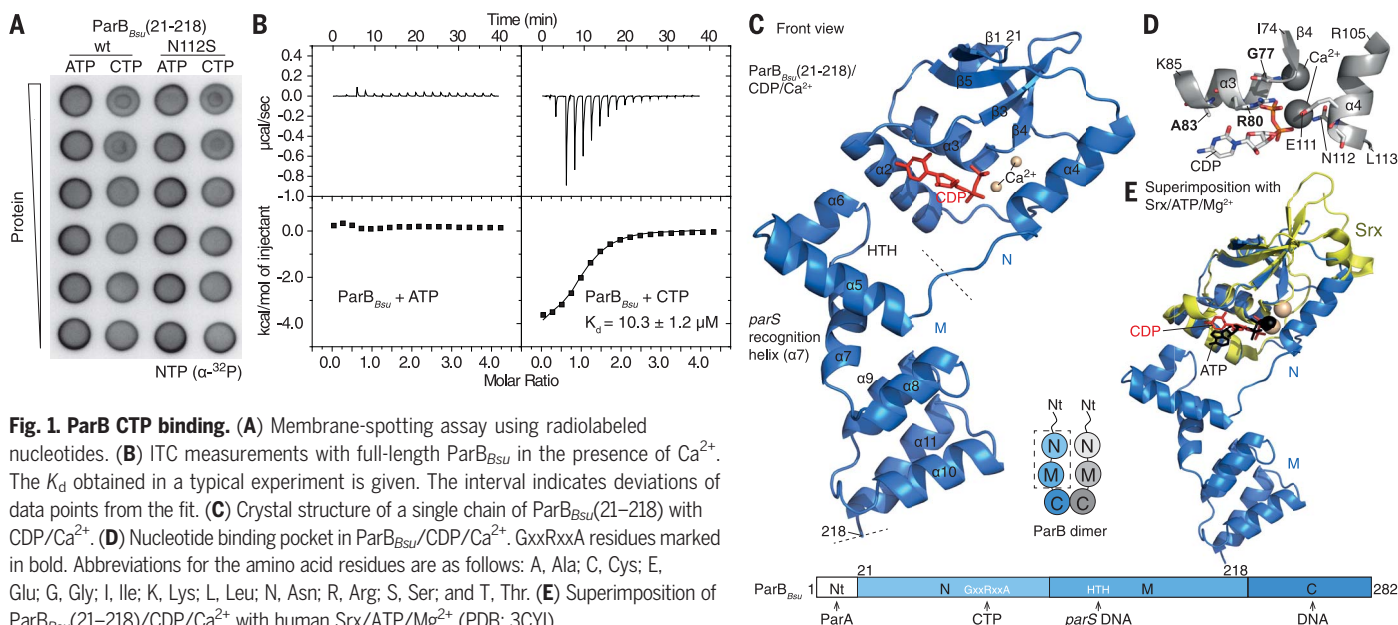
stituted in vitro, indicating the lack of an essential component.

ParB proteins harbor three globular domains (Fig. 1). A helix-turn-helix (HTH) motif in the middle domain (M) recognizes *parS* DNA. The C-terminal domain (C) homodimerizes and in chromosomally encoded ParB also supports sequence-nonspecific DNA binding (14). The N-terminal domain (N) harbors conserved amino acid residues that produce strong phenotypes when mutated (5–7, 9, 15), but its function is unclear. Domain N shares marginal sequence similarity with a functionally unrelated eukaryotic enzyme, called sulfiredoxin (Srx) (fig. S1A) (16). Srx catalyzes the repair of peroxiredoxin by transferring ATP  $\gamma$ -phosphate groups onto hyperoxidized cysteine moieties. A conserved GxxRxxA motif forms the ATP binding pocket in Srx (16, 17). Mutations in corresponding ParB residues (G77S and R80A)

lead to loss of function and subcellular localization defects in *Bacillus subtilis* (*Bsu*) (5–7). Those subtle similarities invoke the possibility that ParB proteins are not merely DNA binding proteins but enzymes.

Membrane-spotting assays with radiolabeled nucleoside triphosphates (NTPs) (18) unexpectedly indicated that full-length ParB<sub>Bsu</sub> and the fragment ParB<sub>Bsu</sub>(21–218) bind cytidine triphosphate (CTP) rather than ATP (Fig. 1A and fig. S1B). CTP binding was abolished in the ParB<sub>Bsu</sub>(R80A) mutant (fig. S1C). Isothermal titration calorimetry (ITC) confirmed ParB<sub>Bsu</sub> binding to CTP, yielding dissociation constants ( $K_d$ 's) in the range of 10 to 50  $\mu$ M. By contrast, other nucleotides produced little response in ITC (Fig. 1B and fig. S2, A and B). CTP was also bound by plasmid-encoded ParB proteins (F plasmid ParB<sub>F</sub> and P1 prophage ParB<sub>P1</sub>), implying broad evolutionary conservation (fig. S1, B to D) (10, 19).

We then solved the atomic structure of ParB<sub>Bsu</sub>(21–218) (comprising domains N and M) using crystals grown with CTP and Ca<sup>2+</sup> ions. The unit cell contained two ParB<sub>Bsu</sub>(21–218) dimers. Each chain associated with a cytidine diphosphate (CDP) molecule and two coordinated Ca<sup>2+</sup> ions (Fig. 1C). CTP must thus have been hydrolyzed during crystallization. In



the structure, the CDP  $\beta$ -phosphate group contacts G77 and R80, explaining the strict conservation of the GxxRxxA motif (Fig. 1D) and implying that phenotypes associated with GxxRxxA mutations are caused by defective nucleotide binding (or hydrolysis). Individual domains N and M superimposed well with published ParB structures of bacterial and archaeal origin (with few exceptions) (fig. S2C) (20–22). Domain N also superimposed fairly well with human Srx/ATP/Mg<sup>2+</sup> (17), yielding a close overlap of  $\alpha$  and  $\beta$  phosphate

groups (Fig. 1E). This marked resemblance implies that Srx ATP phosphotransferases and ParB CTP phosphohydrolases evolved from a common ancestor.

We next investigated ParB CTPase activity by measuring the accumulation of inorganic phosphate (Fig. 2A and fig. S3A). ParB<sub>Bsu</sub> dimers hydrolyzed about five CTP molecules per hour. CTP hydrolysis was abolished in the CTP-binding mutant R80A and also in the CTP-binding proficient mutant N112S (figs. S2B, S3B, and S4A) (5, 23). Notably, addition

of 40-nucleotide *parS* duplex (*parS*DNA<sub>40</sub>) strongly increased CTP turnover to about 36 molecules per hour (Fig. 2A). Substoichiometric amounts of *parS*DNA<sub>40</sub> (ratio ~40:1) were sufficient to saturate enzymatic activity (Fig. 2B), implying that *parS* only transiently associates with ParB. Noncognate DNA sequences did not alter the activity, even at increased concentrations (Fig. 2A). ParB<sub>F</sub> and the paralog Noc<sub>Bsu</sub> (24) also displayed CTPase activity, which was stimulated by cognate DNA (fig. S3A).

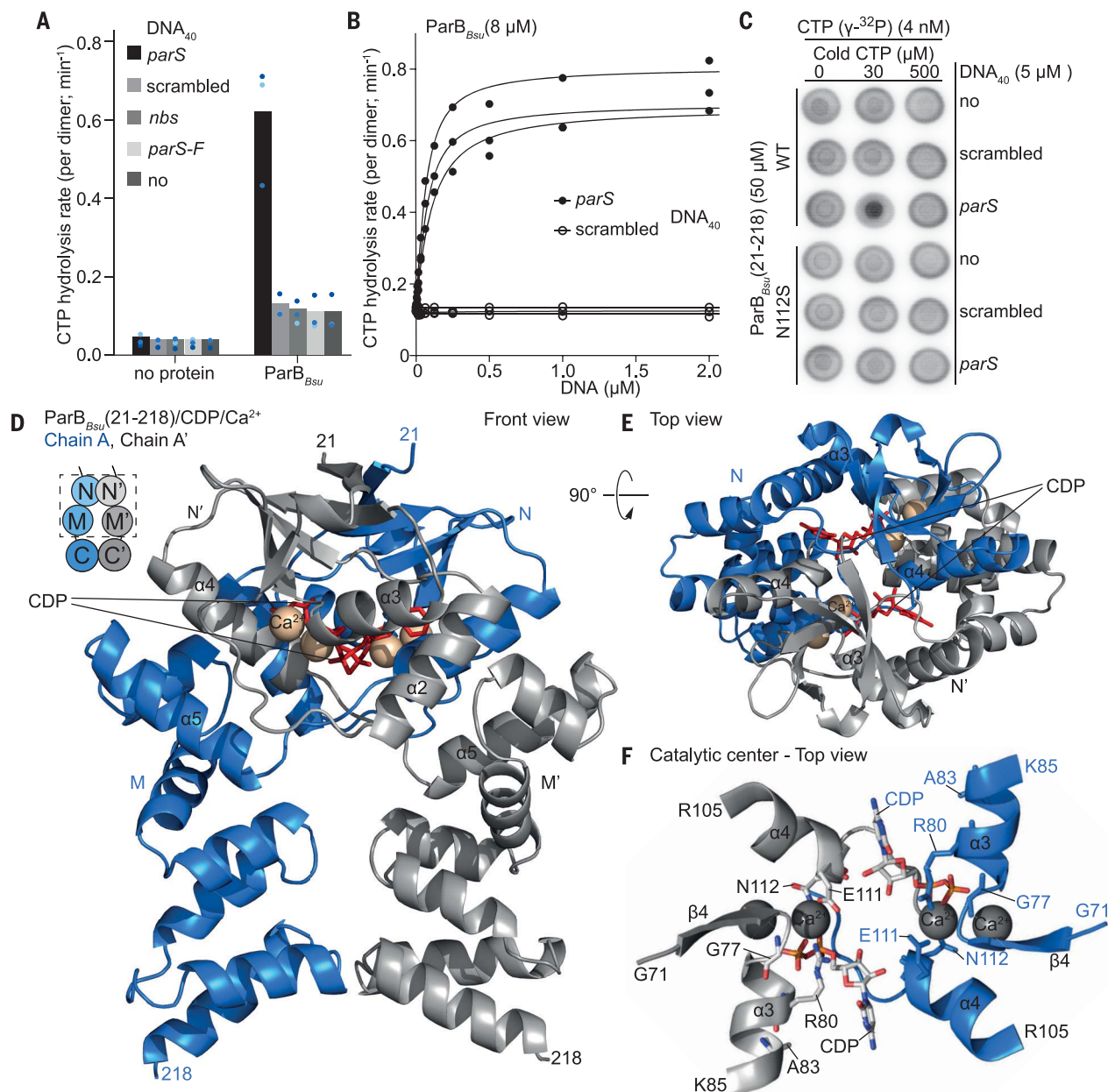


**Fig. 2. ParB CTP hydrolysis.** (A) CTP hydrolysis measured by colorimetric detection of inorganic phosphate using malachite green. Mean values from three repeat measurements. Data points are shown as dots. (B) CTP hydrolysis by ParB<sub>Bsu</sub> dimers with increasing DNA concentrations. Data

points and fits of three repeat measurements. (C) Membrane spotting showing *parS*-stimulated cooperative CTP binding. (D and E) Crystal structure of a ParB<sub>Bsu</sub>(21–218)/CDP/Ca<sup>2+</sup> dimer. (F) Catalytic center in ParB<sub>Bsu</sub>(21–218)/CDP/Ca<sup>2+</sup>.



interface and appear critical for N engagement (Fig. 2F). They are conserved in ParB proteins but absent from monomeric Srx (fig. S1A). Consistent with a role in N engagement, N112S impairs *parS*-stimulated cooperative but not basal CTP binding (Fig. 2C). To detect N engagement in solution, we used site-specific cross-linking of purified ParB(T22C) with bismaleimidoethane (BMOE). T22 is ideally positioned at the symmetry axis of the ParB/ nucleotide structure to support dimer cross-linking (Fig. 3D). ParB<sub>B<sub>200</sub></sub>(T22C) cross-linking

**A**

ParB <sub>BSU</sub> (T22C)										
-	+	+	+	+	+	+	+	+	+	BMOE
-	-	-	-	-	-	-	-	-	-	Nuc
-	-	+	-	-	+	-	-	+	-	parS DNA <sub>40</sub>
-	-	-	+	-	-	+	-	-	+	scrambled DNA <sub>40</sub>

**B**

ParB <sub>BSU</sub> (T22C) CTPyS, no parS								
0	5	10	15	20	25	30	X	
							ParB	

Crosslinked fraction

minutes

**C**

ParB <sub>BSU</sub> ring (XX)					ParB <sub>BSU</sub> oligomer					
-	+	+	+	+	-	+	+	+	+	BMOE
-	-	+	-	+	-	-	+	-	+	CTP
-	-	-	+	+	-	-	-	+	+	parS DNA <sub>40</sub>
-	-	-	-	-	+	+	-	-	-	scrambled DNA <sub>40</sub>

**D**

ParB model

ParB<sub>BSU</sub>(21-218)/CDP

T22C

N

M

C

N'

M'

C'

S278C

Extended linker (219-228) (modelled)

ParB<sub>BSU</sub>(229-282) PDB: 5NOC

**E**

Front view

Side view

90°

N

N'

M

M'

half parS

half parS'

Superimposition  
ParB<sub>BSU</sub>(21-218)/CDP & parS DNA (PDB: 4UMK)

half parS' half parS

single cross-linked dimer species. XX marks double cross-linked ParB rings. Other species are oligomeric forms. **(D)** Model of ParB built from ParB<sub>BSU</sub>(21–218)/CDP/Ca<sup>2+</sup> and ParB<sub>BSU</sub>(229–282) (PDB: 5NOC) dimers. Linker at the M-C junction is manually modeled as fully extended peptide. **(E)** Superimposition of domain M in ParB<sub>BSU</sub>(21–218)/CDP/Ca<sup>2+</sup> and a ParB/*parS* structure (PDB: 4UMK). Only DNA is shown for the latter.

CTPγS supported robust cross-linking even without *parS* after extensive incubation periods (Fig. 3B and fig. S6B). This demonstrates that N engagement is energetically favorable, but the transition to the engaged state is very slow without *parS*. We conclude that *parS*

catalyzes CTP-dependent engagement of domain N in ParB.

To determine whether N engagement occurs within or between ParB dimers, we purified ParB<sub>B<sub>ST</sub></sub>(T22C, S278C) (Fig. 3C). In the presence of CTP and *parS* DNA<sub>40</sub>, double cross-

linked ParB dimers emerged as predominant species, demonstrating that N engagement produces mostly ring-shaped ParB dimers (and few ParB oligomers). This invokes the possibility that domain N serves as a nucleotide-operated DNA gate in ParB rings, which closes at *parS*.

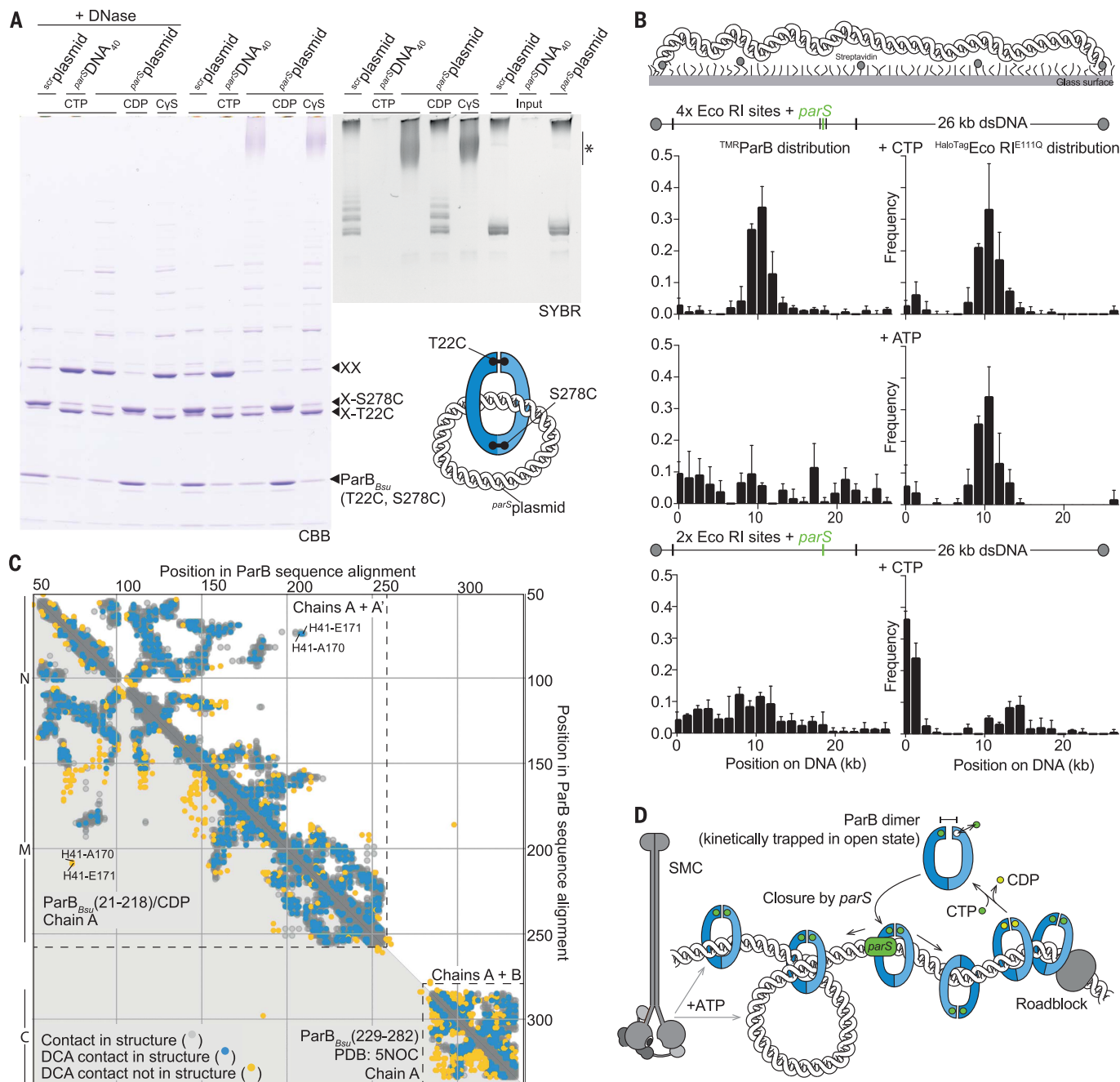


**Fig. 4. ParB DNA loading and sliding.** (A) Polyacrylamide gel analysis of ParB<sub>Bsu</sub> (T22C, S278C) protein species (CBB) and DNA species (SYBR) from BMOE-cross-linked DNA loading reactions. A presumed ParB-XX<sup>par</sup>Sc plasmid adduct is marked by asterisk. CDP and <sup>scr</sup>plasmid (scrambled) only support limited ParB loading. (B) Single-molecule imaging (SMI) of DNA-bound <sup>TMF</sup>ParB in the presence of HaloTagEco RI<sup>E111Q</sup> roadblocks. Mean and SD were calculated from three repeat measurements of a sample. (C) Residue contact maps by

coevolutionary analysis (DCA; blue and yellow dots) and residue proximities (gray dots) in monomeric (below diagonal) and dimeric chains (above diagonal) of ParB<sub>Bsu</sub>(21–218)/nucleotide and ParB<sub>Bsu</sub>(229–282) (PDB: 5NOC). **(D)** Model for ParB spreading by self-loading of DNA sliding clamps at *parS*. The SMC complex (ATP-bound form) is recruited to the chromosome by an interaction with ParB protein or DNA shaped by ParB. ParB triggers nucleotide hydrolysis by ParA ATP dimers (not shown).



Comparing the ParB/nucleotide structure with a ParB/*parS* DNA cocrystal structure, it became apparent that *parS* DNA associating with one HTH motif clashes with the opposing HTH motif (Fig. 3E and fig. S6C). This indicates that *parS* DNA duplexes may detach from the HTH motif upon N engagement (or CTP hydrolysis), possibly explaining the transient nature of ParB/*parS* association. ParB dimers may, however, remain associated with chromosomal DNA even after release from *parS* if they were to entrap the DNA backbone. To test this possibility, we next used circular DNA for in vitro DNA loading experiments (Fig. 4A). ParB<sub>Bsu</sub>(T22C, S278C) was incubated with plasmid DNA (1873 bp) or linear DNA<sub>40</sub> in the presence of CTP and cross-linked with BMOE to preserve topological interactions under protein-denaturing conditions (5). Control samples were nuclease-treated to release proteins from DNA. As expected, ParB<sub>Bsu</sub>(T22C, S278C) generated large fractions of covalently closed ParB rings with *parS* DNA only (Fig. 4A). When nuclease digestion was omitted, the ParB ring species was retained in the *parS*-DNA<sub>40</sub> sample but was eliminated from the *parS*-plasmid sample containing CTP or CTPγS. Instead, a slowly migrating species was observed near the top of the gel, presumably corresponding to *parS*-plasmid interlocked with multiple covalent ParB rings. DNA staining of polyacrylamide and agarose gels supported the notion of multiple ParB rings entrapping *parS*-plasmid (Fig. 4A and fig. S7). The efficient stimulation of ParB-DNA entrapment by CTPγS implies that CTP hydrolysis is dispensable for all steps of DNA loading.

We next used single-molecule imaging to elucidate how CTP binding may relate to ParB spreading (27). The ends of linear 26-kb DNA molecules containing a single *parS* sequence were immobilized in flow chambers. Increased DNA occupancy of labeled ParB (TMR-ParB) was detected in the presence of CTP (fig. S8A). However, no local enrichment of TMR-ParB on DNA was observed, potentially due to ParB spreading from *parS*. We therefore used a labeled and catalytically inactive variant of the Eco RI restriction enzyme to test if this HaloTag-Eco RI<sup>E111Q</sup> protein could function as a roadblock, which might constrain ParB spreading. Intriguingly, under these conditions TMR-ParB became locally enriched on DNA between two Eco RI sites flanking *parS* (Fig. 4B), indicating that HaloTag-Eco RI<sup>E111Q</sup> had indeed restrained ParB spreading. TMR-ParB localized more broadly when these two *parS* flanking Eco RI sites were removed (Fig. 4B). Local enrichment of TMR-ParB was also lost when ATP was used instead of CTP or when HaloTag-Eco RI<sup>E111Q</sup> was added at the end of the experiment, despite normal localization of HaloTag-Eco RI<sup>E111Q</sup> (Fig.

4B and fig. S8B). These results demonstrate that ParB enrichment at *parS* DNA is enhanced by CTP and indicate that ParB translocates onto *parS* flanking DNA, unless it is restrained by roadblocks. These findings support the notion that ParB forms self-loading DNA clamps whose sliding on chromosomal DNA is hampered by protein roadblocks.

ParB<sub>Bsu</sub>(T22C) cross-linking was rather inefficient in vivo (fig. S9), possibly indicating that levels of N engagement are low in the cell. Alternatively, cross-linking might be hampered for technical reasons or by steric blockage by other proteins such as ParA or SMC. To obtain information on ParB architecture by independent means, we extracted residue coevolution signatures from sequence data by direct coupling analysis (DCA) (28). We obtained excellent agreement between the top 900 DCA contacts predicted from an alignment of 157,776 ParB sequences and residue proximities observed in the ParB/nucleotide dimer (Fig. 4C). By contrast, the ParB/nucleotide monomer and published ParB structures failed to explain numerous DCA contacts or produced proximities not observed by DCA (fig. S10). These results strongly suggest that the dimer in the ParB/nucleotide structure closely resembles a state of ParB that is relevant in many bacteria.

Our work shows that the widespread family of ParB proteins are enzymes that bind the atypical nucleotide CTP to promote spreading from cognate DNA sequences. Our data suggest that ParB dimers exist in an open, CTP-bound form in solution (Fig. 4D). Gate closure is energetically favorable but extremely slow in the absence of *parS*. Physical association with *parS* catalyzes gate closure and DNA entrapment, which in turn releases ParB from *parS*. On the chromosome, the ParB DNA sliding clamps may frequently encounter roadblocks formed by RNA polymerase and nucleoid-associated proteins. ParB sliding might thus be stochastically restricted, giving rise to the characteristic gradient distribution patterns observed by chromatin immunoprecipitation (6, 13). CTP hydrolysis is apparently not required for DNA loading or sliding. It might instead play a role in ParB recycling by destabilizing the closed gate, thereby determining the chromosomal residence time of ParB and limiting the extent of ParB spreading. Altogether, CTP utilization enables robust enrichment of ParB at and near rare recognition sequences (~1 cognate per 10<sup>6</sup> noncognate sites) even with little or no sequence specificity in DNA binding (14). The CTPase domain is also present in a large variety of protein sequences with diverse domain organizations (>100; PFAM: PF02195), implying that it plays prominent roles in multiple cellular processes.

## REFERENCES AND NOTES

1. I. V. Surovtsev, C. Jacobs-Wagner, *Cell* **172**, 1271–1293 (2018).
2. D. C. Lin, A. D. Grossman, *Cell* **92**, 675–685 (1998).
3. A. G. Vecchiarelli, L. C. Hwang, K. Mizuuchi, *Proc. Natl. Acad. Sci. U.S.A.* **110**, E1390–E1397 (2013).
4. H. C. Lim et al., *eLife* **3**, e02758 (2014).
5. L. Wilhelm et al., *eLife* **4**, e06659 (2015).
6. T. G. Graham et al., *Genes Dev.* **28**, 1228–1238 (2014).
7. S. Autret, R. Nair, J. Errington, *Mol. Microbiol.* **41**, 743–755 (2001).
8. A. Minnen et al., *Cell Rep.* **14**, 2003–2016 (2016).
9. A. M. Breier, A. D. Grossman, *Mol. Microbiol.* **64**, 703–718 (2007).
10. O. Rodionov, M. Lobocka, M. Yarmolinsky, *Science* **283**, 546–549 (1999).
11. H. Murray, H. Ferreira, J. Errington, *Mol. Microbiol.* **61**, 1352–1361 (2006).
12. O. Rodionov, M. Yarmolinsky, *Mol. Microbiol.* **52**, 1215–1223 (2004).
13. A. Sanchez et al., *Cell Syst.* **1**, 163–173 (2015).
14. G. L. Fisher et al., *eLife* **6**, e28086 (2017).
15. D. Song, K. Rodrigues, T. G. W. Graham, J. J. Loparo, *Nucleic Acids Res.* **45**, 7106–7117 (2017).
16. M. K. Basu, E. V. Koonin, *Cell Cycle* **4**, 947–952 (2005).
17. T. J. Jönsson, M. S. Murray, L. C. Johnson, W. T. Lowther, *J. Biol. Chem.* **283**, 23846–23851 (2008).
18. K. G. Roelofs, J. Wang, H. O. Sintim, V. T. Lee, *Proc. Natl. Acad. Sci. U.S.A.* **108**, 15528–15533 (2011).
19. J. Y. Bouet, Y. Ah-Seng, N. Benmeradi, D. Lane, *Mol. Microbiol.* **63**, 468–481 (2007).
20. T. A. Leonard, P. J. Butler, J. Löwe, *Mol. Microbiol.* **53**, 419–432 (2004).
21. M. A. Schumacher et al., *Science* **349**, 1120–1124 (2015).
22. B. W. Chen, M. H. Lin, C. H. Chu, C. E. Hsu, Y. J. Sun, *Proc. Natl. Acad. Sci. U.S.A.* **112**, 6613–6618 (2015).
23. S. Gruber, J. Errington, *Cell* **137**, 685–696 (2009).
24. L. J. Wu et al., *EMBO J.* **28**, 1940–1952 (2009).
25. R. Gasper, S. Meyer, K. Gotthardt, M. Sirajuddin, A. Wittinghofer, *Nat. Rev. Mol. Cell Biol.* **10**, 423–429 (2009).
26. K. P. Hopfner et al., *Cell* **101**, 789–800 (2000).
27. I. F. Davidson et al., *EMBO J.* **35**, 2671–2685 (2016).
28. D. Malinverni, A. Barducci, *Methods Mol. Biol.* **2022**, 379–397 (2019).
29. Y.-M. Soh, I. F. Davidson, S. Zamuner, J. Basquin, F. P. Bock, M. Taschner, J.-W. Veening, P. De Los Rios, J.-M. Peters, S. Gruber, Deposition of raw data for: Self-organization of *parS* centromeres by the ParB CTP hydrolase, Mendeley Data (2019); <https://doi.org/10.17632/n5jdr55r.1>.

## ACKNOWLEDGMENTS

We thank D. Barilla, M.-L. Diebold-Durand, and B. Funnell for providing purified proteins; L. Lavis for JF646 ligand; D. Malinverni for sharing DCA code; and M. Thanbichler for exchanging unpublished results. We are grateful to R. Vazquez Nunez and D. Tavares for technical help and to S. Martin, A. Vjestica, and members of the Gruber lab for comments and discussions.

**Funding:** The authors acknowledge financial support from the European Research Council (724482 to S.G. and 693949 to J.-M.P.), the Swiss National Science Foundation (170242 to S.G.), the Austrian Research Promotion Agency (FFG-834223, FFG-852936 to J.-M.P.), Boehringer Ingelheim, and the Human Frontier Science Program grant RGP0057/2018 (to J.-M.P.). **Author contributions:** Initial finding, Y.-M.S., S.G., J.-W.V., and M.T.; Crystallography, Y.-M.S. and J.B.; In vivo cross-linking, Y.-M.S. and F.P.B.; SMI, I.F.D. and J.-M.P.; DCA, S.Z. and P.D.L.R.; Other experiments, Y.-M.S.; Writing and visualization, Y.-M.S., S.G.; Supervision, S.G. **Competing interests:** None declared. **Data and materials availability:** Raw data are available at Mendeley Data (29). Structure coordinates are deposited at the Protein Data Bank (PDB: 6SDK). DCA code is deposited at GitHub (<https://gitlab.com/LBS-EPFL/code/lbsDCA/tree/v1.0>).

## SUPPLEMENTARY MATERIALS

[science.sciencemag.org/content/366/6469/1129/suppl/DC1](https://science.sciencemag.org/content/366/6469/1129/suppl/DC1)  
Materials and Methods  
Figs. S1 to S10  
Table S1 and S2  
Reference (30)

20 June 2019; accepted 14 October 2019  
Published online 24 October 2019  
10.1126/science.aay3965

## ENHANCER GENOMICS

## Brain cell type-specific enhancer-promoter interactome maps and disease-risk association

Alexi Nott<sup>1\*</sup>, Inge R. Holtman<sup>1,2\*</sup>, Nicole G. Coufal<sup>3,4\*</sup>, Johannes C. M. Schlachetzki<sup>1</sup>, Miao Yu<sup>5</sup>, Rong Hu<sup>5</sup>, Claudia Z. Han<sup>1</sup>, Monique Pena<sup>3</sup>, Jiayang Xiao<sup>3</sup>, Yin Wu<sup>3</sup>, Zahara Keulen<sup>3</sup>, Martina P. Pasillas<sup>1</sup>, Carolyn O'Connor<sup>6</sup>, Christian K. Nickl<sup>1</sup>, Simon T. Schafer<sup>3</sup>, Zeyang Shen<sup>1,7</sup>, Robert A. Rissman<sup>8,9</sup>, James B. Brewer<sup>8</sup>, David Gosselin<sup>1,10</sup>, David D. Gonda<sup>11</sup>, Michael L. Levy<sup>11</sup>, Michael G. Rosenfeld<sup>12</sup>, Graham McVicker<sup>13</sup>, Fred H. Gage<sup>3</sup>, Bing Ren<sup>5,14</sup>, Christopher K. Glass<sup>1,15†</sup>

Noncoding genetic variation is a major driver of phenotypic diversity, but functional interpretation is challenging. To better understand common genetic variation associated with brain diseases, we defined noncoding regulatory regions for major cell types of the human brain. Whereas psychiatric disorders were primarily associated with variants in transcriptional enhancers and promoters in neurons, sporadic Alzheimer's disease (AD) variants were largely confined to microglia enhancers. Interactome maps connecting disease-risk variants in cell-type-specific enhancers to promoters revealed an extended microglia gene network in AD. Deletion of a microglia-specific enhancer harboring AD-risk variants ablated *BIN1* expression in microglia, but not in neurons or astrocytes. These findings revise and expand the list of genes likely to be influenced by noncoding variants in AD and suggest the probable cell types in which they function.

The central nervous system is a complex organ consisting of diverse and highly interconnected cells. Single-cell-sequencing technologies have advanced our understanding of the molecular phenotypes of human neurons, microglia, astrocytes, oligodendrocytes, and other cell types that reside within the brain (1–3), but the transcriptional mechanisms that control their developmental and functional properties in health and disease remain less well understood. Genome-wide association studies (GWASs) provide a genetic approach to identify molecular pathways involved in complex traits and diseases by defining associations between genetic variants and phenotypes of interest (4, 5). Large-scale GWASs have discovered hundreds of single-nucleotide polymorphisms (SNPs) associated with the risk of neurological and psychiatric disorders. The vast majority of these disease-risk genetic variants are located in noncoding regions of the genome (5). The causal variants and the specific cell type(s) in which the disease-risk variants may be active is often unclear. GWAS-identified risk variants in noncoding regions of the genome can exert phenotypic effects through perturbation of transcriptional gene promoters and enhancers (4). Enhancers are short regions of DNA that bind transcription factors to enhance messenger

RNA expression from target promoters. Clusters of multiple enhancers, referred to as super-enhancers, are particularly important in driving the expression of cell-identity genes (6). Enhancer repertoires underlie particular patterns of gene expression and enable cell-type-specific responses (7). The activity of enhancers depends on three-dimensional enhancer-promoter interactions (8); however, the enhancer-promoter interactome of different brain cell types in vivo remains largely unknown.

To characterize transcriptional regulatory elements within different cell types of the human brain, PU.1<sup>+</sup> microglia, NEUN<sup>+</sup> neuronal, OLIG2<sup>+</sup> oligodendrocyte, and NEUN<sup>neg</sup> LHX2<sup>+</sup> astrocyte nuclei were isolated from resected cortical brain tissue from six individuals by fluorescent-activated nuclei sorting (fig. S1, A and B, and table S1). Cell-type-specific populations of 200,000 nuclei were subjected to the assay for transposase-accessible chromatin sequencing (ATAC-seq), which identifies open regions of chromatin (9), and cell-type-specific populations of 500,000 nuclei were subjected to H3K27ac and H3K4me3 chromatin immunoprecipitation sequencing (ChIP-seq), which predominantly identifies active chromatin regions and promoters, respectively (10, 11). These datasets clustered

according to cell type of origin and exhibited cell-type-specific patterns (Fig. 1A and fig. S1, C to E). Promoter H3K27ac signal correlated with gene expression of the corresponding cell type more closely than ATAC-seq and H3K4me3 ChIP-seq (fig. S1F) (12). Promoters associated with cell-type signature genes preferentially exhibited corresponding H3K27ac profiles (fig. S1G) (13). Oligodendrocyte nuclei contain a low signal for oligodendrocyte precursor cell signature genes, whereas neuronal nuclei represent a mixture of excitatory and inhibitory subtypes (fig. S1G). ATAC-seq and H3K27ac ChIP-seq profiles generated from PU.1 nuclei were highly correlated with those previously defined in ex vivo microglia (fig. S1, C and D) (14). Promoter H3K27ac signal was increased at microglia signature genes compared with genes associated with other myeloid populations (fig. S1H) (15). Cell-type-specific promoter activity defined by differential H3K27ac mirrored cell-type patterns of gene expression (12), as well as ATAC-seq and H3K4me3 enrichment, and were associated with gene ontologies representative of each cell type (fig. S2, A to D, and table S2).

We identified putative active promoters and enhancers in each cell type and found a one-to-many relationship between promoters and enhancers (8). Whereas active promoters are largely shared between cell types (Fig. 1B), a relatively small fraction of active enhancers overlap between cell types (Fig. 1C), indicating that cell-type specificity is mainly captured within the enhancer repertoire. Most bulk brain-enhancer regions identified by PsychENCODE overlapped with the nuclei cell-type enhancers (94%) (13). However, analysis of cell-specific nuclei expanded the total number of putative brain enhancers by 87%.

To determine the enrichment of genetic variants associated with complex traits and diseases in cell-type-specific regulatory regions, we performed linkage disequilibrium score (LDSC) regression analysis of heritability (16). LDSC uses GWAS summary statistics to determine whether genetic heritability for a trait or disease is enriched for SNPs within genome annotations while accounting for linkage disequilibrium. We obtained GWAS summary statistics for neurological and psychiatric disorders and neurobehavior traits (17) (table S3). We found a strong enrichment of heritability for variants within neuronal

<sup>1</sup>Department of Cellular and Molecular Medicine, University of California, San Diego, La Jolla, CA 92093, USA. <sup>2</sup>Section Molecular Neurobiology, Department of Biomedical Sciences of Cells & Systems, University Medical Center Groningen, University of Groningen, 9713 AV Groningen, the Netherlands. <sup>3</sup>Laboratory of Genetics, The Salk Institute for Biological Studies, La Jolla, CA 92037, USA. <sup>4</sup>Department of Pediatrics, University of California, San Diego, La Jolla, CA 92093, USA. <sup>5</sup>Ludwig Institute for Cancer Research, La Jolla, CA 92093, USA. <sup>6</sup>Flow Cytometry Core Facility, The Salk Institute for Biological Studies, La Jolla, CA 92037, USA. <sup>7</sup>Department of Bioengineering, University of California, San Diego, La Jolla, CA 92093, USA. <sup>8</sup>Department of Neurosciences, University of California, San Diego, La Jolla, CA 92093, USA. <sup>9</sup>Veterans Affairs San Diego Healthcare System, San Diego, CA 92161, USA. <sup>10</sup>Centre de Recherche du Centre Hospitalier Universitaire de Québec–Université Laval, Département de Médecine Moléculaire, Faculté de Médecine, Université Laval, Québec G1V 4G2, Canada. <sup>11</sup>Department of Neurosurgery, University of California, San Diego–Rady Children's Hospital, San Diego, CA 92123, USA. <sup>12</sup>Howard Hughes Medical Institute, Department and School of Medicine, University of California, San Diego, La Jolla, CA 92093, USA. <sup>13</sup>The Salk Institute for Biological Studies, La Jolla, CA 92037, USA. <sup>14</sup>Department of Cellular and Molecular Medicine, Center for Epigenomics, University of California, San Diego, School of Medicine, La Jolla, CA 92093, USA. <sup>15</sup>Department of Medicine, University of California, San Diego, La Jolla, CA 92093, USA.

\*These authors contributed equally to this work.

†Corresponding author. Email: ckg@ucsd.edu



enhancers and promoters for all psychiatric disorders and behavioral traits (Fig. 1D), which was substantially lower in PsychENCODE bulk brain enhancers (Fig. 1D) (13). By contrast, AD SNP heritability was most highly enriched in microglia-regulatory elements (Fig. 1D), specifically microglia enhancers (18–23).

De novo motif analyses at open chromatin within enhancers identified transcription factor-binding motifs associated with each cell type (fig. S3). In addition, H3K27ac-defined active promoters identified 288 human transcription factors that were active in a cell-type-specific manner (fig. S4 and table S2) (24), several of which have been associated with

disease (fig. S5 and table S4). Integrating cell-type-specific transcription factors with enhancer motifs of the corresponding cell type identifies major drivers of cell ontogeny.

The relationship between promoters and distal regulatory regions for different cell types in the brain is largely unknown. We used proximity ligation-assisted ChIP-seq (PLAC-seq), in which proximity ligation preceded an enrichment for active promoters by H3K4me3 ChIP-seq (25). Chromatin loops were identified between active promoters and distal regulatory regions in microglia, neurons, and oligodendrocytes (26). An example is the *SALL1* locus, which has interactions with cell-type-specific

enhancers, including chromatin loops to a microglia-specific super-enhancer (Fig. 2A). There were 219,509 significant interactions across cell types, and replicates clustered according to origin (fig. S6, A and B, and table S5). A strong H3K4me3 signal did not dictate that an interaction would occur (fig. S6C), suggesting that PLAC-seq captures a unique dimension of the chromatin conformation.

A subset of chromatin interactions was significantly more active in each cell type and colocalized with increased ATAC-seq, H3K27ac, and H3K4me3 ChIP-seq signal in a cell-type-specific manner (Fig. 2B and fig. S6D). Active

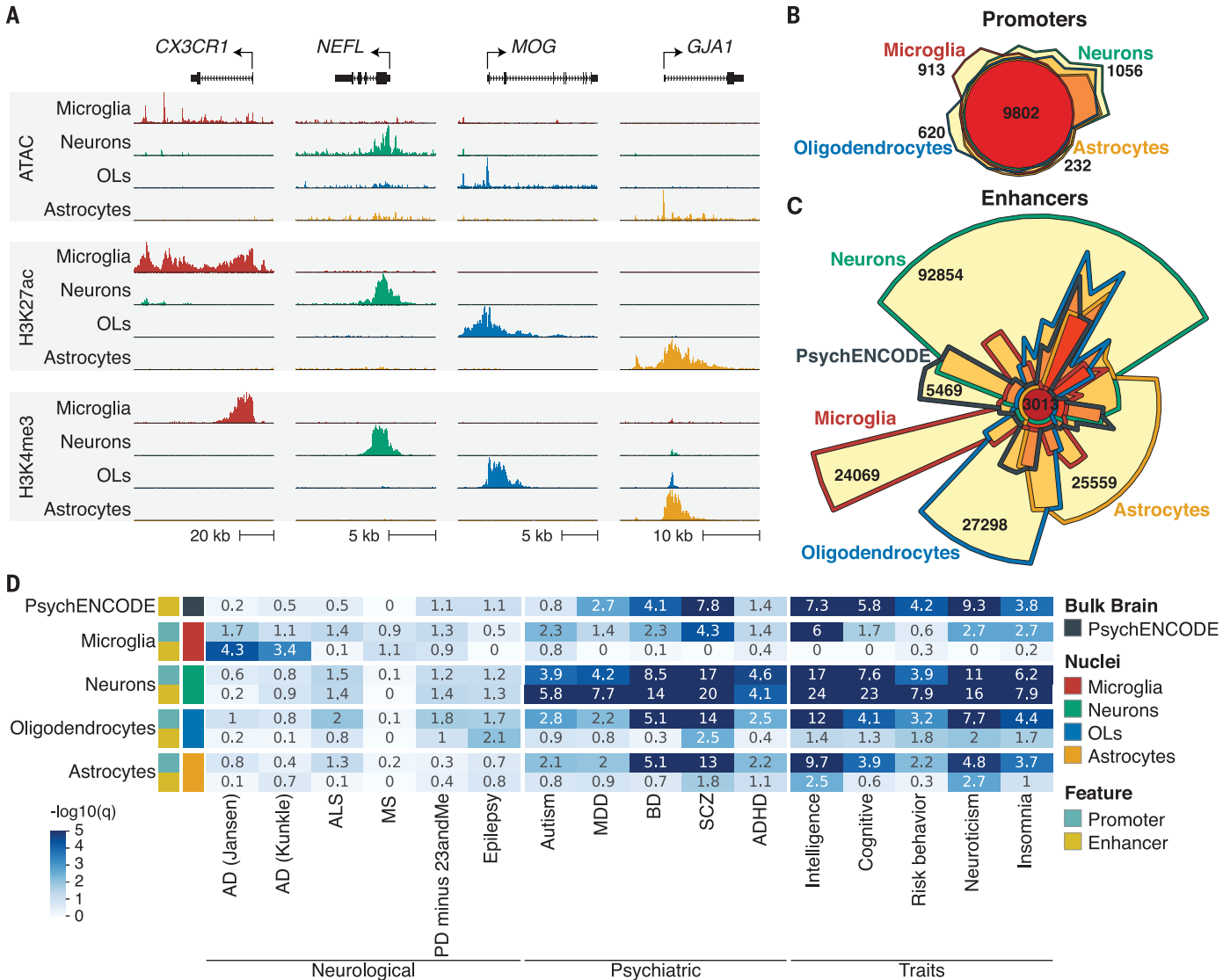


**Fig. 1. Cell-type-specific genomic regulatory region enrichments for GWAS risk variants for brain disorders and behavioral traits.** (A) UCSC genome browser visualization of ATAC-seq (top panel), H3K4me3 ChIP-seq (middle panel), and H3K27ac ChIP-seq (bottom panel) for brain nuclei populations. Shown is a representative gene for microglia (*CX3CR1*), neurons (*NEFL*), oligodendrocytes (*MOG*), and astrocytes (*GJA1*). (B) Chow-Ruskey plot

of promoter regions defined for cell populations. (C) Chow-Ruskey plot of enhancer regions defined for cell populations and PsychENCODE enhancers defined using bulk brain. (D) Heatmap of LDSC analysis for genetic variants associated with brain disorders and behavior traits displayed as  $-\log_{10}(q)$  value for significance of enrichment for promoter and enhancer regions of cell populations and PsychENCODE bulk brain enhancers. OL, oligodendrocytes.

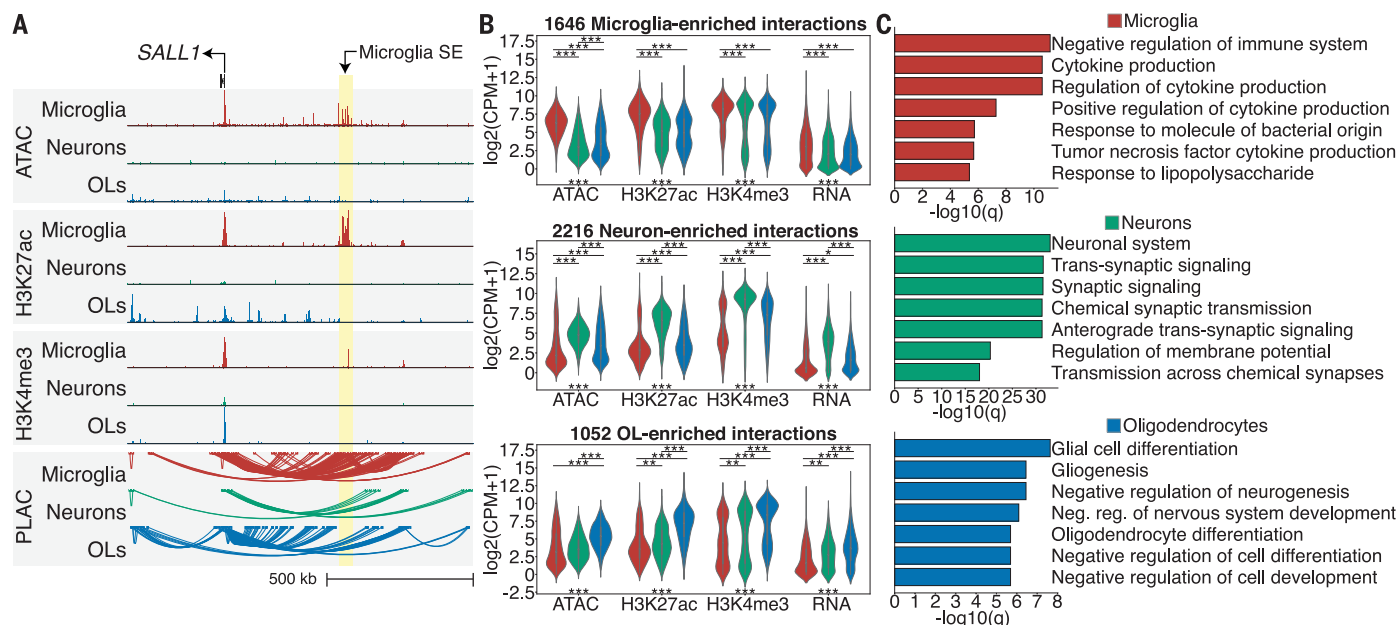


**Fig. 2. Chromatin loops link promoters to active gene-regulatory regions.**

(A) UCSC genome browser visualization of ATAC-seq, H3K27ac ChIP-seq, H3K4me3 ChIP-seq and PLAC-seq loops at the *SALL1* locus. The microglia-specific super-enhancer is associated with microglia interactions (highlighted yellow). (B) Violin plots of ATAC-seq, H3K27ac ChIP-seq, H3K4me3 ChIP-seq and

RNA-seq  $\log_2(\text{CPM}+1)$  values at PLAC-seq up-regulated interactions shown in fig. S6D for microglia, neurons, and oligodendrocytes; \*\*\* $p < 1e-12$ ; \*\* $p < 1e-5$ ; \* $p < 1e-3$  by Kruskal–Wallis between-groups test. (C) Metascaple enrichment analyses of active genes identified at PLAC-seq up-regulated interactions shown in fig. S6D for microglia, neurons, and oligodendrocytes shown as  $-\log_{10}(q)$  values.

promoters linked to microglia-, neuron-, and oligodendrocyte-enriched interactions were associated with gene ontology terms representative of each cell type, supporting the ability of the PLAC interactome to annotate cell-type-specific promoter–enhancer interactions (Fig. 2C).

We identified 2,954 super-enhancers in microglia, neurons, and oligodendrocytes, of which 83% had PLAC interactions and were linked to promoters with elevated H3K27ac levels compared with promoters linked to regular enhancers (fig. S7, A and B). Many super-enhancers harbored GWAS disease-risk variants and were connected to cell-type-specific genes, suggesting that a subset of GWAS variants act on super-enhancers to affect gene expression (fig. S7A and table S6).

To better understand AD genetics and the microglia interactome, we distinguished likely causal variants from those in linkage disequilibrium by applying fine mapping and identified 261 credible set variants (18). In many instances, such as the *BIN1*, *PICALM*, and *SORL1* loci, the fine-mapped variants overlapped with microglia-specific enhancers that were PLAC linked to corresponding gene promoters (Fig. 3A). Next, we determined PLAC interactions between active promoters and AD-risk-credible set variants (19) and identified 41 genes that were linked to these variants across cell types (fig. S8). Twenty-five of the PLAC-linked AD-risk genes were identified in microglia, of which 14 were not de-

tected in the other cell types (Fig. 3B and fig. S8). A broader set of 134 putative risk genes were identified by applying the same analysis to all genome-wide significant variants found in two AD GWASs (figs. S8 and S9, A and B, and table S7) (18, 19).

Protein–protein interaction (PPI) network analysis showed that microglia AD-risk genes identified by PLAC-seq were highly connected with GWAS-assigned genes and centered around *APOE*, whereas PPI networks for neurons and oligodendrocytes were smaller in scope (fig. S9, C to E). Microglia AD-assigned genes were associated with gene ontology terms for immune function, whereas gene ontology terms for amyloid-beta processing were associated with neurons, microglia, and oligodendrocytes (fig. S9F).

PLAC interactions altered the interpretation of AD-risk variants for three reasons. First, we found AD-risk variants that were linked to more distal active promoters and not the closest gene promoter. An example is the *SLC24A4* locus, which had AD-risk variants that were connected to the proximal active promoters of *ATXN3*, *TRIP11*, and *CPSF2*, but not to *SLC24A4* (Fig. 3C). Second, we observed enhancers harboring AD-risk variants that were PLAC linked to active promoters of both GWAS-assigned genes and an extended subset of genes not assigned to GWAS loci. An example is the *CLU* locus, which had PLAC-linked AD-risk variants to the GWAS-assigned genes *CLU* and *PTK2B* and an extended set

of genes: *TRIM35*, *CHRNA2*, *SCARA3*, and *CCDC25* (Fig. 3D). Finally, we identified cell-type-specific enhancers harboring AD-risk variants that were linked to genes expressed in multiple cell types, implicating cell-type-specific disease susceptibility. Examples are the *PICALM* and *BIN1* loci, which, despite being expressed in multiple cell types (12), had microglia-specific enhancers harboring AD-risk variants (Figs. 3E and 4A).

The *BIN1* microglia-specific enhancer is PLAC linked to the *BIN1* promoter (Fig. 4A), binds to PU.1 (14), and contains the AD-risk variant rs6733839, which has the second-highest AD-risk score after *APOE* and was fine mapped as a causal variant (Fig. 3A). Functionality of this microglia-specific enhancer was validated by CRISPR/Cas9-mediated deletion of a 363-bp region in two human pluripotent stem cell (PSC) lines (fig. S10, A to C). PSC control (*BIN1*<sup>control</sup>) and *BIN1* enhancer deletion (*BIN1*<sup>enh.del</sup>) lines had normal karyotypes (fig. S10D) and were differentiated into microglia, neurons, and astrocytes (Fig. 4B and figs. S11, A to D, and S12, A and B). Gene-expression analysis of *BIN1*<sup>control</sup> and *BIN1*<sup>enh.del</sup> lines in PSC and PSC-derived microglia, neurons, and astrocytes showed high correlation between samples, with clustering according to cell type (fig. S12, C and D). However, gene expression of *BIN1* was nearly absent in the *BIN1*<sup>enh.del</sup> PSC-derived microglia, whereas *BIN1* expression in *BIN1*<sup>enh.del</sup> PSCs and PSC-derived neurons and astrocytes was equivalent to that in



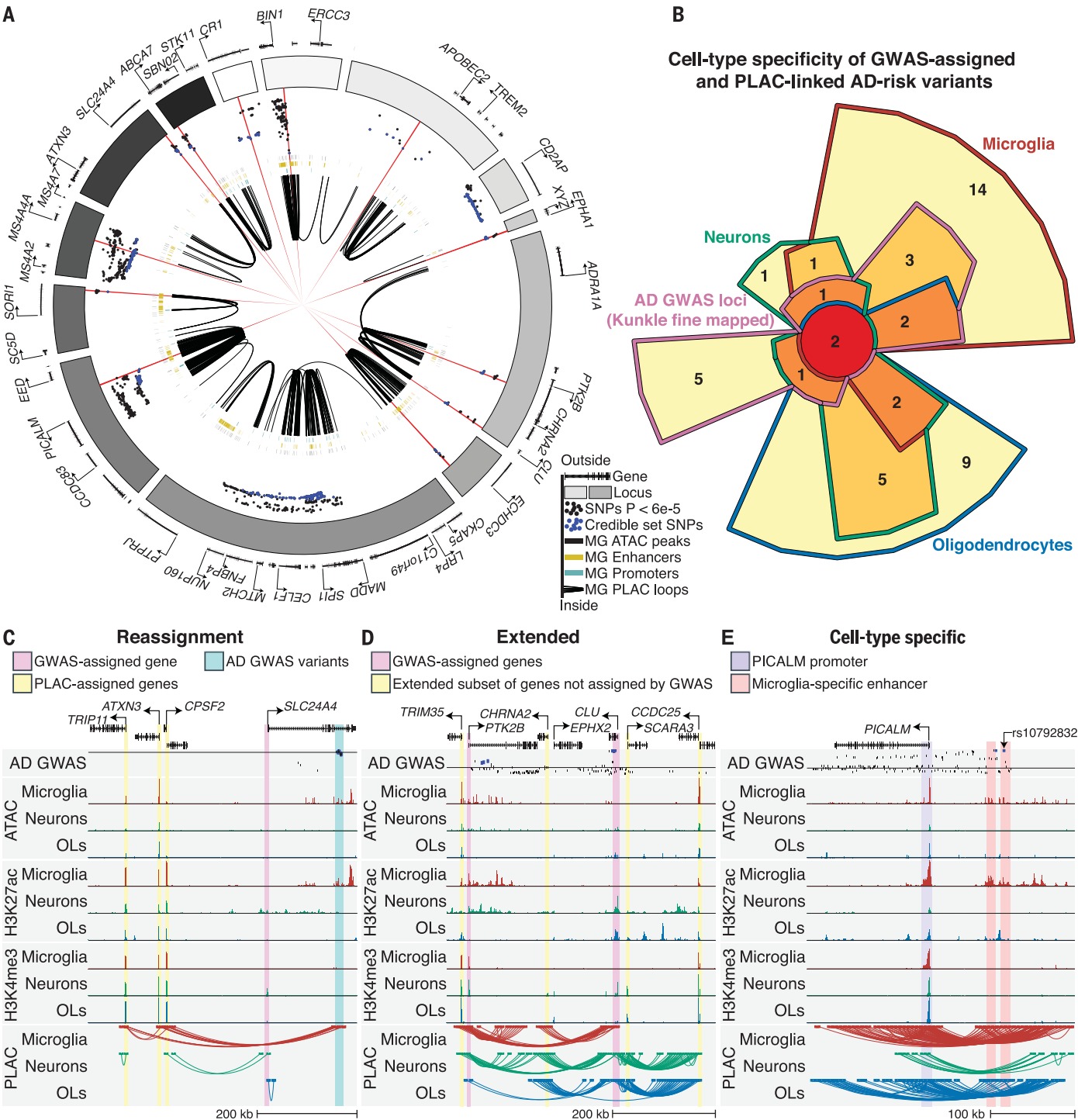
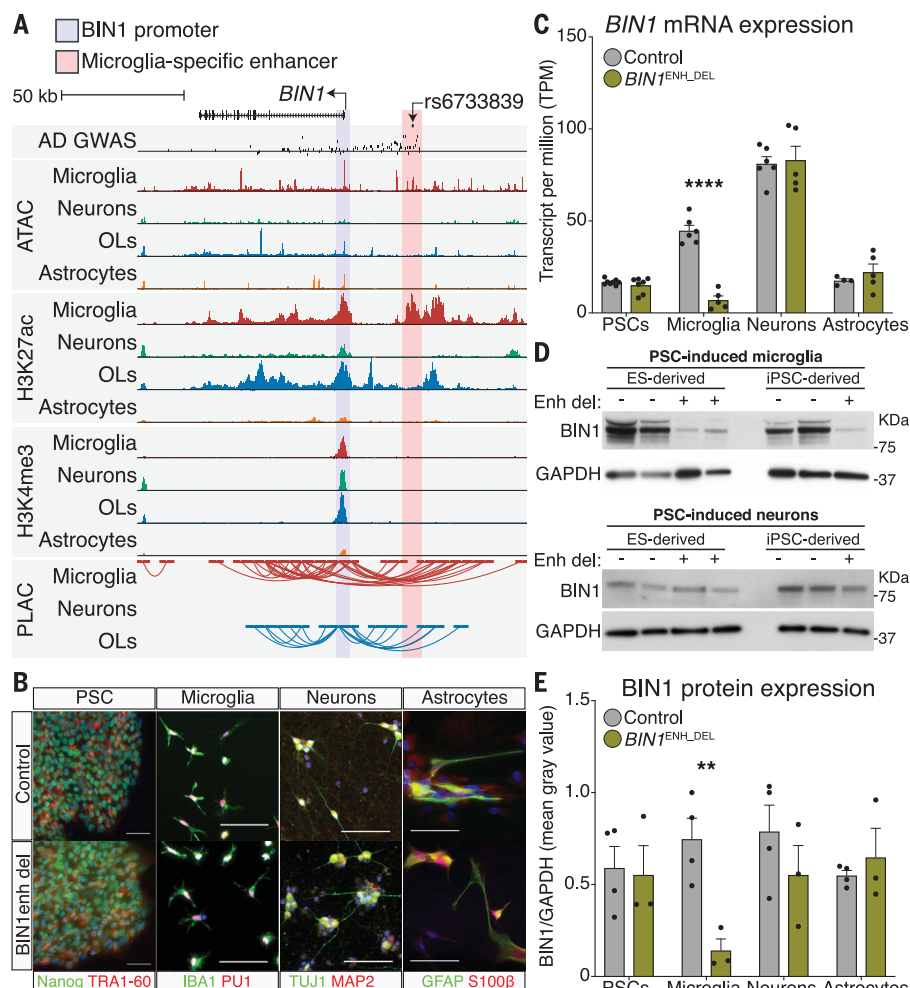


**Fig. 4. Deletion of a microglia-specific enhancer harboring a lead AD-risk variant affects microglia BIN1 expression.** (A) UCSC genome browser visualization of the *BIN1* locus showing AD-risk variants, ATAC-seq, H3K27ac ChIP-seq, H3K4me3 ChIP-seq, and PLAC-seq in different brain cell types. The shared active promoter region is highlighted in light blue; the microglia-specific enhancer region is highlighted in pink. The AD GWAS track shows meta-analysis *p*-values of stage 2 variants (18); line indicates *p*-value =  $5 \times 10^{-8}$ ; blue dots are fine-mapped 95% credible set variants. (B) Immunohistochemistry of PSCs, microglia, neurons, and astrocytes in control and *BIN1*<sup>enh<sub>del</sub></sup> lines stained for the indicated cell lineage markers. (C) *BIN1* gene expression in control and *BIN1*<sup>enh<sub>del</sub></sup> PSCs (*N* = 8,7), microglia (*N* = 6,5), neurons (*N* = 6,5), and astrocytes (*N* = 4,5) as RNA-seq TPM. \*\*\*\**p* < 0.0001, Benjamini–Hochberg adjusted. (D) Western blot of BIN1 and GAPDH in control and *BIN1*<sup>enh<sub>del</sub></sup> PSC-derived microglia (top) and neurons (bottom). (E) Protein expression of BIN1 in control and *BIN1*<sup>enh<sub>del</sub></sup> PSCs, microglia, neurons, and astrocytes determined as Western blot BIN1/GAPDH mean gray intensity. *N* = 4 controls, 3 *BIN1*<sup>enh<sub>del</sub></sup> per cell type. \*\**p* < 0.01 by unpaired two-tailed *t* test.



*BIN1*<sup>control</sup> cells (Fig. 4C, fig. S12E, and table S8). Western blot confirmed BIN1 protein in *BIN1*<sup>control</sup> PSCs and PSC-derived microglia, neurons, and astrocytes (Fig. 4, D and E, and fig. S12F). BIN1 expression was unchanged in *BIN1*<sup>enh<sub>del</sub></sup> PSC-derived microglia precursor hematopoietic stem cells, indicating that microglia derivation was unaffected (fig. S12F). However, BIN1 was substantially reduced in *BIN1*<sup>enh<sub>del</sub></sup> microglia and not in neurons and astrocytes (Fig. 4, D and E). This finding that the most significant GWAS risk allele associated with *BIN1* resides in a microglia-specific enhancer provides a rationale for further investigation of its function in these cells (27).

The present study provides evidence that the identification of cell-type-specific promoter-enhancer interactomes enables substantial advances in the interpretation of GWAS-risk alleles and establishes a new resource for this purpose in a broad spectrum of neurological and psychiatric diseases. Major goals will be to extend these approaches to diseased tissues and to refine nuclear-sorting protocols to interrogate enhancer landscapes of informative cell subsets such as amyloid plaque-associated microglia (28). Disease-specific regulatory ele-

ments are likely to be influenced by genetic variation, which, because of our limited sample size, may partly explain the lack of overlap of a subset of risk alleles with the current regulatory atlases. The acquisition of more samples will provide further opportunity to evaluate inter-individual variation on enhancer selection and function. We expect that these approaches will provide qualitatively new insights into disease mechanisms that may be of value in developing new approaches for prevention and treatment.

#### REFERENCES AND NOTES

- B. B. Lake et al., *Science* **352**, 1586–1590 (2016).
- B. B. Lake et al., *Nat. Biotechnol.* **36**, 70–80 (2018).
- H. Mathys et al., *Nature* **570**, 332–337 (2019).
- M. D. Gallagher, A. S. Chen-Plotkin, *Am. J. Hum. Genet.* **102**, 717–730 (2018).
- M. T. Maurano et al., *Science* **337**, 1190–1195 (2012).
- D. Hnisz et al., *Cell* **155**, 934–947 (2013).
- S. Heinz, C. E. Romanoski, C. Benner, C. K. Glass, *Nat. Rev. Mol. Cell Biol.* **16**, 144–154 (2015).
- M. R. Mumbach et al., *Nat. Methods* **13**, 919–922 (2016).
- X. Chen et al., *Nat. Methods* **13**, 1013–1020 (2016).
- M. P. Creighton et al., *Proc. Natl. Acad. Sci. U.S.A.* **107**, 21931–21936 (2010).
- N. D. Heintzman et al., *Nat. Genet.* **39**, 311–318 (2007).
- Y. Zhang et al., *Neuron* **89**, 37–53 (2016).
- D. Wang et al., *Science* **362**, eaat8464 (2018).
- D. Gosselin et al., *Science* **356**, eaal3222 (2017).

- M. J. C. Jordão et al., *Science* **363**, eaat7554 (2019).
- B. Bulik-Sullivan et al., *Nat. Genet.* **47**, 1236–1241 (2015).
- Materials and methods are available as supplementary materials.
- B. W. Kunkle et al., *Nat. Genet.* **51**, 414–430 (2019).
- I. E. Jansen et al., *Nat. Genet.* **51**, 404–413 (2019).
- K. L. Huang et al., *Nat. Neurosci.* **20**, 1052–1061 (2017).
- G. Novikova, G. Novikova, M. Kapoor, J. TCW, E. M. Abud, A. G. Efthymiou, H. Cheng, J. F. Fullard, J. Bendl, P. Roussos, W. W. Poon, K. Hao, E. Marcara, A. M. Goate, Integration of Alzheimer's disease genetics and myeloid cell genomics identifies novel causal variants, regulatory elements, genes and pathways. bioRxiv 694281 [Preprint]. 6 July 2019. <https://www.biorxiv.org/content/10.1101/694281v1>.
- K. E. Tansey, M. J. Hill, *Transl. Psychiatry* **8**, 7 (2018).
- K. E. Tansey, D. Cameron, M. J. Hill, *Genome Med.* **10**, 14 (2018).
- S. A. Lambert et al., *Cell* **175**, 598–599 (2018).
- R. Fang et al., *Cell Res.* **26**, 1345–1348 (2016).
- I. Juric et al., *PLOS Comput. Biol.* **15**, e1006982 (2019).
- A. Crotti et al., *Sci. Rep.* **9**, 9477 (2019).
- H. Keren-Shaul et al., *Cell* **169**, 1276–1290.e17 (2017).

#### ACKNOWLEDGMENTS

We thank J. Collier for technical assistance, L. Van Ael for manuscript preparation, D. Skola and M. L. Gage for manuscript editing, and M. Gymrek and S. Konermann for scientific discussions. **Funding:** Support was provided by NIH grant nos. RF1 AG061060-01, R01 AG056511-01A1, and R01 AG057706-01; the Cure Alzheimer's Fund Gifford Neuroinflammation Consortium; and UCSD Shiley-Marcos ADRC grant no. IP30AG062429. A.N. was supported by the Alzheimer's Association (grant no. AARF-18-531498) and the Altman Clinical & Translational Research Institute



at UCSD (National Center for Advancing Translational Sciences, supported by NIH grant no. KL2TR001444). I.R.H. was supported by the VENI research program, which is financed by the Netherlands Organization for Scientific Research. N.G.C. was supported by NIH grant no. K08 NS109200-01 and The Hartwell Foundation. C.Z.H. was supported by the Cancer Research Institute Irvington Postdoctoral Fellowship Program. C.O. was funded by NIHNCI CCSG grant nos. P30 014195 and S10-OD023689. Salk facilities are supported by the Salk Cancer Center (NCI grant no. P30-CA014195). F.H.G. was supported by the JPB Foundation, the Engman Foundation, an AHA-Allen Initiative in Brain Health and Cognitive Impairment award made jointly through the American Heart Association and The Paul G. Allen Frontiers Group; 19PABH134610000, and the Dolby Foundation. J.B.B. and R.A.R. were supported by the UCSD Shiley-Marcos ADRG grant no.

AG062429-01. Sequencing was conducted at the IGM Genomics Center, UCSD; the center was supported by grant nos. P30DK063491 and P30CA023100. **Author contributions:** A.N., N.G.C., J.C.M.S., and C.K.G. conceived the study. N.G.C. coordinated tissue acquisition. D.D.G. and M.L.L. resected brain tissue. A.N., C.K.N., M.P.P., and D.G. isolated nuclei and cells. N.G.C., M.P., J.X., Y.W., Z.K., and C.O. performed PSC experiments. A.N., M.Y., and R.H. prepared sequencing libraries. I.R.H., A.N., and Z.S. analyzed datasets. A.N., I.R.H., and C.K.G. wrote the manuscript with contributions from N.G.C., C.Z.H., J.C.M.S., M.G.R., F.H.G., and B.R. **Competing interests:** B.R. is a cofounder of Arima Genomics, Inc., which sells Hi-C and PLAC-seq kits. **Data and materials availability:** Data are available on dbGap ([https://www.ncbi.nlm.nih.gov/projects/gap/cgi-bin/study.cgi?study\\_id=phs001373.v2.p2](https://www.ncbi.nlm.nih.gov/projects/gap/cgi-bin/study.cgi?study_id=phs001373.v2.p2)). The UCSC genome browser session

(hg19) containing the processed ATAC-seq, ChIP-seq, and PLAC-seq datasets for each brain cell type is available at: [https://genome.ucsc.edu/s/nottalexi/glassLab\\_BrainCellTypes\\_hg19](https://genome.ucsc.edu/s/nottalexi/glassLab_BrainCellTypes_hg19).

#### SUPPLEMENTARY MATERIALS

[science.sciencemag.org/content/366/6469/1134/suppl/DC1](https://science.sciencemag.org/content/366/6469/1134/suppl/DC1)  
Materials and Methods  
Figs. S1 and S2  
Captions for Tables S1 to S8  
References (29–66)  
Tables S1 to S8

[View/request a protocol for this paper from Bio-protocol.](#)

27 May 2019; accepted 30 October 2019  
10.1126/science.aay0793

## MOLECULAR BIOLOGY

# Comprehensive AAV capsid fitness landscape reveals a viral gene and enables machine-guided design

Pierce J. Ogden<sup>1,2,3\*</sup>, Eric D. Kelsic<sup>1,2,4\*,†</sup>, Sam Sinai<sup>1,2,4,5</sup>, George M. Church<sup>1,2,3,4,†</sup>

Adeno-associated virus (AAV) capsids can deliver transformative gene therapies, but our understanding of AAV biology remains incomplete. We generated the complete first-order AAV2 capsid fitness landscape, characterizing all single-codon substitutions, insertions, and deletions across multiple functions relevant for in vivo delivery. We discovered a frameshifted gene in the VP1 region that expresses a membrane-associated accessory protein that limits AAV production through competitive exclusion. Mutant biodistribution revealed the importance of both surface-exposed and buried residues, with a few phenotypic profiles characterizing most variants. Finally, we algorithmically designed and experimentally verified a diverse in vivo targeted capsid library with viability far exceeding random mutagenesis approaches. These results demonstrate the power of systematic mutagenesis for deciphering complex genomes and the potential of empirical machine-guided protein engineering.

Since the discovery of the adeno-associated virus (AAV) in 1965 (1), AAV capsids have become a powerful tool for therapeutic in vivo gene delivery (2, 3). However, the transduction efficiency of natural capsids is still limiting for therapeutic purposes (4). Furthermore, engineering of enhanced capsids has proven challenging because of the complexity of genotype-phenotype relationships and the many functional properties that must be simultaneously optimized (5).

To better understand AAV function and inform capsid engineering, we generated all single-codon mutants of the AAV2 *cap* gene. AAV2 is the most well-characterized AAV serotype and is a component of the first U.S. Food and Drug Administration-approved gene therapy (2). Additionally, the AAV2 *rep* gene and inverted terminal repeat (ITR) sequences are commonly used for recombinant AAV production. Whereas recent high-throughput AAV mutagenesis studies have focused on limited capsid regions (6, 7), we examined the effects of mutations systematically across all 735 positions. Moreover, we included all synonymous codons for each amino acid to enable detection of noncoding elements. Wild-type (WT) AAV2 sequences and stop codon substitutions were included as positive and negative controls, respectively. In addition to codon substitutions, we generated all single-codon insertions and deletions. The full library was generated through mutant synthesis and plasmid assembly: final constructs contained ITRs flanking the full-length capsid gene with an upstream

promoter and a downstream barcode, enabling pooled measurements of mutant frequencies by high-throughput sequencing (Fig. 1A and fig. S1).

To understand how mutations affect virus production (e.g., capsid assembly and genome packaging), we transfected the plasmid library into human embryonic kidney (HEK) 293T cells to produce recombinant AAV and purified the resulting virus. We calculated the fitness of each variant as normalized enrichment relative to WT (Fig. 1B), summing counts for all synonymous codons of the same amino acid. VP1, VP2, and VP3 are *cap* isoforms that assemble into capsids with a 1:1:10 ratio (8). We observed that nonsense mutations in the VP3 region were more strongly depleted than those in VP1 and VP2 (Fig. 1C), consistent with only VP3 being essential for capsid assembly (9).

We found that mutations at buried positions and those near the 5-fold axis of symmetry were more deleterious, whereas exposed residues and those at the 3-fold axis were better tolerated (Fig. 1, D and E). Additionally, mutations in variable regions identified from evolutionary capsid alignments (10) had greater average fitness than nonvariable regions (Fig. 1E). Outside of the variable regions, substitution to amino acids found within other serotypes were better tolerated than substitutions to amino acids never observed across a set of commonly studied AAVs (Fig. 1F). In contrast to alanine scanning, comprehensive mutagenesis revealed the importance of amino acid biochemical properties: positive charge was more deleterious across all positions, whereas negative charge was beneficial mainly at external projections, especially near the 3-fold axis (Fig. 1D). Mutations to methionine (ATG) were deleterious throughout the VP1 region, likely because the early initiation of translation there reduced the production of VP2 and VP3 monomers or because truncated VP1 products inhibit capsid formation.

We also developed assays for measuring the evasion of neutralizing antibodies and thermostability. We identified mutations that escape neutralization by the A20 monoclonal antibody, whose binding epitope on the capsid surface has been identified through cryo-electron microscopy (11). Many mutants escaped neutralization, with escaping mutations being more likely to arise from known A20 epitope positions (fig. S4). We further measured capsid thermostability by incubating the library at varying temperatures and then digesting any genomes released from capsids. Most mutations that decreased thermostability occurred at the 3-fold axis, suggesting that capsid disassembly initiates at these positions (fig. S5). These in vitro assays showed the utility and versatility of such libraries for studying complex AAV functions.

Our comprehensive codon-scanning approach enabled the detection of hidden gene products and genetic elements. In particular, functions independent of coding for the capsid could manifest as fitness differences among synonymous codons. We devised a Frameshift Score (FS) to detect the presence of frameshifted open reading frames (ORFs) by comparing the differences in fitness observed among synonymous *cap* mutants when stop codons in alternative reading frames were present or absent. We evaluated this metric using AAV production data across Assembly Activating Protein (AAP), a known frameshifted ORF within *cap* (9). We observed significant FS in the +1 frame (Fig. 2A), as expected given AAP's essential role in AAV2 capsid assembly (9). Other frameshifted ORFs, such as the X gene, have been proposed (12), however, we detected no highly significant FS within this region.

Instead, we detected a +1 frameshifted ORF in the VP1 region (Fig. 2A). Guided by differences in fitness of synonymous codons, we identified *cap* positions 27 to 147 as the most likely ORF location. We hypothesized that the ORF starts with CTG, a noncanonical start codon. Supporting this hypothesis, all mutations to P27(CCT) were deleterious, except those that preserved the CTG start codon (fig. S6A). In this frame, translation continues until reaching a TAG stop codon, creating a protein 119 amino acids in length (fig. S7). A pBLAST search for this sequence on the National Center for Biotechnology Information (NCBI) website against the nonredundant protein database returned no proteins with significant homology.

To validate the ORF's translation in the native context we added a FLAG tag at the C terminus and transfected the plasmid construct into HEK293T cells. Using Western blotting, we confirmed the presence of a protein migrating near the expected size of 16 kDa (Fig. 2B and fig. S6B). Synonymous changes to

<sup>1</sup>Harvard Medical School, Boston, MA 02115, USA. <sup>2</sup>Wyss Institute for Biomedically Inspired Engineering, Boston, MA 02115, USA. <sup>3</sup>Harvard Graduate Program in Biological and Biomedical Sciences, Boston, MA 02115, USA. <sup>4</sup>Dyno Therapeutics, Inc., Cambridge, MA 02139, USA. <sup>5</sup>Department of Organismic and Evolutionary Biology, Harvard University, Cambridge, MA 02138, USA.

\*These authors contributed equally to this work.

†Corresponding author. Email: eric.kelsic@dynotx.com (E.D.K.); gchurch@genetics.med.harvard.edu (G.M.C.)



*cap* that mutated the hypothesized CTG start codon ablated the primary protein product, as did a *cap* mutation creating an early stop codon (Fig. 2B). Light bands at lower molecular weight indicated the potential presence of additional downstream start codons.

Intriguingly, although AAV2 assembles in the nucleolus (13), anti-FLAG immunofluo-

rescence imaging revealed the ORF protein to be membrane associated (fig. S6C). We confirmed this by replacing the FLAG tag with a C-terminal GFP fusion and also by testing sequences derived from AAV5, AAV8, and AAV9. In all cases, the protein was associated with the cell membrane (Fig. 2C and figs. S6, C and D, and S8). On the basis of these obser-

variations, we proposed the name “membrane-associated accessory protein” (MAAP).

To understand the functional role of MAAP, we repeated the production experiment while supplementing the library with MAAP expressed in trans. This rescued the packaging abilities of VP mutants containing MAAP-null mutants (Fig. 2D). Although MAAP-null

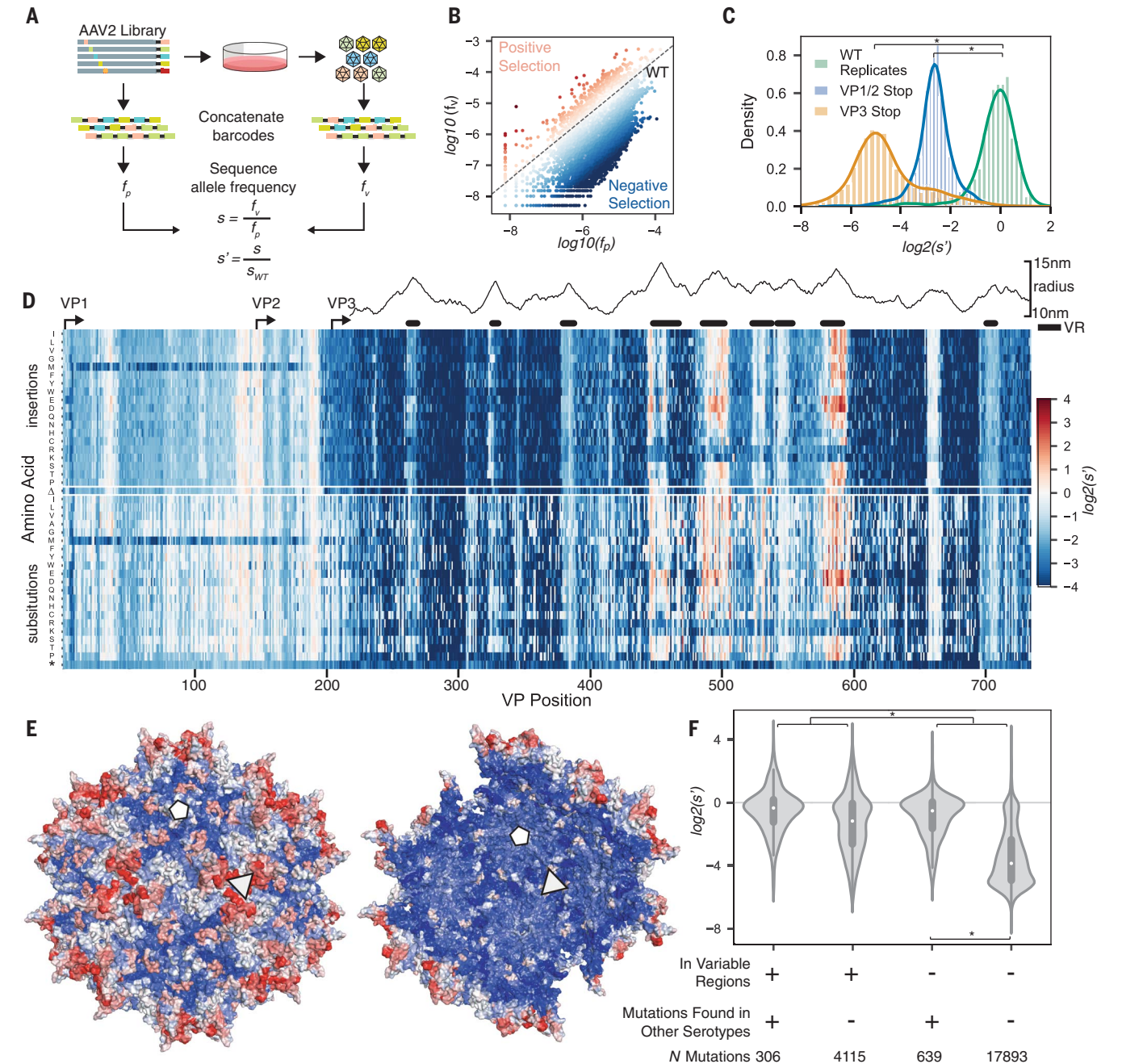
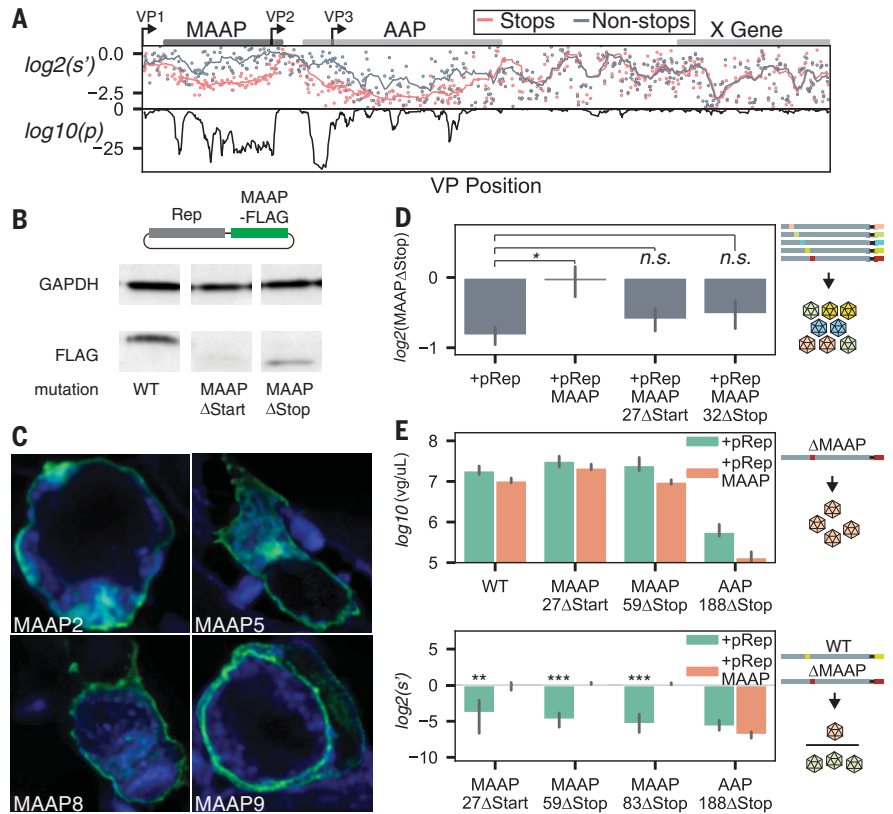


**Fig. 1. Measurement of all single AAV2 capsid mutations in a multiplexed viral production assay.** (A) Assay and calculation of production fitness ( $s'$ ). (B) Barcode frequencies: plasmid ( $f_p$ ) versus virus ( $f_v$ ). (C) Fitness for WT replicates and stop codons in VP1, VP2, and VP3. (D) Fitness for all single-amino-acid insertions, deletions ( $\Delta$ ), stop codons (\*), and substitutions.

Radius is from capsid center. VR, variable regions. (E) Average fitness for insertions at each position colored on the 3D structure. The triangle is the 3-fold axis and the pentagon is the 5-fold axis. (F) Fitness distributions split by conservation and location within or outside of variable regions. In all panels,  $*p < 10^{-20}$  (Mann-Whitney  $U$  test).

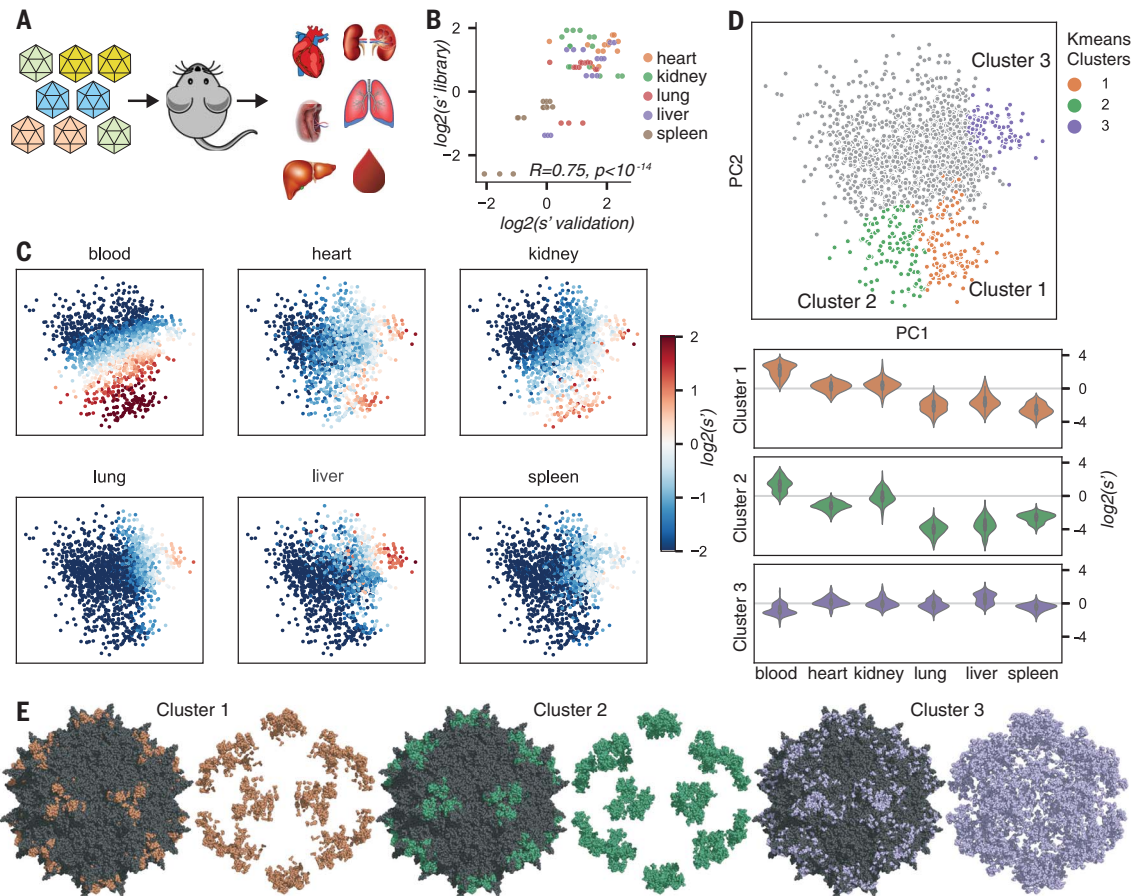
**Fig. 2. A frameshifted protein expressed from the VP1 region functions through competitive exclusion.**

(A) Discovery of MAAP, a frameshifted ORF in the VP1 region. Top: Production fitness for mutations with stop codons in the +1 frame (red) and for cap codons synonymous to the red points but without creating stops in the +1 frame (gray). Solid lines indicate the 10-position moving average. Bottom: p-value for the observed difference in +1 frame stops and non-stops for the moving window of 10 positions. (B) Western blot of MAAP-3xFLAG with M2 anti-FLAG HRP antibody and an anti-GAPDH loading control. (C) Membrane association: confocal imaging of MAAP-GFP localization for AAV serotypes 2, 5, 8, and 9. Blue is membrane stain and green is green fluorescent protein. (D) Deleterious effects on production for MAAP stop codons relative to other synonymous codons in the cap gene, supplying in trans: pRep, pRep+MAAP, or pRep+MAAP negative controls. \* $p < 10^{-5}$  (Mann-Whitney  $U$  test). (E) MAAP mutants produce at levels similar to WT when expressed individually (top) are outcompeted by WT in a head-to-head format, but then rescued by pRep+MAAP in trans (bottom). \*\* $p < 0.05$ , \*\*\* $p < 0.01$  (one-way t-test).



**Fig. 3. Multiplexed measurement of in vivo bio-distribution reveals phenotypic clustering and structural design principles.**

(A) Biodistribution assay. (B) In vivo selection values for validation mutants in library format versus individual assays. (C) Projection of individual mutants onto PC1 and PC2 derived from PCA, colored by tissue enrichment. (D) Top: Highlighting k-means clusters of mutants with enhanced tissue targeting. Bottom: Mutant biodistribution values within each cluster. (E) Position of cluster mutants in capsid structure, rendering first all residues and then only residues from each cluster to show the importance of buried residues for cluster 3.





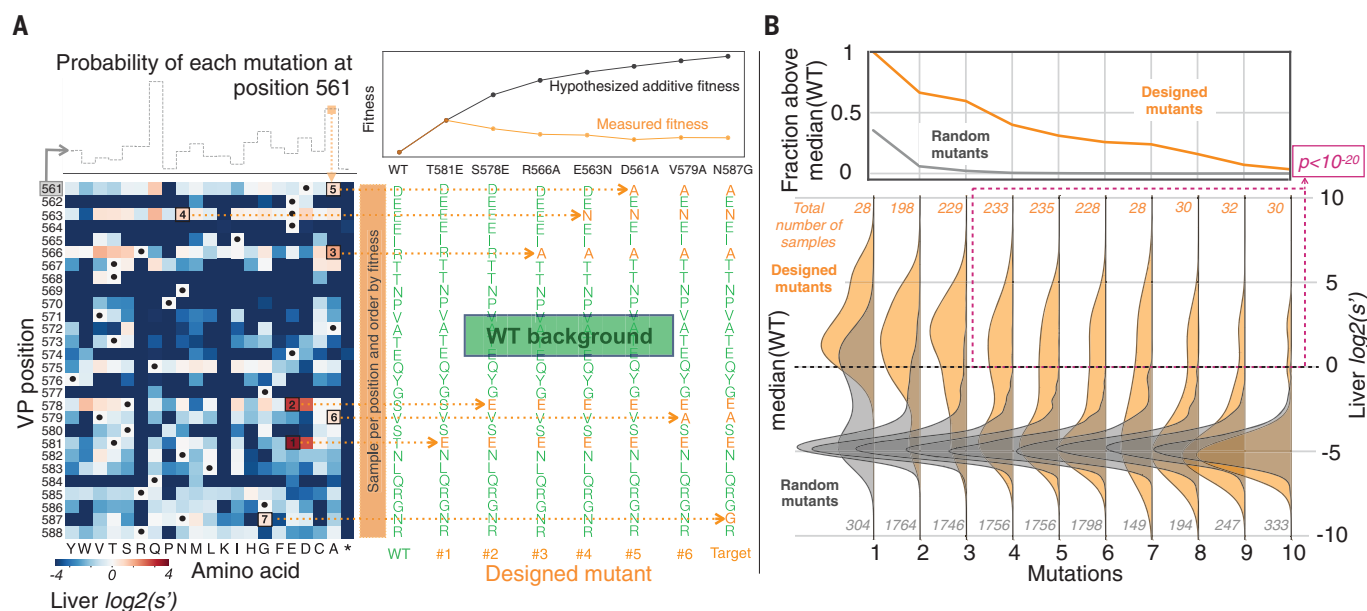


**Fig. 4. Machine-guided design of AAV capsids outperforms random mutagenesis.** (A) Left: Generation of multimutants from individual amino-acid liver-biodistribution measurements (black dots: WT). Mutation probability distributions for each position are calculated from single-amino-acid mutant fitness (top). Right: Sampled mutations are combined to generate a multimutant target variant and then all mutants from WT to target are synthesized and

experimentally measured (top shows ordering by increasing fitness). (B) Top: Fraction of designed mutants with liver biodistribution values greater than WT for random (gray) and machine-guided design mutants (orange). Bottom: Distribution of biodistribution values for random and designed mutants separated by number of mutations. Even at distances farther than four mutations, the designed approach outperforms random mutagenesis (pink box).

mutants produced individually did not have reduced titers relative to WT, when we assayed individual MAAP mutants in head-to-head competition with WT, MAAP mutants were outcompeted unless complemented in trans with functional MAAP (Fig. 2E). MAAP's function therefore manifests through competitive exclusion, possibly explaining the high genome-capsid coupling observed for libraries of engineered AAV capsids (14).

We studied the effects of mutations on in vivo delivery by administering the virus library to mice through retroorbital injection. We collected blood 1 hour later; spleen, liver, kidney, heart, and lung 18 days later; and then sequenced barcodes from purified virus genomes (Fig. 3A and fig. S9). We chose five mutants with divergent biodistribution profiles and verified that biodistribution from individual variants matched our library-based measurements (Fig. 3B).

Principal component analysis (PCA) revealed distinct relationships between tropism profiles and capsid structure. The first two principal components explained 80% of the variance in tropism profiles. We identified three mutant clusters that increased biodistribution to at least one tissue (Fig. 3CD and fig. S10). Cluster 1 included the well-studied R585 and R588 mutants (15), which were depleted from the liver and enriched in the blood, as expected, and enriched in the heart and kidney. Cluster 2 mutants were similar, but selectively

depleted from the heart. Cluster 3 mutants were depleted from the blood and spleen but enriched across the other tissues. The structural locations of these clusters were distinct: Mutants from cluster 1 and cluster 2 occurred in tight patches on the capsid surface near the 3-fold axis, whereas cluster 3 mutations were dispersed in buried positions throughout the capsid (Fig. 3E).

With most single-amino-acid changes being deleterious, introducing multiple mutations without breaking capsid function has been a limitation for engineering through random mutagenesis (16). We hypothesized that an additive model built from our data would approximate the fitness of nearby variants with multiple mutations, enabling the design of functional variants with greater throughput than rational design and higher efficiency than random mutagenesis.

To validate this hypothesis, we focused on capsid positions 561 to 588, a region containing both surface-exposed and buried positions. Informed by liver-biodistribution data from an additional in vivo mouse experiment focused on single mutations only at these positions (Fig. 4A), we designed multimutant variants by sampling mutations at each position proportional to their measured effect on liver delivery. Within the library, each designed target variant was tested either alone or with a complete path of stepwise edits from WT to the target itself (Fig. 4A).

Using this strategy, we designed 1271 variants in addition to 10,047 randomly generated mutants with 1 to 10 mutations from the WT reference and measured liver biodistribution in mice. The designed set contained a much higher fraction of mutants targeted to the liver. This trend was most pronounced when the number of mutations was four or more: 147 designed mutants (25.6% of those tested) were functional, whereas nearly all of the 4477 randomly generated mutants were not viable or had weaker liver tropism than WT (99.8%; Fig. 4B).

Our comprehensive, machine-guided design strategy generated viable mutants in a principled and high-throughput manner and is generalizable to other proteins and engineering challenges. Applied to AAV, such methods now enable the systematic optimization of natural capsids into synthetic variants with enhanced properties for emerging gene therapies.

## REFERENCES AND NOTES

1. R. W. Atchison, B. C. Casto, W. M. Hammon, *Science* **149**, 754–755 (1965).
2. S. Russell et al., *Lancet* **390**, 849–860 (2017).
3. J. R. Mendell et al., *N. Engl. J. Med.* **377**, 1713–1722 (2017).
4. D. Wang, P. W. L. Tai, G. Gao, *Nat. Rev. Drug Discov.* **18**, 358–378 (2019).
5. D. Grimm, S. Zolotukhin, *Mol. Ther.* **23**, 1819–1831 (2015).
6. K. Adachi, T. Enoki, Y. Kawano, M. Veraz, H. Nakai, *Nat. Commun.* **5**, 3075 (2014).
7. M. Davidsson et al., Barcoded rational AAV vector evolution enables systematic in vivo mapping of peptide binding motifs. bioRxiv 335372 [Preprint]. 31 May 2018.
8. A. Srivastava, E. W. Lusby, K. I. Berns, *J. Virol.* **45**, 555–564 (1983).

9. F. Sonntag, K. Schmidt, J. A. Kleinschmidt, *Proc. Natl. Acad. Sci. U.S.A.* **107**, 10220–10225 (2010).
10. V. V. Lukashov, J. Goudsmit, *J. Virol.* **75**, 2719–2740 (2001).
11. D. M. McCraw, J. K. O'Donnell, K. A. Taylor, S. M. Stagg, M. S. Chapman, *Virology* **431**, 40–49 (2012).
12. M. Cao, H. You, P. L. Hermonat, *PLOS ONE* **9**, e104596 (2014).
13. A. Wistuba, A. Kern, S. Weger, D. Grimm, J. A. Kleinschmidt, *J. Virol.* **71**, 1341–1352 (1997).
14. M. Nonnenmacher, H. van Bakel, R. J. Hajjar, T. Weber, *Mol. Ther.* **23**, 675–682 (2015).
15. A. Kern *et al.*, *J. Virol.* **77**, 11072–11081 (2003).
16. E. D. Kelsic, G. M. Church, *Cell Gene Ther. Insights* **5**, 523–536 (2019).

## ACKNOWLEDGMENTS

We thank S. Biswas, N. Davidsohn, D. Goodman, N. Jain, G. Kuznetsov, M. Schubert, D. Thompson, and members of the Church lab for helpful discussions and J. Aach, R. Kishony, S. Slomovic, and H. Wang for feedback on early versions of the manuscript. **Funding:** This work was supported by grant nos. NIH-P50-HG005550 and NIH-RM1-HG008525, and by internal funding from the Harvard Wyss Institute. Computational resources for this work were provided by the AWS Cloud Credits for Research Program. **Author contributions:** Conceptualization, methodology, writing: P.J.O., E.D.K., S.S., and G.M.C.; Investigation: P.J.O. and E.D.K.; Formal analysis, Software: P.J.O., E.D.K., and S.S.; Supervision: E.D.K. and G.M.C. **Competing interests:** P.J.O., E.D.K., S.S., and G.M.C. are inventors on patent applications filed by Harvard University related to this work. E.D.K., S.S., and G.M.C. hold equity in Dyno Therapeutics,

Inc. G.M.C.'s tech transfer and advisory roles are listed at: <http://arep.med.harvard.edu/gmc/tech.html>. **Data and materials availability:** These data are available at the GEO website under accession number GSE139657. Barcode scripts are available at [https://github.com/churchlab/AAV\\_fitness\\_landscape](https://github.com/churchlab/AAV_fitness_landscape). Commit hash: e42505099b6d5f1f64770e4fa90f17c198915662.

## SUPPLEMENTARY MATERIALS

[science.sciencemag.org/content/366/6469/1139/suppl/DC1](https://science.sciencemag.org/content/366/6469/1139/suppl/DC1)  
Materials and Methods

Figs. S1 to S10

References (17–20)

[View/request a protocol for this paper from Bio-protocol.](#)

7 December 2018; accepted 5 November 2019  
10.1126/science.aaw2900



## MICROBIOME

# Lactose drives *Enterococcus* expansion to promote graft-versus-host disease

C. K. Stein-Thoeringer<sup>1,2,3</sup>, K. B. Nichols<sup>1,2</sup>, A. Lazrak<sup>1,2</sup>, M. D. Docampo<sup>1,2</sup>, A. E. Slingerland<sup>1,2</sup>, J. B. Slingerland<sup>1,2</sup>, A. G. Clurman<sup>4</sup>, G. Armijo<sup>1,2</sup>, A. L. C. Gomes<sup>1,2</sup>, Y. Shono<sup>1,2</sup>, A. Staffas<sup>1,2</sup>, M. Burgos da Silva<sup>1,2</sup>, S. M. Devlin<sup>5</sup>, K. A. Markey<sup>1,2,4</sup>, D. Bajic<sup>6</sup>, R. Pinedo<sup>7</sup>, A. Tsakmaklis<sup>8,9</sup>, E. R. Littmann<sup>1,10</sup>, A. Pastore<sup>1</sup>, Y. Taur<sup>11</sup>, S. Monette<sup>12</sup>, M. E. Arcila<sup>13</sup>, A. J. Pickard<sup>14</sup>, M. Maloy<sup>4</sup>, R. J. Wright<sup>1</sup>, L. A. Amoretti<sup>1</sup>, E. Fontana<sup>1</sup>, D. Pham<sup>15</sup>, M. A. Jamal<sup>15</sup>, D. Weber<sup>16</sup>, A. D. Sung<sup>17</sup>, D. Hashimoto<sup>18</sup>, C. Scheid<sup>8</sup>, J. B. Xavier<sup>19</sup>, J. A. Messina<sup>20</sup>, K. Romero<sup>21</sup>, M. Lew<sup>17</sup>, A. Bush<sup>17</sup>, L. Bohannon<sup>17</sup>, K. Hayasaka<sup>22</sup>, Y. Hasegawa<sup>18</sup>, M. J. G. T. Vehreschild<sup>8,9,23</sup>, J. R. Cross<sup>14</sup>, D. M. Ponce<sup>2,4</sup>, M. A. Perales<sup>2,4</sup>, S. A. Giralt<sup>2,4</sup>, R. R. Jenc<sup>15</sup>, T. Teshima<sup>18,22</sup>, E. Holler<sup>16</sup>, N. J. Chao<sup>17</sup>, E. G. Pamer<sup>1,2,10</sup>, J. U. Peled<sup>1,2,4,\*</sup>†, M. R. M. van den Brink<sup>1,2,4,\*</sup>†

Disruption of intestinal microbial communities appears to underlie many human illnesses, but the mechanisms that promote this dysbiosis and its adverse consequences are poorly understood. In patients who received allogeneic hematopoietic cell transplantation (allo-HCT), we describe a high incidence of enterococcal expansion, which was associated with graft-versus-host disease (GVHD) and mortality. We found that *Enterococcus* also expands in the mouse gastrointestinal tract after allo-HCT and exacerbates disease severity in gnotobiotic models. *Enterococcus* growth is dependent on the disaccharide lactose, and dietary lactose depletion attenuates *Enterococcus* outgrowth and reduces the severity of GVHD in mice. Allo-HCT patients carrying lactose-nonabsorber genotypes showed compromised clearance of postantibiotic *Enterococcus* domination. We report lactose as a common nutrient that drives expansion of a commensal bacterium that exacerbates an intestinal and systemic inflammatory disease.

The healthy gut is inhabited by a diverse community of mostly anaerobic bacteria, and a hallmark of microbial imbalance (dysbiosis) observed in many disease states involves the expansion of facultative anaerobic bacteria (1). Enterococci are facultative anaerobes that colonize the intestines of almost every species, from insects to mammals (2), and make up a very small proportion (<0.1%) of the gut microbiota in healthy humans (3). However, enterococci are also pathogens; the species *Enterococcus faecium* and *Enterococcus faecalis* are important causes of multidrug-resistant infections in patients (4). In single-center studies, *E. faecium* has been observed to dominate the fecal microbiota of immunocompromised patients after allogeneic hematopoietic cell transplantation (allo-HCT), a curative-intent therapy for hematological malignancies (5–7). Moreover, fecal domination with vancomycin-resistant enterococci increases the risk of

bloodstream infection in allo-HCT patients (5, 8). Patients with severe graft-versus-host disease (GVHD) after allo-HCT have poor outcomes with only ~30% long-term survival (9). Gut microbiota perturbations caused by broad-spectrum antibiotics and a reduction in microbial diversity are associated with increased transplant-related mortality and lethal GVHD in humans and mice (10–13). Besides causing infections, experimental studies in gnotobiotic mice have revealed that enterococci play an important role in colitis (14) by stimulating antigen-presenting cells and CD4<sup>+</sup>RORγ<sup>+</sup> T cell infiltration, causing intestinal inflammation (15). In this study, we investigated the role of enterococci in the development of acute GVHD, both in allo-HCT patients and preclinical allo-HCT mouse models.

We used 16S ribosomal RNA (rRNA) gene sequencing to study the fecal microbiota of 1325 adult allo-HCT recipients at four HCT centers: Memorial Sloan Kettering Cancer

Center (MSKCC) (United States), Duke University (United States), Hokkaido University (Japan), and University Hospital Regensburg (Germany). Patient characteristics are shown in table S1. We observed high abundance of enterococci soon after transplantation in samples from all four transplant centers (Fig. 1B and fig. S1B). We defined *Enterococcus* domination as relative genus abundance ≥0.3 (≥30%) in any fecal sample, following a threshold we have used previously (5) (materials and methods and fig. S2C). The incidence of domination rose comparably across centers, with up to 65% of patients exhibiting a domination event after allo-HCT (Fig. 1A). *E. faecium* was the dominant species in both the MSKCC and the multicenter-validation cohort (Duke, Hokkaido, and Regensburg) (Fig. 1B, fig. S1, and table S2), where 40.1% of MSKCC patients (441 of 1101 patients) and 46.0% of multicenter-validation patients (103 of 224 patients) met criteria for domination at any time point between day –20 and day +80 relative to the date of allo-HCT, in which cells are infused on day 0.

Fecal domination by *Enterococcus* in the early posttransplant period (day 0 to +21) was associated with significantly reduced overall survival and increased GVHD-related mortality in both the MSKCC and multicenter-validation cohort, as well as an increased risk of moderate-to-severe acute GVHD in the MSKCC cohort (Fig. 1, C and D, fig. S2, A and B, and table S3). The risk of relapse or disease progression was not associated with enterococcal domination in either cohort. The association of domination by genus *Enterococcus* with clinical outcomes in the MSKCC cohort remained significant in a multivariate analysis adjusted for graft source, disease, conditioning intensity, gender, and age (table S4). In a subset of MSKCC patients, the *vanA* operon was found in 152 (37.4%) of 406 patients that had samples available for analysis, indicating the presence of vancomycin-resistant enterococci (VRE) (fig. S2E). Notably, expansions of several different taxa were detected in fecal samples in this study, but the *Enterococcus* genus was the one most commonly observed dominating the microbiota in all four transplant centers (fig. S3 and tables S5 and S6).

<sup>1</sup>Department of Immunology, Sloan Kettering Institute, Memorial Sloan Kettering Cancer Center, New York, NY, USA. <sup>2</sup>Weill Cornell Medical College, New York, NY, USA. <sup>3</sup>German Cancer Research Center (DKFZ), Heidelberg, Germany. <sup>4</sup>Adult Bone Marrow Transplantation Service, Department of Medicine, Memorial Sloan Kettering Cancer Center, New York, NY, USA. <sup>5</sup>Epidemiology and Biostatistics, Memorial Sloan Kettering Cancer Center, New York, NY, USA. <sup>6</sup>Department of Internal Medicine II, Technical University of Munich, Munich, Germany. <sup>7</sup>Gnotobiotic Facility, Memorial Sloan Kettering Cancer Center, New York, NY, USA. <sup>8</sup>Department I of Internal Medicine, Center for Integrated Oncology Aachen Bonn Cologne Duesseldorf, University of Cologne, Cologne, Germany. <sup>9</sup>German Center for Infection Research, Partner site Bonn-Cologne, Cologne, Germany. <sup>10</sup>Department of Medicine, Section of Infectious Medicine and Global Health, University of Chicago, Chicago, IL, USA. <sup>11</sup>Infectious Disease Service, Department of Medicine, Memorial Sloan Kettering Cancer Center, New York, NY, USA. <sup>12</sup>Laboratory of Comparative Pathology, Memorial Sloan Kettering Cancer Center, The Rockefeller University, Weill Cornell Medicine, New York, NY, USA. <sup>13</sup>Diagnostic Molecular Pathology Laboratory, Memorial Sloan Kettering Cancer Center, New York, NY, USA. <sup>14</sup>Donald B. and Catherine C. Marron Cancer Metabolism Center, Memorial Sloan Kettering Cancer Center, New York, NY, USA. <sup>15</sup>Department of Genomic Medicine, The University of Texas MD Anderson Cancer Center, Houston, TX, USA. <sup>16</sup>Internal Medicine III, University Clinic Regensburg, Regensburg, Germany. <sup>17</sup>Division of Hematologic Malignancies and Cellular Therapy, Department of Medicine, Duke University Medical Center, Durham, NC, USA. <sup>18</sup>Department of Hematology, Hokkaido University, Faculty of Medicine, Sapporo, Japan. <sup>19</sup>Computational and Systems Biology Program, Memorial Sloan Kettering Cancer Center, New York, NY, USA. <sup>20</sup>Division of Infectious Diseases, Department of Medicine, Duke University, Durham, NC, USA. <sup>21</sup>Office of Clinical Research, Duke University School of Medicine, Durham, NC, USA. <sup>22</sup>Division of Laboratory and Transfusion Medicine, Hokkaido University Hospital, Sapporo, Japan. <sup>23</sup>Department of Internal Medicine, Infectious Diseases, Goethe University Frankfurt, University Hospital Frankfurt, Frankfurt am Main, Germany.

\*These authors contributed equally to this work.

†Corresponding author. Email: peledj@mskcc.org (J.U.P.); vandenbm@mskcc.org (M.R.M.v.d.B.)

To further investigate these clinical observations, we examined the fecal microbiota of mice early after transplantation using well-established mouse models of allo-HCT. In a major histocompatibility complex (MHC)-matched, minor-antigen-mismatched allo-HCT model [C57BL/6-to-129S1/Sv transplant (C57BL/6→129S1/Sv)], we performed 16S rRNA gene sequencing of fecal samples and found that *E. faecalis* dominated the fecal microbiota at posttransplant day +8 in mice who received T cell-replete grafts and developed lethal, acute GVHD (Fig. 2A and fig. S4A). In contrast to the patients who had prolonged antibiotic exposures, this expansion of *E. faecalis* was independent of antibiotic administration and dependent upon GVHD, as it was not observed in control recipients of T cell-depleted allografts in which GVHD did

not develop. This posttransplant expansion of enterococci was consistently found in two additional lethal GVHD models: C57BL/6→BALB/c mice (MHC-disparate model after irradiation conditioning) (Fig. 2B) and LP/J→C57BL/6 mice [MHC-matched, minor-antigen-mismatched after busulfan and cyclophosphamide conditioning (16)] (Fig. 2C). The expansion of enterococci in murine allo-HCT recipients with GVHD was accompanied by an increase in *Enterococcus* colony-forming units recovered from mesenteric lymph nodes, consistent with increased bacterial translocation (Fig. 2B).

Although we observed *E. faecium* domination in patients and a transient expansion of *E. faecalis* in GVHD mice, we hypothesized that both members of this genus might be associated with GVHD. Of note, *E. faecium*

only recently became recognized as a major human pathogen; before the 1990s it was *E. faecalis* that caused >90% of clinical infections (17). Because *E. faecalis* expands in mice with GVHD and is the major *Enterococcus* species in laboratory mice, we next investigated whether *E. faecalis* contributes to GVHD. We colonized germ-free C57BL/6 mice with a community of six bacterial strains (*Akkermansia muciniphila*, *Lactobacillus johnsonii*, *Blautia producta*, *Bacteroides sartorii*, *Clostridium bolteae*, and *Parabacteroides distans*; see materials and methods) (10, 18, 19) 21 days prior to allo-HCT (LP/J→gnotobiotic C57BL/6). One group of mice was cocolonized on day -21 with *E. faecalis* OG1RF, which remained detectable in mouse feces on days 0 and +7 (Fig. 2D, right panel, and fig. S4E). GVHD was exacerbated in *E. faecalis*-harboring mice

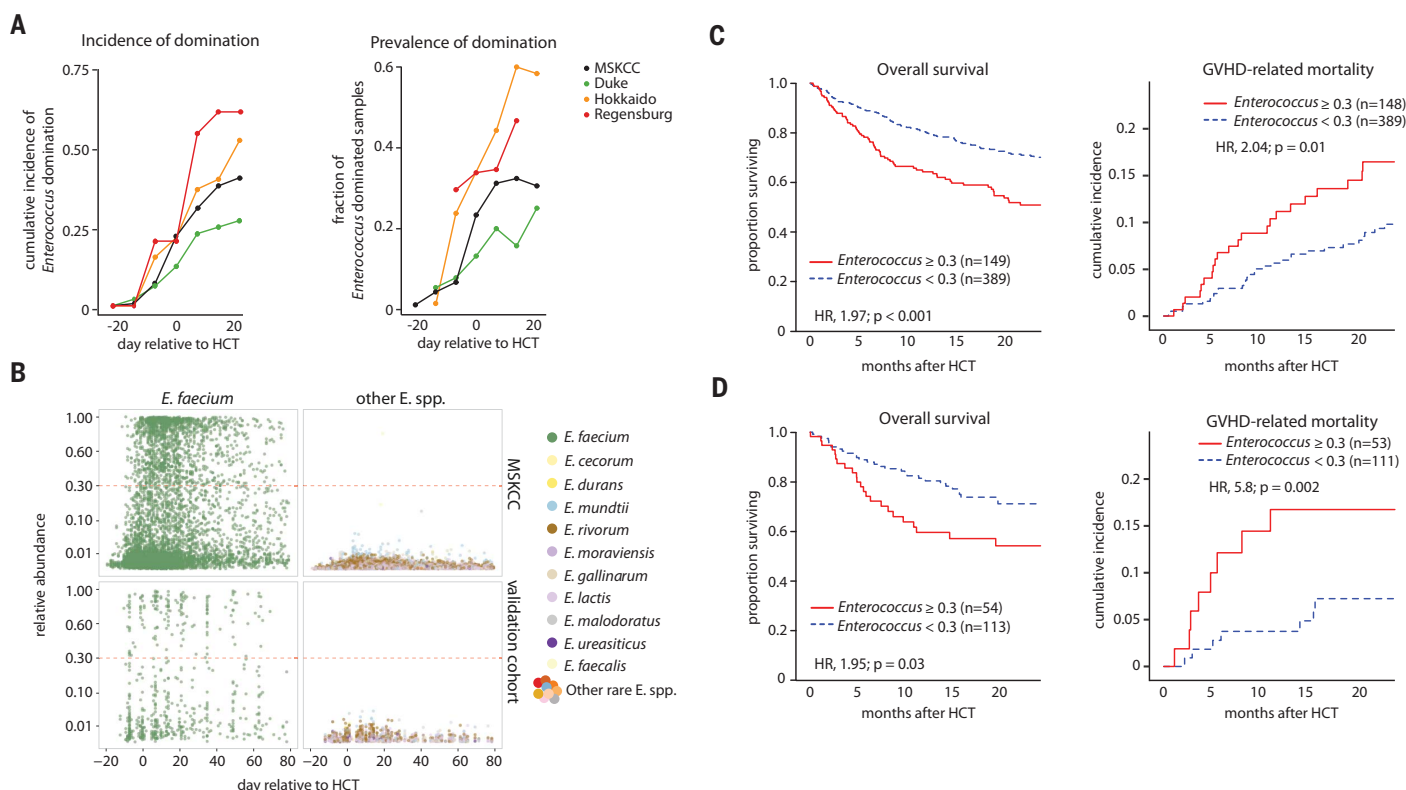


**Fig. 1. *Enterococcus* domination occurs globally and increases risk of GVHD and mortality after allo-HCT.** Fecal microbiota were profiled using 16S rRNA gene sequencing of 1325 adult allo-HCT recipients. The patients attended one of four HCT centers in different countries: MSKCC (United States), Duke University (United States), Hokkaido University (Japan), and University Hospital Regensburg (Germany). **(A)** (Left) Cumulative incidence of patients who experienced at least one instance of genus *Enterococcus* domination of the gut microbiota [domination defined as a genus relative abundance of  $\geq 0.3$  (on a unitless scale from 0 to 1) over the course of allo-HCT (day -20 to +24 relative to HCT; using 7-day sliding windows) at different transplant centers]. (Right) Fraction of fecal specimens with enterococcal domination of the gut microbiota. **(B)** Relative abundance of different *Enterococcus* spp. in the microbiota of allo-HCT patients from the MSKCC and multicenter-validation cohort over the course of HCT, determined by 16S rRNA gene sequencing of fecal samples. Each

point represents a fecal sample, and color indicates the different *Enterococcus* spp.; the red dotted line indicates the threshold for domination set at a relative abundance  $\geq 0.3$ . **(C)** Overall survival (left) and cumulative incidence of GVHD-related mortality (right) in the T cell replete graft recipients in the MSKCC patient cohort (see table S3), stratified into nondominated and *Enterococcus*-dominated groups (domination is defined as the relative genus abundance  $\geq 0.3$  in at least one sample between day 0 and +21). *n*, number of individuals. **(D)** Overall survival (left) and cumulative incidence of GVHD-related mortality (right) in *Enterococcus*-dominated (at genus level) versus nondominated allo-HCT patients in the combined multicenter-validation cohort (table S3). Clinical outcomes in (C) and (D) were analyzed using the R packages *survival* and *cmprsk*. Wald values of  $P < 0.05$  signify higher risks (HR, hazard ratios) of mortality among patients with *Enterococcus* domination as compared with those without domination.

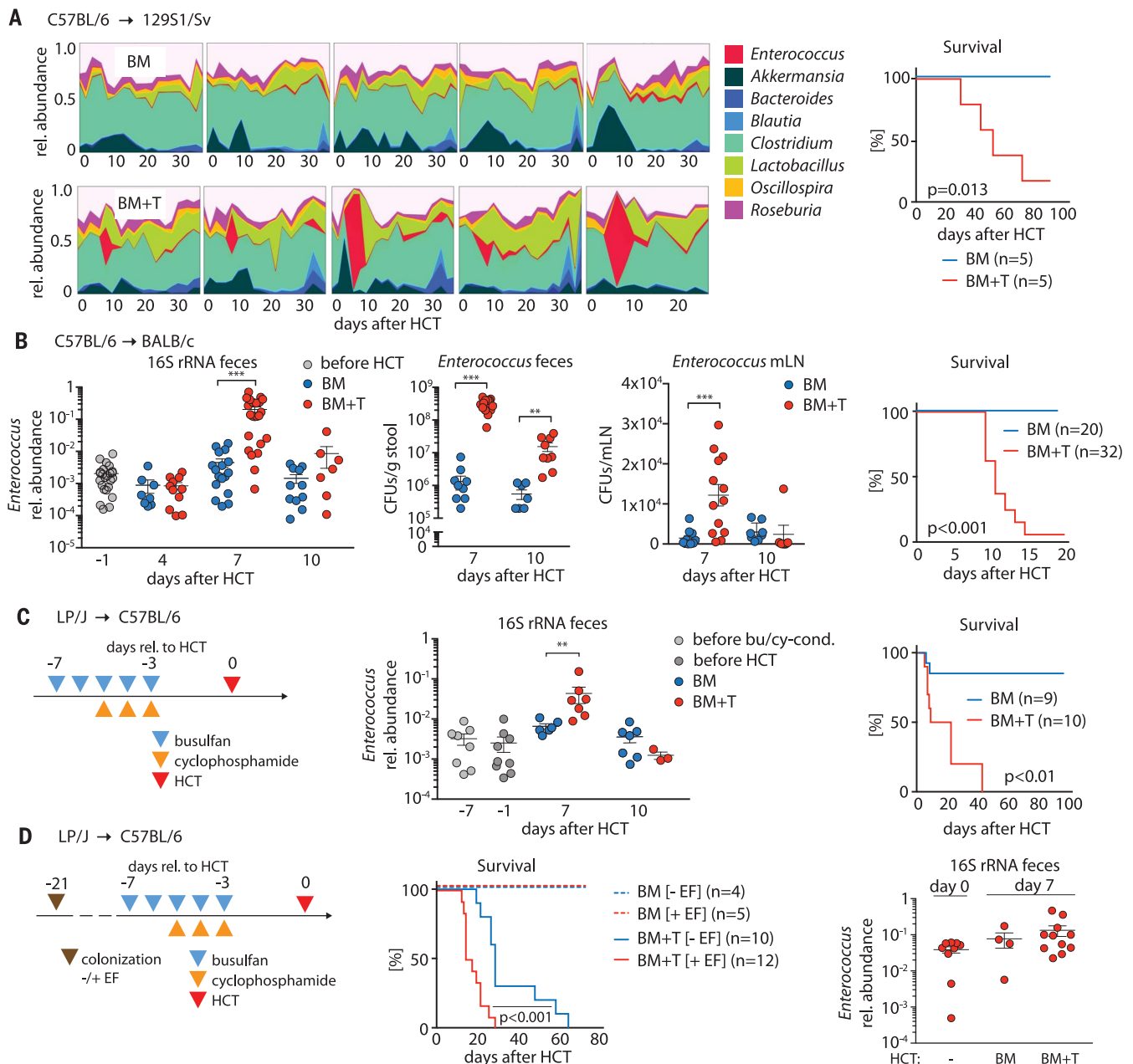


**Fig. 2. *Enterococcus* dominates mouse gut microbiota after HCT and can exacerbate GVHD.**

(A) (Left) High-density sampling and 16S rRNA gene sequencing of fecal microbiota from 129S1/Sv mice (1 box = 1 mouse) receiving bone marrow (BM; upper row) or T cell-replete bone marrow [BM+T ( $2 \times 10^6$  T cells); lower row]. (Right) BM+T transplanted mice develop lethal GVHD as shown by survival analysis. rel., relative. (B) (Left) Relative abundance of the genus *Enterococcus* in BALB/c host mice transplanted with C57BL/6 BM or BM+T ( $1 \times 10^6$  T cells) at different time points relative to HCT. (Middle) Colony-forming units (CFUs) of enterococci in fecal samples and in mesenteric lymph nodes (mLN). Scatter plot data show means  $\pm$  SEM. (Right) Survival of BALB/c recipient mice after HCT [BM versus BM+T ( $1 \times 10^6$  T cells)]. (C) (Left) Schematic showing HCT of LP/J BM versus BM+T ( $4 \times 10^6$  T cells) into C57BL/6 mice after chemotherapy conditioning. (Middle) Relative abundance of the genus *Enterococcus* in the feces of

transplanted mice at different time points relative to HCT. (Right) Comparison of overall survival between BM and BM+T mice. bu/cy-cond., busulfan/cyclophosphamide conditioning. (D) (Left) Schematic showing colonization of germ-free C57BL/6 mice with a 6-strain minimal microbiota with (+EF) or without (-EF) *E. faecalis* OG1RF ( $2 \times 10^7$  CFUs per mouse); after 14 days, colonized mice received chemotherapy conditioning with busulfan and cyclophosphamide and, subsequently, an HCT of LP/J BM versus BM+T ( $4 \times 10^6$  T cells). (Middle) Comparison of overall survival. (Right) Relative abundances of *E. faecalis* spiked to the minimal microbiota in the EF+ group with samples collected at the day of HCT (day 0) and 7 days later ( $n = 4$  to 11 mice per group;  $P = 0.09$ , paired testing of relative abundances of enterococci of day 0 versus BM+T day 7). Scatter plot data are presented as means  $\pm$  SEM.  $**P < 0.01$ ,  $***P < 0.001$  (independent *t* test for BM versus BM+T); survival data were statistically analyzed using Mantel-Cox log-rank test.



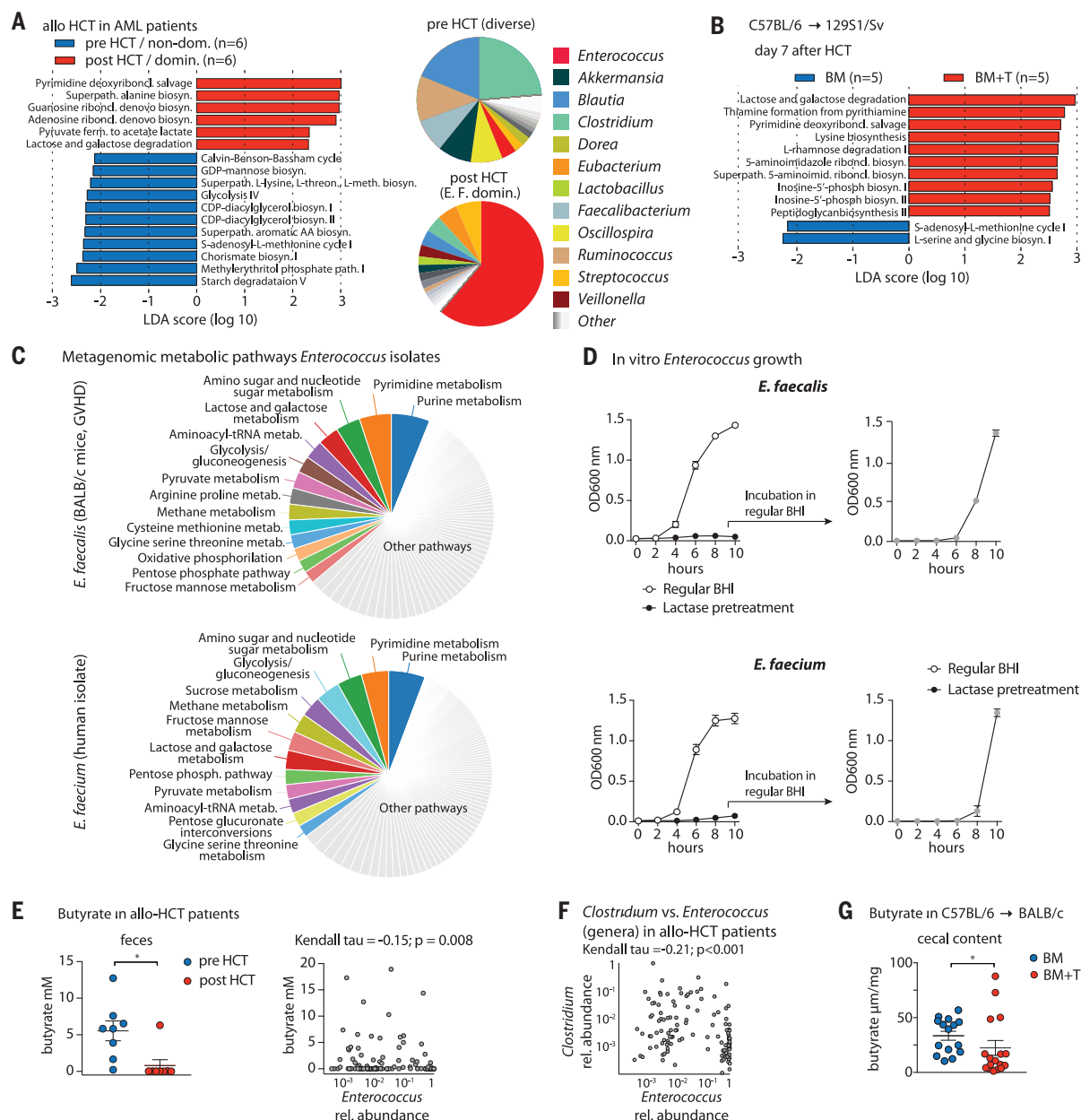


**Fig. 3. Metagenomic and metabolomic analyses of *Enterococcus*-dominated fecal specimens in human HCT patients and mice.** (A) (Left) Differential abundances of shotgun-sequenced and HUMAnN2-annotated bacterial metabolic pathways between paired pre- and post-HCT fecal samples from MSKCC patients who received allo-HCT for acute myeloid leukemia (AML) analyzed by linear discriminant analysis (LDA) coupled with effect size measurements (LEfSe). pre HCT, day -8 to -1 before allo-HCT; post HCT, day +3 to +25 after allo-HCT. (Right) Pie chart showing mean relative abundances of bacterial genera (analyzed by MetaPhlAn2) found in patient fecal samples pre- and post-HCT; data are aggregated across all patients. non-dom., non-dominated; domin., dominated. (B) LEfSe analysis of bacterial metabolic pathway abundances in HCT day +7 fecal samples of 129S1/SV mice transplanted with C57BL/6 BM versus BM+T ( $2 \times 10^6$  T cells) (see Fig. 2A). (C) Pie charts with metabolic pathway abundances determined by whole-genome sequencing of *E. faecalis* (isolated from feces of a BALB/c GVHD mouse, day +7 after HCT; upper panel) and *E. faecium* (human isolate; ATCC #700221; lower panel); only pathways with an abundance  $\geq 2\%$  are shown in both panels. (D) (Left) In vitro growth of *E. faecalis* (mouse GVHD isolate; upper panel) and *E. faecium* (ATCC #700221; lower panel) in nontreated BHI broth

or in BHI broth pretreated with lactase. (Right) *E. faecalis* or *E. faecium* incubated in lactase-pretreated BHI were put into regular BHI broth after 8 hours to assess growth dynamics in regular BHI (gray symbols). Data are results of four experiments combined; values represent means  $\pm$  SEM. (E) (Left) Fecal butyrate concentrations (means  $\pm$  SEM) from pre- and posttransplant fecal samples from AML patients from MSKCC, who received allo-HCT and were selected based on a highly diverse pre-HCT microbiota and a posttransplant *E. faecium* domination [by 16S rRNA gene sequencing; 6 (out of 8) patients are presented in (A)]. (Right) Correlation of butyrate concentrations with relative abundances of the genus *Enterococcus* ( $n = 139$  patients; 8 patients from left panel), and 131 allo-HCT patients from a dataset published by Haak *et al.* (28); statistical analysis was performed using Kendall's tau rank correlation coefficient. (F) Stool samples were collected at the time of engraftment (~24 days after allo-HCT). Data show Kendall's tau rank correlation of relative abundances of the genera *Clostridium* and *Enterococcus* from the dataset of Haak *et al.* (G) Butyrate concentration (mean  $\pm$  SEM) in cecal contents of BALB/c mice transplanted with C57BL/6 BM or BM+T ( $1 \times 10^6$  T cells) at day +7 after HCT. Statistical analysis: \* $P < 0.05$  [paired *t* test (E) or independent *t* test (F)].

(Fig. 2D and fig. S4B). Serum interferon- $\gamma$  concentrations were significantly elevated in *E. faecalis*-colonized mice (fig. S4C), and we observed a significantly increased number of donor T cells, an increase of acti-

vated and proliferating CD4<sup>+</sup> T cells (fig. S4D; CD4<sup>+</sup>CD25<sup>+</sup>; CD4<sup>+</sup>Ki67<sup>+</sup>), and an increased number and percentage of CD4<sup>+</sup>ROR $\gamma$ <sup>+</sup> T helper 17 (T<sub>H</sub>17) cells in colon lamina propria (fig. S4D). Posttransplant administration of *E. faecalis*

*OGIRF* to conventionally housed, T cell-replete bone marrow (BM+T)-transplanted BALB/c mice also aggravated GVHD (fig. S5A). These findings indicate that *E. faecalis* can aggravate GVHD severity.

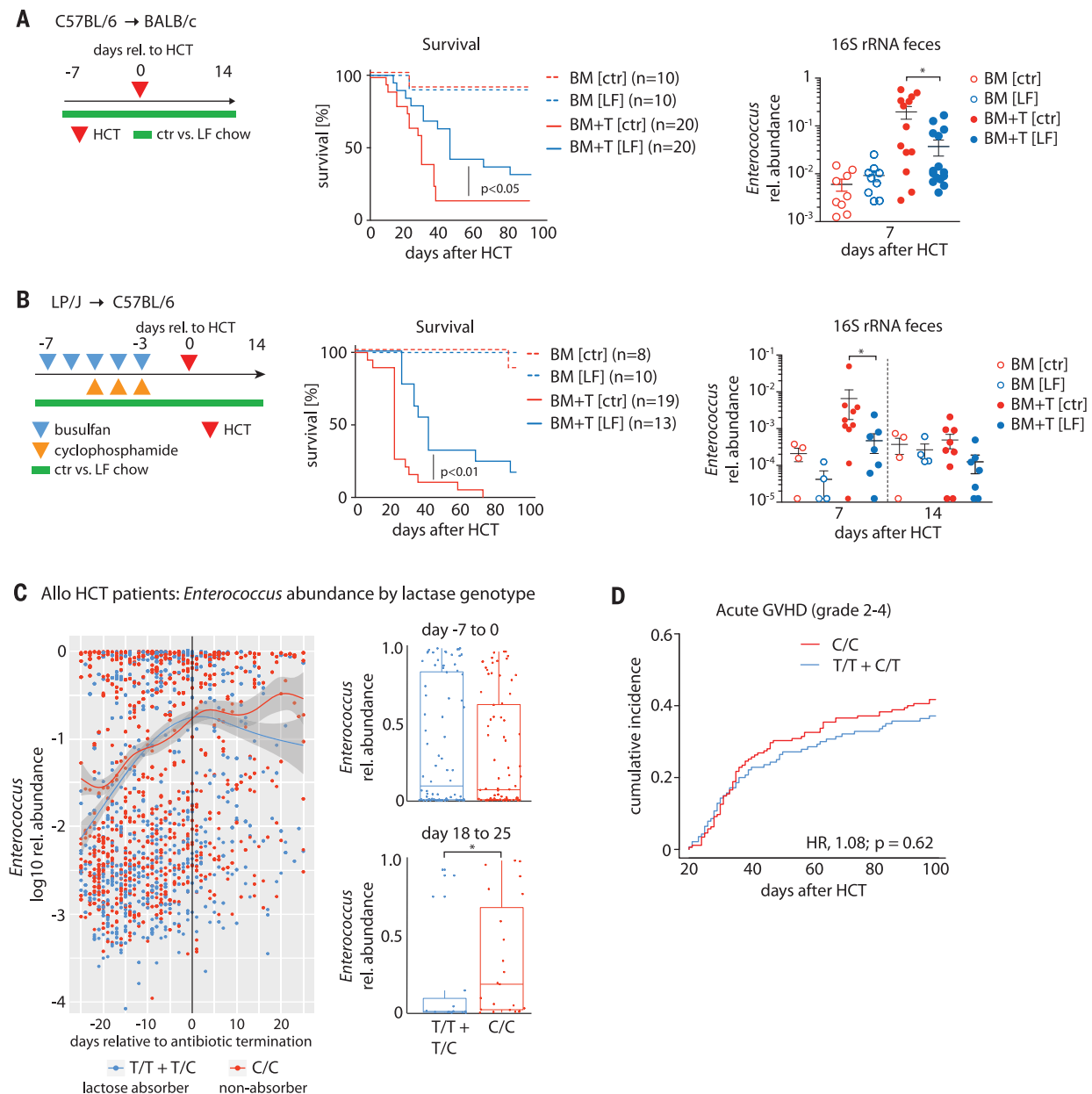


**Fig. 4. Lactose-free diet reduces experimental GVHD and lactase genotypes associated with microbiota dynamics after allo-HCT in humans.**

(A) (Left) Schematic showing that BALB/c recipient mice received C57BL/6 BM or BM+T ( $5 \times 10^5$  T cells) and were fed control chow (ctr) versus lactose-free chow (LF) from day -7 to +14 relative to transplant. Comparison of survival between BM and BM+T mice (middle) and relative abundance of the genus *Enterococcus* in mouse feces (right) are shown. Scatter plot data presented as means  $\pm$  SEM; \* $P < 0.05$  (independent  $t$  test). (B) (Left) Schematic showing HCT of LP/J BM versus BM+T ( $4 \times 10^6$  T cells) into C57BL/6 mice after chemotherapy conditioning. Comparison of survival between BM and BM+T mice (middle) and relative abundance of the genus *Enterococcus* at different time points relative to HCT (right) are shown. Scatter plot data presented as means  $\pm$

SEM; \* $P < 0.05$  (independent  $t$  test). (C) (Left) Relative abundance ( $\log_{10}$ ) of *Enterococcus* (genus) by days relative to the day of antibiotic cessation (broad-spectrum antibiotics for neutropenic fever: intravenous piperacillin-tazobactam, intravenous imipenem-cilastatin, or intravenous meropenem). Box plot inserts display the median relative abundances of the genus *Enterococcus* of time binned in the indicated day ranges relative to antibiotic cessation; whiskers represent maximum and minimum. Statistical analysis of box plot data: \* $P < 0.05$  (Wilcoxon rank test). (D) Cumulative incidence of acute GVHD grade 2 to 4 in rs4988235 SNP-genotyped MSKCC patients (T cell-depleted grafts excluded; graft source: BM/PBSC unmodified = 213 patients; cord blood = 102 patients; C/C = 175, T/C+T/T = 140). The cumulative incidence of grade 2 to 4 acute GVHD was compared between genotype groups using the R package *cmprsk*.

We next considered whether posttransplant defects of mucosal defense mechanisms facilitate enterococcal expansion. Immunoglobulin A (IgA) coating of intestinal bacteria can be protective in colitis and is important for maintaining mucosal integrity (20). However, we did not observe members of the genus *Enterococcus* to be enriched in either IgA-negative or IgA-positive fecal fractions, even though total fecal IgA was significantly reduced in allo-HCT recipients with GVHD (fig. S5, B to D). Reduction of IgA by transplanting IgA-deficient bone marrow (BM) from activation-induced cytidine deaminase knockout mice did not further increase enterococcal expansion (fig. S5E). Intestinal antimicrobial peptides of the Reg3 family can suppress the growth of VRE (21) and are reported to play a major role in GVHD (22). Accordingly, we found that both Reg3B/G transcripts and interleukin-22 protein, which regulates Reg3 expression (23), were reduced in the ileum of GVHD mice (fig. S5F).

Next, we analyzed microbiota-intrinsic factors and used shotgun metagenomic sequencing to characterize the metabolic potential of the *Enterococcus*-dominated fecal microbiota. Pre- and posttransplant fecal samples from MSKCC patients who received allo-HCT for acute myeloid leukemia were selected for sequencing on the basis of having a highly diverse pre-HCT microbiota and posttransplant *E. faecium* domination (by 16S rRNA gene sequencing). We focused on microbial metabolic pathways that specifically characterize domination by comparing them with the highly diverse pretransplant microbiota from the same patients. Pathways involved in DNA synthesis and, notably, in lactose and galactose degradation were enriched in the *E. faecium*-dominated, posttransplant microbiota. In contrast, amino acid synthesis and starch-degradation pathways were more prevalent in pretransplant specimens (Fig. 3A). The lactose-and-galactose degradation pathway was also significantly enriched in the posttransplant *E. faecalis*-dominated samples of mice with GVHD (Fig. 3B). Comparison of whole-genome sequencing from isolates of *E. faecium* (from a human allo-HCT patient) and of *E. faecalis* (from a mouse with GVHD) revealed that genes encoding lactose and galactose metabolism accounted for ~3% of their genomes (Fig. 3C). In silico analysis of these *Enterococcus* genomes and publicly available genomes of other members of the gnotobiotic six-strain consortium revealed that enterococci are specifically enriched in enzymes of the tagatose-type galactose pathway for galactose-to-glucose degradation (24) (materials and methods and fig. S6, A and B). Enterococcal growth depends on lactose in vitro, as both *E. faecalis* and *E. faecium* strains cultured in brain-heart

infusion (BHI) broth depleted of lactose (by lactase; fig. S7A) did not grow (Fig. 3D). Growth was reinstated upon transfer to regular BHI, excluding antibacterial effects of lactase treatment (Fig. 3D). Enterococcal expansion after allo-HCT was accompanied by a loss of *Clostridium* spp. in the microbiota of allo-HCT patients (Fig. 3, A and F) and of mice with GVHD (fig. S8, A to C, and table S7). This may be important for allo-HCT patients, as high abundances of clostridia are associated with better survival and lower incidence of GVHD (12, 25). Commensal clostridia are known to produce large amounts of butyrate (26), which mitigates lethal GVHD in mice through protecting energy homeostasis of enterocytes (27). We observed that posttransplant enterococcal domination and a loss of clostridia were accompanied by a significant reduction in fecal butyrate in both allo-HCT patients and mice with GVHD (Fig. 3, E and G) (28). A loss of this key metabolite may contribute to the poor outcomes in *Enterococcus*-dominated patients and mice.

Given that the optimal growth of enterococci depends on lactose availability in vitro, we investigated whether enterococcal expansion can be mitigated by feeding mice lactose-free chow (fig. S7B and table S8). In the C57BL/6→BALB/c model, the absence of dietary lactose significantly reduced posttransplant *Enterococcus* bloom and mitigated GVHD (Fig. 4A and fig. S9B). Flow cytometric analysis of donor T cells on day +14 revealed a reduction in the percentage of activated and proliferating CD4<sup>+</sup> T cells (CD4<sup>+</sup>CD69<sup>+</sup>; CD4<sup>+</sup>Ki67<sup>+</sup>) as well as a reduction in the percentage of CD4<sup>+</sup>Tbet<sup>+</sup> (T<sub>H</sub>1) T cells (fig. S9). The effect of a lactose-free diet on enterococcal outgrowth and GVHD was replicated in the LP/J→C57BL/6 mouse model (Fig. 4B and table S9 for changes in non-enterococcal taxa). Intestinal mucosal damage by irradiation or allo-reactive T cells may affect the expression of lactase, the enzyme found on small-intestine enterocytes that facilitates lactose absorption through disaccharide cleavage. Duodenal lactase transcript abundance progressively declined in BM+T recipients over the course of transplantation (fig. S9C), which may induce a lactose-intolerant-like state in mice, allowing nondigested lactose to reach the lower intestinal tract and serve as a carbon source for bacteria.

Next, we explored whether enterococci expansion is associated with lactose tolerance in human allo-HCT patients by genotyping 602 patients from the MSKCC cohort with available pretransplant germline DNA samples for the gene polymorphism rs4988235 (-13910\*T). This single-nucleotide polymorphism (SNP) regulates lactase expression and predicts lactose absorption and/or tolerance (C/T

or T/T alleles) and malabsorption (C/C alleles) in the upper gut (29). Although abundance of the genus *Enterococcus* increased comparably during exposure to broad-spectrum antibiotics in both lactose absorbers and malabsorbers, enterococcal domination was significantly prolonged in malabsorbers after cessation of antibiotics (Fig. 4D and fig. S10). This finding suggests that the maintenance of enterococcal domination and microbiota recovery after broad-spectrum antibiotic exposure is significantly modulated by the luminal availability of lactose as a growth substrate.

Fecal domination by *Enterococcus* spp. is a significant risk factor for the development of acute GVHD and for increased overall and GVHD-related mortality after allo-HCT. Our findings extend previous reports from smaller single-center analyses that posttransplant VRE bacteremia and fecal domination are associated with worse outcomes after allo-HCT (7, 8, 30). In gnotobiotic mouse models, enterococci exacerbate GVHD, consistent with previous reports of aggravated colitis in models of inflammatory bowel disease (14) or systemic autoimmune responses (31). We previously identified *Blautia* abundance (a genus within class Clostridia) as a predictor of protection from lethal GVHD (12), whereas here we describe *Enterococcus* domination as a risk factor for GVHD. These two findings are noteworthy in light of our recent observation that a *B. producta* strain can inhibit VRE growth via the production of a lantibiotic protein (32). We identified a microbiota-intrinsic mechanism that is dependent on lactose utilization and favors the expansion of enterococci. This process may be triggered through a loss of lactase produced by enterocytes damaged by conditioning or allo-reactive T cells. We validated this concept experimentally, by showing that depletion of lactose in vitro and in vivo inhibited enterococcal expansion and mitigated GVHD, and clinically, by showing that patients harboring a lactose-malabsorption allele experienced prolonged *Enterococcus* domination after antibiotic exposure. These observations in mice and allo-HCT patients provide proof-of-concept for a novel, non-antibiotic-based therapeutic strategy, such as a lactose-free diet, to attenuate the outgrowth of pathobionts like enterococci and possibly improve clinical outcomes by modulating dietary sources of nutrients for pathogenic bacteria.

## REFERENCES AND NOTES

1. Y. Litvak, M. X. Byndloss, A. J. Bäuml, *Science* **362**, eaat9076 (2018).
2. M. S. Gilmore, F. Lebreton, W. van Schaik, *Curr. Opin. Microbiol.* **16**, 10–16 (2013).
3. S. Schloissnig et al., *Nature* **493**, 45–50 (2013).
4. F. Lebreton et al., *Cell* **169**, 849–861.e13 (2017).
5. Y. Taur et al., *Clin. Infect. Dis.* **55**, 905–914 (2012).
6. C. Ubeda et al., *J. Clin. Invest.* **120**, 4332–4341 (2010).
7. E. Holler et al., *Biol. Blood Marrow Transplant.* **20**, 640–645 (2014).



8. C. D. Ford *et al.*, *Biol. Blood Marrow Transplant.* **23**, 340–346 (2017).
9. H. J. Khoury *et al.*, *Haematologica* **102**, 958–966 (2017).
10. Y. Shono *et al.*, *Sci. Transl. Med.* **8**, 339ra71 (2016).
11. Y. Taur *et al.*, *Blood* **124**, 1174–1182 (2014).
12. R. R. Jenq *et al.*, *Biol. Blood Marrow Transplant.* **21**, 1373–1383 (2015).
13. Y. Taur *et al.*, *Sci. Transl. Med.* **10**, eaap9489 (2018).
14. N. Steck *et al.*, *Gastroenterology* **141**, 959–971 (2011).
15. N. Geva-Zatorsky *et al.*, *Cell* **168**, 928–943.e11 (2017).
16. K. Riesner, M. Kalupa, Y. Shi, S. Elezkurtaj, O. Penack, *Bone Marrow Transplant.* **51**, 410–417 (2016).
17. K. Dubin, E. G. Pamer, *Microbiol. Spectr.* doi:10.1128/microbiolspec.BAD-0014-2016 (2014).
18. R. R. Jenq *et al.*, *J. Exp. Med.* **209**, 903–911 (2012).
19. S. Caballero *et al.*, *Cell Host Microbe* **21**, 592–602.e4 (2017).
20. N. W. Palm *et al.*, *Cell* **158**, 1000–1010 (2014).
21. K. Brandl *et al.*, *Nature* **455**, 804–807 (2008).
22. D. Zhao *et al.*, *J. Clin. Invest.* **128**, 4970–4979 (2018).
23. C. A. Lindemans *et al.*, *Nature* **528**, 560–564 (2015).
24. K. H. Schleifer, A. Hartinger, F. Götz, *FEMS Microbiol. Lett.* **3**, 9–11 (1978).
25. D. Weber *et al.*, *Biol. Blood Marrow Transplant.* **23**, 845–852 (2017).
26. P. A. Gill, M. C. van Zelm, J. G. Muir, P. R. Gibson, *Aliment. Pharmacol. Ther.* **48**, 15–34 (2018).
27. N. D. Mathewson *et al.*, *Nat. Immunol.* **17**, 505–513 (2016).
28. B. W. Haak *et al.*, *Blood* **131**, 2978–2986 (2018).
29. C. J. Ingram, C. A. Mulcare, Y. Itan, M. G. Thomas, D. M. Swallow, *Hum. Genet.* **124**, 579–591 (2009).
30. J. Vydra *et al.*, *Clin. Infect. Dis.* **55**, 764–770 (2012).
31. S. Manfredo Vieira *et al.*, *Science* **359**, 1156–1161 (2018).
32. S. G. Kim *et al.*, *Nature* **572**, 665–669 (2019).

## ACKNOWLEDGMENTS

We thank G. M. Dunny and J. Willett (Department of Microbiology, University of Minnesota) as well as R. Zbasnik and V. Schlegel (Department of Food Science, University of Nebraska) for helpful discussion and for providing materials for revision of the manuscript. **Funding:** This work was supported by a German Research Foundation (DFG) scholarship to

C.K.S.-T.; a Young-Investigator-Award by American Society of Bone Marrow Transplantation to C.K.S.-T.; partially supported by the DFG research consortium TR221 “GvH/GvL” (project B13) to E.H.; by NCI awards R01-CA228358 (M.R.M.v.d.B.), R01-CA228308 (M.R.M.v.d.B.), MSKCC Cancer Center Core Grant P30 CA008748, and Project 4 of P01-CA023766 (M.R.M.v.d.B.); NHLBI award R01-HL125571 (M.R.M.v.d.B.), R01-HL123340 (M.R.M.v.d.B.), and K08-HL143189 (J.U.P.); NIA National Institute of Aging award Project 2 of P01-AG052359 (M.R.M.v.d.B.); NIAID award U01 AI124275 (M.R.M.v.d.B.); R01 AI032135 (E.G.P.); AI095706 (E.G.P.); U01 AI124275 (E.G.P. and J.B.X.); Tri-Institutional Stem Cell Initiative award 2016-013 (M.R.M.v.d.B.); the Lymphoma Foundation (M.R.M.v.d.B. and N.K.); the Susan and Peter Solomon Divisional Genomics Program (M.R.M.v.d.B.); the Parker Institute for Cancer Immunotherapy at Memorial Sloan Kettering Cancer Center (M.R.M.v.d.B. and J.U.P.); the Sawiris Foundation (J.U.P.); the Society of Memorial Sloan Kettering Cancer Center (J.U.P.); MSKCC Cancer Systems Immunology Pilot Grant (J.U.P.); Empire Clinical Research Investigator Program (J.U.P.); Seres Therapeutics (M.R.M.v.d.B., J.U.P., J.B.S., A.L.C.G., A.G.C., A.E.S., and A.D.S.); Japan Society for the Promotion of Science KAKENHI (17H04206 to T.T. and 17K09945 to D.H.); the Center of Innovation Program from Japan Science and Technology Agency (T.T.); Mochida Memorial Foundation for Medical and Pharmaceutical Research (D.H.); R56 AI137269-01 (J.B.X.); Conquer Cancer Foundation Young Investigator Award/Gilead Sciences (N.K.); NIH KL2 TR001115-03 (NCATS CTSA to A.D.S.); NIA P30AG028716-11 (Claude D. Pepper Older Americans Independence Center to A.D.S.); NCI R01CA203950-01 (to N.J.C., A.D.S., L.B., M.L. and A.B.); NIH 1R01HL124112-01A (A.D.S. and R.R.J.); and NIA R21AG066388-01 (A.D.S. and N.J.C.). **Author contributions:** C.K.S.-T., E.G.P., J.U.P. and M.R.M.v.d.B. conceptualized the project; C.K.S.-T., A.L.C.G., A.S., S.D., A.P., J.R.C., Y.T., R.R.J., J.B.X., E.R.L., and J.U.P. were involved in data curation and formal analyses; C.K.S.-T., K.B.N., A.L., M.D.D., A.E.S., J.B.S., A.G.C., G.A., Y.S., M.B.d.S., K.A.M., D.B., R.P., A.T., S.M., M.E.A., A.J.P., M.M., R.J.W., L.A.A., E.F., D.P., M.A.J., D.W., A.D.S., D.H., C.S., J.A.M., K.R., M.L., A.B., L.B., K.H., and Y.H. conducted research and collected data; M.J.G.T.V., D.M.P., M.A.P., S.A.G.,

T.T., E.H., N.J.C., E.G.P., and M.R.M.v.d.B. supervised the project and provided validation; and C.K.S.-T., J.U.P., A.L.C.G., and M.R.M.v.d.B. prepared data presentation and wrote the manuscript with contributions from all other authors.

**Competing interests:** M.R.M.v.d.B. has received research support from Seres Therapeutics; has consulted, received honorarium from, or participated in advisory boards for Seres Therapeutics, Flagship Ventures, Novartis, Evelo, Jazz Pharmaceuticals, Therakos, Amgen, Magenta Therapeutics, Merck & Co, Inc., Acute Leukemia Forum (ALF), and DKMS Medical Council (Board); and has IP Licensing with Seres Therapeutics and Juno Therapeutics and stock options from Smart Immune. J.U.P. reports research funding, intellectual property fees, and travel reimbursement from Seres Therapeutics and consulting fees from Davolterra. A.D.S. received research support from Seres Therapeutics, Merck, and Novartis. E.G.P. has received speaker honoraria from Bristol-Myer Squibb, Celgene, Seres Therapeutics, MedImmune, Novartis, and Ferring Pharmaceuticals; is an inventor on patent application number WPO2015179437A1, entitled “Methods and compositions for reducing *Clostridium difficile* infection,” and patent number WPO2017091753A1, entitled “Methods and compositions for reducing vancomycin-resistant *Enterococci* infection or colonization”; and holds patents that receive royalties from Seres Therapeutics Inc. Other authors have no competing interests. **Data and materials availability:** All data are available in the manuscript or the supplementary materials. Sequencing data have been deposited into Sequence Read Archive under Bioproject number PRJNA545312.

## SUPPLEMENTARY MATERIALS

science.sciencemag.org/content/366/6469/1143/suppl/DC1  
Materials and Methods  
Table S1 to S10  
Fig S1 to S10  
References (33–53)

[View/request a protocol for this paper from Bio-protocol.](#)

18 March 2019; accepted 22 October 2019  
10.1126/science.aax3760

## PROTEIN FOLDING

# Watching helical membrane proteins fold reveals a common N-to-C-terminal folding pathway

Hyun-Kyu Choi<sup>1,2,3\*</sup>, Duyoung Min<sup>4,5\*</sup>, Hyunook Kang<sup>2\*</sup>, Min Ju Shon<sup>2,3</sup>, Sang-Hyun Rah<sup>1,2,3</sup>, Hak Chan Kim<sup>2</sup>, Hawoong Jeong<sup>1</sup>, Hee-Jung Choi<sup>2†</sup>, James U. Bowie<sup>4†</sup>, Tae-Young Yoon<sup>2,3†</sup>

To understand membrane protein biogenesis, we need to explore folding within a bilayer context. Here, we describe a single-molecule force microscopy technique that monitors the folding of helical membrane proteins in vesicle and bicelle environments. After completely unfolding the protein at high force, we lower the force to initiate folding while transmembrane helices are aligned in a zigzag manner within the bilayer, thereby imposing minimal constraints on folding. We used the approach to characterize the folding pathways of the *Escherichia coli* rhomboid protease GlpG and the human  $\beta_2$ -adrenergic receptor. Despite their evolutionary distance, both proteins fold in a strict N-to-C-terminal fashion, accruing structures in units of helical hairpins. These common features suggest that integral helical membrane proteins have evolved to maximize their fitness with cotranslational folding.

**T**ens of thousands of mutations associated with diseases are thought to affect membrane protein folding and trafficking (1). The biogenesis of most helix-bundle membrane proteins has been divided conceptually into two stages (2, 3). First, cotranslational insertion of the hydrophobic protein into the membrane occurs through the Sec translocon pathway (4, 5), thereby establishing much of the transmembrane helical structure and initial topology. Second, the protein completes folding to its final tertiary structure. The two stages, however, are not necessarily cleanly separable (6–9). Studying folding mechanisms of membrane proteins by single-molecule force spectroscopy has been challenging and limited mostly to observing unfolding (10–13), because folding intermediates are usually invisible at the lower forces where folding occurs on a practical time scale. Here, we use physicochemical conditions that strongly favor folding, thereby enabling the observation of folding at forces high enough to achieve 1-nm resolution.

To develop an experimental method that can be generally applied to the observation of the folding pathways of polytopic membrane proteins, we built on a single-molecule approach that we have developed using magnetic tweezers (MT) (Fig. 1A) (14, 15). We linked DNA handles to the N- and C-termini of the protein using a SpyTag-SpyCatcher attachment system (16). The handles are in turn attached to a magnetic bead and a polymer-coated glass

surface, respectively. The target membrane protein is embedded in bicelles that provide a lipid bilayer-like environment (Fig. 1A). While applying pN- to tens-of-pN-scale force to the magnetic bead, we record the vertical position of the bead relative to a reference bead stuck on the surface (referred to as the extension value) (fig. S1).

We applied this method to study the folding of *Escherichia coli* rhomboid protease GlpG. Figure 1B shows force-extension curves (FECs) averaged over multiple cycles of mechanical stretching and relaxation for single GlpG proteins. At high-force levels above 20 pN, the single GlpGs show cooperative unfolding of six transmembrane (TM) helices to an unstructured polypeptide (referred to as the unfolded coil or  $U_c$  state) while exhibiting two unfolding intermediates, as we described previously (Fig. 1B, upper inset) (14, 15). When relaxing the mechanical tension, we detected a gradual transition in the FEC from the theoretical curve for  $U_c$  to a more compact state that is dependent on the presence of bicelles (Fig. 1, B and C, and fig. S2). We designate the new state as unfolded helical ( $U_h$ ) because it fits the FEC expected for a state in which all  $\alpha$ -helical structures are restored for the TM helices and linkers. But the protein remains fully stretched along the pulling direction (Fig. 1B). Below the  $U_c$ -to- $U_h$  transition, the FEC shifts to a yet more compact state (Fig. 1B, bottom inset), which we call the  $U_z$  state (unfolded zigzag state). As discussed below, the  $U_z$  state appears to consist of bilayer-inserted, but weakly interacting, TM helices arranged in a zigzag-like fashion. Finally, at low forces, GlpG finds its folded, native conformation (referred to as the N state) (Fig. 1B). Because formation of the native state could only be achieved at low tension below 2 pN, Brownian motions of the magnetic bead preclude observation of any detailed intermediates during the refolding process under these conditions.

In hopes of seeing folding at higher forces where extension measurements can be more precise, we screened for more favorable folding conditions using a simple force-jump experiment (fig. S3) (10, 17, 18). We found that addition of 1,2-dimyristoyl-*sn*-glycero-3-phosphorylglycerol (DMPG) is effective in enhancing GlpG refolding. When we add 30 mole % (mol %) DMPG lipids in the bicelle phase, the refolding probability after a waiting time of 200 s at 5-pN tension increases by a factor of seven (Fig. 1D). The FECs obtained with and without 30 mol % DMPG lipids almost exactly overlap with one another, preserving the coil-to-helix transition as well as the formation of the  $U_z$  state (figs. S2 and S4). These observations suggest that the addition of negatively charged lipids does not fundamentally alter the folding pathway but selectively enhances refolding commencing from the  $U_z$  state.

With the ability to observe folding at higher forces, we tested the potential for achieving high resolution by examining the Brownian motion of magnetic beads in the bicelle phase. With high-speed tracking at 1.2 kHz and the force above 5 pN, we obtained an Allan deviation (i.e., uncertainty in our tracking) of less than 1 nm when median filtered at 5 Hz (200 ms), corresponding to a resolution of a few amino acids (Fig. 1E). Also, we observed folding with a reasonable probability up to 8-pN tension, the force at which the  $U_z$  state starts to form (Fig. 1D).

On the basis of these observations, we developed a force-application protocol to monitor the folding process of single GlpG proteins (Fig. 2). We first induced full unraveling of GlpG to the  $U_c$  state by applying a high mechanical tension above 20 pN and then made a force jump to a low-force level between 5 and 8 pN (Fig. 2A). The force jump takes a finite time of ~300 ms, during which single GlpGs relax to the  $U_z$  state (Fig. 2B, right). We experimentally confirmed that the force jump indeed reaches the same extension state as that reached through slow gradual force relaxation at ~1 pN s<sup>-1</sup> (Fig. 2B, left). When maintained at the low-force level, the magnetic bead begins to show complex up-and-down movements, finally culminating in a compact N state (Fig. 2A, 5-pN phases). Achievement of the N state is verified by observing the extension expected for the N state after jumping the tension back to ~20 pN. By repeating our designed mechanical cycle, we can observe the folding of single GlpG molecules multiple times.

With the reduced Brownian motion of the magnetic bead in the 5- to 8-pN force window, we can see distinct conformational changes during refolding when the extension traces are median filtered down to 5 Hz (Fig. 2C, black traces). Application of hidden Markov modeling (HMM) and Bayesian information criteria (BIC) to the time-resolved extension traces indicates that the data are best fit by a

<sup>1</sup>Department of Physics, Korea Advanced Institute of Science and Technology, Daejeon 34141, South Korea. <sup>2</sup>School of Biological Sciences, Seoul National University, Seoul 08826, South Korea. <sup>3</sup>Institute for Molecular Biology and Genetics, Seoul National University, Seoul 08826, South Korea. <sup>4</sup>Department of Chemistry and Biochemistry, University of California–Los Angeles, Los Angeles, CA 90095, USA. <sup>5</sup>Department of Chemistry, Ulsan National Institute of Science and Technology, Ulsan 44919, South Korea.

\*These authors equally contributed to this work.  
†Corresponding author. Email: chohij@snu.ac.kr (H.-J.C.); bowie@mbi.ucla.edu (J.U.B.); tyoon@snu.ac.kr (T.-Y.Y.)

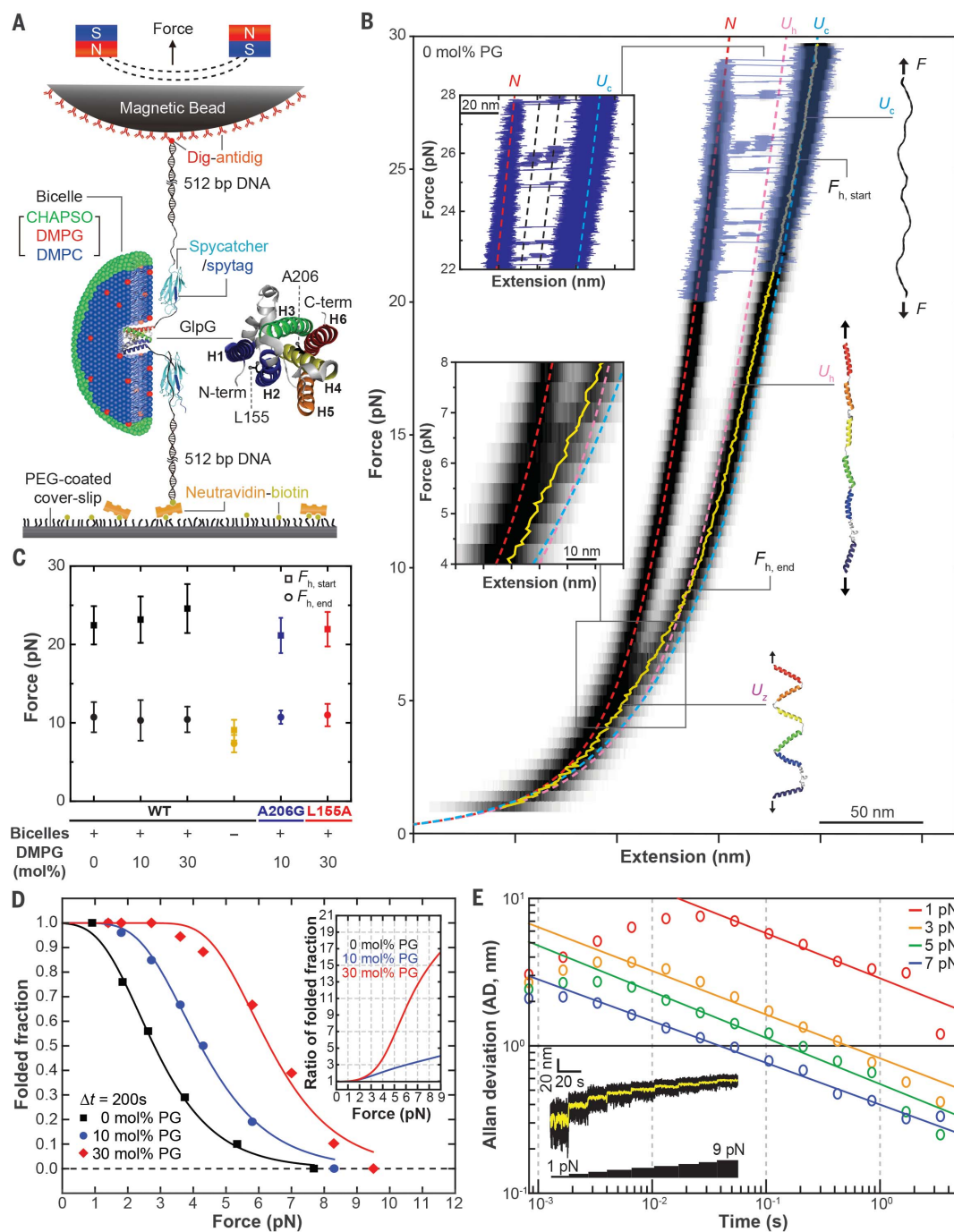


**Fig. 1. Physicochemical search for refolding conditions of polytopic helical membrane proteins.** (A) Schematic of single-molecule MT folding experiment for a single GlpG protein reconstituted in a bicelle. N, north; S, south; Dig-anti-dig, digoxigenin-anti-digoxigenin; CHAPSO, 3-[[3-cholamidopropyl]dimethylammonio]-2-hydroxy-1-propanesulfonate; DMPG, 1,2-dimyristoyl-*sn*-glycero-3-phosphocholine; H1 to H6, TM helices 1 to 6; bp, base pairs; PEG, polyethylene glycol.

(B) FEC of single GlpG proteins averaged over 28 cycles of mechanical stretching and relaxation (black heat map). To show individual unfolding events, representative raw traces are overlaid above 20 pN tension (blue traces). The yellow trace shows the mean extension value in the relaxation phase.  $F_{h,start}$  and  $F_{h,end}$  indicate the force levels at which the coil-to-helix transition starts and ends. Theoretical FECs for the N,  $U_c$ , and  $U_h$  states are shown as red, light blue, and pink dashed lines, respectively. The upper inset shows a close-up view of the

unfolding events. The lower inset shows a close-up view of the FEC between 4- and 8-pN force. PG, DMPG. (C) Average  $F_{h,start}$  and  $F_{h,end}$  values determined under different refolding conditions.  $n = 34, 42$ , and  $58$  FECs for the 0, 10, and 30 mol % DMPG cases.  $n = 16$  for the no bicelle case.  $n = 6$  and  $10$  for the A206G and L155A single-point GlpG mutant cases. All error bars represent mean  $\pm$  SD. (D) Refolding probability determined using a simple force-jump experiment (see fig. S3) at different applied force levels ( $n = 125, 147$ , and  $111$  force-jump experiments for the 0, 10, and 30 mol % PG cases, respectively). The inset shows the refolding probability normalized to the 0 mol % PG case. (E) Allan deviation of the magnetic-bead fluctuation at different force levels. The inset is a representative trace showing the Brownian fluctuation of a magnetic bead at different force levels (black trace, raw data at 1.2-kHz sampling; yellow trace, a median-filtered data with a 5-Hz window).



total of four states: two intermediate states (referred to as  $I_1$  and  $I_2$ ) in addition to the  $U_z$  and  $N$  states (Fig. 2, C to E, and fig. S5) (19).

The magnetic beads show many upward (i.e., local unfolding) and downward movements (i.e., local folding) before reaching the native  $N$  state extension. Thus, the resultant time-resolved traces report reversible intermediate folding-unfolding events—equilibrium processes from which we can directly reconstruct

the folding energy landscape. The local folding and unfolding processes pass through the same  $I_1$  and  $I_2$  intermediate states, justifying a one-dimensional representation of the energy landscape (20, 21). Our HMM analysis indicates that although rates connecting non-neighboring states are negligible, the transitions connecting the neighboring states are well described by single rates falling in a narrow region between 0.1 to 10  $s^{-1}$  (Fig.

2F and fig. S6). An exception is the  $N$ -to- $I_2$  transition that shows two different rates. One  $N$ -to- $I_2$  transition is relatively fast, with an average dwell time in  $N$  of only  $\sim 5$  s, indicating incomplete refolding (Fig. 2F, red symbols, and fig. S6). The other subset of the  $N$  states has higher stability, requiring higher forces ( $\sim 8$  pN) to show unfolding within our observation time, and presumably corresponds to a correctly folded state (Fig. 2F, inset, and fig. S7).

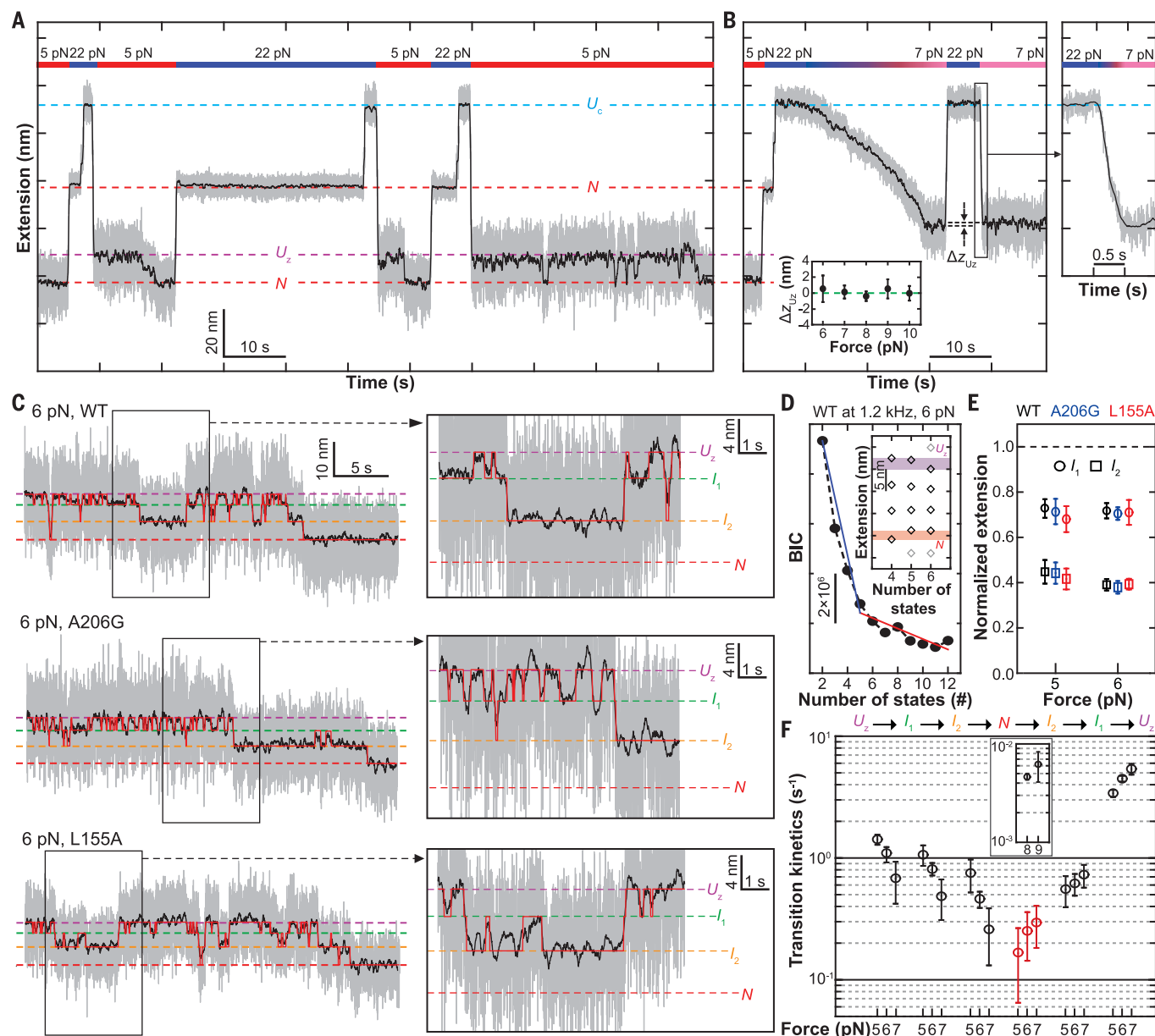


**Fig. 2. Direct observation of single GlpG folding.** (A) Designed mechanical cycle for inducing refolding of single GlpG proteins. The gray and black traces are 1.2-kHz raw data and 5-Hz median-filtered data, respectively. (B) Representative time-resolved traces comparing the extensions following slow force relaxation and force jump. The lower inset shows the extension difference ( $\Delta z_{Uz}$ ) at the indicated force levels. The right inset shows a close-up view of the trace of the force jump that takes  $\sim 300$  ms. (C) Representative folding traces for wild-type (WT), A206G, and L155A GlpG under 6-pN tension. The insets to the right show close-up views of the traces

exhibiting reversible transitions among the  $U_z$ ,  $I_1$ , and  $I_2$  states. (D) BIC values for the indicated number of states.  $n = 20, 21$ , and 11 low-force folding-unfolding traces for the WT, A206G, and L155A cases, respectively. (E) Positions of the intermediate states in the normalized extension space [at 6 pN,  $n$  is same as in (D); at 5 pN,  $n = 21, 24$ , and 14 low-force folding-unfolding traces for WT, A206G, and L155A, respectively]. Error bars represent SEM. (F) Transition kinetics between the neighboring states at the indicated force levels. In the  $N$ -to- $I_2$  transition, both slow (inset, black) and fast (red) rates are displayed. Error bars represent SEM.

We next examined whether we could extend our MT folding experiment to true bilayers by reconstituting GlpG in vesicles produced through slow detergent removal (Fig. 3A and fig. S8). For the vesicle-reconstituted GlpGs, we observed cooperative unraveling of six TM helices to the  $U_c$  state, similar to what is observed for the bicelle-reconstituted GlpGs (Fig. 3B, first stretching cycle). We also observed the expected coil-to-helix transition during the relaxation phase (Fig. 3C) as well as complete refolding, albeit with low probability (Fig. 3B, sixth stretching cycle). Because there are no free vesicles, these observations suggest that single GlpGs remain bound to the vesicle membranes after their unraveling to unstructured polypeptides. Nevertheless, many of the vesicle-reconstituted GlpGs fail to refold (e.g., Fig. 3B, second and fifth stretching cycles). The refolding probability at 1 pN is only ~15% with a 200-s wait time, in contrast with a refolding probability approaching 100% seen for the bicelle-reconstituted GlpGs. We also found that the FECs of vesicle-reconstituted GlpGs persistently follow the  $U_h$  curve and fail to form the loosely stretched  $U_z$  state (Fig. 3C, lower inset).

We hypothesized that polypeptide insertion into bilayers may be more difficult in vesicles compared with bicelles, which would explain the barrier to folding and the block to formation of the  $U_z$  state if the  $U_z$  state was indeed membrane inserted. To explore this possibility, we tested whether decreasing vesicle size would enhance folding, because increased bilayer curvature may allow more facile insertion of the TM helices into the membrane (22). Indeed, when we decreased the diameter of reconstitution vesicles to 100 nm by extrusion, the refolding probability at 1 pN increased to ~60% (Fig. 3D and fig. S8).

We next attempted to avoid membrane extraction and directly access the  $U_z$  state by applying a moderate force of 8 pN, a tension at which the  $U_z$  state was seen to form in FEC (referred to as the direct- $U_z$  protocol). We tested the feasibility of this protocol first with the bicelle-reconstituted GlpGs and found that application of 8 pN indeed directly induces the  $U_z$  state (Fig. 3E, left). Subsequent lowering of the force leads to complete refolding in bicelles (fig. S9). When we applied 8 pN to the vesicle-reconstituted GlpGs, the resultant unfolding step was almost identical to that expected for the  $U_z$  state (Fig. 3E, right and inset). When we subsequently induced refolding by lowering the force to 1 pN, the refolding probability in vesicles increased relative to refolding from the  $U_c$  state (~50 versus ~15%) (Fig. 3, D and E), consistent with the possibility that this 8-pN unfolding selectively disrupts the tertiary structure while decreasing exposure of the TM helices to the outside of the lipid bilayer, thereby reducing the need to reinsert TM helices during refolding.

Our analysis of the end-to-end distance of the  $U_z$  state further suggests that the penetration depths of TM helices in the  $U_z$  state might not be enough to completely reach the other side of the lipid bilayer (Fig. 3F, right, and fig. S10). If so, tertiary structure formation would be intimately coupled with the membrane insertion (Fig. 3F, right; compare  $I_2$  and N at 6 pN). To determine whether membrane insertion or tertiary structure formation dominates the energy barriers, we examined the local folding-unfolding kinetics of two single-point GlpG mutants in the bicelle phase (23). The N-terminal [L155A (Leu<sup>155</sup>→Ala) on TM helix 2] and C-terminal [A206G (Ala<sup>206</sup>→Gly) on TM helix 4] mutants selectively slow down the  $I_1$ -to- $I_2$  and the  $I_2$ -to-N transitions, respectively (Fig. 3F, left, and fig. S11). These observations suggest that the tertiary structure formation makes a major contribution to the observed energy barriers. Moreover, these mutant data are consistent with GlpG folding occurring in a unidirectional manner from the N to C terminus.

To map the partially folded structures in  $I_1$  and  $I_2$ , we made force jumps to ~20 pN while the protein sampled either  $I_1$  or  $I_2$  in the course of refolding (Fig. 3G). Surprisingly, the extensions after the force jump exactly coincide with the two intermediates of the high-force unfolding (Figs. 3G and 1B, upper inset), which indicates that the low-force folding-unfolding and the high-force unfolding intermediates share the same partially folded structures, albeit with different levels of stretching in the unfolded regions (Fig. 3F, right; compare  $I_2$  at 6 pN with  $I_2$  at 22 pN). We therefore used the extension difference between  $I_2$  and N at 22 pN to estimate that  $I_2$  is positioned at the C terminus of TM helix 4 (Fig. 3H, inset). Likewise, we used the extension difference between  $U_c$  and  $I_1$  at 22 pN to estimate that  $I_1$  is positioned after TM helix 2. Combined with the mutant data above, we conclude that GlpG folds in an N-to-C-terminal direction, largely in units of helical hairpins.

On the basis of the structural assignments made above, we examined one more GlpG mutant in which two hydrophobic residues in the long linker region between TM helices 1 and 2 are mutated to negatively charged residues [L121E/F133E (Leu<sup>121</sup>→Glu/Phe<sup>133</sup>→Glu)] (Fig. 3H, inset, and fig. S12B). Although such mutations reportedly increase the energy barrier for membrane insertion and flip-flop (24, 25), we did not detect any sign of slowing down in the transition between  $U_z$  and  $I_1$  (fig. S12). This data supports again our conclusion that the TM helices have made their initial membrane integration as the  $U_z$  state forms. In particular, because of the many polar and charged residues in the long linker, we suspect that TM helices 1 and 2 of GlpG are inserted more deeply than other TM helices in the zigzag-aligned  $U_z$  state.

Finally, we constructed one-dimensional energy landscapes for the reversible folding-unfolding process of single GlpG proteins using the Bell (26) and the Dudko-Hummer-Szabo models (27). Both models indicate a free-energy difference ( $\Delta G_0$ ) of 15.2  $k_B T$  (where  $k_B$  is the Boltzmann constant and  $T$  is temperature) between the native N state and the zigzag  $U_z$  state, albeit with slightly different intermediate positions (Fig. 3H). As expected, this  $\Delta G_0$  value is slightly larger than the estimates from previous ensemble measurements under less favorable folding conditions (7.1 to 13.9  $k_B T$ ) (23, 28, 29). When we apply the Crooks fluctuation theorem to the FECs as shown in Fig. 1B, we obtain an estimate of ~115  $k_B T$  for a free-energy difference between the N and the  $U_c$  states (fig. S13 and table S1), almost eightfold larger than 15.2  $k_B T$  estimated between the N and  $U_z$  states. We attribute this larger free-energy difference to additional processes imposed on the high-force unfolding, such as pulling TM helices out of the membrane and disruption of secondary structures. These observations attest to the fundamental difference between the energy barriers seen during high-force unfolding and the low-force folding-unfolding processes. At lower forces, we can explore rearrangements of intact TM helices that occur largely within the lipid bilayer, more closely reflecting the process expected for second-stage folding (2).

Using the experimental methods established with GlpG, we next sought to observe the folding process of a single human  $\beta_2$ -adrenergic receptor ( $\beta_2$ AR), which belongs to the G protein-coupled receptor family (Fig. 4A). We first examined the FEC and again observed a large mechanical hysteresis in the unfolding and refolding of  $\beta_2$ AR (Fig. 4B). Because  $\beta_2$ AR has an odd number of TM helices, the DNA handles are pulling on opposite sides of the bilayer, and we note the possibility that after the cooperative unraveling, some part of  $\beta_2$ AR may reside within the lipid bilayer (most likely the first TM helix; see fig. S14). During the relaxation phase, we observed the coil-to-helix transition in nearly the same force range as that observed for GlpG. Moreover, below 8 pN, the FEC of  $\beta_2$ AR became shorter than the  $U_h$  extension, consistent with the formation of a zigzag-aligned  $U_z$  state (Fig. 4B and fig. S15).

To observe the folding process of human  $\beta_2$ AR, we used the original folding protocol starting from the  $U_c$  state (Fig. 4C). We first induced mechanical unraveling of a single  $\beta_2$ AR  $U_c$  state by applying 25-pN tension and then induced the  $U_z$  state through force quenching to 5 pN. We reconfirmed that the force quenching within 300 ms yielded the same  $U_z$  state as that obtained through slow force relaxation (fig. S16). With the mechanical tension kept at 5 pN, the magnetic bead

showed complex up-and-down movements, ending in a compact N state (confirmed to be the native state through reapplication of high force) (Fig. 4C).

By applying the HMM and BIC analyses to the time-resolved extension traces of the magnetic beads, we identified six major states (thus four intermediates) in the folding process of human  $\beta_2$ AR (Fig. 4, D and E). Both local folding and unfolding processes share these four intermediate states (referred to as  $I_{f1}$ ,  $I_{f2}$ ,  $I_{f3}$ , and  $I_{f4}$ ), indicative of the one-

dimensionality of the folding energy landscape. The transition rates connecting the neighboring states fall between  $10^{-1}$  and  $10$  s $^{-1}$ , whereas all other rates are negligibly small (Fig. 4F and fig. S17). As was the case for GlpG, we observed two groups of the N states: one with a lower stability (Fig. 4F, red symbol) and the other reflecting a correctly folded structure (Fig. 4F, inset).

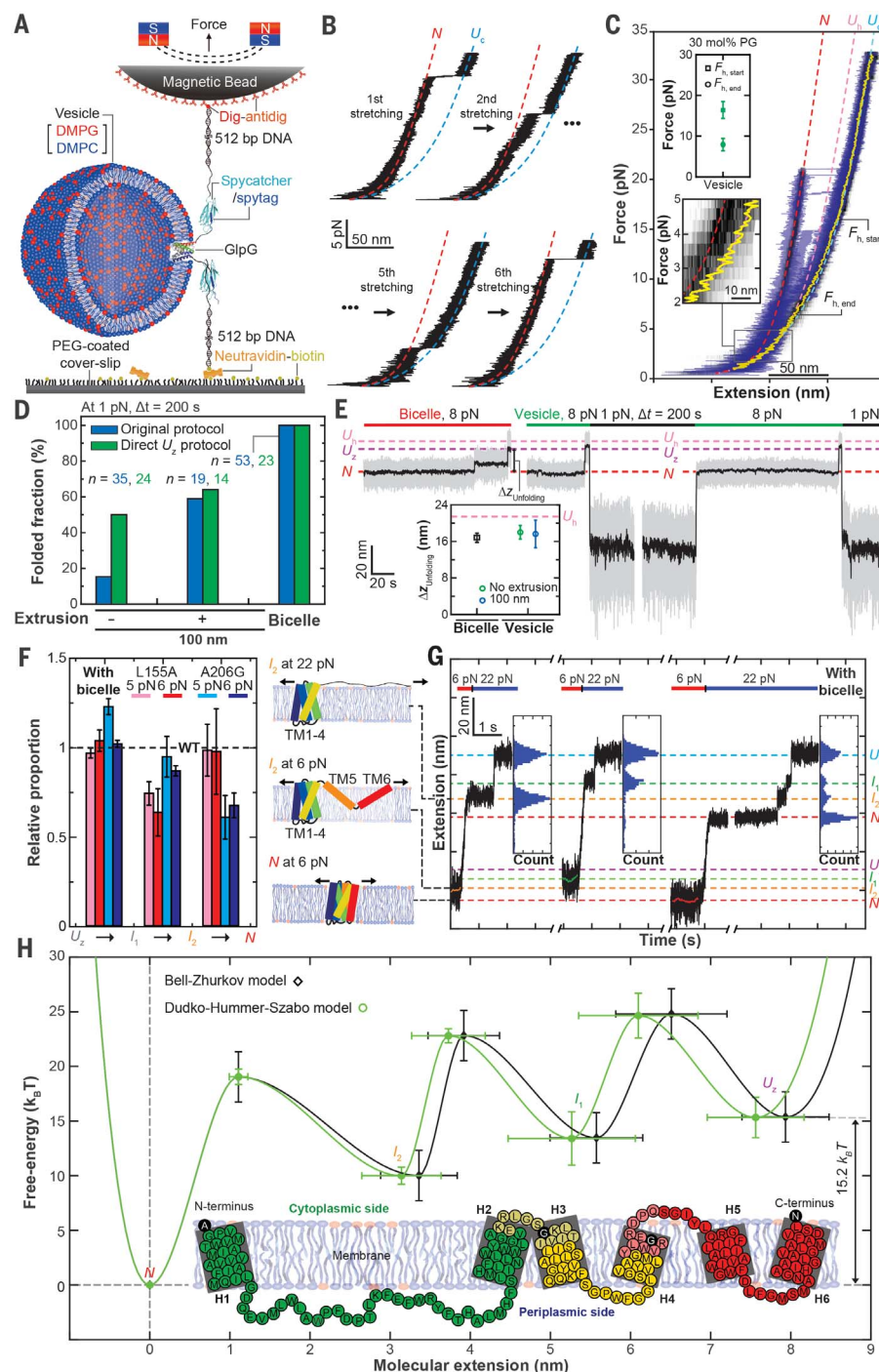
To measure the number of amino acids unfolded in the structures of the four intermediates, we applied the force-jump technique to each intermediate observed during the low-force folding-unfolding processes. We found that all four intermediates correspond to distinct extension states at 25 pN, reflecting a direct connection between the low-force folding-unfolding and the high-force unfolding intermediates (Fig. 4G). We thus sought to use the extension states of the high-force unfolding intermediates to infer the partially folded structures in individual low-force intermediates. The distribution of intermediate extension states during high-force unfolding

### Fig. 3. Characterization of folding properties for vesicle- and bicelle-reconstituted single GlpGs.

(A) Schematic of single-molecule MT folding experiments for GlpGs reconstituted in vesicle membranes. (B) Representative FECs showing successive stretching cycles applied to a single GlpG protein in a vesicle membrane. (C) FEC of vesicle-reconstituted single GlpG proteins averaged over five cycles of mechanical stretching and relaxation (black heat map). To show individual unfolding events, representative raw traces during stretching are overlaid (blue traces). Other definitions are the same as in Fig. 1B. The upper inset shows the average  $F_{h,start}$  and  $F_{h,end}$  values. The lower inset shows a close-up view of the FEC between 2- and 5-pN force. (D) Refolding probability determined under different membrane conditions.  $n$  is the number of trials;  $\Delta t$  is the waiting time at 1-pN force. (E) Representative traces of the folding protocol that directly induces the  $U_z$  state. The inset shows the extension changes ( $\Delta z_{unfolding}$ ) during unfolding at 8 pN under indicated membrane conditions. The pink dashed line is the expected extension change when reaching the  $U_h$  state.

(F) Normalized transition rates determined for the A206G and L155A single-point mutants relative to the WT case (dashed line). The illustrations to the right show an anticipated conformational status of GlpG in each indicated state. Error bars represent SEM. (G) Representative force-jump experiments applied for the intermediate states. Each inset shows the distribution of extension values recorded during high-force unfolding. Estimated extensions for individual states are shown as the dashed lines.

(H) Folding energy landscapes of a single GlpG protein along the molecular extension reconstructed on the basis of the Bell-Zhurkov (black trace) and the Dudko-Hummer-Szabo models (green trace). The inset shows detailed structural segments in the folding pathways of GlpG. Each structural segment is indicated by a different color. Black-colored amino acids correspond to the boundaries of the intermediate states. Faint colors around the boundaries represent the measurement errors (SD). Single-letter abbreviations for the amino acid residues are as follows: A, Ala; C, Cys; D, Asp; E, Glu; F, Phe; G, Gly; H, His; I, Ile; K, Lys; L, Leu; M, Met; N, Asn; P, Pro; Q, Gln; R, Arg; S, Ser; T, Thr; V, Val; W, Trp; and Y, Tyr.





clearly revealed a total of nine peaks (Fig. 4, H and I).

To map the unfolded structures on the high-force unfolding intermediates, we took advantage of the fact that in the native structure of human  $\beta_2$ AR, there is one conserved disulfide bond formed between Cys<sup>106</sup> (C106)

and Cys<sup>191</sup> (C191), which locks TM helices 3 and 4 and the extracellular linker 2 (ECL2) into one structural unit (Fig. 4, I and J, upper insets). We reasoned that with removal of the reducing agent tris(2-carboxyethyl)phosphine (TCEP), the high-force unfolding intermediates related to the region linked by the

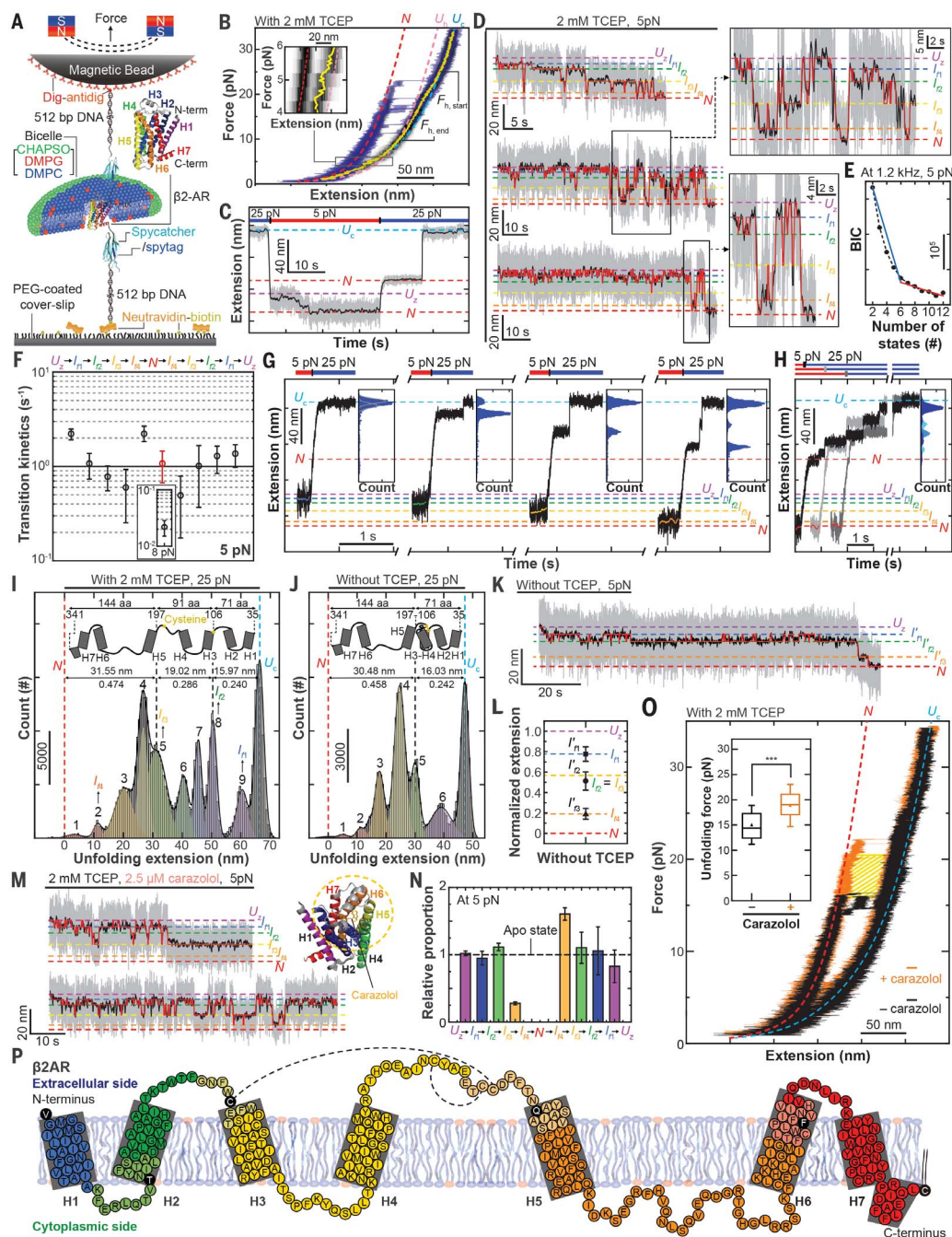
disulfide bond might disappear from the extension distribution. Indeed, in the absence of TCEP, the first five peaks (peaks 1 to 5) and the last two peaks (peaks 9 and  $U_c$ ) are essentially preserved, but the three peaks in the middle (peaks 6 to 8) selectively disappear (Fig. 4, I and J). We further note that in the

**Fig. 4. Direct observation of the complete folding pathway of human  $\beta_2$ AR.**

(A) Schematic diagram of the single-molecule MT folding experiment for  $\beta_2$ AR. (B) FEC of single  $\beta_2$ AR proteins averaged over six cycles of mechanical stretching and relaxation (black heat map). To show individual unfolding events, representative raw traces during stretching are overlaid (blue traces). Other definitions are the same as in Fig. 1B. The inset shows a close-up view of the FEC between 4- and 6-pN force.

(C) Designed mechanical cycle for inducing refolding of human  $\beta_2$ AR at low-force levels. (D) Representative time-resolved traces for  $\beta_2$ AR folding under 5-pN tension (with 2 mM TCEP). Right insets show close-up views of trajectories. Red traces show the transitions between four intermediates identified by the HMM. (E) BIC values for the indicated numbers of states ( $n = 18$  low-force folding-unfolding traces). (F) Transition kinetics between the neighboring states at 5 pN. For the N-to- $I_{14}$  transition, both slow (inset, black) and fast (red) rates are displayed. Error bars represent SEM. (G and H) Representative traces for the force-jump experiments applied to individual folding intermediates (G) and the native state (H). Each inset shows an extension distribution during high-force unfolding.

(I and J) Extension distribution during high-force unfolding initiated from the native N state ( $n = 29$  and 13 low-force folding-unfolding traces for the cases with 2 mM TCEP and without TCEP, respectively). The peaks indicate the fit centers of multiple Gaussian functions (colored for each function). The upper insets show structural diagrams of  $\beta_2$ AR to guide mapping onto the structure. (K) Representative  $\beta_2$ AR folding trace at 5 pN with no TCEP ( $n = 10$  low-force folding-unfolding traces). HMM analysis finds three intermediate states ( $I_{11}'$ ,  $I_{12}'$ , and  $I_{13}'$ ). (L) Normalized extensions for  $\beta_2$ AR folding intermediates in the absence of TCEP. Dashed lines are anticipated extensions for the intermediates in the presence of 2 mM TCEP. Error bars indicate SD. (M) Representative folding traces for  $\beta_2$ AR at 5 pN in the presence of 2.5  $\mu$ M carazolol (with 2 mM TCEP). The right inset shows the structure of carazolol-bound human  $\beta_2$ AR. The dashed yellow circle indicates interaction regions between carazolol and  $\beta_2$ AR. (N) Normalized rates determined for carazolol-bound  $\beta_2$ AR relative to the apo  $\beta_2$ AR case (dashed



line). (O) Representative FECs of  $\beta_2$ AR showing high-force cooperative unfolding in the presence (orange) and absence (black) of 2.5  $\mu$ M carazolol (with 2 mM TCEP). N and  $U_c$  are defined the same way as in (B). The inset shows distributions of unfolding forces with (orange,  $n = 26$  FECs) and without (black,  $n = 35$  FECs) carazolol. Error bars indicate SD. (P) Detailed structural segments in the folding pathways of  $\beta_2$ AR. Each structural segment is indicated by a different color. Other notations are the same as those for the inset in Fig. 3H.

absence of TCEP, the extension-change spanning the first five peaks is distinctly larger than that spanning the last two peaks by a factor of 1.98. This value closely matches the 2.02 ratio of the number of amino acids placed C-terminal to the disulfide bond [144 amino acid residues (aa)] to that placed N-terminal to the disulfide bond (71 aa) (Fig. 4I). Thus, our observations point to a hypothesis that the first five peaks correspond to unfolding from the C terminus to TM helix 5. In the absence of TCEP, unfolding from ECL2 to TM helix 3 is prevented by the disulfide bond, so that the last two peaks correspond to unfolding of the two N-terminal helices and ECL1. By aligning the unfolding traces in Fig. 4, G and H, with one another, we find that folding intermediates  $I_{f1}$ ,  $I_{f2}$ ,  $I_{f3}$ , and  $I_{f4}$  correspond to the high-force unfolding intermediate peaks 9, 8, 5, and 2, respectively (Fig. 4I and fig. S18). Together, our data suggest that the human  $\beta_2$ AR shows unidirectional folding from the N to the C terminus.

To test the validity of our structural assignment, we monitored the folding process at 5 pN in the absence of TCEP. The HMM and BIC analyses indicate a reduction in the number of folding intermediates to three (Fig. 4K and fig. S19). The positions of these three folding intermediates ( $I_{f1}'$ ,  $I_{f2}'$ , and  $I_{f3}'$ ) matched well with those expected when  $I_{f2}$  and  $I_{f3}$  are merged (Fig. 4L), reaffirming that the transition from  $I_{f2}$  to  $I_{f3}$  corresponds to folding of TM helices 3 and 4 and ECL2.

We also examined the effect of carazolol, a partial inverse agonist of human  $\beta_2$ ARs, on the 5-pN folding process. Although the presence of 2.5  $\mu$ M carazolol did not change the positions of the four intermediates in the extension space, it markedly inhibited any transition beyond  $I_{f3}$  (Fig. 4M and fig. S19). This inhibition was highly selective because the transition  $U_z$  to  $I_{f3}$  remained minimally affected (Fig. 4N), suggesting that single human  $\beta_2$ ARs fold normally up to ECL2 but fail to fold TM helices 5 and 6 onto the growing structure in the presence of carazolol. When we examined unfolding by force ramping, carazolol increased the forces at which unfolding occurred by 4.5 pN on average (Fig. 4O, inset), indicating that additional work of more than 50  $k_B T$  is required to induce the unraveling of single  $\beta_2$ ARs in the presence of carazolol (Fig. 4O, shaded area). Thus, our observations suggest distinct effects of carazolol on human  $\beta_2$ AR folding and unfolding. Carazolol inhibits the addition of TM helices 5 and 6 during folding, perhaps being loosely located in the incomplete ligand binding pocket formed by TM helices 1 to 4 and sterically interfering with incoming TM helices 5 and 6. In the presence of excess carazolol, it is also possible that carazolol is already bound to TM helices 5 and 6, because carazolol makes an extended aromatic network with the residues on these

helices. However, once folded, carazolol binding dramatically stabilizes the tertiary structure, as expected (30, 31).

The identified folding pathway of the human  $\beta_2$ AR reveals several interesting features (Fig. 4P). The first intermediate  $I_{f1}$  corresponds to an association between the first TM helix and the following linker helix, completing insertion of this nascent structure with respect to the residing membrane structure. The second TM helix folds onto this structure to form the first helical hairpin, completing intermediate  $I_{f2}$ . The next folding step involves the addition of TM helices 3 and 4 as well as ECL2 (forming  $I_{f3}$ ). We note that the positions of  $I_{f2}$  and  $I_{f3}$  closely map to the cysteine residues of C106 and C191, thereby potentially consolidating the formed tertiary structure by means of disulfide bonding. The transition from  $I_{f3}$  to  $I_{f4}$  involves formation of the helical hairpin consisting of the TM helices 5 and 6. This folding step is found to be markedly inhibited in the presence of carazolol. The last step from  $I_{f4}$  to N involves addition of the TM helix 7 and the C-terminal membrane-associated helix onto the structure, completing the known structure of human  $\beta_2$ AR (30, 31). Although our experimental data consistently support the folding pathway delineated above, we cannot rule out the possibility that an alternative folding pathway exists in the physiological milieu. We also note that the folding pathway presented here is a coarse-grained one down to a 5-Hz sampling rate. Enhancing the bandwidth of our methods would reveal a more complex and dynamic nature of the polytopic membrane protein folding (12). Finally, we note the possibility that the strategy of using disulfide bonds to map the four folding intermediates of  $\beta_2$ AR can be extended to other membrane proteins.

Although *E. coli* GlpG and human  $\beta_2$ AR are at an enormous evolutionary distance, both integral membrane proteins accrue structure largely in units of helical hairpins, with a unidirectional N-to-C-terminal folding as a single, predominant pathway out of a countless number of permutations in the possible folding pathways. Unidirectional N-to-C-terminal folding is consistent with several prior studies (28, 32–36) and would permit the nascent N-terminal chain to commence folding without needing to wait for the more C-terminal TM helices to be translated, thereby reducing the risk of generating misfolded structures. Thus, the folding processes of integral membrane proteins may be evolutionarily selected and tailored to fit with cotranslational folding.

## REFERENCES AND NOTES

- C. R. Sanders, J. K. Myers, *Annu. Rev. Biophys. Biomol. Struct.* **33**, 25–51 (2004).
- J.-L. Popot, D. M. Engelman, *Biochemistry* **29**, 4031–4037 (1990).
- J. U. Bowie, *Nature* **438**, 581–589 (2005).
- H. Mori, K. Ito, *Trends Microbiol.* **9**, 494–500 (2001).
- S. H. White, G. von Heijne, *Annu. Rev. Biophys.* **37**, 23–42 (2008).

- F. Cymer, G. von Heijne, S. H. White, *J. Mol. Biol.* **427**, 999–1022 (2015).
- N. B. Woodall, Y. Yin, J. U. Bowie, *Nat. Commun.* **6**, 8099 (2015).
- N. B. Woodall, S. Hadley, Y. Yin, J. U. Bowie, *Protein Sci.* **26**, 824–833 (2017).
- W. Dowhan, H. Vitrac, M. Bogdanov, *Protein J.* **38**, 274–288 (2019).
- A. Kedrov, H. Janovjak, C. Ziegler, W. Kuhlbrandt, D. J. Muller, *J. Mol. Biol.* **355**, 2–8 (2006).
- T. Serdiuk et al., *Nat. Chem. Biol.* **12**, 911–917 (2016).
- H. Yu, M. G. Siewny, D. T. Edwards, A. W. Sanders, T. T. Perkins, *Science* **355**, 945–950 (2017).
- P. Lu et al., *Science* **359**, 1042–1046 (2018).
- D. Min, R. E. Jefferson, J. U. Bowie, T.-Y. Yoon, *Nat. Chem. Biol.* **11**, 981–987 (2015).
- D. Min, M. A. Arbing, R. E. Jefferson, J. U. Bowie, *Protein Sci.* **25**, 1535–1544 (2016).
- B. Zakeri et al., *Proc. Natl. Acad. Sci. U.S.A.* **109**, E690–E697 (2012).
- F. Oesterhelt et al., *Science* **288**, 143–146 (2000).
- J. M. Fernandez, H. Li, *Science* **303**, 1674–1678 (2004).
- T.-H. Lee, *J. Phys. Chem. B* **113**, 11535–11542 (2009).
- K. Neupane, A. P. Manuel, M. T. Woodside, *Nat. Phys.* **12**, 700–703 (2016).
- K. Neupane et al., *Science* **352**, 239–242 (2016).
- N. S. Hatzakis et al., *Nat. Chem. Biol.* **5**, 835–841 (2009).
- R. P. Baker, S. Urban, *Nat. Chem. Biol.* **8**, 759–768 (2012).
- R. C. Van Lehn, B. Zhang, T. F. Miller III, *eLife* **4**, e08697 (2015).
- M. Seuring, M. Ek, G. von Heijne, N. Fluman, *Nat. Chem. Biol.* **15**, 945–948 (2019).
- G. I. Bell, *Science* **200**, 618–627 (1978).
- O. K. Dudko, R. Hummer, A. Szabo, *Phys. Rev. Lett.* **96**, 108101 (2006).
- W. Paslawski et al., *Proc. Natl. Acad. Sci. U.S.A.* **112**, 7978–7983 (2015).
- R. Guo et al., *Nat. Chem. Biol.* **12**, 353–360 (2016).
- S. G. Rasmussen et al., *Nature* **450**, 383–387 (2007).
- V. Cherezov et al., *Science* **318**, 1258–1265 (2007).
- P. Curnow, P. J. Booth, *Proc. Natl. Acad. Sci. U.S.A.* **106**, 773–778 (2009).
- D. Min et al., *Nat. Chem. Biol.* **14**, 489–496 (2018).
- N. Ismail, R. Hedman, N. Schiller, G. von Heijne, *Nat. Struct. Mol. Biol.* **19**, 1018–1022 (2012).
- F. Cymer, G. von Heijne, *Proc. Natl. Acad. Sci. U.S.A.* **110**, 14640–14645 (2013).
- O. B. Nilsson et al., *Nat. Struct. Mol. Biol.* **24**, 221–225 (2017).
- M. J. Shon, tyoonlab/Science\_aaw8208: Science\_aaw8208. Zenodo (2019); doi:10.5281/zenodo.3528913.

## ACKNOWLEDGMENTS

**Funding:** This work was supported by the National Creative Research Initiative Program (Center for Single-Molecule Systems Biology to T.-Y.Y.; NRF-2011-0018352), the Bio Medical Technology Development Program (NRF-2018M3A9E2023523 to T.-Y.Y.), the Basic Science Research Program (NRF-2016R1A6A3A03007871 to D.M.), and a NRF grant (NRF-2016R1A2B4013488 to H.-J.C.), all funded by the National Research Foundation of South Korea. This work was also supported by a National Institutes of Health grant (R01GM063919 to J.U.B.). **Author contributions:** T.-Y.Y. conceived of the project. H.-K.C., H.-J.C., J.U.B., and T.-Y.Y. designed the experiments. H.-K.C. and H.C.K. performed magnetic tweezers experiments. H.-K.C., S.-H.R., H.J., and T.-Y.Y. analyzed the magnetic tweezers data. M.J.S. built the high-speed magnetic tweezers setup. D.M. and J.U.B. expressed and purified GlpG proteins. H.K. and H.-J.C. expressed and purified  $\beta_2$ AR proteins. H.-K.C., D.M., J.U.B., and T.-Y.Y. wrote the manuscript with input from other authors.

**Competing interests:** The authors declare no competing interests. **Data and materials availability:** All data that support the findings of our study are available in the manuscript or supplementary materials. A program, written in LabView, to control the entire magnetic tweezers setup, which includes a high-speed complementary metal-oxide semiconductor (CMOS) camera, translation and rotation motors, and a piezo lens positioner and allows tracking of three-dimensional positions of magnetic beads at a frequency of up to 1.2 kHz has been deposited in GitHub ([https://github.com/tyoonlab/Science\\_aaw8208](https://github.com/tyoonlab/Science_aaw8208)) and is available at Zenodo (37).

## SUPPLEMENTARY MATERIALS

science.sciencemag.org/content/366/6469/1150/suppl/DC1  
Materials and Methods  
Figs. S1 to S19  
Tables S1 to S3  
References (38–66)

[View/request a protocol for this paper from Bio-protocol.](#)

28 January 2019; resubmitted 30 August 2019

Accepted 5 November 2019

10.1126/science.aaw8208



# The science of being a scientist

Science and Life Webinar Series



Throughout 2019, *Science* and Fondation Ipsen are offering free Science and Life webinars that tackle the issues researchers face in the field.

**Sign Up Today**

<https://scim.ag/35mLvNv>



**ScienceWebinars**





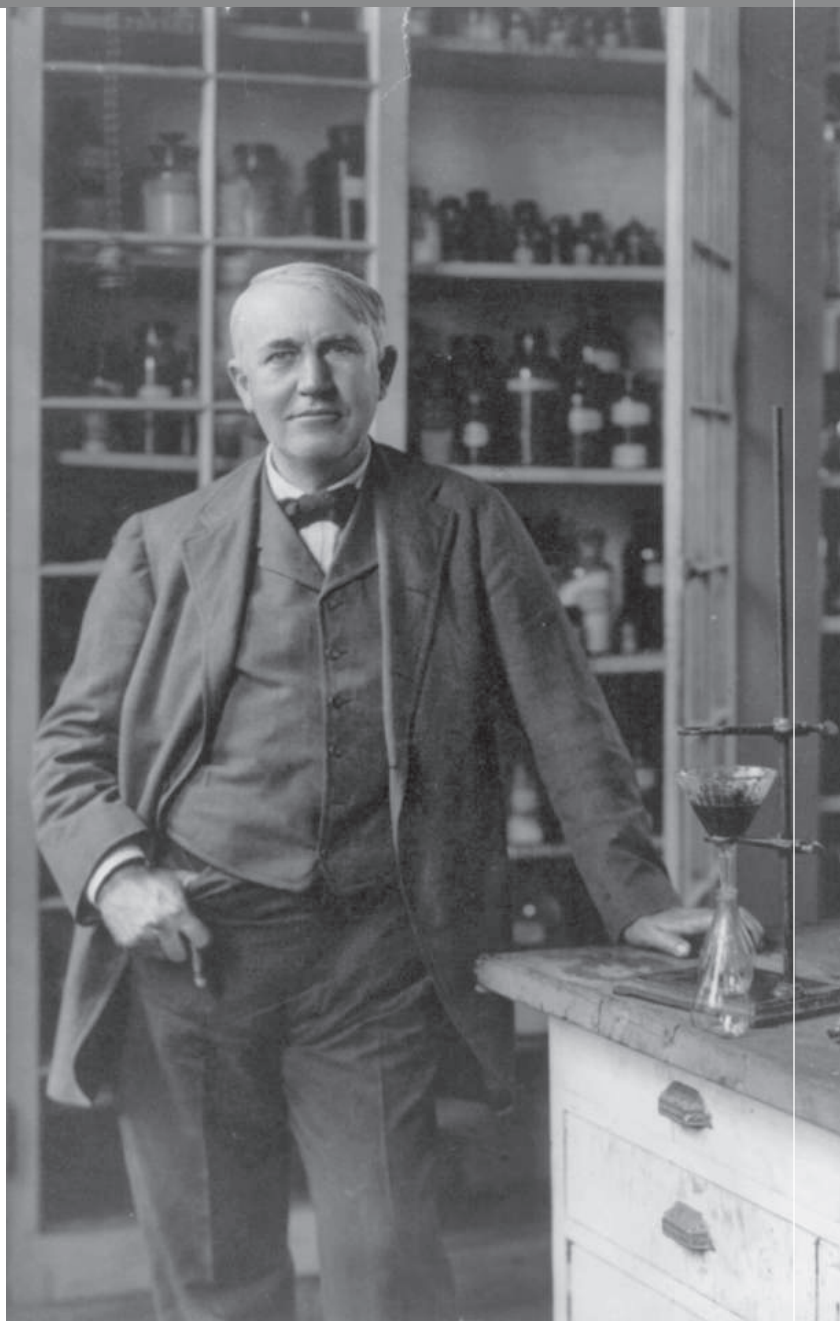
# WHAT DO YOU AND THOMAS EDISON HAVE IN COMMON?

## AAAS.

By investing in AAAS you join Thomas Edison and the many distinguished individuals whose vision led to the creation of AAAS and our world-renowned journal, *Science*, more than 150 years ago.

Like Edison, you can create a legacy that will last well into the future through planned giving to AAAS. By making AAAS a beneficiary of your will, trust, retirement plan, or life insurance policy, you make a strong investment in our ability to advance science in the service of society for years to come.

To discuss your legacy planning, contact Juli Staiano, Chief Philanthropy Officer, at (202) 326-6636, or [jstaiano@aaas.org](mailto:jstaiano@aaas.org), or visit [aaas.org/1848society](http://aaas.org/1848society) for more information.



"I feel great knowing that I will leave behind a legacy that will be channeled through the AAAS. It also means a lot to me to be able to honor my late parents, too."

—PETER ECKEL  
Member, 1848 Society and AAAS Member since 1988



## Chengdu Tianfu Life Science Park: Building a world-class life sciences hub

**C**hengdu, the capital of China's Sichuan Province and a national central city, is one of the fastest growing and most promising cities in China. It is also a crucial high-tech industrial base as well as a trade and logistics center, enjoying its reputation as the heart of "The Land of Abundance," known in Chinese as "Tianfu"—a name long held by the Chengdu Plain.

As clearly defined, the Chengdu High-Tech Industrial Development Zone (CDHT) is the core area of bioindustry in Sichuan and Chengdu. It pools the traditional national Chinese medicine modern technology industry base together with Chengdu's national biological industrial base, national medicine export base, national high-tech industrialization base for biomedical materials and medical devices, and national demonstration base for transfer and transformation of key new drug development achievements.

CDHT furthers the buildup of an innovative ecological environment with the concept of the industrial ecological circle (involving circular resource loops), thus facilitating talent cultivation and innovation, and accelerating development and new competitive advantages. In addition, with the goal of developing biomedicine, biomedical engineering, biological services, and the new health economy, CDHT is focusing on six major areas: biotechnology drugs, new chemical medicine preparations, high-performance medical devices, modern traditional Chinese medicine, smart health and precision medicine, and professional outsourcing services. In recent years, CDHT has witnessed the rapid growth of over 20 % of the biomedical industry. Chengdu High-Tech Zone ranks sixth in the comprehensive competitiveness of national biomedical industrial parks.

### Better together: Creating collaborations

As a specialized biomedical industrial park, the Tianfu Life Science Park (TLSP) was officially launched in 2010 with a total construction area of 220,000 m<sup>2</sup>. It serves as one of China's most vital biomedical R&D innovation and industrial incubation centers, and is ideally located in CDHT, the gateway for the life science and technology industry in western China, an important base for international medicine and medical institutions to cooperate with

R&D institutions there, and a platform for domestic industry–university–research cooperation.

TLSP mainly provides innovative and entrepreneurial incubation services for overseas returnees engaged in biomedical R&D, leading figures in the biomedical industry, outstanding researchers in universities and research institutes, excellent small and medium-sized biomedical technology companies at home and abroad, contract research organizations (CROs), and others who can contribute to the rapid growth of cutting-edge enterprises.

TLSP attaches great importance to collaborative innovation between industry, university, and research institutes, with a total of 27 participating institutions, laboratories, and professional platforms; 134 results in patents, publications, and clinical drug trials obtained through industry–university–research cooperation; and nine awards (titles) in industry–university–research cooperation. TLSP has proposed several development plans that involve increased physical space, talent introduction, project introduction, enterprise gathering, capital accumulation, and collaboration between business, academia, and research institutions. Through TLSP's "park + hospital," "park + research institutions," and other collaborative modes, it has made great progress in introducing innovative talent, driving transformative results, and optimizing resource allocation. TLSP also aims to propel the evolution of the biomedical industry from the traditional industry–university–research cooperation model to the more dynamic, integrated model of government–industry–university–research–application, thus building the biomedical industry ecosystem and accelerating the healthy, rapid growth of business in a multilevel, multichannel way. As an entrepreneurial hub for global bioenterprises, TLSP has gradually grown into a national first-class science and technology park integrating R&D and innovation of medicine and related disciplines, industrial value-added services, and business-supporting facilities. It also represents the comprehensive integration of medical technology, capital, management, talent, and policy.

The Phase II project of TLSP, the Biomedical Innovation Incubation Park, has a total construction area of approximately 290,000 m<sup>2</sup>. It is positioned in Xinchuan Innovation Science Park (jointly built by Singapore and Sichuan) as

a new core area and strategic source for the innovation and development of cutting-edge medicine in Chengdu, and will endeavor to become a world-class landmark park for the new health economy, concentrating on the new business model incorporating cross-border integration of smart health, precision medicine, and cosmetic medicine. It was begun in late 2018 when some institutions cooperated with Sichuan University to build a cutting-edge medical center like the Chengdu Advanced Medical Sciences Center in the city.

## Technology-driven: Focusing on innovation

Moreover, the Chengdu Advanced Medical Sciences Center (AMSC) keeps its focus on the latest basic medical research and clinical innovation driven by burgeoning technologies such as big data, artificial intelligence (AI), the Internet of Things, genomics, and more. With translational medicine as its innovation target and market application as its value orientation, the center has built a "community of shared interests, innovation, and development" to form a new model of business partners for school-site cooperation, in order to realize the integration and enhancement of innovation capabilities and the in situ metamorphosis of scientific and technological achievements.

So far, Chengdu Advanced Medical Sciences Center has initially introduced eight high-level R&D platform projects, including the Frontier Science Center for Disease-Related Molecular Network, the Medical Big Data Center, the Frontier Innovation Translational Platform for Dental Medicine Plus, the Leading Research Center for Stress Medicine, and the West China Rare Disease Research Institute. These platforms will drive the development of AMSC and help TLSP and phase II industry. It is home to 10 new drug R&D projects initiated by professors from Sichuan University, such as Biotech Solution and Discovery Co., Ltd., and 10 interactive cooperation projects, such as the collaboration between PerkinElmer and Farsoon Turing Additive Manufacturing Technology Co., Ltd. It has also introduced two top scientists at the academician level, 20 scientists recognized by the National Science Fund for Distinguished Young Scholars Program and the Changjiang Scholars Program, and over 100 professors and researchers. Thanks to the professional carrier space provided by the Chinese government and the high-level research centers and innovation teams introduced from Sichuan University, TLSP has successfully implemented the sequence of "innovation and R&D, incubation of results, and implementation of industrialization."

AMSC, as the innovation center of university and local government cooperation, integrates global high-quality resources through cooperation of government, industry, university, research, and application; realizes the transformation of technological achievements; and finally, radiates Chengdu and even Sichuan, which will help it become globally competitive in the future.

## Who we are

Welcome to TLSP. Centering on the needs of businesses, our service team commits itself to establishing a public technology service platform for innovative drug R&D, building the Information Center of Tianfu Life Science Park, attracting talent, organizing various industrial exchange meetings and medical lectures, and assisting enterprises to apply for awards. Through these comprehensive activities, it is wedded to facilitating the development of business and biomedical industry.

Sponsored by



Produced by the Science/AAAS  
Custom Publishing Office



## Company profiles



**Geneus Technologies, Ltd.**, founded in 2017, is a private company focusing on developing nanopore-based gene (DNA/RNA) sequencing devices and solutions. The key technologies include disruptive single-molecule sequencing chemistry, highly accurate and supersensitive current detecting circuits, large-scale integration of microelectromechanical systems-integrated circuits (MEMS-IC) chips, supercapacitor electrode, deep learning, etc.



**MaxHealth Biotech, LLC**, focuses on development and commercialization of safe and effective vaccines to serve global public health. By employing its cutting-edge technologies of antigen engineering and novel adjuvant formulations, MaxHealth has built a rich pipeline of prophylactic and therapeutic vaccines against major infectious diseases, allergies, and cancers; two lead candidates are expected to enter clinical development in 2020.



**Chengdu FANXI Biopharma Co., Ltd.**, is a newly founded biomed company engaged in developing first-in-class or best-in-class innovative medicines, with an emphasis on the areas of oncology, viruses, and liver disease.



**Cunde Therapeutics Co., Ltd.**, is an innovative biotechnology company specializing in manufacturing therapeutically valuable immune cells, and dedicated to developing cutting-edge cell-based therapies to combat medical conditions such as cancer and liver cirrhosis.



**Xiling Lab Co., Ltd.**, a Chengdu-based biopharmaceutical company, was founded by Drs. Jinkun Huang and Dejian Xie in August 2016. The company has built a unique technology platform by utilizing modern homogeneous, heterogeneous, and biocatalysis technologies for the production of pharmaceutical intermediates, drug substances, and related specialty chemicals.



**Farsoon Turing Additive Manufacturing Technology Co., Ltd.**, is a high-tech enterprise focusing on overall solutions for medical 3D printing. The company was founded in 2018, and is located in the Advanced Medical Sciences Center of the Biomedical Innovation Incubation Park in the Chengdu High-Tech Zone.



CALL FOR PAPERS



# BioDesign Research

 OPEN ACCESS

*BioDesign Research* is a Science Partner Journal published in affiliation with **Nanjing Agricultural University (NAU)** and distributed by the **American Association for the Advancement of Science (AAAS)**. *BioDesign Research* publishes high quality breakthrough research, reviews, editorials, and perspectives focusing on in silico biosystems design, genetic or epigenetic modifications, and genome writing or rewriting in any organism.

**Submit your research to *BioDesign Research* today!**

Learn more at [spj.sciencemag.org/bdr](http://spj.sciencemag.org/bdr)

The Science Partner Journals (SPJ) program was established by the American Association for the Advancement of Science (AAAS), the non-profit publisher of the *Science* family of journals. The SPJ program features high quality, online-only, editorially independent open-access publications produced in collaboration with international research institutions, foundations, funders and societies. Through these collaborations, AAAS expands its efforts to communicate science broadly and for the benefit of all people by providing a top-tier international research organization with the technology, visibility, and publishing expertise that AAAS is uniquely positioned to offer as the world's largest general science membership society.

Learn more at [spj.sciencemag.org](http://spj.sciencemag.org)



@SPJournals



@SPJournals

ARTICLE PROCESSING CHARGES WAIVED UNTIL 2022



### Western Blot Processor

Scientists seeking reproducible Western blot assays can do so reliably using BlotCycler Mini, a hands-free Western blot processing system. By automating the blocking, primary and secondary antibody binding, and washing steps, the system consistently delivers a strong signal with low

background. Users simply add reagents and antibody to the tanks and place their blots in the trays. BlotCycler Mini is equipped with two trays and can process from one to eight blots with two different primary and secondary antibodies simultaneously. Blocking time (from 10 min to 120 h), washing steps, addition of antibodies, and incubation time are programmable using the system's touchscreen. BlotCycler Mini works with new and established protocols, uses standard reagents, requires about 17.25 in x 10.25 in of bench space, and works with standard electrical power.

#### Precision Biosystems

For info: 888-490-4443  
[www.blotcycler.com](http://www.blotcycler.com)

### Heater/Shaker

The Teleshake 95 heater/shaker module is now available for use with the BRAND Liquid Handling Station pipetting robots. The heater/shaker module can be heated up to 90°C depending on the labware material. It can also be used to shake samples with rotation speeds from 100 rpm to 1,900 rpm. The heater and shaker is compatible with microplates; PCR plates, strips, and tubes; and some low-profile reservoirs and polypropylene plates. Adapter plates are available for different consumables.

#### BrandTech Scientific

For info: 888-522-2726  
[www.brandtech.com/product/new-teleshake-95](http://www.brandtech.com/product/new-teleshake-95)

### Cell Labeling Kits

Spend more time on your science and less time making cell lines with System Biosciences' (SBI's) Lenti-Labeler Lentivector Constructs. These constructs are available with a range of reporters (GFP, RFP, BFP, luciferase), selection markers (puro, blast), and promoters (CMV, EF1 $\alpha$ ). Perfect for cell tracking, high-throughput assays, and more, SBI's Lenti-Labeler Constructs are a reliable way to generate fluorescent- and luciferase-labeled cell lines. Available as either fully propagatable, sequence-verified plasmid DNA or ready-to-transduce prepackaged lentivirus, all Lenti-Labeler constructs are designed for reliability, so you can get to valuable insights faster.

#### System Biosciences

For info: 888-266-5066  
[systembio.com/lenti-labeler-constructs](http://systembio.com/lenti-labeler-constructs)

### RNA-Seq Library Prep Kit

Zymo Research introduces its total RNA-Seq library prep kit, which allows users to go from sample to sequencer in a single day. This probe-free technology makes RiboFree total RNA libraries from any organism in as little as 3.5 h. It also depletes ribosomal RNA (rRNA)

and globin from any RNA source. Zymo-Seq RiboFree Total RNA Library Kit minimizes the number of reagents and steps needed to generate stranded, rRNA-depleted total RNA-Seq libraries.

#### Zymo Research

For info: 888-882-9682  
[www.zymoresearch.com/pages/total-rna-seq-library-prep](http://www.zymoresearch.com/pages/total-rna-seq-library-prep)

### Artificial Intelligence for Chemistry Projects

Augmented Chemistry software and services from Optibrium bring groundbreaking artificial intelligence technologies that continuously learn from all available data to supplement your experience and skills. We are delighted to announce the first component of the Augmented Chemistry platform, a unique deep-learning capability called Alchemite that has already been demonstrated to provide more accurate, more confident results than conventional predictive models. Developed in an exclusive partnership with Intellegens, Alchemite deep learning brings unparalleled modeling capabilities that learn simultaneously across all experimental endpoints in your project or corporate database, even based on limited data. Confidently identify your most valuable compounds and the most important experiments to perform. Fill in the gaps in your database with confident results to target high-quality compounds. Run virtual screens to find new starting points for your projects.

#### Optibrium

For info: 978-234-4329  
[www.optibrium.com/augmentedchemistry](http://www.optibrium.com/augmentedchemistry)

### Matrix for Organoid Culture

Corning's new Matrigel matrix for organoid culture is a ready-to-use solution formulated to support organoid growth and differentiation. Each lot is measured for its elastic modulus, which is indicative of matrix stiffness. Additionally, each lot is qualified to form stable 3D dome structures commonly used in organoid culture. The matrix has been demonstrated to successfully grow mouse and human organoids from both healthy and diseased cell origins. It reduces the need for time-consuming screening, while providing the reproducibility and consistency essential for organoid research.

#### Corning

For info: 800-492-1110  
[www.corning.com](http://www.corning.com)

### Liquid Handling Pipette Tip Filters

Porvair Sciences introduces a range of Liquid Handling Pipette Tip Filters that block out aerosol and liquid contaminants. Using its proprietary Vyon porous plastics, the new pipette tip filters are fully compliant with U.S. FDA, U.S. Pharmacopeia Class VI, and European Pharmacopoeia statutory regulations as well as being free from heavy metals. Manufacturing to tight tolerances with an excellent edge finish ensures that these filters always provide an optimum fit into pipette tips, enabling labs to routinely achieve superior liquid handling and dispensing.

#### Porvair Sciences

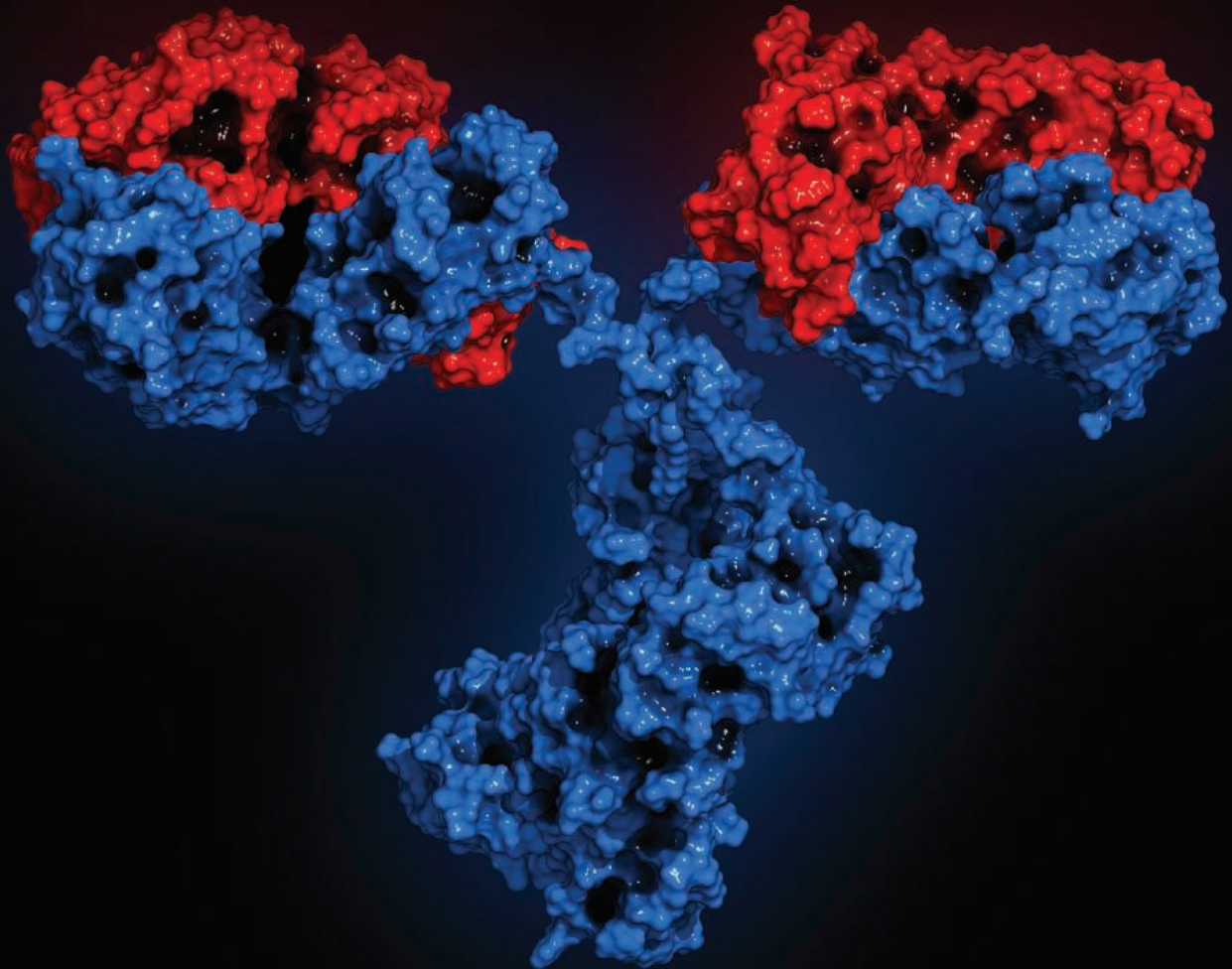
For info: +44-(0)-1978-661144  
[www.vyonporousplastics.com/pipette-tip-filters](http://www.vyonporousplastics.com/pipette-tip-filters)

Electronically submit your new product description or product literature information! Go to [www.sciencemag.org/about/new-products-section](http://www.sciencemag.org/about/new-products-section) for more information.

Newly offered instrumentation, apparatus, and laboratory materials of interest to researchers in all disciplines in academic, industrial, and governmental organizations are featured in this space. Emphasis is given to purpose, chief characteristics, and availability of products and materials. Endorsement by *Science* or AAAS of any products or materials mentioned is not implied. Additional information may be obtained from the manufacturer or supplier.

# Antibodies Recognize Antigens...

How will you get **recognized** for your immunology research?



*Science Immunology* publishes original, peer-reviewed, science-based research articles that report critical advances in all areas of immunological research, including important new tools and techniques.

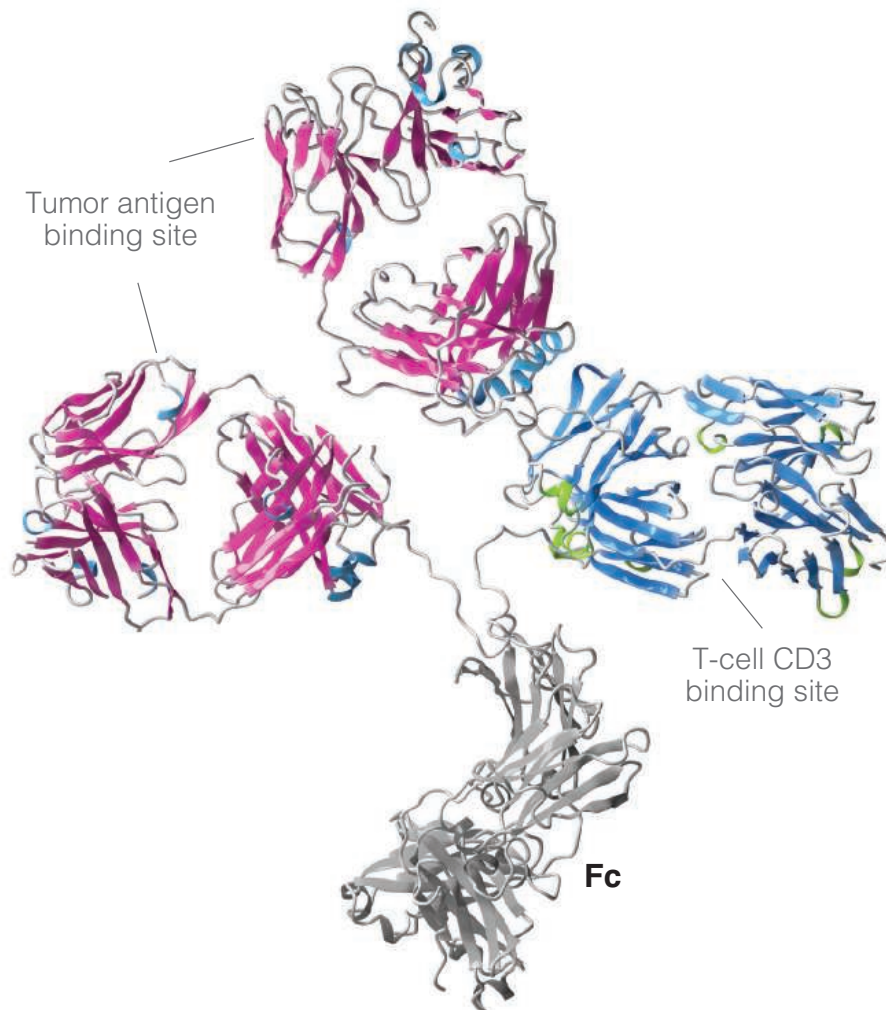
Submit your research today. Learn more at: [ScienceImmunology.org](https://www.scienceimmunology.org)

Science  
Immunology  
AAAS



# Bispecific Antibody Generation

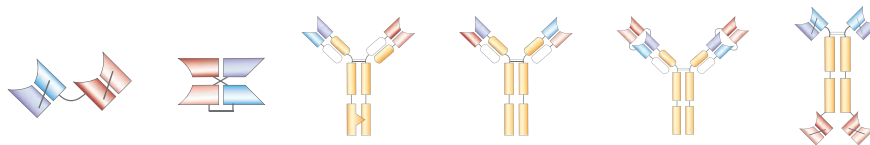
Custom Antibody Engineering Services



With nearly 20 years of experience, ProMab can help streamline your antibody project from start to finish

## Custom Antibody Solutions

- Hybridoma Sequencing
- Antibody Humanization
- Antibody Producing Stable Cell Line
- Rabbit Monoclonal Antibody
- Human Monoclonal Antibody
- Mouse / Rat Monoclonal Antibody



Discover more | [www.promab.com](http://www.promab.com)



2600 Hilltop Dr, Building B, Suite C320, Richmond, CA 94806

1.866.339.0871 | [info@promab.com](mailto:info@promab.com)

# HIGH-LEVEL GLOBAL TALENTS RECRUITMENT

*Welcome back to hometown.*

*Thousands of academic job vacancies are in fast-developing China.*

## On-the-spot Recruitment in UK

Dec. 10, 2019 Imperial College London

Dec. 11, 2019 Queen Mary University of London

## On-the-spot Recruitment in France

Dec. 14, 2019 Pierre and Marie Curie University

Dec. 15, 2019 Université Paris-Sud

## Participating Universities

Jiangsu Normal University

Xuzhou Medical University

Shanghai Institute of Technology

The First Affiliated Hospital of Jinan University

Northeastern University

Shanghai University of Electric Power



Scan the QR code to apply  
for UK&France Job Fair

## Online Job Fair

Dec. 21, 2019(GTM+8) [www.edu.cn/cv](http://www.edu.cn/cv)

## Participating Universities

Shanghai University of Political Science and Law, China Three Gorges University

Shanghai International Studies University, Hubei University of Technology

Xi'an Technological University, Northeastern University

Inner Mongolia University of Technology, Wuhan Polytechnic University

Inner Mongolia University of Finance and Economics, Inner Mongolia University

Hunan University of Technology and Business, Nanchang University



Scan the QR code to  
apply for Online Job Fair

## Qualification for Applicants

Overseas scholars, Doctor and Post-doctor

## Participating Approach

Please send your CV to [consultant@acabridge.edu.cn](mailto:consultant@acabridge.edu.cn) for  
on-the-spot Recruitment in UK and France and Online Job Fair.

**Job Vacancies in China's Universities and Institutes**

Please visit <https://www.acabridge.edu.cn/>

Contact [consultant@acabridge.edu.cn](mailto:consultant@acabridge.edu.cn)



乡愁，  
是那一汪大海，  
我在这头，  
家人在那头。

千万个  
不回的理由，  
难抵  
一个归根的念头。

Nostalgia,  
is like an ocean,  
I am here,  
the family is over there.

Thousands of reasons  
to stay abroad,  
but one decision to  
return to the roots.

## Overseas Chinese Scholars' Visit to Top Chinese Universities

Check the Details from [www.edu.cn/zgx](http://www.edu.cn/zgx)

- 10,000+ academic job vacancies in China
- Free one-to-one consultation service

Send your CV to [consultant@acabridge.edu.cn](mailto:consultant@acabridge.edu.cn)



上海外国语大学  
SHANGHAI INTERNATIONAL STUDIES UNIVERSITY



贵州医科大学  
GUIZHOU MEDICAL UNIVERSITY



南京工业大学  
NANJING TECH  
UNIVERSITY



天津师范大学  
Tianjin Normal University



青岛大学



山东第一医科大学 (山东省医学科学院)  
Shandong First Medical University & Shandong Academy of Medical Sciences





## Air Force Science & Technology Fellowship Programs Postdoctoral and Senior Research Awards

The National Academies of Sciences, Engineering, and Medicine administers postdoctoral and senior research awards at the U.S. Air Force Research Laboratory (AFRL), the U.S. Air Force Institute of Technology (AFIT), and the U.S. Air Force Academy (USAF) under the Air Force Science & Technology Fellowship Program (AF STFP).

We are actively seeking highly qualified candidates including recent doctoral recipients and senior researchers. Applicants must be U.S. citizens and should hold, or anticipate receiving, an earned doctorate in science or engineering. Awards are contingent upon completion of the doctoral degree.

### Application deadline dates (four annual review cycles):

- February 1
- May 1
- August 1
- November 1

### Awardee opportunities:

- Conduct independent research in an area compatible with the interests of the Air Force laboratories
- Devote full-time effort to research and publication
- Access the excellent and often unique Air Force research facilities
- Collaborate with leading scientists and engineers

### Awardee benefits:

- Base stipend starting at \$76,542; may be higher based on experience
- Health insurance (including dental and vision), relocation benefits, and professional travel allowance

Applicants should contact prospective AFRL, AFIT, and USAFA Research Adviser(s) at the lab(s) prior to the application deadline to discuss their research interests and funding opportunities.

For detailed information, visit [www.nas.edu/afstfp](http://www.nas.edu/afstfp) or e-mail [afstfp@nas.edu](mailto:afstfp@nas.edu).

*The National Academies of*  
**SCIENCES • ENGINEERING • MEDICINE**

## NRC Research Associateship Programs

The National Academy of Sciences, Engineering, and Medicine administers postdoctoral and senior research awards at participating federal laboratories and affiliated institutions at locations throughout the U.S. and abroad. All research opportunities are open to U.S. citizens; some are open to U.S. permanent residents and foreign nationals. We are actively seeking highly qualified candidates including recent doctoral recipients and senior researchers. Applicants should hold, or anticipate receiving, an earned doctorate in science or engineering. Awards are contingent upon completion of the doctoral degree. A limited number of opportunities in select fields are also available for graduate students. Degrees from universities abroad should be equivalent in training and research experience to a degree from a U.S. institution.

### Application deadline dates (four annual review cycles):

- February 1
- May 1
- August 1
- November 1

### Awardee opportunities:

- Conduct independent research in an area compatible with the interests of the sponsoring laboratory
- Devote full-time effort to research and publication
- Access the excellent and often unique facilities of the federal research enterprise
- Collaborate with leading scientists and engineers at the sponsoring laboratories

### Awardee benefits:

- One-year award, renewable for up to three years
- Stipend ranging from \$45,000 to \$83,000; may be higher based on experience
- Health insurance (including dental and vision), relocation benefits, and professional travel allowance

Applicants should contact prospective Research Adviser(s) at the lab(s) prior to the application deadline to discuss their research interests and funding opportunities.

For detailed information, visit [www.nas.edu/rap](http://www.nas.edu/rap) or e-mail [rap@nas.edu](mailto:rap@nas.edu).

*The National Academies of*  
**SCIENCES • ENGINEERING • MEDICINE**



## Who's the Top Employer for 2019?

Science Careers' annual survey reveals the top companies in biotech & pharma voted on by *Science* readers.

Read the article and employer profiles and listen to podcasts at [sciencecareers.org/topemployers](http://sciencecareers.org/topemployers)

The Yale Institute for Biospheric Studies (YIBS) was established in 1990 through a generous bequest from Yale alumnus Edward P. Bass. YIBS is an umbrella environmental science organization that supports the environmental community at Yale University through research and training, grants and fellowships, and weekly seminars and events ([yibs.yale.edu](http://yibs.yale.edu)). The newly established Hutchinson Environmental Program, named in honor of G. Evelyn Hutchinson, the father of modern ecology, is intended to support the environmental priorities identified in Yale's strategy to advance the sciences.

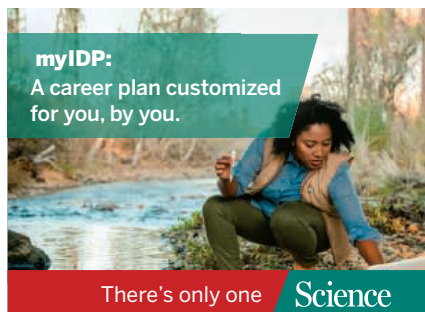
We seek to attract as many as 10 Hutchinson Environmental Postdoctoral Fellows in the summer and fall of 2020. Cohorts of postdoctoral fellows, representing multiple disciplines, will be centered around the two broad themes outlined below: Environment and Evolution, and Climate and Greenhouse Gases. The Hutchinson Fellows will share space in the Osborn Memorial Laboratories on Yale's Science Hill. Postdoc cohorts will engage in research and synthesis activities with a network of Yale faculty mentors spanning multiple schools and departments. Priority will be given to applicants whose research incorporates data-driven synthesis, modeling, and/or conceptual unification of knowledge as a means to address these core themes. These are two-year postdoctoral fellowships (contingent on success in year one) with a starting salary of \$62,000, plus \$10,000 for research and travel. Funds will also be available to support cohort projects, symposia, workshops, and training in science communication.

**THEME I Environment and Evolution.** Human-accelerated environmental changes are affecting the flux of energy and nutrients in ecosystems, in many cases by altering the structure and function of species interactions. We are seeking candidates whose research addresses how species interactions are reshaped by ecological and evolutionary responses to environmental change and/or how this reshaping determines processes and patterns at larger scales. Successful applicants will work in a highly collaborative environment around themes including, but not limited to: (1) eco-evolutionary dynamics in ecosystems driven by human-accelerated change; (2) the genomic basis of evolving species interactions; and (3) contemporary effects of environmental change from a paleoecological perspective. *Faculty lead for Theme I: David Vasseur, Department of Ecology & Evolutionary Biology. Other relevant faculty are affiliated with the Yale School of Forestry & Environmental Studies, and the Departments of Geology & Geophysics and Anthropology. See [yibs.yale.edu/hutchinson-fellowship](http://yibs.yale.edu/hutchinson-fellowship) for additional details and affiliated faculty.*

**THEME II Climate and Greenhouse Gases.** Atmospheric levels of CO<sub>2</sub>, CH<sub>4</sub> and N<sub>2</sub>O are increasing, leading to planetary warming. We are seeking candidates whose research can contribute to our general understanding of the generation and management of greenhouse gases (GHG). Because of growing interest in global methane among a group of Yale faculty, we are particularly interested in building a cohort of postdoctoral fellows who can advance knowledge of the production and control of CH<sub>4</sub> losses from natural and human-managed systems. Successful applicants will work in a highly collaborative environment around themes including, but not limited to: (1) GHG fluxes from ecosystems and the energy sector; (2) microbial ecology and evolution relevant to GHGs; (3) GHG pathways in plants; (4) GHG dynamics in deep time; and (5) natural climate solutions. *Faculty lead for Theme II: Peter Raymond, Yale School of Forestry & Environmental Studies. Other relevant faculty are affiliated with the Departments of Geology & Geophysics, Ecology & Evolutionary Biology, Chemical & Environmental Engineering, and the Yale School of Management. See [yibs.yale.edu/hutchinson-fellowship](http://yibs.yale.edu/hutchinson-fellowship) for additional details and affiliated faculty.*

**APPLICATIONS.** Interested candidates should have, or will soon receive, a Ph.D. in a relevant discipline. Applications must be submitted by **Monday, January 13, 2020**. Submit a CV (with a complete bibliography), the names and email addresses of three references, and a research statement detailing potential connections to one (or both) of the themes described above; please also identify one or more potential Yale faculty mentors. Applications should be submitted to <http://apply.interfolio.com/71435>. Applicants will be notified of the results of the selection process by mid-February 2020.

Yale University considers applicants for employment without regard to, and does not discriminate on the basis of, an individual's sex, race, color, religion, age, disability, status as a veteran, or national or ethnic origin; nor does Yale discriminate on the basis of sexual orientation or gender identity or expression. Title IX of the Education Amendments of 1972 protects people from sex discrimination in educational programs and activities at institutions that receive federal financial assistance. Questions regarding Title IX may be referred to the University's Title IX Coordinator, at [TitleIX@yale.edu](mailto:TitleIX@yale.edu), or to the U.S. Department of Education, Office for Civil Rights, 8th Floor, Five Post Office Square, Boston MA 02109-3921. Telephone: 617.289.0111, Fax: 617.289.0150, TDD: 800.877.8339, or Email: [ocr.boston@ed.gov](mailto:ocr.boston@ed.gov).



**myIDP:**  
A career plan customized  
for you, by you.

There's only one **Science**

**Features in myIDP include:**

- Exercises to help you examine your skills, interests, and values.
- A list of 20 scientific career paths with a prediction of which ones best fit your skills and interests.



Visit the website and start planning today!

[myIDP.sciencecareers.org](http://myIDP.sciencecareers.org)

**Science  
Careers**  
MAAS

In partnership with:



**CASE WESTERN RESERVE  
UNIVERSITY** EST. 1826

**TENURE TRACK/TENURED FACULTY POSITION IN CANCER RESEARCH**  
Case Western Reserve University School of Medicine  
**Case Comprehensive Cancer Center**

The Case Comprehensive Cancer Center (<https://case.edu/cancer/>), an NCI-designated Comprehensive Cancer Center at CWRU, with affiliates University Hospitals Cleveland Medical Center and Cleveland Clinic, invites applications for tenure track/tenured faculty positions at the level of Assistant, Associate, or Full Professor. Applicants are being sought that have basic/translational research expertise in one of the following areas of cancer focus: Tumor Immunology, Drug Discovery, Genomics, Brain Tumors, Adolescent and Young Adult, and Women's Cancers. Qualified individuals should have a PhD with established expertise in the specific cancer to be studied. Applicants for Assistant Professor must have a track record of outstanding cancer research and publications and potential for extramural funding. Candidates applying for consideration at a senior rank must possess national (Associate Professor) or international (Professor) reputations in collaborative cancer research, a distinguished record of publication and funding, a commitment to mentoring, teaching, and leadership, and they must fulfill other qualifications necessary for a tenured appointment at CWRU.

Successful candidates will be expected to interact closely with members of established basic and translational cancer center research programs. Primary appointment will be in the CWRU School of Medicine department of expertise or in the Cancer Center.

Please send curriculum vitae and a cover letter outlining your research interests, and experience in mentoring electronically to: Stanton L. Gerson, MD, Director, Case Comprehensive Cancer Center, c/o [cancersearch@case.edu](mailto:cancersearch@case.edu). After initial review, you will be asked for a list of three or more references. Please include "Cancer Faculty Search" in the subject line.

*In employment, as in education, Case Western Reserve University is committed to Equal Opportunity and Diversity. Women, veterans, members of underrepresented minority groups, and individuals with disabilities are encouraged to apply.*

*Case Western Reserve University provides reasonable accommodations to applicants with disabilities. Applicants requiring a reasonable accommodation for any part of the application and hiring process should contact the Office of Inclusion, Diversity and Equal Opportunity at 216-368-8877 to request a reasonable accommodation. Determinations as to granting reasonable accommodations for any applicant will be made on a case-by-case basis.*

By Barbara Gastel

# Giving thanks in China

**G**olden autumn. The best time of year in Beijing. I'd just flown in from the United States to start a position teaching scientific writing in English. I hadn't been to China before, much less taught there, so I didn't know what to expect. "Will I be able to establish rapport with my students?" I wondered. "Will we communicate adequately?" At the start of my first class, I looked around at my students: 17 scientists. The year was 1983, and some wore jackets that resembled the type popularized by the late Chinese leader Mao Zedong. The students gave me hesitant but welcoming smiles, and I proceeded to tell them that my main goal was to help them publish internationally. I hoped this venture would work out for them—and me.

My path to China began the previous autumn. I was an assistant professor at the time, teaching science writing in the United States. One evening, I returned to my apartment and saw the light flashing on my answering machine. The message was from the head of a U.S. institute devoted to furthering academic exchange with China. He suggested that I apply for a position teaching scientific writing at a medical college in Beijing.

I had dreamed of international work ever since I'd received my medical and public health degrees and embarked on a science communication career 4 years earlier. Yet I hesitated about applying for the opportunity in Beijing. I felt unsure about spending a school year in then-isolated China and putting my tenure-track position at risk. I also worried about venturing so far from my parents, one of whom had been seriously ill.

My parents, however, encouraged me to explore the opportunity. My program director offered me a leave of absence. And there was a good omen: Months before I ever thought of moving to China, my New Year's resolution—one of the few I've kept—had been to master chopsticks.

So I found myself in Beijing. Most of my students were female faculty members approaching my parents' age. They made a point of taking care of me outside the classroom—inviting me to make dumplings, showing me where to shop, and taking me to Chinese operas—and I immersed myself in my host culture. In return, I enjoyed sharing bits of U.S. culture with my students. In November, I told them about U.S. Thanksgiving and the traditional dishes, such as sweet potatoes and turkey. Within a week, the students proposed having a potluck Thanksgiving dinner. They would provide the main courses; I would bring dessert.



**"I hope younger colleagues will take chances on unexpected opportunities."**

When I reached the potluck, sweet potatoes and Chinese favorites awaited. But the main dish had not arrived. Eventually, one student brought a package—and an apology. Turkeys were hard to get, he said, so he hoped we wouldn't mind Peking duck. We went on to eat a delicious meal, complete with the best Thanksgiving bird I've tasted yet. The potluck gave us a chance to meld cultures and build bonds—some of which endure to this day—and in that moment I knew I had much to be thankful for.

My first year in China proved so rewarding that I gave up my U.S. faculty position to work there for one more year. Fortunately, I was able to land a faculty job after I returned to the United States, and I've now been tenured for more than 25 years.

I look back fondly on my time in Beijing. I've been proud to see class members publish internationally and to see one elected to the Chinese Academy of Sciences. Some have shared what I taught them with their own students.

The experience showed me that I greatly enjoy exploring other cultures and helping nonnative speakers communicate science in English. I've pursued those interests ever since. I've given workshops in many countries, and each year I welcome international researchers to my university to take an intensive writing course, treasuring the chance to establish bonds with scientists from other countries.

I hope younger colleagues will take chances on unexpected opportunities. The bird that appears might exceed all expectations. ■

Barbara Gastel is a professor at Texas A&M University in College Station. Send your career story to [SciCareerEditor@aaas.org](mailto:SciCareerEditor@aaas.org).